SCHOLARLY PUBLICATIONS

A CURRENT AWARENESS BULLETIN
OF RESEARCH OUTPUT

@DTU

(42nd Edition)

JUNE 2016

BY: CENTRAL LIBRARY

DELHI TECHNOLOGICAL UNIVERSITY
(FORMERLY *DELHI COLLEGE OF ENGINEERING)*
GOVT. OF N.C.T. OF DELHI
SHAHBAD DAULATPUR, MAIN BAWANA ROAD
DELHI 110042

PREFACE

This is the **Forty two** Issue of Current Awareness Bulletin started by Delhi Technological University, Central Library. The aim of the bulletin is to compile, preserve and disseminate information published by the faculty, students and alumni for mutual benefits. The bulletin also aims to propagate the intellectual contribution of Delhi Technological University (DTU) as a whole to the academia.

The bulletin contains information resources available in the internet in the form of articles, reports, presentations published in international journals, websites, etc. by the faculty and students of DTU. The publications of faculty and student which are not covered in this bulletin may be because of the reason that the full text either was not accessible or could not be searched by the search engine used by the library for this purpose.

The learned faculty and students are requested to provide their uncovered publications to the library either through email or in CD, etc to make the bulletin more comprehensive.

This issue contains the information published during **June 2016**. The arrangement of the contents is alphabetical. The full text of the article which is either subscribed by the university or available in the web is provided in this bulletin.

Central Library

CONTENTS

1. A critical review on production of biodiesel from various feedstocks Deepak Verma, Janmit Raj***, 3.Amit Pal***, Manish Jain, Mechanical Engineering, DTU

2. A New and Robust Segmentation Technique Based on Pixel Gradient and Nearest Neighbors for Efficient Classification of MRI Images ***3.Sanchit Kumar*** and ***3.Sahil Dalal,*** ECE, DTU

3. STUDY OF THE IMPLICATIONS OF PROFESSION ON INVESTMENT BEHAVIOR OF WOMEN ENGINEERS***, 6.Priya Kansal*** and ***3.Dr. Seema Singh***, Humanities, DTU

4. Channel Capacity of Different Adaptive Transmission Techniques over Log-Normal Shadowed Fading Environment, ***3. P. K. Verma*** ,***3.Priyanka Jain***, sanjay Soni and R.S Raw, ECE, DTU

5. Classification of EMG Signals using SVM-kNN, ***3. Preeti Meena*** and ***3.Malti Bansal***, ECE, DTU

6. Classification of Pseudo Random Numbers Using Support Vector Machine Classifier***, 3.Preeti Meena*** and ***3.Malti Bansal,*** ECE, DTU

7. Computational Studies of Synthetic and Plant-Derived Compounds against Cardiovascular Disease Targets N. Jauhari, S. Gupta, S. Saxena and ***3.N. Bharadvaja***, Biotechnology, DTU

8. Design and analysis of BFOA-optimized fuzzy PI/PID controller for AGC of multi-area traditional/restructured electrical power systems,Yogendra Arya· ***3.Narendra Kumar,*** Electrical Engineering, DTU

9. Effect of Different Carbon Sources and Elicitors on Shoot Multiplication in Accessions of Centella asiatica Koyel Kundu, Arpita Roy, Gaurav Saxena, Lakhan Kumar and ***3.Navneeta Bharadvaja*** Plant Biotechnology, DTU

10. Effect of Nose Radius On Surface Roughness During CNC Turning Using Response Surface Methodlogy, Devendra Singh, ***3.Vimanyu Chadha*** and ***3.Ranganath M Singari***, Mechanical, Production and Industrial Engineering, DTU

11. Eliciting Information Requirements for DW systems, ***6.Deepika Prakash*** , DTU

12. Excellent electromagnetic interference shielding effectiveness of chemically reduced graphitic oxide paper at 101 GHz, Parveen Saini, Sachin Kaushik, Rahul Sharma, Disha Chakravarty, ***3.Rishi Raj***, and Jyotirmay Sharma, DTU

13. First principles study of Li terminated armchair graphene nanoribbons, ***3.Neha Tyagi*****,** Neeraj K. Jaiswalb and Pankaj Srivastava, Applied Physics, DTU

14. Greenhouse Gas Emissions from Landfills: A Case of NCT of Delhi, India ***3.Singh SK***, ***3.Anunay G***, 3.***Rohit G, 3.Shivangi G*** and ***3.Vipul V***, Environmental Engineering, DTU

15. Human Activity Recognition based on Spatial Distribution of Gradients at Sub-levels of Average Energy Silhouette Images, ***3.Dinesh K Vishwakarma*** and Kuldeep Singh, Member, IEEE, ECE, DTU

16. Implementation of green supply chain management in India: Bottlenecks and remedies, ***6.Sheetal Soda***, Anish Sachdeva,and Rajiv Kumar Garg, M.E. in Production Engineering, DTU

17. In-situ electrosynthesized Nanostructured Mn3O4-Polyaniline Nanofibers-Biointerface for Endocrine Disrupting Chemical Detection, Nawab Singh Md.

Azahar Ali, Kali Suresh, Ved Varun Agrawal, Prabhakar Rai ,Ashutosh Sharma ***3.B.D. Malhotra***, Renu John, Biotechnology, DTU

18. Large-mode-area single-polarization single-mode photonic crystal fiber: design and analysis, ***3.AJEET KUMAR***, ***3.THAN SINGH SAINI***, ***3.KISHOR DINKAR NAIK***, AND RAVINDRA KUMAR SINHA, Advanced Photonics Simulation Research Laboratory, Applied Physics, DTU

19. Linking mitochondrial dysfunction, metabolic syndrome and stress signaling in Neurodegeneration, ***3.Saurabh Kumar Jha***,***3. Niraj Kumar Jha***, ***3.Dhiraj Kumar, 3.Rashmi K Ambasta*** and ***3.Pravir Kumar,*** Biotechnology, DTU

20. Microstructural and dielectric investigations of vanadium substituted barium titanate ceramics ***3.Aditya Jain***, ***3.Neelam Maikhuri***, ***3.Rakesh Saroha***, Mukul Pastor, A. K. Jha, and ***3.A. K. Panwar***, Applied Physics, DTU

21. Middle Node Optimization Aigorithm for Global Optimal Path Planning, ***3.Ananya Chandra, 3.Vibhu Jawa, 3.Ishan Mishra,*** and ***3.M. Sameer Khan***, DTU

22. Nanocarbon-based Electrochemical Detection of Heavy Metals, Shailendra Kumar Pandey**,** ***7.Priti Singh***, Jyoti Singh, Sadhana Sachan, Sameer Srivastava and Sunil Kumar Singh, DTU

23. Pilot based Channel Estimation and SCGNN based Equalization for MIMO-OFDM System, Zeeshan A. Abbasi and ***7.Zainul Abdin Jaffery***, Electrical Engineering, DTU

24. Question Answering over Knowledge Base using Factual Memory Networks, ***3.Sarthak Jain,*** Computer Engineering, DTU

25. Rear contact SiGe solar cell with SiC passivated front surface for >90-percent external quantum efficiency and improved power conversion efficiency, ***3.Rahul Pandey*** and ***3.*****Rishu Chaujar**, Engineering Physics**,** DTU

26. Role of interleukin-6 in cancer progression and therapeutic resistance, 3.**Neeraj Kumari**, *B. S. Dwarakanath,* ***3.*****Asmita Das** and *Anant Narayan Bhatt*, Biotechnology, DTU

27. Rural Empowerment in India through Small scale Power generation using Vegetable oil based Fuels ,**3.Rajiv Chaudhary**, P B Sharma, S. Maji, Naveen Kumar and R C Singh, Mechanical Engineering, DTU

28. Structural, dielectric and ferroelectric studies of Ba12xSrxTiO3 ceramics prepared by mechanochemical activation technique, ***3.Aditya Jain, 3.A. K. Panwar*** and A. K. Jha, Applied Physics, DTU

29. Supplementary Materials: Sympy: Symbolic Computing In Python Aaron Meurer, Christopher P. Smith, Mateusz Paprocki, Ondrej Certík, Matthew Rocklin, ***3.Amit Kumar***, Sergiu Ivanov, Jason K. Moore, Sartaj Singh, Thilina Rathnayake, Sean Vig, Brian E. Granger, Richard P. Muller , Francesco Bonazzi, Harsh Gupta,Shivam Vats, Fredrik Johansson, Fabian Pedregosa, Matthew J. Curry, Ashutosh Saboo, Isuru Fernando, Sumith, Robert Cimrman, And Anthony Scopatz, DTU

30. Sympy: Symbolic Computing In Python, Aaron Meurer, Christopher P. Smith, Mateusz Paprock, Ondrej Certík§, Matthew Rocklin, ***Amit Kumar***, Sergiu Ivanov, Jason K. Moore, Sartaj Singh, Thilina Rathnayake, Sean Vig ,***Brian E. Granger,*** Richard P. Muller, Francesco Bonazz, Harsh Gupta, Shivam Vats, Fredrik Johansson, Fabian Pedregosa, Matthew J. , Curry, Ashutosh Saboo, Isuru Fernando, Sumith Kulal, Robert , Cimrman1, And Anthony Scopat, DTU

31. Synthesis, characterization and fluorescence turn-on behavior of new porphyrin analogue: meta-benziporphodimethenes, ***3.Ravi Kumar Sharma***, ***3.Lale Kiran Gajanan, 3.Mohan Singh Mehata***, Firasat Hussain, ***3.Anil Kumar,***Applied physics and Chemistry, DTU

32. Tunable unidirectional scattering of ellipsoidal single nanoparticle, Reena, Yogita Kalra, Ajeet Kumar, and R. K. Sinha, Applied Physics DTU

1. Chancellor

2. Pro Vice Chancellor	***2.1. Ex Pro Vice Chancellor***
3. Faculty	***3.1. Ex Faculty***
4. Teaching-cum-Research Fellow	
5. Alumni	
6. Research Scholar	***6.1. Ex Research Scholar***
7. PG Scholar	***7.1. Ex PG Scholar***
8. Undergraduate Student	***8.1. Ex Undergraduate Student***

Journal of Scientific and Innovative Research 2016; 5(2): 51-58
Available online at: www.jsirjournal.com



Review Article

ISSN 2320-4818
JSIR 2016; 5(2): 51-58
© 2016, All rights reserved
Received: 26-03-2016
Accepted: 27-04-2016

Deepak Verma
Research Scholar, Department of Automobile Engineering, Rustam Ji Institute of Technology, Tekanpur, Gwalior (M. P.)- 475005, India

Janmit Raj
Assistant Professor, Department of Automobile Engineering, Rustam Ji Institute of Technology, Tekanpur, Gwalior (M. P.)- 475005, India

Amit Pal
Associate Professor, Department of Mechanical Engineering, Delhi Technological University, Bawana Road, Delhi- 110042, India

Manish Jain
Assistant Professor, Department of Automobile Engineering, Rustam Ji Institute of Technology, Tekanpur, Gwalior (M. P.)- 475005, India

Correspondence:
Deepak Verma
Research Scholar, Department of Automobile Engineering, Rustam Ji Institute of Technology, Tekanpur, Gwalior (M. P.)- 475005, India

A critical review on production of biodiesel from various feedstocks

Deepak Verma, Janmit Raj, Amit Pal, Manish Jain

Abstract

Biodiesel fuel produced by alcoholysis of edible, non-edible and waste cooking oil is viewed as a promising renewable fuel source. Diminishing petroleum reserves and increasing environmental regulations have made the search for renewable fuel. This paper focuses on review of a work carried out by researchers in the field of production of biodiesel from different types of oil. The raw oil used by researchers for production of biodiesel first briefly summarized followed by a description of biodiesel production method applied and yield percentage, FFA content, molar ratio and the reaction time of the biodiesel produced from the raw oil. The review is divided into three categories viz. production of biodiesel from edible oil, non-edible oil and waste cooking oil. This review paper contains the work of past researchers published between 2005 and 2015.

Keywords: Biodiesel, Transesterification, FFA Content, Reaction time.

INTRODUCTION

With the increasing use of diesel fuel, many initiatives have become more attractive to search for alternate fuels to supply or replace fossil fuels. Biodiesel is synthesized from edible, non-edible and waste cooking oil or animal oil can be regarded as an alternative diesel fuel. The various alternative fuel options tried in place of hydrocarbon oils are mainly biogas, producer gas, ethanol, methanol and vegetable oils. Out of all these, biodiesel offers an advantage because of their comparable fuel properties with that of diesel. The emissions produced from biodiesel are cleaner compared to petroleum-based diesel fuel. Particulate emissions, soot, and carbon monoxide are lower since biodiesel is an oxygenated fuel. The biodiesel could be used as pure fuel or as blend with petro diesel, which is stable in all ratio. Alternative new and renewable fuels have the potential to solve many of the current social problems and concerns, from air pollution and global warming to other environmental improvements and sustainability issues.

BRIEF DESCRIPTION OF BIODIESEL

Biodiesel is an alternative fuel made from renewable biological sources such as vegetable oils both (edible and non-edible oil) and animal fats According to the US standard specification for biodiesel (American Society for Testing and materials (ASTM) 6751), biodiesel is defined as a fuel comprised of mono alkyl esters of long chain fatty acids from vegetable oils or animal fats [1]. The dominant bio-diesel production process, namely transesterification, typically involves the reaction of an alkyl-alcohol with a long chain ester linkage in the presence of a catalyst to yield mono-alkyl esters (bio-diesel) and glycerol [2, 3].

Production of Biodiesel by Transesterification

Generally, biodiesel is produced by means of transesterification. Transesterification is the reaction of a lipid with an alcohol to form esters and a byproduct, glycerol. It is, in principle, the action of one alcohol displacing another from an ester, referred to as alcoholysis (cleavage by an alcohol). In Transesterification mechanism, the carbonyl carbon of the starting ester ($RCOOR^1$) undergoes nucleophilic attack by the incoming alkoxide (R^2O^-) to give a tetrahedral intermediate, which either reverts to the starting material, or proceeds to the transesterified product ($RCOOR^2$). Transesterification consists of a sequence of three consecutive reversible reactions. The first step is the conversion of triglycerides to diglycerides, followed by the conversion of diglycerides to monoglycerides, and finally

monoglycerides into glycerol, yielding one ester molecule from each glyceride at each step. The reaction is represented in equation 1. The reactions are reversible, although the equilibrium lies towards the production of fatty acid esters and glycerol. This reaction proceeds well in the presence of some homogeneous catalysts such as potassium hydroxide (KOH)/sodium hydroxide (NaOH). Depending on the undesirable compounds (especially FFA and water), each catalyst has its advantages and disadvantages. Sodium hydroxide is very well accepted and widely used because of its low cost and high product yield. The most common alcohols widely used are methyl alcohol and ethyl alcohol. Among these two, methanol found frequent application in the commercial uses because of its low cost.

$$\text{Triglycerides} + \text{ROH} \rightleftharpoons \text{Diglycerides} + R^1COOR$$

$$\text{Diglycerides} + \text{ROH} \rightleftharpoons \text{Monoglycerides} + R^2COOR$$

$$\text{Monoglycerides} + \text{ROH} \rightleftharpoons \text{Glycerol} + R^3COOR$$

Equation 1 Chemistry of transesterification

PREVIOUS RESEARCHES

Previous work done on production of biodiesel from edible oil.

Over the last few years, there has been increasing amounts of research and interest in the different edible feedstocks that can be used to make biodiesel and the effects of the different feedstocks on the quality of the biodiesel. Currently, biodiesel is produced from different crops such as, Jojoba oil, palm oil, soybean oil, canola, rice bran, sunflower, coconut, rapeseed, soybean and sunflower oil [4, 5, 6]. The major difference between various edible oils is the type of fatty acids attached in the triglyceride molecule. Fatty acid composition effects the yield percentage, reaction temperature, FFA content and molar ratio of the biodiesel oil [7].

Leung D.Y.C and Guo Y. [8], compared the transesterification reaction conditions for fresh canola oil and used frying oil. Higher molar ratio (7:1, methanol/used frying oil), higher temperature (60° C) and higher amount of catalyst (1.1 wt% NaOH) was maintained in used frying oil when compared to fresh canola oil where optimal conditions maintained were 315-318 K, 1.0 wt% NaOH and 6:1 methanol/oil molar ratio. However, less reaction time (20 min) was observed for used frying oil when compared to fresh canola oil reaction time (60 min). The Fig. 1 shows the effect of temperature on the transesterification of (a) neat Canola oil; and (b) UFO. In the further work Lingfeng Cui *et al.* [9] developed biodiesel from cottonseed oil by using KF/γ-Al2O3 as heterogeneous catalysts for the transesterification of cottonseed oil with methanol. The operation variables used were methanol/oil molar ratio (6:1–18:1), catalyst concentration (1–5 wt %), temperature (50–68 °C), and catalyst type. The biodiesel with the best properties was obtained using a methanol/oil molar ratio of 12:1, catalyst (4%), and 65°C temperature with the catalyst KF/γ- Al2O3. Later Sinha Shailendra *et al.* [4] determined the optimum condition for transesterification of rice bran oil with methanol and NaOH as catalyst by mechanical stirring method. The condition was found at 55° C reaction temperature, 1 h reaction time, 9:1 molar ratio of rice bran oil to methanol and 0.75% catalyst (w/w). Further, the physical properties of rice bran methyl ester were tested and compared with other biodiesels and diesel. The result showed that characteristics of rice bran methyl ester were comparable to diesel.

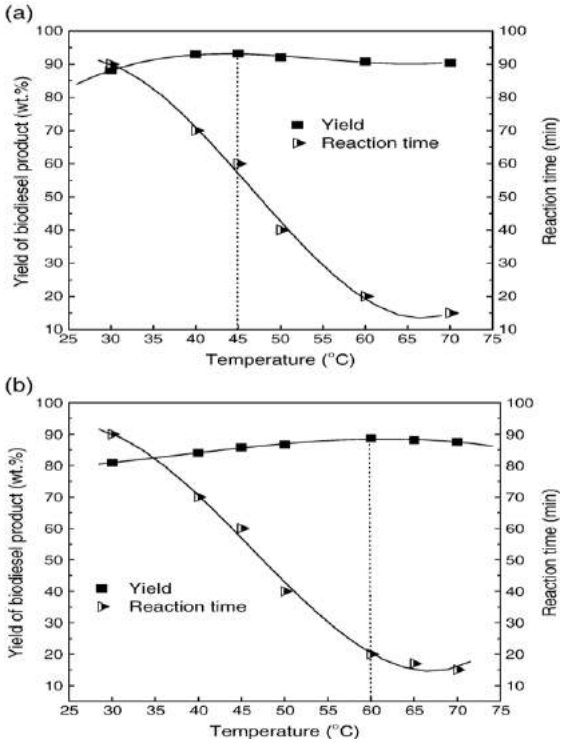


Figure 1: Effect of temperature on the transesterification of (a) neat Canola oil; and (b) UFO.

In an important research Georgogianni K.G. *et al.* [2] studied transesterification reaction of rapeseed oil with methanol, in the presence of homogeneous (NaOH) and heterogeneous (Mg MCM-41, Mg–Al Hydrotalcite, and K+ impregnated zirconia) using low frequency ultrasonication (24 kHz) and mechanical stirring (600 rpm) for the production of biodiesel fuel. The study concluded that that the homogeneous catalyst accelerated significantly the transesterification reaction, as compared to all heterogeneous catalysts, using both mechanical stirring (15 min vs. 24 h) and ultrasonication (10 min vs. 5 h). The table 1 shown below gives the Conversion of rapeseed oil in the presence of different catalysts using both mechanical stirring and ultrasonication. Further, Issariyakul Titipong and Dalai K. Ajay [5] carried out work on transesterification of canola oil and greenseed canola oil via KOH-catalyzed along with methanol, ethanol and a mixture of methanol and ethanol. The reaction was conducted at 60°C and a stirring speed of 600 rpm for 90 min. Prior to transesterification, greenseed canola oil was bleached to remove pigments using various adsorbents at different conditions. The result of the research work disclosed that Biodiesel derived from the treated greenseed canola oil showed an improvement in oxidative stability (induction time of 0.7 h) as compared to that derived from crude greenseed canola oil (induction time of 0.5 h).

Table 1: Conversion of rapeseed oil in the presence of different catalysts using both mechanical stirring and ultrasonication

	Time (h)	Yield (%)			
		Type of catalyst			
		Mg/MCM-41	MgAl hydrotalcite	10K/ZrO_2	20K/ZrO_2
Mechanical stirring	5	21	28	30	38
	10	43	54	37	42
	15	56	73	49	56
	20	73	89	61	69
	24	85	97	67	89
Ultrasonication	1	25	32	29	35
	2	48	58	39	48
	3	59	76	52	59
	4	75	89	63	73
	5	89	96	70	83

Afterwards Alamu J Oguntola et al. [10], produced the biodiesel from through transesterification 100g coconut oil, 20.0% ethanol (wt% coconut oil) and 0.8% potassium hydroxide catalyst at 65°C reaction temperature with 120 min. reaction time. Low yield of the biodiesel (10.4%) was obtained. While Tang Ying et al. [7], developed a new method catalyst, benzyl bromide-modified CaO for production of biodiesel from rapeseed. The improved catalytic activity was obtained by better fat diffusion to the surface of the benzyl bromide-modified CaO. Further, a 99.2% yield of fatty acid methyl esters in 3h was obtained in comparison to by better fat diffusion to the surface of the benzyl bromide-modified CaO. The normal and modified CaO is shown in Fig.2. Further, Silva F. Giovanilton *et al.* [6], produced biodiesel from soybean oil by transesterification with ethanol. Optimum conditions for the production of ethyl esters were the following: mild temperature at 56.7 °C, reaction time in 80 min, molar ratio at 9:1 and catalyst concentration of 1.3 M. For esterification reaction, H*R*2*R*SO*R*4*R* was added as a catalyst and for transesterification KOH was added as the catalyst with methanol. In the investigation of Wakil Abdul Md. *et al.* [11], chosen Cottonseed oil, Mosna oil and Sesame oil for producing biodiesel. Biodiesel is produced by transesterifying the oil with an alcohol such as methanol under mild conditions in the presence of a base catalyst. Satisfactory amount of biodiesel is produced from Cottonseed oil at 3:1 molar ratio of methanol and oil. Three types of oil (cottonsed oil, mosna oil, sesame oil) are extracted from the seeds and chemically converted via an alkaline transesterification reaction to fatty acid methyl ester. The optimum conditions established for the methanolysis of crude cotton seed oil in the investigation were recorded to be: 3:1 molar ratio of methanol to oil and 1.00% (w/w) catalyst. For Mosna oil the optimum conditions were recorded to be 3. 5:1 M ratio of methanol to oil and 1.00% (w/w) catalyst. But small amount of biodiesel was found from this oil and production cost is higher than cottonseed oil. And for Sesame oil the optimum conditions were recorded to be 3.5:1 M ratio of methanol to oil and 1.00% (w/w) catalyst.

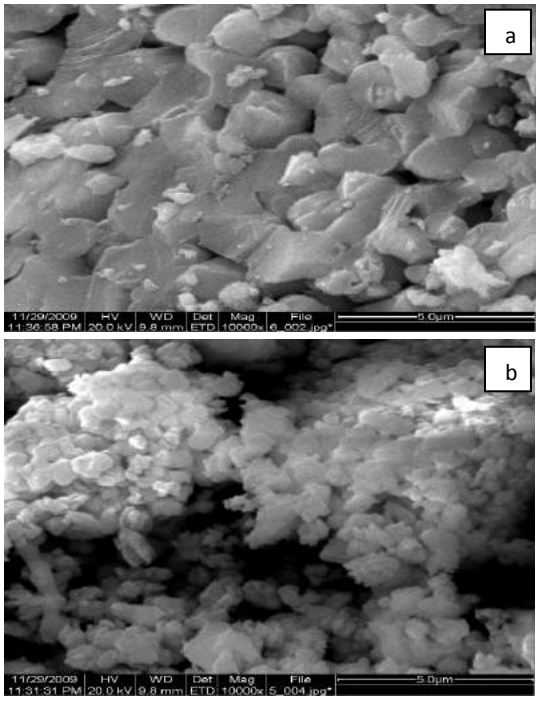


Figure 2: SEM Photo of (a) CaO and (b) Modified CaO

Ali N. Eman and Tay Isis Cadence [12], investigated characteristics of biodiesel produced from palm oil via base catalyst transesterification process. To find the optimum yield value of biodiesel, three important parameters were selected such as reaction temperature 40, 50, and 60°C, reaction time 40, 60 and 80 min. and methoxide ratio 4:1, 6:1 and 8:1. By conducting the experiments the optimum yield value 88% was achieved by the parameters such as reaction temperature 60°C, reaction time 40 minutes and methoxide ratio 6:1. From the optimum yield value, the physical properties were calculated like, density is 876.0 kg/m3, kinematic viscosity of 4.76 mm2/s, cetane number of 62.8, flash point of 170°C, cloud point of 13°C. The produced biodiesel had similar properties of ASTM D 6751, and EN 14214. In the important study Banerjee Madhuchanda *et al*. [13], determined the catalytic activity of bimetallic Gold–silver core–shell nanoparticles toward biodiesel production from Sunflower oil through transesterification. The structure of nanoparticles was examined by UV–vis spectroscopy, transmission electron microscopy (TEM) and energy dispersive X-ray (EDX) analysis. The result of studied showed that at certain catalyst concentration, temperature and reaction time, highest yield of biodiesel (86.9%) is attained. Further, the catalyst showed sustained activity for 3 cycles of transesterification. The effect of variable on the yield of biodiesel is shown in Fig. 3. In the most recent work Nikhom Ruamporn and Tongurai Chakrit [14], examined the continuous deglycerolisation (CD) for the production of ethyl ester biodiesel from palm oil. In this work, $KOCH_3$ was selected as the catalyst in transesterification and the reaction temperature was maintained at 60°C. The result showed that ethyl ester production using CD process could obtain good purity and yield in a single step transesterification. The ester content and yield were 98.0 wt.% and 93.1 wt.%, respectively at molar ratio of oil to ethanol of 1:5.5, $KOCH_3$ concentration of 1.2 wt.% and retention time of 30 min. The FFA content of palm oil and ethyl ester is shown in table 2 below.

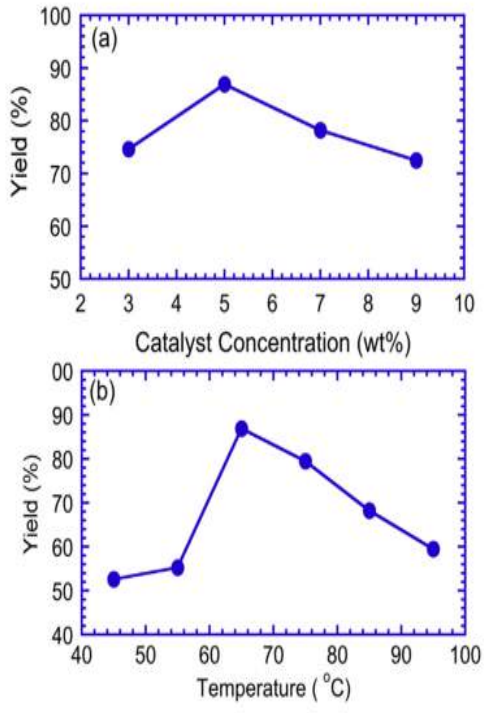


Figure 3: Effects of variables on biodiesel yield; (a) catalyst concentration and (b) temperature.

Table 2: The fatty acid composition of palm oil raw material and Ethyl Ester product

Fatty Acid Composition	Wt.%	
	Palm Oil	Ethyl ester
Lauric acid (C12:0)	1.11	0.24
Myristic acid (C14:0)	1.23	0.97
Palmitic acid (C16:0)	36.58	37.95
Palmitoleic acid (C16:1)	1.39	0.16
Stearic acid (C18:0)	4.5	3.62
Oleic acid (C18:1)	43.38	45.95
Linoleic acid (C18:2)	11.81	11.10
Others	-	2.01

Previous work done on production of biodiesel from non-edible oil.

Azam Mohibbe M. *et al.* [15], found that FAME of Jatropha curcas were most suitable for use as bio- diesel and met the major specification of bio-diesel standards of the European, Germany and USA Standards Organization. Afterwards Sarin Rakesh *et al.* [16], made appropriate blends of Jatropha and palm bio-diesel to improve oxidation stability and low temperature properties because Jatropha bio-diesel has good low temperature property and palm bio-diesel has good oxidative stability. It was found that antioxidant dosage could be reduced by 80-90% when palm oil bio-diesel is blended with Jatropha bio-diesel at about 20-40%. Moreover, Tiwari Kumar Alok *et al.* [17], used response surface methodology to optimize three important reaction variables, including methanol quantity, acid concentration, and reaction time. The optimum the FFA of Jatropha oil from 14% to less than 1% was found to be 1.43% v/v sulphuric acid catalyst, 0.28 v/v methanol-to-oil ration and 88 min reaction time at 60 ºC. The properties of Jatropha oil bio-diesel conform to European and American standards.

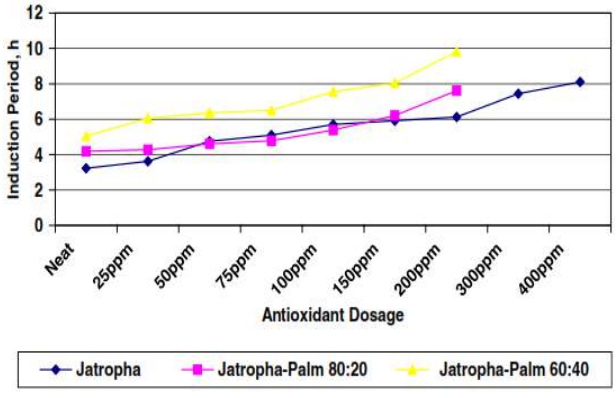


Figure 4: Antioxidant dose optimisation for Jatropha and Palm biodiesel.

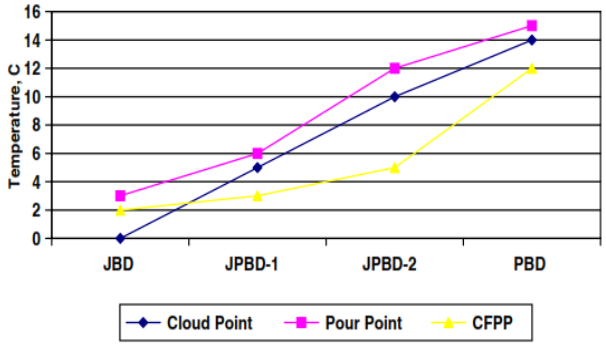


Figure 5: Low temperature property of Jatropha–Palm methyl ester blend

A year later Berchmans Johanes Hanny and Hirata Shizuko [18], developed a two-step pre-treatment process in which the high FFA (15%) of *Jatropha curcas* seed oil was reduced to less than 1%. In the first step, the reaction was carried out with 0.60 w/w methanol-to-oil ratio in the presence of 1 wt.% sulphuric acid as an acid catalyst in 1 h at 50ºC. In the second step, the transesterification reaction was performed using 0.24 w/w methanol-to-oil ratio and 1.4 wt% sodium hydroxide. While Chakrabarti H. Mohammed and Ahmad Rafiq [1], presented work on extraction of oil from castor bean and converting it into biodiesel from transesterification. It was found that reaction mixture containing 65ml of methanol along with 2.4 g of catalyst (KOH) took a good start in half an hour at30°C. In this reaction, amount of glycerine removed as well as ester content produced was considerably increased with rise in temperature of mixture upto 70°C by extending time period (180-360 minutes). The removal of glycerine increased by two and half times and ester content by four times, respectively. When castor oil was subjected to acid esterification, prior to transesterification (a separate investigation), it was found that ester contents up to 95% could be obtained. The comparison of physical-chemical properties of castor oil and diesel done by them is shown in table 3.

Table 3: Physical-chemical properties of mineral diesel, castor oil

Parameter	ASTM Test Method	ASTM Limits	Castor Oil	Diesel
Viscosity (mm^2/s)	ASTM D445	1.9 - 6.0	13.75	3.2
Sulfur (%)	ASTM D5453	0.0015, Max	0.0001	0.20
Density 15°C (g/cm^3)	ASTM D 1298	0.875 - 0.9	0.9279	0.8503
Density 20°C (g/cm^3)	ASTM D 1298	0.86	0.9245	0.8465
Flash point (°C)	ASTM D93	93°C Min.	120	37
Copper corrosion	ASTM D130	No. 3, Max	1	1
Cetane index	ASTM D613	47, Min	50	45
Water and sediment (vol. %)	ASTM D2709	0.050, Max	0.05	Nil

In the further research work Kapilan N and Reddy R.P. [19], produced biodiesel from Mahua oil methyl esters (MOME) by transesterification using potassium hydroxide (KOH) as catalyst and tested the conversion of vegetable oil to biodiesel by nuclear magnetic resonance (NMR) testing method. Further, studied the performance characteristics fuelling with Mahua biodiesel in a diesel engine. They concluded that B20 gave higher thermal efficiency and lower specific fuel consumption then diesel fuel. The physical properties of Mahua oil prepared by them is shown in table 4. In another research work Kansedo Jibrail *et al.* [20], extracted oil from the seeds of C. odollam fruits. The transesterification of the extracted oil was done to form fatty acid methyl esters (FAME). The transesterification reactions were carried out using three different catalysts; sodium hydroxide (NaOH) as a homogenous catalyst, sulfated zirconia alumina and montmorillonite KSF as heterogeneous catalysts. The seeds were found to contain high percentage of oil up to 54% while

the yield of FAME can reach up to 83.8% using sulfated zirconia catalyst. Further, Kafuku Gerald *et al.* [3], examined the feasibility of converting a non-edible oil source croton megalocarpus oil to methyl esters (biodiesel) using sulfated tin oxide with enchansed SiO_2 as super acid solid catalyst. At the following reaction condition 180°C, 2 h and 15:1 methanol to oil molar ratio, while keeping constant catalyst concentration and stirring speed at 3 wt.% and 350–360 rpm the yield up to 95% was obtained without any pre-treatment was obtained. The researcher Padhi S.K. and Singh R.K. [20] produced biodiesel from Mahua oil through the Esterification by varying different parameters. The conditions for produce biodiesel were 8% Sodium Methoxide, 0.33% v/v alcohol/oil ratio, 1 hr reaction time, 65°C temperature and 150% v/v excess alcohol. They concluded this was the best condition for biodiesel production. The results show that 4% H_2SO_4, 0.33% v/v alcohol/oil ratio, 1 hr reaction time and 65°C temperature are the optimum conditions for esterification. Optimum conditions for the production of biodiesel from Mahua oil are 8% Sodium Methoxide, 0.33% v/v alcohol/oil ratio, 1 hr reaction time, 65°C temperature and 150% v/v excess alcohol.

Table 4: Properties of MOME and its blends with diesel

Property	MO	MOME	Diesel	B20
Flash point (°C)	212	129	65	103
Kinematic viscosity at 40 °C (cst)	28.58	5.10	2.4	4.04
Copper strip corrosion	1.5	1	1	1
Cloud point (°C)	17	4	−6	−3
Density at 15 °C (kg/m^3)	897	876	821	838
Calorific value (MJ/kg)	35.614	36.914	42.960	41.750

E.I Bello and A Makanju [22] analyzed castor oil methyl ester as possible alternative fuel for diesel engines. To overcome the high kinematic viscosity of the neat oil, a high molar ratio of 6:1 was used to produce the methyl ester. The viscosity of the ester was high and further reduced by blending with diesel fuel to reduce it to within the American Society for Testing and Materials (ASTM) D6751 limits for biodiesel. The biodiesel was characterized and tested in a single cylinder diesel engine. The results obtained gave properties, torque outputs and specific fuel consumption that are close to those of diesel fuel thus confirming that it can be used as alternative fuel for diesel engines. While Deshpande D.P. *et al.* [23], studied transesterification reaction on castor oil in a batch reactor using potassium hydroxide as a catalyst. The variables chosen for the study were reaction time, Oil to methanol ratio, catalyst concentration; and reaction temperature. The effects of these variables on the viscosity of biodiesel were studied, since this is one of the important specifications in ASTM standard. Apart from viscosity other properties like specific grravity, acid value, and sap value were also determined for the biodiesel product. From the study it was concluded that the optimum operating condition are oil to methanol mole ratio 1:9, temperature 30oC, catalyst concentration 1 wt % and run time 45 min. The variation of viscosity, specific gravity, acid value with time is shown in table 5.

Table 5: Variation of viscosity, specific gravity, acid value with time

Time of Run (min)	30	45	60	90
Kinematic viscosity, (cSt) for Sulfuric Acid as Catalyst	16.56	11.28	12.44	13.93
Kinematic viscosity, (cSt) for Sodium Hydroxide as Catalyst	21.57	13.10	15.33	18.11
Specific gravity for Sulfuric Acid as Catalyst	0.9018	0.9006	0.9012	0.9019
Specific gravity for Sodium Hydroxide as Catalyst	0.9106	0.889	0.9016	0.9039
Acid value for Sulfuric Acid as Catalyst	0.90	0.58	0.562	0.541
Acid value for Sodium Hydroxide as Catalyst	0.92	0.37	0.40	0.52

Afterwards Widayat *et al.* [24], presented work on biodiesel from the rubber seed by situ method. The researcher focused on influence of reaction time, concentration of acid catalyst and ratio of raw material to methanol. This process took 120 minutes at 60°C with maximum yield of FAME 91.05% at HR2RSOR4R 0.25% (v/v) and ratio of raw material to methanol (1:3). Based on the results, ratio of raw material to methanol was quite important to increase yield of FAME significantly. The experimental setup used by the researcher is shown in Fig. 6. Further, the team of researchers Ali Hasan Md. *et al.* [25] produced biodiesel from neem seeds, its properties were close to diesel. The methodology of esterification process was selected and carried out by 1000 ml raw neem oil, 300ml methanol and sodium hydroxide on mass basis as a catalyst usually kept in oven to form methyl ester, and initially to reach equilibrium condition at temperature 55-66°C. The ester and glycerine were separated by stimulating continuously and allow settling under gravity for 24 h. Thus the separated ester contains 3% to 6% methanol and soap agents. The methanol was removed by vaporization. The biodiesel had some catalyst; it was removed by warm water mix with ester. Kinematic viscosity lay between 1.9 to 6.0 according to the ASTM D6751 specification. Hence, 0.95 ltr. biodiesel was production from 1 ltr neem oil.

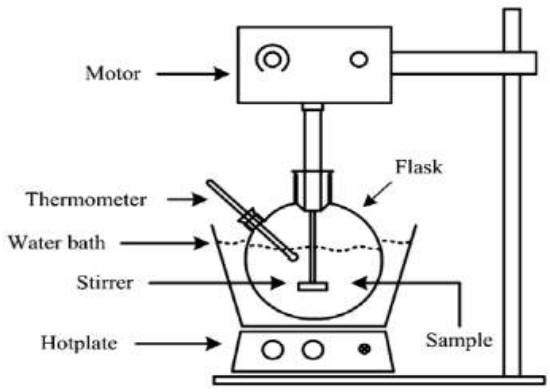


Figure 6: Experimental Setup

In an advance production method of biodiesel Riadi Lieke *et al.* [26], produced biodiesel from karanja oil by two step process. The first step process which was designed for 3 hours reaction time at 30°C and 5.8%

of ozone using either 1 or 1.5 weight % KOH at various percent weight of supporting catalyst had proved simultaneous reaction for both ozonolysis and transesterification. The short chain methyl esters (methyl hexanoate, methyl octanoate and methyl nonanoate) were effectively produced for the first step process using 5.8% mole ozone at 30°C for 3 hours either for 1 or 1.5 weight % KOH at various percent weight of extracted supporting catalyst. From this reaction, the esters predicted by ozone reaction were sufficiently produced. The highest short chain methyl esters and long chain methyl esters produced in the first step process was 85.722 mg/litre and 655.286 mg/ltr respectively, which used 17.3 weight % ash and 1.5 weight % KOH. The presence of extracted ash in methanol as supporting catalyst enhanced the production of total methyl esters compared to that without the presence of ash in the first step process. Higher temperature (60°C) in the second step process without the presence of ozone gave enough vibration of energy, to increase rate of transesterification and decrease the viscosity.In the recent work Hotti R Siddalingappa and Hebbal D Omprakash [27], presented work on non-edible champaca seed oil biodiesel (CBD). The biodiesel was produced by two step process i.e. acid pretreatment process followed by base-catalyzed transesterification process as the free fatty acid (FFA) content found to be 5.30% (corresponding to acid value of 10.55, mg KOH/g). The first step of process was carried out with methanol and sulphuric acid as catalyst, followed by second step, base-catalyzed transesterification process with methanol and sodium hydroxide as catalyst the biodiesel yield was found to be 83.50 %.

Previous work done on production of biodiesel from waste cooking oil.

Zheng S. *et al.* [28] analyzed the reaction kinetics of acid-catalyzed transesterification of waste frying oil. They found that at the methanol/oil molar ratio of 250:1 at 70 ºC or in the range 74:1-250:1 at 80ºC, the reaction was a pseudo-first-order reaction. High yield of 99±1% could be achieved at both 70 ºC and 80 ºC temperatures while stirring at rate of 400 rpm, using a feed molar ratio oil:methanol:acid of 1:245:3.8. A year later Wang Yong *et al.* [29] investigated a two- step catalyzed processes for synthesis of bio-diesel by using WCO from Chinese restaurants. In the first step, ferric sulphate-catalyzed methanolysis was carried out, while potassium hydroxide catalysis was performed in the second step. The authors concluded that compared with one-step sulphur acid catalysis the two-step catalyzed process provided a simpler and more economic method to produce bio-diesel from WCO. The conversion rate is shown in fig. 7. In the further research work Issariyakul Titipong *et al.* [30] also used the two-step process to transesterify waste cooking oil, except that sulphuric acid was selected as acid catalyst and mixtures of methanol and ethanol were used for transesterification in order to use the better solvent properties of ethanol and a more rapid equilibrium using methanol. More than 90% ester was obtained by using the two-stage method compared with yield of ~50% ester by using the single stage alkaline catalyst.

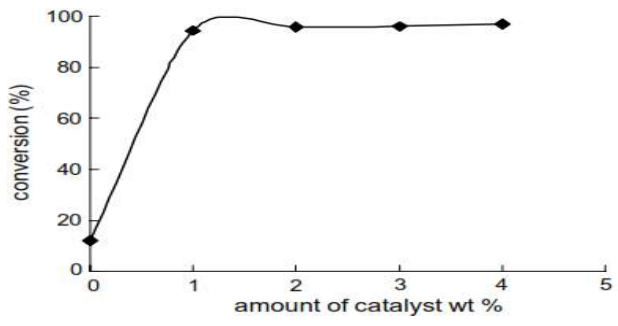


Figure 7: Conversion of FFA VS. Amount of Catalyst

Lin Fen-Ya *et al.* [31] also used WCO to prepare bio-diesel and then conducted a study in which the exhaust tail gas of bio-diesels was compared when the engine was operated using different fuel types, including neat bio-diesel, bio-diesel/diesel blends, and normal diesel fuels. Among the collected data, the authors found that B20 and B50 were the optimum fuel blends. The properties of diesel and biodiesel used by the researcher is shown in table 6. Later Hossain A.B.M.S. and Boyce A.N. [32] in their work compared optimum conditions of alkaline-catalyzed transesterification process for biodiesel production from pure sunflower cooking oil (PSCO) and waste sunflower cooking oil (WSCO) through transesterification process. The highest approximately 99.5% biodiesel yield acquired under optimum conditions of 1:6 volumetric oil-to-methanol ratio, 1% KOH catalyst at 40ºC reaction temperature and 320 rpm stirring speed. Result of the test showed that the biodiesel production from PSCO and WSCO exhibited no considerable differences. Afterwards Bakir T. Emaad and Fadhil B. Abdelrahman [33] presented work on single step transesterification and two step transesterification, namely acid-base and base–base catalyzed transesterification process for production of biodiesel from Chicken fried oil. For this purpose, hydrochloric acid and potassium hydroxide with methanol were used. The results disclosed that two step base catalyzed transesterification was better compared to other methods. It resulted in higher yield and better fuel properties.

Table 6: Major properties of premium diesel and biodiesel used

	Premium diesel	B100	Test method
Density at 20 °C (g/mL)	0.826	0.86	ASTM D 1298
Kinematic viscosity at 40 °C (cSt)	2.73	4.49	ASTM D 445
Cetane index	46.2	44.28 48.05	ASTM D 976 EN ISO 4264
Flash point (°C)	89	122	ASTM D 93
Water and sediment (vol.%)	<1	0.22	ASTM D 2709
Gross Heating Value (cal/g)	11411.4	9850.6	ASTM D 240

Prafulla D. Patil *et al.* [34] carried out comparative study on biodiesel production from waste cooking oil using sulfuric acid (Two-step) and microwave-assisted transesterification (One-step). The two-step transesterification process was used to produce bio-diesel (alkyl ester) from high free fatty acid (FFA) waste cooking oil. While Microwave-assisted transesterification was done by using catalytic BaO and KOH in biodiesel production from waste cooking oil. The study shown that that the microwave-heating method consumes less than 10% of the energy to achieve the same yield as the conventional heating method. Further, fuel properties of biodiesel produced were compared with ASTM Standards for biodiesel and regular diesel. In important study Suvendu Mohanty *et al.* [35] observed that from Waste cooking oil CO emissions are increased with increase in engine load. Further it was found that volume of CO initially decreases but increase at full load indicating better burning conditions at higher temperature assisted by improved spraying qualities with uniform charge preparations of biodiesel. The emissions of unburnt hydrocarbon for biodiesel exhaust due to lower than that of diesel fuel the increased gas temperature and higher cetane number of biodiesel could be responsible for this decrease. Higher temperature of burnt gases in biodiesel fuel helps in preventing condensation of higher hydrocarbon reducing. While Canesin Antonio Edmilson *et al.* [36] produced biodiesel from Residual oils and also check the viability and degradation level of production process. Residual bovine, chicken and soybean oils were used for biodiesel production process. They used four transesterification methods, using acidic and basic catalysis and, gas chromatography with flame ionization detector (GC–FID). They

concluded use of acidic catalysis at a lower temperature were the most efficient in the biodiesel production process. In the recent study Farooq Muhammad and Ramli Anita [37] prepared catalysts from raw chicken bones for transesterification reaction of waste cooking oil for biodiesel production. The study revealed that heterogeneous catalyst calcined at 900°C exhibited good catalytic activity in the transesterification of WCO, providing maximum biodiesel yield of 89.33% at 5.0 g of catalyst loading, 15:1 methanol to oil molar ratio at temperature of 65°C in reaction time of 4 h. The effect of molar ratio, catalyst amount and temperature observed by the researcher on the yield of biodiesel is shown in fig. 8.

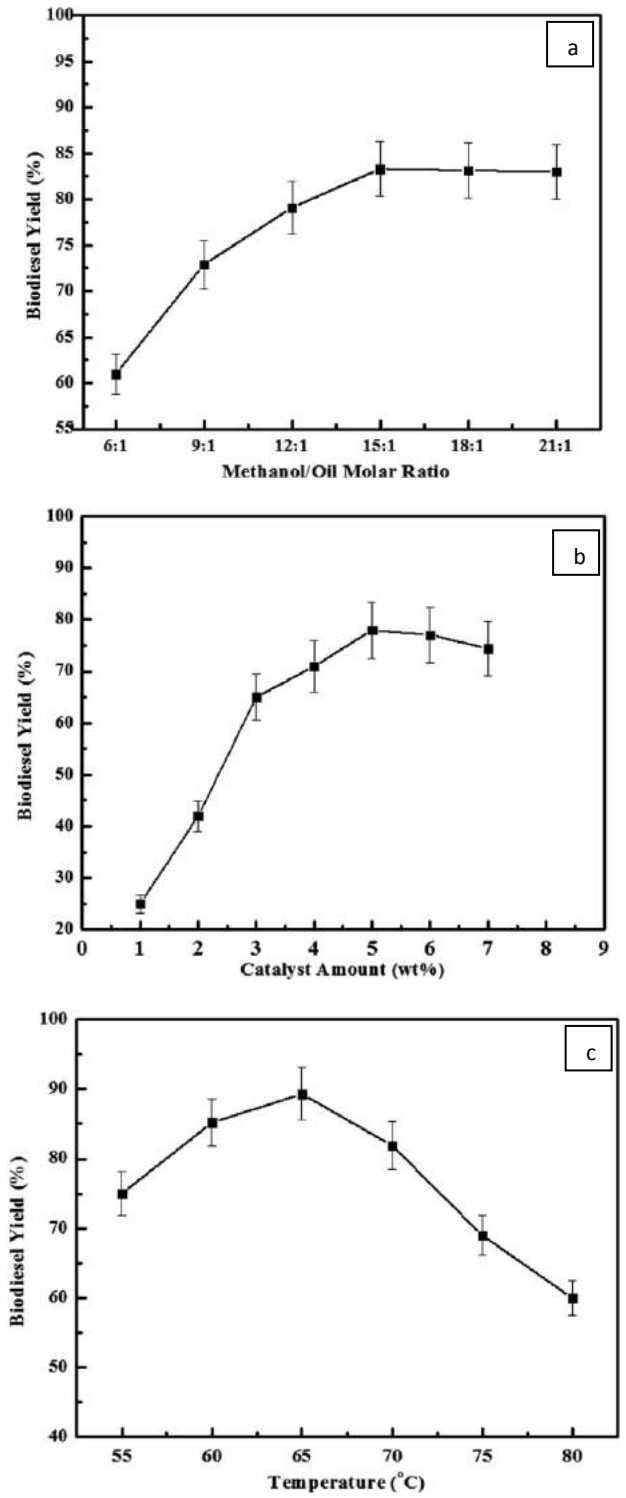


Figure 8: Effect of (a) Molar Ratio (b) Catalyst Amount and (c) Temperature on Biodiesel Yield

CONCLUSION

This work has provided a comprehensive literature review of the previous research work carried out in past years on production of biodiesel from edible, non-edible and waste cooking oil. An effort has been made to comprise all the important contributions and highlighting the most pertinent literature available for investigating the impact attenuator. The conclusion from the current literature survey are as follows: -

a) Biodiesel is an important alternative transportation fuel and it possess properties like renewability, biodegradability, non-toxicity and environmentally friendly benefits.
b) Biodiesel can be produced from different feedstock containing fatty acids such as animal fats, edible oils, non-edible oils, and waste cooking oils and by products of the refining vegetables oils.
c) Transesterification is a commonly employed method for its production. The purpose of this method is to reduce the viscosity of oil or fat using acid or base catalyst in the presence of methanol or ethanol.
d) Transesterification with alkali catalyst (KOH and NaOH) is more economical than acid catalyst and enzyme catalyst.
e) The biodiesel production is strongly affected by parameters such as molar ratio of alcohol, reaction temperature, reaction time and catalyst concentration.

ACKNOWLEDGMENT

The review presented in this work is by no means complete but it gives a comprehensive representation of different methodology adopted for the testing of impact attenuator. The author wishes to apologize for the unintentional exclusions of missing references and would appreciate receiving comments and pointers to other relevant literature for a future update.

REFERENCES

1. Mohammed H. Chakrabarti, Rafiq Ahmad. Trans esterification studies on castor oil as a first step towards its use in bio diesel production. Pakistan Journal of Botany 2008;40:1153-1157.
2. Georgogianni K.G., Katsoulidis A.K., Pomonis P.J., Manos G., Kontominas M.G. Transesterification of rapeseed oil for the production of biodiesel using homogeneous and heterogeneous catalysis. Fuel Processing Technology. 2009;90(7-8):1016-1022.
3. Gerald Kafuku, Man Kee Lam, Jibrail Kansedo, Keat Teong Lee, Makame Mbarawa. *Croton megalocarpus* oil: A feasible non-edible oil source for biodiesel production. Bioresource Technology. 2010;101(18):7000-7004.
4. Sinha Shailendra, Agarwal Kumar Avinash, and Garg Sanjeev. Biodiesel development from rice bran oil: transesterification process optimization and fuel characterization. Energy Conversion and Management. 2008; 49):1248–1257.
5. Issariyakul Titipong and Dalai K. Ajay. Biodiesel production from greenseed canola oil. Energy Fuels 2010;24: 4652–4658.
6. Giovanilton F. Silva, Fernando L. Camargo, Andrea L.O. Ferreira. Application of response surface methodology for optimization of biodiesel production by transesterification of soybean oil with ethanol. Fuel Processing Technology 2011;92:407–413.
7. Ying Tang, Gang Chen, Jie Zhang, Yong Lu. Highly active CaO for the transesterification to biodiesel production from rapeseed oil. Bulletin of the Chemical Society of Ethiopia 2011;25(1):37-42.
8. D.Y.C. Leung, Y. Guo. Transesterification of neat and used frying oil:Optimization for biodiesel production. Fuel Processing Technology 2006;87:883-890.
9. Lingfeng Cui, Guomin Xiao, Bo Xu, and Guangyuan Teng. Transesterification of cottonseed oil to biodiesel by using heterogeneous solid basic catalysts. Energy & Fuels 2007;21:3740–3743.

10. Oguntola J ALAMU, Opeoluwa DEHINBO, Adedoyin M SULAIMA. Production and testing of coconut oil biodiesel fuel and its blend. Leonardo Journal of Sciences 2010;16:95-104.
11. Md. Abdul Wakil, Z.U. Ahmed, Md. Hasibur Rahman, Md. Arifuzzaman. Study on fuel properties of various vegetable oil available in Bangladesh and biodiesel production. International Journal of Mechanical Engineering 2012;2(05):10-17.
12. Eman N. Ali, Cadence Isis Tay. Characterization of biodiesel produced from palm oil via base catalyzed transesterification. Procedia Engineering 2013;53:7-12.
13. Madhuchanda Banerjee, Binita Dey, Jayanta Talukdar, Mohan Chandra Kalita. Production of biodiesel from sunflower oil using highly catalytic bimetallic gold-silver core-shell nanoparticles. Energy. 2014;30:1-5.
14. Ruamporn Nikhom, Chakrit Tongurai. Production development of ethyl ester biodiesel from palm oil using a continuous deglycerolisation process. Fuel 2014;117:926-931.
15. Azam Mohibbe M., Amtul Waris, N.M. Nahar. Prospects and potential of fatty acid methyl esters of somenon-traditional seed oils for use as biodiesel in India. Biomass and Bioenergy 2005;29:293–302.
16. Rakesh Sarin, Meeta Sharma, S. Sinharay, R.K. Malhotra. Jatropha–Palm biodiesel blends: An optimum mix for Asia. Fuel 2007;86: 1365–1371.
17. A.K. Tiwari, A. Kumar, H. Raheman. Biodiesel production from Jatropha (*Jatropha curcas*) with high free fatty acids: an optimized process. Biomass and Bioenergy 2007;31:569-575.
18. Hanny Johanes Berchmans, Shizuko Hirata. Biodiesel production from crude *Jatropha curcas* L. seed oil with a high content of free fatty acids. Bioresource Technology 2008;99:1716–1721.
19. Kapilan N, Reddy R.P. Evaluation of methyl esters of Mahua oil (*Madhuca indica*) as Diesel Fuel. Journal of American Oil Chemists Society. 2008;85:185-188.
20. Kansedo Jibrail, Lee Teong Keat and Bhatia Subhash. *Cerbera odollam* (Sea Mango) oil as a promising non-edible feedstock for biodiesel production. Fuel 2009;88:1148-1150.
21. Padhi S.K and Singh R.K. Optimization of esterification and transesterification of Mahua (*Madhuca indica*) oil for production of biodiesel. Journal of Chemical and Pharmaceutical Research. 2010;5: 599-608.
22. Bello E.I., A. Makanju. Production, characterization and evaluation of castor oil biodiesel as alternative fuel for diesel engines. Emerging Trends in Engineering and Applied Science 2011;2:525-530.
23. Deshpande D.P., Urunkar Y.D., Thakare P.D. Production of Biodiesel from Castor Oil using acid and Base catalysts. Research Journal of Chemical Sciences 2012;2:51-56.
24. Widayat, Agam Duma Kalista Wibowo, Hadiyanto. Study on production process of biodiesel from rubber seed (hevea brasiliensis) by in situ (trans) esterification method with acid catalyst. Energy Procedia. 2013;32:64-73.
25. Hasan Ali Md., Mohammad Mashud, Rowsonozzaman Rubel Md., Rakibul Hossain Ahmad. Biodiesel from Neem oil as an alternative fuel for Diesel engine. ,Procedia Engineering 2013; 56:625- 630.
26. Lieke Riadi, Edy Purwanto, Hendrik Kurniawan and Ria Oktaviana. Effect of Bio-Based Catalyst in Biodiesel Synthesis. Procedia Chemistry, 2014; 9:172-181.
27. Hotti R Siddalingappa and Hebbal D Omprakash). Biodiesel production and fuel properties from non-edible Champaca (*Michelia champaca*) seed oil for use in diesel engine. Journal of Thermal Engineering. 2015;1330-336.
28. S. Zheng, M. Kates, M.A. Dube, D.D. McLean. Acid-catalyzed production of biodiesel from waste frying oil. Biomass and Bioenergy 2006;30:267–272.
29. Yong Wang, Shiyi Ou, Pengzhan Liu, Zhisen Zhang. Preparation of biodiesel from waste cooking oil via two-step catalyzed process. Energy Conversion and Management 2007;48:184–188.
30. Issariyakul, T., Kulkarni, M.G., Dalai, A.K., Bakhshi, N.N. Production of biodiesel from waste fryer grease using mixed methanol/ethanol system. Fuel Process Technol 2007;88:429-436.
31. Ya-fen Lin, Yo-ping Greg Wu, Chang-Tang Chang. Combustion characteristics of waste-oil produced bio-diesel/diesel fuel blends. Fuel 2007;86:1772-1780.
32. Hossain A.B.M.S. and Boyce A.N. Biodiesel production from waste sunflower cooking oil as an environmental recycling process and renewable energy. Bulgarian Journal of Agricultural Science. 2009;15: 312-317.
33. Bakir T. Emaad, Fadhil B. Abdelrahman. Production of biodiesel from chicken frying oil. Pak. J. Anal. Environ. Chem. 2011;12: 95-101.
34. Patil D. Prafulla, Gude Gnaneswar Veera, Reddy K. Harvind, Muppaneni Tapaswy and Deng Shuguang . Biodiesel production from waste cooking oil using sulfuric acid and microwave irradiation processes. Journal of Environmental Protection. 2012;3107-113.
35. Suvendu Mohanty, Dr. Om Prakash. Analysis Of Exhaust Emission Of Internal Combustion Engine Using Biodiesel Blend. International Journal of Emerging Technology and Advanced Engineering 2013;3(05):731-742.
36. Edmilson Antonio Canesin, Cláudio Celestino de Oliveira, Makoto Matsushita, Lucia Felicidade Dias, Mayka Reghiany Pedrao, Nilson Evelazio de Souza. Characterization of residual oils for biodiesel production. Electronic Journal of Biotechnology 2014;17:39-45.
37. Farooq Muhammad and Ramli Anita. Biodiesel production from low FFA waste cooking oil using heterogeneous catalyst derived from chicken bones. Renewable Energy. 2015;76:362-368.

ISSN: 2278 – 909X
International Journal of Advanced Research in Electronics and Communication Engineering (IJARECE)
Volume 5, Issue 6, June 2016

A New and Robust Segmentation Technique Based on Pixel Gradient and Nearest Neighbors for Efficient Classification of MRI Images

Sanchit Kumar, Sahil Dalal

***Abstract*— This paper proposes a new fully automated method for the segmentation of tumour in a tumour affected brain MRI image and its classification from a normal image. The technique detects brain tumour on the basis of differences in pixel intensities between the tumour and the surrounding tissues. It also exploits the connected pixels labelling of the tumour pixels which accurately segments brain tumour. Classification is done using support vector machine (SVM) which uses GLCM technique to calculate feature vector. The classification parameters (i.e. accuracy, sensitivity and specificity) and other parameters (i.e. speed and computational power used) show that our method is better in performance as compared to the other state of the art methods.**

***Keywords*—GLCM, MRI, SVM, Solidity and Thresholding.**

I. INTRODUCTION

Brain tumour [1] [11] is one of the major causes of death among men throughout the world. It is the growth of some abnormal tissues within the brain. It's mainly of two types: one is benign tumour and other is malignant tumour. Malignant tumour is more dangerous than benign tumour as it is cancerous in nature and has the ability to grow inside the brain, thus malignant tumour can result in death if not diagnosed at an early stage. MRI is one of the techniques of medical imaging which helps in detecting tumour accurately. Radiologists can easily examine a brain MRI image to conclude whether it is normal or cancerous. But the problem arises when there are numerous images to be examined leading to decreased accuracy and high time consumption. Hence, in order to increase the accuracy and minimize the time consumption, automated classification with the help of computer technology is needed.

***Sanchit Kumar**, Department of Electronics and Communications Engineering, Delhi Technological University, Delhi, India.*

***Sahil Dalal**, Department of Electronics and Communications Engineering, Delhi Technological University, Delhi, India.*

The methodology includes the following steps: Image pre-processing, segmentation, feature extraction, and classification. Image pre processing is used to remove noise from an image to make it suitable for further processes. It is needed for the accurate segmentation of tumour from the image. Segmentation refers to the process where only the desired part of the image is kept and the unwanted parts removed. It is required to extract the region of tumour in the image making the classification easier and accurate.

Feature extraction is the processing of some calculated parameters from the segmented images which acts as input to the classifier for classification. It further reduces the information in image to a minimum level. For accurate classification, features which are extracted should be meaningful and useful.

Classification process differentiates a normal image from an image having a tumour with the help of algorithms known as classifiers. There are many types of classifiers which can be used for such purposes. Some of them are support vector machine (SVM) [2], k nearest neighbours (KNN) [3], Artificial neural network (ANN) [4], Probabilistic neural network (PNN) [5] etc. Each of the classifier has its own advantages and disadvantages. K-NN [3] has some limitations such as high computation cost, difficulty in finding the proper value of 'K' parameter etc. Even though K-NN [3] has high accuracy in classification, its performance is degraded by its limitations. PNN [5] has a major problem that it is a very slow classifier. ANN [4] performs better than the above mentioned classifiers with the high dimension of feature vector, but it also has high computational cost problem. As feature vector is small in our method, SVM [2] performs the best amongst all the other classifiers.

Classification is divided into two parts: training and testing. In training, known data is given to the classifier for its training. After that unknown images are given to the classifier for classification for testing. The efficiency of classification mainly depends upon the training.

This Paper is organized as follows. Section II describes the methodology utilized for the proposed method .Section III describes experimental work of the proposed method. The tumour classification and experimental results are given in section IV with conclusion in section V.

All Rights Reserved © 2016 IJARECE

II. METHODOLOGY

The methodology used for the classification of brain MRI image of a normal person and a person having brain tumour is shown in fig.1. This system consists of the following modules: pre-processing (RGB to grayscale conversion, resizing and filtering), segmentation, feature extraction, training and testing. Firstly, training dataset of brain MRI images is given to the system for training of classifier. Then testing data set is given to the system which classifies it into two categories normal and abnormal based on the training.

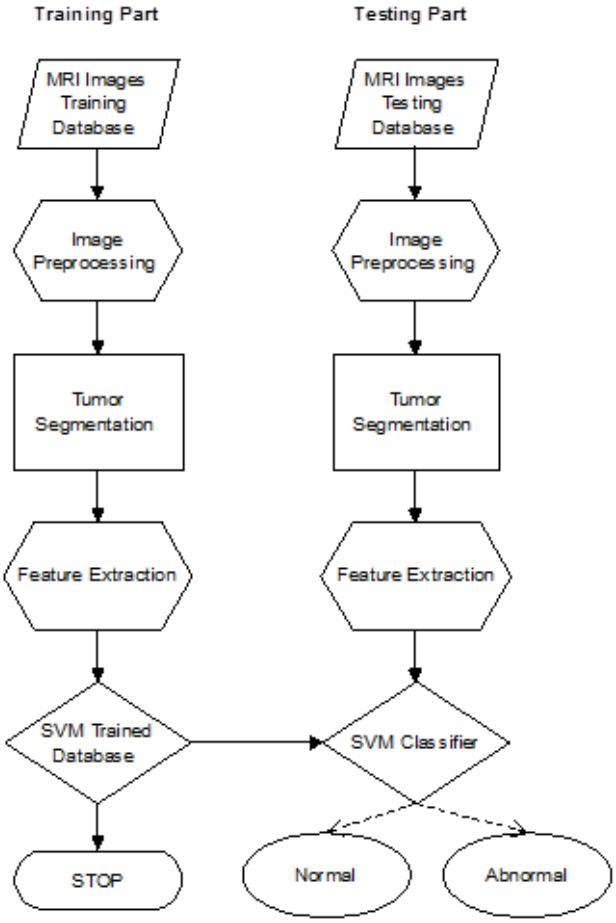
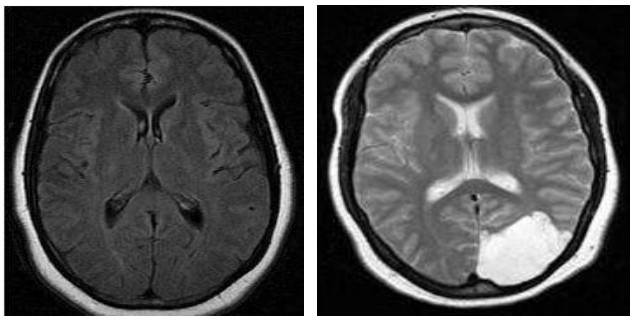


Fig.1. Block Diagram

A. MRI Image

The MRI (magnetic resonance imaging) [6] is one of the best tools used in hospitals and clinics for medical diagnosis of various diseases. Some of its advantages are: (i) It prevents exposure of body from ionizing radiations. (ii) It gives very high contrast between the tissues.

Fig 2 shows the MRI image of normal and abnormal brain respectively. It is clearly seen that the tissues affected from tumour are of higher intensity than the normal tissues. When the image is taken, it is an RGB image. Before giving it to the system, image is first converted to gray scale and resized to a size of 500 X 500.



(a) (b)

Fig.2. Brain MRI (a) Normal and (b) Abnormal

B. Pre-processing of image

Pre-processing includes filtering of image using median filter. At the time of acquisition, the image gets distorted with noise and the contrast is also low which leads to lower efficiency in further steps of the process. Filtering is needed to remove noise and to enhance image contrast. Advantage of using median filter is that it removes the noise while preserving the edges which helps in improving contrast of the image. Accuracy of tumour segmentation is also increased by this step. Filtered image is shown in fig 3.

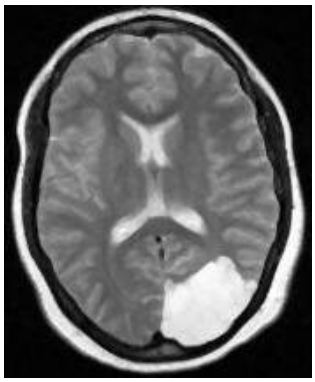


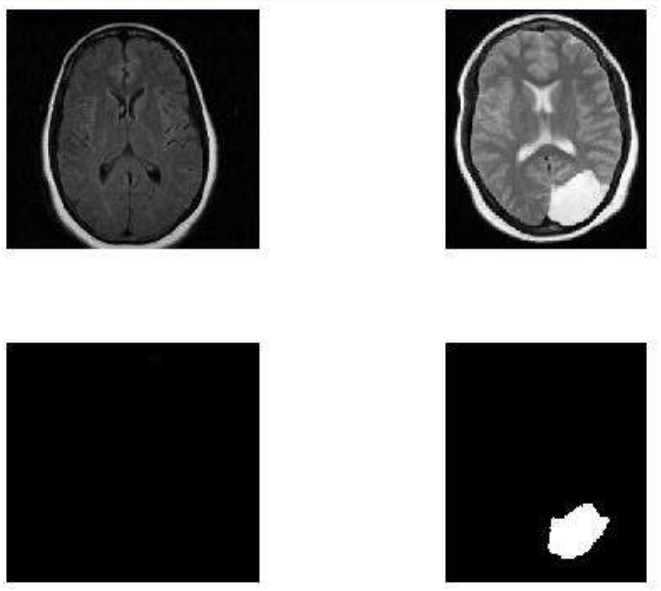
Fig.3. Filtered image

C. Segmentation

In the field of biomedical imaging, tumour detection is a crucial task as brain tumour can be a severe disease if not properly diagnosed. In the acquired MRI image, it can be seen that generally the intensity values where tumour is present is greater in comparison to the surrounding intensities. In our work, segmentation is done using intensity values and solidity of the tumour to detect the tumour from its surrounding tissues. The first step in segmentation is thresholding, where the intensity values greater than predefined thresholds are kept and the values below the threshold level are ignored. The threshold level is found by hit and trial method. We get a value of 164 as our threshold. After thresholding, the image still contains unwanted regions along with the tumour region. For removing these unwanted regions, solidity and area [7] of the segmented regions are calculated. Only those regions having solidity values greater than 0.2 are labelled as tumour

All Rights Reserved © 2016 IJARECE

intensity values. The second criteria is area where the max area of the region is considered as tumour based region. After exploiting these properties, the MRI image is segmented to detect the tumour as foreground and surrounding tissues as background.



(a) (b)

Fig.4. (a) Normal Brain MRI with its segmented image and (b) Abnormal Brain MRI with its segmented image

The segmented results are shown in fig.4 in which the two images are segmented where first image contains a tumour and second image is a normal MRI image. The segmented results are also shown as there counterpart images.

D. Feature extraction

Feature extraction plays a very important role in image processing /computer vision for pattern recognition and classification. A raw segmented image cannot be given directly to the classifier as it contains unwanted data which increases computational time and cost of the process. Some meaningful and important data points are extracted from the image (also called features) using feature extraction process. Features can be of many types such as intensity based features [12], texture based features [13] or shape based features [14]. Several features are calculated from an image which forms a feature vector which is given as input to a classifier for accurate classification of normal and abnormal MRI image. In our work, we are calculating 5 texture features using Grey Level co-occurrence matrix (GLCM) [8] technique which constitutes a feature vector of 5X1 dimension for each image. Features using GLCM are given by:

CONTRAST: Contrast is defined as the separation between the darkest and brightest area.

$$Contrast = \sum_{i,j=0}^{n-1} P_{ij}(i-j)^2 \qquad (1)$$

CORRELATION: Correlation is computed into what is known as the correlation coefficient, which ranges between -1 and +1.

$$Correlation = \sum_{i,j=0}^{n-1} P_{ij} \frac{(i-\mu)(j-\mu)}{\sigma^2} \qquad (2)$$

HOMOGENEITY: Homogeneity is defined as the quality or state of being homogeneous.

$$Homogeneity = \sum_{i,j=0}^{n-1} \frac{P_{ij}}{1+(i-j)^2} \qquad (3)$$

ENTROPY: Entropy is a measure of the uncertainty in a random variable.

$$Entropy = \sum_{i,j=0}^{n-1} -\ln(P_{ij})P_{ij} \qquad (4)$$

ENERGY: It provides the sum of squared elements in the GLCM .Also known as the uniformity or the angular second moment.

$$Energy = \sum_{i,j=0}^{n-1} P_{ij}^2 \qquad (5)$$

Where P_{ij} is the Grey Level Co-occurrence matrix (GLCM).

E. Classification using Support vector machine

Support vector machine (SVM) [2] is a classification algorithm based on the supervised learning model. In SVM, a high dimensional feature space is divided into two halves by constructing a hyperplane where each half belongs to a different class. Hyperplane is given by the equation:

$$G(x) = w^t x + b \qquad (6)$$

Where x is the feature vector, w gives the orientation of the plane, b is the bias i.e. position of the hyper plane w.r.t. origin in high dimensional space. Here values of w and b are optimized by giving training samples from both the classes of image which also maximizes the distance between the two classes, thus forming an accurate classifier. In SVM, feature vector of each class are on either sides of the hyper plane. Class vectors at boundary are called support vectors as the position and orientation of hyper plane depends upon them.

$$G(x_1) = w^t x_1 + b > 0, x_1 \in C_1 \qquad (7)$$

$$G(x_1) = w^t x_1 + b < 0, x_1 \in C_2 \qquad (8)$$

After training the classifier, a feature vector x_1 is given for testing it. G(x_1) is calculated for the given vector if G(x_1)

All Rights Reserved © 2016 IJARECE

value comes out to be positive then x1 belongs to class C_1 and if G(x) comes out to be negative then x_1 belongs to class C_2.

F. Performance Measure

Performance of a classification algorithm can be measured by a specific table layout which is called the Confusion Matrix [9]. It is called so because it makes it easier to see whether the method is confusing the result of classification between the two classes. Each column in confusion matrix shows instances in the predicted class and each row shows instances in the actual class. Confusion matrix is shown in the fig.5.

		PREDICTED CLASS	
		Abnormal	Normal
ACTUAL CLASS	Abnormal	TP	FN
	Normal	FP	TN

Fig. 5 Confusion Matrix

Where TP, TN, FP, and FN are given as:

- True Positive (TP): Abnormal brain correctly identified as abnormal.
- True Negative (TN): Normal brain correctly identified as normal.
- False Positive (FP): Normal brain incorrectly identified as abnormal.
- False Negative (FN): Abnormal brain incorrectly identified as normal.

Parameters that are calculated using confusion matrix are:

1. Accuracy = $\frac{TP+TN}{TP+TN+FP+FN}*100$
2. Sensitivity = $\frac{TP}{TP+FN}*100$
3. Specificity = $\frac{TN}{TN+FP}*100$

III. Experimental Discussion

Our method includes following steps: image pre-processing, segmentation, feature extraction, classification. In image pre-processing step, MRI images are first converted from RGB to grayscale and resized to a size of 500 X 500.Then median filter is used to remove noise from the image and to make segmentation accurate.

In segmentation step, Tumour region from an abnormal brain MRI image is extracted leaving behind all other unwanted parts of the image. These steps play an important role as it makes the classification easier and faster. In feature extraction, we have calculated only 5 features for the classification. As the number of features in our feature vector is so small, our method is fast and takes less computational power compared to other methods.

TABLE I

Features Extracted

GLCM FEATURES	NORMAL IMAGE	ABNORMAL IMAGE
Contrast	1.5571 e-04	2.1322 e-04
Correlation	0.8351	0.9737
Homogeneity	0.9999	0.9999
Entropy	-2.3434 e06	-1.1634 e07
Energy	0.99989	0.9917

The classification processing is divided into two parts i.e. training and testing part. In training part, known data (i.e. 5 features*40 images) is given for the training of classifier. After the completion of training, 50 unknown images are given to the classifier for classification, this is the testing part. The classification is performed using SVM. The accuracy of classification mainly depends upon its training part.

IV. Results & Discussion

In this method, we are using brain MRI images of 90 patients. Out of these 90 images, 40 images have been used for training of classifier and other 50 images for testing. Firstly, features calculated from 40 training images have been given to the classifier (based on SVM). After Training, 50 unknown images have been given to the classifier for classification into normal and abnormal. Accuracy, sensitivity and specificity were calculated based on the confusion matrix shown in Table II and they came out be 96%, 92% and 100% respectively. Table III shows the comparison of accuracy of other methods and our method i.e. SVM with segmentation. It shows that accuracy of our method is greater than the method [10] but slightly lower than method [11].

TABLE II

Confusion Matrix

		PREDICTED CLASS		
		Abnormal	Normal	Accuracy
ACTUAL CLASS	Abnormal	23/25	2/25	92%
	Normal	0/25	25/25	100%

All Rights Reserved © 2016 IJARECE

TABLE III

Comparison of proposed method with other methods used.

REFRENCES	METHOD	ACCURACY
Hari Babu Nandpuru et al [10]	Skull Masking + SVM	84%
Ketan Machhale et al [11]	Skull Masking + SVM-KNN	98%
PROPOSED METHOD	SEGMENTATION + SVM	96%

V. CONCLUSION

This research paper involves using a segmentation technique for the extraction of tumour region in an abnormal image and its classification from normal image using SVM. Results obtained from this method shows that the accuracy attained for classification is 96%. Other advantages of our method are that it is fast and uses small computational power as compared to other methods. For future work, a hybrid SVM algorithm can be used to get better accuracy.

References

[1] http://www.bic.mni.mcgil1.calbrainweb/.

[2] M. F. B. Othman, N. B. Abdullah, N. F. B. Kamal, "MRI brain classification using Support vector machine", IEEE, Centre for Artificial Intelligence & Robotics (CAIRO), University Teknology Malaysia, 2011.

[3] Dr. R J. Ramteke and Khachane Monali Y, "Automatic Medical Image Classification and Abnormality Detection Using K Nearest Neighbor", International Journal of Advanced Computer Research, Volume-2 Number-4 Issue-6 December-20l2.

[4] E. A. El-Dihshan, T. Hosney, A B. M. Salem, "Hybrid intelligence techniques for MRI Brain images classification", ELSEVIER, Digital Signal Processing, Volume 20, pp,433-441, 2010.

[5] Lashkari Amir Ehsan "A Neural Network-Based Method for Brain Abnormality Detection in MR Images Using Zernike Moments and Geometric Moments", UCA-IO.

[6] Chinnu A, "MRI Brain Tumour Classification Using SVM and Histogram Based Image Segmentation", International Journal of Computer Science and Information Technologies, Vol. 6 (2) , 2015, 1505-1508.

[7] K. Somasundaram. T. Kalaiselvi. "Automatic brain extraction methods for TI magnetic resonance images using region labeling and morphological operations", ELSEVIER, Computers in Biology and Medicine 41 (2011) 716-725.

[8] Shweta Jain, "Brain Cancer Classification Using GLCM Based Feature Extraction in Artificial Neural Network", IJCSET, ISSN: 2229-3345, VoL 4 No. 07 JuI2013.

[9] Evangelia I. Zacharaki, Sumei Wang, Sanjeev Chawla, Dong Soo Yoo, Ronald Wolf, Elias R. Melhem, and Christos Davatzikos, "Classification of brain tumour type and grade using MRI texture and shape in a machine learning scheme", PMC 2010 December 1.

[10] Hari Babu Nandpuru, Dr. S. S. Salankar, Vibha Bora, "MRI BRAIN CANCER CLASSIFICATION USING SUPPORT VECTOR MACHINE", 2014 IEEE Students' Conference on Electrical, Electronics and Computer Science.

[11] Ketan Machhale, Hari Babu Nandpuru, Vivek Kapur, Laxmi Kosta, "MRI Brain Cancer Classification Using Hybrid Classifier (SVM-KNN)", 2015 International Conference on Industrial Instrumentation and Control (ICIC) College of Engineering Pune, India. May 28-30,2015.

[12] V.P.GladisPushparathi, S.Palani, "Linear Discriminant analysis for brain tumour classification using Feature Selection",Int. J. Communication and Engineering, vol 5, issue 4 , pp 1179-1185.

[13] Dr.S.Palani, V.P. Gladis Pushpa Rathi, "Detection and characterization of brain tumour using segmentation based on HSOM , Wavelet packet feature spaces and ANN", Ieeeexplore.ieee.org/xpl/freeabstract.jsp/ anumber=5942097(2010).

All Rights Reserved © 2016 IJARECE

ISSN (Print) : 2320-5504

ISSN (Online) : 2347-4793

Asia Pacific Journal of Research
A peer reviewed international Journal
IMPACT FACTOR : 6.58
Print -ISSN -2320 - 5504
Online-E-ISSN - 2347 - 4793

A STUDY OF THE IMPLICATIONS OF PROFESSION ON INVESTMENT BEHAVIOR OF WOMEN ENGINEERS

Priya Kansal

Research Scholar, Department of Humanities,

Delhi Technological University, Delhi

Dr. Seema Singh

Head and Associate Professor, Department of Humanities,

Delhi Technological University, Delhi.

ABSTRACT

The main purpose of this paper is to study the impact of profession on the investment behavior of Women Engineers. Investment behavior includes the investment profile of the investors such as frequency, corpus, experience etc and the behavioral biases. The descriptive type of research is used. Data is collected through a well structured closed ended questionnaire. The five professions of women engineers are chosen viz. core engineering job, teaching, entrepreneurship, administration and research. One sample t-test, chi-square test and one way ANOVA is used for the analysis. The major findings of the study suggest that most of the women engineers are involved in research and development and teaching activities. Profession impact the frequency, corpus and choice of stock. Further, some biases are also impacted by their profession. The main implications of this paper would be for the women investors. The results of this study make them understand that there are many biases due to which their risk and returns varies. These implications would also be important for the policy makers and the portfolio designer who can derive such policy as well as portfolios which lessens the scope of committing biases while investing.

Keywords: *Behavioral Biases, Investment Behavior, Women Engineers.*

Article Classification: G02

1. Introduction

The status of women in India is improving day by day as they are standing with the men at equal level on the basis of their education, their earning capacity, their abilities to accept challenges and taking decisions. Now a days they also have the full support of their family. The general attributes of women such as their patience, less aggressive nature, the humanitarian approach and the ability to be firm in each and every situation make them more successful decision maker at home as well as at work. The women also display the inherent nature of savings. In the ancient time, this saving used to be ideal as women were less aware of the investment option. But with the time as the awareness and importance of investing is improving, women are now more careful about their money and savings. They do regular investments, take risk also and get returns. A plenty of researches are available to discuss the investment behavior of women as investment is proven to be an important activity for the country because it increases the level of country's economy. In developing countries like India investment is even more important because here people,

ISSN (Print) : 2320-5504

ISSN (Online) : 2347-4793

especially women tend to save more and hence invest more. Therefore, the process of investment decision making becomes more important in India. Policy maker, industries, researchers, stock market advisors always look forward to know how women of India invest as women contribute 17% of GDP[1]. They all are interested to know the factors which influence their investment behavior and what are the mistakes committed by them. According to the standard finance, all the investors are rational and have enough capabilities to process each and every information in a rational manner. But the theories of behavioral finance denies the rationality of investors and also proves it with help of the existence of January effect, weekend effect, seasonality etc. Hence it is important to know the reasons behind this irrationality. The evidence of behavioral biases also reflects in the investment behavior of women. Some behavioral biases which reflects in the investment behavior are anchoring, cognitive dissonance, loss aversion, mental accounting, recency/ availability, familiarity, prospect theory, representativeness, hindsight bias, overconfidence, disposition effect, conservatism, endowment effect, herding, self attribution, overconfidence, regret aversion etc. There are many factors which influence their rationality such as, age, marital status, education background, income, profession etc. Besides this, the investment profile of women also cause the variations in the impact of behavioral biases. The present study tries to contribute in the area of behavioral finance by exploring the existence of behavioral biases in the investment behavior of Indian women. It investigates the role of their profession in influencing behavioral biases. Further, for the purpose of study, the researcher has chosen those women who are engineering graduates because they are considered to be more rational by the trait of their education **(Nagarjuna and Mamidenna , 2008).** They take decisions on the basis of facts and figures and not on the basis of emotions **(Moore and Levy, 1951)** also suggested that engineers are practical thinker. Hence the study addresses the following research questions:

i) Are women engineers influenced by behavioral biases?
ii) Is the investment profile of the women engineers influenced by their profession?
iii) Does the influence of behavioral biases change with the change in profession?
iv) Which bias is more prominent in the investment behavior of the women engineers?

For the purpose of finding the answers of the aforesaid questions, a survey has been conducted in Delhi-NCR. With the help of the data collected through the survey, the biases exist in the investment behavior of the women engineers are explored. Further the impact of their profession is studied on the variations in the investment profile and the influence of behavioral biases. Lastly, the most prominent bias in the investment behavior is explored. The main implications of this paper would be for the women investors. The results of this study make them understand that there are many biases due to which their risk and returns varies. These implications would also be important for the policy makers and the portfolio designer who can derive such policy as well as portfolios which lessens the scope of committing biases while investing.

This paper is further divided into five sections. The next sections deals with the discussion of the prior studies related to this topic. Section 3 deals with the research methodology in section. Section 4 is the results and analysis to test the hypotheses. Finally, section 5 deals with the conclusion followed by the scope of future research in next section.

2. Literature Review:

In this paper, we have studied sixteen behavioral biases as the different dimensions of investment behavior. The review of literature is done in two parts. The first part of the literature review consists of the studies which supports the existence of the behavioral biases in investment behavior in reference to the different geographical locations. The second part of the literature deals with the studies which discusses the investment behavior of women.

2.1 Behavioral Biases and their existence:

This part of the literature review deals with the behavioral biases and other irrationalities found in the investment behavior. The recency or availability bias is the tendency of investors to be inclined to the most recent or most easily approachable information (**Tversky and Kaheman, 1974**, **Jahanzeb and Muneer, 2012**). Similarly, when the investor give more weightage to the representative of something rather than logical and relevant facts, the investor is influenced with representative bias. (**Kahneman and Tversky, 1972**; **De Bondt and Thaler, 1990**). According to **Thaler (2008),** when investors put their money into separate mental account, it is known as mental accounting. Investors also have the tendency to follow the mass behavior, known as herd behavior (**Jaiswal and Naela , 2012**). Also, when investors use to sell the stocks whose prices are rising, they are said to be influenced by disposition effect (**Hens and Vlcek, 2011**; **Grinblatt and Keloharju, 2001**). Endowment Effect is the behavioral bias in which people or investors give more importance to the assets which they own and possess rather than the assets which they do not own and possess(**Maddux et al., 2010**; **Harbaugh, Krause, and Vesterlund, 2001**). Further, Prospect theory is the most important theory in the area of behavioral finance. According to this theory, investor' pains due to losses are more than for the happiness for gains **(Tversky and Kahneman, 1981; Kahneman and Tversky, 1979**). Also, the tendency to follow a reference

[1] Source: http://articles.economictimes.indiatimes.com/2015-11-02/news/67953810_1_gender-gap-gender-equality-gdp-growth

ISSN (Print) : 2320-5504

ISSN (Online) : 2347-4793

point or anchor while making investment decision is known as anchoring (**Tversky and Kahneman,1974; Kansal and Singh, 2015**). According to **De Bondt (1998)**, the tendency of investors to overestimate their ability to take decision is known as overconfidence, which leads to self-attribution, in which investors attribute themselves for their success and attribute others or luck for their failures (**Mittal and Vyas, 2009; Mittal, 2010**).

2.2 Investment Behvaior of Women Engineers:

There is always an ongoing debate on the decision making capacity of men and women. This debate is also continued in the investment decision making, for example, **Ramanujam and Devi (2012)** find out that the married women trade more in comparison to single women. Karmakar (2001) reported the same results with the sample of rural investors of the West Bengal, India. Models of investor overconfidence predicted that, since men are more overconfident than women, men trade more and perform worse than women. **Richard & Kim (2006)** suggested through laboratory settings, the risk tolerance can also vary due to group effects. The investrs, especially males respond in a different way if they are with the group. **Herrmann (2007)** provided the estimation results and discussed the facts that supported the initial hypotheses regarding the roles of race/gender in investment preferences. Using multiple specifications and leveraging multiple risk/return measures, the evidence pointed to significant effects with respect to both race and gender. **Croson & Gneezy (2009)** reviewed various of studies that demonstrated how strongly and in what direction social preferences manifest themselves in men and in women. **Shanmugsundaram and Balakrishnan (2011)** found that age, gender, income and education affect investors' preference and attitudes towards investment decisions. **Shaikh and Kalkundrikar (2011)** argued that the factors influencing investors' investment decisions are based on various demographic factors like age, gender, marital status, level of income, level of market knowledge, educational qualification and the number of dependents. Further according to **Ton (2014)** men are prone to be more willing to take risks than women in trading and this result is also proved by **Barber and Odean (2001)**; **Wood and Zaichkowsky (2004)**. These studies suggest that men are often overconfident and trade with a larger volume than women. **Lunderberg, Fox and Puncochar (1994)** also illustrated that men are often more confident than women in trading stock. Although both men and women have the same understanding, the feeling often influences on men's decision making, (**Prince, 1993; Lunderberg, Fox, & Puncochar, 1994**). Besides, due to the characteristics of Vietnamese, women often play an important role in families' spending, so they have to consider carefully in trading stock to minimize the cost and to avoid risks and be unwilling to take risks.

Graham et.al.(2002) found that while men tend to be focused on results, goal directed and single minded with higher risk tolerance levels as well as high overconfidence levels, women, on the other hand, are multi-focussed, process driven, less tolerant of risk and less prone to over confidence. **Davar and Gill (2007)** concluded after an intensive statistical enquiry that females have lower levels of awareness, lower confidence levels and lower risk tolerance capacities and hence are more cautious vis-à-vis males with regard to prospective investment in equity (risky) securities, especially if fund availability is low.

3. Research Methodology:

3.1 Survey Design and sample composition:

A well-structured questionnaire on 5-point LIKERT Scale was designed to collect the data. The questionnaire is distributed to around 200 women engineers involve in different profession viz. are core engineers job, teaching, administration, entrepreneurship and researcher. The criteria used for sample selection was as follows:

i) Respondent should be the resident of Delhi-NCR
ii) Respondent should be engineering graduates.
iii) Respondent should have at least one year experience in stock market.
iv) Respondent should be either core women engineers, teacher, administrator, researcher or entrepreneur by profession and women engineers by education.

Since the size of population is not decided in this study, a snowball sampling technique is used to collect the data. Out of 200 distributed questionnaires, 136 filled questionnaires were received. Out of 136, 14 questionnaires will incomplete and hence discarded.

3.2 Survey Instrument:

The structured questionnaire consists of three sections. The first section consists of the socio-demographic profile of the women investors. Section two measures the investment profile of the women investors. Further, section three consists of scenario based questions measured on 5 Point LIKERT Scale. These questions are designed in a way that helps the respondents to relate themselves with the hypothetical stock market. This section helps the researcher to identify the biases exist in the investment behavior of women investors.

ISSN (Print) : 2320-5504

ISSN (Online) : 2347-4793

3.3 Statistical Tests:

To explore the answers of the research questions mentioned in section one, following statistical tests are conducted:

i) Chi-square test- Chi-square test is used when the independent and dependent variables are categorical. In the present study, this test is used to identify whether the investment profile of the women investor is independent of their profession or not.

H_0: There is no association between the profession and the investment profile of the women engineers.

H_1: There is an association between the profession and the investment profile of the women engineers.

ii) One sample t-test- This test is used to identify the existence of behavioral biases among the investment behavior. For the purpose of comparing the responses of all women engineers, the value assigned to most rational response is taken. The hypothesis is as follows:

H_0: All the women engineers behave rationally while investing i.e. there is no significant difference between the actual response and the most rational response viz. 5.

H_1: All the women engineers do not behave rationally while investing i.e. there is a significant difference between the actual response and the most rational response viz. 5.

iii) One way ANOVA- One way ANOVA is used to identify the differences in the mean responses of two or more groups. Here, in the present study, this test is used to identify the impact of profession on the several behavioral biases. The hypothesis set for the purpose is as follows:

H_0: There is no significant impact of profession on behavioral biases.

H_1: There is a significant impact of profession on behavioral biases.

iv) Ranking of the Behavioral Biases- For the purpose of identifying the most prominent bias exist among the women engineers, the ranking of each bias is done according to the responses selected by the respondents. The behavioral biases are ranked according to the mean value of the responses. The lower the mean, the more prominent the bias because as per the structure of the questionnaire, if the respondent select the least response, she is most influence by the bias. Hence the bias, which has the least mean score, influence most to the women engineers while investing and thus most prominent.

3.4 Limitations:

Although the researcher has tried to do a meaningful research with the aim to imply the results to every stakeholder of the study, yet the study has some limitations:

- Due to the time constraint, the research focuses only on the behavior of women engineers in Delhi NCR Area. It is necessary to have further research for all over the country and also for more professional.
- There are no. of factors remain untouched in this study which can have the significance influence on the behavioral biases such as personality of the investor, financial literacy etc.
- Only sixteen biases are studied in this research, there are other biases also which are detected by the other researchers in foreign stock exchanges. Those biases can also be studied in the reference of Indian Stock market.
- Moreover, this study can also be accompanied the evaluation of the presence of the sixteen biases in Indian stock market with the help of secondary data.
- This study attempts to study the variations in behavior due to the profession of the investors having same educational background. The women engineers can be compared with the other professionals.

4. **Results and Interpretations**:

This section represents the results of the statistical test used to test the various hypotheses. The results are based on the responses selected by the women engineers.

4.1 Results of Cronbach's Alpha:

Reliability analysis is conducted to test the internal consistency of each bias. Table 1 shows the results of reliability analysis.

ISSN (Print) : 2320-5504

ISSN (Online) : 2347-4793

Table 1: Reliability Analysis

Construct	No. of Items	Cronbach's Alpha
Anchoring Bias	2	0.694
Cognitive Dissonance	2	0.83
Conservatism	2	0.637
Prospect Theory	2	0.662
Loss Aversion	2	0.61
Endowment Effect	1	-
Hindsight Bias	2	0.623
Herding Bias	2	0.763
Mental Accounting	3	0.771
Overconfidence	2	0.69
Self-Attribution	2	0.665
Recency Bias	2	0.63
Disposition Effect	1	-
Regret Aversion	2	0.611
Representativeness	1	-
Familiarity Bias	1	-

Source: Author's Compilation

The results shows that the value of Cronbach's alpha of items pertaining to anchoring bis, cognitive dissonance, conservatism, prospect theory, loss aversion, hindsight bias, herding bias, mental accounting, overconfidence, self attribution and regret aversion is greater than the benchmark value of 0.60, which make them a consistent scale. However, the Cronbach's alpha can not be calculated for endowment effect, disposition effect, representativeness and familiarity bias because these construct consists of only one item. Further, when the internal consistency of the full scale is calculated, the Cronbach's alpha 0.846, which is strongly acceptable.

4.2 Frequency Distribution of the respondents:

This section presents the frequency distribution of 122 respondents according to the seven socio-demographic factors taken into consideration. Also, this section provides the frequency distribution of the respondents as per their investment profile.

Table 2: Frequency Distribution of Respondents

Summary Statistics	Count	Percentage
Marital Status		
Married	89	73
Single	33	27
Age Group		
25-30	43	35.2
31-40	69	56.6
41-50	9	7.4
50 Above	1	0.8
No. of Dependents		
No Dependents	36	29.5
1-3	83	68
More than 3	3	2.5

ISSN (Print) : 2320-5504

ISSN (Online) : 2347-4793

Earning Capacity		
Primary Earner	21	17.2
Secondary Earner	101	82.8
Profession		
Job	16	13.1
Administrator	15	12.3
Entrepreneur	8	6.6
Teacher	37	30.3
Scientist	46	37.7
Qualification		
B. Tech/B.E.	24	19.7
M.Tech/M.E.	43	35.2
B.Tech, MBA	17	13.9
B.Tech, M,Tech, PhD	38	31.1
Annual Income		
Below Rs.5,00,000	14	11.5
Rs.5,00,000-Rs.8,00,000	57	46.7
Rs.8,00,000-Rs.10,00,000	28	23
Rs.10,00,000-Rs.12,00,000	8	6.6
Rs.12,00,000-Rs.15,00,000	8	6.6
More than 15,00,000	7	5.7
Investment frequency		
Once in a Year	64	52.5
Once in a Month	42	34.4
Once in a week	5	4.1
Daily	3	2.5
Others	8	6.6
Investment Corpus		
Less than 50,000	95	77.9
50,000-2,00,000	23	18.9
2,00,000-5,00,000	4	3.3
Time Horizon		
Less than one Year	57	46.7
1-3 years	35	28.7
3-5 years	15	12.3
More than 5 Years	15	12.3

ISSN (Print) : 2320-5504

ISSN (Online) : 2347-4793

Investment Experience		
Less than 2 Years	58	47.5
2-5 Years	41	33.6
5-10 Years	23	18.9
Choice of Stock		
Large Cap	35	28.7
Mid Cap	57	46.7
Small Cap	30	24.6

Source: Author's compilation

Results of chi-square Test:

The association between the profession and investment profile is identified with the help of chi-square test. In total, the dependence is detected with the five variables of investment profile. These factors are investment frequency, investment corpus, time horizon, investment experience and the choice of the stock. The findings of the test are summarized in Table 3. The results of chi-square test shows that investment frequency, investment corpus and choice of stock is associated with profession, where as the time horizon and investment experience is independent of profession.

Table 3: Results of chi-Square test

Variable in Investment profile	chi-square value	Sig.
Investment frequency	36.841	0.002**
Investment Corpus	15.816	0.045*
Time Horizon	11.015	0.201
Investment Experience	20.519	0.058
Choice of Stock	35.061	0.000**

*Source: Author's compilation; * significant at 5% level, ** significant at 1% level*

Further, Table 4 shows that the women engineers who are in core engineering job, administration, and entrepreneurship have more investment frequency. They invest in stock market once in a month. However, the women engineers who are engaged in teaching and research are less active in market. They usually invest on yearly basis. Table 4 also shows that the women engineers usually prefer to invest less than Rs.50000 quarterly. Also, when it comes to the choice of stock, Table 4 suggest that, the women engineers engaged in core engineering job prefer large cap stocks for the investments, administrators, entrepreneurs, teachers prefer to invest in mid cap stocks where as scientist prefer small cap stocks for the investment.

Table 4: Profession wise Investment Corpus

Profession	Most Preferred Investment Frequency	Most Preferred Investment Corpus	Most Preferred Type of stock
Job	Once in a month	Less Than 50000	Large Cap
Administrator	Once in a month	Less Than 50000	Mid Cap
Entrepreneur	Once in a month	Less Than 50000	Mid Cap
Teacher	Once in a Year	Less Than 50000	Mid Cap
Scientist	Once in a Year	Less Than 50000	Small Cap

Source: Author's compilation

ISSN (Print) : 2320-5504

ISSN (Online) : 2347-4793

Results of One Sample t-test

The one sample t-test is performed to explore the existence or non existence of behavioral bias among the women engineers. For the purpose of test value, the value assigned to the most rational response (5) is chosen. This value represents the non existence of behavioral bias in the investment behavior of women engineers. The results of one sample t-test are represented in Table 5.

Table 5: Results of One-Sample t-test

Biases	Mean	SD	t-statistics	df	Sig. (two-tailed)
Anchoring Bias	2.3150	.94714	-63.389	499	0.000
Cognitive Dissonance	2.3500	.74808	-79.211	499	0.000
Conservatism	2.4460	.92834	-61.518	499	0.000
Prospect Theory	2.3730	.94666	-62.051	499	0.000
Loss Aversion	2.6440	.85950	-61.293	499	0.000
Endowment Effect	2.4880	1.08268	-51.880	499	0.000
Hindsight Bias	3.0690	.76019	-56.799	499	0.000
Herding Bias	3.1680	.92438	-44.316	499	0.000
Mental Accounting	2.3580	.66101	-89.374	499	0.000
Overconfidence	2.6440	.82074	-64.188	499	0.000
Self-Attribution	2.3440	.75485	-78.677	499	0.000
Recency Bias	2.4750	.79947	-70.623	499	0.000
Disposition Effect	2.4000	1.02474	-56.734	499	0.000
Regret Aversion	2.6890	.85630	-60.348	499	0.000
Representativeness	2.4060	.89821	-64.577	499	0.000
Familiarity Bias	2.2720	.90091	-67.709	499	0.000

Source: Author's Compilation

These results are in the line of previous finding such as **Fama (1970)** and **Statman (2012)** which states that people investing in stock market are not rational in their decision making. The present study finds that the women engineers are also anchored (**Sudgen et. al ,2013**), suffering from cognitive dissonance (**Pompain, 2006**), conservative to update their beliefs (**Chen, Chin & Liu 2009**), prioritize losses over gains **(Kahneman and Tversky, 1979**), loss averse (**Berkelaar and Kouwenberg, 2008; Coval and Shumway, 2005**), give more value to the owned asset (**Kahneman et. al, 1990**), overrate their capacity to predict the future events (**Monti and Legranzi,2009**), follow herd (**Economou, Kostakis and Philippas, 2010**), have several mental accounts (**Thaler, 2008**), attribute themselves for their success **(Mittal,2010**), give more preference to recent information **(Lee et.al., 2007),** quick in disposing the gains (**Chen et.al,2007**) and regret on their wrong decision (**Pompain,2006**). These women engineers are also show representativeness (**Gilovich, 1981**) and familiarity (**Abreu et al., 2011**).

Result of One Way ANOVA:

The five categories of profession are tested for studying the impact of profession on the behavioral biases. The five categories of the profession taken into consideration are engineers doing job, administrators, entrepreneur, teacher and scientists. One way ANAVA is used to test whether the engineers differ due to profession in terms of behavioral biases. The results are shown in Table 6. These results indicate that out of sixteen biases, eight biases are significantly impacted by profession. The profession of women engineers significantly influence their investment behavior in terms of anchoring bias *[F (4,495)=6.135, p= 0.000]*, prospect theory *[F (4,495)=2.465, p= 0.044]*, loss aversion *[F (4,495)=3.934, p= 0.004]*, hindsight bias *[F (4,495)=3.976, p= 0.003]*, self-attribution *[F (4,495)=3.676, p= 0.006]*, recency bias *[F (4,495)=2.672, p= 0.032]*, disposition effect *[F (4,495)=3.697, p= 0.006]* and Familiarity bias *[F (4,495)=2.23, p= 0.031]*

ISSN (Print) : 2320-5504

ISSN (Online) : 2347-4793

Table 6: Results of One way ANOVA

Behavioral Biases	Professions					$F_{(4,495)}$
	Job (N=16)	**Administration (N=15)**	**Business (N=8)**	**Teacher (N=37)**	**Scientist (N=46)**	
Anchoring Bias	1.96[a] (0.84)	2.6[b] (0.97)	2.32[b] (0.89)	2.34[b] (0.94)	2.37[b] (1)	6.135**
Cognitive Dissonance	2.21 (0.79)	2.34 (0.72)	2.44 (0.72)	2.37 (0.74)	2.41 (0.77)	1.357
Conservatism	2.29 (0.81)	2.64 (1.02)	2.58 (0.88)	2.39 (0.92)	2.34 (0.96)	2.677
Prospect Theory	2.16[a] (0.9)	2.55[b] (0.93)	2.45[a,b] (0.85)	2.32[a,b] (0.96)	2.4[a,b] (1.05)	2.465*
Loss Aversion	2.4[a] (0.83)	2.81[b] (0.83)	2.69[a,b,c] (0.86)	2.55[a,b,c] (0.83)	2.78[b,c] (0.89)	3.934**
Endowment Effect	2.24 (0.99)	2.46 (1.07)	2.55 (1.07)	2.58 (1.16)	2.61 (1.11)	1.922
Hindsight Bias	3.22[a] (0.66)	3.15[a,b,c] (0.87)	3.17[a,b,c] (0.76)	2.9[b] (0.71)	2.92[b,c] (0.73)	3.976**
Herding Bias	3.14 (0.96)	3.28 (1)	3.15 (0.97)	3.07 (0.84)	3.21 (0.83)	0.707
Mental Accounting	2.36 (0.74)	2.36 (0.69)	2.44 (0.66)	2.36 (0.59)	2.27 (0.62)	0.859
Overconfidence	2.52 (0.91)	2.68 (0.82)	2.77 (0.82)	2.64 (0.78)	2.62 (0.76)	1.29
Self-Attribution	2.11[a] (0.83)	2.49[b] (0.76)	2.37[a,b,c] (0.72)	2.36[a,b,c] (0.7)	2.4[b,c] (0.73)	3.673**
Recency Bias	2.26[a] (0.73)	2.58[b] (0.94)	2.46[a,b,c] (0.76)	2.51[a,b,c] (0.72)	2.57[b,c] (0.81)	2.672*
Disposition Effect	2.66[a] (1.12)	2.18[b] (0.93)	2.32[a,b] (1.04)	2.54[a,b] (0.94)	2.3[a,b] (1.03)	3.697**
Regret Aversion	2.73 (0.87)	2.51 (0.88)	2.65 (0.89)	2.78 (0.79)	2.79 (0.83)	1.814
Representativeness	2.24 (0.84)	2.44 (0.94)	2.44 (0.9)	2.46 (0.91)	2.45 (0.89)	1.077
Familiarity Bias	2.25[a,b] (0.95)	2.15[a] (0.82)	2.21[a,b] (0.96)	2.5[b] (0.93)	2.25[a,b] (0.82)	2.23*

*Source: Author's Compilation; Note: *significant at 5%; numbers within parentheses shows the value of standard deviation; any common superscripts do not differ significantly.*

Further, to test the nature of differences among the five different categories of professions in which women engineers are engaged, post – hoc comparison is conducted using Tukey HSD.

i) Anchoring Effect: Post hoc results showed that the women engineers who were in core engineering job (M=1.96, SD=0.8) behave differently and more anchored than the women engineers who were engaged in any other profession such as administration (M=2.60, SD== 0.97), entrepreneurship (M=2.32, SD=0.89), teaching (M=2.34, SD=0.94) and research and development (M=2.37, SD=1.00). The reason is can be detected from Table 6 where we find that the people who are doing job are youngest. According to the study done by **Kornotis and Kumar (2008)**, rationality increases with the age.

ii) Prospect Theory: Results indicate that there is a significant difference between the influence of prospect theory on the women engineers involved in core engineering jobs and administration. The core women engineers *(M=2.16, SD=*

ISSN (Print) : 2320-5504

ISSN (Online) : 2347-4793

0.9) are more influence by prospect theory than the administrators *(M=2.55, SD = 0.93)*. However, the other professional do not have any significant impact on prospect theory.

iii) Loss Aversion: Post hoc results showed that the women engineers who were involve in core engineering job (M=2.40, SD=0.83) behave differently and more loss averse than the women engineers who were engaged in administration (M=2.81, SD== 0.83) and research and development (M=2.78, SD=0.89).

iv) Hindsight Bias: Post hoc results show that the women engineers who were in core engineering job (M=3.22, SD=0.66) behaved differently and were affected more by hindsight bias than the women engineers who were engaged in teaching (M=2.90, SD== 0.71) and research and development (M=2.92, SD=0.73)

v) Self-Attribution: According to the statistics of Tukey HSD, there is a significant difference between the level of self-attribution of the women engineers involved in core ing jobs (M= 2.11, SD=0.83) and administration (M=2.49, SD= 0.76). Further, there is also a significant difference between the core women engineers and the entrepreneurs *(M=2.37, SD = 0.72)*. However, the other professional do not have any significant impact on self-attribution.

vi) Recency Bias: According to the Table 6 of Tukey HSD, there is a significant difference between the women engineers involved in core engineering jobs (M= 2.26, SD=0.73) and administration (M=2.58, SD= 0.94). Further, there is also a significant difference between the core engineers and the scientists *(M=2.57, SD = 0.81)*. Taken up together, core engineers rely more on recent information than the administrators and scientists. However, the other professional do not have any significant impact on recency bias.

vii) Disposition Effect: The results of Tukey HSD indicate that there is a significant difference between the engineers involved in core engineering jobs (M= 2.66, SD=1.12) and administration (M=2.18, SD= 0.93). Further, there is also a significant difference between the core engineers and the scientists *(M=2.30, SD = 1.03)*. Taken up together, core engineers have fewer tendencies to dispose their gains from the portfolio than the administrators and scientists. However, the other professional do not have any significant impact on disposition effect.

viii) Familiarity Bias: Table 6 shows that there is a significant different between the administrators (M=2.15, SD=0.82) and teachers (M=2.5, SD=0.82). The administrators have more tendencies to invest in the familiar stocks than the teachers.

Results of Rank Test:

The responses of the women engineers are captured on 5 Point LIKERT Scale for various hypothetical stock market conditions. The scale varies from Strongly Agree (1) to Strongly Disagree (2). According to the nature of the statement, provided to them, if the response chosen by any women engineer is 1, she is strongly biases and vice versa. For the purpose of exploring the most prominent bias, the mean responses of each bias is calculated and then ranked. The bias which has the lowest mean is the most prominent bias in the investment behavior of investors. The result of rank test is as follows:

Table 7: Ranking of Behavioral Biases

Behavioral Bias	N	Mean	SD	Rank
Familiarity Bias	122	2.27	0.9	1
Anchoring Bias	122	2.32	0.95	2
Self Attribution	122	2.34	0.75	3
Cognitive Dissonance	122	2.35	0.75	4
Mental Accounting	122	2.36	0.66	5
Prospect Theory	122	2.37	0.95	6
Disposition Effect	122	2.4	1.02	7
Representativeness	122	2.41	0.9	8
Conservatism	122	2.45	0.93	9
Recency Bias	122	2.48	0.8	10
Endowment Effect	122	2.49	1.08	11
Loss Aversion	122	2.64	0.86	12
Overconfidence	122	2.64	0.82	13
Regret Aversion	122	2.69	0.86	14
Hindsight Bias	122	3.07	0.76	15
Herding Bias	122	3.17	0.92	16

Source: Author'

ISSN (Print) : 2320-5504

ISSN (Online) : 2347-4793

From Table7, it can be concluded that women engineers are mostly influenced by familiarity bias (M=2.27, SD=0.90), followed by anchoring (M=2.32. SD=0.95), self attribution bias (M=2.34, SD= 0.75), cognitive dissonance (M=2.35, SD=0.75), mental accounting (M=2.36, SD=0.66), prospect theory (M=2.37, SD=0.95), disposition effect (M=2.40, SD=1.02), representativeness (M=2.41, SD=0.90), conservatism (M=2.45, SD=0.93), recency bias (M=2.48, SD=0.80), endowment effect (M=2.49, SD=1.08), overconfidence (M=2.64, SD=0.82), loss aversion (M=2.64, SD=0.86), regret(M=2.69, SD=0.86), hindsight (M=3.07, SD=0.76) and herding (M=3.17, SD=0.92).

5. Conclusions and Implications:

The global stock markets are experiencing the major turbulent and so the Indian stock market. There are major swings and changes happened in Indian stock market sometimes due to global stock markets and sometimes due to investors' behavior. Hence it is very important to study the investment behavior. Further, with the changing position of women in India, now they are actively participating in investment decision making and hence the research should be done in isolation on the various aspects of investment decision making of women. This study is an attempt to study the various aspect of the investment behavior of women engineers. The study reveals that women engineers are engaged majorly in teaching and research. The investment frequency, investment corpus and choice of stock are dependent on their profession. The women investors who are engaged in job, administration and entrepreneurship are more active than the other professional like teaching and research. . Similarly, the women engineers who are in job prefer to invest in large cap stock, who are in teaching, administration and business prefer to invest in mid cap. However, the women engineers who are engaged in research usually invest in small cap. But, it is also important to note that whatever the frequency and choice of stock, women engineers prefer to invest the least amount in the stock market. Further, there is no study which has compared five professions simultaneously, yet the study done by Rastogi (2015) support the findings of the present study. Rastogi (2015) investigated the influence of occupation (salaried and business men) on overconfidence, self attribution, overreaction, anchoring, loss aversion and framing effect, where he finds that there is no impact of occupation on overconfidence, self attribution, framing biases. In the present study also, there is no impact of profession on overconfidence and self-attribution. However, Rastogi (2015) also concluded that influence of anchoring bias do not differ significantly among the occupation, which do not support the present study. Also he investigated that occupations are significantly different in terms of loss aversion which is also true in the present study. The main implications of this paper would be for the women investors. The results of this study make them understand that there are many biases due to which their risk and returns varies. These implications would be also important for the policy makers and the portfolio designer who can derive such policy as well as portfolios which lessens the scope of committing biases while investing.

References:

1. Abreu, M., V. Mendes, J. Santos (2011), "Home Country Bias: Does Domestic Experience Help Investors Enter Foreign Markets?", *Journal of Banking and Finance* Vol.35 No..9, pp. 2330-2340.
2. Berkelaar, A and Kouwenberg, R (2008), "From Boom till Bust: How Loss Aversion Affects Asset Prices", *SSRN Working Paper*, viewed on 03 January 2014, http://papers.ssrn.com/sol3/papers.cfm?abstract_id=229548.
3. Chen. H.W, Chin S.W. & LiuV.W, (2009), The conservatism bias in an emerging stock market: Evidence from Taiwan, *Pacific Basin Finance Journal*, Vol.17, pp 494-505.
4. Coval, JD and Shumway, T (2005), "Do Behavioral Biases Affect Prices?", *The Journal of Finance*, vol. 60, no. 1, pp. 1-34.
5. Croson, R., & Gneezy, U. (2009), "Gender Differences in Preferences" *Journal of Economic Literature*, 448-474.
6. Davar, YP and Gill, S (2007), "Investment decision making: an exploration of the role of gender", *Decision*, vol. 34, no. 1, pp. 95-120.
7. De Bondt, W. M. M. and R. H. Thaler (1990), "Do security analysts overreact?" *American Economic Review*, Vol.80 No.2, pp. 52-57.
8. De Bondt, W. F. M. (1998), "A portrait of the individual investors", *European Economic Review*, Vol. 42 (3-5), pp. 831-844.
9. Fama.F, (1970), "Efficient capital markets: A review of theory and empirical work", *Journal of Finance*, Vol.25 No.2, pp. 383-417.
10. Graham, J. F., Stendardi, E. J., Myers, J. K., & Graham, M. J. (2002), "Gender differences in investment strategies: an information processing perspective." *International journal of bank marketing*, Vol. 20 No. 1, pp.17-26. http://dx.doi.org/10.1108/02652320210415953
11. Grinblatt, M. and M. Keloharju (2001) "What makes Investors trade?" *Journal of Finance*. Vol.56, No.2, pp 589-616.
12. Harbaugh, W. T., K. Krause, and L. Vesterlund (2001), "Are adults better behaved than children? Age, experience, and the endowment effect." *Economics Letters*, Vol.70 No.2, pp. 175-181.
13. Hens, T. and M. Vlcek (2011), "Does prospect theory explain the disposition effect?" *Journal of Behavioral Finance*, Vol. 12 No. 3, pp. 141-157.
14. Herrmann, A. F. (2007), "People Get Emotional About Their Money: Performing Masculinity in a Financial Discussion Board", *Journal of Computer-Mediated Communication*, Vol. 12 pp. 499–522. doi: 10.1111/j.1083-6101.2007.00335.x

ISSN (Print) : 2320-5504

ISSN (Online) : 2347-4793

15. Hoang Thanh Hue Ton, T. M. (2014), "The Impact of Demographical Factors on Investment Decision: A Study of Vietnam Stock Market", *International Journal of Economics and Finance* , Vol. 6 No.11.
16. Jahanzeb, A. and S. Muneer. (2012), "Implication of behavioral finance in investment decision making process", *Information Management & Business Review,* Vol. 4 No.10 pp. 532-536.
17. Gilovich, T. (1981), "Seeing the Past in the Present: The Effect of Associations to Familiar Events on Judgments and Decisions", *Journal of Personality and Social Psychology,* Vol. 40, pp. 797-808.
18. Kahneman, D., J. Knetsch, and R. Thaler (1990), "Experimental test of the endowment effect and the coase theorem", *Journal of Political Economy*, Vol. 98 No. 6, pp. 1325-1348.
19. Kahneman, Daniel; Tversky, Amos (1979), "Prospect theory: An analysis of decision under risk", *Econometrica*, Vol. 47, pp. 263-291.
20. Jaiswal, B. and K. Naela. (2012), "Gender, Behavioral finance and the Investment decision". *IBA Business Review,* Vol. 7 No. 2, pp.8-22.
21. Kahneman, Daniel; Tversky, Amos (1972), "Subjective probability: a judgment of representativeness" *Cognitive Psychology*, Vol 3, pp. 430-454.
22. Kansal, P. and Singh Seema (2015). "Anchoring Effect in Investment: A Systematic Literature Review", *Asia Pacific Journal of Research,* Vol.1 No.32, pp. 17-27
23. Korniotis, George M., and Kumar Alok (2008), "Do Portfolio Distortions Reflect Superior Information or Psychological Biases?" Working Paper, University of Texas at Austin.
24. Lee, Y.-J., Wang, G.-L., Kao, K.-S., Chen, C.-Y., & Zhu, F.-P. (2010), "The Investment Behavior, Decision Factors and Their Effects". *Journal of Global Business Management* , Vol. 6 No.2, pp. 1-12.
25. Lundeberg, M. A., Fox, P. W., & Punccohar, J. (1994). "A Critique of "Highly Confident but Wrong: Gender Differences and Similarities in Confidence Judgments", *Journal of Educational Psychology*, pp. 114–121. http://dx.doi.org/10.1037/0022-0663.86.1.114
26. Maddux, W. W. , H. Yang, C. Falk, H. Adam, W. Adair, Y. Endo, Z. Carmon and S. J. Heine. (2010), "For whom is parting with possessions more painful? Cultural differences in the endowment effect", *Psychological Science,* Vol. 21 No.12, pp. 1910–1917.
27. Mittal, M. (2010). "Study of differences in behavioral biases in investment decision-making between the salaried and business class investors". I*UP Journal of Behavioral Finance*, Vol.7 No. 4, pp. 20-34.
28. Mittal, M. and R. K. Vyas. (2009), "Does irrationality in investment decisions vary with income?" *The ICFAI University Journal of Behavioral Finance*, Vol. 6 No.1, pp. 26-42.
29. Moore, H.B., & Levy, S.L. (1951), "Artful contrivers: A study of engineers", *Personnel*, Vol.23, pp.148-153.
30. Monti M., and Legrenzi P., (2009), "Investment decision making and hindsight bias". *Annual meeting of cognitive science society.* Amsterdam
31. Nagarjuna, Laxmi, V. and Mamidenna Sireesha (2008), "Personality Characteristics of Commerce and Engineering Graduates- A Comparative Study", *Journal of Indian Academy of Applied Psychology,* Vol.34 No.2, pp. 303-308.
32. Pompian, M.M. (2006), *Behavioral Finance and Wealth Management,* John Wiley & Sons, Inc. Hoboken, NJ.
33. Prince, M. (1993). "Women, Men, and Money Styles", *Journal of Economic Psychology*, pp. 175–182. http://dx.doi.org/10.1016/0167-4870(93)90045-M
34. Ramanujam, V., & Devi, K. C. (2012), "A study on impact of socio-economic profile on investment pattern of salaried and business people in Coimbatore city" *International Journal of Management & Information Technology*, Vol.2 No.1, pp. 67-77.
35. Rastogi Shailesh (2015), "Differences in Behavioral Biases in Investment Decision making: Gender and Occupation Perspective", *Journal of International Business and Economy, Vol.*16 No.1, pp. 13-25
36. Ronay., Richard.,& Kim, Do-Yeong. (2006). "Gender differences in explicit and implicit risk attitudes: A socially facilitated phenomenon", *British Journal of Social Psycholog*,Vol. 45, pp. 397-419.
37. Shaikh, A. R. H., & Kalkundrikar, A. B. (2011b) "Impact on demographic factors on retail investors' investment decisions - An exploratory study" *Indian Journal of Finance*, Vol. 5 No.9, pp. 35-44.
38. Shanmugasundaram, V., & Balakrishnan, V. (2011) "Investment decisions-Influence of behavioural factors", *Indian Journal of Finance*, Vol. 5 No.9, pp. 25-34.
39. Statman, M, "Rational is Stupid" (2012), viewed 2 February 2014, http://blogs.cfainstitute.org/investor/2012/10/16/rational-is-stupid-learn-the-science-ofinvesting-to-be-a-normal-smart-investor-meir-statman/.
40. Sugden, R. and Zheng, J., Zizzo, D.J. (2013), "Not all anchors are created equal" *Journal of Economic Psychology*, Vol. 39, pp. 21-31.

ISSN (Print) : 2320-5504

ISSN (Online) : 2347-4793

41. Tversky, A and Kahneman, D (1974), "Judgment under Uncertainty: Heuristics and Biases", *Science*, vol. 185, no. 4157, pp. 1124-1131.
42. Thaler, R. H. (2008), "Mental accounting and consumer choice" *Marketing Science*, Vol. 27 No.1, pp. 15-25.
43. Tversky, A. and D. Kahenman (1981), "The framing of decision and psychology of choice", *Science*, Vol. 211 No.4481, pp.435-458.
44. Wood, R., & Zaichkowsky, J. L. (2004). "Attitudes and trading behavior of stock market investors: a segmentation approach" *Journal of Behavioral Finance*, Vol.5, No.3, pp.170–17. http://dx.doi.org/10.1207/s15427579jpfm0503_5.

ResearchGate

See discussions, stats, and author profiles for this publication at: https://www.researchgate.net/publication/294891946

Channel Capacity of Different Adaptive Transmission Techniques over Log-Normal Shadowed Fading Environment

Conference Paper · March 2016

DOI: 10.13140/RG.2.1.1330.0884

READS

21

3 authors, including:



P. K. Verma

Delhi Technological University

4 PUBLICATIONS **2** CITATIONS

SEE PROFILE



Priyanka Jain

Delhi Technological University

9 PUBLICATIONS **16** CITATIONS

SEE PROFILE

All in-text references underlined in blue are linked to publications on ResearchGate, letting you access and read them immediately.

Available from: P. K. Verma
Retrieved on: 07 June 2016

Proceedings of the 10th INDIACom; INDIACom-2016; IEEE Conference ID: 37465
3rd 2016 International Conference on "Computing for Sustainable Global Development", 16th – 18th March, 2016
Bharati Vidyapeeth's Institute of Computer Applications and Management (BVICAM), New Delhi (INDIA)

Channel Capacity of Different Adaptive Transmission Techniques over Log-Normal Shadowed Fading Environment

P. K. Verma
Department of Electronics & Communication Engineering,
Delhi Technological University, New Delhi, India
vermapk87@gmail.com

Priyanka Jain
Department of Electronics and Communication Engineering,
Delhi Technological University, New Delhi, India
priyajain2000@rediffmail.com

Sanjay Soni
Department of Electronics and Communication Engineering,
G. B. Pant Engineering College, Pauri, UK, India
sanjoo.ksoni@gmail.com

R. S. Raw
Department of Computer Science and Engineering,
Ambedkar Institute of Advance Communication Technologies and Research, New Delhi, India
rsrao08@yahoo.in

***Abstract* - Channel capacity is an important parameter to analyses the performance of wireless communication. To model the shadowing effect of the wireless channel, lognormal distribution is widely used. In this paper, our aim to develop the closed-form expression of average channel capacity of slow fading channel categorized by the log-normal distribution. The channel capacity in closed form expression for four different adaptive transmission schemes such as optimal power and rate adaption, channel inversion with fixed rate optimal rate adaption and truncated channel inversion with fixed rate are derived using Holtzamn approximation. The channel capacity results are compared under light and heavy shadowing condition and some interesting observations are made.**

Keywords* - *Log-normal Distribution; Probability Distribution Function; Holtzman Approximation; Channel Capacity; Channel Side Information

I. INTRODUCTION

The analysis of channel capacity (CC) under log-normal shadowed fading environment for different transmission schemes is an important measurement for the valuation of the transmission rate that the transmission medium or channel can sustenance with slight probability of error [1-5]. So, channel capacity preserves the very imperative character in small scale and large scale fading environment. There are several classifications of channel capacity, present in the literature for different type of fading environments i.e. for multipath fading and shadowing [1-4, 6]. In the wireless communication, log-normal distribution is widely used model to capture the phenomenon called shadowing [6, 7], indoor fading environment which is having fading envelope probably similar as log-normal probability distribution function and ultra wideband slow fading shadowed transmission channel [8].

The channel capacity mostly depends on characteristics of the transceiver i.e. what type of parameters are known to the transmitter and receiver, considering different scenario regarding this knowledge. Channel capacity is defined for different adaptive transmission techniques/schemes for the flat fading channel [9], such as optimal power and rate adaption, optimal rate adaption, channel inversion with fixed rate and truncated channel inversion with fixed rate. In this work, mathematical expression of these adaptive transmission channel capacity over lognormal shadowing environment is obtained using the approximation named Holtzman approximation [10], which gives the simple expression as a sum of in three terms.

The main involvement of paper is to formulate accurate and simple expressions of capacity for ORA, OPRA, TIFR and CIFR. The representation of this paper is as tracks. In Section 2, we present the system and channel model for log-normal shadowed fading environment and explain about Holtzman approximation, Channel capacity of different adaptive transmission schemes are explained and mathematical expression derived in Section 3. In section 4, describes the result and discussion of channel capacity and paper concludes in the Section 5.

II. SYSTEM AND CHANNEL MODELS

A. Log-normal (LN) Distribution

A γ is LN, random variable, i.e. $\gamma \sim LN(\mu, \sigma^2)$, if and only if $\ln(\gamma) \sim N(\mu, \sigma^2)$. A LN, RV has the PDF [12]

$$p(\gamma) = \frac{1}{\sigma\gamma\sqrt{2\pi}} e^{-\frac{(\ln\gamma-\mu)^2}{2\sigma^2}} \quad (1)$$

Copy Right © INDIACom-2016; ISSN 0973-7529; ISBN 978-93-80544-20-5

The PDF in (2) can also be shown in decibel form as

$$p(\gamma)=\frac{\xi}{\sigma_d\gamma\sqrt{2\pi}}e^{-\frac{(10\log_{10}\gamma-\mu_d)^2}{2(\sigma_d)^2}} \quad (2)$$

Where, $\mu_d=\xi\mu$ and $\sigma_d=\xi\sigma$, $\xi=10/\ln(10)=4.3429$. For any $\sigma^2 > 0$, the mean/expected value of γ is $E(\gamma)=e^{(\mu+0.5\sigma^2)}$ and the variance of γ is $Var(\gamma)=[\exp(\sigma^2)-1]e^{(2\mu+\sigma^2)}$.

B. Holtzmann Approximation

If z is RV with mean μ and variance σ^2, then, $k(z)$ can be expanded as [10]

$$k(z)=k(\mu)+(z-\mu)k'(\mu)+\frac{1}{2}(z-\mu)^2k''(\mu)+\ldots \quad (3)$$

Taking expectation,

$$\begin{aligned}E[k(z)]&\cong k(\mu)+\frac{1}{2}\sigma^2k''(\mu)\\&=k(\mu)+\frac{1}{2}\sigma^2\left[\frac{k(\mu+f)-2k(\mu)+k(\mu-f)}{f^2}\right]\end{aligned} \quad (4)$$

Select, $f=\sqrt{3}\sigma$,

$$E[k(z)]\cong\frac{2}{3}k(\mu)+\frac{1}{6}k(\mu+\sqrt{3}\sigma)+\frac{1}{6}k(\mu-\sqrt{3}\sigma) \quad (5)$$

If z is Gaussian distributed and $k(z)$ is either monotonically increasing or decreasing function, then, we can write

$$E[k(z)]=\int_0^\infty\frac{k(z)}{\sqrt{2\pi}\sigma}\exp\left(-\frac{(z-\mu)^2}{2\sigma^2}\right)dz \quad (6)$$

Comparing (5) and (6),

$$\begin{aligned}E[k(z)]&=\int_0^\infty\frac{k(z)}{\sqrt{2\pi}\sigma}\exp\left(-\frac{(k-\mu)^2}{2\sigma^2}\right)dz\\&\cong\frac{2}{3}k(\mu)+\frac{1}{6}k(\mu+\sqrt{3}\sigma)+\frac{1}{6}k(\mu-\sqrt{3}\sigma)\end{aligned} \quad (7)$$

III. CHANNEL CAPACITY (CC)

The analysis of channel capacity (CC) for fading Channel is a significant performance metric as it gives an estimation of the information rate that the channel can sustenance with small amount of the probability of error. In this section, the closed-form mathematical model of CC of log-normal shadowed fading environment is obtained for different adaptive transmission schemes, such as, OPRA, ORA, CIFR and TIFR respectively.

A. Shannon Average Channel Capacity

The Shannon average CC (also known as ergodic channel capacity) is results in [11] as

$$C=B\int_0^\infty\log_2(1+\gamma)\,p(\gamma)\,d\gamma \quad (8)$$

B. Optimal Power and Rate Adaptation (OPRA)

If the CSI of the both transmitter and receiver have in perfect state then the average transmitting power constraint is maximized for the channel capacity using OPRA i.e. optimal power and rate schemes and the mathematical expression for this OPRA is given in [9] as

$$C_{OPRA}=B\int_{\gamma_0}^\infty\log_2\left(\frac{\gamma}{\gamma_0}\right)p(\gamma)\,d\gamma \quad (9)$$

Where, the channel bandwidth is denoted by B and its unit is in *Hz* and γ_0 is defined as the optimal cutoff signal-to-noise ratio level, below this cutoff level any kind of transmission will not takes place.

Substituting (1) in (9), then (9) becomes as

$$C_{OPRA}=B\int_{\gamma_0}^\infty\log_2\left(\frac{\gamma}{\gamma_0}\right)\frac{1}{\sqrt{2\pi}\sigma\gamma}\exp\left(-\frac{(\ln\gamma-\mu)^2}{2\sigma^2}\right)d\gamma \quad (10)$$

Now substituting $\ln\gamma=x$ then (10) becomes,

$$C_{OPRA}=B\frac{1}{\ln(2)}\int_{\ln(\gamma_0)}^\infty(x-\ln(\gamma_0))\frac{1}{\sqrt{2\pi}\sigma}\exp\left(-\frac{(x-\mu)^2}{2\sigma^2}\right)dx \quad (11)$$

Here, considering $\gamma_0=1$, so limits of integration now changes 0 to ∞, now applying Holtzman approximation, (11) becomes,

$$C_{OPRA}=B\frac{1}{\ln(2)}\int_0^\infty(x-\ln(\gamma_0))\frac{1}{\sqrt{2\pi}\sigma}\exp\left(-\frac{(x-\mu)^2}{2\sigma^2}\right)dx \quad (12)$$

Now, applying Holtzman approximation (7), so (12) becomes as,

Copy Right © INDIACom-2016; ISSN 0973-7529; ISBN 978-93-80544-20-5

$$C_{OPRA} = B\frac{1}{\ln(2)}\begin{bmatrix}\frac{2}{3}\left(\mu-\ln(\gamma_0)\right)\\ +\frac{1}{6}\left(\mu+\sqrt{3}\sigma-\ln(\gamma_0)\right)\\ +\frac{1}{6}\left(\mu-\sqrt{3}\sigma-\ln(\gamma_0)\right)\end{bmatrix} \quad (13)$$

Expression (13) is the channel capacity of OPRA in closed form using Holtzman approximation.

C. Optimal Rate Adaptation (ORA)

If the CSI is only present at the receiver side that means transmitter power always remain constant. The mathematical expression of channel capacity for the optimal rate adaptation is given in [9] as

$$C_{ORA} = B\log_2(e)\int_0^\infty \ln\left(\frac{\gamma}{\gamma_0}\right)p(\gamma)\,d\gamma \quad (14)$$

Substituting PDF of log-normal in (14) from (1), (14) becomes as,

$$C_{ORA} = B\log_2(e)\int_0^\infty \ln\left(\frac{\gamma}{\gamma_0}\right)\frac{1}{\sqrt{2\pi}\sigma}\exp\left(-\frac{(\ln\gamma-\mu)^2}{2\sigma^2}\right)d\gamma \quad (15)$$

Now substituting $\ln\gamma = x$ then (15) becomes,

$$C_{ORA} = B\log_2(e)\int_0^\infty \ln\left(1+\exp(\mu)\right)\frac{1}{\sqrt{2\pi}\sigma}\exp\left(-\frac{(x-\mu)^2}{2\sigma^2}\right)dx \quad (16)$$

According to Holtzaman approximation, (16) becomes as,

$$C_{ORA} = B\log_2(e)\begin{bmatrix}\frac{2}{3}\ln\left(1+\exp(\mu)\right)\\ +\frac{1}{6}\ln\left(1+\exp\left(\mu+\sqrt{3}\sigma\right)\right)\\ +\frac{1}{6}\ln\left(1+\exp\left(\mu-\sqrt{3}\sigma\right)\right)\end{bmatrix} \quad (17)$$

Eq. (17) is the closed form expression of channel capacity of ORA using Holtzman approximation.

D. Channel Inversion with Fixed Rate (CIFR)

According to this CIFR scheme, constant SNR should be maintained at the receiver side therefore transmitter can deed the channel side information. In this type of scheme, channel after the inversion behaves like additive white Gaussian noise (AWGN) channel because if it uses fixed communication data rate. When the CSI is present on the both transmitter and receiver, it produces the minimum amount of complexity and also shows in zero outage capacity. So, the channel capacity of the CIFR is originates from the CC of an AWGN channel and the mathematical expression of the CIFR is given in [9] as

$$C_{CIFR} = B\log_2\left(1+\frac{1}{\int_0^\infty \frac{p(\gamma)}{\gamma}d\gamma}\right) \quad (18)$$

Substituting (1) in (18), (18) becomes as,

$$C_{CIFR} = B\log_2\left(1+\frac{1}{\int_0^\infty \frac{1}{\gamma}\frac{1}{\sqrt{2\pi}\sigma\gamma}\exp\left(\frac{(\ln\gamma-\mu)^2}{2\sigma^2}\right)d\gamma}\right) \quad (19)$$

Now substituting $\ln\gamma = x$ then (19) becomes,

$$C_{CIFR} = B\log_2\left(1+\frac{1}{\int_0^\infty \exp(x)\frac{1}{\sqrt{2\pi}\sigma}\exp\left(\frac{(x-\mu)^2}{2\sigma^2}\right)dx}\right) \quad (20)$$

Now, applying Holtzman approximation in (20), (20) becomes as,

$$C_{CIFR} = B\log_2\left(1+\frac{1}{[g]}\right) \quad (21)$$

$$\text{Where, } g = \begin{bmatrix} \frac{2}{3}\exp(-\mu) \\ +\frac{1}{6}\exp\left(-\left(\mu+\sqrt{3}\sigma\right)\right) \\ +\frac{1}{6}\exp\left(-\left(\mu-\sqrt{3}\sigma\right)\right) \end{bmatrix}$$

E. Truncated Channel Inversion with Fixed Rate (TIFR)

Another mode to CIFR is the truncated CIFR scheme known as the TIFR. In this scheme, channel fading is reversed above the fixed cutoff SNR level γ_0. On comparing between TIFR and CIFR, on the basis of the outage probability then the channel capacity of TIFR scheme is far better than the CIFR scheme. The mathematical expression of outage capacity for TIFR is given in [9] as

$$C_{out} = B\log_2\left(1+\frac{1}{\int_0^{\infty}\frac{p(\gamma)}{\gamma}d\gamma}\right)\left(1-P_{out}\right) \qquad (22)$$

Where, P_{out} is defined as, $P_{out} = p(\gamma_0)$. By maximizing the outage capacity, the channel capacity of the TIFR is obtained as

$$C_{TIFR} = \max_{\gamma_0} C_{out} \qquad (23)$$

Substituting C_{out} and P_{out}, (23) becomes,

$$C_{TIFR} = \max_{\gamma_0} C_{CIFR}\left(1-p(\gamma_0)\right) \qquad (24)$$

$$C_{TIFR} = \max_{\gamma_0}\left\{\begin{matrix} B\log_2\left(1+\frac{1}{[g]}\right) \\ \times\left(1-\frac{1}{\sigma\gamma_0\sqrt{2\pi}}e^{-\frac{(\ln\gamma_0-\mu)^2}{2\sigma^2}}\right)\end{matrix}\right\} \qquad (25)$$

$$\text{Where, } g = \begin{bmatrix} \frac{2}{3}\exp(-\mu) \\ +\frac{1}{6}\exp\left(-\left(\mu+\sqrt{3}\sigma\right)\right) \\ +\frac{1}{6}\exp\left(-\left(\mu-\sqrt{3}\sigma\right)\right) \end{bmatrix}$$

Expression (25) is the final mathematical expression of the TIFR using Holtzman approximation.

IV. RESULT AND DISCUSSION

We present the graphical results of channel capacity (CC) in the closed form expression for different transmission schemes such as OPRA, ORA, CIFR and TIFR in the log-normal shadowed fading environment.

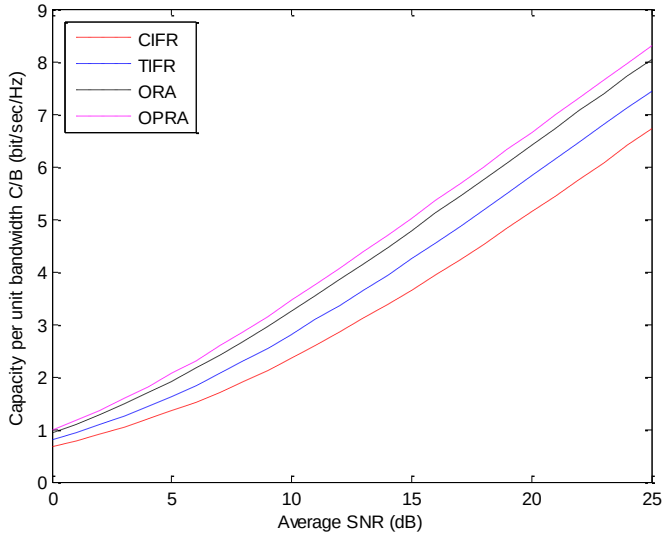


Fig. 1: *Capacity/bandwidth against average signal-to-noise ratio for different adaptation scheme at light shadowing* ($\sigma = 0.55$)

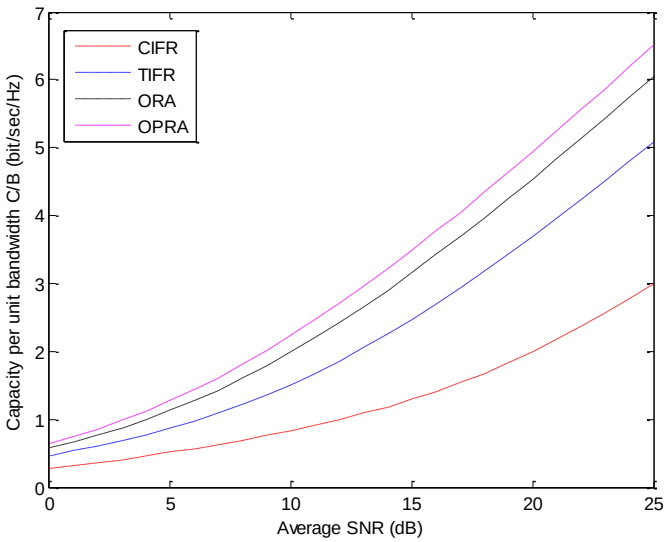


Fig. 2: *Capacity/bandwidth against average signal-to-noise ratio for different adaptation scheme at heavy shadowing* ($\sigma = 5.55$)

Fig. 1 and Fig. 2 show the channel capacity/bandwidth verses average signal-to-noise ratio (dB) for four different

Copy Right © INDIACom-2016; ISSN 0973-7529; ISBN 978-93-80544-20-5

adaptive transmission schemes in light shadowing ($\sigma = 0.55$) and heavy shadowing ($\sigma = 5.55$) conditions in a log-normal fading environment. As expected from the plots, the channel environments improve, all the channel capacities increases, with average SNR having a significant effect on the performance. Comparing Fig. 1 and Fig. 2, it is witnessed that CC decreases with the increase in the shadowing parameter; a very obvious deleterious effect of shadowing and it is quite obvious that as the average SNR increases CC also increases.

It is witness that as fading severity decreases the difference in the capacity between the different adaptive schemes diminishes. On comparing channel capacity among OPRA, ORA, CIFR and TIFR, CIFR losses its channel capacity which is more prominent as shadowing severity increases, on increase with the average SNR, the channel capacity of TIFR losses, and at lower SNRs, the channel capacity of the ORA loss turn into non-negligible.

V. CONCLUSION

We have presented mathematical expression for CC over the log-normal shadowed fading environment. Channel capacity in closed form expression for different transmission schemes were obtained in three terms using Holtzman approximation yielding a very accurate and simple expression. Furthermore, the results have been examined for light as well as heavy shadowing conditions and some important observations were made.

References

[1] A. Goldsmith, P. Varaiya, "Capacity of fading channels with channel side information," *IEEE Transaction on In Theory*, vol. 43, no. 6, pp. 1986–1992, 1997.

[2] W. C. Y. Lee, "Estimate of channel capacity in Rayleigh fading environment," *IEEE Transactions on Vehicular Technology*, vol 93, no. 3, pp.187–189, 1990.

[3] M. S. Alouni, & A. J. Goldsmith, "Capacity of rayleigh fading channels under different adaptive transmission and diversity-combining techniques" *IEEE Transactions on Vehicular Technology*, vol. 48, no. 4, pp. 1165–1181, 1999.

[4] N. C. Sagias, G. S. Tombras & G. K. Karagiannidis, "New results for the Shannon channel capacity in generalized fading channels," *IEEE Communication Letters*, vol. 9 no. 2, pp. 97–99, 2005.

[5] D. B Da Costa & M. D. Yacoub, "Average channel capacity for generalized fading scenarios," *IEEE Communication Letters*, vol. 11, no. 12, pp. 949–951, 2007.

[6] A. Goldsmith, "Wireless communications," *Cambridge: Cambridge University Pres*, 2006.

[7] M. K. Simon & M. S. Alouni, "Digital communication over fading channels: a unified approach to performance analysis," *London: Wiley*, 2000.

[8] A. F. Molisch, J. R. Foerster & M. Pendergrass, "Channel models for ultra wideband personal area networks," *IEEE Wireless Communications Magazine*, vol. 10, no. 6, pp. 14–21, 2003.

[9] G. P. Efthymoglou, N. Y. Ermolova, V. A. Aalo, Channel capacity and average error rates in genralised-K fading channels," *IET Communication*, vol. 11, no. 4, pp. 1364-1372, 2010.

[10] J. M. Holtzman, A simple, accurate method to calculate spread multiple-access error probabilities," *IEEE Transactions on Communication*, vol. 40, pp. 461–464, 1992.

[11] F. El . Bouanani, H. Ben-Azza and M. Belkasmi, "New results for the Shannon channel capacity over generalized multipath fading channels for MRC diversity," *EURASIP Journalon Wireless Communications and Networking*, vol. 336, pp. 1-12, 2012.

[12] R. Singh, S. K. Soni, P. K. Verma, S. Kumar, "Performance analysis of MRC combiner output in log-normal shadowed fading," *IEEE International Conference on Computer Communication & Automation (ICCCA)*, pp. 1116-1120, 2015.

ISSN: 2278 – 909X
International Journal of Advanced Research in Electronics and Communication Engineering (IJARECE)
Volume 5, Issue 6, June 2016

Classification of EMG Signals using SVM-kNN

PREETI MEENA, MALTI BANSAL

Abstract **–Electromyography (EMG) is a way to measure the electrical activity of the contraction of muscles and nerves.There are so many methods already developed, in the time and frequency domains, for EMG signals analysis. In this research, a method is proposed for the EMG signals analysis using their coiflet wavelet transform and with their features such as mean, energy and standard deviation. These features are then utilized on three different types of EMG signals like normal, myopathic and neuropathic signals to classify them. The method proposed can automatically classifies these signals into their respective classes. For this, various classifiers are used in this research but it is observed that SVM-kNN classifies the signals with highest accuracy in comparison to the other classifiers. SVM-kNN has come with 95% (approximately) accuracy which is also very compared to the other methods used earlier.**

Index terms **--- Electromyography, Wavelet transform, SVM, SVM-kNN.**

I. INTRODUCTION

Electromyography (EMG) is an analytic way to access the health of muscles and nerves. Motor neurons present in the body transmit electrical signals that cause muscles to contract. These changes in muscles contraction is recorded in the form of graph using EMG.

EMG signals classification is an important analysis and anorganisedstudy is required for their classification. For the same reason, number of computer-based quantitative

Preeti Meena, *Department of Electronics and Communication Engineering, Delhi Technological University, Delhi, India.*

Malti Bansal, *Department of Electronics and Communication Engineering, Delhi Technological University, Delhi, India.*

EMG analysis algorithms have been developed.Among these algorithms, some of the already used feature extraction techniques includes Discrete wavelet transform (Daubechies-6) [1], AR modelling [2], autoregressive cepstral analysis [3], PSO [4], wavelet packet energy [5] etc. These methods were utilized by other researchers for the features extraction in the EMG signals that were used during their research. Then, these features are exploit in the classifiers to classify the signals used. Classifiers that are already exploitedincludes Fuzzy [5], Artificial neural networks (ANN) [6], Fuzzy-genetic [7], Neuro-fuzzy [8], Deep fuzzy neural network [1], SVM [9]etc. All these models give satisfactory and even good results. But, for better result performance in terms of accuracy,SVM-kNN is utilized here because SVM-kNN can also provide efficient results in the field of classification.

In this paper, a method is proposed for EMG signals classification. A brief overview of the proposed method is shown in the block diagram in Fig.1. As shown in the figure, three different types of EMG signals (Normal, Myopathy and Neuropathy) are taken. Detail coefficients of coiflet of order 5 of the EMG signals are computed. Then, for D4 coefficient, features like mean, energy and standard deviation are calculated. At last, using these calculated features, classifiers like SVM and SVM-kNN are exploited to classify the EMG signals and the best classifier from them is find out.

The organisation of different sections of the paper is as follows: Section 2 provides a brief overview of the proposed method in the form of a block diagram. Section 3 provides details about the dataset used, definitions and explanations of the methods used. Section 4 provides the process, explained using block diagram, of the proposed method. Section 5 contains the classification results followed by conclusion in Section 6.

II. BLOCK DIAGRAM

A brief outline of the work is shown in the block diagram in Figure. As shown in the figure, three different types of EMG signals (Normal, Myopathy and Neuropathy) are taken. Detail coefficients of coiflet of order 5 of the EMG signals are computed.

All Rights Reserved © 2016 IJARECE

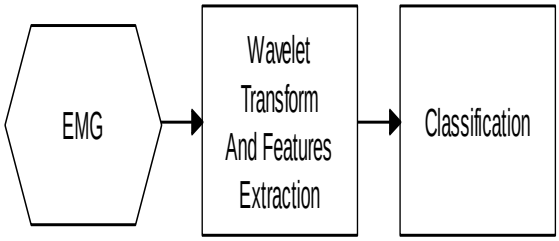


Fig.1.EMG Signals Classification

Then, for D4 coefficient, features like mean, energy and standard deviation are calculated. At last, using these calculated features, classifiers like SVM and SVM-kNN are exploited to classify the EMG signals and the best classifier from them is find out.

III. PROPOSED METHOD

A. Data Set Used

Data set of EMG signals is loaded from the MIT-BIH database.

From the data set, waveforms of three types of EMG signals are taken and shown in the Fig. 2. These waveforms represent the normal, myopathy and neuropathy signals.

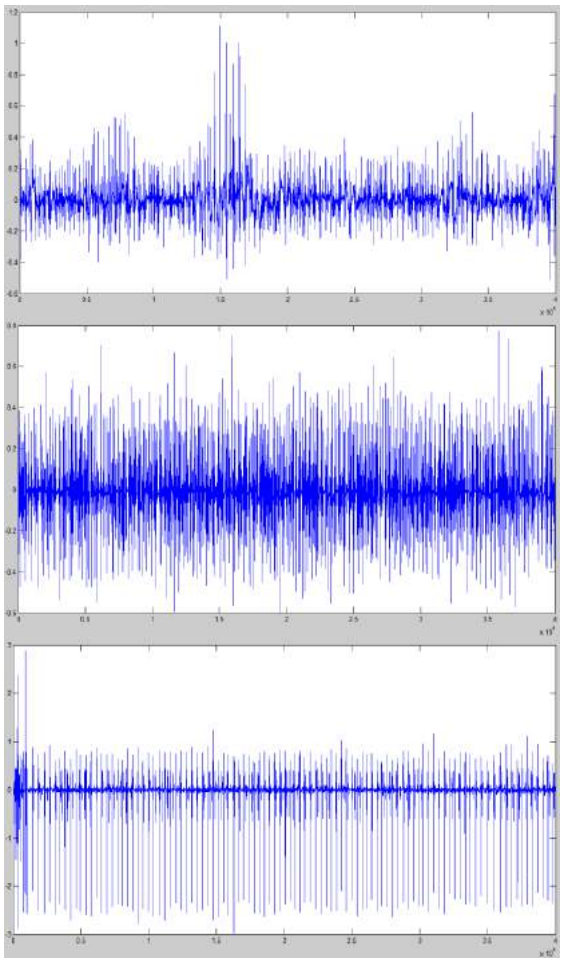


Fig.2. EMG Signals – Normal, Myopathy and Neuropathy

A description of the data set is shown in the Table I.

Table I
Description of dataset used

EMG Signals	Total
Normal	500
Myopathy	500
Neuropathy	500

B. WAVELET TRANSFORM

Wavelet transformis the representation of any signal in the time–frequency domain[10] simultaneously. It can provide time and frequency information at the same point of time, thus giving a time–frequency representation of the signal. It is an already known fact that the higher frequency elements are resolved, better, in time domain while the lower frequency components are resolved, better, in frequency domain. Hence, the wavelet transform can be defined as:

$$C(\alpha,\beta)=\int_{-\infty}^{\infty}x(t)\frac{1}{\sqrt{\alpha}}\varphi\left(\frac{t-\beta}{\alpha}\right)dt \quad (1)$$

It can be seen from the above equation that the resultant signal obtained is a function of two variables, α and β. Here, φ is the transforming function called as the mother wavelet, α is the translation parameter and β is the scale parameter.

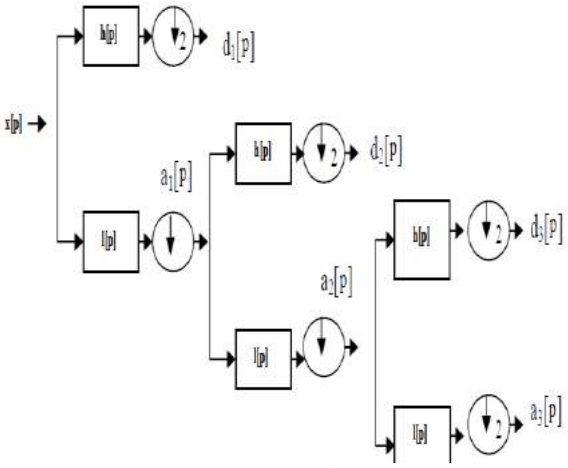


Fig. 3. Sub-band decomposition of DWT implementation; h[p] is the high pass filter, l[p] the low pass filter.

For this, the signal is passed through various high- and low-pass filters. This process is repeated for the either portion or both of the filter's output.

All Rights Reserved © 2016 IJARECE

This process is known by the name decomposition. This constitutes one level of decomposition and can be expressed as:

$$y_{hi}(m) = \sum_{p} x(p).h(2m - p) \quad (2)$$

$$y_{lo}(m) = \sum_{p} x(p).l(2m - p) \quad (3)$$

Here, yhi[k] is the output from the high-pass filter and ylo[k] is the outputfrom the low-pass filter after sub-sampling by 2. It is shown in the Fig.3. Decomposition of any signal halves its time resolution, that is, only half the number of samples is required to describe the entire signal. However, this will also result in double the frequency resolution. The process shown in Fig.3 is known as the sub-band coding. This can be further repeated for more decomposition levels. In Fig.3 shows is the process of level decomposition. In the figure, x[n] represents the original signal that need to be decomposed.l[p] and h[p] are low- and high-pass filters, respectively. Thisdecomposition of the x[p] will give the detail and the approximation coefficients. The approximation coefficient may further be decomposed as the process is shown in Fig.4.For the EMG signal, these approximation and detail coefficients are calculated for the Coiflet 5 (coif5) wavelet transform.

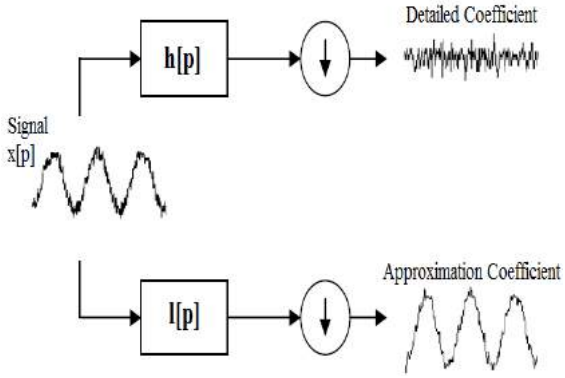


Fig. 4. EMG signal and its wavelet decomposition into Approximation and Detailed coefficients.

Wavelet coefficients extracted as detailed and approximation ones gives the representation of the distribution of EMG signal in time and frequency domain simultaneously.

Now, detail coefficients computed for the EMG signals are selected and the coefficient which highly resembles its original signal is taken out. Here, this coefficient is 4th one i.e. D4 coefficient. It is shown in the Fig. 5 that D4 coefficient resembles its original signal. Feature extraction of the EMG signals is now begins. Features that are going to be calculated for these signals D4 coefficient are mean, energy and standard deviation [11]. These are briefly described as follows:

(1) Mean of the absolute values of the coefficient 4 in each sub-band.

$$Mean = \frac{\sum_{w} z_w}{w} \quad (4)$$

(2) Energy of the wavelet coefficient 4 in each sub-band.Energy of the sub-signal xwk (t) is calculated by

$$Energy = \sum_{w}\sum_{j} \left| D_j^w \right|^2 \quad (5)$$

(3) Standard deviation of the coefficient 4 in each sub-band.

$$\text{Standard Deviation} = \sqrt{\frac{\sum_{w} (z_w - mean)^2}{w}} \quad (6)$$

The features extracted as mean, energy and standard deviation are now utilized to train and test on the classifiers which are going to be explained in the next sub-sections.

C. SVM

The Classifiers are now applied using the features computed in the previous sub-section that includes coiflet wavelet transform of the EMG signals and features like mean, energy and standard deviation for the D4 coefficient of the transform. These features are now utilized to train the SVM model and then test on the same trained SVM for the classification.

SVM (Support Vector Machine) is a classifier which requires training of the model for the testing of the samples and such technique in which training is given is called as supervised learning technique. In this, model is firstly trained to learn according to the features of the classes which need to be classified. Then that trained model is exploited in the classification process. Learning given to the classifier provides better results compared to the other classifiers in which unsupervised learning is used. This classifier is simple and easy to understand as it constructs a hyperplane between the different classes which need to be classified. The classifier used may be linear or non-linear. In linear SVM, training samples of the classes are linearly separable. But it is very difficult in practical situations that a straight line is sufficient to classify each and every sample. For such cases, non-linear classifier is exploited.

All Rights Reserved © 2016 IJARECE

In these, kernel functions may also be utilized to increase the dimensionality of the mapping. If the samples are not distinguishable in lower dimensional space, then kernel functions are used. In this, a non-linear operator maps the inputs to the classifier into a higher dimensional space so that samples can be classified easily.
If a linear function is given by the equation

$$g(z) = az + b \tag{7}$$

Then its dimensionality can be increased by using the equation as

$$g(z) = a.\phi(z) + b \tag{8}$$

In this, after plotting the samples in a space, a hyperplane is drawn according to the condition that margin between the support vectors and the hyperplane need to be maximized. It can be seen in [9].

However, classification skill of SVM is better as compared to the other methods, but, some complications still persists in its applications which includesclassifying accuracy as low in the complex applications. It is also difficultto choose the kernel function parameters. In an attempt to find solution for these problems, SVM is combined with k-nearest neighbour classifier (kNN). It will be seen in the results section that doing this is a good approach and better results are obtained using the SVM-kNN. This explained in the next sub-section.

D. *SVM-kNN*

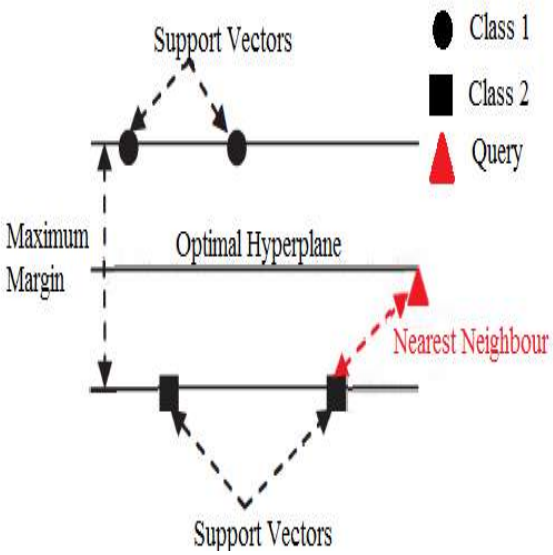


Fig.5. SVM-kNN Classification

SVM-kNN classifier is a hybrid of Support Vector Machine and k-Nearest Neighbour classifiers. In the previous section studied, SVM is a 1NN classifier [9]. That is, according to the nearest neighbour approach, SVM uses only a single representative point as support vectors for each class. But on combining the SVM with kNN, more than one points are chosen from the sample points i.e. say k-points are selected and accordingly, the class is decided for the tested sample.

It can be seen from the Fig.5 that this hybrid algorithm (SVM-KNN) considers more than one support vectors as the representative points of a class. This is much better than the SVM in which samples present nearest to the hyperplane represents the support vectors. In that, only one representative point is chosen for support vectors in each class and this representative point only represents the whole class which becomes quite complicated in the complex situations. In SVM-kNN, all support vectors are considered as representative points for the class and hence, maximum of information of a class is exploited in the classification process. In this classifier, radial basis kernel function is used with SVM to train the classifier. And, during the testing of the signals, nearest neighbour (that is, support vector) is computed as the query point using k-nearest neighbour algorithm. In the next section, the experimental point of view is shown.

IV. EXPERIMENTAL VIEW

EMG Dataset: Data set of EMG signals is loaded from the MIT-BIH database. It is described in the table shown in Table II.

Table II
Description of dataset used

EMG Signals	Training	Testing	Total
Normal	350	150	500
Myopathy	350	150	500
Neuropathy	350	150	500

Computing the wavelet transform and their features: Discrete wavelet transform (DWT) of the EMG signals are computed using the coiflet wavelet transform of the order of 5. Then, Features such as Energy, Mean and Standard Deviation for the D4 coefficient are computed for each and every sample of dataset of the different types of EMG signals used during the research. These calculated features in the form of mean, energy and standard deviation serve as an input to train and test the various classifiers.

Classification: During the classification, computed features of the EMG signals in the second stage are

All Rights Reserved © 2016 IJARECE

exploited by the classifiers like SVM and SVM-kNN to determine the corresponding class of the samples. This feature set consists of mean, energy and standard deviation of the D4 coefficient of the

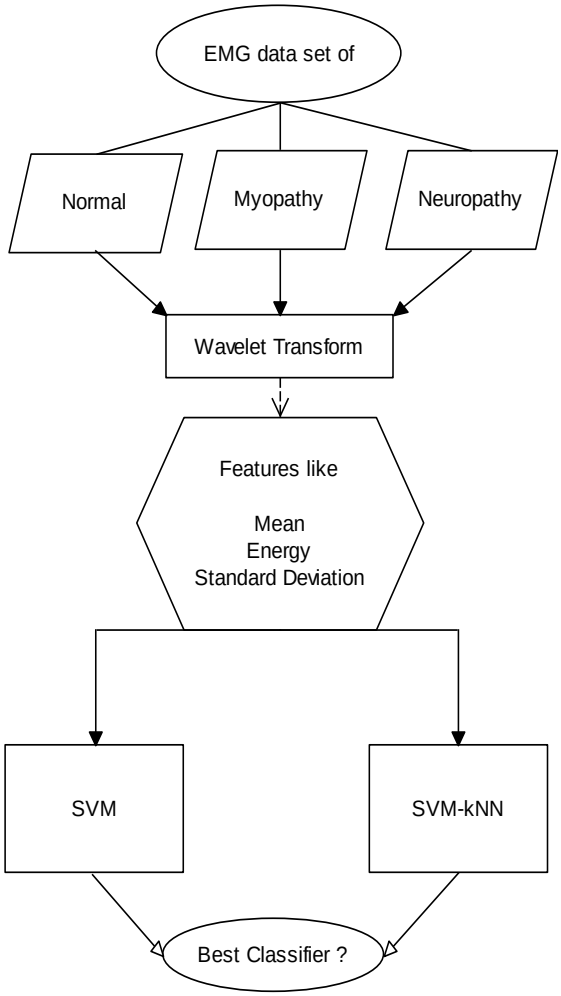


Fig.6. Block Diagram of EMG Signals Classification

coiflet wavelet transform that should efficiently characterize the variations in the input signals for accurate detection and classification of the EMG signals. The calculated features will be applied to the classifiers like SVM and SVM-kNN classifiers as training and testing data to classify the EMG signals in their corresponding classes.

V. RESULTS

In this study, SVM and SVM-kNN classifiers are utilized for the classification of three different types of EMG signals (Normal, Myopathy and Neuropathy). As the features required to train the classifiers, D4 coefficient of the coiflet wavelettransform is used. Then, as the features, mean, energy and standard deviation is used.

Now, data set utilized for this research is shown in the Table I. For this data of the EMG signals, firstly, wavelet transform is applied. In the wavelet transform, coiflet family of order 5 is used. The results for each type of data set used is shown in the figures 7, 8 and 9.

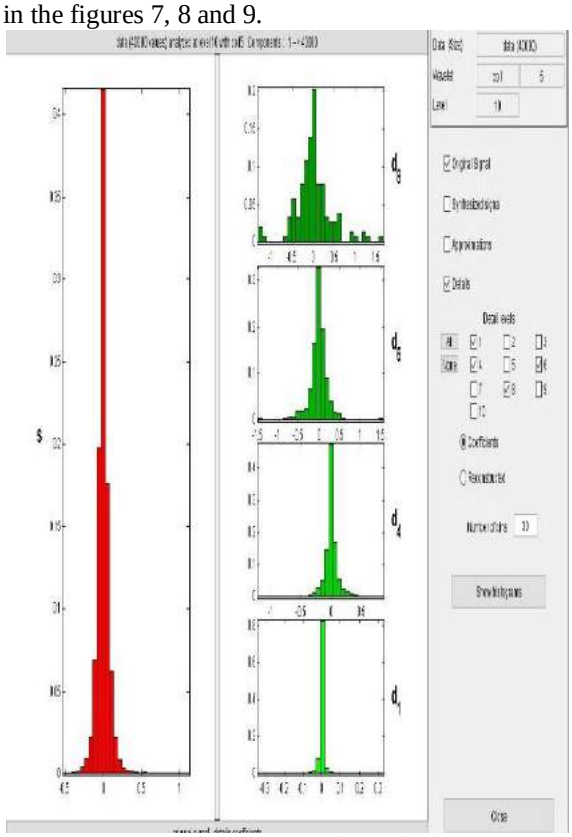


Fig.7. Histogram of wavelet transform of normal person EMG

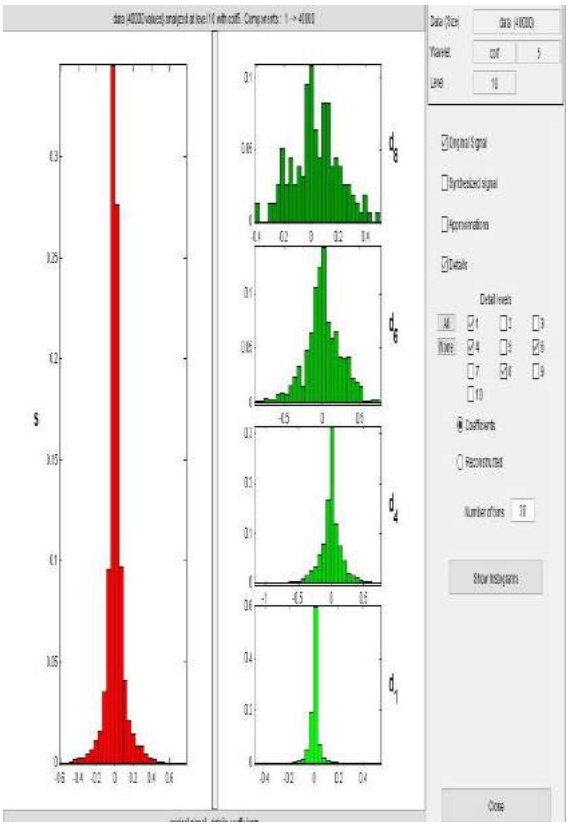


Fig.8. Histogram of wavelet transform of myopathy person EMG

All Rights Reserved © 2016 IJARECE

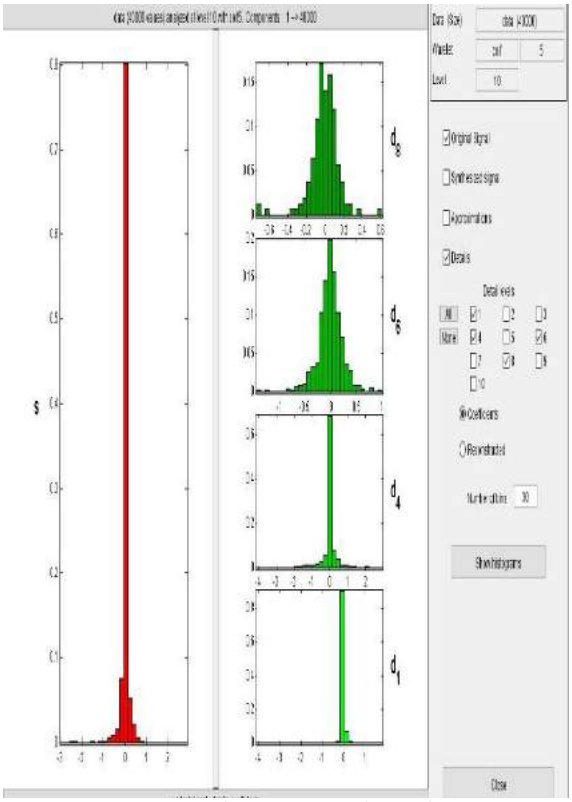


Fig.9. Histogram of wavelet transform of myopathy person EMG

These figures shows the EMG signals wavelet transform in the form of histograms. And it can be observed from the figures that histogram of D4 coefficient maximally resembles the original signals histogram. This implies that maximum information lies in that coefficient and hence, for further analysis, D4 coefficient is sufficient to give the maximum features alone. Therefore, mean, energy and standard deviation is computed for D4 coefficient only. Sample values for these features are shown in the Table III.

Table III. Sample values of features for EMG signals

EMG Signal	Mean	Energy	Standard Deviation
Normal	7.43	56.58	1.173
Myopathy	5.26	28.46	0.890
Neuropathy	9.48	85.34	1.212

In the Table III shown is the sample values for the features computed for the D4 coefficients of the coiflet of order 5. These features include mean, energy and standard deviation values of the signal. These features are calculated for each and every sample of data set of the three types of EMG signals used.

Now, from these features computed, features of 350 samples from each class are selected and used to train the SVM. After that, remaining 450 samples (Normal-150, Myopathy-150 and Neuropathy-150) are tested on the same trained SVM. Its classification results are in the Table IV in the form of a confusion matrix.

Table IV. SVM Classification

Targets → / Outputs ↓	Normal	Myopathy	Neuropathy	Accuracy
Normal	141/150	3/150	6/150	94%
Myopathy	11/150	134/150	5/150	89.33%
Neuropathy	7/150	4/150	139/150	92.67%

The confusion matrix shown in the Table IV shows a good result in terms of classifying the EMG signals into their respective classes. SVM gives 92% of accuracy in classifying these signals. This is quite good but SVM-kNN is utilized further to increase this percent of accuracy in classification of EMG signals.

Next, SVM-kNN classifier is used for the EMG signals classification. In this also, features of 1050 samples (Normal-350, Myopathy-350 and Neuropathy-350) are utilized to train the SVM-kNN. Then, the remaining samples are used to test on the same trained SVM-kNN.

Table V. SVM-kNN Classification

Targets → / Outputs ↓	Normal	Myopathy	Neuropathy	Accuracy
Normal	147/150	2/150	1/150	98%
Myopathy	8/150	137/150	5/150	91.33 %
Neuropathy	3/150	5/150	142/150	94.67 %

And, it can can be clearly seen from the Table V that increase in the accuracy of classification is observed. Table V shows the confusion matrix of SVM-kNN classification and from this classifier an accuracy of approximately 95% is observed.

VI. CONCLUSION

In the research, a method is presented for the classification of three different types of EMG signals (i.e. Normal, Myopathy and Neuropathy) using the classifier SVM-kNN. This method is based on the extraction of features like mean, energy and standard deviation for the coiflet family of wavelet transform of the order of 5. Results achieved from the classification show that the proposed method can beconsidered as an

All Rights Reserved © 2016 IJARECE

alternative approach, compared to the other methods, for extracting relevant features and classification for EMG signals.

This method exploits only three features of the EMG signals compared to other existing methods. And, hence, this also allows an efficient classification results with 95% accuracy with only a small number of features.Therefore, now,it can be concluded that,with some more efforts in achieving more accuracy in classification, the expensive tests of diagnosing the EMG can be replaced by this automatic techniques of classifying EMG signals.

REFERENCES

1. Subasi, A., "Classification of EMG signals using combined features and soft computing techniques," Applied Soft Computing, vol. 12, pp 2188- 2198, 2012.
2. Kaur, G. Shatru-Aurora, A., Kumar-Jain, Vijendra., "EMG Diagnosis via AR Modeling and Binary Support Vector Machine Classification," Int Journal Of Eng. Science and Tech., vol. 2, pp. 1767-1772. 2010
3. C.S. Pattichis, A.G. Elia, Autoregressive cepstral analyses of motor unit action potentials, Medical Engineering & Physics 21 (1999) 405–419.
4. Subasi, A., "Classification of EMG signals using PSO optimized SVM for diagnosis of neuromuscular disorders," Computers in Biology and Medicine, vol. 43, pp 576-586, 2013.
5. Khushaba RN, Al-Jumaily A, Al-Ani, "A. Novel feature extraction method based on fuzzy entropy and wavelet packet transform for myoelectric Control," 2007 Int Symp Commun Inf Technol., pp. 352– 357, 2007.
6. Y. Becerikli, On three intelligent systems: dynamic neural, fuzzy and wavelet networks for training trajectory, Neural Computing & Applications 13 (4) (2004) 339–351.
7. C.A. Pena-Reyes, M. Siper, A fuzzy-genetic approach to breast cancer diagnosis, Artificial Intelligence in Medicine 17 (1999) 131–155.
8. S.E. Hussein, M.H. Granat, Intention detection using a neuro-fuzzy EMG classifier, IEEE Engineering in Medicine and Biology November/December (2002) 123–129.
9. Subasi, A., "Classification of EMG signals using PSO optimized SVM for diagnosis of neuromuscular disorders," Computers in Biology and Medicine, vol. 43, pp 576-586, 2013.
10. C. Parameswariah, S. Member, M. Cox, and S. Member, "Frequency Characteristics of Wavelets," vol. 17, no. 3, pp. 800–804, 2002
11. Sepulveda-Cano LM, Acosta-Medina CD, Castellanos-Dominguez G "Relevance Analysis of Stochastic Biosignals for Identification of Pathologies," 2011 EURASIP J. Adv. Sig. Proc. 2011.
12. Phinyomark, a. Quaine, F., Charbonnier, S., Serviere, C., Tarpin- Bernard, F., Laurillau, Y., "EMG feature evaluation for improving myoelectric pattern recognition robustness", Expert systems with applications, vol. 40, pp. 4832-4840, 2013.

All Rights Reserved © 2016 IJARECE

IJARCCE

ISSN (Online) 2278-1021
ISSN (Print) 2319 5940

International Journal of Advanced Research in Computer and Communication Engineering
Vol. 5, Issue 5, May 2016

Classification of Pseudo Random Numbers Using Support Vector Machine Classifier

Preeti Meena[1], Malti Bansal[2]

Department of ECE, Delhi Technological University, Delhi, India[1, 2]

Abstract: The paper studies about the randomness and its application in the field of cryptography. It is already known to have randomness having applications in the fields of gaming, gambling, statistics etc. But, in applications such as cryptography, randomness has a vital role. As with the use of these random numbers only, a highly secure message can be formed. So, Pseudo Random numbers classification is proposed in this paper so that sources of these random numbers can be classified for the enhancement in the security level. The result shows good accuracy of classification of these random numbers i.e. classified using multi-SVM.

Keywords: Cryptanalysis, Multi-SVM, PRNGs, TRNGs.

I. INTRODUCTION

In this world, randomness is the dearth of certainty in an event. It can be easily understood with the help of randomness that proper random numbers generation is a quite complicated process. Random numbers are helpful in various purposes which include creating files keys for encryption, creating a representation for selecting the random trials from large datasets. A random sequence for any event has no particular order and does not follow a logical pattern.

Randomness has found its applications in the fields of art, science, statistics, cryptanalysis, gaming etc. In the field of cryptanalysis, goal is to make a message as hard to crack as possible. It is done by disguising the parameters used to encode the message from the context in which it is conceded. For example, randomness, in randomized trials, are helpful in testing the hypotheses. Pseudo Random numbers are useful in video games such as video poker. In 1946, [1] introduced a method to generate Pseudo Random numbers. In this method, middle digit of the previous number takes the place of the next successive number. First of all they took a kernel value, and calculated the square in which they nominated the middle digits of that number and took it as the kernel value for next successive Pseudo Random number. This way, middle digits of previous numbers act as the kernel value for the successive number. In 1949, [2] proposed a method named Linear Congruential Generator (LCG). This algorithm comes out as the best algorithm for the generation of Pseudo Random numbers. It is very fast and easy to comprehend at the same time. Its execution is also very informal. In this, with the help of a simple linear equation, they attained a Pseudo Random sequence. The source of the equation was the modulo arithmetic. Modulo arithmetic is a very useful tool in which numbers wrap around after reaching a certain value. Quadratic congruential generator 1 and Quadratic congruential generator 2, uses a quadratic equation, are very greatly based on the idea of Linear congruential generator as these two do not use the linear equation. [3] also generates another Pseudo Random number generator, named Blum Blum Shub, that was proposed in 1986. These Pseudo Random numbers generated using various different methods can increase their number of applications if the source of that random number is identified. Support Vector Machine is a model which is derived from a theory known as statistical learning [4]. Compared to Neural Network (NN) approaches [5], SVMs exhibit higher generalization capability, robustness, lower efforts are required for classifier selection during the training period [6] and finest solution is obtained by this algorithm. [7] proposed a technique which performs classification of multi-classes problem (known as multiclass SVM) into the single one, rather into binary classification of multiple sets. Now, through this paper, an experiment has been done for separating the different kinds of Pseudo Random numbers generated from different sources. For this, three set of Pseudo Random numbers are selected with different sources, each representing a separate class. Then using the model named SVM, classification of these numbers are done and results are represented in the form of an image output showing three classes of Pseudo Random numbers which are well separated using the SVM.

The paper is organised as follows. Section II provides details about definitions and explanations of the methods used. Section III provides the process, explained using algorithm, of the proposed method. Section IV contains the classification results followed conclusion in Section V.

II. PROPOSED METHOD

A. True Random Numbers Generator (TRNG)

In the applications like cryptography, sources for generating the random numbers should be of high quality so that a high quality design may produce. There are so many good quality sources exists for the generation of true random numbers, at present, to design a cryptographic system. But, unfortunately, cryptographic analysis is done with only few of the existing true random number

IJARCCE
ISSN (Online) 2278-1021
ISSN (Print) 2319 5940
International Journal of Advanced Research in Computer and Communication Engineering
Vol. 5, Issue 5, May 2016

generators. This is because a design made using TRNGs produces the sequence of numbers of such kind that these numbers show a definite level of association due to its bandwidth and temperature drift limitations.
So, due to issues in manipulating the TRNGs, there is difficulty in designing such a system. TRNGs also create deterministic disturbances in the cryptographic system design. Solution to this problem is to design such a system which can use analogue randomness sources. Therefore, due to design flaws occurring using TRNGs and lack of random data in TRNGs, Pseudo random numbers generators came in use.

B. Pseudo Random Numbers Generators (PRNG)
Theories of researches on Pseudo Random numbers with the results being so positive that Pseudo Random numbers generated using modern algorithms look exactly as they are really random. According to the meaning of the word 'Pseudo', Pseudo Random numbers are not as such as we might presume. Essentially, PRNGs are the algorithms which utilize simple pre-calculated data and mathematical formulaes [11] to generate the random numbers. Linear congruential is a good design of PRNGs.
The linear Congruential Generator (LCG) is defined by using a recurrence relation:

$$Y_{k+1} = (\alpha.Y_k + \gamma).(|r|) \qquad (3)$$

where,
α, 0 < α < r = multiplier
γ, 0 <= γ < r = incremental
r, r > 0 = modulus
Y_0, 0 <= Y_o < r = seed value
And, Y is the sequence of Pseudo Random values

$$Gcd(\gamma, r) = 1 \qquad (4)$$

β = (α - 1) is multiple of q for every q dividing r
β is multiple of 4 if r is multiple of 4

Another PRNG that exists is Quadratic Congruential Generator i.e., shown in the equation

$$Y_{k+1} = (\alpha Y_k^2)(|r|) \qquad (5)$$

Quadratic congruential generator 2 is defined as,

$$Y_{k+1} = (\alpha Y_k^2 + \beta Y_k + \gamma)(|r|) \qquad (6)$$

Blum Blum Shub is another PRNG which follows the equation for PRNG as:

$$Y_{k+1} = Y_k^2(|r|) \qquad (7)$$

Here, Y_r = seed value
Y_{k+1} = Pseudo Random number generated
r = uv, where u and v be the two prime numbers of large values. In this algorithm, output is derived from Y_K at each step. Then the output is the least significant bit of Y_{K+1}.

Blum Blum Shub follows the following steps:
1. Generate u and v as two big prime numbers.
2. k := u · v
3. Choose t belongs to R [1, k − 1], the random seed. Choose a random number s, such that neither u nor v is a factor of t.
4. $Y_0 := t_2 \pmod k$
5. The sequence is defined as $Yj = Y_{2j-1} \pmod k$ and $Z_j :=$ parity(Y_j).
6. The output is $Z_1, Z_2, Z_3, \ldots$.

PRNGs are efficient [12] which means that they can generate the random numbers in a short extent. These are deterministic also as certain sequence can be reproduced at the future stage if the primary point of the structure is known. If determinism is handy, same sequence is to be repeated at further stage. Efficiency can also be considered as a distinguishing characteristic if there are large number of pseudo random numbers are present. PRNGs also have one more property which is hardly desirable and i.e. periodic nature [13]. This property states that the sequence obtained should be repeatable. At present, modern algorithms of PRNGs are periodic with such a period that it can be ignored for most practical cases as it is so long.

As it is beneficial to have a sequence which can be easily repeatable, hence, the above stated characteristics of PRNGs make them a very much suitable for the applications where randomness is the basic necessity. Among such applications, popular ones includes simulation and modeling applications but are not suitable for the applications such as gambling and data encryption, where the numbers are really unpredictable.

C. Comparison of PRNGs with TRNGs
In comparison with PRNGs [14], the characteristics of TRNGs are quite different. These characteristics are helpful in distinguishing both. Firstly, TRNGs are ineffective as compared to PRNGs because former takes considerably a very large time to generate the numbers. They are also known by the name of non-deterministic random number generators because it is not possible with the help of TRNGs that random numbers sequence can be reproduced.

Athough, by chance, same numbers sequence may, of course, occur several times. TRNGs is non-periodic. The basic differences [15] between PRNGs and TRNGs are very easy to understand because PRNGs produce random numbers by using pre-calculated data and mathematical formulaes. An outlook is shown in the Table I in which the characteristics of the two types of random number generators are compared.

Even the numbers generated from TRNG seems random, but they are really predetermined. TRNGs are considered more suitable, approximately, in such applications in which PRNGs are failed to find their applications. These includes security in data transfer, gambling, games etc. However, less efficient and non-deterministic nature of TRNGs doesn't allow such generated random numbers to produce satisfactory results for the applications like simulation and modeling. This is because TRNG is not able to generate the amount of data which is required for these applications.

IJARCCE
ISSN (Online) 2278-1021
ISSN (Print) 2319 5940
International Journal of Advanced Research in Computer and Communication Engineering
Vol. 5, Issue 5, May 2016

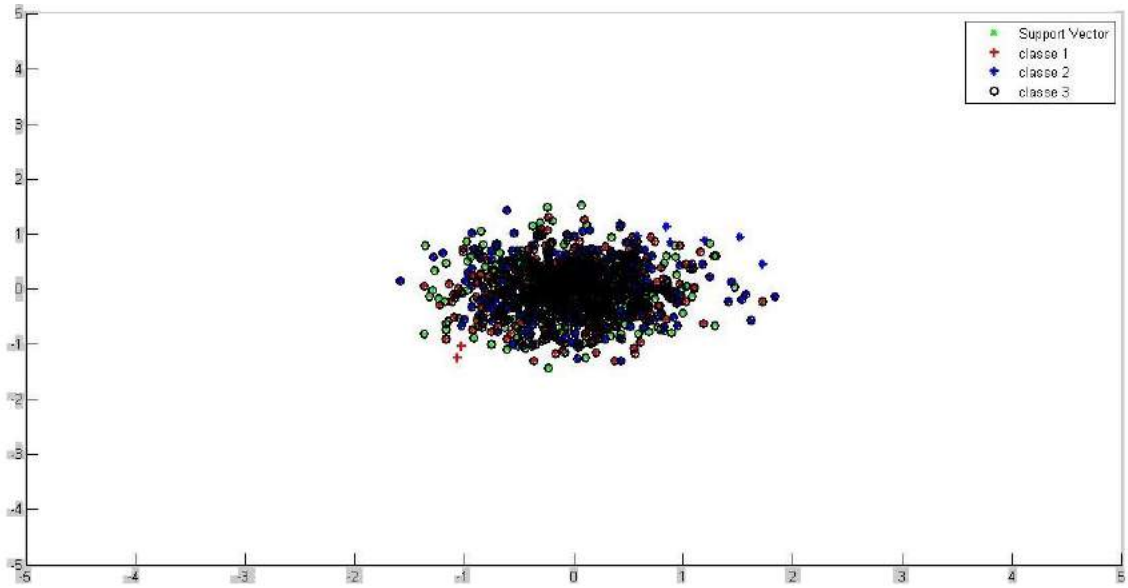


Fig. 1. Mixture of three classes Pseudo Random Numbers

TABLE I COMPARISON OF PRNGS AND TRNGS

Characteristics	True RNGs	Pseudo RNGs
Efficient	Less	more
Nature	Random	Deterministic
Repeatablity	Non-repeatable	Repeatable

Table II shows the various fields of applications and generators suitable in each field.

TABLE II SUITABLITY OF GENERATOR : APPLICATION-WISE

Application	Most Suitable Generator
Generation of keys for data encryption	True RNG
Random Sampling (e.g., medicine selection)	True RNG
Sports and Gambling	True RNG
Lotteries and Draws	True RNG
The Arts	Varies
Simulation and Modelling	Pseudo RNG

Hence, according to its application in the simulation and modelling, Pseudo Random numbers are used during this research. Three different types of Pseudo Random numbers generated are mixed and classified again separately using a classifier. The classifier is explained in the next sub-section.

D. Classifier

In the classification of the pseudo random numbers generated using different sources, SVM is a classifier which is used. It is a supervised learning model [16] as it is firstly trained using the associated learning algorithms with the labelled data. Then with the help of this trained model, tested data is analyzed. These are exploited in the regression analysis. SVMs can be helpful in various applications. These includes text categorization, hand-written characters recognition etc. Experimental results shows, SVM achieves higher accuracy than other traditional models. SVMs also find its application in the field of medical sciences with nearly 80% of accuracy in classifying the samples accurately. For this, a set of training random numbers, each marked for one of the classes is used to train the SVM. Then the pseudo random numbers are tested on this trained SVM and the random numbers are classified into the classes to which they belong. SVM can easily with efficient results performs non-linear classification using kernel trick in which dimensionality is increased for the feature space. Let y_i, j =1, 2, . . . ,K, be the pseudo random numbers for the training Y. Numbers taken belong to one of the three sources (or classes). These random numbers are supposed to be separable linearly. Now, the objective is to design a hyperplane such as

$$h(y) = \omega^T y + \omega_0 = 0 \tag{8}$$

Then the separation of a support vector from the hyperplane is given by

$$D = \frac{|h(y)|}{\|\omega\|} \tag{9}$$

Now, ω, ω_0 are selected such that the value of h(y) should be at the support vector points. This is equivalent with

1. Having a margin of

$$\frac{1}{\|\omega\|} + \frac{1}{\|\omega\|} = \frac{2}{\|\omega\|}$$

IJARCCE

ISSN (Online) 2278-1021
ISSN (Print) 2319 5940

International Journal of Advanced Research in Computer and Communication Engineering
Vol. 5, Issue 5, May 2016

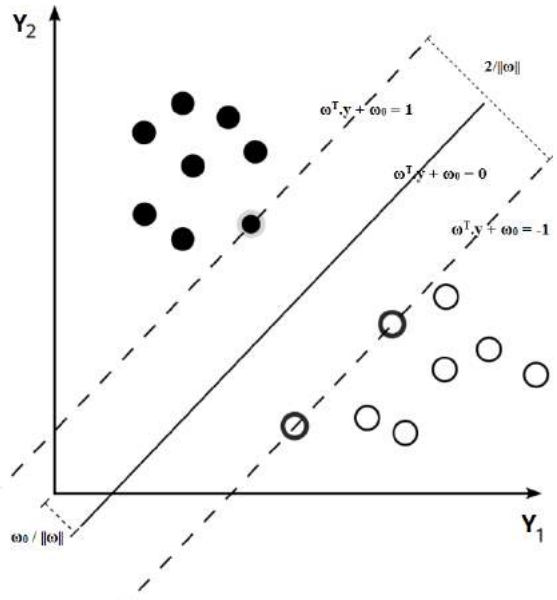


Fig. 2. Linear Classifiers

2. Requiring that

$$\omega^T y + \omega_0 \geq 1, \forall y \in \omega_1 \quad (10)$$

$$\omega^T y + \omega_0 \geq -1, \forall y \in \omega_2 \quad (11)$$

Now, for each value of y_j, we represent the corresponding class by z_j. Hence, for this, calculate ω, ω_0 so that:

$$\text{minimize } F(\omega, \omega_0) \equiv \frac{1}{2}\|\omega\|^2 \quad (12)$$

subject to

$$z_j(\omega^T y + \omega_0) \geq 1 \quad , j = 1, 2, \ldots, \quad (13)$$

This is done as minimizing (12) will make the separation between support vector and hyperplane maximum. Some constraints need to be followed by the SVM. Here are the Karush–Kuhn–Tucker (KKT) conditions [17] that the minimizer has to satisfy are as follows:

$$\frac{\partial}{\partial \omega} L(\omega, \omega_0, \eta) = 0 \quad (14)$$

$$\frac{\partial}{\partial \omega_0} L(\omega, \omega_0, \eta) = 0 \quad (15)$$

$$\eta_j \geq 0 \quad , j = 1, 2, \ldots, K \quad (16)$$

$$\eta_j[z_j(\omega^T y + \omega_0) - 1] = 0 \quad , j = 1, 2, \ldots, K \quad (17)$$

More formally, SVM will design a hyperplane in a higher dimensional space using the kernel trick which can be exploited for the classification purpose. But here, three classes of random number are present generated from different sources and no need of kernel function is there during this classification. Here, multiclass SVM is sufficient for the given set of pseudo random numbers generated from three different sources.

E. Multiclass SVM

Multiclass SVM aims to label the test datasets of random numbers by exploiting SVMs. In this, the main approach used is to convert the multiclass problem into binary problem which will be done multiple times.

There are some methods through which such conversion is possible. Such methods include: (i) one-versus-one (or Pairwise approach), (ii) one-against-all. In the Pairwise classification, every classifier is assigned with instance to one of the classes. Then, the votes are counted for the assigned class. Finally, the class with maximum number of votes is assigned the instance classification.

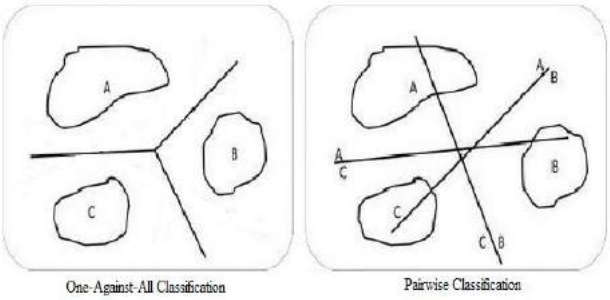


Fig. 3. Multiclass SVM

For this research work, one-versus-all approach is used. In this approach, Tested dataset is classified using an output function whose highest value defines the class to which that data is to be allocated.

III. EXPERIMENTAL VIEW

Here, multiple 1-dimensional data points to be categorised into three different classes. These different types of classes are the Pseudo Random numbers generated using three different types of PRNGs. Thus we have vectors. In addition to binary classification, we also scrutinize the use of multiclass classification for the problem at hand which we have used in this research. In one-against-all classification approach, there is a single binary SVM is exploited for each class so that members of that class can be separated from the members of other classes. We create sequences of Pseudo Random numbers and extract attributes pertaining to runs of various lengths which are then normalized and given as input to the SVM for training and cross validation. These three types of Pseudo Random numbers are first mixed and used as a single collection of all the numbers. A different set of sequences is generated by changing the bias of occurrence of particular outcomes and this set is tested on the trained classifier. And the algorithm for the same process is shown here as under:

Algorithm

Classification of Pseudo random numbers generated from three different types of sources using SVM Classifier.

Input: I: Input data, V: Support vectors

1. Assigning different class labels to each of the three set of pseudo random numbers, divide them into their

classes for training.
2. Add these training datasets to the support vector set named as V.
3. Then make a loop for these divided set of random numbers.
4. If any random number does not belongs to any of the class labels, then add that random number to the set V.
5. Break, if inadequate random numbers are found.
6. end loop.
7. Trained exploiting the resulting classifier i.e. SVM model.
8. Test, with the unlabelled random numbers, so as to validate the results.

IV. RESULTS

Now, in the results of the research, matlab simulation is shown. Matlab simulation shows the results as the outcomes of classification of the Pseudo Random numbers using the SVM classifier. In the fig. 4 shown, three classes (Class 1, 2 and 3) of Pseudo Random numbers are classified using SVM classifier.

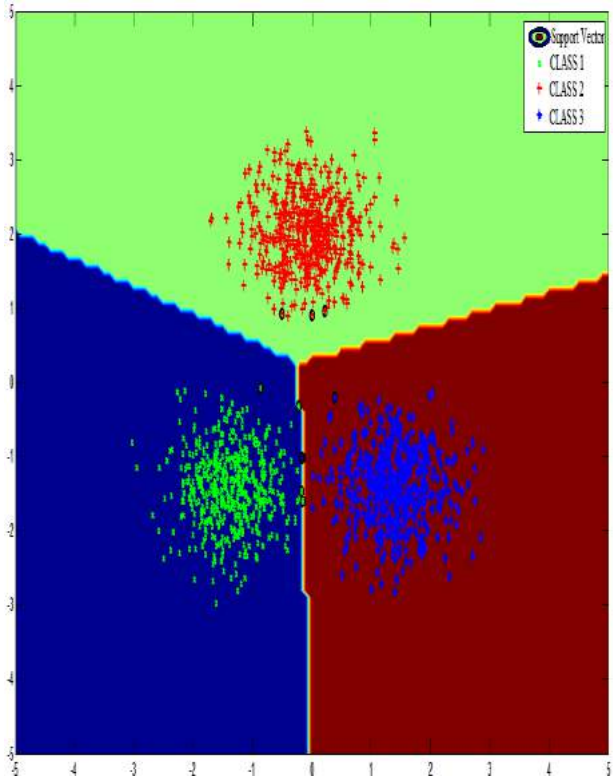


Fig. 4. Classification using SVM

As it was already shown in the fig. 1 that, firstly, three types of Pseudo Random nubmers generated using three different sources were mixed. Then these are very well classified by the SVM classifier using the algorithm that is already discussed in section III. Random numbers shown with green colour is class 1, red colour is class 2 and shown with blue colour is class 3. From the results, it can be seen that Pseudo Random numbers are very well separated using the SVM classifier. And it shows nearly 100% accuracy in classifying the Pseudo Random numbers.

V. CONCLUSION

This paper shows the successful classification of Pseudo Random numbers in their one-to-one classes using Support vector machine (SVM) classifier. We are able to get the optimum path to get the specific results which other classifiers were not able to deliver accurately and this accuracy can be further improved by using some more invariances as the features which can be used to classify these Pseudo Random numbers.

Our research can be helpful in the field of cryptanalysis. Cryptanalysis includes security in sending a message. Hence, this classification of Pseudo Random number's sources helps in enhancing that level of security in sending those messages. This enhancement in cryptanalysis surely booms the field of security.

REFERENCES

[1] J. K. Heinrich, Pangrat and Hans Weinrichter, "Pseudo Random Number Generator Based on Binary and Quinary Maximal-Length Sequences", Ieee Transactions On Computers, Vol. C-28, No. 9, September 1979

[2] D. H.Lehmer, "Random number generation on the BRL highspeed computing machines," by M. L. Juncosa. Math. Rev. 15, 559, 1954.

[3] L. Blum, M. Blum, and M. Shub. A simple unpredictable Pseudo Random number generator. SIAM Journal on computing, 15(2):364–383, 1986.

[4] V. N. Vapnik, "An overview of statistical learning theory", IEEE Transactions on Neural Networks, Volume: 10, Issue: 5, Pages: 988 – 999, 1999.

[5] F. Dehghan; H. Abrishami-Moghaddam, "Comparison of SVM and neural network classifiers in automatic detection of clustered microcalcifications in digitized mammograms", 2008 International Conference on Machine Learning and Cybernetics, Volume: 2, Pages: 756 – 761, 2008.

[6] T. Joachims. Text categorization with support vector machines: Learning with many relevant features. Technical Report 23, Universit~it Dortmund, LS VIII, 1997.

[7] Koby Crammer and Yoram Singer, "On the Algorithmic Implementation of Multiclass Kernel-based Vector Machines", Journal of Machine Learning Research 2 Page: 265-292, 2001.

[8] R.C. Fairfield, R.L. Mortenson, and K.B. Coulthart. An LSI Random Number Generator (RNG). In Advances in Cryptanalysis: Proceedings of Crypto 84, pages 203–230. LNCS 0196, Springer-Verlag, 1984.

[9] D. Eastlake, S. Crocker, and J. Schiller. Randomness recommendations for security. Network Working Group, RFC 1750, 1994.

[10] U. Vazirani and V. Vazirani. Efficient and secure Pseudo Random number generation. In Proc. 25th IEEE Symp. on the Foundations of Comput. Sci., pages 458–463, 1984.

[11] T. Stojanovski, J. Pil, and L. Kocarev. Chaos-based random number generators. Part II: practical realization. IEEE Transactions on Circuits and Systems – I: fundamental Theory and Application, 48(3):382–385, March 2001.

[12] A. J. Menezes, P. C. van Oorschot, and S. A. Vanstone. Handbook of Applied Cryptanalysis. CRC Press, 5th edition, 2001.

[13] R.C. Fairfield, R.L. Mortenson, and K.B. Coulthart. An LSI Random Number Generator (RNG). In Advances in Cryptanalysis: Proceedings of Crypto 84, pages 203–230. LNCS 0196, Springer-Verlag, 1984.

[14] A New Approach to Machine Generation of Random Variables With Any Distribution P. T. Jeswani S. Sikdar, Senior Member Ieee Ieee Transactions On Reliability, Vol. R-27, No. 1, April 1978.

[15] C. Q. Li, S. J. Li, and G. Alvarez. Cryptanalysis of two chaotic encryption schemes based on circular bit shift and xor operations. Physics Letters (a), 369:23–30, 2007.

[16] C. Cortes and V. Vapnik. Support vector networks. Machine Learning, 20:273–297, 1995. R. Courant and D. Hilbert. Methods of Mathematical Physics. Interscience, 1953.

[17] C.J.C. Burges. Geometry and invariance in kernel based methods. In B. Sch¨olkopf, C.J.C. Burges, and A.J. Smola, editors, Advances in Kernel Methods: Support Vector Learning, pages 89–116. MIT Press, 1999.

Available online at www.ijpsdr.com

International Journal of Pharmaceutical Sciences and Drug Research
2016; 8(3): 144-148



Research Article

ISSN: 0975-248X
CODEN (USA): IJPSPP

Computational Studies of Synthetic and Plant-Derived Compounds against Cardiovascular Disease Targets

N. Jauhari, S. Gupta, S. Saxena, N. Bharadvaja*

Department of Biotechnology, Delhi Technological University (formerly Delhi College of Engineering), Delhi, India

ABSTRACT

Knowledge of cardiovascular diseases and improved diagnostic capacity is rapidly expanding with the advancement of medical sciences. However, heart diseases are a challenge to human life. Few important therapeutic targets for cardiovascular diseases were collected from mining of various bibliographic sources. Different proteins and bioactive small molecules are taken into consideration for target search. From ancient times, medicinal plants are shown to have remedial effect on cardiovascular system of human body, yet their modes of action are not completely understood till now. Selected plant derivatives, which have been examined under *in vitro* conditions to be effective against various heart diseases, were subjected to molecular docking with proposed targets using a bioinformatics tool, Hex 8.0. We have explored eight targets for five types of cardiovascular diseases and ten different ligands from herbal plants with a brief description about the cardiovascular diseases, their symptoms, target, ligand, source of the ligand and their mechanism of action. All the reported synthetic and phytocompounds were found to have good binding energies with all potential disease targets. Among all, Forskolin is found to be the best inhibitor of Angiotensin II type I receptor with the E-score of -369.96 for Atherosclerosis.

Keywords: Molecular docking; cardiovascular; Hex; phytocompounds.

INTRODUCTION

Cardiovascular diseases (CVD) are the group of disorders of heart and circulation, responsible for premature death. CVDs include: ischemic heart disease (IHD), stroke, hypertensive heart disease, rheumatic heart disease (RHD), aortic aneurysms, cardiomyopathy, atrial fibrillation, congenital heart disease, endocarditis, and peripheral artery disease (PAD). Risk factors of CVDs are mainly unhealthy diet, lack of physical activity, high blood pressure, high blood cholesterol, diabetes, smoking, obesity and sometimes-family history. According to WHO (Fact sheet N°317, 2015), 17.5 million people died from CVDs in 2012, which is the 31% of all worldwide deaths. Among these, coronary heart disease was responsible for 7.4 million deaths and 6.7 million were died due to stroke. However, CVDs are no more age related disorders; still most of the cardiovascular diseases affect older persons. We have studied five important cardiovascular diseases, which are important and seek global attention. These are cardiomyopathy (heart muscle disease) is the decrease in the ability of the myocardium (the heart muscle) to contract, mostly resulting in heart failure. Myocardial infarction (Pain), commonly known as a heart attack, is the damage of heart muscle, occurring when blood does not flow to the heart on any part of it. Coronary artery disease (CAD) is also known as ischemic heart disease (IHD).

***Corresponding author: Dr. N. Bharadvaja,**
Delhi Technological University (formerly Delhi College of Engineering), New Delhi-110042, India; **Tel.:** +91-9868446613; **E-mail:** navneetab@dtu.co.in
Received: 28 March, 2016; **Accepted:** 10 May, 2016

Atherosclerotic or coronary heart disease includes symptoms like stable and unstable angina, myocardial infarction as well as sudden artery death. Myocardial Ischemia (MI), a heart condition, occurs through decreased blood flow to the myocardium due to a partial or complete blockage of coronary arteries. Blood clotting disorder is the condition of shock and possible death when the loss of blood from the damaged or cut blood vessels was not stopped.

CVDs are the consequence of multiple pathogenic factors, reflecting the changed interaction between interconnected genes and their products. A number of chemicals, synthetic drugs, NSAIDs have been used to cure CVDs but demand for compounds with lesser side effects is increasing. In addition to the tremendous growth of biochemical data and the progress of network pharmacology, the analysis of mechanisms of action of medicinal herbs at *in silico* level has become possible. Walker (1996) has reviewed plant foods and extracts for prophylactic and curative effects in reducing cardiovascular disease. [1] Table 1 shows all studied targets their ligands, source of ligand and their corresponding associated diseases.

Literature survey reveals that the majority of current CVD drugs develop adverse effects. On the contrary, natural and few industrially produced compounds contain the remedial properties without any harmful effects on human being even after long-term use. These compounds can play a vital role in the production of novel treatment amenity for cardiovascular diseases. Therefore, objective of the present study is to identify the inhibitors having the potential to inhibit various targets of cardiovascular diseases and explore their interaction capability with selected ligands. In the present study, we worked on eight potential molecular targets for five types of cardiovascular diseases and docked them with ligands of medicinal plants and safe synthetic compounds to test their binding affinity for probable phytomedicine as well as synthetic but harmless drug for humans. The selected ligands are Forskolin (Fig. 1), Naproxen (Fig. 2), Pinocembrin (Fig. 3), Resveratrol (Fig. 4), Morin hydrate (Fig. 5), Tamarixetin (Fig. 6), Epicatechin (Fig. 7), Cocoa flavanols (Fig. 8), Cannabidoids (Anandamide) (Fig. 9) and Aspirin (Acetylsalicyclic acid) (Fig. 10). Except naproxen and aspirin all are plant-derived compounds. Various bioinformatics tools like Swiss prediction, Hex, OpenBabel Graphical User Interface (GUI), various databases (uniprot, PDB, RCBS, NCBI), pc3 viewer and argus lab have been used to explore the findings.

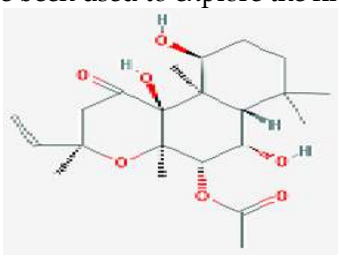


Fig. 1: Forskolin

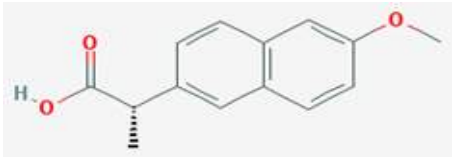


Fig. 2: Naproxen

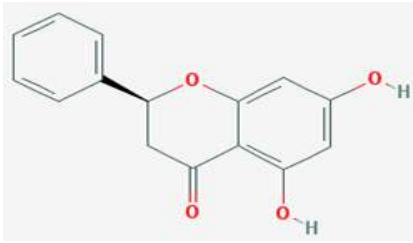


Fig. 3: Pinocembrin

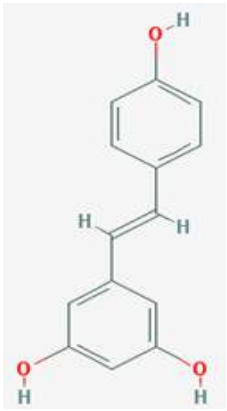


Fig. 4: Resveratrol

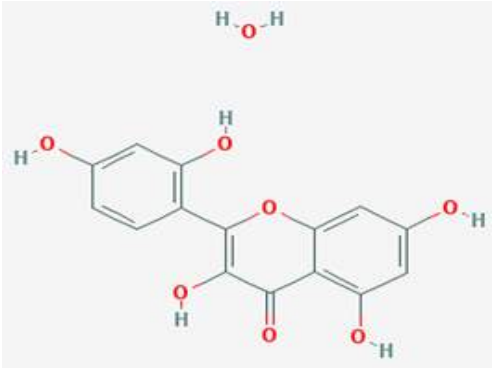


Fig. 5: Morin Hydrate

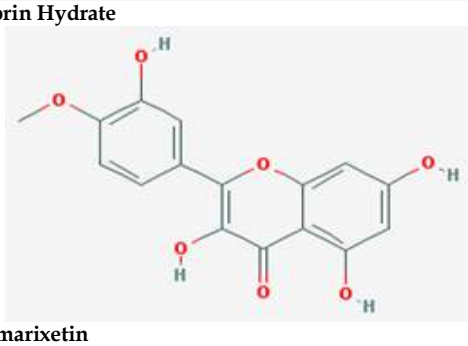


Fig. 6: Tamarixetin

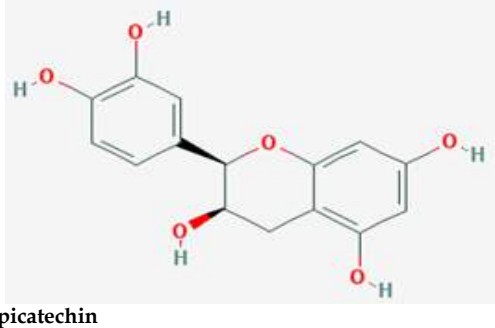


Fig. 7: Epicatechin

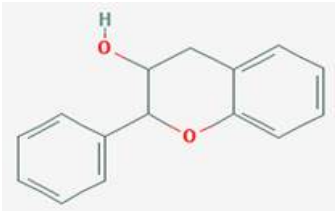


Fig. 8: Cocoa Flavanol

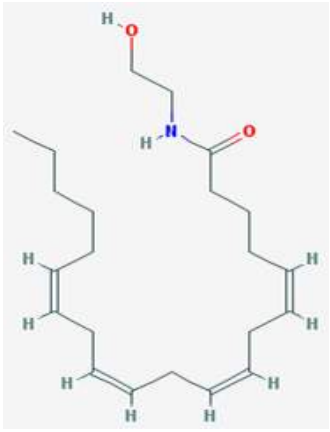


Fig. 9: Anandamide

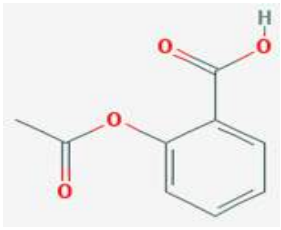


Fig. 10: Aspirin

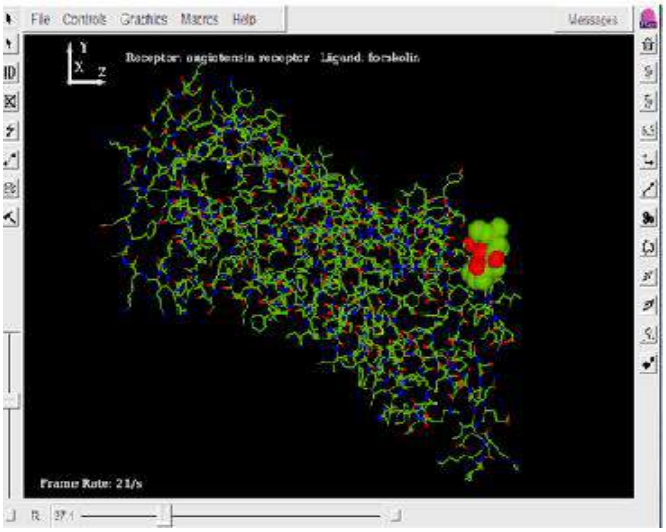


Fig. 11: Docked complex of ATR and Forskolin (red and green balls)

MATERIALS AND METHODS

Inverse (or reverse) docking (for target prediction)

Molecular docking is a computational process, which helps to determine the energy associated with a ligand-target complex and how the energy level changes according to configuration in the form of E values. Once the genes responsible for causing diseases are found, it would be possible to design lead molecules, which could modulate those genes or their protein products. The growth in the number of 3D structure databases of proteins eg. PDB and the increase in computing power have made virtual screening of lead molecules an easier and faster process. However, in reverse docking, protein targets are searched, which can bind to a specific known ligand. The procedure is as follows -a compound with known biological activity is docked to the binding sites of all 3D structures of proteins in a given database. Protein 'hits' identified from this docking can further be used as potential candidates for validation. This approach is referred to as reverse docking. The software that was used to do reverse docking was SwissTargetPrediction.

Ligand preparation

The 3D structures of the 10 plant derived compounds were obtained from PubChem in PDB format. The ligands were available in XML, SDF, JSON and ASN.1 formats. Most structures were obtained in SDF format. These conformations were used as starting conformations to perform docking. [2]

Target preparation

Most appropriate targets were obtained through Swiss target search. Secondary research via literature survey has been done for the validation of the selected targets. Target structures were obtained from Protein Data Bank in PDB format. Targets were downloaded in such a way that heteroatoms like water, ions etc. were not present and they did not complex with other bioactive molecules. Those structures, which were found complexes with other bioactive molecules, were individually modeled using SWISS MODEL. It uses the FASTA format of protein sequences. [2]

Ligand visualization

The ligand and target in the PDB format were visualized in Argus Labs [3] and in PC3 viewer. ArgusLab and PC3 viewer are both freely licensed. The structure files obtained from ChemSketch, Pubchem were not in PDB format. They were converted to PDB format using OpenBabel. Molecular Docking technique was done using Hex 8.0.0 with 10 plant-derived compounds. Hex is an interactive molecular graphics program used for calculating and displaying feasible docking pairs of protein-DNA or, protein-ligand molecules, assuming the ligand is rigid.

RESULTS AND DISCUSSION

Each compound was docked to the same or a different target. In order to compare docking interactions between selected natural compounds and the known inhibitor/activators (as required) of each target, docking was also performed with specific compounds that are reported to have activity against the studied targets, via previous studies. Table 2 shows the E-score of all interactions.

Docking results for binding between Adenylate cyclase and Forskolin showed adequate binding. Adenylyl cyclase (AC) is an effector molecule that catalyzes the conversion of ATP to cAMP in β-adrenergic receptor (βAR) signaling. Forskolin has the ability to activate cAMP-generation systems reversibly in intact cells. It acts as an activator for adenylate cyclase.

Table 1: Cardiovascular diseases their therapeutic targets and corresponding ligands

S. No.	Disease	Target	Ligands	Source of Ligand
1	Atherosclerosis/Coronary Artery Diseases	Angiotensin II type 1 Receptor [14]	Forskolin	Plant- *Coleus forskhohlii*
			Resveratrol	Plant- grapes, nuts and berries
			Morin hydrate	Plant- *Morus alba L.*
			Tamarixetin	Plant- *Tamarix gallica*
		NF-κB	Epicatechin	Plant-*Theobroma cacao*
			Quercetin reductase [15]	Plant-*Theobroma cacao*
			Cocoa Polyphenols [16]	Plant-*Theobroma cacao*
			Cocoa Flavanols	Plant-*Theobroma cacao*
		Angiotensin Converting enzyme (ACE)	Epicatechin	Plant-*Theobroma cacao*
			Cocoa flavanols	Plant-*Theobroma cacao*
		SOD	Epicatechin	Plant-*Theobroma cacao*
			Cocoa flavanols	Plant-*Theobroma cacao*
2	Blood Clotting	Thromboxane A_2 [17]	Aspirin	Synthetic- Industrially produced
3	Cardiomyopathy [18]	Adenylate cyclase	Forskolin	Plant- *Coleus forskhohlii*
4	Myocardial Infarction, Pain	COX-2	Naproxen [19]	Synthetic-Industrially produced
			Pinocembrin	Plant- *Curcuma ecalcarata*
			Resveratrol	Plant- grapes, nuts and berries
5	Myocardial Ischaemia	Cannabinoids Receptor 1,2 [20]	Cannabinoids	Plant-*Cannabis sativa*

Table 2: E-score of all docking interactions performed for cardiovascular disorders

S. No.	Targets	Ligands	Total E-score
1	Adenylate cyclase	Forskolin	-313.3
2	Angiotensin II type 1 Receptor	Forskolin	-369.96 [Figure 11]
3	Angiotensin Converting enzyme	Anthocynidine reductase	-769.9
4	Cannabinoids Receptor 1,2	Anandamide	-344.4
5	COX-2	Naproxen	-289
		Resveratrol	-351.0
		Pinocembrin	-286.97
6	NF-KB	Resveratrol	-280.5
		Morin hydrate	-325.3
		Anthocynidine reductase	-245.4
		Quercetine reductase	-325.6
7	SOD	Anthocynidine reductase	-879.1
8	Thromboxane A_2	Aspirin	-132.85

Forskolin elicited marked accumulations of cyclic AMP in rat cerebral cortical slices. [4] Naproxen binds to cyclooxygenase-2 (COX-2) with good interaction energy. All three ligands have been reported as inhibitors of COX-2. The inhibitors suppressed the formation of prostaglandin I_2 as COX-2 was the source of prostaglandins E_2 and I_2, which mediate inflammation. [5] The selective inhibition of this target has been shown to relieve patients of myocardial infections. AT1 (Angiotensin II type 1 receptor) is a well-known vasconstrictor, which causes blood vessels to constrict thereby causing hypertension. Angiotensin II receptor blockers (ARBs) prevent ligand angiotensin II to bind these receptors on blood vessels, providing relief in atherosclerosis. [6] Here, many plant derivatives were found to play this role. Forskolin, Resveratrol, and Morin hydrate have good binding with AT1. Forskolin is found to be the best inhibitor among all docked ARBs. Fig. 11 shows docked complex of angiotensin II type I receptor and Forskolin (red and green balls). Binding of Anthocynidine reductase to SOD leads to its activation. SOD is produced in more amounts. E-score of this interaction is good interaction. *In vivo* interaction between ROS and RNS, results in the formation of peroxynitrite (a powerful oxidant). [7] The reaction between SOD and reactive oxygen species prevents interaction between ROS and NO. Thus, maintaining concentration of NO that is a vasorelaxant. [8] This is beneficial against atherosclerosis. Another target in Atherosclerosis is angiotensin converting enzyme (ACE). Angiotensin-converting enzyme (ACE) inhibitors interfere with the formation of Angiotensin II that can constrict blood vessels. ACE inhibitors lower B.P. and reduce the workload on the heart, which lowers the chances of heart attack. Anthocynidine reductase showed good inhibition when complexes with ACE. Anandamide, an endocannabinoids was docked with CB receptor 1 and resulting complex showed inhibition of the receptor. Cannabinoids provide protective role in atherosclerosis progression and in cerebral and myocardial ischemia. [9-11] Anandamide limits infarct size induced by ischemia-reperfusion injury and the pharmacological profile of this response fails to match with any of the previously known mechanisms of cannabinoid action. [12] Thromboxane-A_2 is the therapeutic target of blood clotting disorder [13] and its ligand Aspirin is helpful in giving relief from skeletal pain, viz. arthritis, fever (antipyretic), prevents platelet coagulation (thus used for preventing heart attacks) and inhibits prostaglandin synthesis. As such, its role is being studied in diseases where blood clotting blocks vessels. Binding with target thromboxane A2 is noticed as least effective.

Among all docked complexes, ligand anthocynidine reductase showed maximum E-score with target SOD (super oxide dismutase) by activating it (or increasing its production) while ligand Forskolin shows maximum E-score with target Angiotensin II type I receptor by activation of target. As such, these interactions have high binding affinity and can be further studied for their role as potential molecular targets in targeted treatment of cardiovascular diseases. However, all the

studied docked complexes can be referred for development of potential drugs for cardiovascular diseases. Experimented computational technique is faster than the traditional drug designing method, cheaper and less laborious. Results of this investigation can further be utilized for the development of safe and potent herbal and synthetic drug after *in vivo* studies and clinical trials to the benefit of humankind.

ACKNOWLEDGEMENT

We would like to thank Vice Chancellor of Delhi Technological University and Head of Department of Department of Biotechnology, for providing the facility and support to conduct the research work.

REFERENCES

1. Walker AF. Of Hearts and Herbs. Biologist. 1996; 43: 177-180.
2. Lisina KV, Piramanayagam S. An *in-silico* Study on Thymoma with Inhibitors from Petiole and Tender Coconut Water *from Cocos nucifera*. Int. J. Pharm. Sci. Drug Res. 2014; 6: 52-59.
3. Baghel MS, Goswami K. Bcl-2 Targeted Structural Based Computer Aided Drug Design (CAAD) For Therapeutic Assessment of Ricin in Prostate Cancer. Int. J. Pharm. Sci. Drug Res. 2015; 7:168-171.
4. Rodbell M. The role of hormone receptors and GTP-regulatory proteins in membrane transduction. Nature. 1980; 284: 17-22.
5. Garret A, Fitz, Gerald MD. Coxibs and Cardiovascular Disease. The New England Journal of Medicine. 2004; 351: 1709-1711.
6. Fu GD, Sun YL, Hamet P, Inagami T. The angiotensin II type 1 receptor and receptor-associated proteins. Cell Research. 2001; 11:165-180.
7. Bilfinger TV, Salzet M, Fimiani C, Deutsch DG, Tramu G, Stefano GB. Pharmacological evidence for anandamide amidase in human cardiac and vascular tissues. International Journal of Cardiology 1998; 64 (Suppl 1): S15-S22.
8. Kim van der heiden, Simon C, Le A. luong, MZ, Paul CE. Role of nuclear factor κB in cardiovascular health and disease. Clinical Science. 2010; 118: 593-605.
9. Hillard CJ. Endocannabinoids and vascular function. Journal of Pharmacology and Experimental Therapeutics. 2000; 294:27-32.
10. Randall MD, Harris D, Kendall DA, Ralevic V. Cardiovascular effects of cannabinoids. Pharmacology and Therapeutics. 2002; 95: 191-202.
11. Pacher P, Bátkai S, Kunos G. Cardiovascular pharmacology of cannabinoids. Handbook of Experimental Pharmacology. 2005; 168: 599-625.
12. Underdown NJ, Hiley CR, Ford WR. Anandamide reduces infarct size in rat isolated hearts subjected to ischaemiareperfusion by a novel cannabinoid mechanism. Br J Pharmacol. 2005; 146: 809-816.
13. Andrew O. Maree, MSc, MD; Desmond J. Fitzgerald, MD. Variable Platelet Response to Aspirin and Clopidogrel in Atherothrombotic Disease. Circulation 2007; 115: 2196-2207.
14. Matsoukas MT, Cordomí A, Ríos S, Pardo L, Tselios T. Ligand binding determinants for angiotensin II type 1 receptor from computer simulations. J Chem Inf Model. 2013; 11: 2874-2883.
15. Kleemann R, Verschuren L, Morrison M, Zadelaar S, van Erk MJ, Wielinga PY, Kooistra T. Anti-inflammatory, anti-proliferative and anti-atherosclerotic effects of quercetin in human *in vitro* and *in vivo* models. Atherosclerosis. 2011; 1: 44-52.
16. Vázquez-Agell M, Urpi-Sarda M, Sacanella E, Camino-López S, Chiva-Blanch G, Llorente-Cortés V, Tobias E, Roura E, Andres-Lacueva C, Lamuela-Raventós RM, Badimon L, Estruch R. Cocoa consumption reduces NF-κB activation in peripheral blood mononuclear cells in humans. Nutr Metab Cardiovasc Dis. 2013; 3: 257-263.
17. Rivera J, Lozano ML, Vicente V. Platelet receptors and signaling in the dynamics of thrombus formation. Haematologica. 2009; 5: 700-711
18. Denniss AR, Marsh JD, Quigg RJ, Gordon JB, Colucci WS. Beta-adrenergic receptor number and adenylate cyclase function in denervated transplanted and cardiomyopathic human hearts.Circulation.1989; 79: 1028-1034.
19. Hippisley-Cox J. Risk of myocardial infarction in patients taking cyclo-oxygenase-2 inhibitors or conventional non-steroidal anti-inflammatory drugs: population based nested case-control analysis. BMJ.2005; 330-1366.
20. Filippo CD, Rossi F, Rossi S, D'Amico M. Cannabinoid CB2 receptor activation reduces mouse myocardial ischemia-reperfusion injury: involvement of cytokine/chemokines and PMN. JLB. 2003; 3: 453-459.

Source of Support: Nil, Conflict of Interest: None declared.

Soft Comput
DOI 10.1007/s00500-016-2202-2

METHODOLOGIES AND APPLICATION

Design and analysis of BFOA-optimized fuzzy PI/PID controller for AGC of multi-area traditional/restructured electrical power systems

Yogendra Arya[1] · **Narendra Kumar**[2]

© Springer-Verlag Berlin Heidelberg 2016

Abstract In this paper, design and performance analysis of bacterial foraging optimization algorithm (BFOA)-optimized fuzzy PI/PID (FPI/FPID) controller for automatic generation control of multi-area interconnected traditional/restructured electrical power systems is presented. Firstly a traditional two-area non-reheat thermal system is considered, and gains of the fuzzy controller are tuned employing BFOA using integral of squared error objective function. The supremacy of this controller is demonstrated by juxtaposing the results with particle swarm optimization (PSO), firefly algorithm (FA), BFOA, hybrid BFOA–PSO-based PI and fuzzy PI controllers based upon pattern search (PS) and PSO algorithms for the same power system structure. The approach is then extended to a two-area reheat system, and improved results are found with the purported FPI/FPID controller in comparison with PSO and artificial bee colony optimized PI controller. Further, the approach is implemented on a traditional multi-source multi-area (MSMA) hydrothermal system and its superb performance is observed over genetic algorithm and hybrid FA–PS tuned PI controller. Additionally, to demonstrate the scalability of the designed controller to cope with restructured power system, the study is also protracted to a restructured MSMA hydrothermal power system. Finally, sensitivity analysis is performed to ascertain the robustness of the controller designed for the systems under study. It is observed that the suggested FPI/FPID controller optimized for nominal conditions is able to handle generation rate constraints and wide variations in nominal loading condition as well as system parameters.

Keywords Multi-area power system · Multi-source power system · Fuzzy logic controller (FLC) · Automatic generation control (AGC) · PI/PID controller · Restructured power system

Communicated by V. Loia.

✉ Yogendra Arya
yarya@msit.in

Narendra Kumar
dnk_1963@yahoo.com

[1] Department of Electrical and Electronics Engineering, Maharaja Surajmal Institute of Technology, Janakpuri, New Delhi 110058, India

[2] Department of Electrical Engineering, Delhi Technological University, Shahbad Daulatpur, Main Bawana Road, Delhi 110042, India

1 Introduction

Modern power systems comprise of several integrated control areas duly interconnected via tie-lines. The control of generation or frequency is the big issue for reliable operation of a power system. For appropriate operation of power system, the frequency and tie-line power exchange should remain almost stable (Kothari and Nagrath 2012). Under normal conditions, the total power generation of power stations should equal to the load demands plus associated losses. However, active and reactive power demands are never stable; so steam input to turbogenerators or water input to hydro generators must then be always regulated to match the active power demand, failing which the machine speed/frequency will violate the prescribed limits. Therefore, a control mechanism is necessary to nullify the effects of the varying load changes. Automatic generation control (AGC), also termed as supplementary control, performs a continuous real-time task to adjust the power generation of the respective generator most economically to match with the randomly changing load demands (Kundur 2011). In an AGC system, each con-

Published online: 06 June 2016

trol area has a coherent group of generators responsible for its own load demand and scheduled power interchanges within neighboring control areas (Elgerd 2014).

The traditional electric power business at present is chiefly handled by vertically integrated utilities (VIUs) which own generation, transmission and distribution systems, and sell power to the consumers at regulated rates. No market players exist in traditional electricity market. The US Federal Energy Regulatory Commission (FERC) has issued order 888 in year 1996 on electricity deregulation or restructuring. This order intended to boost competition in wholesale electrical power markets. The effects of deregulation of the power industry on AGC have been addressed by Christie and Bose (1996). After deregulation and restructuring of power industry, VIUs do not exist and several independent entities such as distribution companies (DISCOs), generation companies (GENCOs), transmission companies (TRANSCOs) and independent system operator (ISO) have been introduced in competitive open market (Arya et al. 2016; Bhateshvar et al. 2015; Sekhar et al. 2016). In this new scenario, consumers will have an opportunity to make a choice among electric service providers to purchase unbundled power at competitive best prices. However, the continuous growth in size and complexity and stochastically changing load demands in electric systems has turned AGC task a challenging one.

2 Literature review

The first attempt in AGC was to control the frequency oscillations of the power system via the flywheel governor of the synchronous machine (Ibraheem et al. 2005). But this method was insufficient to control the deviated frequency, thus a supplementary control action was added to the speed governor using a signal proportional to the integral of the frequency deviation. This scheme is termed as the classical AGC approach. Very early works in classical AGC were based on tie-line bias control strategy (Concordia and Kirchmayer 1953; Cohn 1957). The investigations with large signal dynamics of AGC systems by employing an optimization technique based on nonlinear programming executed by (Aggarwal and Bergseth 1968) might be a maiden attempt. The revolutionary optimal control approach for AGC of interconnected power system was initiated by Fosha and Elgerd (1970). The design of linear optimal AGC regulators with PI controller feedback for a two-area hydrothermal system was presented by Calovic (1984). Although optimal AGC schemes offered palpably enhanced system dynamic performance, they are associated with the measurement of all the system states which is not practically feasible. To circumvent these shortcomings, suboptimal AGC schemes were proposed in the literature (Malik et al. 1985; Aldeen and Trinh 1994). To enhance the dynamic performance of the AGC systems under varying system parameters and operating conditions, variable structure controller has offered better possibilities (Chan and Hsu 1981; Das et al. 1991). Since digital control is more flexible, accurate, reliable, compact and less susceptible to noise/drift, various researchers proposed digital AGC control schemes in AGC of power system (Kumar et al. 1987; Hari et al. 1991).

The literature reviews unveil that over the past decades many researchers have proposed a range of control strategies for AGC of traditional and restructured power systems to preserve the system frequency and tie-line power flows at their scheduled values during normal as well as during small load perturbations (Ibraheem et al. 2005; Pandey et al. 2013). Various conventional and intelligent techniques like ISE-based continuous–discrete control (Nanda et al. 2006), Ziegler Nichols (ZN) method (Chandrakala et al. 2013), variable structure control (Chandrakala et al. 2013), neural networks (Chaturvedi et al. 1999), genetic algorithm (GA) (Abdel-Magid and Dawoud 1996; Chandrakala et al. 2013; Jeyalakshmi and Subburaj 2015), fuzzy control (Indulkar and Raj 1995; Chandrakala et al. 2013; Jeyalakshmi and Subburaj 2015), bacterial forazing optimization algorithm (BFOA) (Ali and Abd-Elazim 2011), firefly algorithm (FA) (Padhan et al. 2014), hybrid particle swarm optimization–pattern search (PSO–PS)-based fuzzy (Sahu et al. 2015a), PSO (Gozde et al. 2010; Abdel-Magid and Abido 2003; Panda et al. 2013), PSO-based fuzzy (Jeyalakshmi and Subburaj 2015), hybrid BFOA–PSO (Panda et al. 2013), artificial bee colony (ABC) (Gozde et al. 2012), hybrid FA–PS (Sahu et al. 2015b, c), hybrid differential evolution–PS (DE–PS)-based fuzzy (Sahu et al. 2014) and BFOA-based fuzzy (Saikia et al. 2013) are prevalent in the literature to solve AGC problem in traditionally interconnected power systems.

In deregulated environment, due to the availability of several GENCOs and DISCOs in the restructured system, DISCOs in an area have the liberty to subscribe contracts with GENCOs operating in any other area for transaction of electric power (Parmar et al. 2014). There can be various types of power transactions between DISCOs and GENCOs such as poolco and bilateral and combination of these transactions. In bilateral transactions, DISCOs of any area show the autonomy to have a contract with GENCOs operating in other control areas, whereas in poolco transactions, GENCOs have contracts within their own areas only. In a competitive electric market, both these transactions may be negotiated simultaneously. TRANSCOs act as medium to wheel the contracted power between GENCOs and DISCOs. For maintaining the electrical system secure and reliable, all transactions have to be mandatorily cleared through ISO. The ISO manage a number of such ancillary services, one of which is AGC (Debbarma et al. 2013). To simulate different transactions, Donde et al. (2001) has introduced the concept of DISCO participation matrix (DPM) and area participation factor (apf) for

AGC study of a two-area restructured thermal system. DPM demonstrates the involvement of a DISCO in contract with a GENCO. In DPM, no. of rows and columns are equivalent to the no. of GENCOs and DISCOs, respectively. Each entry in DPM is termed as contract participation factor (cpf). The cpf_{ij} corresponds to the portion of the total power contracted by a DISCO-j from a GENCO-i (Bhateshvar et al. 2015). It is to be noted that $\sum_i \text{cpf}_{ij} = 0$. The researchers to tackle AGC problem effectively in restructured systems have been suggested many control strategies such as optimal control (Parmar et al. 2014; Arya et al. 2016), BFOA (Debbarma et al. 2013), trajectory sensitivities-based gradient Newton algorithm (Donde et al. 2001), GA-based fuzzy (Bhateshvar et al. 2015) and FA-based fuzzy (Sekhar et al. 2016).

In a realistic power system, each control normally comprises of a mix of thermal, hydro, gas and nuclear power generation. However, due to high efficiency, nuclear plants usually operate at base load close to their maximum power output with no involvement in the system AGC. Gas power plants contribute a very little percentage of total power generation, and they are best suited for meeting the fluctuating peaking load demands (Nanda et al. 2006). Thus, the natural alternative for AGC study, as also presented here, falls on mix of thermal and hydro units in each area of the system under study (Chandrakala et al. 2013; Jeyalakshmi and Subburaj 2015).

In industrial processes the use of classical proportional–integral–derivative (PID) controller is widespread due to their simple/robust design, effectiveness for linear systems and less cost. However, for higher-order systems with time delays and uncertainties, classical PID controller may not be an efficient choice. On the other side, fuzzy logic controller (FLC) is effective to improve the closed-loop performance of PID controller and capable to handle small variations in operating point or system parameters by tuning the controller parameters (Mudi and Pal 1999, 2000). Fuzzy-based PID controller is effective for all nonlinear systems, but fuzzy parameters may not be the optimal as their selection is usually based on certain experiential rules. FLC tuning via rules and membership functions (mfs) tuning is a very complicated assignment which may not be effective. Most common method of FLC tuning is the gain tuning of input and output scaling factors as their values significantly affect the performance of FLC. Therefore, standard rule base and mfs may be utilized for dissimilar applications and input and output scaling factors can be tuned to design optimum fuzzy PI/PID controller (Mudi and Pal 1999, 2000; Yesil et al. 2004; Sahu et al. 2014, 2015a, c; Sekhar et al. 2016). A simplified fuzzy PI controller configuration is visualized for AGC study of different systems (Sahu et al. 2015a), where input scaling factors i.e., the error signal and its derivative are used as the input to the FLC. And, the output of FLC is connected to a conventional PI controller with optimized gains or output scaling factors to get the desired output control signal. With standard rule base and mfs, the scaling factors of fuzzy PI controller are tuned using hybrid PSO–PS (Sahu et al. 2015a) and hybrid DE–PS (Sahu et al. 2014) algorithms to get the desired optimal controlled output. However, for higher-order systems, fuzzy PI controller during the transient phase may not exhibit good performance because of their internal integration operation. To attain an overall improved performance, generally fuzzy PID controller is recommended (Yesil et al. 2004; Sahu et al. 2014, 2015c; Sekhar et al. 2016). A BFOA-based fuzzy integral double derivative structured controller is proposed with optimized mfs and output scaling factors for AGC of a traditional three-area hydrothermal system (Saikia et al. 2013). However, input scaling factors are not optimized but this controller provides an improved performance over its conventional counterpart. A fuzzy PID structured controller optimized using FA technique shows superior performance over conventional I/PI/PID structured controller optimized using the same technique for AGC of a four-area restructured thermal system (Sekhar et al. 2016).

Critical examination of the literature review expressed above indicates that the performance of the AGC systems depends largely on the type of optimization technique utilized and structure of the supplementary controller selected. In context to fuzzy controller, various intelligent techniques and FLC structures are available in the literature (Chandrakala et al. 2013; Saikia et al. 2013; Sahu et al. 2014; Bhateshvar et al. 2015; Jeyalakshmi and Subburaj 2015; Sahu et al. 2015a, b, c; Sekhar et al. 2016). To the best of the authors' knowledge, till date, no research has been reported in the literature to design BFOA-optimized fuzzy PI/PID structured controller for AGC analysis of traditional and restructured power systems. Hence, further study is required. In light of the above, the significant contributions of this piece of work are:

(a) To design a BFOA-optimized fuzzy PI/PID (FPI/FPID) controller for a two-area non-reheat thermal power system and to compare the system results with PI controller based on PSO, FA, BFOA, hybrid BFOA–PSO and fuzzy PI controller based on PS and PSO techniques.
(b) To apply BFOA for the optimization of FPI/FPID controller in a two-area reheat thermal power system and to establish systems' superb dynamic performance over PSO and ABC tuned PI controller.
(c) To design the proposed controller for a traditional multi-source multi-area (MSMA) hydrothermal system and to establish its superiority over GA and hybrid FA–PS algorithm optimized PI controller.
(d) To extend the study to restructured configuration of the MSMA power system stated in (c).
(e) To conduct sensitivity analysis of optimum scaling factors of the proposed FPI/FPID controller obtained at

nominal system conditions to wide variations in nominal loading and parameters of systems mentioned in steps (a–d).

Contrasted with the methods prevalent in the literature, the benefits of the proposed approach are observed through the simulation results over some power system models. Moreover, the design technique is easy to implement.

3 Bacterial foraging optimization algorithm

Recently, bacterial foraging optimization algorithm (BFOA), a powerful nature-inspired evolutionary computation technique was introduced as a new method in which the foraging (methods of locating, handling and ingesting food) behavior of Escherichia coli bacteria present in our intestine is mimicked (Passino 2002). Since the maiden application of BFOA to AGC problem of a traditional three-area thermal system by Nanda et al. (2009), many papers have been witnessed in the literature for different AGC systems (Debbarma et al. 2013; Ali and Abd-Elazim 2011; Panda et al. 2013; Saikia et al. 2013). BFOA follows the law of natural evolution which favors species with better food searching ability and eliminates those with deprived search capability. The genes of stronger species possibly propagate in the evolution chain since they show the greater ability to reproduce better future generations. The foraging strategy of *E. coli* bacteria can be subdivided into four developments namely chemotaxis, swarming, reproduction, and elimination–dispersal (Passino 2002). These four operations among the bacteria are used for searching the total solution space.

3.1 Chemotaxis

Chemotaxis process is attained through swimming and tumbling via Flagella of *E. coli* bacteria. In the entire lifetime, the revolution of Flagella in each bacterium decides whether it should move in a pre-specified direction (swimming) or altogether in different directions (tumbling). Mathematically, tumble of any bacterium can be defined by $\phi(j)^* C(i)$, where $\phi(j)$ is unit length of random direction and $C(i)$ is step length of that bacterium. Let, 'j' is the index of chemotactic step, 'k' is reproduction step and 'l' is the elimination–dispersal event, then $\theta^i(j+1,k,l)$ is the position of ith bacteria at jth chemotactic step, kth reproduction step and lth elimination–dispersal event. In the next chemotactic step, the position of the bacteria after a tumble is given by

$$\theta^i(j+1,k,l) = \theta^i(j,k,l) + C(i)\phi(j) \tag{1}$$

3.2 Swarming

During foraging, the bacterium which discovered best food location provides an attraction signal till a point of time in the search period to other bacteria so that they can swarm together in a group to converge at the desired location more rapidly. In other words, the effect of swarming is to congregate the bacteria into groups and hence travel as concentric patterns of groups with high bacterial density.
Mathematically swarming process is represented by

$$\begin{aligned} &J_{cc}\left(\theta, P\left(j,k,l\right)\right) \\ &= \sum_{i=1}^{S} J_{cc}^{i}\left(\theta, \theta^{i}\left(j,k,l\right)\right) \\ &= \sum_{i=1}^{S}\left[-d_{\text{attract}}\exp\left(-w_{\text{attract}}\sum_{m=1}^{p}\left(\theta_m - \theta_m^i\right)^2\right)\right] \\ &\quad + \sum_{i=1}^{S}\left[h_{\text{repelent}}\exp\left(-w_{\text{repelent}}\sum_{m=1}^{p}\left(\theta_m - \theta_m^i\right)^2\right)\right] \end{aligned} \tag{2}$$

where $J_{cc}(\theta, P(j,k,l))$ is the relative distance of each bacterium from the optimum bacterium or the cost function value to be added to the actual cost function to be minimized to present a time varying cost function. S is the total number of bacteria and p is the total number of parameters to be optimized, θ^m is the position of the fittest bacteria and d_{attract}, ω_{attract}, h_{repelent} and ω_{repelent} are the various coefficients characterizing swarm behavior which are to be chosen accurately.

3.3 Reproduction

In reproduction step, healthiest bacteria (those yielding lower value of objective function) will reproduce and the least healthy bacteria will die. The healthier bacteria replace unhealthy one which gets eliminated owing to their poorer foraging capabilities. This makes the population of bacteria invariable in the evolution process.

3.4 Elimination and dispersal

In the evolution process, a gradual or abrupt unexpected incident in the local environment where a bacterium population lives may drastically alter the even practice of evolution. Events can occur in such a manner that all the bacteria in a region are killed due to significant increase in heat (elimination) or a group is scattered into a new location/environment due to sudden flow of water (dispersal). These events may possibly destroy the chemotactic progress, but they also have the effect to support chemotaxis, as dispersal may posi-

tion a newer set of bacteria nearer good food locations. In a broad perspective, elimination and dispersal are elements of the population-level long-distance motile behavior. Elimination–dispersal step helps to avoid the behavior of stagnation (trapping the optimization process in a premature local optima point) often observed in such parallel search algorithms. In BFOA, to simulate this incident, some bacteria are liquidated haphazardly with a very small prospect, while the new replacements are randomly loaded over the search space.

In the present simulation work, BFOA is initialized considering (a) no. of parameters to be optimized, $p = 4$ or 5, (b) no. of bacteria to be used for total search space, $S = 6$, (c) swimming length, $N_S = 3$, (d) No. of iterations to be undertaken in a chemotactic loop, $N_C = 5(N_C > N_S)$, (e) maximum no. of reproduction steps by bacteria, $N_{re} = 15$, (f) maximum no. of elimination and dispersal events, $N_{ed} = 2$, (g) probability with which the elimination and dispersal will prolong, $P_{ed} = 0.25$, (h) the location of each bacterium p specified by values attained using the trial and error method, (i) the value of step size taken in the random direction, $C(i), i = 1, 2, \ldots, S$, is assumed to be constant for all bacteria to simplify the design approach, (j) the magnitude of secretion of attractant by a cell, $d_{attract} = 0.01$, (k) the chemical cohesion signal diffuses (smaller makes it diffuse more), $\omega_{attract} = 0.04$, (l) the repellant (tendency to avoid nearby cell), $h_{repelent} = 0.01$ and (m) the width of the repellant, $\omega_{repelent} = 10$. The value of $d_{attract}$ and $h_{repelent}$ must be equivalent so that the penalty compelled on the cost function through J_{cc} of Eq. (2) will be zero when all the bacteria will have equal value i.e., they have converged. In the extant work, we present only a concise overview of BFOA and request the readers to refer Nanda et al. (2009) for details of BFOA application to an AGC system. However, the flow chart of BFOA is shown in Fig. 1.

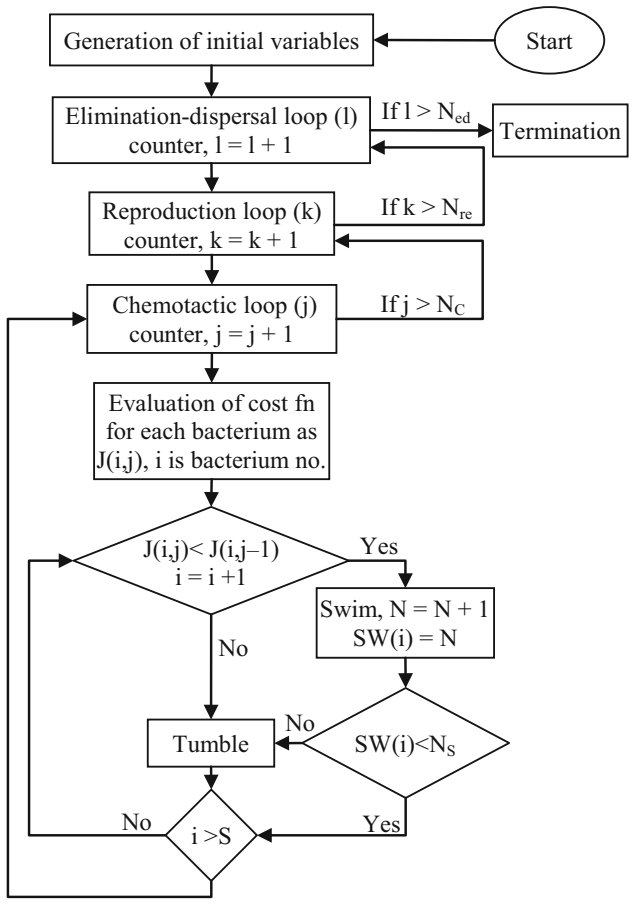


Fig. 1 Flow chart of BFOA for tuning FPI/FPID controller parameters

4 Systems investigated

Investigations have been carried out on a two-area non-reheat thermal power system (NRTPS), a two-area reheat thermal power system (RTPS), a traditional multi-source multi-area (TMSMA) hydrothermal system and a restructured MSMA (RMSMA) hydrothermal system. A bias setting of $B_i = \beta_i$ is considered in both areas. Area capacity of each system under study is 2000 MW with nominal initial loading of 1000 MW. The transfer function model of two-area RTPS is shown in Fig. 2 and that of traditional/restructured MSMA power system in Fig. 11. The nominal parameters for NRTPS are taken from (Ali and Abd-Elazim 2011), for RTPS from (Gozde et al. 2010) and for MSMA system from (Chandrakala et al. 2013) and given in "Appendix".

Each area of the power system consists of speed governor, hydraulic valve actuator (governor), turbine, generator and load as shown in Figs. 2 and 11. To make the frequency domain analysis simpler, transfer function blocks are used to model every component of the power system. The transfer functions of various blocks used in each area of two-area NRTPS model are given below:

The generator and load or power system is represented by the transfer function:

$$G_{PS}(s) = \frac{K_{PS}}{1 + sT_{PS}}. \tag{3}$$

The speed governor valve transfer function:

$$G_G(s) = \frac{1}{1 + sT_G}. \tag{4}$$

Steam turbine transfer function:

$$G_T(s) = \frac{1}{1 + sT_T}. \tag{5}$$

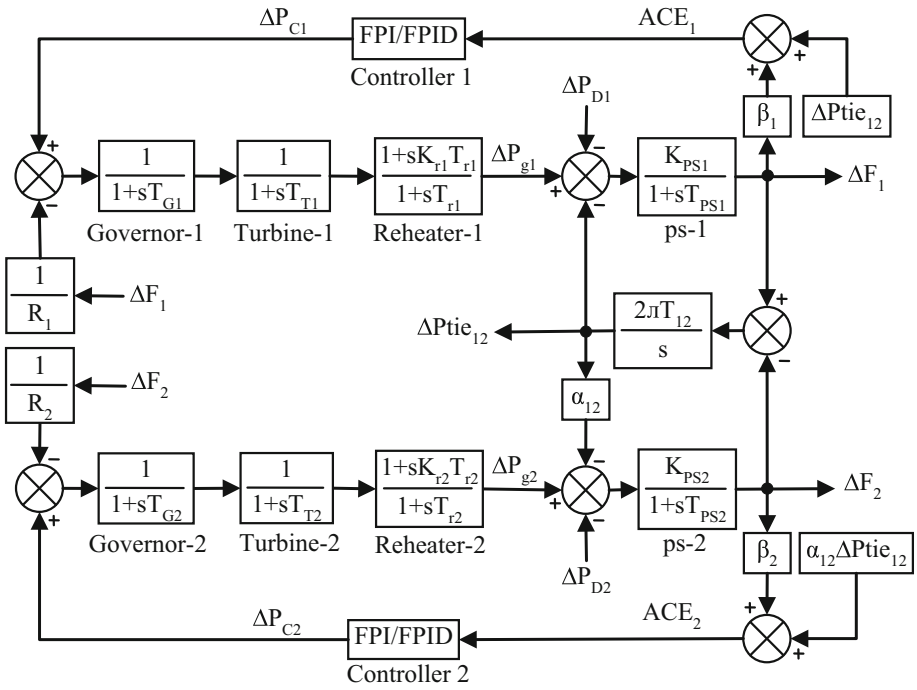


Fig. 2 Transfer function model of two-area RTPS

While simulating two-area RTPS model as shown in Fig. 2, one additional reheater block will be used in every area of two-area NRTPS model as given follows:

Reheater transfer function:

$$G_{\mathrm{r}}(s) = \frac{1 + \mathrm{sK_r}T_{\mathrm{r}}}{1 + \mathrm{sT_r}}. \tag{6}$$

Each area of two-area traditional/restructured MSMA power system model owns two generating units, one non-reheat thermal and other hydro power plant unit. The transfer functions of non-reheat thermal unit are expressed in Eqs. (4–5), while transfer function blocks used for hydro unit are given below:

Hydro turbine transfer function:

$$G_{\mathrm{HT}}(s) = \frac{1 - \mathrm{sT_W}}{1 + 0.5\mathrm{sT_W}}. \tag{7}$$

Mechanical hydraulic governor transfer function:

$$G_{\mathrm{HG}}(s) = \left[\frac{1}{1 + \mathrm{sT_{RH}}}\right]\left[\frac{1 + \mathrm{sT_R}}{1 + \mathrm{sT_{GH}}}\right]. \tag{8}$$

Each area has three inputs such as change in controller input [ΔP_{C}, Eqs. (11–12)], change in load disturbance (ΔP_{D}) and change in tie-line power ($\Delta\mathrm{Ptie}_{12}/\Delta\mathrm{Ptie}_{\mathrm{actual}}$) and two outputs such as change in generator frequency ΔF and area control error (ACE) defined by Eqs. (9–10). In restructured system, one additional input will be ΔP_G, while ΔP_C input will be via apf block (Fig. 11). The generator always regulates its power output to meet the variable load demand. In normal condition, the turbine power (ΔP_{g}) maintains balance with load demand (ΔP_{D}) resulting in zero acceleration and a constant frequency. The difference between these powers will cause deviation in system frequency in negative or positive side. The list of symbols used is provided in "Appendix". The detailed description of the models under study is provided by Kothari and Nagrath (2012) and Kundur (2011).

5 Controller structure

To solve the AGC problem, fuzzy PI/PID (FPI/FPID) controller is provided in each area of the two-area systems under study. The FPID controller structure is shown in Fig. 3 (Sahu et al. 2014, 2015c). The error inputs to the fuzzy logic controller (FLC) are the respective area control error (ACE) represented by:

$$\mathrm{ACE}_1 = \beta_1 \Delta F_1 + \Delta\mathrm{Ptie}_{12} \tag{9}$$

$$\mathrm{ACE}_2 = \beta_2 \Delta F_2 + \alpha_{12}\Delta\mathrm{Ptie}_{12}. \tag{10}$$

Here, area size ratio, $\alpha_{12} = -\frac{P_{r1}}{P_{r2}}$. P_{ri} is the area capacity (MW) and β_i is the area frequency response characteristic (puMW/Hz), ΔF_i is the area frequency deviation (Hz) and $\Delta\mathrm{Ptie}_{12}$ is the tie-line power deviation (puMW). However, Ptie_{12} will be $\mathrm{Ptie}_{\mathrm{error}}$ in restructured system. FLC employ ACE and derivative of ACE as input signals. The FLC output (i.e., y) is multiplied with K_{P}, K_{I} and K_{D} and then added to give the controller output ΔP_{Ci}. Here, ΔP_{C1} and

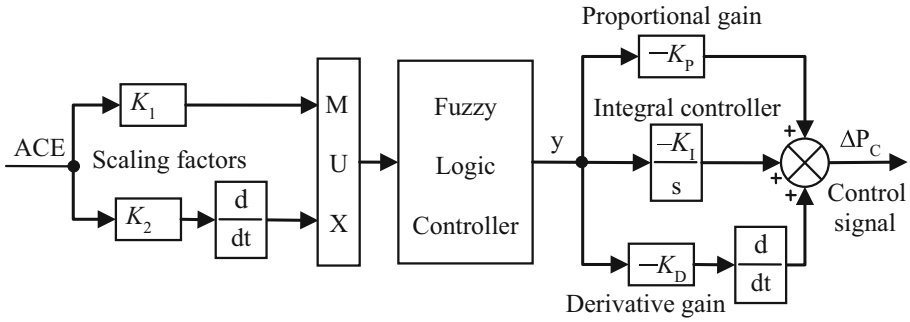


Fig. 3 Structure of fuzzy PID controller

ΔP_{C2} are the control inputs of the power system and K_P, K_I and K_D, respectively, represent the proportional, integral and derivative gains of FLC. K_1, K_2 (input scaling factors) and K_P, K_I, K_D (output scaling factors) are the parameters to be optimized using BFOA to minimize an objective function explained in Eq. (13). With FPI controller, the derivative path will be omitted from Fig. 3. FLC has four components i.e., the fuzzifier, the fuzzy inference engine/system (fis), the rule base and the defuzzifier. The fuzzifier converts the numeric value into fuzzy sets. The fis executes all the logical manipulations. The rule base consists of membership functions (mfs) and control rules. The output of the fis is the fuzzy set which is converted into numeric value by defuzzification method. Commonly, triangular, trapezoidal, bell- and Gaussian-shaped mfs are favored due to their easy functional representation, less memory requirement for the storage and efficient to be handled by the fis. However, triangular mfs are generally accepted in FLC designs of real-time applications because of their economical and improved performance as compared to other options (Sahu et al. 2014; Sekhar et al. 2016). In light of the above, in the existing study five triangular mfs are utilized with five fuzzy linguistic variables like MN (more negative), SN (small negative), Z (zero), SP (small positive) and MP (more positive) for inputs and output of the fuzzy controller. The mfs for ACE, ACE derivative and FLC output are shown in Fig. 4. Also, for aiming simplicity, improved computational efficiency, less memory usage and enhanced performance analysis, identical mfs, with identical horizontal range, are employed for both inputs and output of the FLC (Sahu et al. 2014, 2015a; Sekhar et al. 2016). Mamdani fuzzy interface system and centroid defuzzification method are selected for the study. The control signal of FPI/FPID controller is given by

$$\Delta P_{\mathrm{Ci}}\,(\mathrm{FPI}) = K_{\mathrm{P}} y + K_{\mathrm{I}} \int y \mathrm{d}t, i = 1, 2, \tag{11}$$

$$\Delta P_{\mathrm{Ci}}\,(\mathrm{FPID}) = K_{\mathrm{P}} y + K_{\mathrm{I}} \int y \mathrm{d}t + K_{\mathrm{D}} \frac{\mathrm{d}y}{\mathrm{d}t}, i = 1, 2. \tag{12}$$

The two-dimensional rule base for ACE, ACE derivative and FLC output consisting of twenty-fives rules is shown in Table 1. Identical FPI/FPID controller is designed for the identical two-area systems.

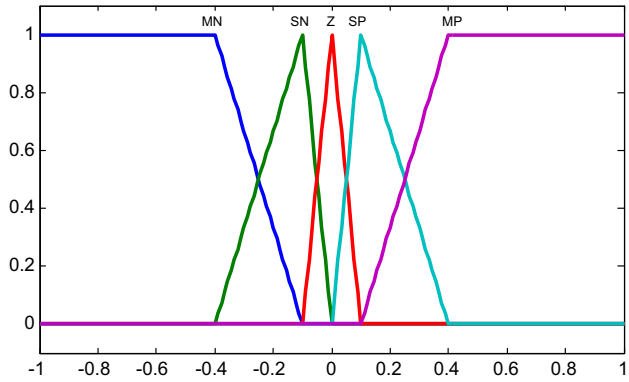


Fig. 4 Membership functions of fuzzy PI/PID controller for ACE, ACE derivative and FLC output

Table 1 Rule base for ACE, ACE derivative and FLC output

ACE	ACE derivative				
	MN	SN	Z	SP	MP
MN	MN	MN	MN	SN	Z
SN	MN	SN	SN	Z	SP
Z	MN	SN	Z	SP	MP
SP	SN	Z	SP	SP	MP
MP	Z	SP	MP	MP	MP

6 Optimization problem

The main objective of an optimization problem is to minimize an objective function selected for the system considering a particular performance index of the system. It should be noted that the performance of an optimization method relies upon the selection of a proper performance index. In this paper, integral of squared error (ISE) is exercised as a performance index (J) to appropriately design the proposed BFOA-FPI/FPID controller. The mathematical expression for J, which is the amalgamation of the frequency devia-

tions of both areas (ΔF_1 and ΔF_2) and tie-line power flow (ΔPtie_{12}) of the two-area system, may be stated by

$$\text{ISE} = J = \int_0^T \left(\Delta F_1^2 + \Delta F_2^2 + \Delta \text{Ptie}_{12}^2\right) \text{d}t. \tag{13}$$

Here, T is the simulation time range. The optimum solution has the lowest value of the J. The constraints of the optimization task are the gains/parameters of FPI/FPID controller within some pre-specified bounds. Hence, the controller design problem can be devised as the following optimization problem:

$$\begin{aligned}
&\text{Minimize } J, \text{ subject to}\\
&K_1^{\min} \le K_1 \le K_1^{\max},\ K_2^{\min} \le K_2 \le K_2^{\max},\ K_{\text{P}}^{\min}\\
&\quad \le K_{\text{P}} \le K_{\text{P}}^{\max}, K_{\text{I}}^{\min} \le K_{\text{I}} \le K_{\text{I}}^{\max}\\
&\quad \text{(FPI controller)}, \qquad (14)\\
&K_1^{\min} \le K_1 \le K_1^{\max},\ K_2^{\min} \le K_2 \le K_2^{\max}, K_P^{\min}\\
&\quad \le K_P \le K_P^{\max}, K_I^{\min} \le K_I \le K_I^{\max},\\
&\quad K_D^{\min} \le K_D \le K_D^{\max} \quad \text{(FPID controller)}. \qquad (15)
\end{aligned}$$

Here, the superscripts min and max stand for the minimum and the maximum values of the respective parameter. The selection of the range of superscripts affects the final optimal solution. The minimum and maximum values of the parameters are selected as 0.0 and 2.0, respectively (Sahu et al. 2014, 2015a). The rationale of minimizing J is to determine the most favorable scaling factors/gains of the controller which may harvest the desired AGC performance of the system models under study. Each bacterium is permitted to take all potential values within specified range, and the objective function is curtailed to derive the optimal parameter values of the controllers. The numbers of tunable parameters for FPI (K_1, K_2, K_{P} and K_{I}) and FPID (K_1, K_2, K_P, K_{I} and K_{D}) controllers would be four and five, respectively. The BFOA optimization process for each model under study is repeated 20 times, and the best final solution among the 20 runs is selected as the parameters of the proposed controller (Panda et al. 2013; Sahu et al. 2014).

To study the comparative assessment between the proposed approach and the other techniques reported in the literature, the settling times (STs) and peak undershoots (PUs) of tie-line/frequency deviation results under sudden load demands are calculated at the end of the developed program. The values of these parameters point out about the speed of the dynamic response profiles of the studied models. To establish further comparisons, in addition to the ISE defined via Eq. (13), three more performance indices (PIs) i.e., integral of time multiplied squared error (ITSE), integral of absolute error (IAE) and integral of time multiplied absolute error (ITAE) are also calculated. These three PIs may be stated by Eqs. (16–18) (Chandrakala et al. 2013; Sahu et al. 2015c).

$$\text{ITSE} = \int_0^T \left(\Delta F_1^2 + \Delta F_2^2 + \Delta \text{Ptie}_{12}^2\right) \cdot t\,\text{d}t, \tag{16}$$

$$\text{IAE} = \int_0^T \left(|\Delta F_1| + |\Delta F_2| + |\Delta \text{Ptie}_{12}|\right) \text{d}t, \tag{17}$$

$$\text{ITAE} = \int_0^T \left(|\Delta F_1| + |\Delta F_2| + |\Delta \text{Ptie}_{12}|\right) \cdot t\,\text{d}t, \tag{18}$$

7 Simulation results and discussion

The SIMULINK models of the power systems under study and the corresponding different programs are developed on an Intel Core 2 Duo processor of 1.66 GHz and 2 GB RAM computer in the MATLAB software version 7.5.0 (R2007b) using the system data and nomenclature given in "Appendix" to study the system dynamic performance against step load perturbation (SLP) in the control areas. The best final optimal results obtained in the 20 runs for various power system models under study are displayed in Table 2. The Results showing best performance are bold faced in their respective tables.

7.1 Two-area non-reheat thermal power system

A two-area non-reheat thermal power system (NRTPS) model is simulated using data given in "Appendix" and considering 10 % SLP at $t = 0$ s in area-1. The entire AGC structure of this model is shown in Fig. 2 which clearly portrays the grid connections and position of SLP inputs. However, reheater blocks available in area-1 and 2 of Fig. 2 are not parts of NRTPS. Each area is equipped with FPI/FPID controller. The system dynamic responses for frequency deviation of area-1 (ΔF_1), area-2 (ΔF_2) and tie-line power deviation (ΔPtie_{12}) are shown in Figs. 5, 6 and 7. To show the advantage of the proposed approach, the simulation results with some newly developed/published approaches like BFOA (Ali and Abd-Elazim 2011), PSO (Panda et al. 2013), hybrid BFOA–PSO (Panda et al. 2013) and FA (Padhan et al. 2014) tuned conventional PI structured controller as well as PS (Sahu et al. 2015a) and PSO (Sahu et al. 2015a) optimized fuzzy PI structured controller for the same power system are also shown in Figs. 5, 6 and 7. Critical analysis of the Figs. 5, 6 and 7 distinctly reveals that with the same structured controller substantial improvements are noticed with the proposed BFOA-optimized FPI controller compared to other PI and fuzzy PI controllers. The system dynamic performance is further improved by adding the derivative block in the FPI controller, i.e., by proposed BFOA-based FPID controller. The numerical values of the

Table 2 BFOA-optimized FPI/FPID controller parameters

Controller parameters	NRTPS		RTPS		TMSMA		RMSMA	
	BFOA: FPI	BFOA: FPID	BFOA: FPI	BFOA: FPID	BFOA: FPI	BFOA: FPID	BFOA: FPI	BFOA: FPID
K_1	1.9902	1.9999	1.1645	1.6601	1.8978	1.9904	0.8023	0.5956
K_2	0.9509	0.7990	0.6711	0.9576	1.1525	1.1099	0.4512	0.3222
K_P	0.5514	1.2914	0.5336	0.6017	0.4111	1.1532	0.9836	1.8231
K_I	0.7991	1.3991	0.7936	1.7598	0.4412	1.0502	1.2082	1.6991
K_D	–	0.0311	–	0.0121	–	0.0719	–	0.0813

An entry "–" means not applicable

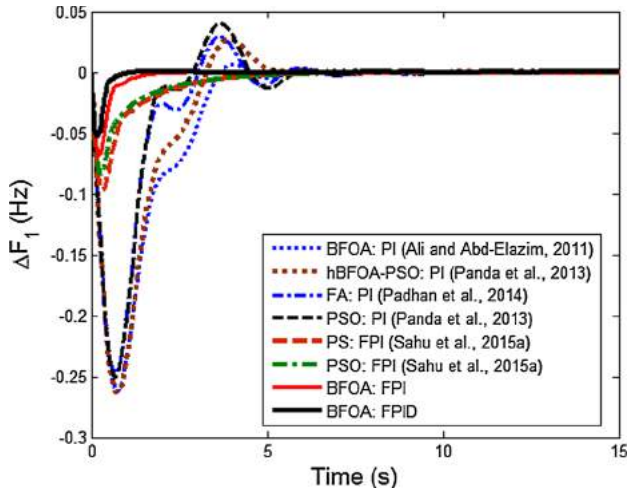


Fig. 5 ΔF_1 response for 10 % SLP in area-1 of NRTPS

responses in terms of settling times (STs), peak undershoots (PUs) and various performance indices (PIs) like ISE, ITSE, IAE and ITAE are noted in Table 3. It is apparent from Table 3 that with the same controller structure (PI controller), using BFOA-optimized FPI controller, smaller ITAE (0.0757), IAE (0.0822), ITSE (0.00093), ISE (0.00207), STs ($\Delta F_1 = 2.05, \Delta F_2 = 4.04, \Delta \text{Ptie}_{12} = 3.38$) and PUs ($\Delta F_1 = -0.0692, \Delta F_2 = -0.0264, \Delta \text{Ptie}_{12} = -0.0099$) values are obtained as compared to PSO optimized FPI controller ITAE (0.4564), IAE (0.2374), ITSE (0.00638), ISE (0.00642), STs ($\Delta F_1 = 7.68, \Delta F_2 = 8.70, \Delta \text{Ptie}_{12} = 7.28$) and PUs ($\Delta F_1 = -0.0834, \Delta F_2 = -0.0366, \Delta \text{Ptie}_{12} = -0.0151$) values. These numerical values due to BFOA-optimized FPI controller are also smaller in comparison with PS optimized FPI controller and conventional PI controller optimized using PSO, FA, BFOA and hybrid BFOA–PSO techniques. It is also palpable from Table 3 that minimal ITAE (0.0325), IAE (0.0428), ITSE (0.00026), ISE (0.00082), STs ($\Delta F_1 = 1.05, \Delta F_2 = 3.16, \Delta \text{Ptie}_{12} = 2.50$) and PUs ($\Delta F_1 = -0.0528, \Delta F_2 = -0.0154, \Delta \text{Ptie}_{12} = -0.0062$) values are obtained with BFOA-optimized FPID controller as compared to all other controllers including BFAO optimized FPI controller. Therefore, it can be concluded that BFOA-tuned FPID controller outperforms other optimal conventional/fuzzy PI structured controllers available for comparison. It should be noted that the STs are received in a band of 5 % (± 0.0005) and PIs values are taken into account for a simulation time of 15 s for all the simulations of the system models under study.

7.2 Two-area reheat thermal system

The study is further extended by incorporating the reheat effect in the NRTPS model. The transfer function model of two-area reheat thermal power system (RTPS) is shown in

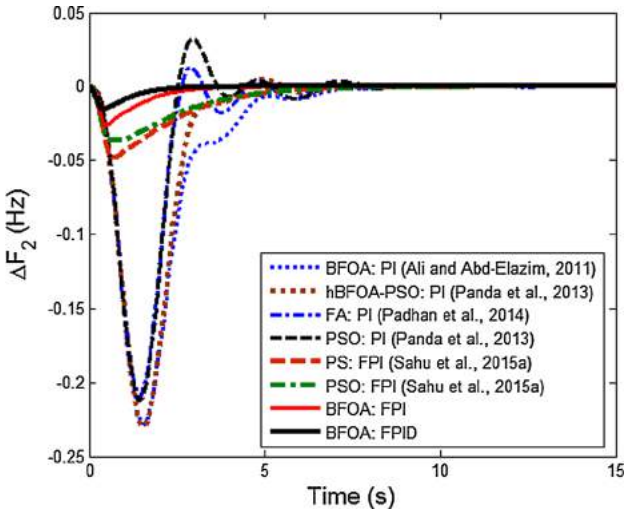


Fig. 6 ΔF_2 response for 10 % SLP in area-1 of NRTPS

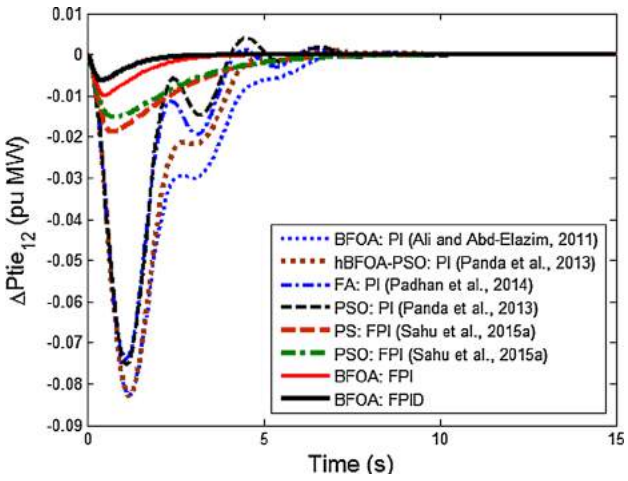


Fig. 7 ΔPtie_{12} response for 10 % SLP in area-1 of NRTPS

Fig. 2. The system data are given in "Appendix". The simulation results of ΔF_1, ΔF_2 and ΔPtie_{12} under 1 % SLP in area-1 at $t = 0$ s are shown in Figs. 8, 9 and 10. The performance of proposed BFOA-optimized fuzzy PI/PID controller is compared with some recently published heuristic techniques such as: PSO optimized PI controller (Abdel-Magid and Abido 2003; Gozde et al. 2010) and ABC optimized PI controller (Gozde et al. 2012) as shown in Figs. 8, 9 and 10 and Table 4. Critical analysis of the system responses shown in Figs. 8, 9 and 10 and Table 4 clearly indicates that proposed control strategy shows favorable performance in comparison with other controllers.

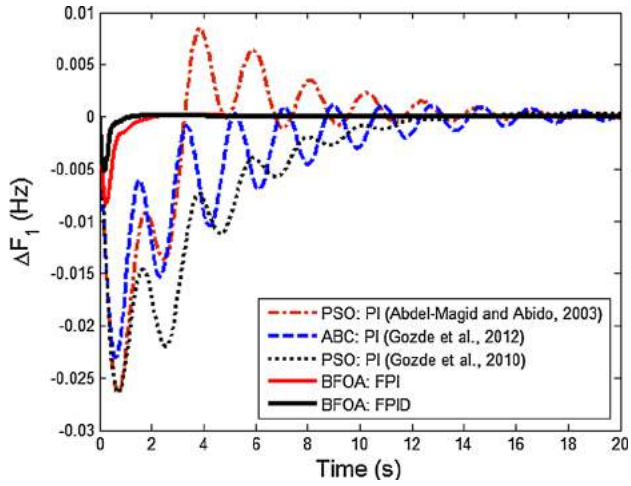


Fig. 8 ΔF_1 response for 1 % SLP in area-1 of RTPS

7.3 Traditional multi-source multi-area system

To manifest the potential of the proposed approach to cope with multi-source generating systems, the study is further stretched to a traditional multi-source multi-area (TMSMA) hydrothermal power system (Chandrakala et al. 2013; Sahu et al. 2015a, b) and its transfer function model is shown in Fig. 11 (without dotted line connections). Each area has two units, one non-reheat thermal and other mechanical governor equipped hydro power plant. The nomenclature and relevant parameters are stated in "Appendix". The dynamic

Table 3 Numerical values of STs, PUs and PIs with NRTPS

Controller	STs (s)			PUs (Hz) (−ve)			PIs			
	ΔF_1	ΔF_2	ΔPtie_{12}	ΔF_1	ΔF_2	ΔPtie_{12}	ISE	ITSE	IAE	ITAE
PSO: PI (Panda et al. 2013)	9.77	10.52	7.85	0.2500	0.2118	0.0754	0.09928	0.11190	0.7519	1.2330
FA: PI (Padhan et al. 2014)	9.26	9.05	6.91	0.2473	0.2076	0.0740	0.09636	0.10680	0.7385	1.1470
BFOA: PI (Ali and Abd-Elazim 2011)	7.79	8.87	7.78	0.2622	0.228	0.0828	0.14090	0.18690	1.030	1.8430
hBFOA–PSO: PI (Panda et al. 2013)	7.87	7.00	7.52	0.2627	0.2293	0.0830	0.13240	0.16500	0.9255	1.4960
PS: FPI (Sahu et al. 2015a)	7.20	8.38	7.03	0.0966	0.0482	0.0188	0.00916	0.00879	0.2725	0.4907
PSO FPI (Sahu et al. 2015a)	7.68	8.70	7.28	0.0834	0.0366	0.0151	0.00642	0.00638	0.2374	0.4564
BFOA: FPI	2.05	4.04	3.38	0.0692	0.0264	0.0099	0.00207	0.00093	0.0822	0.0757
BFOA: FPID	**1.05**	**3.16**	**2.50**	**0.0528**	**0.0154**	**0.0062**	**0.00082**	**0.00026**	**0.0428**	**0.0325**

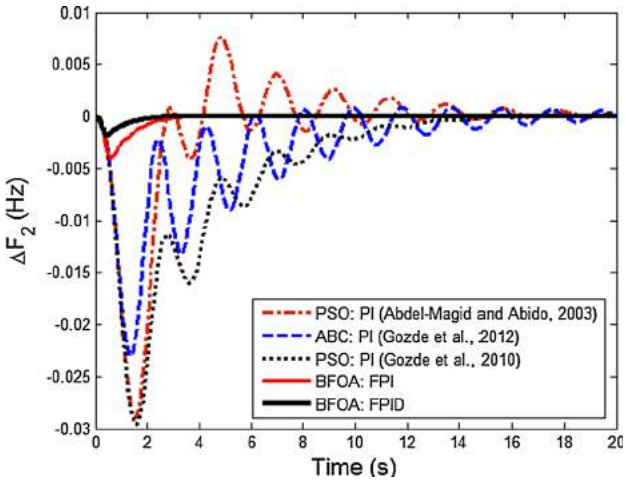


Fig. 9 ΔF_2 response for 1 % SLP in area-1 of RTPS

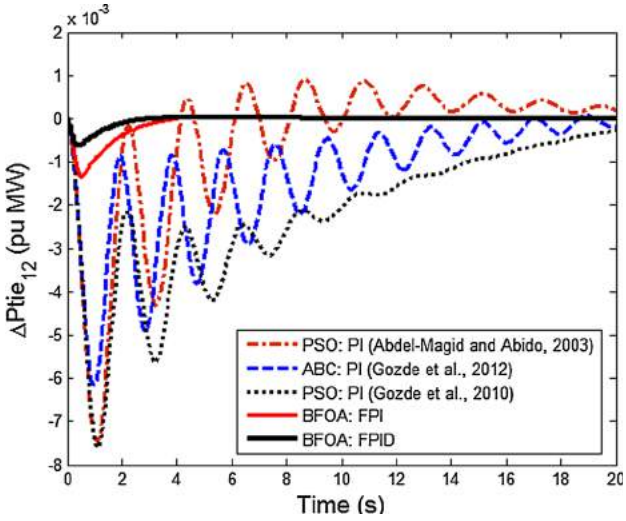


Fig. 10 ΔPtie_{12} response for 1 % SLP in area-1 of RTPS

performance of the system for 1.5 % SLP in area-1 applied at $t = 0$ s using proposed controller is shown in Figs. 12, 13 and 14 and Table 5. For comparison, the simulation results with GA (Sahu et al. 2015b) and hFA–PS (Sahu et al. 2015b) technique-based PI controllers are also provided in these figures and Table 5. It is clear from Figs. 12, 13 and 14 and Table 5 that proposed FPID controller outperforms the other controllers.

7.4 Restrutured multi-source multi-area system

To swell competition in modern wholesale power market, vast VIUs are being deregulated to create competition among generating companies selling unbundled power and retail energy service companies. With growing dimension and complexity of the restructured power system and due to

Table 4 Numerical values of STs, PUs and PIs with RTPS

Controller	STs (s)			PUs (Hz) (−ve)			PIs			
	ΔF_1	ΔF_2	ΔPtie_{12}	ΔF_1	ΔF_2	ΔPtie_{12}	ISE	ITSE	IAE	ITAE
ABC: PI (Gozde et al. 2012)	20.52	19.50	16.24	0.0230	0.0230	0.0061	0.001464	0.003423	0.1547	0.6377
PSO: PI (Abdel-Magid and Abido 2003)	17.03	18.02	15.49	0.0262	0.0289	0.0074	0.001806	0.003187	0.1444	0.4893
PSO: PI (Gozde et al. 2010)	11.63	12.81	18.10	0.0265	0.0296	0.0076	0.003041	0.007425	0.2350	0.9220
BFOA: FPI	1.43	2.27	1.741	0.0083	0.0039	0.0013	$3.694e^{-05}$	$2.290e^{-05}$	0.0134	0.0269
BFOA: FPID	**0.71**	**1.44**	**0.713**	**0.0051**	**0.0018**	**0.0006**	$\mathbf{8.513e^{-06}}$	$\mathbf{3.022e^{-06}}$	**0.0051**	**0.0084**

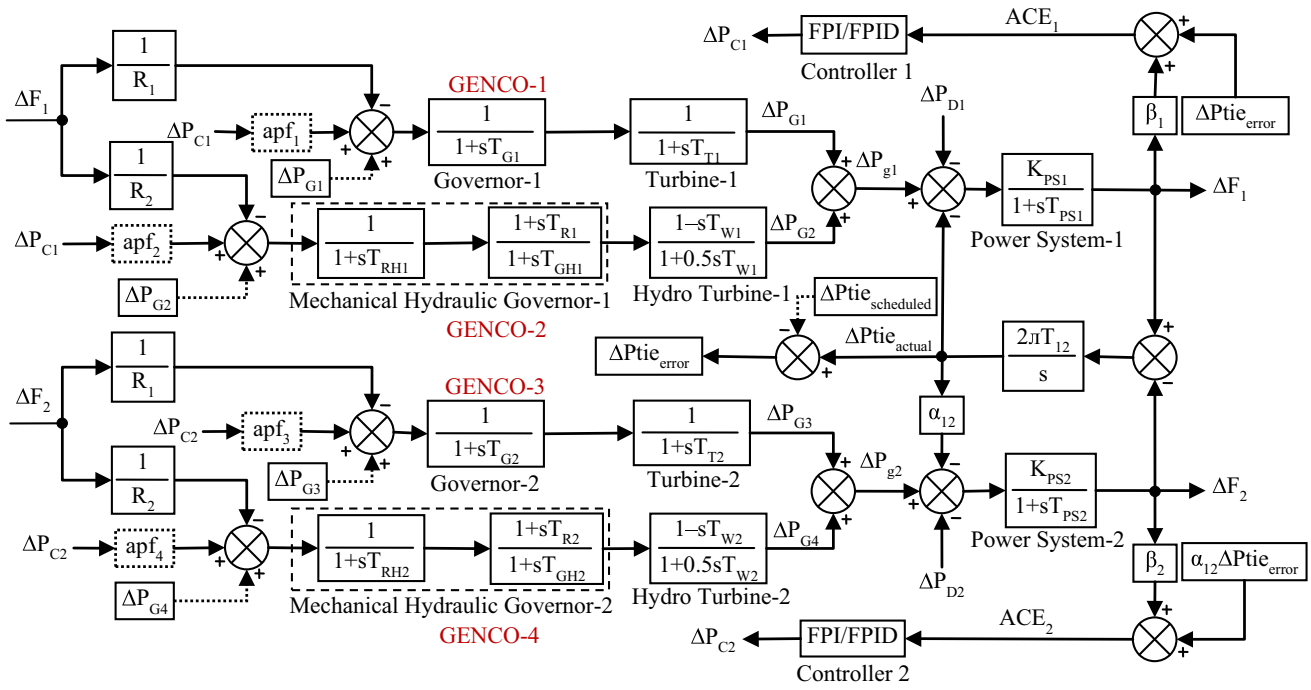


Fig. 11 Transfer function model of MSMA hydrothermal system (traditional: without *dotted line* connections; Restructured: with *dotted line* connections)

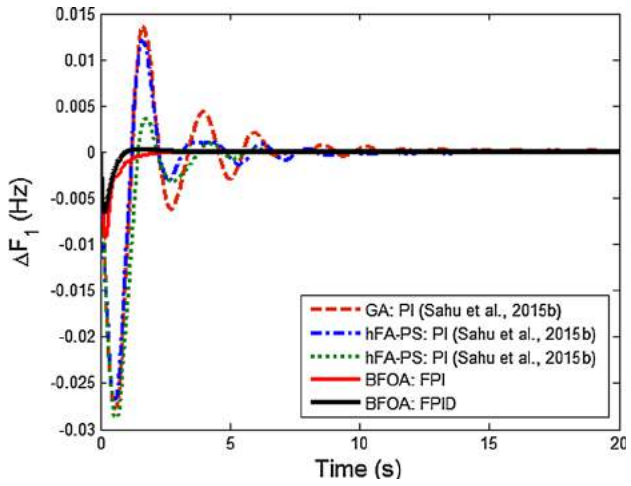


Fig. 12 ΔF_1 response for 1.5 % SLP in area-1 of TMSMA system

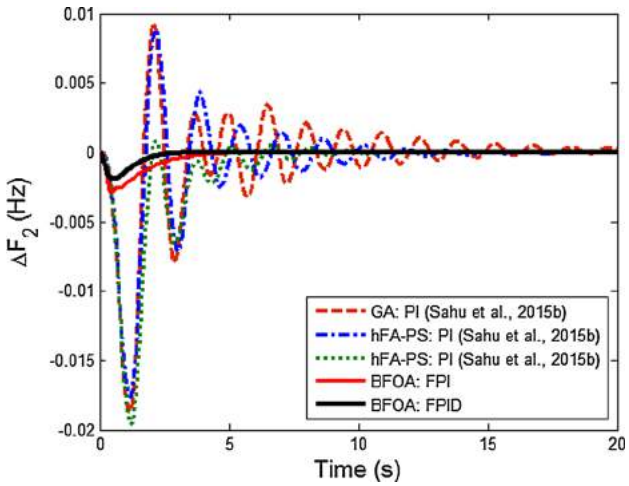


Fig. 13 ΔF_2 response for 1.5 % SLP in area-1 of TMSMA system

introduction of considerable uncertainties and disturbances in power system, it is desired to use some novel control strategies to achieve AGC goals and secure electric power system adequately. In view of this, to demonstrate the aptitude of the proposed approach to tackle restructured system, the study is further extended from TMSMA hydrothermal system to restructured MSMA (RMSMA) hydrothermal system. The transfer function model of RMSMA hydrothermal power system is shown in Fig. 11 (with dotted line connections). Each area owns two generating units and let two DISCOs. GENCO-1 and GENCO-3 are non-reheat thermal, while GENCO-2 and GENCO-4 are hydro power plants. A scenario having combination of poolco and bilateral contracts between DISCOs and available GENCOs is only considered for the present study. It is assumed that all GENCOs participate in the AGC task as per their ACE participation factors (apfs) taken as: $\text{apf}_1 = \text{apf}_2 = \text{apf}_3 = \text{apf}_4 = 0.5$. DPM structure for this scenario is given by Eq. (19).

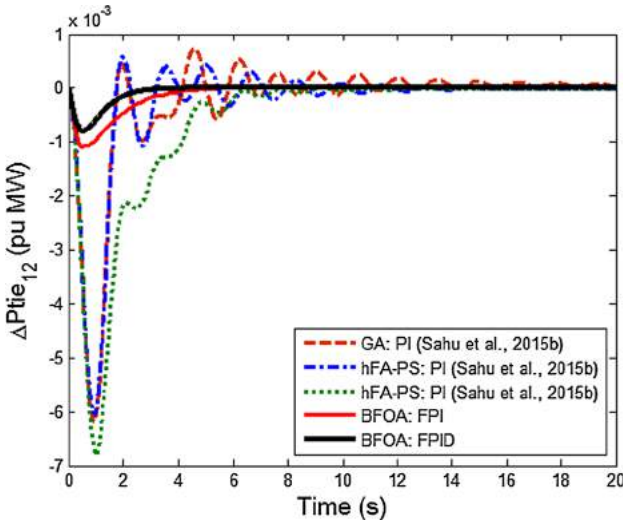


Fig. 14 ΔPtie_{12} response for 1.5 % SLP in area-1 of TMSMA system

$$\text{DPM} = \begin{bmatrix} 0.10 & 0.24 & 0.33 & 0.18 \\ 0.20 & 0.16 & 0.17 & 0.22 \\ 0.27 & 0.40 & 0.50 & 0.00 \\ 0.43 & 0.20 & 0.00 & 0.60 \end{bmatrix}. \tag{19}$$

In this hybrid transaction, let the DISCO-1, DISCO-2, DISCO-3 and DISCO-4 demands equally 1 % puMW of power from GENCOs as per Eq. (19) i.e., $\Delta P_{L1} = \Delta P_{L2} = \Delta P_{L3} = \Delta P_{L4} = 0.01$ puMW. Hence, area power demand of area-1 i.e., $\Delta P_{D1} = \Delta P_{L1} + \Delta P_{L2} = 0.02$ puMW, area-2 i.e., $\Delta P_{D2} = \Delta P_{L3} + \Delta P_{L4} = 0.02$ puMW and uncontracted power demand signals $\Delta P_{\text{UC1}} = \Delta P_{\text{UC2}} = 0$ puMW. The power output of GENCOs in steady state must satiate the contracted demand of the DISCOs. The steady state output of GENCOs is given by Eq. (20) (Donde et al. 2001).

$$\Delta P_{Gi} = \text{cpf}_{i1}\Delta P_{L1} + \text{cpf}_{i2}\Delta P_{L2} + \text{cpf}_{i3}\Delta P_{L3} + \text{cpf}_{i4}\Delta P_{L4}, i = 1, \ldots, 4. \tag{20}$$

Therefore, steady state generations are: $\Delta P_{G1} = 0.0085$ puMW, $\Delta P_{G2} = 0.0075$ puMW, $\Delta P_{G3} = 0.0117$ puMW, $\Delta P_{G4} = 0.0123$ puMW. The scheduled tie-line power flow from area-1 to 2 is the total power exported from area-1 (demand of DISCOs in area-2 from GENCOs in area-1) minus total power imported to area-1 (demand of DISCOs in area-1 from GENCOs in area-2). Therefore, $\Delta\text{Ptie}_{\text{scheduled}}$ is given as (Donde et al. 2001; Arya et al. 2016):

$$\begin{aligned}\Delta\text{Ptie}_{\text{scheduled}} &= (\text{cpf}_{13} + \text{cpf}_{23})\Delta P_{L3} + (\text{cpf}_{14} + \text{cpf}_{24})\Delta P_{L4} \\ &\quad -(\text{cpf}_{31} + \text{cpf}_{41})\Delta P_{L1} - (\text{cpf}_{32} + \text{cpf}_{42})\Delta P_{L2}.\end{aligned} \tag{21}$$

Table 5 Numerical values of STs, PUs and PIs with TMSMA power system

Controller	STs (s)			PUs (Hz) (−ve)			PIs			
	ΔF_1	ΔF_2	ΔPtie_{12}	ΔF_1	ΔF_2	ΔPtie_{12}	ISE	ITSE	IAE	ITAE
GA: PI (Sahu et al. 2015b)	10.48	15.45	6.292	0.0277	0.0187	0.006184	0.000908	0.001140	0.08872	0.25340
hFA–PS: PI (Sahu et al. 2015b)	7.38	10.26	3.054	0.0267	0.0176	0.006066	0.000796	0.000865	0.07420	0.16780
hFA–PS: PI (Sahu et al. 2015b)	5.35	6.18	4.480	0.0287	0.0195	0.006797	0.000903	0.000856	0.07056	0.11770
BFOA: FPI	1.41	2.86	1.923	0.0093	0.0029	0.001080	$3.472e^{-05}$	$1.764e^{-05}$	0.01223	0.01979
BFOA: FPID	**0.82**	**1.79**	**1.173**	**0.0065**	**0.0019**	**0.000792**	$\mathbf{1.601e^{-05}}$	$\mathbf{6.076e^{-06}}$	**0.00688**	**0.00835**

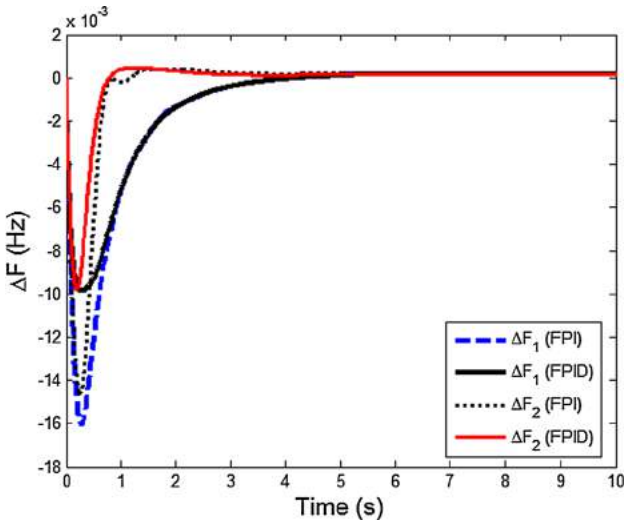


Fig. 15 ΔF_1 and ΔF_2 responses of RMSMA system for FPI and FPID controllers

Hence, $\Delta\text{Ptie}_{\text{scheduled}} = -0.004$ puMW. Referring Fig. 11, the actual tie-line power can be stated as:

$$\Delta\text{Ptie}_{\text{actual}} = \frac{2\pi T_{12}}{s}[\Delta F_1 - \Delta F_2]. \tag{22}$$

The tie-line power flow error can be defined as:

$$\Delta\text{Ptie}_{\text{error}} = \Delta\text{Ptie}_{\text{actual}} - \Delta\text{Ptie}_{\text{scheduled}}. \tag{23}$$

$\Delta\text{Ptie}_{\text{error}}$ reduces to zero in steady state as $\Delta\text{Ptie}_{\text{actual}}$ attains the power flow equal to $\text{Ptie}_{\text{scheduled}}$.

The performance of the BFOA-optimized FPID controller is contrasted with that of BFOA-optimized FPI controller. The simulation results of ΔF_1 and ΔF_2 are shown in Fig. 15 and Table 6. It is evident from Fig. 15 and Table 6 that ΔF_1 and ΔF_2 due to FPI/FPID controller settles to zero in steady state and hence satisfy the AGC requirement. However, FPID shows superior performance in comparison with FPI in terms of superior STs, PUs and PIs. Some other responses of the RMSMA system, only due to FPID controller are shown in Figs. 16, 17, 18 and 19. In these figures the system responses with generation rate constraint (GRC) are also shown to make comparison and ascertain the effectiveness of the BFOA-based FPID controller optimized for linear system, under GRC. There exist constraints on the rate of change of power generation of steam/hydro plants called GRC, and it must be incorporated in AGC study of realistic power systems (Nanda et al. 2006; Kundur 2011; Kothari and Nagrath 2012; Debbarma et al. 2013; Panda et al. 2013; Saikia et al. 2013; Padhan et al. 2014; Sahu et al. 2015a, b, c; Arya et al. 2016). The GRC of ± 0.015 pu/s is considered for non-reheat thermal GENCOs (Yesil et al. 2004) and GRC of +0.045 pu/s for raising generation and -0.06 pu/s for lowering generation is considered for hydro power GENCOs (Nanda et al. 2006; Saikia et al. 2013; Panda et al. 2013; Arya et al. 2016; Sahu et al. 2015a, b). Figure 16 indicates that the frequency of both areas settles to zero in steady state; however, degraded responses are observed with GRC in comparison with without considering GRC. This sluggish trend of the responses continues in Figs. 17 and 18. Figure 17 shows that $\Delta\text{Ptie}_{\text{actual}}$ value equates to $\text{Ptie}_{\text{scheduled}}$ in steady state, hence $\Delta\text{Ptie}_{\text{error}}$ settles to zero. Further, power generations (ΔP_{Gi}) of all four GENCOs attain their desired generation values of Eq. (20) as showcased in Fig. 18. Critical analysis of Fig. 18 and 19 (reduced x axis of Fig. 18) clearly reveals that proposed controller satisfies the AGC obligations efficiently; however, GRC influences the dynamic responses of the system significantly and lead to larger overshoots and longer settling times. The favorable performance of the FPID controller with GRC advocates its robustness.

7.5 Sensitivity analysis

Sensitivity analysis is carried out to study the robustness of the optimized parameters (i.e., $K_{1\text{i}}$, $K_{2\text{i}}$, K_{Pi}, K_{Ii} and K_{Di}) of the proposed FPI/FPID controller, obtained at nominal conditions, to wide variations in the system parameters and initial loading condition (Nanda et al. 2009; Ali and Abd-Elazim 2011; Gozde et al. 2012; Saikia et al. 2013; Panda et al. 2013; Padhan et al. 2014; Sahu et al. 2014; Arya et al. 2016; Sahu et al. 2015a, b, c; Sekhar et al. 2016). The system parameters such as R_i, K_{Pi}, T_{Pi}, T_{Ri} and T_{GHi} are varied by $\pm 25\,\%$ from their nominal values (given in "Appendix") as well as the system loading condition is changed by $\pm 25\,\%$ from its nominal loading of 50 %. The ΔF_1 response for variation in R_i parameter of NRTPS, ΔF_2 response for simultaneous variation in K_{PSi} and T_{PSi} parameters of RTPS, ΔPtie_{12} response for simultaneous variation in T_{Ri} and T_{GHi} parameters of TMSMA system and ΔP_{G3} response for variation in

Table 6 Numerical values of STs, PUs and PIs with RMSMA power system

Controller	STs (s)			PUs (Hz) (−ve)			PIs			
	ΔF_1	ΔF_2	$\Delta\text{Ptie}_{\text{error}}$	ΔF_1	ΔF_2	$\Delta\text{Ptie}_{\text{error}}$	ISE	ITSE	IAE	ITAE
BFOA: FPI	2.85	0.73	2.36	0.0160	0.0146	0.0000	0.00021	9.482e^{-05}	0.02977	0.05316
BFOA: FPID	**2.84**	**0.69**	**2.23**	**0.0098**	**0.0097**	0.0000	**0.00011**	$\mathbf{6.256e^{-05}}$	**0.02458**	**0.04880**

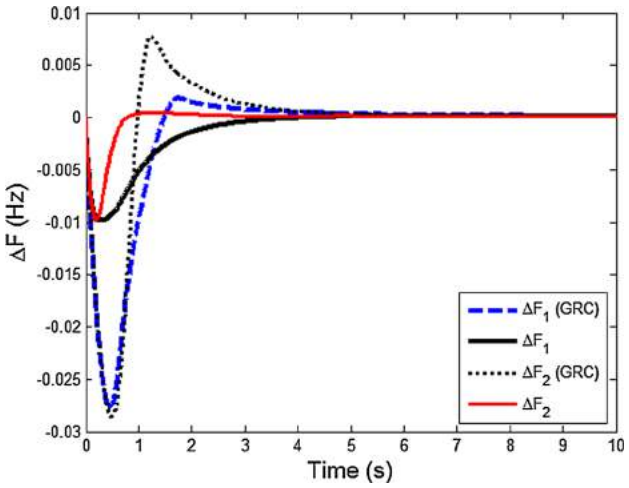


Fig. 16 ΔF_1 and ΔF_2 responses of RMSMA system with/without GRC for FPID controller

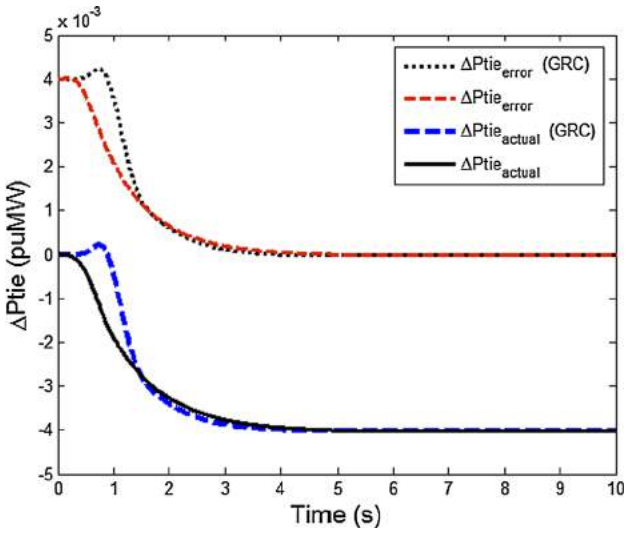


Fig. 17 $\Delta\text{Ptie}_{\text{actual}}$ and $\Delta\text{Ptie}_{\text{error}}$ responses of RMSMA system with/without GRC for FPID controller

initial loading of RMSMA system are shown, respectively, in Figs. 20, 21, 22 and 23. The sensitivity analysis is performed for FPI and FPID controllers designed at nominal conditions for the power system models under study. Critical examination of all frequency, tie-line and output power responses clearly reveals that FPID outperforms FPI controller. It can be observed further from Figs. 20, 21, 22 and 23 that all the system responses due to wide variations in system parameters and operating loading condition are more or less same. Only four sample responses one for each system are provided to validate the said statement. Thus, the optimum values of K_{1i}, K_{2i}, K_{Pi}, K_{Ii} and K_{Di} obtained at the nominal parameters and nominal loading of 50 % are robust enough and need not be reset to wide changes in the system parameters or system loading.

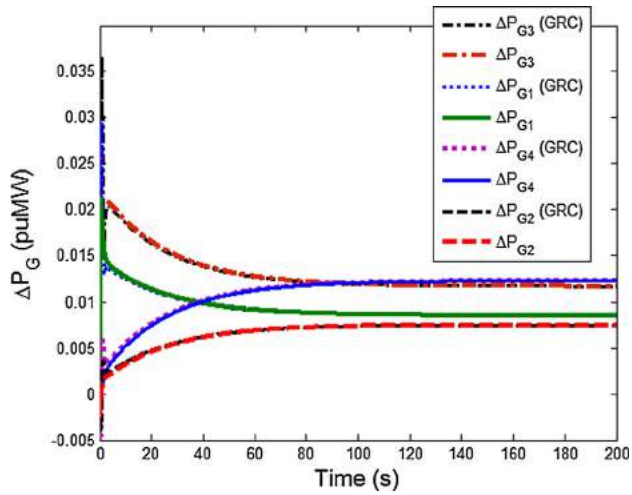


Fig. 18 GENCOs output (ΔP_G) responses of RMSMA system with/without GRC for FPID controller

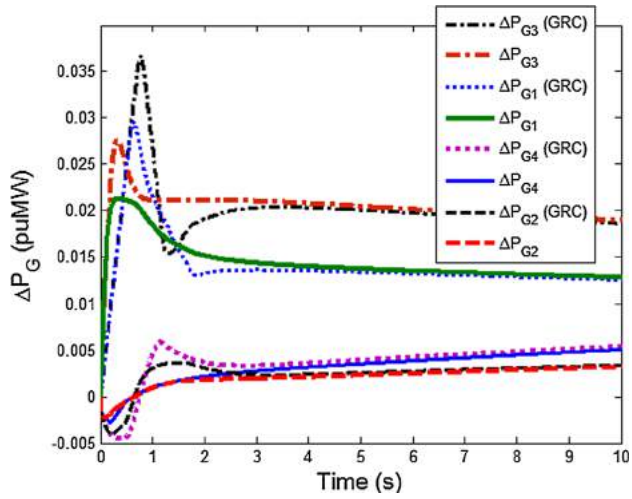


Fig. 19 Fig. 18 with Time = 0–10 s

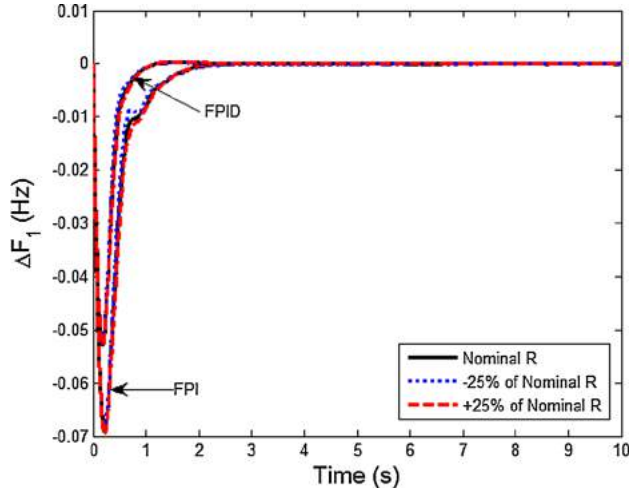


Fig. 20 ΔF_1 response of NRTPS for variation in R parameter

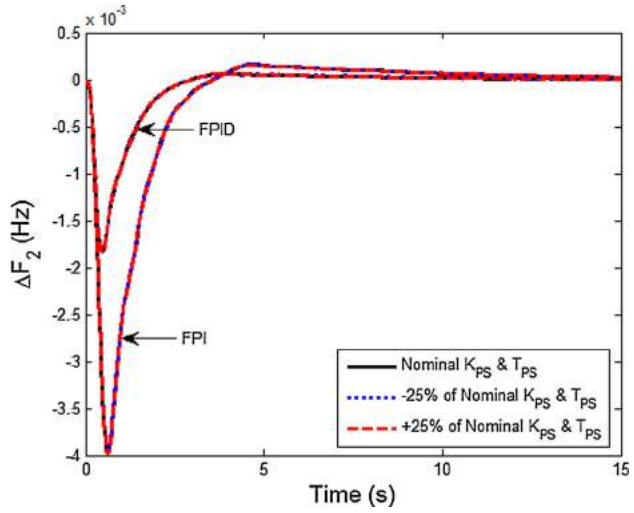


Fig. 21 ΔF_2 response of RTPS for simultaneous variation in K_{PS} and T_{PS} parameters

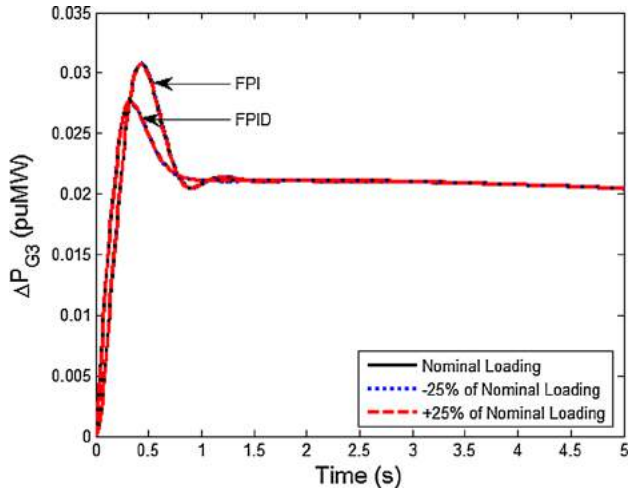


Fig. 23 GENCO-3 power output response of RMSMA system for variation in initial loading

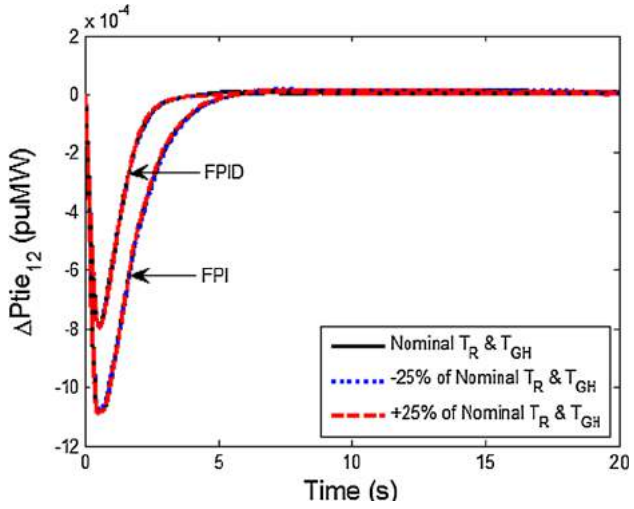


Fig. 22 ΔPtie_{12} response of TMSMA system for simultaneous variation in T_R and T_{GH} parameters

8 Conclusions

In this paper, BFOA-optimized fuzzy PI/PID (FPI/FPID) controller is proposed for AGC of multi-area interconnected power systems. At first, a widely accepted two-area non-reheat thermal system is considered and BFOA is used to optimize simultaneously the input and output scaling factors of FPI/FPID controller. To depict potential benefits yielded by the proposed controller, results are compared with PI controller based on some recently reported approaches such as PSO, FA, BFOA, hybrid BFOA–PSO and fuzzy PI controller based on PS and PSO algorithms for the same power system configuration. It is noticed that significant improvements are achieved with proposed method compared to recently reported PI and fuzzy PI controllers. The proposed approach is then extended to a two-area reheat thermal system and superb dynamic performance is observed with the proposed approach in comparison with PI controller optimized using PSO and ABC algorithms. The approach is further applied on a traditional multi-source multi-area hydrothermal system. From simulation responses, it is observed that BFOA-optimized FPID controller performed better compared to recently published GA and hybrid FA–PS optimized PI controller as well as proposed FPI controller. The system performance indices such as ISE, ITSE, IAE and ITAE, settling times and peak undershoots of frequency and tie-line responses due to above said systems disclose that the proposed approach is better than others. To reveal the capability of the suggested controller to cope with restructured system, the proposed approach is also extended to a restructured multi-source multi-area hydrothermal system. It is observed that FPID outperforms FPI controller. Finally, sensitivity analysis is carried out to test the robustness of the proposed controller parameters optimized at nominal conditions for the systems under study. It is observed that the optimum values of input/output scaling factors of FPI/FPID controller at the nominal 50 % loading condition are quite robust and need not be reset for wide changes in system parameters or loading condition or under the presence of appropriate GRC in thermal/hydro turbines. It may be concluded that the proposed BFOA-optimized fuzzy controller may fruitfully be implemented in the AGC field as well as in some other more complex power engineering problems.

Compliance with ethical standards

Funding This study was not funded by any organization.

Conflict of interest The authors declare that they have no conflict of interest.

Ethical approval This article does not contain any studies with human participants or animals performed by any of the authors.

Appendix: Nomenclature and system data (Chandrakala et al. 2013; Ali and Abd-Elazim 2011; Gozde et al. 2010

i	Subscript referring to area-i ($i = 1, 2$)
ACE_i	Area control error
P_{ri}	2000 MW; rated area capacity
α_{12}	$-1(=-P_{r1}/P_{r2})$; area size ratio coefficient
F^0	60 Hz; nominal system frequency
D_i	0.00833 puMW/Hz ($=\partial P_{\mathrm{Li}}/\partial F P_{\mathrm{ri}}$); system damping constant
R_i	2.4 Hz/puMW, $R_1 = 2$ Hz/puMW for TMSMA/RMSMA; governor regulation parameter
β_i	$D_i + 1/R_i$ puMW/Hz; area frequency response characteristic (AFRC)
B_i	$0.425(=\beta_i)$; frequency bias constant
H_i	5 s; power system inertia constant
K_{PSi}	120 ($=1/D_i$), 100 for TMSMA/RMSMA; power system gain
T_{PSi}	20 s($=2H_i/F^0 D_i$); power system time constant
δ_i	30^0 ($\delta_{12} = \delta_1 - \delta_2$), 45^0 for TMSMA/RMSMA; nominal phase angle of voltages
$\mathrm{Ptie}_{\max}$	$0.1 P_{ri}$ MW; maximum tie-line capacity
T_{12}	0.086 puMW/rad for reheat system, 0.0707 puMW/rad for TMSMA/RMSMA; synchronizing coefficient
$2\pi T_{12}$	0.545 puMW/Hz for non-reheat system; tie-line power synchronizing coefficient
K_{ri}	0.5; high pressure thermal turbine power fraction
cpf_{ij}	Contract participation factor of jth DISCO with ith GENCO
T_{ri}	10 s; reheat thermal turbine time constant
T_{Gi}	0.08 s; speed governor time constant
T_{Ti}	0.3 s; thermal turbine time constant
T_{Ri}	5 s; hydro turbine speed governor reset time
T_{RHi}	48.7 s; hydro turbine speed governor transient droop time constant
T_{Wi}	1 s; water starting time constant
ΔP_{UCi}	Incremental change in uncontracted load power demanded by DISCO
T_{GHi}	0.513 s; hydro turbine speed governor main servo time constant
ΔP_{Di}	Incremental change in load power demand in an area
ΔF_{i}	Incremental change in the area frequency
ΔP_{Ci}	Incremental change in the speed changer position
ΔP_{gi}	Incremental change in area power generation
ΔP_{Gi}	Incremental change in GENCO output
p	Number of parameters to be optimized
S	Number of bacteria
N_S	Swimming length after which tumbling of bacteria will be carry out in a chemotactic loop
N_C	Number of iterations to be undertaken in a chemotactic loop ($N_C > N_S$)
N_{re}	Maximum number of reproduction to be carry out
N_{ed}	Maximum number of elimination–dispersal events
P_{ed}	Probability with which elimination–dispersal will go on

References

Abdel-Magid YL, Dawoud MM (1996) Optimal AGC tuning with genetic algorithms. Electr Power Syst Res 38(3):231–238

Abdel-Magid YL and Abido MA (2003) AGC tuning of interconnected reheat thermal systems with particle swarm optimization. In: Proceedings of 10th IEEE international conference on electronics, circuits and systems, 14–17 December, vol 1, pp 376–379

Aggarwal RP, Bergseth FR (1968) Large signal dynamics of load-frequency control systems and their optimization using nonlinear programming: I & II. IEEE Trans Power Appar Syst PAS–87(2):527–538

Aldeen M, Trinh H (1994) Load frequency control of interconnected power systems via constrained feedback control schemes. Comput Electr Eng 20(1):71–88

Ali ES, Abd-Elazim SM (2011) Bacteria foraging optimization algorithm based load frequency controller for interconnected power system. Int J Electr Power Energy Syst 33(3):633–638

Arya Y, Kumar N, Ibraheem (2016) AGC of a two-area multi-source power system interconnected via AC/DC parallel links under restructured power environment. Optim Control Appl Methods. doi:10.1002/oca.2181

Bhateshvar YK, Mathur HD, Siguerdidjane H, Bhanot S (2015) Frequency stabilization for multi-area thermal-hydro power system using genetic algorithm-optimized fuzzy logic controller in deregulated environment. Electr Power Compon Syst 43(2):146–156

Calovic MS (1984) Automatic generation control: decentralized area-wise optimal solution. Electr Power Syst Res 7(2):115–139

Chan W-C, Hsu Y-Y (1981) Automatic generation control of interconnected power systems using variable-structure controllers. IEE Proc Gener Transm Distrib C 128(5):269–279

Chandrakala KRMV, Balamurugan S, Sankaranarayanan K (2013) Variable structure fuzzy gain scheduling based load frequency controller for multi source multi area hydro thermal system. Int J Electr Power Energy Syst 53:375–381

Chaturvedi DK, Satsangi PS, Kalra PK (1999) Load frequency control: a generalized neural network approach. Int J Electr Power Energy Syst 21(6):405–415

Christie RD, Bose A (1996) Load frequency control issues in power system operations after deregulation. IEEE Trans Power Syst 11(3):1191–1200

Cohn N (1957) Some aspects of tie-line bias control on interconnected power systems. AIEE Trans Power Appar Syst pt III 75(3):1415–1436

Concordia C, Kirchmayer LK (1953) Tie-line power and frequency control of electric power systems. AIEE Trans Power Appar Syst pt III 72(3):562–572

Das D, Kothari ML, Kothari DP, Nanda J (1991) Variable structure control strategy to automatic generation control of interconnected reheat thermal system. IEE Proc D Control Theory Appl 138(6):579–585

Debbarma S, Saikia LC, Sinha N (2013) AGC of a multi-area thermal system under deregulated environment using a non-integer controller. Electr Power Syst Res 95:175–183

Donde V, Pai MA, Hiskens IA (2001) Simulation and optimization in an AGC system after deregulation. IEEE Trans Power Syst 16(3):481–489

Elgerd OI (2014) Electric energy systems theory: an introduction, 2nd ed (42nd reprint). McGraw Hill Education, New Delhi

Fosha CE, Elgerd OI (1970) The megawatt-frequency control problem: a new approach via optimal control theory. IEEE Trans Power Appar Syst PAS–89(4):563–577

Gozde H, Taplamacioglu MC, Kocaarslan I, Senol MA (2010) Particle swarm optimization based PI-controller design to load-frequency control of a two area reheat thermal power system. J Therm Sci Technol 30(1):13–21

Gozde H, Taplamacioglu MC, Kocaarslan I (2012) Comparative performance analysis of artificial bee colony algorithm in automatic generation control for interconnected reheat thermal power system. Int J Electr Power Energy Syst 42(1):167–178

Hari L, Kothari ML, Nanda J (1991) Optimum selection of speed regulation parameters for automatic generation control in discrete mode considering generation rate constraints. IEE Proc Gener Transm Distrib C 138(5):401–406

Ibraheem Kumar P, Kothari DP (2005) Recent philosophies of automatic generation control strategies in power systems. IEEE Trans Power Syst 20(1):346–357

Indulkar CS, Raj B (1995) Application of fuzzy controller to automatic generation control. Electr Mach Power Syst 23(2):209–220

Jeyalakshmi V, Subburaj P (2015) PSO-scaled fuzzy logic to load frequency control in hydrothermal power system. Soft Comput. doi:10.1007/s00500-015-1659-8

Kothari DP, Nagrath IJ (2012) Modern power system analysis, 4th ed. (3rd reprint). McGraw Hill, New Delhi

Kumar A, Malik OP, Hope GS (1987) Discrete variable structure controller for load frequency control of multiarea interconnected power systems. IEE Proc Gener Transm Distrib C 134(2):116–122

Kundur P (2011) Power system stability and control (12th reprint). Tata McGraw-Hill, New Delhi

Malik OP, Hope GS, Tripathy SC, Mital N (1985) Decentralized suboptimal load-frequency control of a hydro-thermal power system using the state variable model. Electr Power Syst Res 8(3):237–247

Mudi RK, Pal NR (1999) A robust self-tuning scheme for PI-and PD-type fuzzy controllers. IEEE Trans Fuzzy Syst 7(1):2–16

Mudi RK, Pal NR (2000) A self-tuning fuzzy PI controller. Fuzzy Sets Syst 115(2):327–338

Nanda J, Mangla A, Suri S (2006) Some new findings on automatic generation control of an interconnected hydrothermal system with conventional controllers. IEEE Trans Energy Convers 21(1):187–194

Nanda J, Mishra S, Saikia LC (2009) Maiden application of bacterial foraging-based optimization technique in multiarea automatic generation control. IEEE Trans Power Syst 24(2):602–609

Padhan S, Sahu RK, Panda S (2014) Application of firefly algorithm for load frequency control of multi-area interconnected power system. Electr Power Compon Syst 42(13):1419–1430

Panda S, Mohanty B, Hota PK (2013) Hybrid BFOA–PSO algorithm for automatic generation control of linear and nonlinear interconnected power systems. Appl Soft Comput 13(12):4718–4730

Pandey SK, Mohanty SR, Kishor N (2013) A literature survey on load-frequency control for conventional and distribution generation power systems. Renew Sustain Energy Rev 25:318–334

Parmar KPS, Majhi S, Kothari DP (2014) LFC of an interconnected power system with multi-source power generation in deregulated power environment. Int J Electr Power Energy Syst 57:277–286

Passino KM (2002) Biomimicry of bacterial foraging for distributed optimization and control. IEEE Control Syst 22(3):52–67

Sahu RK, Panda S, Yegireddy NK (2014) A novel hybrid DEPS optimized fuzzy PI/PID controller for load frequency control of multi-area interconnected power systems. J Process Control 24(10):1596–1608

Sahu RK, Panda S, Sekhar GTC (2015a) A novel hybrid PSO–PS optimized fuzzy PI controller for AGC in multi area interconnected power systems. Int J Electr Power Energy Syst 64:880–893

Sahu RK, Panda S, Padhan S (2015b) A hybrid firefly algorithm and pattern search technique for automatic generation control of multi area power systems. Int J Electr Power Energy Syst 64:9–23

Sahu RK, Panda S, Pradhan PC (2015c) Design and analysis of hybrid firefly algorithm-pattern search based fuzzy PID controller for LFC of multi area power systems. Int J Electr Power Energy Syst 69:200–212

Saikia LC, Sinha N, Nanda J (2013) Maiden application of bacterial foraging based fuzzy IDD controller in AGC of a multi-area hydrothermal system. Int J Electr Power Energy Syst 45(1):98–106

Sekhar GTC, Sahu RK, Baliarsingh AK, Pandam S (2016) Load frequency control of power system under deregulated environment using optimal firefly algorithm. Int J Electr Power Energy Syst 74:195–211

Yesil E, Guzelkaya M, Eksin I (2004) Self tuning fuzzy PID type load and frequency controller. Energy Convers Manag 45(3):377–390

Medicinal & Aromatic Plants

Kundu et al., Med Aromat Plants 2016, 5:4
http://dx.doi.org/10.4172/2167-0412.1000251

Research Article Open Access

Effect of Different Carbon Sources and Elicitors on Shoot Multiplication in Accessions of *Centella asiatica*

Koyel Kundu, Arpita Roy, Gaurav Saxena, Lakhan Kumar and Navneeta Bharadvaja*

Plant Biotechnology Laboratory, Department of Biotechnology, Delhi Technological University, New Delhi, India

Abstract

Centella asiatica is a medicinal herb which has been extensively used in the treatment of nervous disorders and skin diseases. It is distributed throughout the tropical and sub-tropical region of the world. This plant contains various bioactive constituents such as asiaticoside, madecassic acid, flavonoids etc. *Centella* is in huge demand in International market for the preparation of pharmaceuticals and cosmetics which has resulted in its overexploitation. This situation demands the use of biotechnological methods to conserve as well as increase the production of biomass and bioactive compounds. The present study focused the use of different carbon sources (sucrose and fructose) and elicitors (Malt extract, Salicylic acid and Jasmonic acid) for the enhancement of biomass in five accessions of *Centella asiatica*. It was concluded that Murashige and Skoog (MS) medium supplemented with 1 mg/L concentration of Malt extract and 1.5 mg/L concentration of 6-Benzyl amino purine (BAP) showed highest biomass production among all elicitors. Among two carbon sources, MS media supplemented with Sucrose (3 mg/L) along with BAP (1.5 mg/L) showed better result than fructose.

Keywords: *Centella asiatica*; Carbon sources; Elicitors; Sucrose; Fructose; Malt extract; Salicylic acid; Jasmonic acid

Introduction

Centella asiatica is a perennial herb belonging to the family Apiaceae and found throughout tropical and sub-tropical regions of India. This plant is known by different names in different regions of India, Manimunni in Assam, Thankuni in Bengali, Vallari in Decan, Mandookaparni in Hindi and Gotukola in Sinhali [1]. It is a softly perfumed, creeping plant that attains height up to 15 cm. Stem is smooth and rooting occurs at the nodes. It grows extensively in marshy, damp and wet places and flowering occurs during April to June with white to purple or pink flowers. Fruits are approximately 2 inches long, globular in shape and strongly thickened pericarp [2]. This plant has been used since ancient days in Ayurvedic medicines. Use of this plant has been described in the ancient literature Charaka Chikitsa [3]. Whole plant is used for the preparation of drug and these drugs can be used internally or externally. Paste from fresh herbs can be used externally for the treatment of rheumatism and elephantitis. Leaf juice can be applied on forehead in case of headache. An ointment prepared from this plant can be used for the treatment of leprosy or any skin disorder [3]. One of the bioactive compound i.e., asiaticoside helps in collagen I synthesis in human [4]. Asiaticoside shows antitumor activity by apoptosis of cancer cells. This plant can also be used for the treatment of eczema. Internally, it can also be used for the treatment of various diseases such as bronchitis, asthma, gastric, leucorrhea, kidney disease, urethritis and dropsy [5]. *Centella asiatica* contain various types of bioactive compounds like Asiaticoside, Medacassoside, Brahmoside, Alkaloids (Hydrocotylin), triterpene glycoside, Triterpene acid, Anthrone of Asiaticoside, Asiatic acid, Madegascaric or madecassic acid Isothankuniside, Brahmic acid, Centelloside, Centic acid, Indocentoic acid, Indocentelloside, Oligosaccharide, etc. [6,7]. The plant also contains volatile and fatty oils. Glycosides of palmitic, stearic, oleic and linolenic acids are present in fatty oils.

Due to great medicinal importance of *Centella asiatica* in the preparation of different pharmaceutical compounds, this plant has been overexploited and marked as threatened plant species by the International Union for Conservation of Nature and Natural Resources (IUCN), and also as an endangered plant species [8,9]. Thus conservation of this plant is need of the hour. Biotechnological methods not only help in the conservation of endangered plants but also help in the enhancement of biomass and commercially important plant products.

Mass propagation of plants through *in vitro* micro propagation is the most successful commercial application of plant tissue culture technique. *In vitro* propagation may provide a potential solution for cloning of plant and secondary metabolite production. Application of elicitors is one of the most important method to increase the production of secondary metabolites in plants. Elicitors are the molecule that enhances the secondary metabolite production under stress [10]. In plant tissue culture, plants are grown under stress condition but the plant genome has the defense mechanism to protect the plant via some secondary metabolite production. Elicitors are the signal compound of plant defense mechanism [11]. It was reported that elicitors enhance bioaccumulation of asiaticoside in *C. asiatica* [12]. Sugars also have important role in metabolic activity [13] as they enhance the formation of auxiliary buds and branching of adventitious roots [14]. But the above mentioned effects are not universal and depend on the geographical conditions of plant to a great extent. Plant of same species is collected from different locations and is assigned an accession number. Accessions differ in their growth pattern and secondary metabolite content. Therefore the present study was undertaken to determine the effect of different carbon sources like sucrose and fructose and different elicitors, like Malt extract (ME), Salicylic acid (SA), Jasmonic acid (JA) on growth of five different accession of *Centella asiatica* and to assess the response of different accession to variable conditions of carbon sources and elicitors.

***Corresponding author:** Navneeta Bharadvaja, Plant Biotechnology Laboratory, Department of Biotechnology, Delhi Technological University, New Delhi-110 042, India, Tel: 9198684466137; E-mail: navneetab@dtu.co.in

Received April 19, 2016; **Accepted** May 20, 2016; **Published** May 23, 2016

Citation: Kundu K, Roy A, Saxena G, Kumar L, Bharadvaja N (2016) Effect of Different Carbon Sources and Elicitors on Shoot Multiplication in Accessions of *Centella asiatica*. Med Aromat Plants 5: 251. doi:10.4172/2167-0412.1000251

Copyright: © 2016 Kundu K, et al. This is an open-access article distributed under the terms of the Creative Commons Attribution License, which permits unrestricted use, distribution, and reproduction in any medium, provided the original author and source are credited.

Materials and Methods

Cultures of five different accessions i.e., 281374, 383913, 342109, 347492, 331514 of *C. asiatica* were collected from NBPGR New Delhi, India. To study the effect of carbon source and elicitors on shoot multiplication MS media was used. Murashige and Skoog (MS) [15] media was prepared and pH was adjusted to 5.8 using 1 N HCl or 1 N NaOH solution. 0.8% plant agar was used to solidify the media. Sterilization of the media was done by autoclaving for 20 min at 121°C and 15 lb pressure. For experiment on elicitors and carbon sources, MS media was supplemented with 1.5 mg/L 6- Benzyl amino purine along with different elicitors {Malt extract (1 mg/L), Salicylic acid (1 mg/L), Jasmonic acid (1 mg/L)} and different carbon sources {Sucrose (3%) and fructose (3%)} separately. After the solidification of media, sterile shoot nodes from each accession were inoculated in culture tubes (25 × 150 mm) separately. The cultures were incubated at 26 ± 2°C under 16 h photoperiod and light intensity of 3000 lux for four weeks. Each and every experiment was done in triplicates. Visual data was recorded after 4th week of inoculation in terms of number of shoots and length of shoots for *in vitro* growth measurement.

Data analysis

Observations were recorded and are presented as means ± standard deviation of 3 biological replicates to estimate the variability between the accessions.

Results and Discussion

Effect of carbon source and elicitors on shoot regeneration was observed in five accessions of *Centella asiatica*. Observation was recorded as mean value of triplicate samples after four weeks of inoculation (Tables 1 and 2). Among the elicitors used, MS media supplemented with malt extract (1 mg/ltr) showed maximum number and maximum length of shoots (Figure 1). Maximum effect of malt extract was found on accession no. 281374 as maximum number of shoots i.e., 25 were reported in this accession followed by 342109 (16), 331514 (15), 347492 (14) and 383913 (10). Maximum average length was reported in accession number 347492 (3.07) followed by 281374 (2.35), 342109 (1.69), 331514 (1.75), 383913 (1.5).

Two different carbohydrate sources i.e., sucrose and fructose were tested for their potential on shoot regeneration in five different accession of *Centella asiatica* and it was found that sucrose showed better shoot growth than fructose in different accession of *Centella asiatica* (Figure 2). Maximum number of shoots generation was recorded in MS media supplemented with Sucrose (3%). In case of sucrose as carbon source, maximum number of shoots was reported in accession number 347492 (16) followed by 331514 (10), 281374 (8), 342109 (5) and 383913 (3). Maximum average length was reported in accession number 347492 (1.66).

Order of other accession's average length of shoots in sucrose experiment is 281374 (1.5) and 331514 (1.5), 342109 (0.75),

S No	Accession Number	Treatment	No. of shoots (M ± SE)	Length of shoot (cm.) (M ± SE)
1	Accession No. 281374	MS+BAP (1.5 mg/ltr)+ME (1 mg/ltr)	25 ± 1.52	2.35 ± 0.12
		MS+BAP (1.5 mg/ltr)+SA (1 mg/ltr)	4 ± 1.15	1 ± 0.08
		MS+BAP (1.5 mg/ltr)+JA (1 mg/ltr)	2 ± 1	0.75 ± 0.12
2	Accession No. 383913	MS+BAP (1.5 mg/ltr)+ME (1 mg/ltr)	10 ± 0.57	1.3 ± 0.05
		MS+BAP (1.5 mg/ltr)+SA (1 mg/ltr)	1 ± 0.33	1.5 ± 0.12
		MS+BAP (1.5 mg/ltr)+JA (1 mg/ltr)	1 ± 0	0.5 ± 0.05
3	Accession No. 342109	MS+BAP (1.5 mg/ltr)+ME (1 mg/ltr)	16 ± 3.46	1.69 ± 0.09
		MS+BAP (1.5 mg/ltr)+SA (1 mg/ltr)	1 ± 0	2.5 ± 0.28
		MS+BAP (1.5 mg/ltr)+JA (1 mg/ltr)	2 ± 0.57	0.75 ± 0.07
4	Accession No. 347492	MS+BAP (1.5 mg/ltr)+ME (1 mg/ltr)	14 ± 1.15	3.07 ± 0.12
		MS+BAP (1.5 mg/ltr)+SA (1 mg/ltr)	5 ± 1.15	0.9 ± 0.10
		MS+BAP (1.5 mg/ltr)+JA (1 mg/ltr)	5 ± 1.52	0.52 ± 0.03
5	Accession No. 331514	MS+BAP (1.5 mg/ltr)+ME (1 mg/ltr)	15 ± 1.15	1.43 ± 0.07
		MS+BAP (1.5 mg/ltr)+SA (1 mg/ltr)	8 ± 2	1.75 ± 0.07
		MS+BAP (1.5 mg/ltr)+JA (1 mg/ltr)	12 ± 2.88	1.66 ± 0.07

Table 1: Effect of different elicitors on number and length of regenerated shoots in five different accession of *Centella asiatica* after four weeks of inoculation. Values are expressed as mean ± Standard Error (M ± SE). MS: Murashige and Skoog medium; BAP: 6-Benzyl amino purine; ME: Malt Extract; SA: Salicylic acid; JA: Jasmonic acid.

S No	Accession Number	Treatment	No. of shoots (M ± SE)	Length of shoot (cm) (M ± SE)
1	Accession No. 281374	MS+Sucrose+BAP (1.5 mg/ltr)	8 ± 1.15	1 ± 0.06
		MS+Fructose+BAP (1.5 mg/ltr)	2 ± 0.57	1.5 ± 0.16
2	Accession No. 383913	MS+Sucrose+BAP (1.5 mg/ltr)	3 ± 0.57	0.27 ± 0.04
		MS+Fructose+BAP (1.5 mg/ltr)	2 ± 0.57	0.75 ± 0.08
3	Accession No. 342109	MS+Sucrose+BAP (1.5 mg/ltr)	5 ± 1.2	0.52 ± 0.02
		MS+Fructose+BAP (1.5 mg/ltr)	2 ± 0.57	0.75 ± 0.10
4	Accession No. 347492	MS+Sucrose+BAP (1.5 mg/ltr)	16 ± 3.05	1.66 ± 0.15
		MS+Fructose+BAP (1.5 mg/ltr)	5 ± 0.57	0.7 ± 0.05
5	Accession No. 331514	MS+Sucrose+BAP (1.5 mg/ltr)	10 ± 1.15	1.5 ± 0.08
		MS+Fructose+BAP (1.5 mg/ltr)	3 ± 0.57	1 ± 0.09

Table 2: Effect of different carbon sources on number and length of regenerated shoots in five different accession of *Centella asiatica* after four weeks of inoculation. Values are expressed as mean ± Standard Error (M ± SE). MS: Murashige and Skoog medium; BAP: 6-Benzyl amino purine.



Figure 1: *In vitro* culture of five different accession of *Centella asiatica* in malt extract (After four weeks of inoculation).

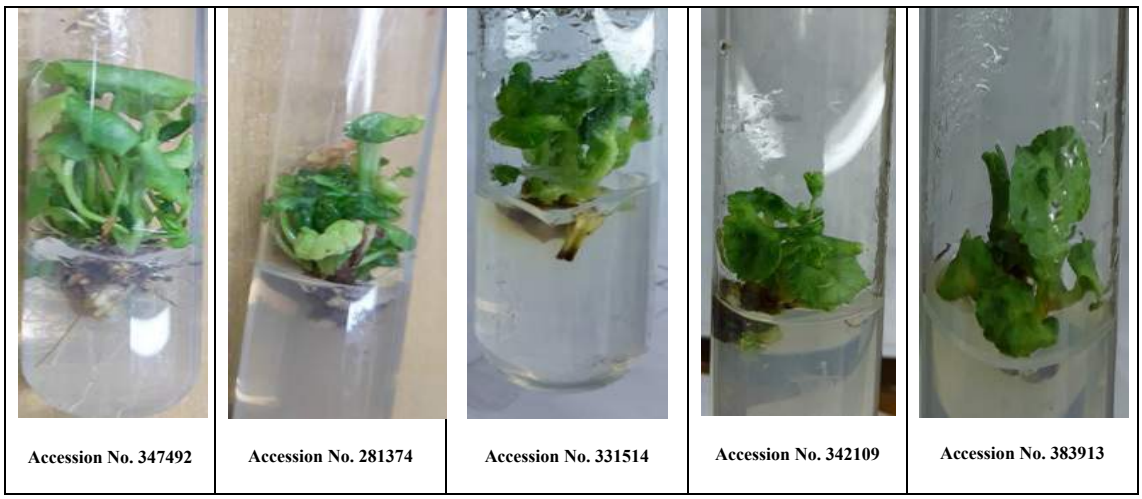


Figure 2: *In vitro* culture of five different accession of *Centella asiatica* in sucrose (After four weeks of inoculation).

383913(0.75). These parameters can be used for maximum production of biomass and bioactive compounds. Focus can be drawn on high yielding accessions for secondary metabolite production. Hossain et al. [16] also reported similar results in *C. asiatica*. They concluded that sucrose showed best results as it helped in the production of maximum shoot length in presence of BA and Kinetin.

Conclusion

From the above study, it can be concluded that different carbon sources and elicitors have significant effect on the shoot formation of *Centella asiatica* as they have the capacity to enhance shoot multiplication as well as shoot length which ultimately increases the growth of the plant. Among the carbon source, sucrose showed better capability to enhance the growth of *Centella asiatica* than fructose. Accession no. 347492 showed maximum number of shoots in MS media containing sucrose. Malt extract showed the highest number of shoots generation among the other elicitors used. Accession no. 281374 showed maximum number of shoots regeneration in MS media containing Malt extract. Shoot proliferation can be used for production of important bioactive compound of this plant i.e., asiaticoside. This study not only finalized the appropriate elicitors and carbon source but also the high yielding accession of *Centella asiatica*. Further study will include the quantitative and qualitative analysis of various secondary metabolites like saponins, terpenoids, and alkaloids extracted from *Centella asiatica*.

Acknowledgements

The authors are grateful to the Department of Biotechnology, Delhi Technological University, Delhi for extending all the laboratory facilities towards successful completion of this investigation and National Bureau of Plant Genetic Resources for providing the plant materials.

References

1. Jamil SS, Nizami Q, Salam M (2007) *Centella asiatica* (Linn.) Urban A Review. Natural Product Radiance 6: 58-170.
2. Tripathi G, Mishra S, Upadhyay P, Purohit S, Dubey GP (2015) Ethno pharmacological importance of *Centella asiatica* with special reference to neuroprotective activity. Asian Journal of Pharmacology and Toxicology 3: 49-53.
3. Bhavna D, Jyoti K (2011) *Centella asiatica*: The elixir of life. International Journal of Research in Ayurveda & Pharmacy 2: 431-438.

4. Bonte F, Dumas M, Chaudagne C, Maybeck A (1994) Influence of asiatic acid, madecassic acid and asiaticoside on human collagen I synthesis. Planta Med 60: 133-135.
5. Evans WC (2002) Saponin, cardioactive drugs and other sterols. Pharmacognosy, Saunders 15: 303-304.
6. Gohil KJ, Patel JA, Gajjar AK (2010) Pharmacological review on *Centella asiatica*: A potential herbal cure-all. Indian J Pharm Sci 72: 546-556.
7. Das KM, Kumar B (2012) Ancient and pharmacological review on *Centella asiatica* (Mandukparni): A potential herbal panacea. International Journal of Research and Reviews in Pharmacy & Applied Science 2: 1062-1072.
8. Singh HG (1989) Himalayan herbs and drugs, importance and extinction threat. Journal of Medicinal Plants Research 10: 47-52.
9. Pandey NK, Tewari KC, Tewari RN, Joshi GC, Pande VN, et al. (1993) Medicinal plants of kumaon Himalaya. In: Dhar U (ed). Strategies for conservation of Himalayas, Himavikas Publication, Nanital, India 3: 293-302.
10. Zhao J, Davis LC, Verpoorte R (2005) Elicitor signal transduction leading to production of plant secondary metabolites. Biotechnol Adv 23: 283-333.
11. Patel H, Krishnamurthy R (2013) Elicitors in plant tissue culture. Journal of Pharmacognosy and Phytochemistry 2: 60-65.
12. Loc NH, Giang NT (2012) Effects of elicitors on the enhancement of asiaticoside biosynthesis in cell cultures of Centella (*Centella asiatica* L. Urban). Chemical papers 66: 642-648.
13. Panathula CS, Mahadev MD, Naidu CV (2014) Effect of different carbohydrates on *in vitro* plant regeneration of *Centella asiatica* (L.), an important antijaundice medicinal plant. International Journal of Medicinal and Aeromatic Plants 4: 41-47.
14. Saad AIM, Elshahed AM (2012) Plant tissue culture media, Recent advances in plant *in vitro* culture. Chapter 2. In Tech Publisher (Online book).
15. Murashige T, Skoog F (1962) A revised medium for rapid growth and bioassays with tobacco tissue cultures. Physiologia Plantarum 15: 473-497.
16. Hossain A, Hossain T, Ali R, Rahman M (2005) Effect of different carbon sources on in vitro regeneration of Indian Pennywort (*Centella asiatica* L.). Pakistan Journal of Biological Science 8: 963-965.

Citation: Kundu K, Roy A, Saxena G, Kumar L, Bharadvaja N (2016) Effect of Different Carbon Sources and Elicitors on Shoot Multiplication in Accessions of *Centella asiatica.* Med Aromat Plants 5: 251. doi:10.4172/2167-0412.1000251

OMICS International: Publication Benefits & Features

Unique features:

- Increased global visibility of articles through worldwide distribution and indexing
- Showcasing recent research output in a timely and updated manner
- Special issues on the current trends of scientific research

Special features:

- 700+ Open Access Journals
- 50,000+ Editorial team
- Rapid review process
- Quality and quick editorial, review and publication processing
- Indexing at major indexing services
- Sharing Option: Social Networking Enabled
- Authors, Reviewers and Editors rewarded with online Scientific Credits
- Better discount for your subsequent articles

Submit your manuscript at: http://www.omicsonline.org/submission

EFFECT OF NOSE RADIUS ON SURFACE ROUGHNESS DURING CNC TURNING USING RESPONSE SURFACE METHODOLOGY

Devendra Singh[1], Vimanyu Chadha[2] and Ranganath M Singari[3]

[1]Department of Mechanical, Production and Industrial Engineering, Sagar Institute Of Technology And Management, Uttar Pradesh, India
jss.devendra@gmail.com

[2,3]Department of Mechanical, Production and Industrial Engineering, Delhi Technological University, New Delhi, India
vimanyuchadha@gmail.com

ABSTRACT

The work and study presented in this paper aims to investigate the effect of nose radius on surface roughness, in CNC turning of Aluminium (6061) in dry condition. The effect of cutting conditions (speed, feed and depth of cut) and tool geometry (nose radius) on surface roughness were studied and analysed. Design of Experiments (DOE) were conducted for the analysis of the influence of the turning parameter on the surface roughness by using Response Surface Methodology (RSM) and then followed by optimization of the results using Analysis of Variance (ANOVA) to minimize surface roughness. The nose radius was identified as the most significant parameter. Surface roughness value decreased with increase in nose radius.

KEYWORDS

Nose Radius, CNC, Design of Experiments, Response Surface Methodology, Central Composite Design, Turning, Speed, Depth of cut, Feed, Surface Roughness, and Aluminium 606.

1.INTRODUCTION

The increase of consumer needs for quality metal cutting related products (more precise tolerance and better surface finish) has driven the metal cutting industry to continuously improve quality control of the metal cutting processes. Quality of the surface roughness is an important requirement of many work pieces in the machining operations. This parameter is increasingly needed in automotive, aerospace, die and mould manufacturing application. Within the metal cutting processes, one of the most fundamental metal removal operations is turning process, which is used in the manufacturing industry. The surface roughness, which is used to determine and evaluate quality of a product, is one of the major quality attribute of the turned product. The surface roughness of a machined product could affect several of the product‘s functional attributes such as contact causing surface friction, light reflection, wearing, ability of distributing and holding a lubricant, heat transmission, resisting fatigue in material. Hence, surface roughness is one of the most important quality aspects in turning operations. Hence, there is a need to optimize the process parameters in a systematic way to achieve the output characteristics/responses by using experimental methods and statistical models[24].

Therefore, in order to obtain better surface roughness, proper setting of cutting parameters is very crucial before the process takes place. Starting point for determining cutting parameters, technologists can use the hands on data tables that are furnished in the machining data handbooks. The trial and error approach could be followed previously in order to obtain the optimal machining conditions for particular operations. Recently, a Design of Experiment (DOE) has been implemented to select manufacturing process parameters that could result in a better quality product. The methods of design such as Taguchi's method, Response Surface Methodology (RSM), factorial designs etc., are finding unbound use nowadays replacing the earlier one factor at a time experimental approach which more costly as well as time-consuming. Surface roughness is the factor which is not only hard to measure but also it is very versatile and it depends upon every minute input parameter. So it becomes highly compulsive to have a detailed study of the process to keep the roughness in limits.

Hasan Gokkaya and Muammer Nalbant[10] investigated the effects of insert radii of cutting tools, depths of cut and feed rates on the surface quality of the work pieces depending on various processing parameters. In the range of importance, the effective parameters on the average surface roughness were determined as the following: speed rate, insert radius, and depth of cut. Thus a good combination among the insert radius, speed rate and depth of cut can provide better surface qualities. Ranganath M S et. al[32] have presented a paper on "Surface Finish Monitoring in CNC Turning Using RSM and Taguchi Techniques". This paper presented the findings of an experimental investigation into the effects of speed, feed rate and depth of cut on surface roughness in CNC turning of Aluminium (KS 1275). The three factors speed, feed rate, depth of cut, which were selected in the screening experiment, were used in CCD. Minitab 15 was used to develop the experimental plan for Taguchi and response surface methodology. The same software was also used to analyze the data collected. The Response surface methodology showed significance of all possible combinations of interactions and square terms, whereas, in Taguchi's technique only three interactions are normally studied. This is because of the fact that the interactions between control factors were aliased with their main effects. Response surface methodology technique required almost double time for conducting experiments as that needed for Taguchi technique. 3D surfaces generated by Response surface methodology could help in visualizing the effect of parameters on response in the entire range specified whereas Taguchi's technique gave the average value of response at given level of parameters. Optimization plot obtained from Response surface methodology was not a feature of Taguchi technique. Thus Response surface methodology is a better tool for optimization and can better predict the effect of parameters on response.

Ranganath M S, Vipin[33] carried out experimental investigation and parametric analysis of surface roughness in CNC turning using design of experiments. Their work integrated the effect of various parameters which affect the surface roughness. The important parameters discussed were cutting speed, feed, depth of cut, nose radius and rake angle Experiments were carried out with the help of factorial method of design of experiment (DOE) approach to study the impact of turning parameters on the roughness of turned surfaces. The following conclusions have been made on the basis of results obtained and analysis performed: Increase in cutting speed improved the surface finish, thus the average surface roughness value decreased. Increase in depth of cut affected the surface finish adversely to a small extent, but as depth of cut increased beyond a certain limit surface finish deteriorated to a large extent. Small increase in feed rate deteriorated surface finish to a large extent as compared to same amount of increase of depth of cut. Surface roughness also decreased as the nose radius increased hence surface finish increased. With increase in back rake angle the surface roughness decreased and improved the surface finish. The ANOVA and F-test revealed that the feed is dominant parameter followed by depth of cut, speed, and nose radius and rake angle for surface roughness. Ranganath M S et. al[35] had predicted the surface roughness model for CNC turning of EN 8 steel using response surface methodology. In

this prediction model of surface roughness had been developed for turning EN-8 steel with uncoated carbide inserts using response surface methodology. The model was developed in the form of multiple regression equations correlating dependent parameter surface roughness, with speed, feed rate and depth of cut, in a turning process. The box-behnken design was used to perform the experiments. The second order model was found suitable for this work. Moreover a good agreement between the predicted and experimental surface roughness was observed within reasonable limit. Zahari Taha et. al[48] have investigated on Effect of insert geometry on surface roughness in the turning process of AISI D2 steel. The objective of his study was to compare measured surface roughness (from experiments) with theoretical surface roughness (from theoretical calculations) of two types of insert, 'C' type and 'T' type. Consequently at high feed rates (0.4 mm/rev) the 'C' type insert resulted in 40% lower roughness compared to the 'T' type due to differences in insert geometry.

In this project various research papers were studied and it was assessed that the surface roughness depended upon various cutting parameters as well as tool geometry (nose radius). RSM was adopted to be used as the optimization technique so that the focused parameters could be obtained in a much better and comprehensive way in the process ANOVA and Taguchi were taken in consideration but due to the ability of RSM to control the surface parameters and also the ability to have a second order fitting curve the RSM was chosen to bring the optimality in the system.

2. EXPERIMENTAL WORK

2.1. Workpiece Material

Aluminium 6061 was selected as the work material. It is one of the most extensively used of the 6000 series aluminium alloys. This standard structural alloy, one of the most versatile of the heat-treatable alloys, is popular for medium to high strength requirements and has good toughness characteristics. Applications range from transportation components to machinery and equipment applications to recreation products and consumer durables. It is widely used for producing automotive components by turning process.

It has excellent corrosion resistance to atmospheric conditions and good corrosion resistance to sea water. This alloy also offers good finishing characteristics and responds well to anodizing. Alloy 6061 is easily welded and joined by various commercial methods. For screw machine applications, alloy 6061 has adequate machinability characteristics in the heat-treated condition. The different alloying elements present in this alloy are shown in the Table 1.

Table 1: Workpiece Composition

Components	% by weight
Aluminium (Al)	95.9 to 98.6 %
Magnesium (Mg)	0.8 to 1.2 %
Silicon (Si)	0.4 to 0.8 %
Iron (Fe)	0 to 0.7 %
Copper (Cu)	0.15 to 0.4 %
Chromium (Cr)	0.04 to 0.35 %
Zinc (Zn)	0 to 0.25 %
Manganese (Mn)	0 to 0.15 %
Residuals	0 to 0.15 %
Titanium (Ti)	0 to 0.15 %

2.2. Cutting Tool Inserts

CNMG cutting tool inserts of nose radius 0.4 mm, 0.8 mm, 1.2 mm. The geometry of the tool was.

Table 2: Details of Cutting Inserts

Insert	Shape	Clearance Angle	Inscribed Circle Size	Thickness	Nose Radius
CNMG120404	Diamond	0^0	12.7 mm	4.76 mm	0.4 mm
CNMG120408	Diamond	0^0	12.7 mm	4.76 mm	0.8 mm
CNMG120412	Diamond	0^0	12.7 mm	4.76 mm	1.2 mm

2.3. Experimental Plan

The experimental work was carried out on CNC turning center LMW LL20TL3



Fig. 1: CNC Turning- LMW LL20TL3 (Lakshmi Machine Works Limited)



Fig. 2: Roughness Measuring Instrument (Taylor Hobson Surtronic 3+)

Surface Roughness of these machined surfaces has been measured by a Surface Roughness measuring instrument Talysurf Surtronic 3+. Surtronic 3+ is a self-contained, portable instrument for the measurement of surface texture and is suitable for use in both the workshop and laboratory. Parameters available for surface texture evaluation are: Ra, Rq, Rz (DIN), Ry and Sm. The parameter evaluation and other functions of the instrument are microprocessor based. The measurement results are displayed on a LCD screen and can be an output to an optional printer or computer for further results[30].

2.4. Design of Experiment

The process was studied with a standard RSM design called a Central composite design (CCD). The factorial portion is a full factorial design with all factors at three levels, the star points are at the face of the cube portion on the design which correspond to value of -1. This is commonly referred to as a face centered CCD. The center points, as implied by the name, are points with all levels set to coded level 0, the midpoint of each factor range, and this is repeated six times. Thirty experiments were performed. For each experimental trial, a new cutting edge was used. The Minitab-17 was used to develop the experimental plan for response surface methodology. The same software was also used to analyze the data collected.

As RSM helps to find out the factor level which will satisfy the desired dimensions. Helps in finding relationships of responses on individual input parameter. Helps in forecasting the properties of the product and find out the responses it would give when obtained settings are given. Helps in finding out all the necessary situations for the stability of the process. Hence on the basis of the above uses, RSM is a better tool for optimization and able to forecast effectively the effect of parameters on response. The design table to be used was made by deciding the values of the parameters to be set in the experiment. Namely, the depth of cut, feed rate, speed or rpm and nose radius were set accordingly. The values were defined on basis of the values available in the machine so as to perform the experiment. The process parameters and their values at three levels are given in Table 3.

Table 3: Process Parameters with their values at three levels

Parameters		Level 1	Level 2	Level 3
A	Speed(RPM)	1600	1900	2200
B	Feed (mm/rev.)	0.12	0.18	0.24
C	Depth of Cut(mm)	0.25	0.50	0.75
D	Nose Radius(mm)	0.4	0.8	1.2

2.5. Analysis

ANOVA was used for analyzing the results obtained. ANOVA is used in the analysis of comparative experiments, those in which only the difference in outcomes is of interest. The statistical significance of the experiment is determined by a ratio of two variances. This ratio is independent of several possible alterations to the experimental observations. Adding a constant to all observations does not alter significance. Multiplying all observations by a constant does not alter significance. So in ANOVA, statistical significance results are independent of constant bias and scaling errors as well as the units used in expressing observations.

3. ANALYSIS AND DISCUSSION

The results from the machining trials performed as per the experimental plan are shown in Table 4. These results were used as input in the Minitab Software for further analysis. The CCD details are given in Table 5.

Table 4: Design Table

Order	Block	Speed(RPM)	Feed(mm/rev)	Depth of Cut(mm)	Nose Radius (mm)	Surface Roughness(µm)
1	3	1900	0.18	0.5	1.2	0.92
2	3	1900	0.18	0.5	0.8	2.86
3	3	1900	0.12	0.5	0.8	0.8
4	3	1600	0.18	0.5	0.8	1.56
5	3	1900	0.18	0.5	0.4	1.76
6	3	1900	0.24	0.5	0.8	2.48
7	3	1900	0.18	0.5	0.8	1.46
8	3	1900	0.18	0.75	0.8	1.40
9	3	2200	0.18	0.5	0.8	2.92
10	3	1900	0.18	0.25	0.8	1.38
11	1	2200	0.24	0.5	0.4	2.30
12	1	2200	0.24	0.25	1.2	1.95
13	1	1600	0.12	0.25	1.2	0.60
14	1	1600	0.12	0.75	0.4	0.94
15	1	1600	0.24	0.75	1.2	0.60
16	1	2200	0.12	0.75	1.2	0.92
17	1	1600	0.24	0.25	0.4	1.56
18	1	1900	0.18	0.5	0.8	0.96
19	1	2200	0.12	0.25	0.4	1.00
20	1	1900	0.18	0.5	0.8	1.48
21	2	1600	0.24	0.25	1.2	0.54
22	2	1900	0.12	0.5	0.8	0.64
23	2	1600	0.24	0.75	0.4	3.04
24	2	2200	0.24	0.25	0.4	2.64
25	2	2200	0.24	0.75	1.2	1.10
26	2	1600	0.12	0.25	0.4	1.36
27	2	1600	0.12	0.75	1.2	1.00
28	2	1900	0.18	0.5	0.8	1.56
29	2	2200	0.12	0.25	1.2	1.60
30	2	2200	0.12	0.75	0.4	1.08

.Table 5: Central Composite Design Details			
Factors:	4	**Replicates:**	1
Base Runs:	30	**Total Runs:**	30
Base Blocks:	3	**Total Blocks:**	3
Two-Level Factorial:	16		
Cube Points:	8		
Centre Points in Cube:	4		
Axial Points:	8		
Center Points in Axial:	2		
Alpha	1		

Table 6: Analysis of Variance					
Source	**DF**	**Adj SS**	**Adj MS**	**F-Value**	**P-Value**
Model	6	8.7527	1.45879	9.04	0.000
Linear	4	6.3277	1.58192	9.81	0.000
S	1	1.3566	1.35665	8.41	0.008
F	1	2.2339	2.23390	13.85	0.001
D	1	0.0348	0.03480	0.22	0,647
N	1	2.6971	2.69712	16.72	0.000
2-Way Interaction	2	2.4299	1.21494	7.53	0.003
s*d_1	1	0.9809	0.98091	6.08	0.022
f*n	1	1.2803	1.28027	7.94	0.010
Error	23	3.7097	0.16129		
Lack-of-Fit	18	3.7097	0.20610	*	*
Pure Error	5	0.0000	0.0000		
Total	29	12.4625			

Table 7: Model Summary			
S	**R-sq**	**R-sq(adj)**	**R-sq(pred)**
0.401614	70.23%	62.47%	45.69%

Regression Equation:

Ra = -5.50 + 0.002678×(Speed) + 15.36×(Feed) + 6.38×(Depth of Cut) + 1.159×(Nose Radius) - 0.00345 (Speed)×(Depth of Cut) - 11.84 (Feed)×(Nose Radius)

Without performing any transformation on the response, examination of the fit summary output revealed that the quadratic model is statistically significant for all the conditions and therefore, it has been used for further analysis. An ANOVA table is commonly used to summarize the tests performed. It is evident that speed, depth of cut, feed and nose radius are significant at 95%

confidence level and thus affects mean value and variation around the mean value of the Ra. The nose radius is the most significant in ANOVA for and thus affects the mean value of Ra followed by feed and then speed.

The value of "P >F" for models less than 0.05 indicates that the model is significant, which is desirable as it indicates that the terms in the model have a significant effect on the response. The value of P < 0.0001 indicates that there is only a 0.01% chance that a "model F-value" could occur due to noise. Values greater than 0.1000 indicate the model terms are not significant. Some of the model terms were found to be significant. However, the main effect of nose radius was found to be the most significant factor followed by feed and then depth of cut.

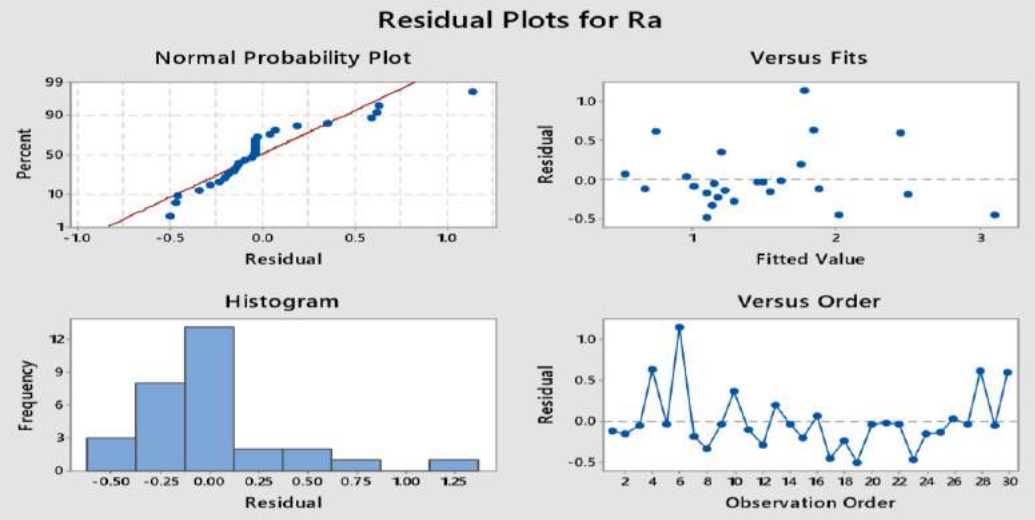


Fig. 3: Residual Plots for Ra

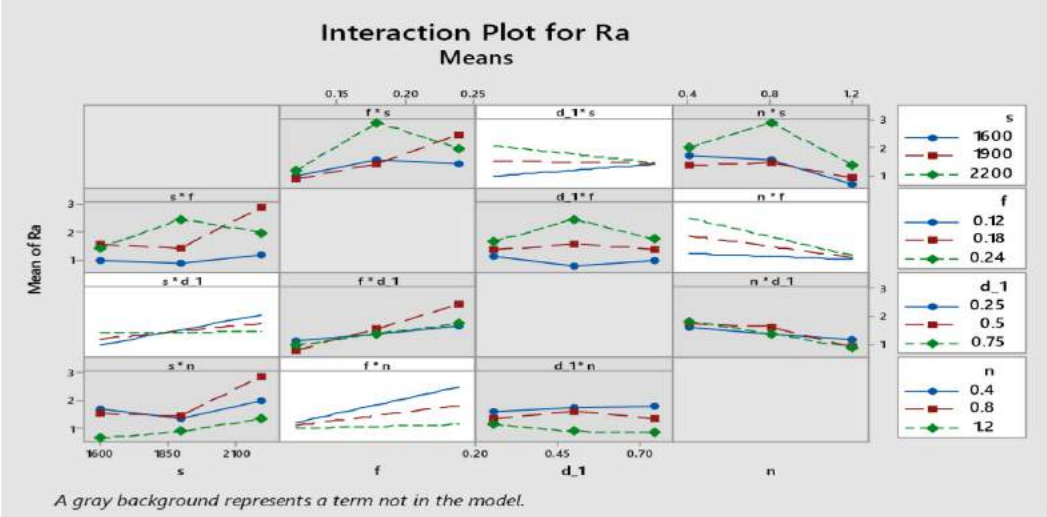


Fig. 4: Interaction Plots of Ra

The normal probability plots of the residuals for Ra shows that the residuals generally fall on a straight line implying that errors are distributed normally. Also in Fig. 3 showing residuals vs order for Ra reveals that they have no visible pattern and unusual structure. This implies that the models proposed are adequate and there is no reason to suspect any violation of the independence or constant variation assumption. Fig.4 shows the interaction plots of Ra for four parameters.

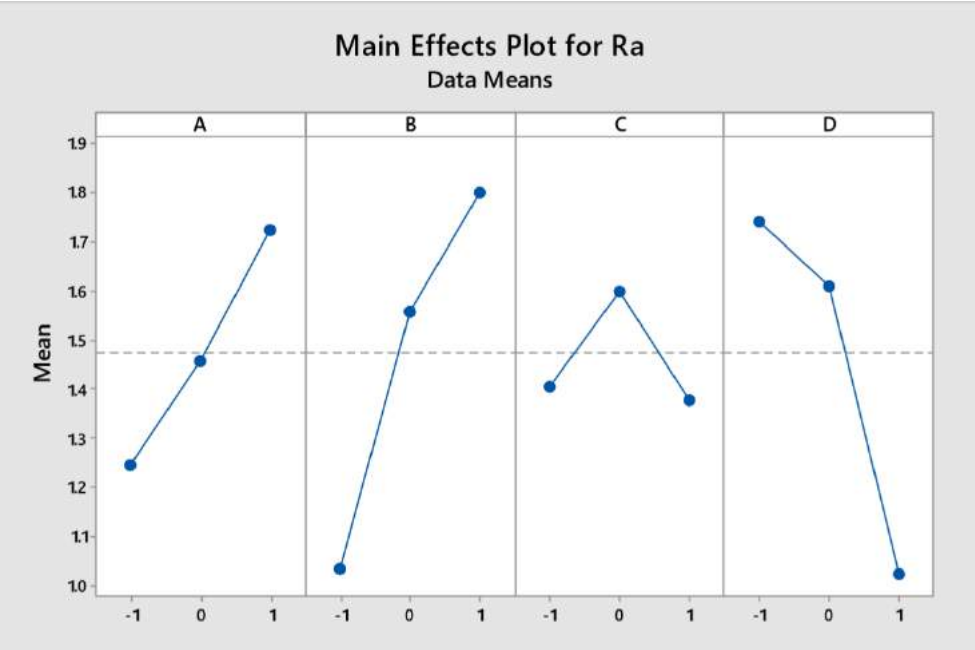


Fig. 5: Main Effects Plot for Means

The main effects plot for Ra is shown in Fig. 5. The optimal values obtained are at 1600 rpm speed, 0.12 m/min feed, 0.25 mm depth of cut and 1.2 mm nose radius. During Optimal Design of A, B, C the Response surface design selected is according to D-optimality. Number of candidate design points are 30, Number of design points in optimal design are 15 and Model terms are A, B, C, D, AA, BB, CC, DD, AB, AC, AD, BC, BD, CD. Initial design generated by Sequential method and Initial design improved by Exchange method. Number of design points exchanged is 1. For Optimal Design Row number of selected design points are 11, 13, 15, 19, 28, 16, 17, 18, 21, 23, 24, 1, 2, 4 and 6.

Condition number:	10.8640
D-optimality (determinant of XTX):	3.47892E+11
A-optimality (trace of inv(XTX)):	5.48611
G-optimality (avg leverage/max leverage):	1
V-optimality (average leverage):	1
Maximum leverage:	1

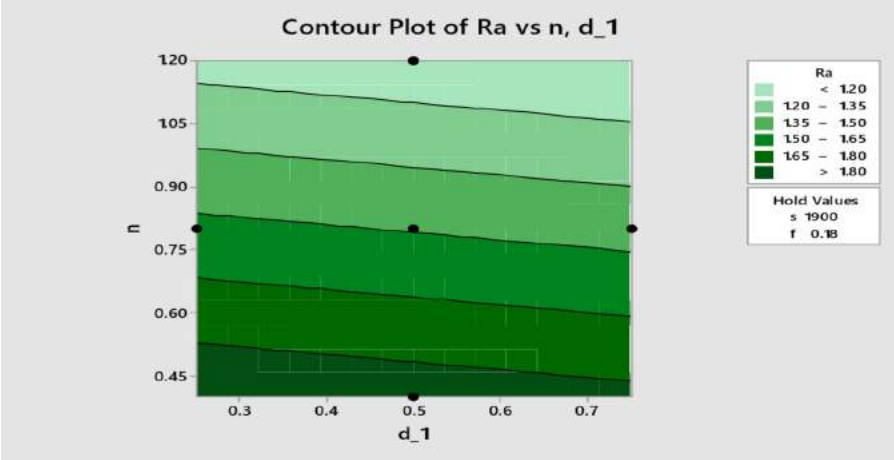


Fig. 6: Contour Plot of Ra vs D, C.

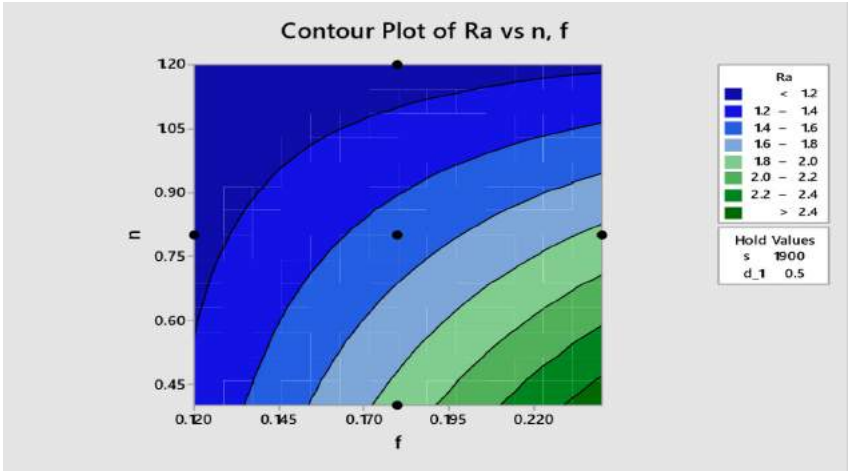


Fig. 7: Contour Plot of Ra vs D, B.

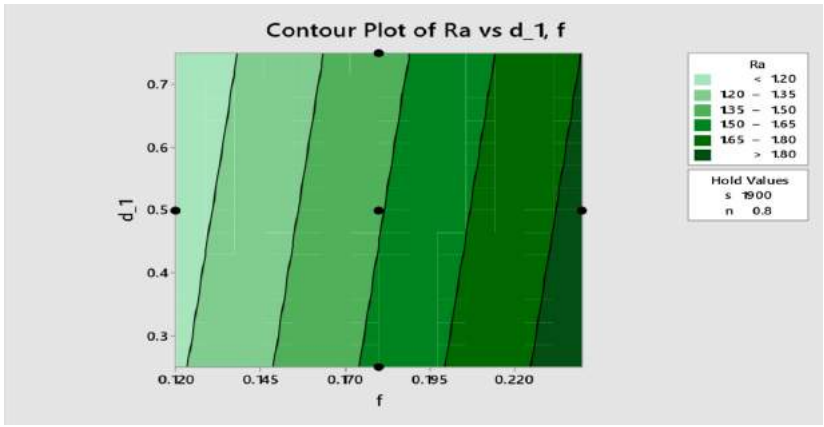


Fig. 8: Contour Plot of Ra vs C, B.

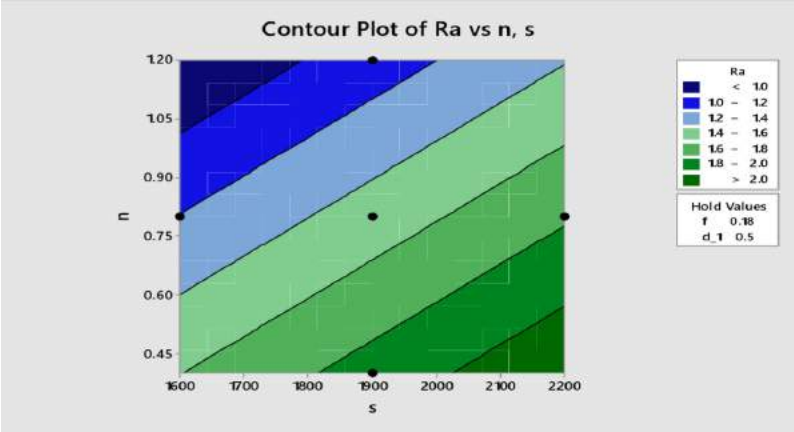


Fig. 9: Contour Plot of Ra vs D, A.

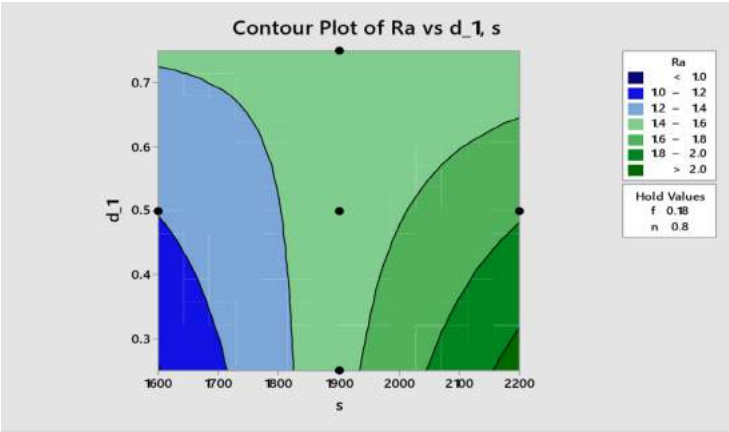


Fig. 10: Contour Plot of Ra vs C, A.

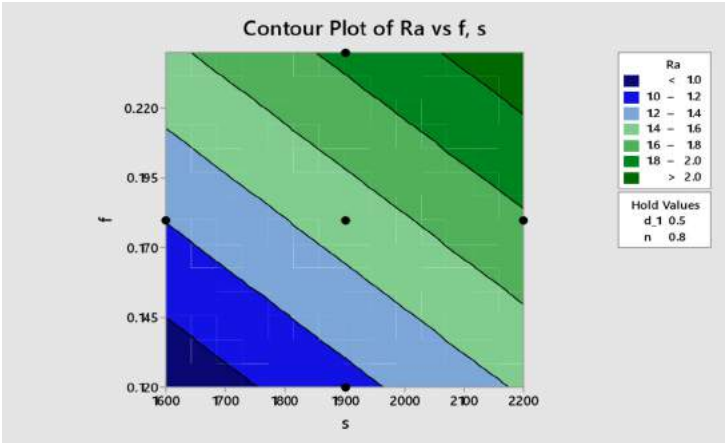


Fig. 11: Contour Plot of Ra vs B, A.

The contour plots for the response, surface roughness are shown Fig. 6 to Fig. 11. The surface roughness decreases with increase in nose radius and increases with increase in feed. Fig. 12 shows 3D surface plot graphs of the effect of nose radius, feed, speed and depth of cut on the surface roughness. It has a curve linear shape according to the model fitted. The entire 3D surface graph for surface roughness has curvilinear profile in accordance to the quadratic model fitted.

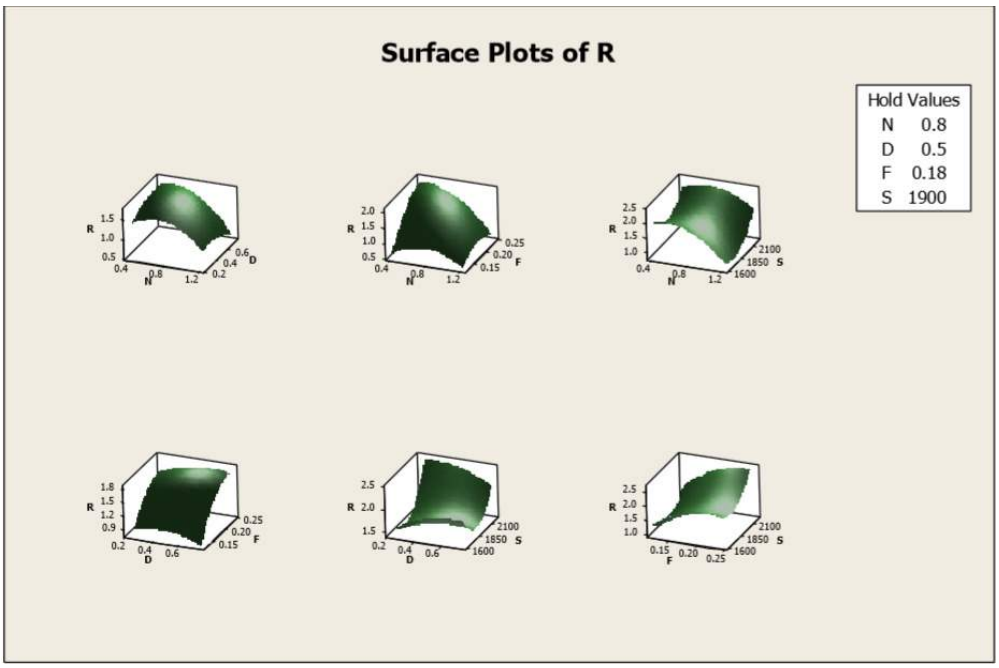


Fig. 12: Various Surface Plots of Ra.

4. CONCLUSIONS

The conclusions which have been drawn on the basis of results obtained and analysis performed are:

- The analysis of the results for surface roughness shows that the nose radius is the most significant factor followed by feed. The 3D surface plots of Response Surface Methodology reveals that nose radius has a very significant effect on the surface roughness.
- The average surface roughness value increases with increase in feed within the specified range.
- Increase in cutting speed within the specified range deteriorates the surface finish, thus the average surface roughness value increases.
- Increase in depth of cut within the specified range affects the surface finish adversely to a small extent.
- Small decrease in nose radius within the specified range deteriorates surface finish to a large extent. Hence, increasing nose radius improves surface finish.
- Empirical models for surface roughness has been determined based on which predictions can be carried out for output response for appropriate applications.

- The optimum value of surface roughness in the given range of parameters as depicted by graphs is 1600 rpm (speed), 0.12 m/min (feed), 0.25 mm (depth of cut) and 1.2 mm (nose radius).
- 3D surfaces generated by Response surface methodology can help in visualizing the effect of parameters on response in the entire range specified, thus Response surface methodology is a better tool for optimization and can better predict the effect of parameters on response.

REFERENCES

[1] A.R.C. Sharman, J.I. Hughes, K. Ridgway, The effect of tool nose radius on surface integrity and residual stresses when turning Inconel 718™, Journal of Materials Processing Technology, Volume 216, February 2015, Pages 123-132, ISSN 0924-0136

[2] Aman Aggarwal, Hari Singh, Pradeep Kumar & Manmohan Singh, "Optimizing power consumption for CNC turned parts using response surface methodology and Taguchi's technique - A comparative analysis", Elsevier Journal, Journal of materials processing technology, pp. 373–384, 2008

[3] Aman Aggarwal and Hari Singh,"Optimisation of machining techniques-a retrospective and literature review", Sadhana, Vol. 30, Part 6, December 2005, pp. 699–711

[4] Anupam Agrawal, Saurav Goel, Waleed Bin Rashid, Mark Price, Prediction of surface roughness during hard turning of AISI 4340 steel (69 HRC), Applied Soft Computing, Volume 30, May 2015, Pages 279-286, ISSN 1568-4946

[5] Chung-Shin Chang, Gwo-Chung Tsai, A force model of turning stainless steel with worn tools having nose radius, Journal of Materials Processing Technology, Volume 142, Issue 1, 10 November 2003, Pages 112-130, ISSN 0924-0136

[6] C. Ahilan, Somasundaram Kumanan, N. Sivakumaran, J. Edwin Raja Dhas, Modeling and prediction of machining quality in CNC turning process using intelligent hybrid decision making tools, Applied Soft Computing, Volume 13, Issue 3, March 2013, Pages 1543-1551, ISSN 1568-4946

[7] C.R. Prakash Rao, M.S. Bhagyashekar, Narendraviswanath, Effect of Machining Parameters on the Surface Roughness while Turning Particulate Composites, Procedia Engineering, Volume 97, 2014, Pages 421-431, ISSN 1877-7058

[8] D. C. Montgomery, Design and Analysis of Experiments, 4th ed. Wi1ey, New York. 1997

[9] Feng C. X. & Wang X., "Development of Empirical Models for Surface Roughness Prediction in Finish Turning, International Journal of Advanced Manufacturing Technology," Vol. 20, 348-356, 2002

[10] Gökkayaa H. & Nalbant M., "The effects of cutting tool geometry and processing parameters on the surface roughness of AISI 1030 steel", Materials & Design, vol. 28(2), 717-721, 2007

[11] H. K. Dave, L. S. Patel & H. K. Raval, "Effect of machining conditions on MRR and surface roughness during CNC Turning of different Materials Using TiN Coated Cutting Tools – A Taguchi approach", International Journal of Industrial Engineering Computations 3, pp. 925-930, 2012

[12] Harish Kumar, Mohd. Abbas, Aas Mohammad, Hasan Zakir Jafri, "Optimization of cutting parameters in CNC Turning", International Journal of Engineering Research and Applications (IJERA), Vol. 3, Issue 3, pp. 331-334, 2013

[13] Ilhan Asilturk & Harun Akkus, "Determining the effect of cutting parameters on surface roughness in hard turning using the Taguchi method", Elsevier Journal, Measurement 44, pp. 1697–1704, 2011

[14] Jakhale Prashant P, Jadhav B. R., "Optimization Of Surface Roughness Of Alloy Steel By Changing Operational Parameters and Insert Geometry in The Turning Process", International Journal of Advanced Engineering Research and Studies, II/ IV, pp. 17-21, 2013

[15] Makadia A.J. and Nanavati J.I., (2013), "Optimisation of machining parameters for turning operations based on response surface methodology," Measurement, 46(4) pp.1521-1529.

[16] Meenu Gupta, Surinder Kumar, Investigation of surface roughness and MRR for turning of UD-GFRP using PCA and Taguchi method, Engineering Science and Technology, an International Journal, Volume 18, Issue 1, March 2015, Pages 70-81, ISSN 2215-0986

[17] Meng Liu, Jun-ichiro Takagi, Akira Tsukuda, Effect of tool nose radius and tool wear on residual stress distribution in hard turning of bearing steel, Journal of Materials Processing Technology, Volume 150, Issue 3, 20 July 2004, Pages 234-241, ISSN 09240136

[18] M. Kaladhar , K. Venkata Subbaiah & Ch. Srinivasa Rao, "Parametric optimization during machining of AISI 304 Austenitic Stainless Steel using CVD coated DURATOMICTM cutting insert", International Journal of Industrial Engineering Computations 3, pp. 577–586, 2012

[19] M. Kaladhar, K. V. Subbaiah, Ch. Srinivasa Rao & K. Narayana Rao, "Application of Taguchi approach and Utility Concept in solving the Multi-objective problem when turning AISI 202 Austenitic Stainless Steel", Journal of Engineering and Technology Review (4), pp. 55-61, 2011

[20] M. Kaladhar, K. Venkata Subbaiah & Ch. Shrinivasa Rao, "Determination of Optimum Process Parameter during turning of AISI 304 Austenitic Stainless Steels using Taguchi method and ANOVA", International Journal of Lean Thinking, Volume 3,Issue 1, 2012

[21] M. Kaladhar, K. Venkata Subbaiah, Ch. Srinivasa Rao and K. Narayana Rao, "Optimization of Process Parameters in Turning of AISI202 Austenitic Stainless Steel", ARPN Journal of Engineering and Applied Sciences, VOL. 5, NO. 9, pp. 79-87, 2010

[22] M. Nalbant, H. Gokkaya & G. Sur, "Application of Taguchi method in the optimization of cutting parameters for surface roughness in turning", Elsevier Journal, Materials and Design 28, pp. 1379–1385, 2007

[23] M. V. R. D. Prasad, Yelamanchili Sravya, and Karri Sai Tejasw," Study of the Influence of Process Parameters on Surface Roughness When Inconel 718 Is Dry Turned Using CBN Cutting Tool by Artificial Neural Network Approach", International Journal of Materials, Mechanics and Manufacturing, Vol. 2, No. 4, November 2014

[24] N. E. Edwin Paul, P. Marimuthu & R. Venkatesh Babu, "Machining Parameter Setting For Facing EN8 Steel with TNMG Insert" American International Journal of Research in Science, Technology, Engineering & Mathematics, 3(1), pp. 87-92, 2013

[25] N. Satheesh Kumar, Ajay Shetty, Ashay Shetty, Ananth K, Harsha Shetty, Effect of Spindle Speed and Feed Rate on Surface Roughness of Carbon Steels in CNC Turning, Procedia Engineering, Volume 38, 2012, Pages 691-697, ISSN 1877-7058

[26] Özel T., Hsu T.K., & Zeren, E., "Effects of cutting edge geometry, workpiece hardness, feed rate and cutting speed on surface roughness and forces in finish turning of hardened AISI H13 steel", International Journal of Advanced Manufacturing Technology, 25(3-4), 262-269, 2005

[27] P. Jayaraman, L. Mahesh kumar, Multi-response Optimization of Machining Parameters of Turning AA6063 T6 Aluminium Alloy using Grey Relational Analysis in Taguchi Method, Procedia Engineering, Volume 97, 2014, Pages 197-204, ISSN 18777058

[28] Ranganath M S, Vipin, R S Mishra, "Optimization of Surface Roughness and Material Removal Rate on Conventional Dry Turning of Aluminium (6061)", International Journal of Advance Research and Innovation, Volume 1, pp 62-71, 2014

[29] Ranganath M S, Vipin, "Optimization of Process Parameters in Turning Operation Using Taguchi Method and Anova: A Review", International Journal of Advance Research and Innovation, Volume 1, pp 31-45, 2013

[30] Ranganath M S, Vipin, Nand Kumar, R Srivastava, "Surface Finish Monitoring in CNC Turning Using RSM and Taguchi Techniques", International Journal of Emerging Technology and Advanced Engineering, Volume 4, Issue 9, September 2014

[31] Ranganath M. S., Vipin, Nand Kumar and Rakesh Kumar, "Experimental Analysis of Surface Roughness in CNC Turning of Aluminium Using Response Surface Methodology", International Journal of Advance Research and Innovation, vol. 3, Issue 1, pp. 45-49, 2015

[32] Ranganath M. S, Vipin, "Experimental Investigation and Parametric Analysis of Surface Roughness in CNC Turning Using Design of Experiments", International Journal of Modern Engineering Research, Vol. 4, Issue 9, September 2014

[33] Ranganath. M. S, Vipin, "Effect of Rake Angle on Surface Roughness in CNC Turning", International Journal of Advance Research and Innovation, Volume 2, 2014

[34] Ranganath M S, Vipin, Harshit, Optimization of Process Parameters in Turning Operation Using RSM: A Review, International Journal of Emerging Technology and Advanced Engineering, (ISSN 2250-2459, ISO 9001:2008 Certified Journal, Volume 4, Issue 10, October 2014) 351-360.

[35] Ranganath M S, Vipin, Harshit, Surface roughness prediction model for CNC turning of EN-8 using Response Surface Methodology, International Journal of Emerging Technology and Advanced Engineering, (ISSN 2250-2459, ISO 9001:2008 Certified Journal, Volume 5, Issue 6, June 2015).

[36] Ranganath. M.S, Vipin, Prateek, Nikhil, Rahul, Nikhil Gaur, "Experimental Investigation and Parametric Studies of Surface Roughness Analysis in CNC Turning", International Journal of Modern Engineering Research, Vol. 4, Issue 10, october 2014

[37] Ravinder Kumar, Santram Chauhan, Study on surface roughness measurement for turning of Al 7075/10/SiCp and Al 7075 hybrid composites by using response surface methodology (RSM) and artificial neural networking (ANN), Measurement, Volume 65, April 2015, Pages 166-180, ISSN 0263-2241
[38] Richárd Horváth, Ágota Drégelyi-Kiss, Analysis of surface roughness of aluminum alloys fine turned: United phenomenological models and multi-performance optimization, Measurement, Volume 65, April 2015, Pages 181-192, ISSN 0263-2241
[39] Rony Mohan, Josephkunju Paul C, George Mathew," Optimization of Surface Roughness of Bearing Steel during CNC Hard Turning Process", International Journal of Engineering Trends and Technology (IJETT) – Volume 17 Number 4 – Nov 2014
[40] Sayak Mukherjee, Anurag Kamal, Kaushik Kumar, Optimization of Material Removal Rate During Turning of SAE 1020 Material in CNC Lathe using Taguchi Technique, Procedia Engineering, Volume 97, 2014, Pages 29-35, ISSN 1877-7058
[41] Shreemoy Kumar Nayak, Jatin Kumar Patro, Shailesh Dewangan, Soumya Gangopadhyay, Multi-objective Optimization of Machining Parameters During Dry Turning of AISI 304 Austenitic Stainless Steel Using Grey Relational Analysis, Procedia Materials Science, Volume 6, 2014, Pages 701-708, ISSN 2211-8128
[42] S. Sivasankaran, P.T. Harisagar, E. Saminathan, S. Siddharth, P. Sasikumar, Effect of Nose Radius and Graphite Addition on Turning of AA 7075-ZrB2 in-situ Composites, Procedia Engineering, Volume 97, 2014, Pages 582-589, ISSN 1877-7058
[43] S. S. Acharya, R. L. Karwande," Investigation and optimization of turning process parameter in wet andMQL system on EN 31", IJMET, Volume 5, Issue 7, July (2014), pp. 134-143
[44] Upinder Kumar Yadav, Deepak Narang & Pankaj Sharma Attri, "Experimental investigation and Optimization of machine parameters for surface roughness in CNC turning by Taguchi method", International Journal of Engineering Research and Application, vol. 2, Issue 4, pp 2060-2065, 2012
[45] V. Mugendiran, A. Gnanavelbabu, R. Ramadoss, Parameter Optimization for Surface Roughness and Wall Thickness on AA5052 Aluminium alloy by Incremental Forming using Response Surface Methodology, Procedia Engineering, Volume 97, 2014, Pages 1991-2000, ISSN 1877-7058
[46] Y.B. Kumbhar, C.A. Waghmare, "Tool life and surface roughness optimization of pvd tialn/tin multilayer coated carbide inserts in semi hard turning of hardened en31 alloy steel under dry cutting conditions", International Journal of Advanced Engineering Research and Studies E-ISSN2249–8974
[47] Y.Kevin Chou, Hui Song, Tool nose radius effects on finish hard turning, Journal of Materials Processing Technology, Volume 148, Issue 2, 15 May 2004, Pages 259-268, ISSN 0924-0136
[48] Zahari Taha, Hani-kurniati LELANA, Hideki AOYAMA,"Effect of insert geometry on surface roughness in the turning process of AISI D2 steel", 11th Asia pacific industrial engineering and management system, Melaka 7-10 december 2010.

AUTHORS

Devendra Singh received his M.Tech degree from Delhi Technological University, Delhi, in 2015.He is currently working as an Assistant Professor in Department of Mechanical Engineering in Sagar Institute of Technology and Management, Barabanki, Uttar Pradesh.



Vimanyu Chadha is currently pursuing (Third Year) his B.Tech degree from Delhi Technological University, Delhi.



Dr. Ranganath M Singari currently the Associate Professor, Department of Production & Industrial Engineering, Delhi Technological University. Dr. Ranganath M Singari Post Graduate and Doctorate from Delhi University.



Eliciting Information Requirements for DW systems

Deepika Prakash
Delhi Technological University, Delhi, India
dpka.prakash@gmail.com
Supervisor: Dr. Daya Gupta

Abstract: Data Warehouse technology addresses business process analysis. However, it ignores upstream decision-making like formulating policies and policy enforcement rules. We provide a requirements engineering approach for building an integrated data for all types of decisions in an organization. To do this, we develop a two level generic platform with the bottom level having generic models of decisions, information, and decision-information association as well as information elicitation techniques for eliciting information for decisions. The higher level is the source of decision for the lower layer and is exemplified by policy enforcement rule decisions as well as operational decisions for managing the business process. Each source produces its own data warehouse requirements specification and these are integrated together using our integration technique.

Keywords: Data Warehouse, Requirements Engineering, Early Information, Decision, Policy enforcement rule, Data Warehouse Integration

1 Introduction

Data Warehouse (DW) failure statistics highlight the crucial role of RE in mitigating system failure [1]. Hayen [2] refers to studies that indicate the typical cost of a DW project to be one million dollars in the very first year. However, one-half to two-third of these projects fail. One of the causes of this failure [1] is inadequate determination of the relationship of the DW with strategic business requirements. These statistics reinforce the need for RE for DW systems.

DWRE techniques identify DW structures like facts, dimensions and finally arrive at star schema. DW structures are identified from existing systems, information gathered from users' of the DW or a combination of the two. DWRE techniques are classified into three broad categories based on the nature and phases of the process. By nature they can be top-down, bottom-up or mixed and by phases they can have a single-derivation phase or multiple phases in which the process is performed.

A more detailed comparison of top-down, bottom-up and mixed approach is as follows:

I. **Bottom-Up or Supply driven approaches** assume that existing, already available, information, needs to only be converted into the multi-dimensional form. Thus, the starting point is existing data bases and data sources. Desired facts and dimensions are then imposed on these available sources. There are two basic approaches, (a) Database Driven approach that starts from existing databases [3], and (b) ER schema driven approach that starts from ER schema [4].

ER driven techniques have been criticised on several grounds. According to [5] "Entity relation models cannot be used for enterprise data warehouses". Information is limited to what has been captured by the ER diagram. These techniques do not give primary importance to the users' perspective [6].

II. **Top-Down or Demand driven approaches** determine information contents of a DW To-Be from scratch. These approaches directly adopted model driven techniques developed in software/information systems RE like goal-orientation and scenario-orientation. User driven and Goal driven approaches of DWRE belong to this category.

Some User driven approaches include techniques developed by [7, 8]. However, it has been observed that some users may not be able to describe their requirements [9]. Users do not see their organization from a "broad angle" and so the requirements are "narrow" [10].

Goal driven approaches [9], [13] suffer from the inherent limitation of goal orientation. Firstly, goals are fuzzy concepts. [11] points out that goal are "informal and incomplete" and "difficult to precisely define". GORE is subjective, dependent on the requirements engineer view of the real world from where goals are identified [12]. Further, the process of goal reduction is unguided.

III. **Mixed Driven Approaches** In purely demand driven techniques, the information needed for decision making may not necessarily be available in existing data sources, whereas in purely supply driven techniques decision making may require information outside of that available in existing data sources. This led to the development of **mixed driven techniques** where the needed information was identified and the available data was determined.

According to the approach of [6], there is a change of perspective required that views nodes of a goal hierarchy as goals in the first perspective and as decisional alternatives later. This treats all alternatives uniformly and deals with 'what is to be achieved'. In the approach of [14], there is little guidance on what questions to ask even though the metrics determined are critically dependent on these questions.

We notice the following drawbacks currently facing DWRE:

1. Lack of DW support for upstream decision-making in an organization:

   According to [15], the primary concern of data warehouse technology is to provide support to decision makers for managing business processes better. Thus, the focus is on "what to do next" type of decisions that are operational in nature. Information support for operational decision-making is provided to all levels in an organization.

   In [16], there is compartmentalization of operational, business analytics and content analytics in separate modules. The authors recognize multiple levels of

decision makers for long term goals. In terms of decision making, the nature continues to be operational.

OMG, in its Business Motivation Model [17] conceptualizes a business in terms of policies and directives that govern their enforcement. This suggests yet another classification of decisions that is based on the nature of the task to be carried out, namely, policy formulation, determination of policy enforcement rules, operational decisions. Notice that the first two of these are **upstream** to the third and not supported by DW technology. Thus, there is a need to develop specific techniques for these as well.

2. Limited understanding of the Decision-Information Link :

Decisional and Information perspectives have been introduced by [6] [14] respectively. However, we find that

(a) The relationship between the notions of decision and information is not fully explored. Thus, the decision-information association is left un-articulated and remains implicit. This inhibits a full investigation into what information is needed for which decision and vice-versa.

(b) DWRE does not take into account the structure of a decision and the semantic notions underlying decisions. The former means that it is not possible to adopt model driven requirements engineering leading to relatively poor guidance in the elicitation task. The latter implies that the conceptual basis for adopting the notion of a decision itself remains weak.

(c) Information models are assumed to be multi-dimensional in nature. This leads to an emphasis on determining facts and dimensions at the expense of determining information properties like required aggregations and historical information needs. As for decisions, this implies that only partial guidance can be provided in the information elicitation task.

There is a need to explicitly model the decision-information relationship and treat both decision and information as first class concepts of DWRE.

3. Limited techniques specific to Information Elicitation:

DWRE techniques are highly oriented towards arriving at information in the form of Facts, Dimensions and Measures. This is either done directly without analyzing information and or without sufficiently exploring information before structuring it. Techniques like [6] belong to the former class and techniques like [3], [13, 14], [18] to the latter. Even though some investigation of information was done with Information scenarios of [13] there is no guidance provided for developing these scenarios.

While arriving at MD structures is essential, it is equally important to elicit, examine and analyze information that is unstructured and also to elicit information in a guided manner.

To sum up, there is *need to treat decision and information as first class concepts of RE models, develop decision and information models for conceptual clarity and*

effective guidance, and to lay emphasis on eliciting early, unstructured information before arriving at multi-dimensional structures.

With three inter-related DW systems, policy formulation, policy enforcement, and operational, there may be common data across them. Therefore, need for integrating these arises. Existing approaches do star schema/data mart integration by identifying conformed dimensions. However, this implies long lead times due to first arriving at the star schemas and then integrating them. Requirements may change during this period and the integrated system may be out of step with desired one.

We can now define the following research questions:

1. What are the different kinds of decisions, the applications from which they originate and their inter-relationship?
2. Can we define information elicitation techniques that are neutral to the types of decisions?
3. Having determined information relevant to decisions of each application, do we keep separate Data Warehouses application-wise or do we maintain one integrated form?

2. Solution Approach

In order to answer the research questions, we propose a solution divided into the following steps:

2.1. Defining upstream and operational decisions and the decision continuum

We start by establishing the 'Decision Environment' and derive a typology of decisions. We define two broad categories of decisions: Imperative decisions and Managerial decisions. Managerial decision-making is upstream and is of two kinds. One kind of Managerial decisions' is those that deal with formulation of norms and standards that are to be followed in organizations. These decisions are Policy Decisions. The other kind are concerned with the enforcement of given policies. **The decision problem here is that of defining an appropriate set of rules that the organization will follow during its operations.** These decisions are Policy Enforcement Rule (PER) Decisions**.** Imperative decisions are derived from policy enforcement rules and consist of operational actions. **The imperative decision making problem is that of selecting the most appropriate action in a given situation such that it also does not violate policy enforcement rules.**

Imperative decisions can be taken once Policy enforcement rule decisions are taken. Policy enforcement rule decisions are taken once policy decisions have been taken. Thus, there is a continuum between policy, policy enforcement rule decisions and operational decisions.

Policy formulation is done in a number of contexts with varied stakeholders [19, 20], shows dependence on related policies [21] and consensus building [20]. Since policy formulation is a many-facetted and complex task, we have left it for a separate

investigation. Therefore, in this thesis, we assume a policy representation system and consider DWRE for PER decisions and operational decisions only.

2.2. Developing a Generic Platform

Our RE process is rooted in Decision Requirement which we model as a tuple <decision, information>. Decision Requirement implies that RE process has two steps, first to determine the choice set of decisions and then to elicit information to choose one from the choice set.

This and our treatment of decision and information as first class concepts leads us a two level generic platform. The bottom of Fig 1 shows the generic platform having generic models of Decision Requirement, decision and information. Information elicitation techniques for decisions are defined in this layer. The higher layer is the source of decisions for this lower layer. Decisions are obtained from PER formulation and operational decisions. This means that the lower layer is neutral to the source of decisions and can be used for any kind of decisions. It is generic.

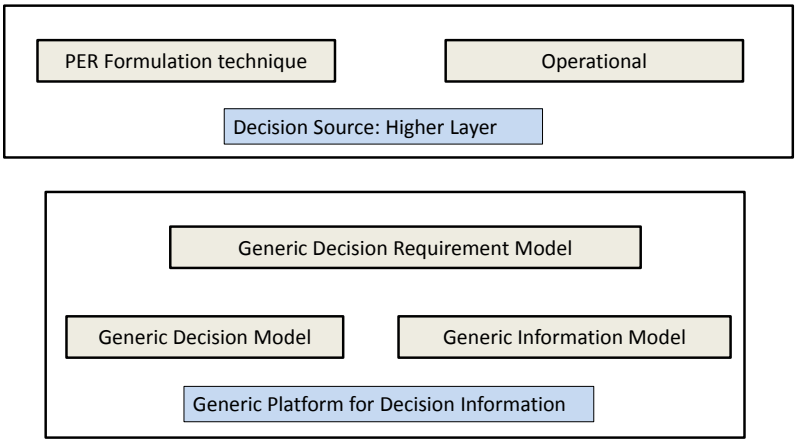


Fig 1: The Generic Platform

For the bottom layer, we propose three information elicitation techniques namely, CSFI, ENDSI and MEANSI as a set of generic techniques for eliciting information for the DW to-be. The elicited information has to be converted to multi-dimensional form and conforms to a *generic information model* developed in the Generic Platform.

For the higher layer, we propose to develop RE approaches for our two sources of decisions. Once this is done, an integration process has to be developed to arrive at the integrated DW.

2.3. Building an integrated DW

Our process begins with first developing Policy Enforcement Rule DW and operational DW. For the former, we propose a PER life cycle thus address the issue of providing support for strategic decision making. For the latter we propose the operational life cycle. Now the remaining question is to integrate the two DWs into one comprehensive DW for the entire organization. .This makes the integrated DW a single enterprise resource that supports ALL forms of decision making. The integration is done using our Vertical integration technique.

Let us consider the RE process in each individual life cycle.

PER Life Cycle

PER life cycle creates a DW for PER decision making, DWper, with a rule base and information in its own operational early information base. The input to the PER life cycle is operational policies. The PER life cycle has two parts; one is to formulate rules and the other to elicit relevant information. We assume that organizational policies are represented in our extended first order logic. Thereafter, we propose guidelines to arrive at PERs. PERs are of the form "WHEN triggering action IF condition THEN correcting action". In general there can be more than one correcting action for a given condition and the decision maker must formulate the appropriate set of correcting actions. In order words, the decision maker works with the choice set {select action, modify action, reject action}. Choosing one of these constitutes the decision problem.

We now need to elicit information that the decision maker will refer to in the decision making task of choosing the appropriate correcting action from the choice set. The generic early information elicitation approaches namely ENDSI, MEANSI and CSFI, defined in the platform of Fig 1 are used. This constitutes early information, $EI_{per,}$

EI_{per} can be:

1. a source of information for the vertical integration life cycle
2. converted to late, structured information

For the latter we have proposed guidelines to convert early information into ER diagram. Subsequently, ER can be converted to star schema by applying existing algorithms of [4]. DWper thus obtained can be used by PER level decision maker.

We applied our process to AYUSH policies consisting of 151 policies. The RE methodology was implemented in a tool called ELISPE and it was used to elicit the required information.

Operational Life Cycle

Operational life cycle creates a DW for operational decision making, DWop. Actions are first extracted from PERs and each action, a, of the PER layer is treated as a decision, d, to be taken at the operational level. This yields the initial set of decisions and is the input to the operational life cycle.

Applying the generic decision model mentioned in Fig 1, each decision is subjected to AND/OR decomposition and generalization-specialization process and leaf nodes are determined. The next task is to elicit information for every decision using CSFI, ENDSI, and MEANSI. The elicited information is $EI_{op.}$

Again, EI_{op}, can be either be converted to ER diagram, for which we propose guidelines, or can be used as a source of early information for vertical integration. In the case of the former, once the ER diagram is converted to star schema we obtain a stand-alone DWop.

Vertical Integration Life Cycle

We found that there are two problems with keeping separate Data Warehouses. These arise if there is common data in them.

- Difference in refresh cycles between DWper and DWop cause common data to have differen values in the two DWs. Thus, rule formulators and operational decision makers end up taking decisions on different data in this temporal window. The larger this window, the longer this inconsistency exists.
- Loss of business control occurs when data of an operational DW calls for decision makers of the policy enforcement DW to take decisions, but the decisions are not taken because daa in the latter do not suggest this need.

Thus, integration is required to maintain compatibility between PER and operational level.

We show that there are in fact two forms of integration that can exist, horizontal and vertical. While the former integrates data marts at the same level of decision-making, the latter integrates data marts across PER and operational levels. For vertically integrating DWper and DWop, we propose a 'build by integrating' approach that works pair-wise pair-wise. When a new data mart is to be built, its requirements specification is integrated with an existing one. The integrated requirements specification then goes through the development cycle. Thus, the point of integration is moved upstream into the requirements stage. In other words, early information is integrated. The advantages of integrating upstream and in a pair-wise fashion are:

- downstream development effort is minimized.
- it never allows un-integrated data marts to be built. Thus, pre-empting our two problems.
- A complete logical DW is available for decision making.

Integration is done as a four-step process, Metadata reading, Correspondence Drafting, Information Mapping and Conflict Resolving. The integrated early information obtained is then converted into ER schema and finally into star schema.

Through vertical integration, an integrated DW is obtained that can be used for both forms of decision making.

3 Contribution of research work

A summary of the contributions made is as follows:

1. Addressing full decisional making continuum: DW support has been extended from providing just operational support to providing policy enforcement and operational support.

2. Elicited Information can be traced back to members of the choice set thereby facilitating decision making. In the case of PERs the choice set is {select A, modify A, delete A} where A is an action and {select A1, select A2, select A3} for operationa decisions. For each alternative, information is elicited, thus relating information to a particular member of the choice set.

3. Discovery of early information: Information is obtained in a two-step process, early information elicitation step, using ENDSI, MEANSI and CSFI and late information elicitation step where early information is converted into ER diagram which is subsequently converted to a star schema.

4. Development of a requirements integration approach that pre-empts the problems of inconsistency in decision-making and loss of business control.

4 Conclusion and future work

This work addresses the issue of providing support to different kinds of decisional needs in a unified, enterprise wide DW system. A two level generic platform is proposed with generic models at the bottom level and decision sources at the higher level.

We develop RE process to arrive at separate DWs for the PER and operational decisions respectively. The two DWs are integrated upstream in the requirements engineering phase. The integrated requirements specification is then converted into multi-dimensional form.

Future work includes developing a policy life cycle for eliciting information for policy decisions and integrating it with 'lower' levels of the decision continuum.

5 References

1. Alshboul, R. (2012). Data Warehouse Explorative Study. *Applied Mathematical Sciences*, *6*(61), 3015-3024
2. Hayen R., Rutashobya C., Vetter D., (2007), An Investigation Of The Factors Affecting Data Warehousing Success, Issues In Information Systems, Volume VIII, No. 2, 547-553, 2007
3. Golfarelli M., Maio D., Rizzi S. (1998, January). Conceptual Design of Data Warehouses from E/R schemes. In System Sciences, 1998., Proceedings of the Thirty-First Hawaii International Conference on (Vol. 7, pp. 334-343). IEEE.

4. Moody L.D., and Kortink M.A.R. (2000), From Enterprise Models to Dimensional Models: A Methodology for Data Warehouses and Data Mart Design, Proc. of the Intl Workshop on Design and Management of Data Warehouses, Stockholm, Sweden, (pp. 5.1-5.12)
5. Kimball, R. (1996): The Data Warehouse Toolkit, New York: J. Wiley & Sons.
6. Giorgini, P., Rizzi, S., Garzetti, M. (2005). Goal-oriented requirement analysis for data warehouse design. In Proceedings of the 8th ACM international workshop on Data warehousing and OLAP (pp. 47-56). ACM.
7. Winter, R., and Strauch, B. (2003, January). A method for demand-driven information requirements analysis in data warehousing projects. In *System Sciences, 2003. Proceedings of the 36th Annual Hawaii International Conference on* (pp. 9-pp). IEEE.
8. Bruckner, R., List, B., &Scheifer, J. (2001). Developing requirements for data warehouse systems with use cases. *AMCIS 2001 Proceedings*, 66.
9. Boehnlein, M., and Ulbrich vom Ende, A. (2000). Business Process Oriented Development of Data Warehouse Structures. In Proceedings of Data Warehousing 2000 (pp. 3- 21). PhysicaVerlag HD
10. List, B., Bruckner, R. M., Machaczek, K., & Schiefer, J. (2002, January). A comparison of data warehouse development methodologies case study of the process warehouse. In *Database and Expert Systems Applications* (pp. 203-215). Springer Berlin Heidelberg.
11. Horkoff, J., and Yu, E. (2010). Interactive analysis of agent-goal models in enterprise modeling. *International Journal of Information System Modeling and Design (IJISMD)*, *1*(4), 1-23.
12. Haumer, P., Pohl, K., and Weidenhaupt, K. (1998). Requirements elicitation and validation with real world scenes. *Software Engineering, IEEE Transactions on*,*24*(12), 1036-1054.
13. Prakash N., and Gosain A. (2008). An Approach to Engineering the Requirements of Data Warehouses. Requirements Engineering Journal, Springer, 13 (1), 49-72
14. Bonifati A.. Cattaneo F., CeriS., A. Fuggetta, and S. Paraboschi (2001). Designing Data Marts for Data Warehouses. ACM Trans. Software. Eng. Methodology, 10(4). (pp. 452–483).
15. Adamson (2010) The complete reference: Star Schema. Tata McGraw-Hill
16. Imhoff, C., & White, C. (2008). Full Circle: Decision Intelligence (DSS 2.0). *B-Eye-Network, Published: August*, *27*.
17. BRG, 2010 BRG, Business Rules Group (2010), The Business Motivation Model: Business governance in a volatile world, Release 1.4, July 2010
18. Prakash, N., and Bhardwaj, H. (2014). Functionality for Business Indicators in Data Warehouse Requirements Engineering. In *Advances in Conceptual Modeling* (pp. 39-48). Springer International Publishing.
19. Lindbloom C.E. (1993), Woodhouse E.J., 3rd edition, Prentice Hall, 1993
20. Ritchie J.R.B. (1988), Consensus policy formulation in tourism: Measuring resident views via survey research, Tourism Management, 9,3, 199-212, 1988
21. Park Y. T. (2000), National systems of Advanced Manufacturing Technology (AMT): hierarchical classification scheme and policy formulation process, Technovation, 20,3, 151-159, 2000

Eur. Phys. J. B (2016) 89: 137
DOI: 10.1140/epjb/e2016-60624-7

THE EUROPEAN PHYSICAL JOURNAL B

Regular Article

Excellent electromagnetic interference shielding effectiveness of chemically reduced graphitic oxide paper at 101 GHz*

Parveen Saini[1,a], Sachin Kaushik[1], Rahul Sharma[1,2], Disha Chakravarty[1], Rishi Raj[3], and Jyotirmay Sharma[4]

[1] Conjugated Polymers and Graphene Technology Lab., Polymeric and Soft Materials Section, CSIR-National Physical Laboratory, 110012 New Delhi, India
[2] Academy of Scientific & Innovative Research (AcSIR), 110012 New Delhi, India
[3] Delhi Technological university (DTU), Bawana Road, 110042 New Delhi, India
[4] Maharaja Surajmal Institute of Technology, Janakpuri, 110058 New Delhi, India

Received 1 August 2015 / Received in final form 2 March 2016
Published online 1 June 2016 – © EDP Sciences, Società Italiana di Fisica, Springer-Verlag 2016

Abstract. Graphitic oxide (GO) was synthesized by oxidation of graphite powder using Hummer's method and the formed GO is solution processed into paper-like macroscopic form. Subsequently, chemically reduced graphitic oxide paper (CRGOP) is prepared by hydrazine vapours induced reduction of formed GO precursor based paper. The formation of GO and its successful reduction to RGO phase is confirmed by FTIR, Raman Spectroscopy and X-ray diffraction. It has been observed that due to high electrical conductivity ∼200 micron thick CRGOP display excellent EMI shielding performance at very high frequency of 101 GHz frequency with total shielding effectiveness (SE) value of −35.49 dB (i.e. >99.97% blocking of incident EM radiation) which is much higher compared to pristine GO paper (−1.55 dB) or comparable to expanded graphite (EG) sheet (−35.61 dB). Due to their lightweight nature, these freestanding CRGOPs display average specific SE value of −221.8 dB cm^3/g. Besides, their excellent flexibility and makes them potential candidate for lightweight EMI gasketing material compared to other forms of flexible carbons like EG.

1 Introduction

With the rapid growth of science and technology, the usage of electronic equipments and power sources are in vogue. However, electromagnetic (EM) interference (EMI) effects due to EM radiation emitted or received by these devices, can be dangerous, as the susceptible electronic components are backbone of many critical applications like aircraft, nuclear reactors, transformers, control and communication channels, healthcare systems, etc. [1–3]. Therefore, EMI shielding is highly desirable for protecting electronic devices from malfunctioning and avoiding harmful health effects on human beings [4,5]. The conventional metal based shielding materials are bulky, costly, corrosion prone and highly reflective. Some promise has also been shown by magnetic or dielectric particulate based compositions and conducting polymer based blends, copolymers or micro- or nano-composites [6–26]. However, their processing, stability and commercial viability issues remained an open challenge [1,3]. In this context, carbon based materials have shown definite promise and considered as excellent choice for EMI shielding, due to their light weight, metallic electrical conductivity, good mechanical properties, corrosion resistance, ease of synthesis and good processability [4,6,9,14,27–33]. In particular, carbonaceous nanomaterials, including carbon nanofibers, carbon nanotubes (CNTs) and graphene have received extreme attention for EMI related applications due to excellent electrical, mechanical and thermal properties, facile processing via chemical route, high surface-to-volume ratio and very low percolation threshold in filled nanocomposites [4,9,26,34–42]. Among them graphene is considered as most promising EMI shielding material candidate due ultra-high mechanical strength (Young's modulus ∼1.0 TPa), and tensile strength ∼130 GPa outstanding electrical conductivity (∼10^6 S/m) and excellent thermal stability/conductivity [1,14,32,35,38,41,43]. Further, ability to be chemically and morphologically manipulated provides means to regulate its shielding efficiency as well as underlying shielding mechanism. Consequently, various graphene analogues including bulk or foamed nanocomposites, graphene foams, paper-like materials, laminates, etc. [14,32,38,41,44–46] have been extensively studied for EMI shielding applications. Among them, graphene paper is considered as important EMI shielding material due to combination of good electrical properties, lightweight and flexibility. However, only few

* Contribution to the Topical Issue "Materials for Dielectric Applications", edited by Maciej Jaroszewski and Sabu Thomas.

[a] e-mail: pksaini@nplindia.org

brief reports are available [45,46] on the same and none of them explored the very high frequency shielding performance especially in the W band range (75−110 GHz) which is used for defence satellite communication, remote sensing or radar navigation.

In this work, we report synthesis and high frequency EMI shielding measurements of graphene like paper. The graphitic oxide paper (GOP) is synthesized by chemical oxidation of graphite followed by solution casting route. Subsequently, the formed GOP is chemically converted into reduced GO paper (CRGOP) by exposure to hydrazine vapors. The formation of GO and its successful reduction to RGO phases is confirmed by optical images, FTIR and Raman Spectroscopy and XRD patterns. The EMI shielding performance of GOP and CRGOP is measured at 101 GHz frequency by free space technique and compared with attenuation of other flexible form of carbon i.e. expanded graphite (EG) sheet (EGS). We would like to emphasize that Shielding effectiveness studies of graphene analogues at such a higher frequency have not been reported till date. The excellent shielding performance of CRGOP with total shielding effectiveness (SE) value of −35.49 dB (i.e. >99.97% blocking of incident EM radiation) and specific SE value of −221.8 dB $cm^3\,g^{-1}$ alongwith good flexibility, makes them potential candidate for lightweight EMI gasketing material.

2 Experimental section

2.1 Materials

Graphite powder (CDH, India), sulfuric acid 98% (Merck), sodium nitrate (Fischer scientific), potassium permanganate (Fischer scientific), hydrogen peroxide 30% solution (Specpure, India), hydrazine hydrate (Sigma Aldrich) were used as received. Double distilled water (resistivity $>10^6$ Ω cm) was used for synthesis and washing.

2.2 Synthesis of graphitic oxide (GO)

Natural graphite powder was oxidized to GO using modified Hummers' method [43,47]. In a typical synthesis, 150 mL of sulphuric acid was taken in glass beaker and magnetically stirred. In next step, 3 g of graphite powder and 3 g of sodium nitrate were added successively to the acid and the contents were stirred further for 30 min to form a homogeneous mixture. The system was placed in an ice bath while maintaining the magnetic stirring. Subsequently, 9 g of $KMnO_4$ flakes were added gradually to above mixture continuous stirring and keeping temperature below 25 °C. After 18 h stirring at room temperature, a thick purple color paste was formed that was gradually added to 400 mL distilled water. After stirring the brown solution for 30 min, 30% hydrogen peroxide solution was added in small increments untill solution is turned into bright yellow color suspension. The suspension was centrifuged and washed several times with HCl and distilled water to get a neutral pulp of GO. The GO flakes were obtained by vacuum drying of the brown pulp at 60 °C.

2.3 Fabrication of graphitic oxide paper (GOP)

The GO powder was dispersed in distilled water by ultrasonication process followed by solvent casting over pertidish. The water was removed by evaporation at 35 °C for 24 h resulting in free standing GO paper of ∼150 micron thickness and resistivity $\sim 10^6$ Ω/square.

2.4 Fabrication of chemically reduced graphitic oxide paper (CRGOP)

The GO paper was exposed to hydrazine vapors for 12 h in a closed chamber containing a solution of hydrazine. The color of GO paper turned from brownish to black, which was an indication of chemical reduction of GO paper. The resulted CRGOP had a thickness of 200 micron due to slight expansion of constituent graphitic stacks.

2.5 Characterization and measurements

The XRD patterns were recorded using Bruker D8 Advance X-ray diffractometer in the diffraction (2θ) range of 10−80°, at a scan rate of 0.02°/s, slit width of 0.1 mm using CuKα line (λ = 1.540598 Å) as radiation source. The Fourier transform infrared (FTIR) spectra of GO and RGO papers was recorded in the wave number range 400−4000 cm^{-1} (at a resolution of 4 cm^{-1} and averaged over 32 scans) using diamond attenuated total reflectance (ATR) assembly attached to FTIR spectrometer (Agilent Technologies, Carry 630). Raman microscope (Renishaw In Via) was used for recording Raman spectrum of samples in 1000 cm^{-1}−3000 cm^{-1} wavenumber range with 514.5 nm laser as excitation source. Shielding effectiveness (SE) was measured using a homemade free space measurement system containing a DC source powered 101 GHz microwave source-antenna couple and a horn-powermeter assembly based detector. Density is calculated from the weight of the rectangular samples (20 mm × 10 mm) and their thickness.

3 Results and discussion

Figure 1a shows the optical image of freshly prepared GO pulp which display characteristic brownish color of oxidized grapitic phase, that reflects the successful oxidation of graphite powder precursor and presence of oxygen functionalities. The ability of GO phase to be processed via aqueous dispersion and vacuum drying route, into a flexible paper like material having brownish hue, is depicted in Figure 1b.

The successful oxidation of the graphite into GO and presence of different oxygen functionalities is also confirmed by FTIR and XRD measurements. It has been observed that the FTIR spectra of GO film (Fig. 1c) shows a broad peak at 3396 cm^{-1} corresponding to O-H stretching vibrations of the C-OH groups and water. Further, narrow peaks at 1708 cm^{-1} and 1225 cm^{-1} can be

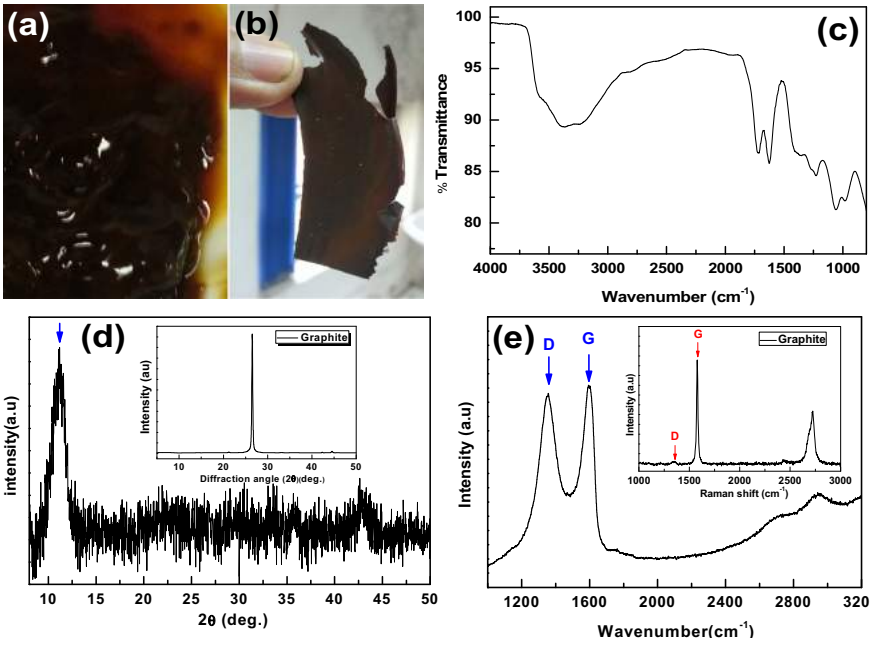


Fig. 1. Optical image of (a) GO pulp and (b) GO paper (GOP) depicting characteristic brown color. (c) FTIR spactra, (d) XRD pattern and (e) Raman specta of GOP. Inset of (d) and (e) shows the XRD and Raman details of graphite powder, respectively.

attributed to the characteristic stretching vibrations of carbonyl (-C=O) and expoxide (C-O-C) groups respectively. Besides, the absorption band at 1620 cm^{-1} can be ascribed to the C=C stretch of the unoxidised sp^2 carbon domains. The coexistence of functional features of various oxygen functionalities and graphitic phase confirmed the formation of GO phase. The formation of GO is also confirmed from increased XRD interlayer spacing (d-value) of GO ($d \sim 7.97$ Å, Fig. 1d) compared to pristine graphite ($d \sim 3.34$ Å, inset Fig. 1d), which is caused by the expansion of graphitic stack due to introduction of oxygen functionalities over constituent graphitic layers. The Raman spectra of GO (Fig. 1e) gives two prominent features at ∼1359 cm^{-1} and ∼1599 cm^{-1} corresponding to D- and G-bands, respectively [43,48,49]. The G-peak corresponds to the first order scattering of the E_{2g} optical mode of sp^2 domains whereas the D-peak is contributed by the disordered regions containing oxidation introdced sp^3 carbons. In contrast, the Raman spectra of graphite (inset Fig. 1e) display prominent G-band with negligible D-band signal, that confirms the very small ratio of I_D/I_G and ordered structure of graphite in terms of defects, ripples and edges.

Figure 2a shows the actual picture of chemically reduced GO paper (CRGOP) which display blackish appearance characteristic of graphitic materials, thereby reflecting successful reduction of GO. The reduction and consequent removal of oxygen functionalities is also confirmed by XRD pattern (Fig. 2d) and Raman spectra (Fig. 2e) of CRGOP which display shifting of its 2θ diffraction peak to higher angle (∼24.9°; $d \sim 3.57$) and systematic variation of intensity of D- and G-bands, respectively. Further, reduction also leads to restoration of conjugation that was supported by very low resistance value of CRGOP (∼264 Ω, Fig. 2c, conductivity of 15 S/cm compared to 6.7×10^{-5} S/cm for GOP). The low resistance reflects high electrical conductivity which is most important criteria for achieving good attenuation levels. Therefore, good EM radiation blocking performance is expected. The removal of oxygen functionalities lead to reduction in density (from ∼0.96 g/cm^3 for GOP to ∼0.16 g/cm^3 for CRGOP) as confirmed by flotation of piece of CRGOP over water's surface (Fig. 2b). Further, the CRGOP also display good bending ability and can easily tolerate repeated bending load (Fig. 2c). These are considered additional advantages from the viewpoint of designing of lightweight and flexible EMI shields.

The radiation blocking efficiency of a shielding material is expressed in terms of quantity called shielding effectiveness (SE) that can be mathematically expressed by logarithmic ratio of strength of incident and transmitted power (electric or magnetic field) as [1,15,50]:

$$SE(\text{dB}) = 10\ \log_{10}\left(\frac{P_T}{P_I}\right) = 20\ \log_{10}\left(\frac{E_T}{E_I}\right) = 20\ \log_{10}\left(\frac{H_T}{H_I}\right) \quad (1)$$

where P_I (E_I or H_I) and P_T (E_T or H_T) are the power (electric or magnetic field intensity) of incident and transmitted EM waves, respectively. As the ratio P_T/P_I (E_T/E_I or H_T/H_I) is always less than unity therefore, SE_T (total shielding effectiveness) is a negative quantity such that a shift towards more negative value means increase in magnitude of SE_T [3,12].

Figure 3 shows the schematic of the EMI shielding measurement setup which consists of a regulated DC power supply to give input to a 101 GHz frequency microwave source coupled to a circular horn type antenna.

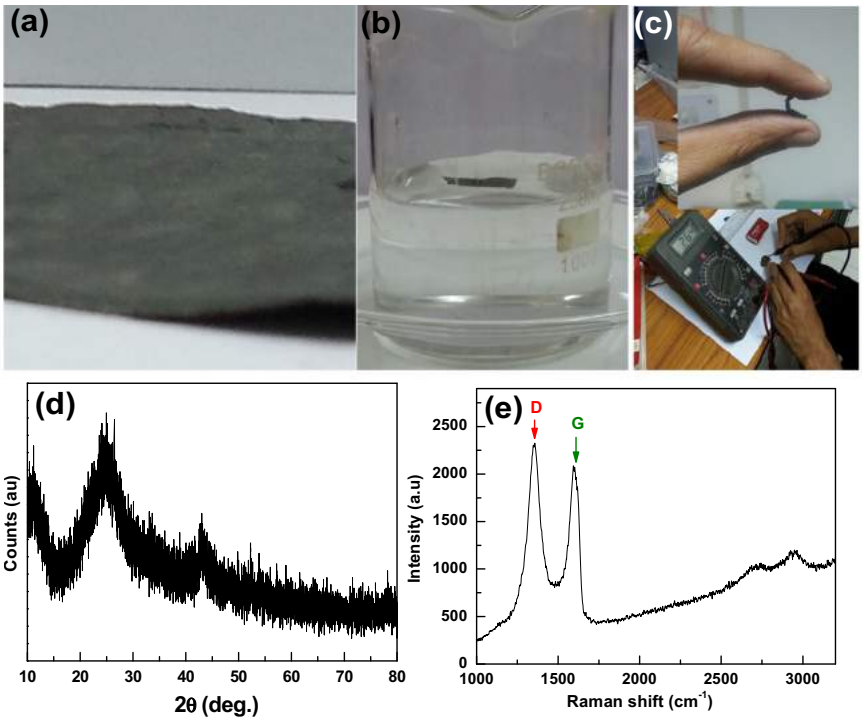


Fig. 2. Optical image of (a) chemically reduced GO paper (CRGOP), (b) piece of CRGOP floating over water and (c) electrical resistance of measurement of sample via multimeter. Inset shows flexibility/bendability of paper. The XRD pattern (d) and Raman spectra (e) confirm the successful reduction of GO phase and restoration of conjugation.

Table 1. EMI shielding effectiveness (SE) and specific SE values for samples.

Material	Input power (mW)	Transmitted power (nW)	Shielding effectiveness (SE) (dB)	Specific SE (SSE) (dB $cm^3\,g^{-1}$)
GOP	0.296	2.07×10^5	−1.55	−1.61
CRGOP	0.298	84.2	−35.49	−221.8
EGS	0.296	81.3	−35.61	−34.57

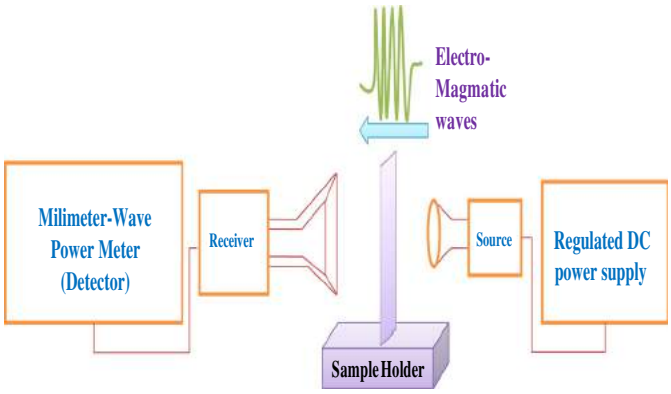


Fig. 3. Schematic of EMI shielding measurement setup.

The antenna generates a beam of microwave energy which is propelled through free space to reach a rectangular type antenna connected to a detector (i.e. millimetre wave power meter). The measurements are completed by alternatively measuring the power reaching the detector in the absence and presence of the sample to assess corresponding incident power (P_I) and transmitted power (P_T), respectively. The calculated SE value for GOP, CRGOP and EGS samples is reported in Table 1.

It can be seen that the GO paper gives negligible attenuation (only 30% radiation blocking) with SE_T value of only −1.55 dB (Fig. 3a). The low SE value of GOP may be linked to the poor conductivity and related conduction loses, due to loss of conjugation via oxidation induced sp^3 defects (oxygen functionalities). In contrast, the CRGOP shows very high attenuation with SE_T value of −35.49 dB, which represent its capability of blocking more than 99.97% of the incident EM energy. Such high SE of can be ascribed to the high electrical conductivity owing to restoration of conjugation upon reduction process. In order to compare the attenuation characteristics of CRGOP with other carbon analogues, SE of expanded graphite sheet (EGS) is also measured and reported in Table 1. Interestingly, it is observed that despite its very high conductivity (120 S/cm); EGS display similar attenuation levels as CRGOP. This suggests that EMI shielding mechanisms of EGS and CRGOP are different and further studies in the direction are necessary to unveil the same. Nevertheless, in order to demonstrate

the superiority of CRGOP, SSE values (SE per unit density [1,18]) were calculated and it was observed that SSE value of CRGOP (~ -221.8 dB cm^3 g^{-1}) is much higher compared to EGS (~ -34.57 dB cm^3 g^{-1}). Indeed, this value is significantly higher than low SSE value of copper sheet ~ -10 dB cm^3 g^{-1} [18,31], carbon foams, conducting polymers or filled nanocomposites. Additionally, their excellent flexibility and ability to be formed into any shape makes them potential candidate for lightweight EMI gasketing material compared to other forms of flexible carbons like EG.

4 Conclusion

The chemically reduced GO paper is successfully synthesised by chemical reduction of solution casted GO paper. The formed paper found to display good electrical conductivity and, light weight nature leading to excellent SE performance with a very high value of -221.8 dB cm^3 g^{-1}. In addition, their good flexibility and ease of fabrication makes them potential candidate for EMI gasketing materials.

Authors are thankful to Director NPL for necessary facilities. DST is acknowledged for providing financial assistance via Fast Track Young Scientist Proposal. Rahul Sharam is thankful to UGC for award of junior research fellowship. Disha and Jyotirmay are thankful to Dr. Biradr to accord permission to work on this project. Sachin and Rishi are thankful to HRD, NPL for allowing to do M. Tech Project work at NPL.

References

1. P. Saini, in *Fundamentals of Conjugated Polymer Blends, Copolymers and Composites*, edited by P. Saini (John Wiley & Sons, Inc., 2015), pp. 449−518
2. H.W. Ott, *Electromagnetic Compatibility Engineering* (John Wiley & Sons, Inc., 2009)
3. P. Saini, M. Arora, in *New Polymers for Special Applications*, edited by A. De Souza Gomes, (InTech, 2012), pp. 71−112
4. N. Li et al., Nano Lett. **6**, 1141 (2006)
5. P. Saini et al., Nanoscale **5**, 4330 (2013)
6. C.-Y. Huang, C.-C. Wu, Eur. Polym. J. **36**, 2729 (2000)
7. T. Taka, Synth. Met. **41**, 1177 (1991)
8. J. Joo, A.J. Epstein, Appl. Phys. Lett. **65**, 2278 (1994)
9. P. Saini, in *Thermoset Nanocomposites*, edited by V. Mittal (Wiley-VCH Verlag GmbH & Co. KGaA, 2013), pp. 211−237
10. *Fundamentals of Conjugated Polymer Blends, Copolymers and Composites: Synthesis, Properties and Applications*, edited by P. Saini (John Wiley & Sons, Inc., 2015)
11. P. Xu et al., J. Phys. Chem. B **112**, 10443 (2008)
12. P. Saini, M. Arora, J. Mater. Chem. A **1**, 8926 (2013)
13. X.L. Dong, X.F. Zhang, H. Huang, F. Zuo, Appl. Phys. Lett. **92**, 013127 (2008)
14. H. Yu et al., J. Mater. Chem. **22**, 21679 (2012)
15. N.F. Colaneri, L.W. Schacklette, IEEE Trans. Instrum. Meas. **41**, 291 (1992)
16. P. Saini, V. Choudhary, B.P. Singh, R.B. Mathur, S.K. Dhawan, Mater. Chem. Phys. **113**, 919 (2009)
17. S.M. Abbas, M. Chandra, A. Verma, R. Chatterjee, T.C. Goel, Composites Part A **37**, 2148 (2006)
18. P. Saini, V. Choudhary, N. Vijayan, R.K. Kotnala, J. Phys. Chem. C **116**, 13403 (2012)
19. W. Li et al., ACS Appl. Mater. Interfaces **5**, 883 (2013)
20. T.-H. Ting, K.-H. Wu, J. Polym. Res. **20**, 127 (2013)
21. C.C. Yang, Y.J. Gung, W.C. Hung, T.H. Ting, K.H. Wu, Compos. Sci. Technol. **70**, 466 (2010)
22. C.C. Yang, Y.J. Gung, C.C. Shih, W.C. Hung, K.H. Wu, J. Magn. Magn. Mater. **323**, 933 (2011)
23. P. Saini, V. Choudhary, B.P. Singh, R.B. Mathur, S.K. Dhawan, Synth. Met. **161**, 1522 (2011)
24. S.W. Phang, M. Tadokoro, J. Watanabe, N. Kuramoto, Synth. Met. **158**, 251 (2008)
25. S.W. Phang, N. Kuramoto, Polymer Compos. **31**, 1548 (2010)
26. P. Saini, V. Choudhary, J. Mater. Sci. **48**, 797 (2013)
27. D.D.L. Chung, J. Mater. Eng. Perform. **9**, 350 (2000)
28. J. Wu, D.D. Chung, Carbon **40**, 445 (2002)
29. P. Saini, V. Choudhary, K.N. Sood, S.K. Dhawan, J. Appl. Polym. Sci. **113**, 3146 (2009)
30. P. Saini, V. Choudhary, S.K. Dhawan, Polym. Adv. Technol. **20**, 355 (2009)
31. Y. Yang, M.C. Gupta, K.L. Dudley, R.W. Lawrence, Nano Lett. **5**, 2131 (2005)
32. Z. Chen, C. Xu, C. Ma, W. Ren, H.-M. Cheng, Adv. Mater. **25**, 1296 (2013)
33. S.D. Khan, M. Arora, M.A. Wahab, P. Saini, J. Polym. **2014**, 193058 (2014)
34. R.H. Baughman, Science **297**, 787 (2002)
35. A.K. Geim, Science **324**, 1530 (2009)
36. J.C. Meyer et al., Nature **446**, 60 (2007)
37. Y. Yang, M.C. Gupta, K.L. Dudley, R.W.A. Lawrence, J. Nanosci. Nanotechnol. **5**, 927 (2005)
38. V. Eswaraiah, V. Sankaranarayanan, S. Ramaprabhu, Macromol. Mater. Eng. **296**, 894 (2011)
39. M.M. Bernal et al., RSC Advances **4**, 7911 (2014)
40. R. Kumar, S.R. Dhakate, P. Saini, R.B. Mathur, RSC Advances **3**, 4145 (2013)
41. J. Liang et al., Carbon **47**, 922 (2009)
42. P. Verma, P. Saini, R.S. Malik, V. Choudhary, Carbon **89**, 308 (2015)
43. S.N. Tripathi, P. Saini, D. Gupta, V. Choudhary, J. Mater. Sci. **48**, 6223 (2013)
44. H.-B. Zhang, Q. Yan, W.-G. Zheng, Z. He, Z.-Z. Yu, ACS Appl. Mater. Interfaces **3**, 918 (2011)
45. W.-L. Song et al., J. Mater. Chem. C **2**, 5057 (2014)
46. L. Zhang et al., Carbon **82**, 353 (2015)
47. W.S. Hummers, R.E. Offeman, J. Am. Chem. Soc. **80**, 1339 (1958)
48. I.K. Moon, J. Lee, R.S. Ruoff, H. Lee, Nat. Commun. **1**, 1 (2010)
49. S. Stankovich et al., Nature **442**, 282 (2006)
50. R.B. Schulz, V.C. Plantz, D.R. Brush, IEEE Trans. Electromag. Compatibility **30**, 187 (1988)

Available online at www.sciencedirect.com

ScienceDirect

Materials Today: Proceedings 3 (2016) 2241–2246

materialstoday: PROCEEDINGS

www.materialstoday.com/proceedings

Recent Advances In Nano Science And Technology 2015 (RAINSAT2015)

First principles study of Li terminated armchair graphene nanoribbons

Neha Tyagi*[a], Neeraj K. Jaiswal[b], Pankaj Srivastava[c]

[a]*Department of Applied Physics, Delhi Technological University, New Delhi, India*
[b]*Discipline of Physics, PDPM-Indian Institute of Information Technology, Design & Manufacturing, Jabalpur, India*
[c]*Nanomaterials Research Group,ABV-Indian Institute of Information Technology & Management, Gwalior, India*

Abstract

We have investigated the consequences of Li termination on the electronic and structural properties of armchair graphene nanoribbons (AGNR) by employing first-principles calculations. We considered the effect of Li termination on one edge as well as on both the edges of ribbons and revealed their potential applications. It is observed that Li termination has a profound effect on the electronic structure of AGNR. The analysis of binding energy suggests that all the structures are energetically feasible to obtain. Further, AGNR with larger widths are comparatively more stable than the narrow width nanoribbons. A semiconducting to metallic transition can be observed depending upon the ribbon width. Our results indicate that Li termination could be a potential way to tailor the electronic and transport properties of AGNR.

© 2015Elsevier Ltd.All rights reserved.
Selection and Peer-review under responsibility of [Conference Committee Members of Recent Advances In Nano Science and Technology 2015.].

Keywords: Graphene; nanoribbon; electronic structure; binding energy; Fermi level

1. Introduction

Graphene, the first atomically thick material observed by the scientific community, has proven its potential for variety of applications [1-5]. Patterned strips of graphene, formally known as graphene nanoribbons (GNR) can be

* Corresponding author.
E-mail address: nehatyagi.phy@gmail.com

2214-7853© 2015 Elsevier Ltd.All rights reserved.
Selection and Peer-review under responsibility of [Conference Committee Members of Recent Advances In Nano Science and Technology 2015.].

used for H-storage, chemical and bio-sensors, electronic/spintronic devices and even in Li-ion batteries [6-12]. What makes these GNR really special is the presence of their edges which also govern the electronic behavior of GNR [13, 14]. The band gap of armchair graphene nanoribbons (AGNR) oscillates as a function of their width whereas zigzag graphene nanoribbons (ZGNR) exhibit a band gap that continuously decreases with increasing the width [13-16]. Owing to the crucial role of edge geometry, researchers have investigated various potential applications of GNR with different functionalization or passivating elements [17-20]. It is reported that substitutional doping or adsorption of different guest atoms can be used to tune the electronic and magnetic properties of graphene and GNR [21-23]. Plenty of literature is available investigating the interaction of B/N doping in graphene and graphene GNR [20, 24]. Li et al., revealed that edge magnetism of zigzag ribbons can be preserved by ethylene termination [25]. Moreover, it is reported that presence of metallic impurity can induce magnetism as well as metallicity in AGNR which are otherwise nonmagnetic semiconductors [1, 13]. As far as metallic impurities are concerned, most of the researchers have concentrated only on Transition metals (TM) impurities [15, 18, 25, 26]. On the other hand, rests of other metallic impurities are almost neglected which can also reveal remarkable physical properties. Uthaisar et al., [27] reported strong interaction between Li adatoms and GNR which depends upon the morphology of ribbon edges. Wang and Zhao [28] studied the effect of substitutional Li doping on the electronic properties of AGNR, however, the effect of ribbon edge termination was not investigated in their study. Previous analysis revealed that edge-termination is energetically more favourable as compared to substitutional doping of same impurity atoms [15, 18]. Motivated from this, in the present manuscript we have investigated the interaction of AGNR with Li adatoms as a terminating element.

2. Computational details

For the present work, we employed density functional theory (DFT) based first principle calculations using ATK-VNL[†] package to study the structural stability and electronic properties of Li terminated AGNR. The ribbons were modelled periodic along z axis and supercell approach has been used to calculate the electronic band structures. The k-point sampling was selected 1×1×50 and the vacuum space of 10 Å was considered in the supercell along non periodic directions to avoid the artificial interactions of ribbon with its periodic images. The energy mesh cut off value of 70 Rydberg was opted for optimization of the structures. We used generalized gradient approximation (GGA) as proposed by Perdew-Burke- Ernzerhof (PBE) to account the exchange correlation potential [29]. All the calculations were completed using double ζpolarized basis set. The geometry optimization was performed without any restriction on the supercell and its constituent atoms. Further, the optimization process was continued in a self-consistent manner until the forces on each participating atom of the supercell was reduced to less than 0.05 eV/Å.

3. Results and discussion

We adopted the previously defined notation to describe the ribbon width (N_a) as the number of C-C pairs across the ribbon [15, 16]. To account for width effects, we considered the ribbons of symmetric widths N_a = 5, 7 and 9. The interaction of AGNR with Li was investigated by considering Li as a terminating element. We considered the termination of AGNR by Li atoms at one edge as well as at both the edges of ribbons. The schematic figures of structures under investigation and the way of defining the ribbon widths are depicted in Fig. 1 for N_a = 5, 7 and 9. For any structure, stability plays a crucial role to reveal its potential applications. Therefore, the structural stability of Li terminated AGNR has been investigated in terms of binding energy (BE), defined as

$$BE = E_T - E_b - nE_a$$

Where, E_T, E_b, E_a are the total energies of the Li-terminated ribbons, bare ribbons and isolated atom (H or Li) used for ribbon termination, n is the number of terminating atoms. The calculated BE per atoms is presented in

[†] www.quantumwise.com

Table (1). The analysis of computed BE reveals that one edge Li terminated ribbons are energetically preferred over both edges terminated structures. The energy differences between these structures are even greater than 6 eV [Table 1]. Moreover, as the ribbon width increases, the thermodynamic stability of AGNR improves for one edge Li terminated as well as for both edges Li terminated configurations.

In order to study the electronic properties of considered ribbons, we investigate the electronic band structures as shown in Fig. 2. Previously, pristine ribbons were found to be semiconducting [15, 16]. It is noticed that both edges termination of AGNR with Li atoms introduces additional electronic bands in the vicinity of Fermi level. The existence of these additional states are responsible for introducing metallicity in both edges terminated structures [Fig. 2 (a)-(c)]. On the other hand, ribbons with only one edge Li termination, maintain their semiconducting nature, however, the band gap is significantly reduced as compared to H-terminated counterparts [15]. The observed band gaps for N_a = 5, 7 and 9 are found to be 0.12 eV, 0.20 eV and 0.05 eV respectively for one edge Li termination. We noticed that the band gap is indirect for N_a = 9 whereas for widths N_a = 5 and 7, a direct band gap has been observed. Interestingly, these observed band gaps do not exhibit any peculiar width dependency which was the characteristic signature of H terminated AGNR [15, 16]. For further understanding of the origin of observed additional states, we computed density of states (DOS) profiles for both edges Li termination [Fig. 3]. Since these additional states are independent of the ribbon widths, to be concise, we depicted the DOS and partial density of states (PDOS) only for N_a = 5 as a representative width. We observed a sharp peak at the Fermi level and a higher peak in the valence band just below the Fermi level. The analysis of PDOS reveals that states near the Fermi level are mainly contributed by *Li-s* and *Li-p* orbital [Fig. 3(c)-(d)]. On the other hand, *C-p* orbital contribute towards the first conduction band peak and a high peak in the valence band region around -2 eV [Fig. 3 (b)].

Table 1. The calculated binding energy (eV) per atom for considered structures

Ribbon width	Both edges-termination	One edge Li-termination
Na = 5	-2.81	-9.09
Na = 7	-3.18	-9.86
Na = 9	-3.57	-10.67

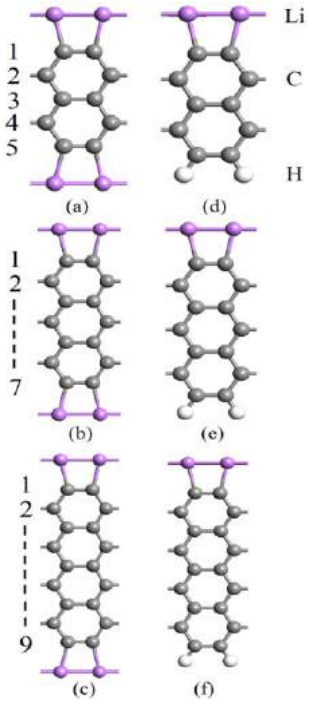


Fig. 1: The schematics of considered both edges Li terminated AGNR for width (a) N_a =5, (b) N_a =7, (c) N_a =9 and that of one edge Li terminated AGNR for width (d) N_a =5, (e) N_a =7 and (f) N_a =9. The purple, grey and white spheres represent Li, C and H atoms respectively.

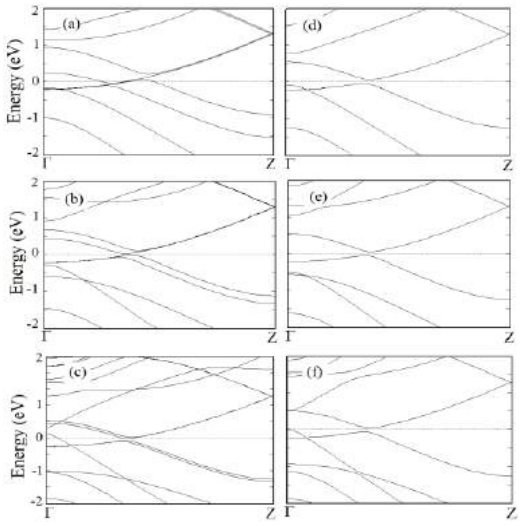


Fig. 2: The calculated band structures of both edges Li terminated AGNR for width (a) N_a =5, (b) N_a =7, (c) N_a =9 and that of one edge Li-terminated AGNR for width (d) N_a =5, (e) N_a =7 and (f) N_a =9. The Fermi level is set at 0 eV.

To reveal the potential applications of the considered structures, we investigate the current-voltage *(I-V)* characteristics using the two-probe model. The schematic figures of considered two-probe geometries are depicted in Fig. 4 (a)-(c). In two-probe geometry, the left and right electrodes (shown by rectangular boxes) are joined with the central region in a seamless way [1] to avoid interface scatterings. The analysis reveals that current is significantly enhanced in Li terminated AGNR as compared to pristine ribbon. The *I-V* characteristics of both edges Li terminated AGNR as depicted in Fig. 5 (b) indicates that current starts to increase instantaneously as a function of bias voltage which is in consistent with the metallic behaviour of this configuration as predicted by the corresponding band structure [Fig. 2(a)]. The behavior of *I-V* curves for both edges and one edge Li terminated ribbons are similar to each other, however, the magnitude of current is significantly lager for both edges Li termination [Fig. 5(b)]. The highest current values observed at 1 V are about 75 μA and 45 μA respectively for both edges Li termination and one edge Li termination while the same for pristine ribbon was only about 14 μA.

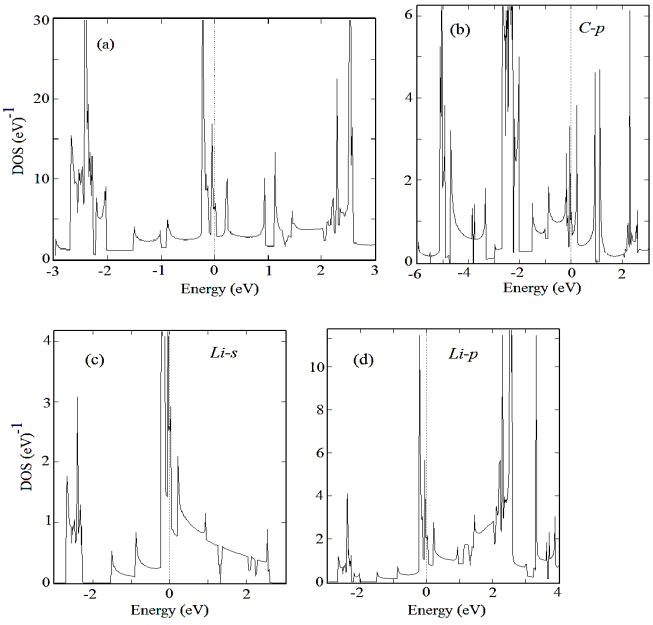


Fig. 3: (a) The DOS profiles for both edges Li terminated AGNR (Na = 5) and the corresponding PDOS for (b) C-p (c) Li-s and (d) Li-p orbital. The dotted line at 0 eV corresponds to Fermi level.

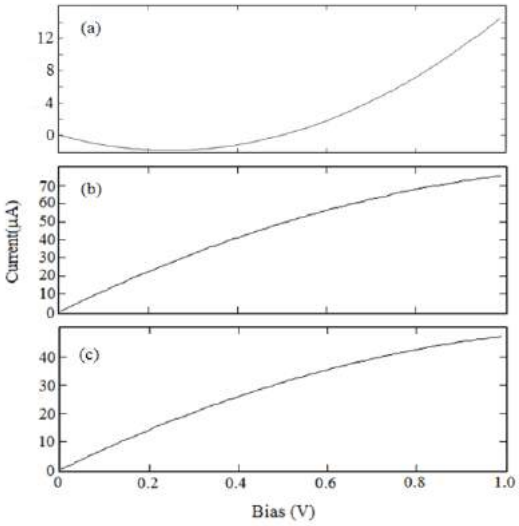


Fig. 4: (a) The schematics of two-probe models used for calculating *I-V* characteristics of (a) Pristine AGNR (b) Both-edges Li terminated AGNR and (c) One-edge Li terminated AGNR [1].

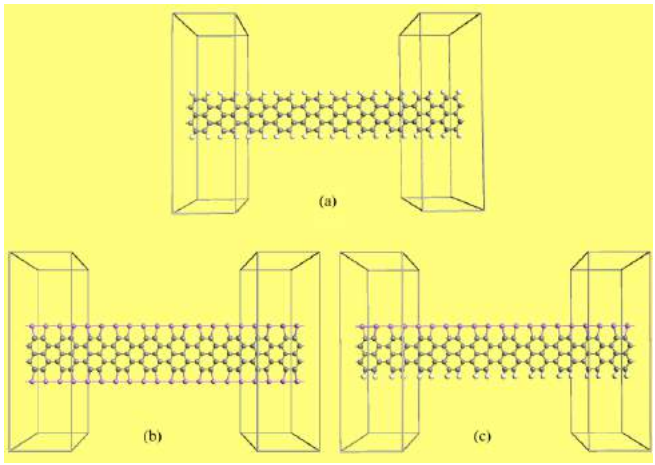


Fig. 5: The calculated *I-V* characteristics of AGNR (N_a =5) for (a) Pristine (b) both edges Li terminated and (c) one edges Li terminated configurations.

4. Conclusion

We revealed the interaction of Li atoms with symmetric AGNR as a terminating element at one edge as well as at both the edges of ribbons. It is observed that Li terminated AGNR are energetically viable to achieve and One edge termination is energetically more favourable. The Li termination introduces metallicity in both edges terminated AGNR while reduces the band gap for one edge terminated ribbons. The enhanced current values through these structures suggest that considered structures could be useful for nano interconnects applications.

Acknowledgements

Authors are thankful to Computational Nanoscience and Technology Lab. (CNTL), ABV-Indian Institute of Information Technology & Management, Gwalior for providing computational resources.

References

[1] N. K. Jaiswal, P. Srivastava, IEEE Trans. Nanotech. 12 (2013) 685-691.
[2] N. D. Robinson, L. Edman, M. Chhowalla, Phys. Scr. T 146 (2012) 014023-1-9.
[3] Z. M. Ao, J. Yang, S. Li, Q. Jiang, Chem. Phys. Lett. 461 (2008) 276-279.
[4] G. Moddel, Z. Zhu, S. Grover, S. Joshi, Solid State Commun. 152 (2012) 1842-1845.
[5] X. Huang, Z. Yin, S. Wu, X. Qi, Q. He, Q. Zhang, Q. Yan, F. Boey, H. Zhang, Small 7 (2011) 1876-1902.
[6] D. Li, Y. Ouyang, J. Li, Y. Sun, L. Chen, Solid State Commun. 152 (2012) 422-425.
[7] Y. Chen, B. Gao, Jing-Xiang Zhao, Qing-Hai Cai, Hong-Gang Fu, J. Mol. Model. 18 (2012) 2043-2054.
[8] J. Kailashiya, N. Singh, S. K. Singh, V. Agrawal, D. Dash, Biosens. Bioelectron. 65 (2015) 274-280.
[9] L. Li, R. Qin, H. Li, L. Yu, Q. Liu, G. Luo, Z. Gao, J. Lu, ACS Nano 5 (2011) 2601-2610.
[10] F. Rana, IEEE Trans. Nanotech. 7 (2008) 91-99.
[11] C. R. Dean, A. F. Young, I. Meric, C. Lee, L. Wang, S. Sorgenfrei, K. Watanabe, T. Taniguchi, P. Kim, K. L. Shepard, J. Hone, Nat. Nanotech. 5 (2010) 722-726.
[12] W. Sun, Y. Wang, Nanoscale 6 (2014) 11528-11552.
[13] M. Ezawa, Phys. Rev. B 73 (2006) 045432-1-8.
[14] Young-Woo Son, M. L. Cohen, S. G. Louie, Phys. Rev. Lett. 97 (2006) 216803-1-4.
[15] N. K. Jaiswal, P. Srivastava, Physica E 44 (2011) 75-79.
[16] K. Nakada, M. Fujita, G. Dresselhaus, M. S. Dresselhaus, Phys. Rev. B 54 (1996) 17954-17961.
[17] S. Dutta, A. K. Manna, S. K. Pati, Phys. Rev. Lett. 102 (2009) 096601-1-4.
[18] N. K. Jaiswal, P. Srivastava, J. Comput. Theo. Nanosci. 10 (2013) 1441-1445.
[19] H. Zheng, W. Duley, Phys. Rev. B 78 (2008) 045421-1-5.
[20] L. L. Song, X. H. Zheng, R. L. Wang, Z. Zeng, J. Phys. Chem. C 114 (2010) 12145-12150.
[21] Y. Mao, G. M. Stocks, J. Zhong, N. J. Phys. 12 (2010) 033046-1-10.
[22] N. Gorjizadeh, A. A. Farajian, K. Esfarjani, Y. Kawazoe, Phys. Rev. B 78 (2008) 155427-1-6.
[23] P. O. Lehtinen, A. S. Foster, A. Ayuela, A. Krasheninnikov, K. Nordlund, R. M. Nieminen, Phys. Rev. Lett. 91 (2003) 017202-1-4.
[24] M. Gupta, N. Gaur, P. Kumar, S. Singh, N. K. Jaiswal, P. N. Kondekar, Phys. Lett. A 379 (2015) 710-718.
[25] Y. Li, Z. Zhou, C. R. Cabrera, Z. Chen, Sci. Rep. 3 (2013) 2030-1-6.
[26] G. Giovannetti, P. A. Khomyakov, G. Brocks, V. M. Karpan, J. v. d. Brink, P. J. Kelly, Phys. Rev. Lett. 101 (2008) 026803-1-4.
[27] C. Uthaisar, V. Barone, J. E. Peralta, arXiv:0910.5154v1[cond-mat.mtrl-sci] (2009) 1-6.
[28] W. Wang, G. Zhao, Solid State Commun. 166 (2013) 6-11.
[29] J. P. Perdew, K. Burke, M. Ernzerhof, Phys. Rev. Lett. 77 (1996) 3865-3868.

Journal of Climatology & Weather Forecasting

Singh et al., J Climatol Weather Forecasting 2016, 4:1
http://dx.doi.org/10.4172/2332-2594.1000157

Research Article Open access

Greenhouse Gas Emissions from Landfills: A Case of NCT of Delhi, India

Singh SK, Anunay G*, Rohit G, Shivangi G and Vipul V

Department of Environmental Engineering, Delhi Technological University, Delhi, India

***Corresponding author:** Anunay G, Assistant Professor, Department of Environmental Engineering, Delhi Technological University, Delhi, India, Tel: +91-11-27871018; E-mail: anunaygour@live.in

Received date: Feb 09, 2016; **Accepted date:** Mar 03, 2016; **Published date:** Mar 19, 2016

Copyright: © 2016 Singh SK, et al. This is an open-access article distributed under the terms of the Creative Commons Attribution License, which permits unrestricted use, distribution, and reproduction in any medium, provided the original author and source are credited.

Abstract

The quantity of municipal solid waste (MSW) generated in Delhi is increasing at an alarming rate. Presently Delhi generates 8360 tons per day of MSW, which is projected to rise up to 18,000 tons/day by 2021.This would place immense pressure on the existing infrastructure and soon become a challenge for the local and municipal bodies responsible for waste management. The paper surveys the present state of the solid waste management in the NCT of Delhi and the propagation of greenhouse gas from the landfill sites. The bulk of the waste generated in Delhi is disposed at the three landfill sites viz. Bhalswa, Ghazipur, and Okhla. Waste at landfills is acted upon chemically and biologically to yield stabilized solids, liquid leachate and gases. The degradable organic carbon in the waste is broken down by microorganisms into methane gas which is released as a major contributor to global anthropogenic CH_4 emissions. The paper further calculates the GHG emission potential for the three landfill sites in Delhi using IPCC Methodology - Default Method and First Order Decay Model. The results obtained from both the methods are compared and it is found out that Default Method gave higher GHG emission values than the First order decay model. MSW in Delhi has been found to have enormous waste-to-energy potential, which if employed may cater to Delhi's energy needs and simultaneously reduce the GHG emissions.

Keywords: Municipal solid waste; Landfill; Greenhouse gas; GHG emissions; IPCC - default method; IPCC - FOD method

Introduction

Solid waste management have become a worldwide problem and is getting increasingly complicated day by day mostly due to the rise in population, industrialization and the consequent changes introduced in the lifestyle of people. Hence the per capita generation of solid waste bears strong correlation with the economic development at global as well as local scale. There are six functional elements complementing solid waste management (SWM) practices. It takes off with waste generation, followed by storage and handling of waste at source, waste collection, transfer and transport, followed by treatment and transformation, and at last the disposal [1]. Presently majority of the waste generated is disposed in open dumps or ordinary landfills in the developing rural areas or in sanitary landfills in the developed ones. Of the various SWM techniques, landfilling is found to be the cheapest and easiest to dispose municipal solid waste (MSW) all over the globe [2]. With the increasing urbanization and evolving life styles, Indian cities are generating eight times more MSW compared to that generated during 1947. Annually about 90 million tons of solid waste is produced as by-products of industrial, mining, municipal, agricultural and other activities. While the average collection efficiency in metropolitan cities (population > 1 million) is below 70% and that for smaller cities, it is less than 50% [3-5]. Waste at the landfills have been known to be one of the major sources of anthropogenic greenhouse gas (GHG) emission and a key contributor to global warming [6]. Methane (CH_4) emission from landfill is estimated to account for 3% - 19% of the anthropogenic sources in the world [6]. India, one of the world's largest emitter of CH_4 from landfills, currently produces about 16 tons of CO_2 equivalent per year which is predicted to increase to almost 20 tons of CO_2 equivalent per year by 2020 [7]. CH_4 alone constitutes about 29% of the total GHG emissions in India which is nearly twice the worldwide average of 15%. Moreover the emission from wastes is also twice (6%) than the global average of (3%) [8]. Major part of MSW constitutes of biodegradable organic materials, which undergo anaerobic decomposition in landfills generating a variety of gases collectively called landfill gas (LFG). It is composed of approximately 60% methane (CH_4) and 40% carbon dioxide (CO_2) in concert with low amounts of non-methane organic compounds and other trace gases [9-11]. Both CH_4 and CO_2 are GHGs. Over a time period of 100 years, the global warming potential (GWP) of CH_4 is 25 times of the GWP of CO_2 and has an atmospheric residence time of 12 ± 3 years [12]. Moreover percolating rainwater through the landfills produces leachate which contaminates the ground water [13,14]. Presently, approximately 8360 tons of MSW is generated daily in Delhi, out of which 87% is collected which amounts to 7273 tons per day (TPD). Moreover of the collected 7273 TPD of waste only 28%, i.e., 2000 TPD is treated [15]. As only one waste to energy plant at Timarpur - Okhla with a capacity of 1950 MTD is operational.

State of Municipal Solid Waste Management in Delhi

Population of Delhi is increasing at an alarming rate and it is estimated that the waste generation is expected to touch 18,000 TPD by 2021 [16]. State of the Delhi's landfills is not very encouraging with all the landfills being used way beyond their design life. Bhalswa landfill (BL), Ghazipur landfill (GL) and Okhla landfill (OL) are the three operational landfill sites in Delhi while two landfill sites in Jaitpur and Bawana are proposed. MSW is treated at three composting plants at Bhalswa, Narela / Bawana and Okhla; two incineration plants at Okhla which also generates 16 MW of power from the waste; one RDF plant at Narela / Bawana; and one construction and demolition waste dump at Burari [17]. Also all the three landfill sites have crossed the 30 metre height ceiling. Since landfills are major contributor of methane emissions [16], emissions from waste-water treatment plants [18,19]

and other waste management practices have not been considered in scope of the present study.

Study area

The NCT of Delhi is spread over an area of 1483 sq. km., located in the northern part of India. It is divided into three parts Delhi Ridge, Yamuna flood plains and plains. The air quality is poor and highly variable [20,21]. Hence periodic critical assessment of air quality by analytic and statistical tests is necessary [22]. It is the hub for employment for millions from the periphery, i.e., the NCR. As a result of which a huge mass of population survive in Delhi, which produces huge quantity of waste. Literature related to MSW management in Delhi shows that wastes are handled by three municipal agencies namely, Municipal Corporation of Delhi [23], New Delhi Municipal Corporation (NDMC) and Delhi Cantonment Board. All the MSW generated in the city is transported to landfill sites at Ghazipur in East Delhi, Bhalswa in North Delhi and Okhla in South East Delhi [16]. Brief descriptions about these landfills are given in (Table 1).

Characteristics	Bhalswa (BL)	Ghazipur (GL)	Okhla (OL)
Starting year	1992	1984	1996
Location	28 44'27.16" N, 77 9'27.92" E	28 37' 22.4" N, 77 19' 25.7" E	28 30'42" N, 77 16' 59" E
Area (Hectare)	26.22	29.62	16.89
Slope ()	60-70	60-70	70 80
Average height (m)	18	25.5 - 30.5	27 - 40
Dumping quantity (TPD)	1500	2200	1200
Type of waste	Household, vegetable market, C and D waste	Household, animal waste from poultry, fish market and slaughter house	Mainly household with C and D waste
Zones supplying waste	Civil Lines, Karol Bagh, Rohini, Narela, Najafgarh and West	Shahdara (North andWest), City zone, Sadar Pahargunj, NDMC	Central, Najafgarh, South Delhi and Cantonment Board
Depression, below ground level (m)	4	3	4

Table 1: Salient features of Delhi's landfills [16].

All the landfills have been receiving waste from more than 15 years; with GL being the oldest site operating since 1984; followed by BL which started in 1992 and OL became operational in 1996. Based on the municipal records, it has been estimated that the cumulative waste quantities reached at GL, BL and OL landfills till 2008 - 2009 are 11 million tons, 9.2 million tons and 6.1 million tons respectively [16]. Figure 1 shows a five-point summary and comparison of the quantity of solid waste received at BL, GL and OL landfill sites on a logarithmic y-axis of the box plot.

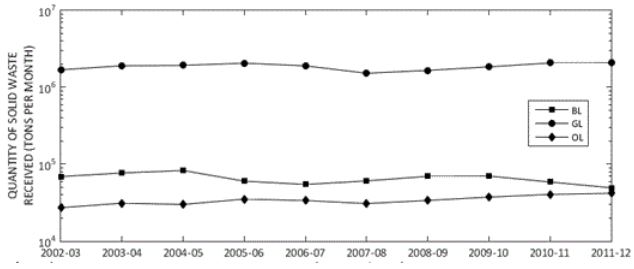


Figure 1: Box plot for quantity of solid waste received by BL, GL and OL landfill sites.

Overall trend of quantity of solid waste received at the landfill sites have been found to be increasing (except OL). Figure 2 shows the annual variation in average monthly garbage received at BL, GL and OL sites from year 2002 to 2012.

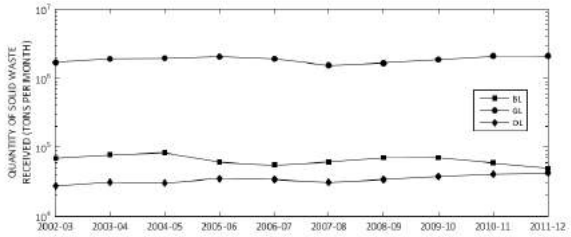


Figure 2: Annual variation in average monthly garbage received at BL, GL and OL sites.

Composition

The composition of MSW is the key to estimate the GHG emissions from landfills. Table 2 shows the relative content of various parameters of Indian MSW. It reveals that the amount of recyclables is very less in the waste owing to the rag-pickers who pick up recyclable matter (paper, plastic, glass, and metal) at dhalaos (garbage bins) before the waste reached the landfill [24].

Methane Emission from Landfills: Methodology for Inventory Estimation

Due to disposal of solid waste to landfills, emissions of methane take place due to anaerobic decomposition of organic matter. IPCC suggests two methods for calculating methane emissions from landfills.

The Default IPCC methodology based on the theoretical gas yield (a mass balance equation).

Theoretical first order kinetic methodologies, through which the IPCC Guidelines introduces the 'First order decay (FOD) model'.

Sr. No	Parameter	Content (%)
1	Biodegradables (includes green matter, kitchen waste, paper, textiles, dry leaves)	73.7
2	Recyclables (includes glass, rubber / leather, metal, plastic)	9.2
3	Inert (include concrete, sand, brick, stone)	17.1
4	Others (includes dead animals, etc.)	6.3
5	Moisture	47

Table 2: Composition of waste reaching the landfill site in Delhi [23].

The main difference between the two methods is that method IPCC-Default method does not reflect the time variation in solid waste disposal and the degradation process as it assumes that all potential methane is released the year the solid waste is disposed whereas the effect of timing of the actual emissions is reflected in FOD method [25].

IPCC Default method

The method assumes that all the potential methane emissions are released during the same year the waste is disposed. The method is simple and emission calculations require only input of a limited set of parameters, for which the IPCC Guidelines provide default values, where country-specific quantities and data are not available.

The Default Method is based on the following equation:-

Methane emissions (Gg/yr) = (MSWT * MSWF * MCF * DOC * DOCF * F * 16/12-R) * (1-OX)

Where,

Symbol	Parameter	Value
MSWT	Total municipal solid waste (MSW) generated (Gg yr/yr.)	MSWT * MSWF = Waste disposed at landfill site (see Tables 4-6)
MSWF	Fraction of MSW disposed of at the disposal sites.	
MCF	Methane correction factor	0.6 (IPCC default value)
DOCF	Fraction DOC dissimilated	0.77 (IPCC default value)
DOC	Fraction of degradable organic carbon in the waste	0.5 (IPCC default value)
F	Fraction of methane in the landfill gas	0.5 (IPCC default value)
R	Recovered methane (Gg/yr)	Recovery of LFG is not adopted in India, hence the value is zero
OX	Oxidation factor	0 (IPCC default value)

Parameters and values of the equation are tabulated above.

Methane generation by first order decay method

The amount of methane generated from the landfill site is calculated based on a First Order Decay Model. In this method, methane generation in the landfill is described as a function of time. Nationally adjusted FOD model has been used for calculating yearly emissions from the waste dumped in landfills.

QT, x = k * MSWT(X) * MSWF(X) * MCF(X) * Lo(X) * e - k (T-X) * F

Where,

Symbol	Parameter	
QT, x	The amount of methane generated in the current year from waste disposed in the year X	
X	The historical year of the disposal of the relevant national MSW quantities	
K	Ln (2)/$t^{½}$. (1/yr) and $t^{½}$ is half-life period for degradation process	
MSWT(X)	Total MSW generated (Gg/yr) in year X	
MSWF(X)	Fraction of MSW disposed to solid waste disposal sites in year X	
MCF(X)	Methane correction factor (fraction) for year X	
Lo(X)	DOC x DOCF for the year X (Gg CH_4 / Gg waste) Where:	
	DOC	Fraction of degradable organic carbon in the waste
	DOCF	Fraction DOC dissimilated
T	The current year (year of the emission estimate) (Gg/yr)	

Parameters of the equation are tabulated above.

The value of is taken as 7 years (default value) for tropical countries and rest all parameters have same values as that in IPCC default method.

Results and Discussion

IPCC- Default methodology and IPCC-FOD methodology has been utilized to yield the values of net methane emission from the three landfills at Bhalswa, Ghazipur and Okhla. Table 3 shows the descriptive statistics, geometric increase / decrease occurred in the average monthly solid waste received at the landfills over the years 2002 to 2012. It also presents the correlation of quantities of solid waste received, which indicates stronger correlation between GL and OL than others. This may be due to the geographic proximity of the landfills, similarity in generation, logistics and transport of wastes. Bhalswa Landfill is the fastest growing landfill as the solid waste received here is growing at a rate of 9.61% per year. Whereas the solid waste received at Okhla Landfill is declining i.e. at a negative growth rate. The quantities of solid waste received at the respective landfills are

presented in Tables 4-6 along with the calculated methane emission by Default Method and FOD Method.

	Correlation			Mean	Std. Dev.	Geometric Increase (%)
	BL	GL	OL			
BL	1			65215.8	9789	9.61
GL	-0.26	1		1867657	180209	5.76
OL	-0.62	0.64	1	34185.7	4450	-7.75*

* % decrease is observed

Table 3: Correlation between solid waste reaching landfill sites and their descriptive statistics [17].

Various values and parameters required for calculation of methane emission potential are described in the methodology. The discussion of the results is discussed here.

Bhalswa landfill (BL)

Bhalswa Landfill was started in 1992 and receives household, vegetable market and Cand D waste. It receives around 1500 tonne per day of wastes from Civil Lines, Karol Bagh, Rohini, Narela, Najafgarh and West Delhi Area. It is a major source of ground water pollution. The quantity of solid waste received at BL and the respective methane emission by IPCC-Default method and IPCC-FOD Methods are given in Table 4. The emissions have been found to gradually decrease from 127.66 Gg/yr to 91.23 Gg/yr by Default method and 86.71 to 61.97 Gg/yr by FOD method as the waste reaching this landfill has decreased over the years.

Year	MSW received at BL (tons per month)	Methane emission by Default Method (Gg/yr)	Methane emissions by FOD Method (Gg/yr)
2002-2003	69072	127.66	86.71
2003-2004	77009	142.30	96.67
2004-2005	82773	153.00	103.91
2005-2006	60236	111.32	76.62
2006-2007	54566	100.84	68.49
2007-2008	60674	112.13	76.17
2008-2009	69617	128.65	87.39
2009-2010	70134	129.61	88.04
2010-2011	58711	108.50	73.70
2011-2012	49366	91.23	61.97

Table 4: Methane emissions from Bhalswa landfill (BL).

Ghazipur landfill (GL)

Ghazipur Landfill was started in 1984 and receives household, animal waste from poultry, fish market and slaughter house. It receives around 2200 tonne per day of wastes from Shahdara (North and West), City zone, Sadar, Pahargunj, NDMC municipal areas. It receives the highest quantity of solid waste to be disposed. The quantity of solid waste received at GL and the respective methane emission by IPCC-Default method and IPCC-FOD Methods are given in Table 5. The quantity of waste reaching GL has increased; hence the CH_4 emissions have also been observed to increase gradually from 3125.121 Gg/yr to 3845.20 Gg/yr by default method and increased from 2122.85 Gg/yr to 2611.99 Gg/yr by FOD method. GL shows the maximum emission as it received the largest quantity of solid waste. Also the methane emissions calculated by First order decay method are less than of Default method.

Year	MSW received at GL (tons per month)	Methane emission by Default Method (Gg/yr)	Methane emissions by FOD Method (Gg/yr)
2002-2003	1691083	3125.12	2122.85
2003-2004	1907599	3525.24	2394.65
2004-2005	1929465	3565.65	2422.10
2005-2006	2061538	3809.72	2587.89
2006-2007	1903583	3517.82	2389.61
2007-2008	1524059	2816.46	1913.18
2008-2009	1659741	3067.20	2083.51

2009-2010	1845896	3411.21	2317.20
2010-2011	2072873	3830.67	2602.12
2011-2012	2080736	3845.20	2611.99

Table 5: Methane emissions from Ghazipur landfill (GL).

Okhla landfill (OL)

Okhla Landfill was started in 1996 and receives mainly household waste with some C and D waste. It receives around 1200 tonne per day of wastes from Central, Najafgarh, South Delhi and Cantonment Board. The quantity of solid waste received at OL and the respective methane emission by IPCC-Default method and IPCC-FOD Methods are given in Table 6. The emissions have been found to gradually decrease from 350.29 Gg/yr to 77.42 Gg/yr by default method and increased from 34.16 Gg/yr to 52.60 Gg/yr as the waste reaching this landfill has increased but the rate at which waste is received at OL is reducing over time. OL shows a geometric growth rate of -7.75% of solid waste received.

Year	MSW received at OL (tons per month)	Methane emission by Default method (Gg/yr)	Methane emissions by FOD Method (Gg/yr)
2002-2003	27216	50.29	34.16
2003-2004	31180	57.62	39.14
2004-2005	30004	55.48	37.66
2005-2006	35249	65.14	44.25
2006-2007	33736	62.34	42.35
2007-2008	30836	56.98	38.71
2008-2009	33807	62.48	42.44
2009-2010	37379	69.08	46.92
2010-2011	40554	74.94	50.91
2011-2012	41896	77.42	52.60

Table 6: Methane emissions from Okhla landfill (OL).

Figure 3 shows the methane emission from years 2002 to 2012 calculated by IPCC- Default method (DM) and FOD Method at BL, GL and OL landfill sites. It is observed that Default Method yields higher value of emission than FOD method because any change in the amount of MSW disposed is reflected immediately in the results of IPCC-Default method whereas the FOD method responds slowly to the changes. The IPCC-Default Method is easy to implement and the result are also lucid. The FOD method requires adequate knowledge of the decay process at solid waste disposal sites and comparatively more data is required (Table 7).

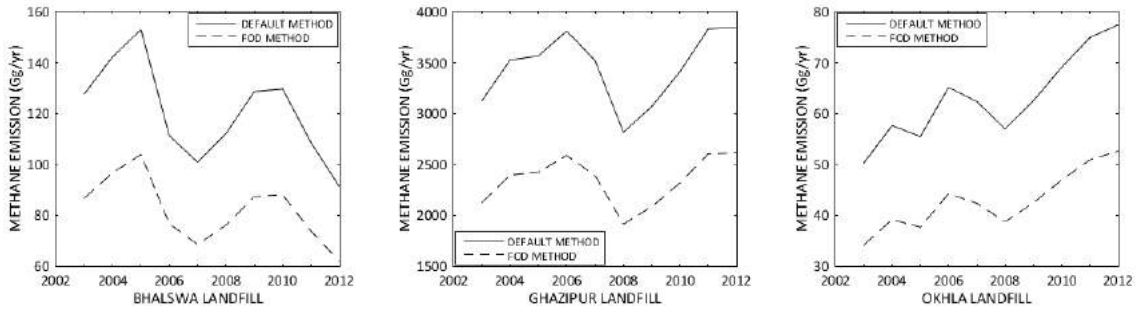


Figure 3: Methane emissions from BL, GL and OL landfill sites (Gg/yr).

In consonance with the total quantity of solid waste received at the landfills, Ghazipur emits the largest share of methane emission from both methods. The variation in methane emissions is found to be fluctuating the most at GL with a standard deviation of 333 in Default Method CH_4 emission results and 226.2 in FOD method CH_4 emission results.

Landfill	BL		GL		OL	
IPCC Method	DM	FOD	DM	FOD	DM	FOD
Mean	120.5	82.0	3451.4	2344.5	63.2	42.9
St. Dev.	18.1	12.2	333.0	226.2	8.2	5.6

Table 7: Descriptive statistics of methane emission from BL, GL and OL landfills.

Uncertainty in quantity and composition of waste received at landfill sites, oxidation mechanism and rate of methane generation in upper crust of landfill, fraction of DOC and DOCF contribute to the uncertainties in GHG emission estimation from landfills. IPCC model that predict the amount of methane generated (mass balance, first order decay) need to be precise for accurate results. Therefore, even a small variation in the DOC or methane generation rate constant may lead to large variations in CH_4 emission estimates.

Conclusion

Municipal solid waste disposal is a significant source of methane emissions globally. The increasing pressure of waste from the population needs an alternative for waste management and disposal other than landfilling in topographic depressions. Present study revealed that the methane emissions from Bhalswa, Ghazipur and Okhla Landfills for the year 2011-2012 was 91.23 Gg/yr, 3845.20 Gg/yr and 77.42 Gg/yr by Default Method; and 61.97 Gg/yr, 2611.99 Gg/yr and 52.60 Gg/yr by First Order Decay method. Hence there emerges an urgent need to initiate mitigation steps for controlling GHG emission from landfill areas. Moreover the quantity of methane emission has been increasing as a result of increased consumption. The first step of waste management practice to be employed is the segregation of organic component from solid waste at the source, which will be effective for composting. Secondly, construction of scientifically planned sanitary landfill site with provision of tapping landfill gas for its fuel value [11]. Hence the huge quantity of MSW in Delhi has enormous waste to energy potential [3,19] which if utilized can cater to Delhi's increasing energy needs.

References

1. Tchobanoglous G, Theisen H, Vigil SA (1993) Integrated Solid Waste Management: Engineering Principles and Management Issues, McGraw Hill International editions, pp: 978.
2. Jhamnani B, Singh SK (2007) Solid Waste Management by land filling in new Urban Growth Centres. National Seminar on Integrated Development of Towns as new growth Centers. Indian Buildings Congress 17-19.
3. Kumar A, Sharma MP (2014) Estimation of GHG emission and energy recovery potential from MSW landfill sites. Sustainable Energy Technologies and Assessments 5: 50-61.
4. Singh SK, Bisht A (2015) Environmental Management in Mass Gatherings, Int J of Engg Sci and Mgmt 5: 130-138.
5. Sahai S, Sharma C, Mitra AP, Singh SK, Gupta PK (2011) Assessment of trace gases, carbon and nitrogen emission from field burning of agricultural residues in India. Nutrient Cycling in Agroecosystems 89: 143-157.
6. Intergovernmental Panel on Climate Change (IPCC) (1996) Report of the Twelfth Season of the Intergovernmental Panel on Climate Change, Mexico City.
7. Singh SK, Singh N (1998) Solid Waste Management of Bathinda City. Proceedings of Thirteenth International Conference on Solid Waste technology and Management. Philadelphia, USA.
8. Siddiqui FZ, Khan ME (2011) Landfill gas recovery and its utilization in India: current status, potential prospects and policy implications. J Chem Pharm Res 3: 174-83.
9. Hegde U, Chang TC, Yang SS (2003) Methane and carbon dioxide emissions from Shan chu-ku landfill site in northern Taiwan. Chemosphere 52: 1275-1285.
10. Singh J, Ramanathan AL (2015) Solid Waste Management: Present and Future Challenges. In: Singh SK, Mahour M (eds18.) Clean Development Machanism: An Opportnity in Solid Waste Perspective, pp: 178-185.
11. Singh J, Ramanathan AL (2015) Solid Waste Management: Present and Future Challenges In: Singh SK, Mahour M (eds2.) Methane Estimation from Landfill Site, pp: 19-28.
12. Solomon S, Qin D, Manning M, Chen Z, Marquis M, et al. (2007) Climate Change 2007: The Physical Science Basis, IPCC Fourth Assessment Report.
13. Singh SK (2007) Ground water Modeling-Trends and Practices. Journal of American Society of Civil Engineers-IS 4(1).
14. Chawla A, Singh SK (2014) Modelling of Contaminant Transport from Landfills. International Journal of Engineering Science and Innovative Technology 3: 222-227.
15. Govt. of Delhi, Department of Environment (2015) Waste Management.
16. Chakraborty M, Sharma C, Pandey J, Singh N, Gupta PK (2011) Methane Emission Estimation from Landfills in Delhi: A comparative Assessment of Different Methodologies. Atmospheric Environment 45: 7135-7142.
17. Kumar A (2013) Existing Situation of Municipal Solid Waste Management in NCT of Delhi, India, Research Forum: International Journal of Social Sciences 1: 6-17.
18. Gupta D, Singh SK (2012) Green House Gas Emission from Waste Water Treatment Plants: A Case Study of Noida, India. Journal of Water Sustainability 2: 131-139.
19. Gupta D, Singh SK (2015) Energy use and Greenhouse Gas emissions from Waste Water Treatment Plants, Journal of Environmental Engineering 7: 1-10.
20. Gour AA, Singh SK, Tyagi SK, Mandal A (2013) Weekday/Weekend Differences in Air Quality Parameters in Delhi, India. International Journal of Research in Engineering and Technology 1: 69-76.
21. Gour AA, Singh SK, Tyagi SK, Mandal A (2015) Variation in Parameters of Ambient Air Quality in National Capital Territory (NCT) of Delhi (India). Atmospheric and Climate Sciences 5: 13-22.
22. Aenab AM, Singh SK, Lafta AJ (2013) Critical Assessment of Air Pollution by ANOVA Test and Human Health Effects. Atmospheric Environment 71: 84-91.
23. Municipal Corporation of Delhi (2004) Feasibility study and master plan for Optimal Waste Treatment and Disposal for the Entire State of Delhi on Public Private Partnership Solution. Volume 6: Municipal Solid Waste Characterization Report.
24. Sastry DBSSR. Composition of Municipal Solid Waste- Need for Thermal Treatment in the present Indian context.
25. Frøiland-Jensen JE, Pipatti R. CH_4 emissions from Solid Waste Disposal. Good Practice Guidance and Uncertainty Management in National Greenhouse Gas Inventories 419-439.

This article has been accepted for publication in a future issue of this journal, but has not been fully edited. Content may change prior to final publication. Citation information: DOI 10.1109/TCDS.2016.2577044, IEEE Transactions on Cognitive and Developmental Systems

Human Activity Recognition based on Spatial Distribution of Gradients at Sub-levels of Average Energy Silhouette Images

Dinesh K Vishwakarma, *Member, IEEE*, Kuldeep Singh, *Member, IEEE*

***Abstract*—The aim of this paper is to present a unified framework for human action and activity recognition by analysing the effect of computation of spatial distribution of gradients (SDGs) on average energy silhouette images (AESIs). Based on the analysis of SDGs computation at various decomposition levels, an effective approach to compute the SDGs is developed. The AESI is constructed for the representation of the shape of action and activity and these are the reflection of 3D pose into 2D pose. To describe the AESIs, the SDGs at various sub-levels and sum of the directional pixels (SDPs) variations is computed. The temporal content of the activity is computed through R–transform (RT). Finally, the shape computed through SDGs and SDPs, and temporal evidences through RT of the human body is fused together at the recognition stage, which results in a new powerful unified feature map model. The performance of the proposed framework is evaluated on three different publicly available datasets i.e. Weizmann, KTH, and Ballet and the recognition accuracy is computed using hybrid classifier. The highest recognition accuracy achieved on these data sets is compared with the similar state-of-the-art techniques and demonstrate the superior performance.**

***Index Terms*— Human action recognition, Human action analysis, Computation of spatial distributions, The sum of directional pixels, Texture segmentation, Hybrid Classifier.**

I. INTRODUCTION

DURING the past few years, the dynamic interaction between the machine and human have grown tremendously, which encompasses the recognition of human action and activity which is a new domain of computer vision. The human action and activity recognition using video sequences have become the focal point of the research, the effort of which is the enlargement of a harsh scheme that recognizes the human action and activity competently. The advances in this field leads to variety of promising such as medical diagnostic, robotics, video surveillance, smart rooms, human-computer interaction, elderly health care, etc. [1] [2] [3]. The recent literature reviews [1] [3] [4] [5] [6] indicates that there are some popular approaches used for HAR such as spatio-temporal interest points (STIPs), optical flow, bag of words (BoWs), point trajectories, and silhouette models. The major issues in the concerned area are cluttered background, camera motion, angular variations and lighting settings. To address these problems, a unified framework is presented based upon the shape description of human silhouette and its orientation. The shape of posture is represented by forming the AESIs based on the global characteristics of a human silhouette. To enhance the effectiveness of the shape computation using SDGs, the region of interest (ROI) of AESI is selected so that the redundant information is eliminated. In addition, to SDGs feature, the sum of directional pixels (SDPs) values are computed, which shows the variation of the sum of pixels in the x-y direction and preserve the structural information. This shape information is further integrated with the rotational feature based upon the action dynamics. The motion based rotational information is computed by applying R- transform on the binary silhouette of the human activity. Hence, our unified feature map model has abundant discriminating power for the representation of human activity. The earlier works [7] [8] [9] [10] [11] have proved that fusion techniques based on multiple features have superior performance as compared to the individual features. The central theme of motivation is proposing a unified framework based on the analysis of the effect of computation of spatial distribution of gradients. Thus, the descriptor designed by fusion of shape and motion characteristics of human activity is more effective, robust, and capable of handling occlusion. The theme of this paper is based on the earlier work in [11], where the recognition of human activity is done by computing the spatial distribution of average energy images using a pyramid of the histogram of oriented gradients. While in this article, the effect of spatial distribution at various decomposition levels is analysed and assessed. Based on the analysis and assement, a novel modified algorithm for computation of spatial distribution is presented, which is superior in terms of cost of computation in comparision with earlier work in [11] and recognition accuracy than the similar state-of-the-art.

The organization of the reminder of this paper is as follows. In Section 2, the earlier state-of-the-art techniques used for the HAR based on human silhouettes are discussed which

Dinesh K. Vishwakarma is working as Assistant Professor in the Department of Electronics and Communication Engineering, Delhi Technological University (Formerly Delhi College of Engineering), Delhi-110042, India (e-mail: dvishwakarma@gmail.com, dinesh@dtu.ac.in).

Kuldeep Singh is working as Senior Scientist in Central Research Laboratory, Bharat Electronics Limited (Ministry of Defense, GOI), Ghaziabad, U.P.-201010, India (e-mail: kuldeep.er@gmail.com).

2379-8920 (c) 2016 IEEE. Personal use is permitted, but republication/redistribution requires IEEE permission. See http://www.ieee.org/publications_standards/publications/rights/index.html for more information.

This article has been accepted for publication in a future issue of this journal, but has not been fully edited. Content may change prior to final publication. Citation information: DOI 10.1109/TCDS.2016.2577044, IEEE Transactions on Cognitive and Developmental Systems

highlights merits and demits of these techniques. The detailed of the proposed framework is described in Section 3, which comprehends the binary silhouette extraction, 3D to 2D pose representation, computation of modified SDGs, SDPs and Orientation of a human silhouette. Experimental setup and performance evaluation is presented in Section 4. Conclusions are outlined in Section 5.

II. RELATED WORK

In the past, numerous efforts have been made for the recognition of human action in video sequences. Moslty, the HAR techniques are based on the representation of local features, global features, key points, spatial-temporal features, bags of words etc. [1] [3] [4] [5] [6] [12].

The spatio-temporal interest points (STIPs) based action recognition as introduced in [13], where it has been observed that the performance of this approach is not stable and effective for manifold actions. The issues involved in the interest point based approach is countered by proposing separable linear filers [14]. A biological model [15] based on the visual cortex is developed for processing of motion evidences and used for the recognition of human and animals actions, where it is also quantified that shape is important feature and can be integrated with motion feature for the recognition of human actions in future.

A complicated but effective approach for action recognition is based on the extension 2D motion templates to 3D space time volume is developed [16] . The issue of space time volume approach is addressed using probabilistic latent sematic analysis (PLSA) and Latent Dirichlet Allocation (LDA) models [17] but they do not compromise temporal and scale invariance. A combined approach [18] of HOG with histogram of optical flow (HOF) is developed for the grouping of human action centred on the subsequence, which is reasonably stable and robust to the portion based approaches. A holistic approach centred on spatial-temporal steerable pyramid (STSP) [19] is proposed to recognize human actions, which is compact in representation and turns as a global descriptor. Somasundaram et al. [20] develops, another compact representation used for HAR based on spatio-temporal characteristics, which address the problem of large and scale variant datasets. Shao et al. [21] presented, a novel Laplacian pyramid coding technique, which is free from tracking of features or localization of STIP's. MHI/MEI template based representation of human action is proposed in [22], which depends on time parameter, action speed, and view. A low resolution videos are used for action recognition in [23], where they are used to compute the parameters by correlating the optical flow measurements. Hung et al. [24] present an approach based on space time volume. [24], where they formed average energy image and adaptive discriminant analysis for human identification. Similarly, the silhouette energy images [25] and gait energy images [26] are also used for the recognition of human activity, but these methods are less accurate due to the insufficiency of motion evidence. To enhance the accuracy, a hybrid approach is proposed by Shao *et al.* [27], where they use the motion and shape feature of the human activity. Zhang et al. [28] developed a shape based descriptor, where they used the RT to compute the shape of human silhouette and reported that its performance is better for the activities involving more rotation in comparison with translation. Another approach proposed by Khan & Sohn [29], which recognizes the abnormal activities and they used to compute the shape of the activity using RT. A recent approach [30] is based on silhouette orientation to detect the abnormal human activities using the orientation of human silhouette. The orientation is computed by forming an approximated ellipse around the moving human silhouette. The angle between the major and minor axis of the ellipse gives the orientation of human silhouette.

In more recent, multiple feature based techniques [8] [9] [10] [28] [31] are becoming popular for the recognition of human activity. Sedai et al. [31] propose a multiple features based HAR model, which combines the shape and appearance feature, which gives improved performance over the single feature based methods for HAR. Shao et al. [7] use multiple features for the recognition of human activity, and these features are 3D gradients and wavelet transform. The major difference between existing methods which combines motion and shape features is the proposed descriptor itself. In an attempt to provide an alternate model of HAR, which can handle the challenge of representation of complex activities, the variation of lighting conditions, noise, and occlusion, etc., a modified algorithm is presented. This is based on the previous work done in [11] and the significant contributions are as follows:

- The proposal and evaluation of a new framework in which shape (AESIs, SDPs, and Modified SDGs) and motion (R-transform) evidence are combined for the recognition of human activity.
- The shape of human activity is characterized using modified proposal of computation of spatial distribution while in [11], the spatial distribution is based on the traditional way of computation of pyramid of histogram oriented gradients [32], which was less effective in terms of feature representation.
- The proposed algorithm of spatial distribution computation in this paper are analysed in terms of the dimensionality of the feature vector and the recognition accuracy on various standard human activity datasets, where it is inexpensive in terms of cost of computation and higher recognition accuracy than [11] with the similar state-of-the-art.
- Additionally, the effect of proposed algorithm is tested on Ballet Human Movement dataset [33], which is highly challenging in terms of interclass similarity, intra-class dissimilarity, clothing variation, and illumination change, while in [11] only Weizmann [16] and KTH [34] human action dataset result were presented.
- The comparative performance analysis of the proposed algorithms with similar state-of-the-art techniques is more exhaustive than the earlier work [11].

III. PROPOSED FRAMEWORK OF HAR

The proposed framework is established by exploring the local and global evidence, which allows the recognition of human action and activity in an effective manner. An outline of the proposed framework is as illustrated in Fig.1. In input video

2379-8920 (c) 2016 IEEE. Personal use is permitted, but republication/redistribution requires IEEE permission. See http://www.ieee.org/publications_standards/publications/rights/index.html for more information.

This article has been accepted for publication in a future issue of this journal, but has not been fully edited. Content may change prior to final publication. Citation information: DOI 10.1109/TCDS.2016.2577044, IEEE Transactions on Cognitive and Developmental Systems

sequences is captured using CCTV or digital camera. To remove the unwanted evidence, the foreground object i.e. the human blob is segmented using texture based approach. The foreground frames containing human blobs are spatially and temporally arranged. Further, these are described by computing the shape and motion of human blob. The shape is computed using modified SDGs and SDPs. The motion of human blob is computed using RT.

A. *Formation of AESIs*

The average energy silhouette images are formed in two steps: first is the extraction of human silhouette while other is the summation and averaging of silhouettes.

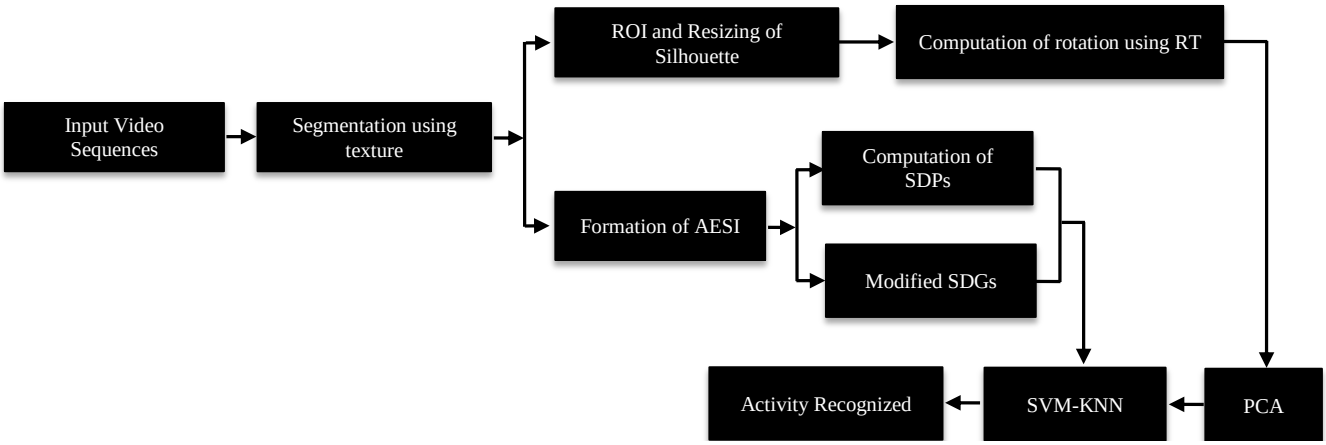


Fig.1. Work flow diagram of proposed framework

Human silhouette extraction is considered as one of the stiff tasks of action recognition based on silhouette due to the illumination change, cluttered background, shadows, video noise, etc. [35]. The simplest way of silhouette extraction is the background subtraction, but the modelling of background is again a complex task. Earlier, Gaussian Mixture Model (GMM) and Local Binary Pattern (LBP) based background models are usually used but for the noisy video sequence, the parameter estimation is unpredictable in the case of GMM. LBP is a very efficient textural operator, which labels the pixels of the image by thresholding the neighbourhood of each pixel, resulting in a binary pattern. Initially, Haralick *et al.* [36], proposed a textural feature based segmentation approach using Gray Level Co-occurrence Matrix (GLCM). After that, numerous textural feature based segmentation techniques have been proposed [37] [38] [39]. Chua et al. [38] developed a robust texture feature based approach using LBP for background subtraction and also they have demonstrated that the textural feature based segmentation method gives more effective and accurate results under the noise and illumination change [40] [41] for video surveillance applications. Also, the same is implemented on field-programmable gate array (FPGA) board [37] [39] for different real life applications. The realization of texture based algorithm in real life applications has encouraged us to use textural feature based background subtraction model in this work. A textural feature based segmentation approach proposed by Haralick *et al.* [36], in which the entropy is measured as one of the important parameters to express the texture information and which is described as:

$$\mathcal{S} = \sum_i \sum_j \not{f}(i,j) \log(\not{f}(i,j)) \quad (1)$$

where in Eq.1 $\not{f}(i,j) = \frac{\mathcal{M}(i,j)}{\sum_{i,j} \mathcal{M}(i,j)}$ is the probability density function, and i and j are indices to the co-occurrence matrix $\mathcal{M}$. The binary silhouette image is having greater area of back as compared to the white area, hence for effectiveness of the feature representation the ROI containing the white pixels of human blob is cropped as in [12].

In the process of ROI selection, first the image is scanned from left to right, and the first white pixel location is taken as the extreme left of the ROI while the last white pixel is taken as the extreme right of the ROI. This is achieved by scanning column-wise from the left and the first column containing one or more white pixels is the desired starting point, and the last column containing one or more white pixels is the desired end point of the ROI. Similarly, the image is then scanned from top to bottom, and the first white pixel location is taken as the topmost part of the ROI while the last white pixel location is taken as the lowest part of the ROI. This is achieved by scanning row-wise from the top and the first row containing one or more white pixels is the desired topmost point and the last row containing one or more white pixels are the desired bottom-most point of the ROI. Finally, the rectangle comprised of these extreme points is then extracted which

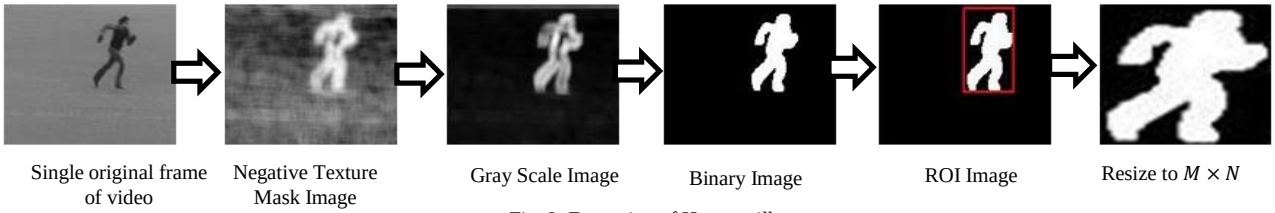


Fig. 2. Extraction of Human silhouette.

2379-8920 (c) 2016 IEEE. Personal use is permitted, but republication/redistribution requires IEEE permission. See http://www.ieee.org/publications_standards/publications/rights/index.html for more information.

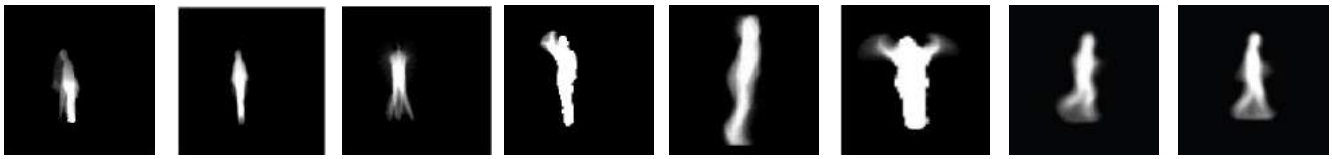
This article has been accepted for publication in a future issue of this journal, but has not been fully edited. Content may change prior to final publication. Citation information: DOI 10.1109/TCDS.2016.2577044, IEEE Transactions on Cognitive and Developmental Systems

forms the ROI.

Han & Bhanu [42] introduced the Gait energy image (GEI) concept that is similar to AESI but in this approach, the alignment of binary silhouettes is done using a reference point. Further, these silhouette sequences are compressed into a sole image based on cumulative process, which takes into consideration the changes of subsequent silhouettes. The main limitation of this approach is the lack of temporal content of activity but simultaneously it has a richness of the structural information, which makes the use of AESI more pertinent. In the next section, the limitation of temporal content is removed by the addition rotation information. The AESI is represented using the equation:

$$A_E(x,y) = \frac{1}{n}\sum_{\tau=1}^{n}|\psi_\tau(x,y)|^2 \quad (2)$$

Eq.2, represents the AESI formation, where, 'n' is the total number of frames in a whole cycle, '$\psi_\tau(x,y)$' is demarcated as a binary frame at time instant 'τ', and (x,y) are the pixel coordinates in 2D image. The benefit of utilizing images is that they eliminate the time dependency issues [22] and easily differentiate the alike depiction of actions of dissimilar groups on the basis of the intensity of pixel values.



Bending Jump in place Jumping Jack One hand waving Jump Two hand waving Running Walking

Fig. 3. The depiction of AESIs of different types of Human Activities.

B. Shape Features

The computation of shape feature is done via the computation of spatial distribution of gradients (SDGs) and the sum of directional pixels (SDPs) values of AESIs. The details of the process of computation of these features are as explained in the subsequent sections.

1) Modified SDGs

This approach is an extension of the previous approach *[11]* of computation of edge spatial distribution of average energy images. The main aim of this approach is to provide an improved spatial distribution computation model with an optimal cost of computation. As it is described that the SDGs computation at K orientation bins and v decomposition level, the feature vector is $K\sum_v 4^v$. To get a better estimate about the SDGs feature vector size and its effect, let us consider an example where $K = 8$ and $v = 0,1,2,3$.

$$At\ v = 0 \quad SDGs_{v=0} = 8\sum_v 4^v = 1 \times 8 \quad (3)$$
$$At\ v = 1 \quad SDGs_{v=1} = 8\sum_v 4^v = 1 \times 40 \quad (4)$$
$$At\ v = 2 \quad SDGs_{v=2} = 8\sum_v 4^v = 1 \times 168 \quad (5)$$
$$At\ v = 3 \quad SDGs_{v=3} = 8\sum_v 4^v = 1 \times 680 \quad (6)$$

From Eq. 3-6, it can be seen that the size of SDGs feature vector increases exponentially, but the effect of SDGs feature vector at a higher level of decomposition is comparable (level 2 and 3) since the variation in the magnitude of SDGs at level 2 and 3 are quite similar in respect of maximum and minimum value of magnitude as depicted in Fig. 4. The magnitude of spatial distribution is decreased for increase in the level of decomposition and can be seen in Fig. 4, while the dimension of the SDGs feature vector increase exponentially. Hence, it can be said that to get the better and more effective spatial distribution, the higher level of decomposition is not a good approach in respect of effect as well as dimension. Therefore, to enhance the effect of SDGs with less computation as compared to level 3 a modified approach of computation of spatial distribution is proposed, which is explained in Algorithm 1.

Fig. 4 shows the spatial distribution variation at various levels and the highest level is 3, where the spatial distribution of an image shows that the magnitudes of the histogram are decreasing vary fast as compared to other levels (0, 1, and 2). A histogram of a mixed level (modified) of the same AESI is also presented in the same figure, where the magnitude of the histogram of spatial distribution is comparatively higher than the level 3 with the lesser dimension of the feature vector. The computation of mixed (modified) level spatial distribution is as explained in Algorithm 2.

Algorithm 1: Computation of modified SDGs

Input: Input an AESI $\mathrm{A_E(x,y)}$ as computed using Eq. 2.

Step1. Crop the ROI of AESI and denoted as $\mathrm{R_E(x,y)}$.

Step2. Compute the magnitude and gradient of each pixel of $\mathrm{R_E(x,y)}$ the image at different decomposition levels (v) using $\mathcal{M}(x,y) = \sqrt{R_{E_x}(x,y)^2 + R_{E_y}(x,y)^2}$ and $\theta(x,y) = \arctan\left[\frac{R_{E_y}(x,y)}{R_{E_x}(x,y)}\right]$.

Step3. Quantize the computed magnitude of intensity at various levels (v) into K- orientation bins.

Step4. Sum all the regions together at level (v) $\mathrm{f_{SDGs}} = \mathrm{K}\sum_{\mathrm{v}} 4^{\mathrm{v}}$

Step 5. Concatenate the level (0, 1, 2) of SDGs together and a modified (mixed) SDGs feature vector is as: $\mathrm{f_{MSDGs}} = \mathrm{K}\left(\underbrace{\sum_{\mathrm{v}} 4^{\mathrm{v}}}_{\text{level v=0}} ; \underbrace{\sum_{\mathrm{v}} 4^{\mathrm{v}}}_{\text{level v=1}} ; \underbrace{\sum_{\mathrm{v}} 4^{\mathrm{v}}}_{\text{level v=2}}\right)$.

Output: The histogram of modified SDGs feature vector as shown in Fig. 4.

2) SDPs

The SDPs of an AESI is used to compute the sum of directional pixels for representing the shape of an action along x and y directions and variations of these values are distinct for different actions, which can be seen in the Fig. 5. The computation SDPs in the $x-y$ direction is defined as:

$$H_x(k) = \sum_{l=0}^{Q-1}\frac{A_E(k,l)}{\max(A_E(k))}, G_y(l) = \sum_{k=0}^{P-1}\frac{A_E(k,l)}{\max(A_E(l))} \quad (7)$$

where P and Q are the number of rows and columns of the

2379-8920 (c) 2016 IEEE. Personal use is permitted, but republication/redistribution requires IEEE permission. See http://www.ieee.org/publications_standards/publications/rights/index.html for more information.

This article has been accepted for publication in a future issue of this journal, but has not been fully edited. Content may change prior to final publication. Citation information: DOI 10.1109/TCDS.2016.2577044, IEEE Transactions on Cognitive and Developmental Systems

AESIs, respectively. To eliminate the effects of noise in x and y direction, the mean of SDPs are calculated as:

$$\mu_x = \frac{1}{m}\sum_{i=1}^{m} H_x(i), \mu_y = \frac{1}{n}\sum_{j=1}^{n} G_y(j) \quad (8)$$

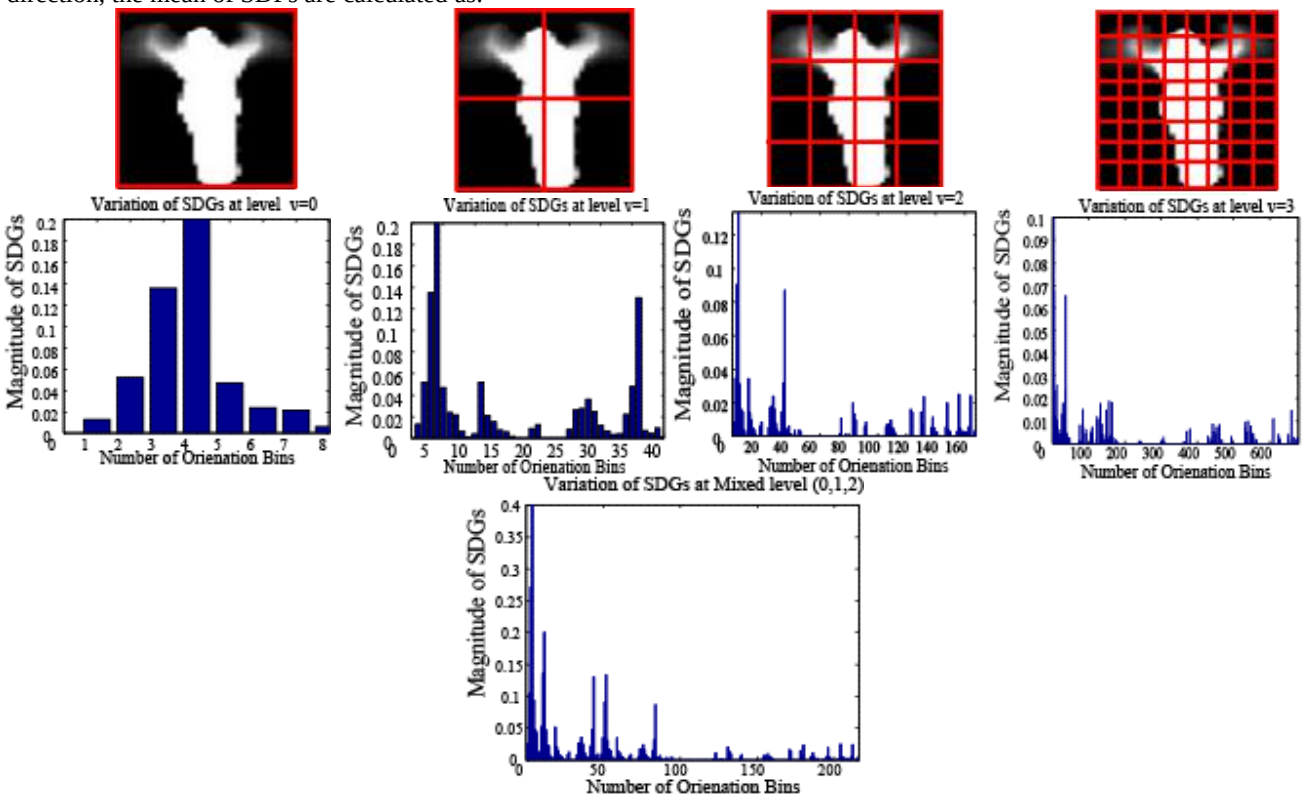
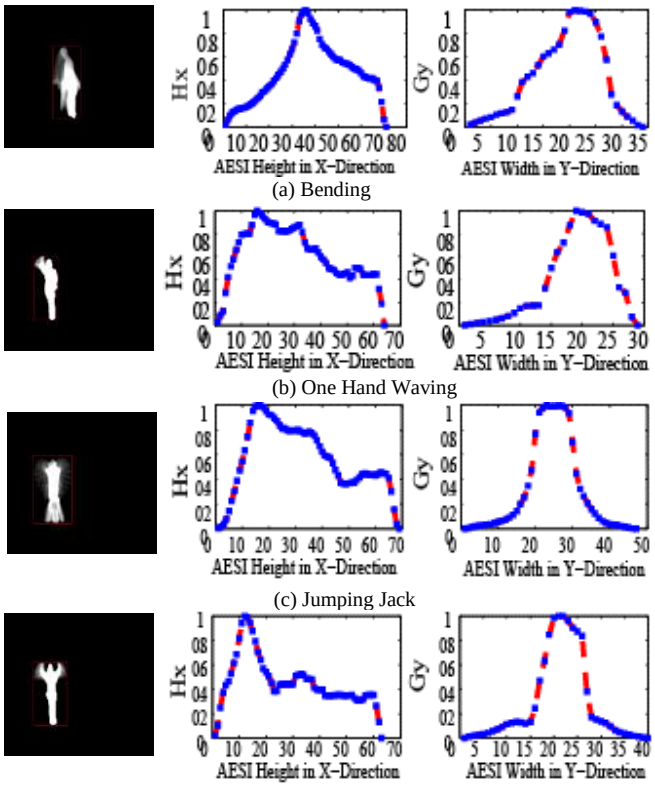


Fig. 4. Representation of levels composition and spatial distributions



(a) Bending

(b) One Hand Waving

(c) Jumping Jack

(d) Two Hand Waving

Fig. 5. Show in Column 1: AESI of dirrenert human activties, Column 2: SDPs value variations in the x-direction and Column 3: SDPs value variations in the y-direction.

where m and n are the number values in x-y direction SDPs. The mean values of SDPs are exemplified as a feature: $\mathcal{F}_d = [\mu_x, \mu_y]$.

In Fig.5, the variation of SDPs values of different activities are presented. The SDPs values variation in horizontal and vertical directions are different for different activities, and these variations correspond to the true reflection the shape of AESI like in the case of two hand wave activity, peak at the centre shows more variation of SDPs as a move in column wise (y-pixel). As a move in the x-axis, it represents the existence of more pixels in the upper portion (x-pixel). Similarly, for bending activity, the major part of the information is present in the lower half of the image and thus, there are peaks in the second half of the graph. If the shape of any object is constant is x-y direction then there wolud not any variation in the SDPs.

The SDGs and SDPs features are mixed with the motion based rotational feature, which is calculated on the binary silhouettes of the human body poses using the RT.

C. Rotation Features

The rotational features of the human activity are computed using RT and the properties of RT as depicted in Fig. 6 reveals that it is robust to the translation and scaling. The sensitivity of the RT can be observed from the Fig. 6, where the variation in rotation reflects a higher deviation in the RT signal. The discernable capability of RT can also be observed in the Fig. 7, where the 3D and 2D representation of RT signals are different for different types of activities. Hence, RT is used to

2379-8920 (c) 2016 IEEE. Personal use is permitted, but republication/redistribution requires IEEE permission. See http://www.ieee.org/publications_standards/publications/rights/index.html for more information.

This article has been accepted for publication in a future issue of this journal, but has not been fully edited. Content may change prior to final publication. Citation information: DOI 10.1109/TCDS.2016.2577044, IEEE Transactions on Cognitive and Developmental Systems

calculate the rotational based orientation information of the human silhouettes and also the performance of RT is proven for the representation of abnormal human activities [29], which have more rotation as compared to the translation. Tabbone *et al.* [43] presented the RT, and defined that RT is an integral transform of the squared values of Radon transform (R_d). It characterizes the features in compressed fashion by transforming 2D representation in to 1-D of R_d. The RT is defined as:

$$R(\theta) = \int_{-\infty}^{\infty} R_d^2(\rho, \theta) \partial\rho \quad (9)$$

where R_d of a binary human silhouette image $\mathcal{I}(x, y)$ is expressed as:

$$R_d(\rho, \theta) = \int_{-\infty}^{\infty} \int_{-\infty}^{\infty} \mathcal{I}(x, y).\delta(\rho - xcos\theta - ysin\theta)\, \partial x \partial y \quad (10)$$

where $\rho \in [-\infty, \infty]$ is the perpendicular distance of the Radon line from the origin expressed as $\rho = xcos\theta + sin\theta$, $\theta \in [0, \pi)$ is the range of θ in which R_d offers the directional features of the image $\mathcal{I}$ and $\delta(.)$ is the Dirac delta function. The normalization of RT is defined to improve the likeness and shows the features in a squeezed manner as follows:

$$R_{norm}(\theta) = \frac{\int_0^{\pi} R(\theta) d\theta}{\max(R(\theta))} \quad (11)$$

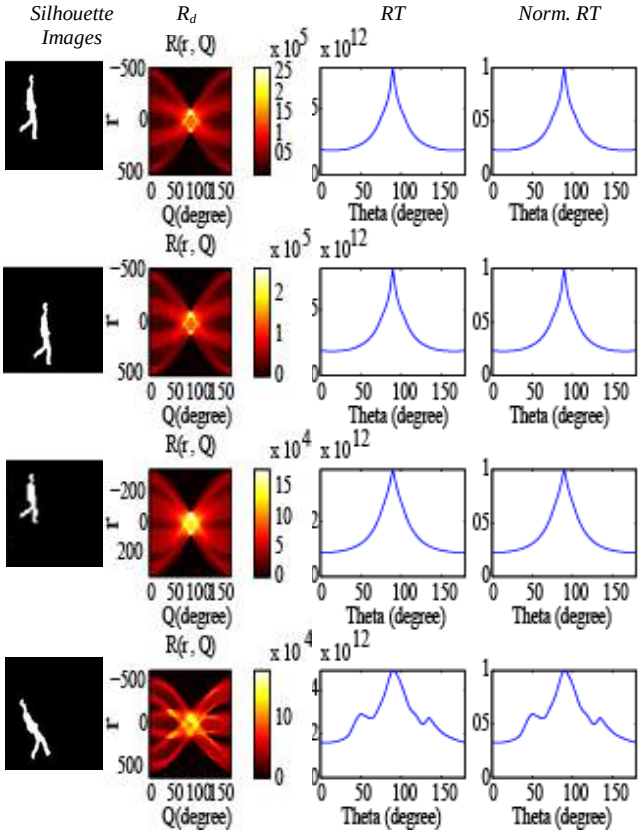
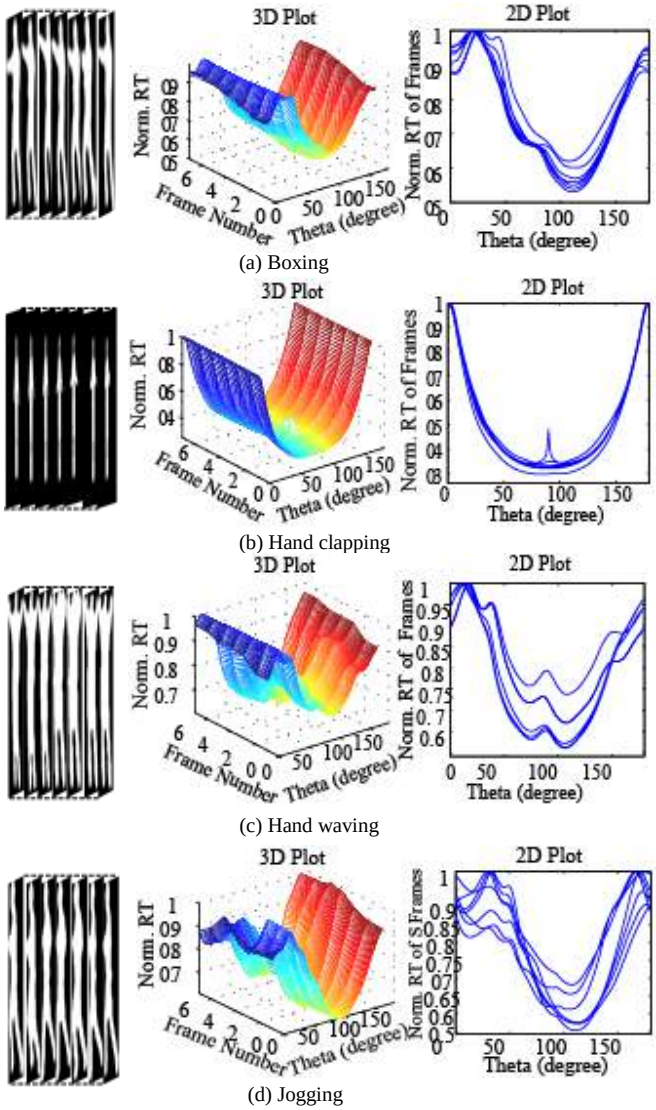


Fig.6. The depiction of RT properties. Column 1: Original silhouette image, translated, scaled, and rotated, Column 2: Radon transform (R_d), Column 3: RT signal and Column 4: Normalized RT signal.

Using the RT, motion features are computed by selecting the key poses of the human silhouettes. The key poses are chosen on the basis of high energy of the human silhouette frames. To compute energy of frame, a total number of white pixel count in the silhouette frame is determined. The benefit of key poses is to reduce the redundancy of silhouette frames and compactness in representation. These key poses are extremely discerning among all the frames of the video sequences. For convenience, eleven keyframes are chosen for the computation of motion feature. The size of binary silhouette frames are selected 50×50 and hence after concatenation; it is represented as1×2500. When RT is applied on these frames, then the dimensions of silhouette image is 1×180, and for an action representation of the video, the size of the feature vector is 11×180. Additional, to get a compact representation of feature vector, the Principal component analysis (PCA) [44] is applied, which reduces the dimension of the feature vector to the size 1×11.



(a) Boxing

(b) Hand clapping

(c) Hand waving

(d) Jogging

Fig. 7. Representation of RT for different human activities: Column 1: Silhoutte frames, Column 2: 3D-Normalized RT and Column 3: 2D projection of Normalized RT

2379-8920 (c) 2016 IEEE. Personal use is permitted, but republication/redistribution requires IEEE permission. See http://www.ieee.org/publications_standards/publications/rights/index.html for more information.

This article has been accepted for publication in a future issue of this journal, but has not been fully edited. Content may change prior to final publication. Citation information: DOI 10.1109/TCDS.2016.2577044, IEEE Transactions on Cognitive and Developmental Systems

D. Final Feature Map Model

The feature map model (F_{Map}) is developed by participating the feature set obtained in the sub section *B* and *C*. The flow of mixing of feature vectors are as shown in Fig. 8.

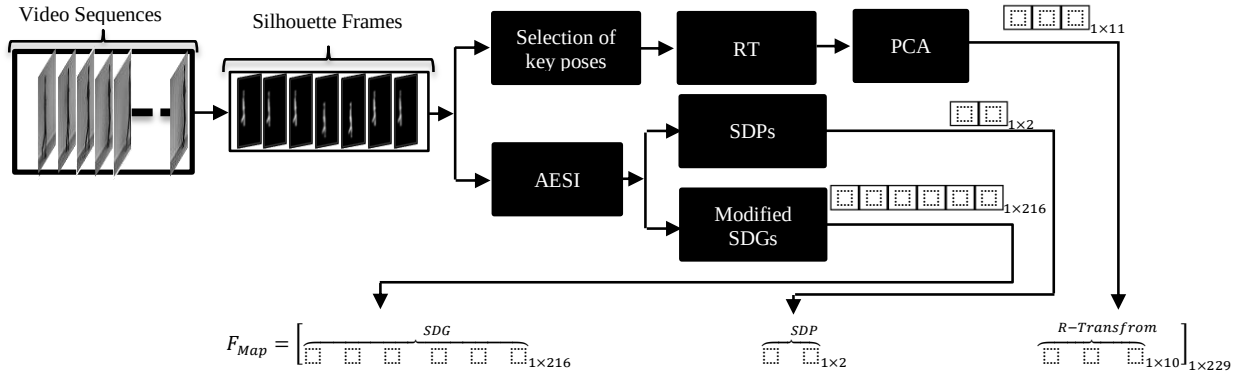


Fig. 8. Depiction of feature map model

The shape based SDGs and SDPs feature vectors are united with the rotation feature vectors which is calculated using the RT. The grouping of shape and rotation formulates, a unique descriptor for the depiction of human activity. The SDGs and SDPs feature vectors are calculated as described in sub section *B* and *C* and have a dimension of 1×216 and 1×2, correspondingly. Moreover, these feature vectors are concatenated with RT features vector, which have the size of 11×180. Finally, the SDGs, SDPs and RT feature vectors are concatenated and which gives the resultant the feature map model of the size [1×216+1×2+1×11]=[1×229]. The performance of descriptor is estimated in terms of classification accuracy by performing an experiment using a hybrid classification model.

E. Hybrid Classification Model

To enhance the recognition accuracy, a hybrid form of "SVM-NN" classification model is used in [45] and as shown in Fig. 9, which utilizes the individual benefits of SVM and K-NN model.

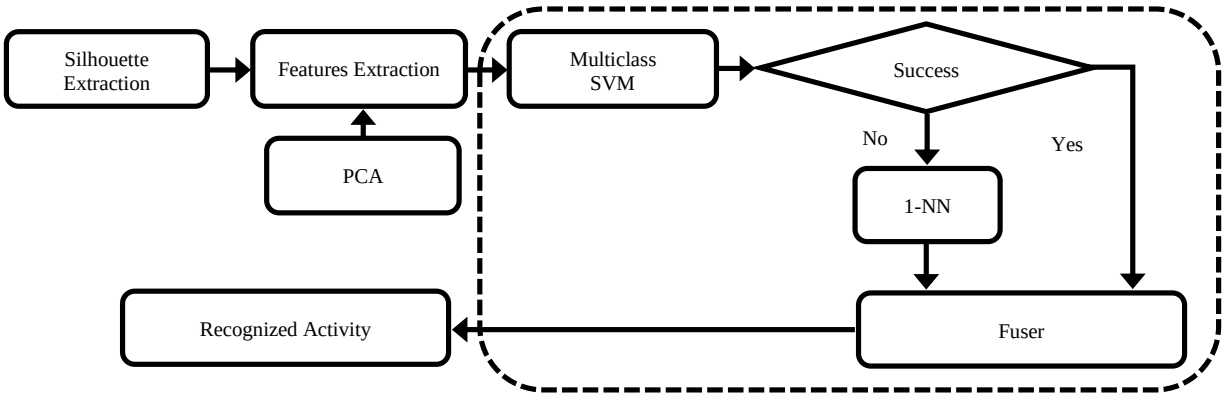


Fig.9 Hybrid classification model for HAR.

A hybrid classification model presented in [46] uses K-NN model for initial pruning of the data samples which makes the cluster of sample points of the similar classes and then SVM is used for the prediction on smaller set samples. In other words, it can be said that KNN is used for creating optimal decision hyperplane for SVM. A recent model [47] on SVM-KNN is developed to predict the stock market, where SVM works as a classification model and K-NN works as a prediction model. The prediction is based on the trained samples of SVM. In our method, keeping the issues of SVM optimal hyperplane design, a simple and effective approach of classifying samples based on the empirical testing of datasets is created to classify human activities, which offers certain benefits such as: no need to handle design of optimal hyperplane, keep the generalization proficiency of SVM and avoid the over fitting problem of KNN.

The K-NN classifier [48] picks the K-closest samples of training feature set to the new instance, and the nearest class having highest voting is mapped to test instance. The major advantages of this classifier is its non-parametric nature. It can easily classify the higher dimensional data without any assumption.

The SVM is a machine learning classifier built on the structural risk minimization principle [49]. For the human activity classification, it is one of the widely [50] used classifier. The term support vectors are features of the samples, which are close to the hyperplane of an SVM. Therefore, the determination of the location of most important data is near the hyperplane and it is formed by the set of lines drawn between the class samples.

A hybrid classification model is developed, which comprises SVM and K-NN classifier. The support vectors are samples of feature set, which are close to the decision

2379-8920 (c) 2016 IEEE. Personal use is permitted, but republication/redistribution requires IEEE permission. See http://www.ieee.org/publications_standards/publications/rights/index.html for more information.

This article has been accepted for publication in a future issue of this journal, but has not been fully edited. Content may change prior to final publication. Citation information: DOI 10.1109/TCDS.2016.2577044, IEEE Transactions on Cognitive and Developmental Systems

boundary and play a decisive role in the classification of a test sample. If a particular test sample is close to the hyperplane, then an accurate classification is not always possible, and SVM may classify these sample inaccurately. Therefore, in this classification model, the wrongly classified samples are further classified by clustering these samples.

It is also vital to mention here that the wrongly classified test samples through SVM, which are close to the hyperplane, become the representative points for K-NN. These wrongly classified samples are further classified using the 1-NN classifier, and if the 1-NN correctly classifies any wrongly classified sample of SVM, then the original classification result obtained by SVM is updated. Otherwise, it remains unaltered. Hence, by use of multiple classifications, the overall classification accuracy can be improved.

The performance of the hybrid classifier is evaluated using the model of HAR system whose block diagram is as shown in Figure 10, where the dotted box is the hybrid classifier model. The proposed model is the partial cascading of two classifiers (SVM, KNN), where the human activity feature sets are extracted from human silhouettes and subsequently, these sets are dimensionally reduced by PCA. Further, the reduced feature sets are used for training and testing of the SVM classifier. The test scheme used for the classification of these feature sets is leave-one-out cross-validation (LOOCV).

In the LOO scheme, the samples of one class are input together, and the result is predicted by the classifier based on the training. If there are N-number of classes, then the testing is performed N times, and a confusion matrix of N×N order is formed and passed to the fuser unit. The confusion matrix consists of the predicted class samples against the input class samples in the form of true positive (TP), true negative (TN), false positive (FP), and false negative (FN).

The correctly predicted sample are stored as TP and wrongly predicted sample are stored as FN. The FN samples of each class are further classified using the 1-NN classifier, and if any sample of FN is classified as a TP sample category, then the original confusion matrix having TP sample values of each class is updated by the fuser unit, else it remains unchanged. Hence, in this way the overall accuracy is improved. The detailed performance analysis of the hybrid classifier is presented in the subsequent section.

IV. EXPERIMENTAL RESULT, COMPARISON AND ANALYSIS

In order to evaluate the performance of the proposed framework, an experiment is done using three publicly available datasets i.e. Weizmann [16], KTH [34], and Ballet [33]. The recognition accuracy is computed through a hybrid classification model of SVM-NN using leave-one-out cross-validation strategy for all data sets. In leave-one-out strategy, one sequence is used as a test video while others are used as training sets. This procedure continues until all the sequences are tested for a single activity and it further proceeds for other activities. The advantage of this method is that whole information of the data set is used to calculate the accuracy. The effectiveness of proposed approach is evaluted using comparison with the earlier techniques; a comparison table is presented with all datasets at the similar state-of-the-art in term of average recognition rate (ARR). The classification strategies used in the different techniques are quite similar and are named as leave one out cross validation (LOOCV), leave-one-sequence-out cross validation (LOSOCV), leave-one-video-out cross validation (LOVOCV) and leave-one-person-out cross validation (LOPOCV). The ARR is computed using Eq.12.

$$\text{ARR} = \frac{\text{TP+TN}}{\text{TP+TN+FP+FN}} \times 100 \text{ (In percentage)} \quad (12)$$

A. *Weizmann Dataset*

Weizmann dataset is one of the commonly used preparatory human action datasets for the recognition of human action. This dataset is presented by Gorelick et al. [16], and the recording setting of the dataset is at a frame rate of 25 fps and size of the frame is 144×180 with a total of 90 videos. The dataset has 9 actors, each executing ten dissimilar actions which are grouped as walk, run, jump_jack, bend, jump forward on one leg, jump, jumping in place, sideways jump, one hand wave, and two hand wave and the sample images of these actions are as shown in Fig. 10.

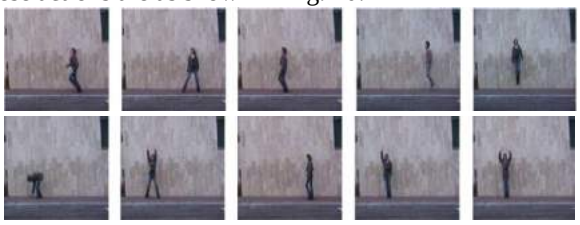


Fig. 10. Sample frames from Weizmann human action dataset.

1) *Recognition Result and Comparison on Weizmann Dataset*

In Weizmann dataset, the extraction of binary silhouettes does not offer great challenge due to the clean background and stable environmental setting. Hence, an accurate silhouette is extracted from all the videos of the dataset, which depicts the effectiveness of the proposed approach. The result presented for this dataset gives the effectiveness of overall approach as well as the effect of SDGs vector at different levels.

SDGs Levels	ARR (%)
0	65
1	85
2	97.7
m	***100***

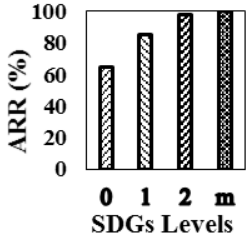


Fig. 11 ARR achieved on Weizmann data set at different level of SDGs

From Fig.11, the recognition accuracy increases with the increase of the level of computation of SDG vector. At level '0' the value of ARR indicates the minimum effect of SDG vector, which results in the ARR of 65%, due to the dominance of RT and variation directional pixel feature vector. At the higher level (2, m) the ARR is 100%, which indicates that the computation of spatial distribution is much finer at a higher level. The highest recognition accuracy is compared with the similar state-of-the-art and is shown in

2379-8920 (c) 2016 IEEE. Personal use is permitted, but republication/redistribution requires IEEE permission. See http://www.ieee.org/publications_standards/publications/rights/index.html for more information.

This article has been accepted for publication in a future issue of this journal, but has not been fully edited. Content may change prior to final publication. Citation information: DOI 10.1109/TCDS.2016.2577044, IEEE Transactions on Cognitive and Developmental Systems

Table I.

TABLE 1
COMPARISON OF ARR WITH THE SIMILAR STATE-OF-THE-ART METHODS

Method	Classifier	Test Scheme	ARR (%)
Gorelick et al. [16]	*KNN*	*LOOCV*	*97.5*
Chaaraoui et al. [51]	*KNN*	*LOSOCV*	*92.8*
Wu & Shao [52]	*SVM*	*LOSOCV*	*97.78*
Goudelis et al. [53]	*SVM*	*LOPOCV*	*95.42*
Melfi et al. [54]	*SVM*	*LOOCV*	*99.02*
Touati & Mignotte [55]	*KNN*	*LOOCV*	*92.3*
Yao et al. [56]	*FUZZY*	*LOOCV*	*94.03*
Proposed Method	***Hybrid***	***LOOCV***	***100***

The experimental setting used in this experiment is similar to the Gorelick et al. [16]. In all these methods [16] [51] [52] [54] [55] [56], the inputs are the human silhouette of activity. Hence, there is a need for effective background subtraction in all these methods. The recognition accuracy achieved through proposed approach is higher than that of many earlier techniques.

B. KTH Dataset

This dataset was introduced by Schuldt et al. [34] and is a more challenging dataset as compared to the Weizmann dataset. The sample frames of the dataset are as depicted in Fig 12. The dataset consists of six basic activities, namely; Walking (k1), Jogging (k2), Running (k3), Boxing (k4), Hand-waving (k5), and Hand-clapping (k6). Each activity has 100 videos for four different scenarios (S1, S2, S3 and S4) in different light conditions, indoor and outdoor conditions. All these video sequences are recorded in a uniform background with a static camera of frame rate 25fps and further down-sampled to the spatial resolution of 160x120 pixels. The recording conditions of the videos in the KTH data set are not stationary and there is a significant amount of camera movement and lighting effects in some cases. Therefore, the silhouette extraction is not straight forward and simple background subtraction method may not be suitable. Hence, for the silhouette extraction, a texture based segmentation method is utilized.



Fig.12. Sample images of KTH dataset.

1) Recognition Result and Comparison on KTH Dataset

KTH dataset is more challenging as compared to Weizmann dataset in terms of recording conditions, which includes zoom in and zoom out of the camera, variation in viewing angle, and lighting conditions. Due to these variations, the extraction of the silhouette is difficult as compared to the previous data set. Therefore, the less ARR is achieved.

As it is seen in Fig.11, the highest ARR is achieved at level 2 and 'm'. Hence, for this data set the ARR is computed at the level of 2 and 'm'. The ARR achieved on this data set is as presented in Table II.

TABLE II
RECOGNITION RESULT FOR KTH DATASET

Activity \ SDG level	k1	k2	k3	k4	k5	k6	ARR (%)
2	*100*	*92.5*	*90*	*100*	*100*	*92.5*	*95.83*
'm'	*100*	*95*	*92.5*	*100*	*100*	*95*	*97.08*

The ARR achieved on this dataset is 97.08% which is higher than the ARR achieved at the level 2. Moreover, from Table II, the recognition accuracy of the similar classes like Jogging, and Running at the 'm' level is boosted. Hence, it is concluded that the SDGs computation at 'm' level is more effective than the individual levels. The highest ARR is compared with the comparable state-of-the-art datasets and presented as in Table III.

TABLE III
COMPARISON OF ARR WITH THE SIMILAR STATE-OF THE-ART METHODS

Method	Classifier	Test Scheme	ARR (%)
Saghafi & Rajan [57]	*KNN*	*LOOCV*	92.6
Goudelis et al. [53]	*SVM*	*LOPOCV*	93.14
Melfi et al. [54]	*SVM*	*LOOCV*	95.25
Rahman et al. [58]	*KNN*	*LOOCV*	94.49
Benmokhtar [59]	*SVM*	*LOOCV*	92.50
Vishwakarma & Kapoor [11]	*SVM-NN*	*LOOCV*	95.5
Proposed Method	***Hybrid***	***LOOCV***	**97.08**

C. Ballet Dataset

Ballet dataset is introduced by Fathi & Mori [33], which consists of highly complex ballet movements of different actors. The dataset is obtained from instructional ballet DVD. The background in the dataset is simple, but the actions performed are complex. Each video sequence consists of only one actor. The dataset consists of 44 video sequences, and each sequence is pre-labelled into eight different actions. These actions are labelled as hopping (b1), jumping (b2), left-to-right hand opening (b3), leg swinging(b4), right-to-left hand opening (b5), standing hand opening (b6), standing still (b7) and turning (b8). The sample frames of the dataset are as depicted in Fig.13.

2379-8920 (c) 2016 IEEE. Personal use is permitted, but republication/redistribution requires IEEE permission. See http://www.ieee.org/publications_standards/publications/rights/index.html for more information.

This article has been accepted for publication in a future issue of this journal, but has not been fully edited. Content may change prior to final publication. Citation information: DOI 10.1109/TCDS.2016.2577044, IEEE Transactions on Cognitive and Developmental Systems

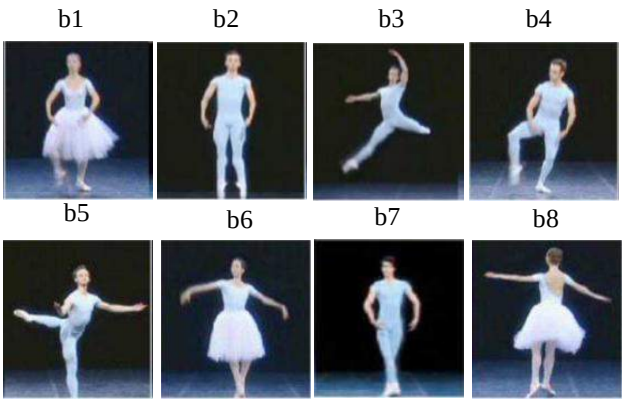


Fig. 13. Images of the Ballet data set depicting eight movement of actions

1) Recognition Result and Comparison on Ballet Dataset

The recognition accuracy is computed on this dataset is at level 'm' because it is seen from the earlier experiment that the mixed 'm' gives the highest recognition accuracy. The detail of classification result of different activities of this dataset is presented in Table IV. The highest ARR achieved is 94.5%, which is less than the earlier datasets used in this work. The key reason for the decrease in the accuracy is the complex motion pattern, which differentiates due to execution of the motion from actor to actor and high misclassification error is introduced due to the "hopping" movement as it is confused with a much-related movement "jumping". It is also observed that the formation of the AESI is difficult because of the complexity.

TABLE IV
RECOGNITION RESULT FOR BALLET DATASET

Activity \ SDG level	b1	b2	b3	b4	b5	b6	b7	b8	ARR (%)
'm'	*90*	*72*	*100*	*100*	*100*	*100*	*100*	*94*	*94.5*

TABLE V
COMPARISON OF ARR WITH THE SIMILAR STATE-OF THE-ART METHODS

Method	Classifier	Test Scheme	ARR (%)
Fathi & Mori [33]	*Adaboost*	*LOOCV*	*51*
Wang & Mori [60]	*S-CTM*	*LOO*	*91.3*
Guha & Ward [61]	*RSR*	*LOO*	*91.1*
Ming et al. [62]	*RVM*	*LOO*	*90.8*
Iosifidis et al. [63]	*SVM*	*LOO*	*91.1*
Vishwakarma & Kapoor [45]	*SVM-NN*	*LOOCV*	*94.0*
Proposed Method	***Hybrid***	***LOOCV***	***94.5***

The ARR achieved on this dataset is compared with the original work [33] on this dataset as well as the others on the comparable state-of-the-art as presented in Table V. The experimental settings used for this dataset is similar to the original paper. The performance of proposed approach can be clearly seen from the comparison Table V, where the recognition rate achieved through our approach is comparatively fair, and performance is significantly better.

D. Assessment of the Experimental Results

The depth analysis of the SDGs feature vector with the integration of RT and directional variation of pixels reveals promising annotations:

- The recognition accuracy achieved with our approach is better than that of the many earlier existing approaches. Hence, the proposed approach has a good discriminative power of representing different kinds of activities and also the discriminating power is increased with an increase in the number of levels of SDGs computation.
- The final feature descriptor formed with the integration of mixed level 'm' of SDGs, SDPs and RT is superior in terms of recognition accuracy as compared to the individual level (0, 1, 2) of SDGs features integration.
- Significant improvement in the recognition accuracy on KTH and Ballet data set shows the robustness of proposed approach against the variation of lighting conditions, intra-class dissimilarity of actions in terms of speed, and spatiotemporal scaling, the camera zooming in and zooming out, clothing, etc.
- As the number of key poses increases for the motion estimation information using RT, the dimension of the feature vector increases and the speed of computation also drops significantly.
- For computation of shape using SDGs, an increase in the number of levels of bins gives improved accuracy in the recognition rate, but the dimension of the distribution vector is increased rapidly, which makes the system slow.

V. CONCLUSION

In this paper, a human action recognition approach using shape and motion features of the human silhouette in the video sequence is presented, which addresses the problem of less recognition rate under challenging environmental conditions and complex motion pattern. The shape information is computed through modified SDGs and the SDPs of AESI. The motion feature is computed by applying RT on the key poses of the human silhouette. As the increase in the decomposition levels of SDGs feature vector, the quality and effectiveness of spatial distribution is less, while the complexity increases exponentially. The RT computed feature vector results in high dimension and hence, a dimension reduction technique is applied for the compact representation and improved classification.

The approach is based on the human silhouette. Hence, there is a strong need for effective segmentation technique to extract the foreground object as it is very difficult to recognize actions of multiple persons in a single video. The parameters like the number of levels of SDGs computation and the number key frames used for motion estimation may be optimized for a higher recognition accuracy with minimal computation.

For future work, a more robust technique can be developed for the HAR, which does not require the segmentation of object. A still image based action recognition may lead to a new destination of HAR, which would require only visual information to recognize the human action.

There are some practical applications, where this approach can be usefull in developing an intelligent system, which can perform the subsequent tasks: (i) To provide assistance to perform the perfect physical exercise, (ii) Gait analysis, which can open the dam for biometric identification, and study of Gait disorder and (iii) To detect the abnormal activity for the elderly monitoring system.

2379-8920 (c) 2016 IEEE. Personal use is permitted, but republication/redistribution requires IEEE permission. See http://www.ieee.org/publications_standards/publications/rights/index.html for more information.

This article has been accepted for publication in a future issue of this journal, but has not been fully edited. Content may change prior to final publication. Citation information: DOI 10.1109/TCDS.2016.2577044, IEEE Transactions on Cognitive and Developmental Systems

REFERENCES

[1] J. Agrawal and M. Rayoo, "Human Activity Analysis: A Review," *ACM Computing Survey*, pp. 16-43, 2011.

[2] D. K. Vishwakarma and R. Kapoor, "An efficient interpretation of hand gestures to control smart interactive television," *International Journal of Computational Vision and Robotics*, pp. 1-18, 2015.

[3] A. A. Chaaraoui, P. Pérez and F. F. Revuelta, "A review on vision techniques applied to Human Behaviour Analysis for Ambient-Assisted Living," *Expert Systems with Applications*, vol. 39, pp. 10873-10888, 2012.

[4] M. Ziaeefard and R. Bergevin, "Semantic human activity recognition: A literature review," *Pattern Recognition*, vol. 48, no. 8, pp. 2329-2345, 2015.

[5] R. Poppe, "A survey on vision-based human action recognition," *Image and Vision Computing*, vol. 28, no. 6, pp. 976-990, 2010.

[6] D. Weinland, R. Ronfard and B. Edmond, "A survey of vision-based methods for action representation, segmentation and recognition," *Computer Vision and Image Understanding*, vol. 115, no. 2, pp. 224-241, 2011.

[7] L. Shao, R. Gao, Y. Liu and H. Zhang, "Transform based spatio-temporal descriptors for human action recognition," *Neurocomputing*, vol. 74, no. 6, pp. 962-973, 2011.

[8] M. Bregonzio, T. Xiang and S. Gong, "Fusing appearance and distribution information of interst points for action recognition," *Pattern Recognition*, vol. 45, no. 3, pp. 1220-1234, 2012.

[9] D. Zhao, L. Shao, X. Zhen and Y. Liu, "Combining appearence and structural features for human action recogntion," *Neurocomputing*, vol. 113, no. 3, pp. 88-96, 2013.

[10] J. Dou and J. Li, "Robust human action recognition based on spatio-temporal descriptors and motion temopral templates," *Optik*, vol. 125, no. 7, pp. 1891-1896, 2014.

[11] D. K. Vishwakarma and R. Kapoor, "Integrated Approach for Human Action Recognition using Edge Spatial Distribution, Direction Pixel, and R -Transform," *Advanced Robotics*, vol. 29, no. 23, pp. 1551-1561, 2015.

[12] D. K. Vishwakarma and R. Kapoor, "Simple and intelligent system to recognize the expression of speech disabled person," in *4th IEEE international Conference on Intelligent Human Computer Interaction*, Kharagpur, India, 2012(11).

[13] I. Laptev, "On Space-Time Interest Points," *International Journal of Computer Vision*, vol. 64, no. 2/3, pp. 107-123, 2005.

[14] P. Dollar, V. Rabaud, G. Cottrell and S. Belongie, "Behavior Recognition via Sparse Spatio-Temporal Features," in *Proceedings 2nd Joint IEEE International Workshop on VS-PETS*, Beijing, 2005.

[15] H. Jhuang, T. Serre, L. Wolf and T. Poggio, "A Biologically Inspired System for Action Recognition," in *International Conference on Computer Vision*, Rio de Janeiro, 2007.

[16] L. Gorelick, M. Blank, E. Shechtman, M. Irani and R. Basri, "Actions as space-time shapes," *IEEE Transactions on Pattern Analysis and Machine Intelligence*, vol. 29, no. 12, pp. 2247-2253, 2007.

[17] J. Nibeles, H. Wang and L. Fei-Fei, "Unsupervised learning of human action categories using spatial-temporal words," *International Journal of Computer Vision*, vol. 79, no. 3, pp. 299-318, 2008.

[18] L. Onofri, P. Soda and G. Iannello, "Multiple subsequence combination in human action," *IET Computer Vision*, vol. 8, no. 1, pp. 26-34, 2014.

[19] X. Zhen, L. Shao and X. Li, "Action recognition by Spatio-temporal oriented energies," *Information Sciences*, vol. 281, pp. 295-309, 2014.

[20] G. Somasundaram, A. Cherian, V. Morellas and N. Papanikolopoulos, "Action recognition using global spatio-temporal features derived from sparse representations," *Computer Vision and Image Understanding*, vol. 123, pp. 1-13, 2014.

[21] L. Shao, X. Zhen, D. Tao and X. Li, "Spatio-Temporal Laplacian Pyramid Coding for Action Recognition," *IEEE Transactions on Cybernetics*, vol. 44, no. 6, pp. 817-827, 2014.

[22] A. F. Bobick and J. W. Davis, "The recognition of human movement using temporal templates," *IEEE Transactions on Pattern Analysis and Machine Intelligence*, vol. 23, no. 3, pp. 257-267, 2001.

[23] A. A. Efros, A. C. Berg, G. Mori and J. Malik, "Recognizing action at a distance," in *IEEE International Conference on Computer Vision*, 2003.

[24] T.-Y. Hung, J. Lu, J. Hu, Y.-P. Tan and Y. Ge, "Activity based Human Identification," in *IEEE International Conference on Acoustics, Speech and Signal Processing (ICASSP)*, Vancouver, BC, 2013.

[25] M. Ahmad and S.-W. Lee, "Variable silhouette energy image representations for recognizing human actions," *Image and Vision Computing*, vol. 28, no. 5, pp. 814-824, 2010.

[26] T. Whytock, A. Belyaev and N. Robertson, "GEI + HOG for Action Recognition," in *Fourth UK Computer Vision Student Workshop*, 2012.

[27] L. Shao, L. Ji, Y. Liu and J. Zhang, "Human action segmentation and recognition via motion and shape analysis," *Pattern Recognition Letters*, vol. 33, pp. 438-445, 2012.

[28] Y. Zhang, H. Lu, L. Zhang and X. Ruan, "Combining Motion and Appearance Cues for Anomaly Detection," *Pattern Recognition*, vol. 51, pp. 443-452, 2015.

[29] Z. Khan and W. Sohn, "Abnormal human activity recogntion system based on R-Transform and Kernel Discriminant Technique for Eldely Home Care," *IEEE Transactions on Consumer Electronics*, vol. 57, no. 4, pp. 1843-1850, 2011.

[30] D. K. Vishwakarma, R. Kapoor, R. Maheshwari, V. Kapoor and S. Raman, "Recognition of abnormal human activity using the changes in orientation of silhouette in key frames," in *2nd IEEE International Conference on Computing for Sustainable Global Development (INDIACom)*, Delhi, 2015.

[31] S. Sedai, M. Bennamoun and D. Q. Huynh, "Discriminative fusion of shape and appearance features for human pose estimation," *Pattern Recognition*, vol. 46, no. 12, pp. 3223-3237, 2013.

[32] A. Bosch, A. Zisserman and X. Munoz, "Representing shape with a spatial pyramid kernel," in *Proceedings of the 6th ACM international conference on Image and video retrieval*, New York, 2007.

[33] A. Fathi and G. Mori, "Action Recognition by Learning Mid-level Motion Features," in *Proc. of IEEE Conference on Computer Vision and Pattern Recognition*, 2008.

[34] C. Schuldt, I. Laptev and B. Caputo, "Recognizing Human Actions: a local SVM approach," in *Proc. of the International Conference on Pattern Recognition*, 2004.

[35] S. Brutzer, B. Hoferlin and G. Heidemann, "Evaluation of Background Subtraction Techniques for Video Surveillance," in *IEEE Conference on Computer Vision and Pattern Recognition (CVPR)*, 2011.

[36] R. Haralick, K. Shanmugam and I. Dinstein, "Textural Features for Image Classification," *IEEE Trasactions on Systems Man, and Cybernetics*, vol. 6, pp. 610-621, 1973.

[37] M. A. Tahir, A. Bouridane and F. Kurugollu, "An FPGA Based Coprocessor for GLCM and Haralick Texture Features and their Application in Prostate Cancer Classification," *Analog Integrated Circuits and Signal Processing*, vol. 43, no. 2, pp. 205-215, 2005.

[38] T. W. Chua, Y. Wang and K. Leman, "Adaptive Texture-Color based Background Subtraction for Video Surveillance," in *19 th IEEE International Conference on Image Processing (ICIP)*, Orlando, FL, 2012.

[39] M. Komorkiewicz and M. Gorgon, "Foreground object features extraction with GLCM texture descriptor in FPGA," in *IEEE Conference on Design and Architectures for Signal and Image Processing (DASIP)*, Cagliari, 2013.

[40] H. Tian, Y. Liu and J. H. Lai, "A Histogram-Based Chan-Vese Model Driven by Local Contrast Pattern for Texture Image Segmentation," in *International Conference on Pattern Recognition (ICPR)*, Stockholm, 2014.

[41] Q. Wu, Y. Gan, B. Lin, Q. Zhang and H. Chang, "An active contour model based on fused texture features for image segmentation," *Neurocomputing*, vol. 150, no. 3, pp. 1133-1141, 2015.

[42] J. Han and B. Bhanu, "Individual Recognition Using Gait Energy

2379-8920 (c) 2016 IEEE. Personal use is permitted, but republication/redistribution requires IEEE permission. See http://www.ieee.org/publications_standards/publications/rights/index.html for more information.

This article has been accepted for publication in a future issue of this journal, but has not been fully edited. Content may change prior to final publication. Citation information: DOI 10.1109/TCDS.2016.2577044, IEEE Transactions on Cognitive and Developmental Systems

Image," *IEEE Transactions on Pattern Analysis and Machine Intelligence*, vol. 28, no. 2, pp. 316-322, 2006.

[43] S. Tabbone, L. Wendling and J. P. Salmon, "A new shape descriptors defined on the Randon Transform," *Computer Vision and Image Understanding*, vol. 102, no. 1, pp. 42-51, 2006.

[44] I. T. Jolliffe, Principal Component Analysis, Springer-Verlag New York, 2002.

[45] D. K. Vishwakarma and R. Kapoor, "Hybrid classifier based human activity recognition using the silhouette and cells," *Expert Systems with Applications*, vol. 42, no. 20, pp. 6957-6965, 2015.

[46] H. Zhang, A. C. Berg, M. Maire and J. Malik, "SVM-KNN: Discriminative Nearest Neighbor Classification for Visual Category Recognition," in *IEEE Conference on Computer Vision and Pattern Recognition (CVPR)*, 2006.

[47] R. K. Nayak, D. Mishra and A. K. Rath, "A Naïve SVM-KNN based stock market trend reversal analysis for Indian benchmark indices," *Applied Soft Computing*, vol. 35, pp. 670-680, 2015.

[48] T. Cover and P. Hart, "Nearest neighbor pattern classification," *IEEE Transactions on Information Theory*, vol. 13, no. 1, pp. 21-27, 1967.

[49] V. N. Vapnik, "An overview of statistical learning theory," *IEEE Transactions on Neural Network*, vol. 10, no. 5, pp. 989-999., 1999.

[50] C. W. Hsu and C. J. Lin, "A Comparison of Methods for Multiclass Support Vector Machines," *IEEE Transactions of Neural Network*, vol. 13, no. 2, pp. 415-425, 2002.

[51] A. Chaaraoui, P. C. Perez and F. Revuelta, "Sihouette-based human action recognition using sequences of key poses," *Pattern Recognition Letters*, vol. 34, pp. 1799-1807, 2013.

[52] D. Wu and L. Shao, "Silhouette Analysis-Based Action Recognition Via Exploiting Human Poses," *IEEE Transactions on Circuits and Systems for Video Technology*, vol. 23, no. 2, pp. 236-243, 2013.

[53] G. Goudelis, K. Karpouzis and S. Kollias, "Exploring trace transform for robust human action recognition," *Pattern Recognition*, vol. 46, no. 12, pp. 3238-3248, 2013.

[54] R. Melfi, S. Kondra and A. Petrosino, "Human activity modeling by spatio temporal textural appearance," *Pattern Recognition Letters*, vol. 34, pp. 1990-1994, 2013.

[55] R. Touati and M. Mignotte, "MDS-Based Multi-Axial Dimensionality Reduction Model for Human Action Recognition," in *Proc. of IEEE Canadian Conference on Compter and Robot Vision*, 2014.

[56] B. Yao, H. Hagras, M. J. Alhaddad and D. Alghazzawi, "A fuzzy logic-based system for the automation of human behavior recognition using machine vision in intelligent environments," *Soft Computing*, vol. 19, no. 2, pp. 499-506, 2015.

[57] B. Saghafi and D. Rajan, "Human action recognition using Pose-based disriminant embedding," *Signal Processing: Image Communication*, vol. 27, pp. 96-111, 2012.



[58] S. Rahman, I. Song, M. K. H. Leung and I. Lee, "Fast action recognition using negative space features," *Expert Systems with Applications*, vol. 41, pp. 574-587, 2014.

[59] R. Benmokhtar, "Robust human action recognition scheme based on high-level feature fusion," *Multimedia Tools and Applications*, vol. 69, no. 2, pp. 253-275, 2014.

[60] Y. Wang and G. Mori, "Human Action Recognition by Semi-Latent Topic Models," *IEEE Transactions on Pattern Analysis and Machine Intelligence*, vol. 31, no. 10, pp. 1762-1764, 2009.

[61] T. Guha and R. K. Ward, "Learning Sparse Representations for Human Action Recognition," *IEEE Transactions on Pattern Analysis and Machine Intelligence*, vol. 34, no. 8, pp. 1576-1588, 2012.

[62] X. L. Ming, H. J. Xia and T. L. Zheng, "Human action recognition based on chaotic invariants," *Journal of South Central University*, vol. 20, pp. 3171-3179, 2013.

[63] A. Iosifidis, A. Tefas and I. Pitas, "Discriminant Bag of Words based representation for human action recognition," *Pattern Recognition Letters*, vol. 49, pp. 185-192, 2014.



Dinesh Kumar Vishwakarma (M'16) received his B.Tech. from Dr RML Avadh University, Faizabad, Uttar Pradesh, India, in 2002, M.Tech. from Motilal Nehru National Institute of Technology, Allahabad, Uttar Pradesh, India in 2005, and Ph.D. in Computer Vision from Delhi Technological University, Delhi, India in 2016. Presently, he is working as Assistant Professor, in the Department of Department of Electronics and Communication Engineering, Delhi Technological University, Delhi, India-110042. His research interest includes human action and activity recognition, hand gesture recognition and machine learning. He is reviewer of various IEEE/IET, Springer and Elsevier journals.

Kuldeep Singh (M'16) received his B.E. degree in Electronics & Communication Engineering from Government Engineering College, Ajmer, Rajasthan, India in 2004 and M. Tech. degree in Signal Processing from Delhi University in 2006. He works as scientist at Central Research Laboratory, Bharat Electronics Limited (Ministry of Defense, Government of India), India. His research interest includes image enhancement, sparse representation based image processing and pattern recognition. He is reviewer of various IEEE/IET, Elsevier and Taylor Francis journals.

2379-89 use is permitted, but republication/redistribution requires IEEE permission. See http://www.ieee.org/publications_standards/publications/rights/index.html for more information.

The Electricity Journal 29 (2016) 43–50

Contents lists available at ScienceDirect

The Electricity Journal

journal homepage: www.elsevier.com/locate/electr

Implementation of green supply chain management in India: Bottlenecks and remedies

Sheetal Soda*, Anish Sachdeva, Rajiv Kumar Garg

Department of Industrial and Production Engineering at the National Institute of Technology, Jalandhar, India

ARTICLE INFO

Article history:
Available online xxx

Keywords:
Green supply chain management
Power industry
Bottlenecks
Remedies

ABSTRACT

The Indian power industry has entered a transition from traditional operations to modern practices. An analysis of developments in Punjab shows how state-owned power companies have been in the vanguard in implementing a holistic model of green supply chain management that reduces losses and inefficiencies while also addressing environmental concerns.

© 2016 Elsevier Inc. All rights reserved.

1. Introduction

With their insatiable appetite for power, developed and developing economies all across the world are gearing up to augment their power generation capacities, at a potentially serious threat to the global environment. The power industry has been identified as the second-largest polluting industry, owing to greenhouse gas emissions caused by burning fossil fuels. The pollution caused by the industry is not limited to generation, but is manifested all through the supply chain. Thus, what is called green supply chain management (GSCM) finds extensive application in the power industry, and has the potential to deliver cleaner energy coupled with economic gains for organizations that adopt it. The concept, as applied to the power industry, has matured over a period of time, as various theories and models have been developed by researchers. Yet, there are still relatively unexplored areas of this discipline that could yield even greener supply chains.

Power companies are waking up to the fact that green operations are not only eco-friendly but make acute business sense, too. In India, a few power companies have reworked their supply chains, but much remains to be done by many others. The opportunities created by intensive GSCM practices for state-owned power companies (SOPCs) justify a comprehensive study of the area.

Until recently, the lion's share of activity has occurred at the state electricity boards (SEBs); few efforts have been made by the majority of power companies. Though the PSUs owned by the central government as well as new privately owned generators have exhibited interest in GSCM practices, the role of SEBs and other state-owned, state-level power utilities has not been very encouraging. Though constrained by regulations and a competitive market structure, the SOPCs are gearing up for a major push to absorb GSCM – not only because it addresses environmental concerns, but for the substantial savings it provides. With a sudden rise of environmental awareness over the past decade, a consensus is forming that issues of environmental pollution accompanying industrial development should be addressed together with supply chain management, thus contributing to the initiative of GSCM (Sheu et al., 2005).

This research looks to meet the following objectives:

- To study the existing supply chains of SOPCs in the state of Punjab, and
- To identify bottlenecks in the adoption of GSCM measures.

A study on GSCM practices prevalent in SOPCs, along with the areas where improvisation and modernization can be done, will help the SOPCs' managements in decisively dealing with the problems of losses and inefficiencies in a number of operational domains, while also addressing the environmental concerns.

2. Material and methods

GSCM is an environmentally conscious approach to the traditional concept of supply chain management, identifying eco-friendly practices at all steps of the supply chain (Walker et al., 2008). GSCM encompasses all phases of a product's life cycle, from extraction of raw materials to its designing, production, and distribution phases, and then to the use of the product by

* Corresponding author.
E-mail address: sheetugrey@gmail.com (S. Soda).

http://dx.doi.org/10.1016/j.tej.2016.05.003
1040-6190/© 2016 Elsevier Inc. All rights reserved.

consumers and its eventual disposal. Though the concept start getting acclaim in academic circles around the end of the 1980s, it was in the 1990s that it gained popularity among corporate and manufacturing enterprises as environmental management got integrated with ongoing SCM operations (Srivastava, 2007). But adoption is far trailing potential because it is a relatively recent concept, and because of the cost and technical complications attached to it. The implementation of GSCM practices is expected to result in improved environmental performance as measured by reductions in air emissions, effluent waste, solid waste, and consumption of toxic materials (Green et al., 2008). GSCM finds it applications not only in the manufacturing industry but in the service sector as well. The term "green" in GSCM refers to sustainability in the supply chain through low emissions and recycling strategies for waste generated. Green SCM is getting more attention as a sustainable development mode for modern enterprises and is seen increasingly as a part of broader corporate social responsibility (CSR) initiatives (Ravishankar 2011).

2.1. The relevance of GSCM to the power sector

The electricity sector in India had an installed capacity of 253.389 GW as of August 2014, making it the world's fifth-largest. The country's annual electricity generation capacity has increased in last 20 years by about 120 GW, from about 66GW in 1991 to over 253.389 GW in 2013.[1] The International Energy Agency estimates India will add between 600 GW and 1200 GW of additional new power generation capacity before 2050. This will have a huge detrimental impact on the environment, unless companies and users switch over to more eco-friendly ways of power generation, transmission, distribution, and consumption. In short, the need for an environmentally friendly supply chain is of paramount importance.

The energy sector around the world is plagued by three major problems: rising energy demand, aggregate technical and commercial (AT&C) losses, and the adverse environmental impact. GSCM, to a substantial extent, provides a solution to all these problems, as listed in Table 1.

2.1.1. Increasing energy needs

Along with the transportation sector, the power sector is identified as one of the two largest sources of greenhouse gas (GHG) emissions the world over. With economies on an upswing in recent years, more prominently in developing economies like India, there is a serious threat to the environment in the coming decades. For example, by 2030 India is likely to have a GDP of US $4 trillion and a population of 150 billion (McKinsey & Company, Inc., 2009). This will put extreme pressure on the energy resources of the country, and threaten a subsequent swelling of GHG emissions. This calls for adoption of high-end green technologies, infrastructure, and practices that augments fuel efficiency and also addresses environmental concerns as much as possible.

2.1.2. Aggregate technical and commercial losses

Inefficient supply chains, apart from their detrimental impact on the environment and the ensuing complications, are also responsible for mammoth losses posted by power companies in terms of T&D as well as aggregate technical and commercial (AT&C) losses. According to the CEA, T&D losses on a national level in 2010–11 amounted to 23.97% while AT&C losses amounted to 16.15%.[2] The losses amount to billions of rupees of prospective revenues that might have been saved. Though existing technologies are not yet capable of fully eliminating the losses, a streamlining of the supply chain can cut losses down dramatically, resulting in huge monetary gains for power companies.

Table 1
Problems and solutions.

PROBLEM	SOLUTION
Increasing energy needs	Sustainable development
Losses (AT&C)	Increased efficiencies
Environmental impact	Eco-friendly operations

2.1.3. Environmental impact

With pollution worsening the lives of billions and creating massive losses for power utilities, it is important that new avenues of eco-friendly measures be identified and new technological developments undertaken to bring in greater efficiencies and cut down on emissions and losses. The pressure accompanying globalization has prompted industries to improve their environmental performance (Zhu and Sarkis, 2006). GSCM has greater relevance for the power sector than any other sector as there is tremendous scope for improvement in the existing supply chains.

An integrated power supply chain comprises three major sections: generation, transmission, and distribution. An addition section by the name of "end user consumption" also exists, and has a bearing on supply chain efficiencies. Each section has sub-elements carrying some association with environmental impact.

2.2. GSCM in SOPCs: why choose Punjab?

Punjab is one of India's more economically developed states, with a high rate of per capita energy consumption. The state's power sector has been instrumental in its economic growth, as much of the agriculture sector and small and medium-size enterprises (SMEs) thrive on power made available by the SOPCs. Any improvement in their supply chains is sure to translate into perceptible growth in the economy of the state.

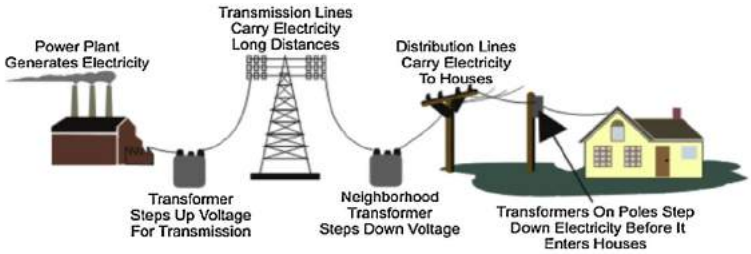
The Punjab State Power Corporation Limited (PSPCL) and Punjab State Transmission Corporation Limited (PSTCL) are also representative of modern power utilities operating in India, which have been transformed into corporations from their erstwhile avatar of being an SEB. The erstwhile SEB, the Punjab State Electricity Board (PSEB), was bifurcated into PSPCL and PSTCL in 2010 on the recommendations of the Central Electricity Regulatory Committee (CERC), thereby presenting an appropriate option to study a state power utility. Further, their relative youth makes them more conducive to identifying and proposing changes than those which are old and characterized by a rigid pattern of operations. The findings of the study on these SOPCs should be more or less applicable to SOPCs in other states.

In a nutshell, the SOPCs of Punjab are nearly ideal choices for a study related to GSCM implementation, since the two SOPCs are identified with the typical power utility set up in most states, and are on the threshold of reforming their supply chains with an intent to leave the remnants of operational mediocrity behind.

3. Theory

Electricity generation is by far one of the biggest culprits in global warming. Electricity generating plants account for one-quarter of all carbon emissions for which human activity is responsible – and their harmful emissions have shot up by 60% over the past two decades, especially as China and India have experienced rapid economic growth (Don Grant et al., 2013).

[1] www.fortunemediagroup.in/Grid%20World/Brochure.pdf.
[2] http://articles.economictimes.indiatimes.com/2013-09-13/news/42042045_1_power-plants-atc-losses-additional-power.



Conventional supply chain

SUPPLY OF COAL: Coal is supplied to the power plant by rail. The coal is crushed to the size of few inches, then sent by conveyor belt to a pulverizer.

PULVERIZATION OF COAL: Coal is crushed to powdered form, then blown into the furnace via hot air.

BOILER: The boiler walls are lined with many kilometers of water-filled pipes. On entering the boiler, the coal ignites and heats up the water in the boiler pipes for conversion into steam.

PRECIPITATORS AND STACK: Emissions (carbon dioxide, sulphur dioxide nitrogen oxides) and ash produced from the burning of coal are vented from the boiler through the stack. Electrostatic precipitators remove nearly all the fly ash before releasing it into the atmosphere. The heavier ash (bottom ash) settles at the bottom.

TURBINE AND GENERATOR: Jets of high-pressure steam propel the blades of a turbine, causing it to spin rapidly. The turbine is connected to a generator, and its spinning causes an electromagnet to turn inside coils of wire in the generator; thus producing

CONDENSERS & WATER COOLING SYSTEM: Steam exits the turbines and passes through a condenser for conversion into water. The water is pumped back to the boiler to repeat the heating process. Condensers are cooled by reservoir water.

ASH DISPOSAL: Ash is removed and sold for use in manufacturing cement, fertilizers, bricks, etc.

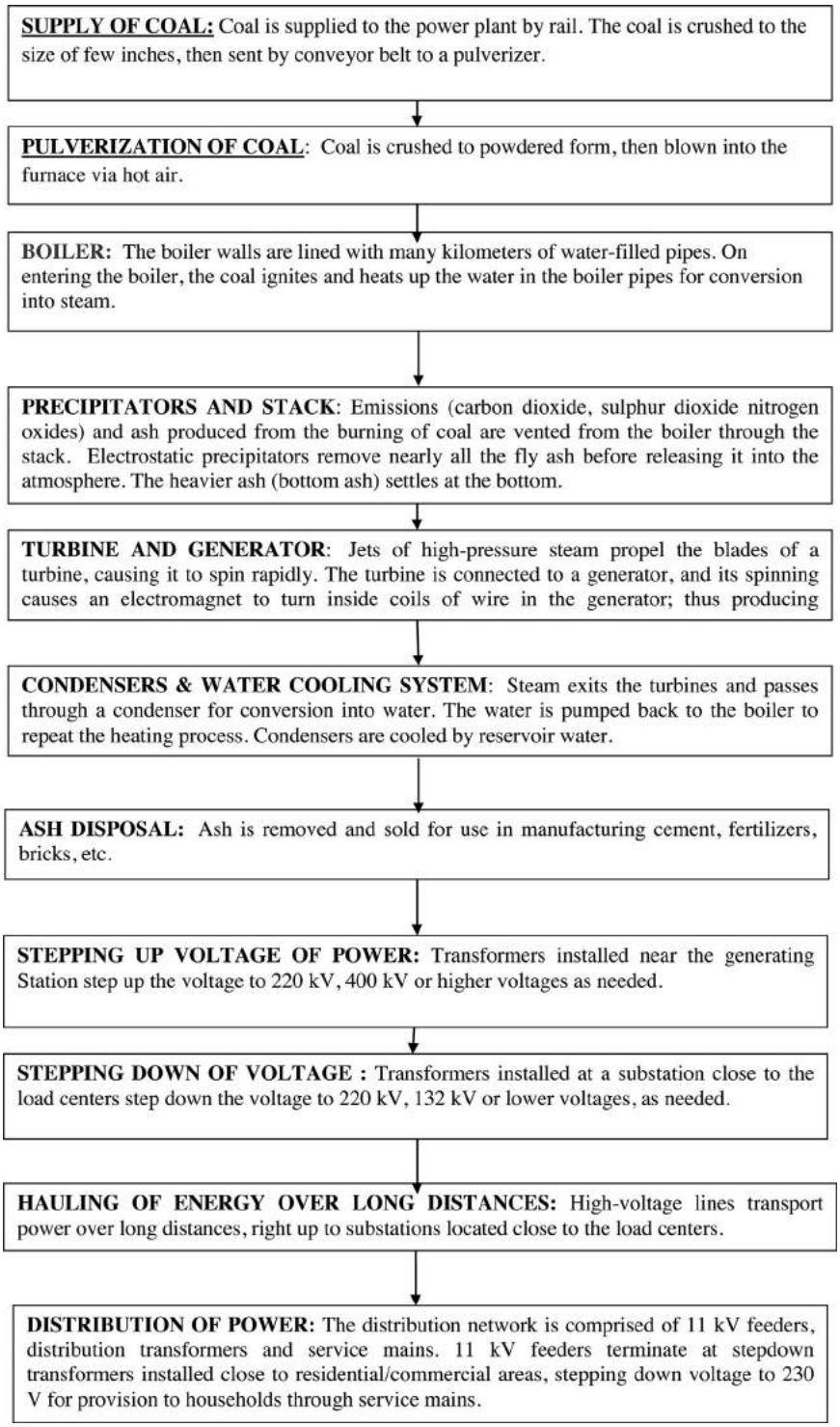
STEPPING UP VOLTAGE OF POWER: Transformers installed near the generating Station step up the voltage to 220 kV, 400 kV or higher voltages as needed.

STEPPING DOWN OF VOLTAGE : Transformers installed at a substation close to the load centers step down the voltage to 220 kV, 132 kV or lower voltages, as needed.

HAULING OF ENERGY OVER LONG DISTANCES: High-voltage lines transport power over long distances, right up to substations located close to the load centers.

DISTRIBUTION OF POWER: The distribution network is comprised of 11 kV feeders, distribution transformers and service mains. 11 kV feeders terminate at stepdown transformers installed close to residential/commercial areas, stepping down voltage to 230 V for provision to households through service mains.

Fig. 1. The supply chain.[3]



Environmental issues in the electricity sector have been addressed directly, through laws and governmental orders, and indirectly, through policies on alternative technologies and efficiency improvement. Solutions to these problems lie in combinations of cleaner and more efficient generation, appropriate control equipment, and more efficient end-use devices (Antonette and Murthy, 2006).

The research study is focused on the SOPCs of Punjab dealing with three major functional domains of generation, transmission, and distribution (GTD), with an intent to assess the environmental consciousness exhibited by them in their infrastructural setup and operational undertakings. In the present scenario, PSPCL and PSTCL are the only two state-owned companies in Punjab associated with GTD of power; hence it is these two that have been analyzed in the context of adoption of GSCM measures in the state.

3.1. Supply chain of power industry

Electricity generation covers a long chain from the fuel source to the ultimate consumer of power.

Table 2
Primary Bottlenecks and Suggested Green Solutions.

S. No.	Stage of Supply Chain	Bottlenecks in GSCM Implementation	Green Measures Suggested
1	Supply of coal	Unavailability of good-quality coal	Securing quality fuel should be a priority among suppliers. Alternative fuels, which are also economical, can be explored.
2	Boiler operations	Limited efficiency	High-end boilers are solutions, but are costly. Regular maintenance of existing boilers may increase efficiency.
3	Flue gas emissions	Outdated technology deployed	Deployment of electrostatic precipitators and elongated chimneys may help in minimizing pollution.
4	Waste disposal	1) Large quantities of ash are produced 2) Toxic wastes (arsenic, mercury, chromium, and cadmium, etc.) contaminate drinking water supplies, leading to cancer and other health hazards.	Ash may be channeled to use in the cement, brickmaking and fertilizer industries.
5	Transmission losses	Technical limitations	Transmission can be undertaken at still higher voltages, which would require an overhaul of the transmission infrastructure.
6	Distribution losses	Lack of auditing of energy, pilferage, commercial Losses, etc.	1) Eliminating LT lines 2) Installations of additional distribution transformers (DTs). 3) Installation of lower-capacity distribution transformers at each consumer premises instead of cluster formation 4) Substitution of DTs with those having lower no-load losses such as amorphous core transformers.
7.	Consumption	Unawareness and unwillingness to go green on part of the consumers	Awareness drives to sensitize awareness of environmental issues and incentives on more judicious use of energy.

The conventional supply chain of the power industry comprises three major parts:

- **Generation**: Power is generated by various means and accordingly it is classified as thermal power, hydro power, solar power, tidal power, geothermal power, bio mass power, etc.
- **Transmission**: Once the power is generated, its voltage is stepped up so that it can be hauled over long distances to reach the load centers.
- **Distribution**: The distribution of power from 11 kV feeders to the premises of the end user forms the distribution network.
- **Consumption**: At the end of the supply chain are consumers, whose role in greening the supply chain is focused on the judicious use of energy (Fig. 1).[3]

3.2. Conventional supply chain

PSPCL – the only SOPC in the generation sector, as of March 2014 had an installed capacity of 4330 MW of energy, both from thermal and hydro sources. Apart from this, the state also draws hydro power to the tune of 1161 MW from Bhakra Beas Management Board, a share of 3071 MW from Central Sector, and 297 MW from PEDA (Punjab Energy Development Agency) and other "new and renewable sources of energy," or NRSE, projects. The energy is first stepped up for transmission and then stepped down consecutively by means of 220 kV substations, 132 kV substations, 66 kV substations and 33 kV substations with a cumulative count of 844 substations. This energy is hauled by the means of 220 kV lines, 132 kV lines, 66 kV lines, and 33 KV lines, with a total length of 19,646 kms. The length of 11 kV feeders, which form the fundamental backbone of distribution, stands at 209,759 kms. At the tail end of the supply chain are consumers, which are distinguished as domestic, non-residential (commercial), industrial, agricultural, bulk consumers railway traction, and street lighting, all adding up to 81,12,286 connections. (Officers' Official Diary, PSPCL: 2015).

In its essence, the supply chain of the power industry remains the same – with generation, transmission, and distribution comprising the basic blocks of the chain, coupled with the last stage of consumption – where the end users stand the potential of contributing at the far end of the extended chain. The green supply chain is an augmented version of the conventional supply chain with an intent to reduce the associated pollution and losses by means of various environment friendly inputs in the shape of new technologies that cause no/lesser damage to environment, selection of suppliers who act in an environment friendly manner, cutting down on wastes, recycling and aware consumers who consumes responsibly thus limiting their adverse impact on environment. In power industry, increased pressure on environment is pushing the producers, governments and consumers to look out for means, methodologies and techniques that can limit the harmful impact of energy generation, its transmission, distribution and final consumption.

3.3. Bottlenecks and proposed measures to push GSCM

If the power industry is one of the leading polluters, it also has an uncommon degree of scope for improvement in operating in an eco-friendly fashion. In the power industry, pollution is not limited to just pollutants, but also to inefficiencies and wastage. From the quality of raw material used to the efficiency of the machines used; from bad workmanship to consumers' behavior; from emissions to management of physical waste; from the accumulation of aggregate and technical losses to the lack of deployment of IT-based technology, there are many features that combine to cause immense pollution. Changes in these would secure significant green gains. After studying the entire supply chain of the Punjab power industry with the help of a detailed literature review and meeting with industry experts, we have identified seven primary bottlenecks, as summarized in Table 2.

3.3.1. Coal supply

The quality of coal has a direct bearing on the waste it generates in the shape of ash and flue gases; that quality itself is dependent on its ash and sulfur content. On average, Indian coal has an ash content of 35–38%, which makes it far more polluting than coal used in relatively developed countries. That environmental impact is not limited to ash production but may also have the potential to lead to energy-water conflicts in places where water supply is

[3] Fig. 1: http://www.netgainenergyadvisors.com/market-overview.php.

scarce, resulting in the diversion of water for power production at the cost of other uses.

To some extent the quality of coal can be upgraded by washing/processing it to get rid of up to 7–8% of ash content and other incombustible content. The government can issue stringent regulations in this regard like one issued on Jan. 1, 2014, which states that thermal power plants located beyond 500 km from the mine should use only treated coal that has a gross calorific value below 4000 kcal/kg. The same applies for a captive thermal power plant of more than 100 MW capacity and located beyond 500 km from the pit head. It has been observed that in India, big players like NTPC have started to lock their horns with state coal suppliers like Coal India Ltd. India is also considering the replacement of some low-grade Indonesian coal with better-quality supplies, either from Southeast Asia or from other producers such as South Africa and Australia.

3.3.2. Boiler operations

Among the major problems associated with boilers, clinker formation occupies a prominent place as it results in forced outages of very long duration and generation losses. A sufficient quantity of water must be provided in the hoppers to flush molten slag and ash so they will not deposit. Soot blowing must be regularly performed to avoid the deposition of soot in the water wall by injecting steam at sufficient pressure and temperature to dislodge soot from the water wall tubes.

Clinker grinders are provided in boilers to grind large pieces of clinkers into small ones so that choking of the exhaust hole may be avoided. The major cause of clinker formation in a boiler is over-firing, which causes ash to fuse, so that firing must be properly adjusted by using the right quantity of primary and secondary air ratio in the boiler. Good-quality coal having a higher gross calorific value, less ash content, less mineral content, and an ash fusion temperature above 1500 °C must be used to avoid clinker formation. Regular watch must be done on poking.

3.3.3. Flue gas emissions

The permissible limits of ash particles specified by the state pollution control boards is normally less than 115 mg/nm^3 in the majority of states in India. However, in many power stations, the concentration of the SPM exceeds the specified limits. The high ash content in our coals (40–45%), low sulfur content (<0.4% – better of course for SO_2 emissions), the acidic to neutral nature of ash (6.8 pH), humidity variation, and above all, gradual deterioration in the performance in the ESP are a few of the reasons for SPM concentrations even in well-managed power stations.

Prevention is better than cure. It is better to use coal that has a lower ash content. Nevertheless, even then, if the problem persists, "flue gas conditioning technology" developed by India's Department of Atomic Energy can be used to alter the resistivity of the ash particles in the charged flue gas medium by using a weak alkaline conditioning agent such as ammonia, thereby ensuring that heavier ash particles are contained effectively and separated from flue gases emitted in the open air.

3.3.4. Ash disposal

After arresting the fly ash in ESP, it is then transported to silos through suction or by pressurized air. When required, this can be obtained in the container for further transportation directly from the silos through chutes at the bottom, or to the delivery point by pipeline using vacuum suction or pressurized air.

The beneficial uses of fly ash include serving as a raw material in concrete, grout, and cement, or as a filler material in stabilization projects and roadbeds. Fly ash is increasingly being used throughout the world as an ingredient for bricks, which get their strength and durability from the chemical reaction of fly ash with water. Fly ash is combined with sand and pigments and compressed via vibrocompaction, then cured with steam for two days and not fired. This method uses 85% less energy than traditional kiln firing and the carbon footprint for a cubic yard of fly ash brick is just 191 pounds.

The leach ability of toxins from fly ash is a critical issue in determining whether fly ash can be put to beneficial use. It is well established that fly ash on its own is highly toxic, with ample an amount of leachable content. Vitrification is a thermochemical process that occurs at high temperatures around 1500° C that melt the ash and turn it into slag, a glasslike substance similar to obsidian in appearance. Vitrified slag has been subjected extensively to analysis via the toxicity characteristic leaching procedure (TCLP) and found to be very stable and reliable at containing all toxins in the glass crystalline matrix. Vitrified slag has been approved for use as a construction aggregate and filler material.

In India, approximately 150 million tons of fly ash is produced every year, and this number is growing as new coal plants are added to meet growing energy demand. In order to combat the growing problem of fly ash waste, the Indian government is mandating the production of fly-ash bricks and compelling their use in new construction projects. Brickmaking is a traditional industry in India with annual production of over 200 billion bricks and 76 million tons of CO_2 emitted from the kilns.

3.3.5. Transmission and distribution losses

In India, the T&D losses in many states are as high as 35–40%, which by itself is an alarming proportion. Methods to reduce transmission losses include replacing existing wires with larger wires (which lowers resistance of the system, thus reducing these losses, known mathematically as I^2R), upgrading transformers and circuits to provide additional energy transformation points closer to the load center. In rural areas, load is scattered over large areas. Thus the primary and secondary distribution lines in rural areas are largely radial, usually extending over long distances. This results in high line resistance and therefore high I^2R losses in the line. The size of the conductors is another consideration in cutting down losses; these should be selected on the basis of KVA × KM capacity of standard conductor for a required voltage regulation. Distribution transformers should be located at minimal distance from the load center with respect to consumers. In order to reduce the voltage drop in the line to the farthest consumers, the distribution transformer should be located at the load center to keep the voltage drop within permissible limits. In most LT distribution circuits, normally the power factor (PF) ranges from 0.65 to 0.75; if the power factor is low, the current drawn in high and the losses proportional to the square of the current will be higher. Thus, line losses owing to the poor PF can be reduced by improving the PF by a number of means such as application of shunt capacitors either in the secondary side (11 kV side) of the 33/11 kV power transformers or at various points along the distribution Line. Bad workmanship contributes significantly towards increasing distribution losses. As joints are a key source of power loss, these should be kept to a minimum, with proper joining techniques used to ensure firm connections.

One of the easiest ways to minimize losses in the distribution system is by balancing current along three-phase circuits. Similarly, balancing load among distribution feeders will lower losses, assuming a similar conductor resistance. This may require installing additional switches between feeders to allow for the appropriate load transfer. Power consumption of customers varies throughout the day and over seasons, thus bringing variations in the load factor. The load factor can be increased by offering customers time-of-use rates, thereby offering a financial incentive for consumers to shift their electricity-intensive activities (such as,

electric water and space heating, air conditioning, irrigating, and pool filter pumping) to off-peak times.

Distribution transformers use copper conductor windings to induce a magnetic field into a grain-oriented silicon steel core. Therefore, transformers have both load losses and no-load core losses. Improved the manufacturing of steel cores and introducing amorphous metals (such as metallic glass) have reduced core losses. Balancing three-phase loads periodically throughout a network can reduce losses significantly. It can be done relatively easily on overhead networks and consequently offers considerable scope for cost-effective loss reduction, given suitable incentives. One method of reducing fixed losses is to switch off transformers during periods of low demand. If two transformers of a certain size are required at a substation during peak periods, only one might be required during times of low demand so that the other transformer might be switched off in order to reduce fixed losses. Other ways of decreasing losses include balancing load distribution among three phases in an L.T system, unloading of overloaded lines, maintaining optimal conditions at which power and distribution transformers can be operated and proper voltages at consumer terminals limiting the higher draw of currents by inductive loads, maintaining good quality of star-rated equipment used in agricultural pumping in rural areas, and cooler air-conditioners and industrial loads in urban areas.

3.3.6. Consumption

The arbitrary fashion with which power is consumed by consumers also accounts for a considerable chunk of environmental damage. In recent years, green energy sources have become more affordable, with solar power emerging as a viable option in a country like India which is blessed with sunny weather for most part of the year.

Environmental effects manifest themselves in two ways: pollutants emitted in the course of generation, and losses occurring in the transmission and distribution. Environmental performance can be improved by capturing pollutants. Capturing and treating pollutants and harmful byproducts at various stages of the supply chain is called pollution control. In contrast, pollution prevention emphasizes approaches that involve fundamental changes to the basic product or manufacturing processes along the supply chain. Pollution prevention reduces or eliminates pollutants by using cleaner alternatives (Freeman et al., 1992). Pollution prevention requires concerted efforts that extend beyond the manufacturing operations of a single plant to suppliers and buyers, or even across a broader supply chain network. Thus, stronger supply chain integration allows suppliers greater access and influence in downstream operations, and can leverage supplier expertise to improve implementation of more environmentally friendly product or process configurations (Geffen and Rothenberg, 2000).

In a fuel audit of thermal power plants of PSPCL by CPRI, Bangalore, in 2012, it was stated that PSPCL can save nearly 31719.59 lakhs by investing 858 lakhs in various technologies associated with efficient fuel management. The disco owns three thermal power plants: GNDTP Bathinda, GGSSTP Ropar, and GHTP, Lehra Mohabbat. It has been proposed that an improvement in coal quality and quantity measurement of both received and bunkered coal at the thermal plant could lead to a saving of nearly 30,610 lakhs; improvements to receiving infrastructure and coal management at the coal yard and reduced demurrages could yield further savings of 197.15 lakhs, improvement in TL could yield a saving of 366.69 lakhs, and a reduction in stones in received coal can yield a saving of 545.75 lakhs (Report – CPRI Bangalore). To boost green energy, PSPCL is also signing power purchase agreements with producers of renewable energy sources.

It is only recently that PSPCL has embarked upon an aggressive drive to adopt technology that can cut losses and be environment friendly. The results to date have been encouraging enough to result in calls for adoption of GSCM on a larger scale. Buoyed by successes to date, PSPCL was aiming to further reduce losses to 15% by 2015. The success achieved by PSPCL is a motivation for other SOPCs of India to adopt green measures in cutting down losses and contributing to greener operations of the Indian power industry.

With specific reference to SOPCs in Punjab, there is great scope for implementing GSCM measures. In the generation sector, procurement of high-quality fuel and induction of new technology will help in reducing emissions. It is not only the SOPCs that have a responsibility to cut down losses; consumers can also play a big part by showing rational consumption and usage behavior.

4. Discussion

GSCM is a cost-intensive practice that calls for new machinery and processes that are specifically deployed to cut down on emissions and wastes. But the increase in operational and production costs should not be viewed in isolation, because there are specific benefits as well. In many cases, deployment of green measures has led to smarter supply chains, lower wastage, and financial savings. There will be cases where the cost attached to GSCM implementation will exceed the resulting gains, and thus will not make much business sense. Hence, the idea of adopting GSCM measures is met with skepticism by a majority of enterprises. Still, even in these cases, particularly among enterprises in the government and social service sectors, some are ready to bear the added costs for the sake of a cleaner environment. More broadly, most organizations today are going green in their business practices as they realize the benefits to their business operations, which also affect suppliers and customers (Ninlawan et al., 2011).

5. Conclusion

GSCM is a new concept, still unfamiliar to many, but with a huge potential in the future. Concern for environment and commercial advantages is going to be a big driver for adoption of the concept, even in face of escalating costs. Extensive and advanced research in this field is vital, as a willingness to embrace it on the part of organizations. Careful planning and implementation of GSCM initiatives tend to yield positive results for the implementers. Organizations should realize that, since they will eventually have to move to green initiatives in SCM, the sooner they address this challenge the better.

References

Antonette D'sa, Narasimha Murthy, K.V., 2006. Environmental Reform in the Electricity Sector: China and India. International Energy Initiative (IEI), India. Report No. CPRI/ERED/EA/117/12 of CPRI Bangalore.

Grant, Don, Longhofer, Wesley, Jorgenson, Andrew K., 2013. Targeting extreme polluters to reduce carbon emissions from the electricity sector. J. Environ. Stud. Sci. 3 (4), 376–380.

Freeman, H., Harten, T., Springer, J., Randall, P., Curran, M.A., Stone, K., 1992. Industrial pollution prevention: a critical review. J. Air Waste Manage. Assoc. 42 (5), 617–656.

Geffen, C., Rothenberg, S., 2000. Sustainable development across firm boundaries: the critical role of suppliers in environmental innovation. Int. J. Oper. Prod. Manage. 20 (2), 166–186.

Green Jr., K.W., Whitten, D., Inman, R.A., 2008. The impact of logistics performance on organizational performance in a supply chain context. Supply Chain Manage. Int. J. 13 (4), 317–327.

McKinsey & Company, Inc, (2009) – Environment & Energy sustainability: An approach for India—A Report .

Ninlawan, C., Seksan, P., Tossapol, K., Pilada, W., 2011. The implementation of green supply chain management practices in electronics industry. Proceedings of the International Multiconference of Engineers and Computer Scientists .

Officers' Official Diary, PSPCL: (2014).

Ravishankar, 2011. Green Supply Chain Management: Logistics and Distribution, White Paper. MPHASIS Company.
Sheu, J.B., Chou, Y.H., Hu, C.C., 2005. An integrated logistics operational model for green supply chain management. Transp. Res. Part E 41 (4), 287–313.
Srivastava, 2007. Green supply-chain management: a state-of the-art literature review. Int. J. Manage. Rev. 9 (1), 53–80.
Walker, H., Di Sisto, L., Mc Bain, D., 2008. Drivers and barriers to environmental supply chain management practices: lessons from the public and private sectors. J. Purchasing Supply Manage. 14 (1), 69–85.
Zhu, Q., Sarkis, J., 2006. An inter-sectoral comparison of green supply chain management in China: drivers and practices. J. Clean. Prod. 14, 472–486.

Sheetal Soda is a Research Scholar with the Department of Industrial and Production Engineering at the Dr. B.R. Ambedkar National Institute of Technology in Jalandhar, India. She obtained her B.Tech. in Mechanical and Automation Engineering from Guru Gobind Singh Indraprashtha University New Delhi (India) and M.E. in Production Engineering from Delhi Technical University (formerly Delhi College of Engineering), also in Delhi.

Anish Sachdeva is working as an Associate Professor in the Department of Industrial and Production Engineering at the National Institute of Technology, Jalandhar and Punjab, India. He obtained his Bachelor in Industrial Engineering from the National Institute of Technology (then the Regional Engineering College) in Jalandhar, India; his Masters in Industrial Engineering from Punjab Technical University, Jalandhar, and Ph.D. from the Mechanical and Industrial Engineering Department of the Indian Institute of Technology (IIT) in Roorkee. His areas of interest are reliability and maintenance engineering, supply chain management, modeling, and simulation.

Rajiv Kumar Garg is a Professor in the Industrial and Production Engineering Department at Dr. B.R. Ambedkar National Institute of Technology, Jalandhar, India. He holds a B.Sc. Engg. (honors) in Mechanical Engineering from the Regional Engineering College Kurukshetra, and an M.E. (honors) in Industrial Engineering and a Ph.D. from the Thapar Institute of Engineering and Technology Patiala (India). He Chief Editor of the *International Journal of Machining and Machinability of Materials (IJMMM)*.

Accepted Manuscript



Title: In-situ electrosynthesized Nanostructured Mn_3O_4-Polyaniline Nanofibers- Biointerface for Endocrine Disrupting Chemical Detection

Author: Nawab Singh Md. Azahar Ali Kali Suresh Ved Varun Agrawal Prabhakar Rai Ashutosh Sharma B.D. Malhotra Renu John

PII: S0925-4005(16)30902-9
DOI: http://dx.doi.org/doi:10.1016/j.snb.2016.06.050
Reference: SNB 20376

To appear in: *Sensors and Actuators B*

Received date: 9-3-2016
Revised date: 31-5-2016
Accepted date: 7-6-2016

Please cite this article as: Nawab Singh, Md.Azahar Ali, Kali Suresh, Ved Varun Agrawal, Prabhakar Rai, Ashutosh Sharma, B.D.Malhotra, Renu John, In-situ electrosynthesized Nanostructured Mn3O4-Polyaniline Nanofibers- Biointerface for Endocrine Disrupting Chemical Detection, Sensors and Actuators B: Chemical http://dx.doi.org/10.1016/j.snb.2016.06.050

This is a PDF file of an unedited manuscript that has been accepted for publication. As a service to our customers we are providing this early version of the manuscript. The manuscript will undergo copyediting, typesetting, and review of the resulting proof before it is published in its final form. Please note that during the production process errors may be discovered which could affect the content, and all legal disclaimers that apply to the journal pertain.

ACCEPTED MANUSCRIPT

In-situ electrosynthesized Nanostructured Mn_3O_4-Polyaniline Nanofibers-Biointerface for Endocrine Disrupting Chemical Detection

Nawab Singh[a], Md. Azahar Ali[b], Kali Suresh[c], Ved Varun Agrawal[d], Prabhakar Rai[e], Ashutosh Sharma[e] *, B. D. Malhotra[f*] and Renu John[a]*

[a] Department of Biomedical Engineering, Indian Institute of Technology Hyderabad, Kandi, Sangareddy-502285 Telangana, India

[b] Department of Electrical and Computer Engineering, Iowa State University, Ames, Iowa-50011, USA

[c] Centre for Nanotechnology, Hyderabad Central University, Hyderabad Telangana-500046, India

[d] Centre on Biomolecular Electronics, Biomedical Instrumentation Section, CSIR-National Physical Laboratory, Dr. K. S. Krishnan Marg, New Delhi-110012, India

[e] Department of Chemical Engineering, Indian Institute of Technology Kanpur, Kanpur, 208016, India

[f] Department of Biotechnology, Delhi Technological University, Shahbad Daulatpur, Main Bawana Road, Delhi-110042, India

ACCEPTED MANUSCRIPT

Highlights

- The Mn_3O_4-PANI nanofibers has been used for detection of bisphenol A.
- The larger surface of Mn_3O_4-PANI helps for loading of tyrosinase.
- This sensor shows a fast response and excellent sensitivity for bisphenol A.
- This sensor exhibits higher selectivity and stability.

ACCEPTED MANUSCRIPT

ABSTRACT

We report results of the studies relating to fabrication of an electrochemical biosensor platform based on *in-situ* electrosynthesized manganese oxide (Mn_3O_4)-polyaniline (PANI) nanofibers for detection of bisphenol A (BPA), an endocrine disrupting chemical. The spherical Mn_3O_4 nanoparticles synthesized using cetyltrimethylammoniumbromide were modified with PANI in presence of polyvinyl sulphonic acid and glutaraldehyde. The tyrosinase (Tyrs) molecules covalently immobilized on the PANI-modified Mn_3O_4 nanofibers surface were characterized using X-ray diffraction, electron microscopy and Fourier transform infrared spectroscopy. This electrochemical biosensor exhibits a response time of 20 s, sensitivity of 0.776 mA μM^{-1} Lcm^{-2}, respectively, and 0.134 mA μM^{-1} Lcm^{-2} in the concentration ranges, 0.004-0.09 $\times 10^{-6}$ mol L^{-1} and 0.2-0.8 $\times 10^{-6}$ mol L^{-1} of BPA.

Keywords: Nanofibers; Mn_3O_4 nanoparticles; Polyaniline; Bisphenol A; Tyrosinase

***Corresponding Authors:** ashutos@iitk.ac.in*, bansi.malhotra@gmail.com*, renujohn@iith.ac.in*, Ph: +91-40-23016097,

1. Introduction

Polymeric materials are currently in increased demand in our daily lives due to their reusability, recoverability and stability [1]. Along with widespread applications of polymeric compounds in food, drinking water and packaging industry, questions have been posed on the harmfulness of these chemicals on human beings and animals. Bisphenol A (2, 2-bis (4-hydroxyphenyl) propane ($C_{15}H_{16}O_2$); BPA) is an example such a chemical that is used in manufacturing drinking water bottles, baby feeding bottles and food packaging industries [2]. It is also used for the synthesis of epoxy resins, polystyrene resins, polycarbonate, inner coating of food cans, dental sealants, food packaging and drug delivery systems [3]. BPA and other similar phenolic compounds are, therefore, a natural threat to our precious environment including drinking water. BPA is

ACCEPTED MANUSCRIPT

considered as an endocrine disrupting compound (EDC) since it may trigger secretion of natural estrogen by the human endocrine system, resulting in elevated estrogenic activity in the human body. EDCs are pollutants chemical that are known to affect the hormonal balance of various species including humans [4,5]. BPA has been reported to have adverse effects such as cancer,[6] decreased semen quality, reduced immunity, heart diseases, obesity and impaired reproduction [7–9] in human beings and animals. Hence the detection of BPA in drinking water and food even at very low concentration is very crucial from a public health perspective. Several techniques such as high-performance liquid chromatography, gas chromatography, capillary electrophoresis, chemiluminescence, [2,10,11] and ELISA technique have been employed for the detection of BPA in a given environment. However, these methods are expensive, time consuming, and require special expertise for handling the complex procedure. Some immunosensors have been reported for detection of BPA using BIACORE 3000 sensor chip, [12] waveguide-based evanescent immunosensor, [13] and piezoelectric immunosensor [14]. In spite of these developments, there is enough scope for the development of an improved biosensing device that can be used for BPA detection.

Manganese oxide (Mn_3O_4) is one of the most stable transition metal oxides with a spinel structure. It is being explored for the development rechargeable lithium ion batteries, catalysis and molecular adsorption [15–17]. Mn_3O_4 is a tetragonal Hausmannite with Mn^{3+} and Mn^{2+} ions occupying octahedral and tetrahedral positions of the spinel structure, respectively. The octahedral symmetry of Mn_3O_4 is tetragonally distorted due to the Jahn–Teller effect on Mn^{3+} ions. The unit cell of Mn_3O_4 contains $Mn_4Mn_8O_{16}$ in which the oxygen atoms are closely packed with Mn^{2+} ion in tetrahedral-site and Mn^{3+} ion in octahedral-site [18,19]. The nMn_3O_4 exhibits ferrimagnetic behavior at Curie temperature (T_c = 40 K) and has excellent electron transport properties [20,21]. Due to excellent electron transfer, stability and electrochemical properties, nMn_3O_4 can perhaps be utilized for biosensing applications [22].

Polyaniline (PANI) is a conducting polymer that is known to be cost-effective, environmentally stable and has interesting tunable conducting properties. The composites of transition metal oxides and conducting polymers have been used for fabrication of supercapacitor electrodes [23,24]. The electrochemical polymerization has been utilized to prepare bioactive nanofiber (NF) of PANI-nMn_3O_4 in presence of aniline, polyvinyl sulphonic acid (PVSA) and

ACCEPTED MANUSCRIPT

hydrochloric acid. PANI-nMn_3O_4 NF is an attractive material that provides a suitable interface for immobilization of proteins due to large specific surface area, highly conductive nature and strong adsorption ability [25–28].

We report results of the studies relating to preparation of spherical nMn_3O_4 via co-precipitation method and electropolymerized with aniline in presence of hydrochloric acid (HCL) and polyvinylsulphonic acid (PVSA) as a binder using chronoamperometric technique. Glutraldehyde (GA) treatment was used to crosslink tyrosinase (Tyrs) with PANI-nMn_3O_4 electrode surface for detection of BPA using amperometric technique. We discuss the merits of this interesting nanohybrid biointerface for BPA detection.

2. Experimental

2.1 Chemicals and reagents

All chemicals used were of analytical grade. Manganese chloride, sodium hydroxide, cetyltrimethylammonium bromide (CTAB), aniline, HCL, PVSA, GA, tyrosinase (Tyrs), BPA, phenol, resorcinol, para-aminophenol, ortho-nitrophenol, and hydroquinone were purchased from Sigma Aldrich, USA. Deionized water used for all experiments was obtained from Millipore. Phosphate buffer saline (PBS) was prepared using sodium monohydrate phosphate (Na_2HPO_4) and sodium dihydrogen phosphate (NaH_2PO_4) reagents, following standard protocols.

2.2 Synthesis of nanostructured manganese oxide

Colloidal solution of Mn_3O_4 was prepared using manganese chloride ($MnCl_2$) as the precursor. 0.5 mol L^{-1} of $MnCl_2$ and 0.2 mol L^{-1} of NaOH were separately dissolved in 250 mL ethanol and distilled water, respectively and then mixed. Spherical nMn_3O_4 was synthesized by co-precipitation method by using cetyltrimethylammoniumbromide (0.4×10^{-3} mol L^{-1}) as a surfactant [29,30]. Thus formed precipitate was washed with deionized water and ethanol seven times and dried at 90 °C for 24 h, and then calcined at 450 °C for 4 h.

ACCEPTED MANUSCRIPT

2.3 Fabrication of the sensor platform

2 mg of nMn_3O_4 was dispersed in 12 mL of 1 mol L^{-1} HCL by stirring constantly for 6 h and ultrasonicated for 90 min after which 100 µL of 0.1 mol L^{-1} distilled aniline was added. After 3 h of constant stirring in a dark place, 100 µL of 0.5 mol L^{-1} PVSA was added drop-wise while shaking. Subsequently, 10 mL of the solution was used for electropolymerization using chronoamperometric technique. The schematic of the thin film fabrication is shown in [Fig. 1(i)]. The solution comprising of distilled aniline, PVSA and nMn_3O_4 dispensed in 1 mol L^{-1} HCL was used to prepare nanocomposite fibers via electropolymerization. During electrochemical deposition, the potential was kept at 1.5 V for three cycles of 100 s. After each cycle, electrode was washed with DI water drop-wise in order to form stable PANI-nMn_3O_4NF/ITO film and the current flowing through the electrode deposition was monitored for 100 s. The high current observed in the initial stage originated due to double layer charging. The stable electrochemical deposition current of PANI-nMn_3O_4 NF [Fig.1 (ii-curve c)] during third cycle was found to be about 10 times higher compared to the second cycle (curve b) and the current observed during the second cycle was about 20 times higher as compared to first cycle (curve a). It was found that the PANI-nMn_3O_4 NF could be uniformly deposited during the third cycle (curve c) after which PANI-nMn_3O_4 NF/ITO electrode was dipped in 1% GA for 2 h in a closed vessel for cross linking with enzyme (Tyrs) molecules. Fresh solution of Tyrs enzyme (0.2 unit/mL) was prepared in PBS (50 $\times 10^{-3}$ mol L^{-1}, pH 7.0) and was uniformly spread (10µL) onto the PANI-nMn_3O_4 NF/ITO electrode surface and kept it in a humid chamber for 12 h at room temperature (27 ^{o} C). The fabricated Tyrs immobilized PANI-nMn_3O_4NF/ITO bioelectrode was stored at 4°C when not in use. The proposed mechanism for fabrication of Tyrs-PANI-nMn_3O_4NF/ITO bioelectrode and immobilization of Tyrs onto this electrode is shown in Fig. 2.

2.4 Real sample preparation

A real sample solution of BPA was prepared using two types of plastic products (polyvinyl chloride and polycarbonate mineral water bottles) available in local market [3,31]. These plastic products were cut into small pieces and washed with double distilled water. Then 15.0 gm. plastic pieces were added into a 100 mL double distilled water and sealed. The solution was then ultrasonicated for 90 minutes at 60 ^{0}C, and kept at 85 ^{0}C with a water bath for 48 h. After filtration, the solution was collected in a flask. The extraction process was repeated three

ACCEPTED MANUSCRIPT

times, and the solutions were collected in the same flask and the concentration of the stock solution with BPA was found to be 0.520 $\times 10^{-6}$ mol L^{-1}. For dilution of this stock solution, we used deionized water with desired concentrations.

2.5 Characterization

Spherical nMn_3O_4 and its composite with PANI were characterized using X-ray diffraction (XRD, Rikagu) and high resolution transmission electron microscope (HRTEM, Jeol/JEM 2100). The surface morphology shapes were studied using field emission scanning electron microscope (FESEM, ZEISS) and atomic force microscope (AFM, BRUKER NanoScope®.V-4498BE). The elemental analysis was conducted using energy dispersive X-ray spectroscopy (EDAX). Fourier transform infra-red spectroscopy (FT-IR) from Perkin Elmer, (Spectrum BX II) was used for confirmation of the functional groups in Tyrs enzyme immobilized on electrode surface. X-ray photoelectron spectroscopy (XPS; PHI 5000 Versa Prob II, FEI Inc.) studies have conducted to investigate the functional groups and chemical bonding of the synthesized materials. Electrochemical studies were performed using Autolab Potentiostat/Galvanostat (Metrohm, Netherlands) in a three-electrode system with PANI-nMn_3O_4 deposited on indium tin oxide (ITO) glass substrate as a working electrode, platinum (Pt) as the auxiliary electrode and Ag/AgCl as reference electrode in phosphate buffer saline (PBS) (50 $\times 10^{-3}$ mol L^{-1}, pH 7.4, 0.9% NaCl) containing 5×10^{-3} mol L^{-1} $[Fe(CN)_6]^{3-/4-}$ as mediator.

3. Results and Discussion

3.1 Structural properties

Fig. 3.i (a–c) shows the X-ray diffraction (XRD) pattern obtained for PANI, nMn_3O_4, and PANI–nMn_3O_4 nanocomposite. The XRD pattern of PANI film [Fig. 3 (i.a)] shows peaks at 2θ = 22.07, 31.16, 35.70, 37.98, 46.22, and 51.65 that correspond to (0 2 1), (0 3 1), (2 2 1), (2 1 3), (1 1 5), and (0 0 6) reflection planes, respectively. These are well-matched with JCPDS file 53-1891. This indicates that PANI film is semi-crystalline [32] and the structure is orthorhombic with cell parameters a = 6.98, b = 8.63, c = 10.44 with respect to α, β, γ, respectively. The additional peaks found in the XRD spectra are ascribed to the ITO substrate. The presence of dominant peaks of nMn_3O_4 in the XRD pattern for synthesized spherical nMn_3O_4 [Fig. 3 (i.b)] reveals high degree of crystallinity as well as purity of the sample. The diffraction peaks seen at

ACCEPTED MANUSCRIPT

2θ = 18.11, 28.84, 32.50, 36.15, 44.44, 51.07, 58.37, 60.02, and 64.60 pertain to (1 0 1), (1 1 2), (1 0 3), (2 1 1), (2 2 0), (1 0 5), (3 2 1), (2 2 4), and (4 0 0) reflection planes, respectively, are well matched to the tetragonal spinel structure of Mn_3O_4. These results are consistent with the values obtained for Mn_3O_4 (JCPDS files, 89-4837, 80-0382 and 24-0734). The average crystallite size of nMn_3O_4 obtained by Debye–Scherrer equation is found to be 25–28 nm for the 2 1 1 plane. The nMn_3O_4 has a tetragonal Hausmanite structure with body centered lattice parameters as a = 5.76 A°, c = 9.44 A° with respect to α, and γ, respectively, which are in agreement with JCPDS 24-0734. The XRD spectra of PANI–nMn_3O_4 nanocomposite [Fig. 3(i.c)] shows diffraction peaks at 2θ = 21.45°, 31.04°, 35.37°, 45.88°, 51°, and 60.60° corresponding to (0 2 1) (1 0 3), (2 2 1) (1 1 5), (1 0 5), and (2 2 4) reflection planes of the tetragonal phase of nMn_3O_4, respectively. The crystallite size for PANI–nMn_3O_4 nanocomposite is found to be 30–35 nm for the (1 0 3) plane. The selected area electron diffraction (SEAD) indicates crystallinity in PANI–nMn_3O_4 nanocomposite with improved charge transfer properties of the electrochemical biosensor [inset, Fig. 4 (iii)]. The results indicate that the nMn_3O_4 interact with the anilinium cation and oligomers, that are formed during the initial stage of the polymerization and act as a template for the self-assembly of the PANI chains in a well-ordered manner.

Fig. 3 (ii) shows the Fourier transform infra-red (FT-IR) spectra of PANI, PANI-nMn_3O_4 NF, and Tyrs-PANI-nMn_3O_4 NF films. The FT-IR spectrum of bare PANI (curve a) shows characteristic vibrational peaks at 1574, 1478, 1298, 1246, and 804 cm^{-1}. The peaks found at 1574 and 1478 cm^{-1} are attributed to the C=C quinoid ring stretching vibrations and benzenoid structure of PANI, respectively. The characteristic peak pertaining to PANI backbone is observed at 804 cm^{-1}. The peaks found at 1298 and 1246 cm^{-1} correspond to the C-N and –C=N stretching vibrations due to emeraldine salt in PANI indicating that aniline is polymerized at the surface of ITO electrode with free $–NH_2$ groups [25]. The FTIR spectra of PANI-nMn_3O_4 NF shown in (curve b) exhibits additional peaks at 1718 cm^{-1} and 1449 cm^{-1} due to carbonyl (C=O) stretching of aldehyde and C-C stretching of the aromatic ring, respectively. The peaks observed at 2948 and 2879 cm^{-1} are attributed to the stretching of -C–H bond. The FTIR spectra obtained for the nanocomposite shows similar characteristic peaks. However, the peaks for bare PANI film are found to be shifted due to the formation of hydrogen bonding between Mn_3O_4 and the -NH groups of PANI. In addition, the nanocomposite exhibits characteristic peaks at 953 and 530

ACCEPTED MANUSCRIPT

cm^{-1} in the fingerprint region arising due to the vibrations of Mn–O are associated with the coupling between Mn–O stretching modes of tetrahedral and octahedral sites [33]. After immobilization of Tyrs on the surface of PANI-nMn_3O_4 NF (curve c), the peaks observed at 1228 cm^{-1} and 1279 cm^{-1} correspond to -C=N stretching vibrations of the amide. The peaks seen at 1539 cm^{-1} and 1656 cm^{-1} are attributed to the NH bending in carbonyl amide bond. These results confirm the surface functionalization of PANI-nMn_3O_4 NF with Tyrs enzyme.

The X-ray photoelectron spectroscopy (XPS) studies were undertaken to confirm the presence of the functional groups in nMn_3O_4, PANI NF, PANI-nMn_3O_4 NF and Tyrs-PANI-nMn_3O_4NF films on ITO electrode and the formation of amide between enzymes and PANI-nMn_3O_4 NF electrodes. The C 1s, N 1s, and O 1s peaks in the wide-scan spectrum of PANI NF, PANI-nMn_3O_4 NF and Tyrs-PANI-nMn_3O_4NF films are shown in Fig. 4 (i-iii). The Mn 2P, Mn 3P, Mn 3s, and O 1s peaks found in the wide-scan spectra of nMn_3O_4 indicate the formation of nMn_3O_4 Fig. 4 (iv). All core-level spectra were deconvoluted into characteristic peaks using a Shirley baseline with a Gaussian profile. The Mn 2P peak for nMn_3O_4 film was deconvoluted and split into two characteristic peaks at binding energies of 639.7 ($Mn2P_{3/2}$) and 644.4 eV ($Mn2P_{1/2}$) due to occurrence of Mn^{4+} (Fig. 4b). The O 1s peaks for nMn_3O_4 film at 530.7, 532.1 and 533.2 eV correspond to Mn-O-C, Mn-O-Mn and Mn-O-H, respectively and are due to the formation of metal–O–C bond, and metal-O (Fig. 4c).

The XPS C 1s peaks at 284.08, 285.4, and 289.4 eV for the PANI NF electrode alone, without nMn_3O_4 and Tyrs enzyme, due to the C–C group in the aromatic ring, C–N bonds, and the p–p* ‘‘shake-up’’ satellite, respectively (Fig. 5a, top graph). On incorporation on nMn_3O_4 into PANI electrode, no significant changes of these C 1s peaks were observed. However, one additional peak at binding energy of 286.09 eV corresponds to the C=N bond present in the composite formation and the peak due to the C–C groups in PANI is shifted to higher binding energy of 0.2 eV (Fig. 5b). After Tyrs immobilization onto PANI-nMn_3O_4 NF, the additional peaks at binding energies of 287.0 and 288.6 eV, correspond to N-C=O and C=O bonds due to covalent amide bond formation between Tyrs enzyme and PANI-nMn_3O_4 in presence of glutaraldehyde cross-linker (Fig. 5c). Fig. 3d shows the N 1s core-level spectra for PANI NF without nMn_3O_4 and Tyrs enzyme. The peaks for N 1s core level of PANI at the binding energies of 397.7, 399.3, and 400.5 eV are due to presence of –N=, -NH-, and $–N^+$-, respectively in PANI matrix (Fig. 5d). These peaks with modification of nMn_3O_4 in PANI matrix were not significantly shifted (Fig. 5e). After enzyme immobilization, the peak found at 297.9 eV correspond to the core-level electrons of N 1s (N1), the peak at 399.2 eV is due to amide bond (CO-NH) formation (N2), and the peak at 402.4 eV is assigned to presence of ≡N species in enzymes (N3) (Fig. 5f). However, the peaks at binding energies of

ACCEPTED MANUSCRIPT

297.9 eV and 399.2 eV for N 1s pertaining to enzymes and PANI are perhaps overlapped. These results confirm the formation of composite and covalent immobilization with Tyrs enzyme molecules.

To investigate the size of the synthesized nMn_3O_4 and PANI NF modified with nMn_3O_4, we conducted high resolution-transmission electron microscopy (HR-TEM). It is found that the nanostructure contains uniformly sized fine granules [Fig. 6(i-ii)] of nMn_3O_4 with hexagonal shape (20-25 nm). The clear lattice fringes seen in SAED pattern [inset, Fig. 6(ii)] indicate highly crystalline structure of the nMn_3O_4. In the atomic scale image (i, inset), two different lattice spacings (d) for (2 1 1) and (1 0 3) planes obtained are 0.248 nm and 0.276 nm, respectively. These results are in support of the JCPDS files 24-0734 and 80-0382, respectively indicating that growth of the nanoparticles occurs mostly along the 2 1 1 and 1 0 3 directions. After electropolymerization with aniline, the PANI coated nMn_3O_4 nanocomposite shows NF network [Fig. 6(iii-iv)]. A single PANI coated nMn_3O_4 NF of about 122.24 nm diameter is shown in image (iv). The SAED pattern of PANI-nMn_3O_4 nanocomposite indicates existence of the (1 0 3), (1 0 5) and (0 2 1) planes (inset, iii) that exactly match with the lattice spacing with d values of 0.280 nm, 0.18 nm and 0.39 nm, respectively (inset in Fig. 6(iv)). These results revealthat electropolymerized PANI-nMn_3O_4 NF provides a suitable biointerface for uniform linking of the Tyrs biomolecules. And it can be seen that Tyrs enzyme is uniformly attached with PANI-nMn_3O_4 NF surface due to inter-particle interactions of PANI-nMn_3O_4 NF and Tyrs enzyme molecules via GA [image (v-vi)].

3.2 Surface morphological studies

The SEM image [Fig. 7(i)] shows that the nMn_3O_4 are closely packed, and porous. The nMn_3O_4 exhibits numerous flower-like aggregations [inset in Fig. 7(i)] and some are elongated in structure. To investigate the atomic ratio and weight % of Mn and O, we carried out elemental (EDAX) analysis for the synthesized nMn_3O_4 [Fig. 7(ii)]. This study confirms the presence of 35 weight % of O and 65 weight % of Mn in the spherical nMn_3O_4 indicating high concentration of manganese and oxygen elements. The EDAX mapping for nMn_3O_4 after calcination containing mixed elements of Mn and O is shown in Fig. S1(a). The EDAX mapping confirms the presence of Mn (image b, Fig. S1) and oxygen elements (image c, Fig. S1) in Mn_3O_4 nanoparticles. It appears that most nanoparticles have spherical flower-like microsphere morphology, with globular 3D structure [Fig. 7 (iii) and (iv)]. After electropolymerization of nMn_3O_4 with PANI

ACCEPTED MANUSCRIPT

on ITO, a fibrous film of PANI-coated nMn_3O_4 is obtained [Fig. 7(v)]. The electropolymerized PANI-nMn_3O_4 results in the formation of symmetrical fibers of PANI-coated nMn_3O_4 deposited on the ITO substrate. The porous surface morphology of nanofibrous PANI-nMn_3O_4 is beneficial for immobilization of Tyrs enzyme molecules. Further, the PANI-nMn_3O_4NF/ITO surface was functionalized with GA via amino groups of the polyaniline surface for binding of the enzyme molecules.After enzyme immobilization, the morphology of Tyrs-PANI-nMn_3O_4NF/ITO surface perhaps occurred [Fig. 7(vi)] due to the covalent interaction of GA and enzyme. The FESEM image of enzyme immobilized on PANI-nMn_3O_4 NF shows a well- arranged and uniform fiber network, that further confirms strong enzyme binding.

The micrograph [Fig.S2 (i)] shows partially uniform spherical nMn_3O_4. The average size of the spherical nMn_3O_4 is calculated as 104 nm with average film roughness of 22.7 nm. The magnified image of nMn_3O_4 and the 3D image are shown in the inset of [Fig. S2 (i.a) and (vi)], respectively. After electropolymerization of PANI-nMn_3O_4 (image ii and iii), the changes in the grain size distribution, structural arrangement and shape of the PANI-nMn_3O_4NF/ITO are observed. The average roughness of PANI-nMn_3O_4NF/ITO film is found to be 90.7 nm. [Fig. S2 (iv)] and its 3D image (v) shows immobilization of the Tyrs enzyme onto the surface of PANI-nMn_3O_4NF/ITO. The Tyrs-PANI-nMn_3O_4NF/ITO electrode surface becomes uneven with increased value of average roughness (331 nm) indicating that Tyrs is adsorbed onto the PANI-nMn_3O_4NF/ITO surface.

3.3 Electrochemical studies

The electrochemical impedance can be represented as the sum of the real (Z') and imaginary (Z'') components that mainly originate from the resistance and capacitance of an electrochemical cell. Fig. 8(i) shows the EIS spectra of various electrodes obtained as a function of frequency (0.01 to 105 Hz) at a bias potential of 0.01V and the equivalent circuit for the EIS measurements [inset in Fig.8 (i)]. The charge transfer resistance (R_{CT}) between the electrolyte and electrode can be described by (Eq.1), [34]

$$Z(\omega) = R_s + \frac{R_{CT}+\sigma\omega^{-1/2}}{(C_d\sigma\omega^{1/2}+1)^2+\omega^2C_d^2(R_{CT}+\sigma\omega^{-1/2})2} - j\frac{\omega C_d(R_{CT}+\sigma\omega^{-1/2})2+\sigma\omega^{-1/2}(\sigma\omega^{1/2}C_d+1)}{(C_d\sigma\omega^{1/2}+1)^2+\omega^2C_d^2(R_{CT}+\sigma\omega^{-1/2})2}$$

Eq.1

ACCEPTED MANUSCRIPT

where R_s is the solution resistance, C_d is the double layer capacitance, ω is the 2πf, where f is the frequency, and σ is defined by

$$\sigma = \frac{RT}{\sqrt{2}F^2A}\left(\frac{1}{\sqrt{D_o}C_o^*} + \frac{1}{\sqrt{D_R}C_R^*}\right)$$

where A is the area of the electrode, D_o and D_R are respectively the diffusion coefficients of oxidant and reductant, C_o^* and C_R^* are the bulk concentrations of oxidant and reductant, respectively, and other symbols have the standard meanings. The R_{CT} value can be calculated from semicircular region in the Nyquist plot and it is found to be lower (551.4 Ω, curve b) for PANI-nMn_3O_4NF/ITO electrode compared to that of the bare ITO electrode (1.94 kΩ, curve a). This is due to the formation of PANI-nMn_3O_4 NF that provides excellent electrical contact between the PANI-nMn_3O_4NF/ITO electrode and electrolyte. The conductive nature of the nanocomposite, facilitates interfacial electron transfer from electrolyte towards the collector. Moreover, it appears that nanofibrous PANI suitably arranges the nMn_3O_4 on its surface and provides a better conformation for enzyme immobilization. Further, immobilization of Tyrs enzyme on PANI-nMn_3O_4NF/ITO surface, increases the R_{CT} value (curve c) due to presence of available functional groups (-NH_2 and -CHO) on the electrode surface. The enhancement of R_{CT} value (5.21 kΩ) for Tyrs-PANI-nMn_3O_4NF/ITO bioelectrode is due to the insulating nature of the Tyrs molecules that covalently bind with -NH_2 group of PANI *via* GA. The amount of immobilized enzyme has been optimized at 10.0 µL and the surface coverage of Tyrs-PANI-nMn_3O_4NF/ITO bioelectrode was calculated to be (62.76%), [3].

The electron transfer resistance can be translated into magnitude of current under the equilibrium (Io), heterogeneous electron-transfer rate constant (HET) and the time constant (τ) of the various electrodes have been calculated by the following Eq. (2-5) [3].

$$R_{CT} = RT/nFI_0 \qquad \text{Eq.2}$$

$$I_0 = nFA\,HET[S] \qquad \text{Eq.3}$$

$$HET = RT/n^2F^2AR_{CT}[S] \qquad \text{Eq.4}$$

$$\tau = R_{CT}C_{dl} \qquad \text{Eq.5}$$

ACCEPTED MANUSCRIPT

where R is gas constant, T is absolute temperature (K), F is Faraday constant, A is the electrode area (cm^2), [S] is the bulk concentration of redox probe (mol cm^{-3}), n is the number of transferred electrons per molecule of the redox probe and C_{dl} is the double layer capacitance. The HET value for ITO is found to be 0.014×10^{-6} cm s^{-1}. The HET value of PANI-nMn_3O_4NF/ITO electrode (0.048×10^{-6} cm s^{-1}) is higher than Tyrs-PANI-nMn_3O_4NF/ITO bioelectrode (0.0051×10^{-6} cm s^{-1}), indicating faster electron transfer among the redox couples. The Tyrs enzyme-immobilized electrode delivers hindrance to the electron transfer resulting in a sluggish electron transfer. Further, high value of time constant (τ) for Tyrs-PANI-nMn_3O_4NF/ITO bioelectrode (44.2 cm s^{-1}) shows slower diffusion rate (8.4 cm s^{-1}) of $[Fe(CN)_6]^{3-/4-}$ ions at the solution/electrode interface.

The cyclic voltammetry (CV) studies have been conducted to investigate the electrochemical properties of the fabricated electrodes in the potential range of -0.7 to 0.7 V at a scan rate of 10 mV/s [Fig. 8(ii)]. After electropolymerization of PANI-nMn_3O_4 nanocomposite on ITO substrate, the oxidation current decreases (0.04 mA) [curve b] compared to that of the bare ITO electrode (1.6 mA) [curve a] revealing that the increased surface area of PANI-nMn_3O_4NF/ITO electrode may obstruct electron transfer. Interestingly, after immobilization of Tyrs enzyme on the surface of PANI-nMn_3O_4NF/ITO, the electrode shows increased current response (0.05 mA, curve c) compared to that of PANI-nMn_3O_4NF/ITO electrode (curve b). This may be attributed to the covalently bonded Tyrs molecules on the surface of PANI-nMn_3O_4NF/ITO providing a promising environment. The available active sites on Tyrs may be electrochemically activated in presence PANI-nMn_3O_4 NF that perhaps acts as a mediator resulting in accelerated electrons from redox reaction. The CV studies of Tyrs-PANI-nMn_3O_4NF/ITO bioelectrode have been conducted as a function of scan rate [Fig. S3]. The anodic (I_A) and cathodic (I_C) peak currents show linear variation with square root of the scan rate [inset in Fig. S3], suggesting that the reaction at the electrode is a quasi-reversible diffusion-controlled process. Both the peak currents are found to increase with increased scan rate (10-100 mV s^{-1}). The linear relationship of peak current versus square root of scan rate ($v^{1/2}$) in Tyrs-PANI-nMn_3O_4NF/ITO bioelectrode can be derived from the Nernst's equation due to presence of electro-active components in the interfacial region. The slope, intercept and correlation coefficient for the bioelectrode obey the following anodic (I_A) and cathodic (I_C) currents given in Eq. (6 and 7):

ACCEPTED MANUSCRIPT

$$I_A(\text{bioelectrode}) = 29.3\ \mu\text{A} + 1.60 \times 10^{-5}(\text{A}^2\text{mV}^{-1}\text{s})^{1/2} \times [\text{Scan rate}(\text{mVs}^{-1})]^{1/2};\ r^2 = 0.999 \quad \text{Eq.6}$$

$$I_C(\text{bioelectrode}) = -26.7\ \mu\text{A} - 0.76 \times 10^{-5}(\text{A}^2\text{mV}^{-1}\text{s})^{1/2} \times [\text{Scan rate}(\text{mVs}^{-1})]^{1/2};\ r^2 = 0.999 \quad \text{Eq.7}$$

The peak current is obtained by the Randles-Sevcik method, as described in Eq. (8)

$$I_p = \frac{n^2F^2CAv}{RT} \quad \text{Eq. 8}$$

where I_p is the peak current (A), n is the number of electrons transferred in the redox process, F is the Faraday constant (C mol^{-1}), C is the concentration (mM), R is gas constant (8.314 J K^{-1} mol^{-1}), υ is the scan rate (40 mV/s), A is the area of fabricated interface (0.25 cm^2) and T is the absolute temperature (298K). The diffusion coefficient of redox probe towards the sensing interface is calculated using Randles-Sevcik Eq. (8)

$$I_{p=2.69\times10^5 n^{3/2}\ A\ D^{1/2}\ C\ v^{1/2}}$$

The diffusion coefficients are found to be 1.41×10^{-6} cm^2/s and 2.21×10^{-6} cm^2/s for PANI-nMn_3O_4NF/ITO electrode and Tyrs-PANI-nMn_3O_4NF/ITO bioelectrode, respectively. The higher diffusion after enzyme immobilization may be due to the formation of PANI-nMn_3O_4 fibrous film that accelerates the transport of electrons due to activation of enzyme active sites.

The reproducibility of Tyrs-PANI-nMn_3O_4NF/ITO bioelectrode [Fig. 8(iii)] was investigated at 0.01×10^{-6} mol L^{-1} of BPA concentration. No significant change in the oxidation current was observed as was evident by relative standard deviation (RSD=6.74 %). The stability of this bioelectrode was tested using repeated measurements at same conditions. Even after 15 times of repeated measurements, [Fig. 8(iv)], the Tyrs-PANI-nMn_3O_4NF/ITO bioelectrode showed identical response as is evident by low relative standard deviation (RSD=2.99 %). The storage stability of the Tyrs-PANI-nMn_3O_4NF/ITO bioelectrode was checked for 8 weeks at an interval of one week. The decrease in the value of current was found to be about 10% up to 4 weeks after which the current value decreases to about 40 % within 10 weeks.

3.4 Bisphenol A Detection

ACCEPTED MANUSCRIPT

Electrochemical response studies of Tyrs-PANI-nMn_3O_4NF/ITO biosensor were conducted using CV technique in presence of 50 $\times 10^{-3}$ mol L^{-1} PBS (pH 7.4, 0.9%NaCl) containing 5 $\times 10^{-3}$ mol L^{-1} $[Fe(CN)_6]^{3-/4-}$. The control experiments were conducted on PANI-nMn_3O_4NF/ITO electrode with and without Tyrs immobilization, using CV technique [Fig. 9(i)] by varying BPA concentrations. A small change in oxidation current (curve a) can be attributed to non-specific reaction with proteins on the sensor surface.

During detection of BPA, the bioelectrode was immersed in PBS solution containing various concentrations of BPA (0.004-0.8 $\times 10^{-6}$ mol L^{-1}). Due to the oxidation of BPA into 2, 2-bis (4-phenylquinone) propane in presence of Tyrs enzyme, two electrons are generated [Fig.9 (ii)] that produce the current. It was observed that magnitude of the current gradually increased with increasing BPA concentration [Fig. 9(ii)]. In addition, this enhancement of electrochemical current may be due to well-arranged and homogenous network of bio-interface of the PANI-nMn_3O_4 nanofibrous film that provides a good path for electron transfer to current collector via manganese ion [35, 36]. The three-dimensional nanofibrous morphology in PANI-nMn_3O_4NF/ITO electrode resulted in improved electronic and ionic transport due to uniform distribution and conductive nature of PANI-nMn_3O_4 NF. The detection time of this biosensor was to be 20 s indicating faster electron communication feature of PANI-nMn_3O_4 NF. The sensor calibration curve [Fig. 9(iii)] showed good linearity for a wide concentration range of 0.004 - 0.8 $\times 10^{-6}$ mol L^{-1}. The current varied linearly with BPA concentration with a correlation coefficient of 0.993. The sensitivity of the fabricated biosensor calculated from the slope of calibration curve was found to be 0.776 mA μM^{-1} Lcm^{-2} and 0.134 mA μM^{-1} Lcm^{-2} for a lower concentration range (0.004-0.09 $\times 10^{-6}$ mol L^{-1}) and higher concentration (0.2-0.8 $\times 10^{-6}$ mol L^{-1}), respectively. The high sensitivity of this biosensor was due to high surface-to-volume ratio and conductive nature of PANI-nMn_3O_4 NF with better electron transportation from electrode surface to the electrolyte. This sensor could be used to detect minute amount of BPA (0.004 $\times 10^{-6}$ mol L^{-1}). The low value of the Michaelis–Menten constant (K_m) obtained [0.0075 $\times 10^{-6}$ mol L^{-1}] using Hanes plot reveals that PANI-nMn_3O_4 NF matrix facilitates increased enzyme activity due to improved conformation of Tyrs. The increased activity of Tyrs with covalent bonding indicates strong affinity between the BPA and the active site of Tyrs resulted in low K_m. The observed higher affinity of Tyrs-PANI-nMn_3O_4NF/ITO based biosensor can be attributed to favorable orientation of Tyrs and higher loading of Tyrs molecules. Table 1 contains

ACCEPTED MANUSCRIPT

characteristics of this sensor along with others reported in literature for BPA detection. The selectivity of Tyrs-PANI-nMn_3O_4NF/ITO bioelectrode [Fig. 9(iv)] was determined in presence of BPA (0.5×10^{-6} mol L^{-1}) concentration with normal concentration of interferent such as phenol (1.0×10^{-6} mol L^{-1}), ortho-nitrophenol (1.0×10^{-6} mol L^{-1}), para-aminophenol (0.8×10^{-3} mol L^{-1}), resorcinol (1.0×10^{-6} mol L^{-1}), hydroquinone (0.8×10^{-6} mol L^{-1}), and all mixers. The response of the Tyrs-PANI-nMn_3O_4NF/ITO bioelectrode was not significantly affected in the presence of interferents during BPA detection. The oxidation current value remained nearly same for all interferents with respect to BPA. The prepared biosensor was tested to detect BPA concentrations in real samples [Fig. 10 (i)]. In comparison to the standard BPA concentrations (curve b), the bioelectrode showed little difference at low real BPA concentrations other than higher concentration of BPA detection (curve a).

Conclusions

A cost-effective, reproducible, selective and highly sensitive PANI-nMn_3O_4 NF based biosensor platform has been demonstrated for BPA detection. We have electropolymerized *in-situ* PANI-nMn_3O_4 NF on an ITO substrate and used that for surface functionalization with Tyrs enzyme molecules via GA treatment. The fibrous surface of PANI-nMn_3O_4 NF performs a cross link with GA molecules for covalent immobilization of Tyrs enzyme resulting in improved sensing characteristics for monitoring BPA concentration. This biosensor is sensitive to 0.004 $\times 10^{-6}$ mol L^{-1} concentration of BPA due to the PANI-nMn_3O_4 NF biointerface, Mn^{2+} ion and cationic polyaniline that improves the charge transfer properties between electrode and electrolyte. The Tyrs-conjugated PANI-nMn_3O_4 NF provides suitable conduction path during oxidation of BPA leading to a fast electrochemical response (20s). This biosensor exhibits higher sensitivity (0.776 mA μM^{-1} Lcm^{-2}), low detection limit of 0.004 $\times 10^{-6}$ mol L^{-1}, lower K_m value 0.0075 $\times 10^{-6}$ mol L^{-1} with linear regression coefficient at 0.993 and a wide linear range of 0.004-0.8 $\times 10^{-6}$ mol L^{-1}. The Tyrs-PANI-nMn_3O_4NF/ITO-based biosensor provides a suitable platform for excellent electrochemical sensing parameters due to the integration of PANI-nMn_3O_4NF and Tyrs via GA. The fabricated biointerface shows excellent sensitivity, selectivity, and good reproducibility and can be explored for monitoring other clinical substances such as low density lipoprotein, glucose, myoglobin etc.

ACCEPTED MANUSCRIPT

References:

[1] K.K. Reza, M.A. Ali, S. Srivastava, V.V. Agrawal, A.M. Biradar, Tyrosinase conjugated reduced graphene oxide based biointerface for bisphenol A sensor, Biosens. Bioelectron. 74 (2015) 644–651.

[2] L.N. Vandenberg, R. Hauser, M. Marcus, N. Olea, W.V. Welshons, Human exposure to bisphenol A (BPA) Reprod Toxicol 24 (2): 139–177, Find This Artic. Online. (2007).

[3] N. Singh, K.K. Reza, M.A. Ali, V.V. Agrawal, A.M. Biradar, Self assembled DC sputtered nanostructured rutile TiO2 platform for bisphenol A detection, Biosens. Bioelectron. 68 (2015) 633–641. doi:10.1016/j.bios.2015.01.041.

[4] J.R. Roy, S. Chakraborty, T.R. Chakraborty, Estrogen-like endocrine disrupting chemicals affecting puberty in humans--a review, Med. Sci. Monit. 15 (2009) RA137–RA145.

[5] M. Regiart, S.V. Pereira, V.G. Spotorno, F.A. Bertolino, J. Raba, Food safety control of zeranol through voltammetric immunosensing on Au–Pt bimetallic nanoparticle surfaces, Analyst. 139 (2014) 4702–4709. doi:10.1039/C4AN00686K.

[6] C. Nichols, X. Ding, G. Miranda-Carboni, S.A. Krum, Abstract 3192: The environmental estrogen bisphenol A (BPA) regulates mammary gland stem cells, Cancer Res. 74 (2014) 3192–3192. doi:10.1158/1538-7445.AM2014-3192.

[7] P. Sohoni, C.R. Tyler, K. Hurd, J. Caunter, M. Hetheridge, T. Williams, C. Woods, M. Evans, R. Toy, M. Gargas, J.P. Sumpter, Reproductive Effects of Long-Term Exposure to Bisphenol A in the Fathead Minnow (Pimephales promelas), Environ. Sci. Technol. 35 (2001) 2917–2925. doi:10.1021/es000198n.

[8] G. Wang, Z. Chen, T. Bartell, X. Wang, Early Life Origins of Metabolic Syndrome: The Role of Environmental Toxicants, Curr. Environ. Health Rep. 1 (2014) 78–89. doi:10.1007/s40572-013-0004-6.

[9] D. Melzer, N.J. Osborne, W.E. Henley, R. Cipelli, A. Young, C. Money, P. McCormack, R. Luben, K.-T. Khaw, N.J. Wareham, T.S. Galloway, Urinary Bisphenol A Concentration and Risk of Future Coronary Artery Disease in Apparently Healthy Men and Women, Circulation. 125 (2012) 1482–1490. doi:10.1161/CIRCULATIONAHA.111.069153.

[10] A. Zafra, M. del Olmo, B. Suárez, E. Hontoria, A. Navalón, J.L. Vílchez, Gas chromatographic–mass spectrometric method for the determination of bisphenol A and its chlorinated derivatives in urban wastewater, Water Res. 37 (2003) 735–742. doi:10.1016/S0043-1354(02)00413-X.

[11] K. Inoue, Y. Yoshie, S. Kondo, Y. Yoshimura, H. Nakazawa, Determination of phenolic xenoestrogens in water by liquid chromatography with coulometric-array detection, J. Chromatogr. A. 946 (2002) 291–294. doi:10.1016/S0021-9673(01)01527-8.

[12] K. Ma, T. Ekblad, M.K. Koerkamp, H. Kelderman, M. van Wijlen, A. Duarah, J. Yue, L. Zhang, M.V.-M. Wong, M.H. Lim, Contaminant detection in treated water using Optiqua's MiniLab^{TM} biosensing system: a case study for Bisphenol A, Int. J. Environ. Anal. Chem. 95 (2015) 366–378. doi:10.1080/03067319.2015.1025223.

[13] Z. Xiao-hong, L. Lan-hua, X. Wei-qi, S. Bao-dong, S. Jian-wu, H. Miao, S. Han-chang, A reusable evanescent wave immunosensor for highly sensitive detection of bisphenol A in water samples, Sci. Rep. 4 (2014). doi:10.1038/srep04572.

ACCEPTED MANUSCRIPT

[14] J.-W. Park, S. Kurosawa, H. Aizawa, Y. Goda, M. Takai, K. Ishihara, Piezoelectric immunosensor for bisphenol A based on signal enhancing step with 2-methacrolyloxyethyl phosphorylcholine polymeric nanoparticle, The Analyst. 131 (2006) 155–162. doi:10.1039/B511662G.
[15] D.K. Kim, P. Muralidharan, H.-W. Lee, R. Ruffo, Y. Yang, C.K. Chan, H. Peng, R.A. Huggins, Y. Cui, Spinel LiMn2O4 Nanorods as Lithium Ion Battery Cathodes, Nano Lett. 8 (2008) 3948–3952. doi:10.1021/nl8024328.
[16] E. Hosono, T. Kudo, I. Honma, H. Matsuda, H. Zhou, Synthesis of Single Crystalline Spinel LiMn2O4 Nanowires for a Lithium Ion Battery with High Power Density, Nano Lett. 9 (2009) 1045–1051. doi:10.1021/nl803394v.
[17] P. Li, C. Nan, Z. Wei, J. Lu, Q. Peng, Y. Li, Mn3O4 Nanocrystals: Facile Synthesis, Controlled Assembly, and Application, Chem. Mater. 22 (2010) 4232–4236. doi:10.1021/cm100831q.
[18] S. Fritsch, J. Sarrias, A. Rousset, G.U. Kulkarni, Low-temperature oxidation of Mn3O4 hausmannite, Mater. Res. Bull. 33 (1998) 1185–1194. doi:10.1016/S0025-5408(98)00108-1.
[19] Z. Weixin, W. Cheng, Z. Xiaoming, X. Yi, Q. Yitai, Low temperature synthesis of nanocrystalline Mn3O4 by a solvothermal method, Solid State Ion. 117 (1999) 331–335. doi:10.1016/S0167-2738(98)00432-9.
[20] P.Z. Si, D. Li, C.J. Choi, Y.B. Li, D.Y. Geng, Z.D. Zhang, Large coercivity and small exchange bias in Mn3O4 / MnO nanoparticles, Solid State Commun. 142 (2007) 723–726. doi:10.1016/j.ssc.2007.04.029.
[21] A. Vázquez-Olmos, R. Redón, G. Rodríguez-Gattorno, M. Esther Mata-Zamora, F. Morales-Leal, A.L. Fernández-Osorio, J.M. Saniger, One-step synthesis of Mn3O4 nanoparticles: Structural and magnetic study, J. Colloid Interface Sci. 291 (2005) 175–180. doi:10.1016/j.jcis.2005.05.005.
[22] K. Kamil Reza, N. Singh, S.K. Yadav, M.K. Singh, A.M. Biradar, Pearl shaped highly sensitive Mn3O4 nanocomposite interface for biosensor applications, Biosens. Bioelectron. 62 (2014) 47–51. doi:10.1016/j.bios.2014.06.013.
[23] Y. Chen, X.H. Wang, J. Li, J.L. Lu, F.S. Wang, Polyaniline for corrosion prevention of mild steel coupled with copper, Electrochimica Acta. 52 (2007) 5392–5399. doi:10.1016/j.electacta.2007.02.057.
[24] Y. Sun, J.A. Rogers, Inorganic Semiconductors for Flexible Electronics, Adv. Mater. 19 (2007) 1897–1916. doi:10.1002/adma.200602223.
[25] C. Dhand, S.K. Arya, S.P. Singh, B.P. Singh, M. Datta, B.D. Malhotra, Preparation of polyaniline/multiwalled carbon nanotube composite by novel electrophoretic route, Carbon. 46 (2008) 1727–1735. doi:10.1016/j.carbon.2008.07.028.
[26] X. Qin, S. Liu, W. Lu, H. Li, G. Chang, Y. Zhang, J. Tian, Y. Luo, A.M. Asiri, A.O. Al-Youbi, X. Sun, Submicrometre-scale polyaniline colloidal spheres: photopolymerization preparation using fluorescent carbon nitride dots as a photocatalyst, Catal. Sci. Technol. 2 (2012) 711–714. doi:10.1039/C2CY00439A.
[27] G. Chang, Y. Luo, W. Lu, X. Qin, A.M. Asiri, A.O. Al-Youbi, X. Sun, Ag nanoparticles decorated polyaniline nanofibers: synthesis, characterization, and applications toward catalytic reduction of 4-nitrophenol and electrochemical detection of H2O2 and glucose, Catal. Sci. Technol. 2 (2012) 800–806. doi:10.1039/C2CY00454B.

ACCEPTED MANUSCRIPT

[28] S. Liu, L. Wang, Y. Luo, J. Tian, H. Li, X. Sun, Polyaniline nanofibres for fluorescent nucleic acid detection, Nanoscale. 3 (2011) 967–969. doi:10.1039/C0NR00873G.
[29] Z.W. Chen, J.K.L. Lai, C.H. Shek, Nucleation site and mechanism leading to growth of bulk-quantity Mn3O4 nanorods, Appl. Phys. Lett. 86 (2005) 181911. doi:10.1063/1.1923753.
[30] H. Kavas, Z. Durmus, M. Şenel, S. Kazan, A. Baykal, M.S. Toprak, CTAB-Mn3O4 nanocomposites: Synthesis, NMR and low temperature EPR studies, Polyhedron. 29 (2010) 1375–1380. doi:10.1016/j.poly.2009.12.034.
[31] Z. Zheng, Y. Du, Z. Wang, Q. Feng, C. Wang, Pt/graphene–CNTs nanocomposite based electrochemical sensors for the determination of endocrine disruptor bisphenol A in thermal printing papers, Analyst. 138 (2012) 693–701. doi:10.1039/C2AN36569C.
[32] A.I. Inamdar, Y.S. Kim, J.S. Sohn, H. Im, H. Kim, D.-Y. Kim, R.S. Kalubarme, C.H. Park, Supercapacitive characteristics of electrodeposited polyaniline thin films grown on indium doped tin oxide substrates, J. Korean Phys. Soc. 59 (2011) 145–149.
[33] D.P. Dubal, D.S. Dhawale, R.R. Salunkhe, S.M. Pawar, C.D. Lokhande, A novel chemical synthesis and characterization of Mn3O4 thin films for supercapacitor application, Appl. Surf. Sci. 256 (2010) 4411–4416. doi:10.1016/j.apsusc.2009.12.057.
[34] B.-Y. Chang, S.-M. Park, Integrated Description of Electrode/Electrolyte Interfaces Based on Equivalent Circuits and Its Verification Using Impedance Measurements, Anal. Chem. 78 (2006) 1052–1060. doi:10.1021/ac051641l.
[35] H. Xia, Y.S. Meng, X. Li, G. Yuan, C. Cui, Porous manganese oxide generated from lithiation/delithiation with improved electrochemical oxidation for supercapacitors, J. Mater. Chem. 21 (2011) 15521–15526. doi:10.1039/C1JM12767E.
[36] H. Jiang, T. Zhao, J. Ma, C. Yan, C. Li, Ultrafine manganese dioxide nanowire network for high-performance supercapacitors, Chem. Commun. 47 (2011) 1264–1266. doi:10.1039/C0CC04134C.
[37] D.C. Apodaca, R.B. Pernites, R. Ponnapati, F.R. Del Mundo, R.C. Advincula, Electropolymerized Molecularly Imprinted Polymer Film: EIS Sensing of Bisphenol A, Macromolecules. 44 (2011) 6669–6682. doi:10.1021/ma2010525.
[38] Q. Li, H. Li, G.-F. Du, Z.-H. Xu, Electrochemical detection of bisphenol A mediated by [Ru(bpy)3]2+ on an ITO electrode, J. Hazard. Mater. 180 (2010) 703–709. doi:10.1016/j.jhazmat.2010.04.094.
[39] H. Yin, Y. Zhou, J. Xu, S. Ai, L. Cui, L. Zhu, Amperometric biosensor based on tyrosinase immobilized onto multiwalled carbon nanotubes-cobalt phthalocyanine-silk fibroin film and its application to determine bisphenol A, Anal. Chim. Acta. 659 (2010) 144–150. doi:10.1016/j.aca.2009.11.051.
[40] M. Portaccio, D. Di Tuoro, F. Arduini, M. Lepore, D.G. Mita, N. Diano, L. Mita, D. Moscone, A thionine-modified carbon paste amperometric biosensor for catechol and bisphenol A determination, Biosens. Bioelectron. 25 (2010) 2003–2008. doi:10.1016/j.bios.2010.01.025.
[41] J. Huang, X. Zhang, S. Liu, Q. Lin, X. He, X. Xing, W. Lian, Electrochemical sensor for bisphenol A detection based on molecularly imprinted polymers and gold nanoparticles, J. Appl. Electrochem. 41 (2011) 1323–1328. doi:10.1007/s10800-011-0350-8.

ACCEPTED MANUSCRIPT

Figure Captions

Fig.1 (i) Schematic representation of In-situ electropolymerization of Mn_3O_4-polyaniline nanocomposite (ii) Chronoamperometric current responses during in-situ electropolymerization of Mn_3O_4 nanoparticles with aniline monomer.

Fig. 2. Schematic representation of fabrication of a biosensor platform for detection of endocrine disrupting chemicals and the mechanism for crosslinking with enzyme molecules.

Fig. 3 (i) X-ray diffraction pattern of (i.a) polyaniline, (i.b) spherical Mn_3O_4 nanoparticle, and (i.c) PANI-nMn_3O_4 nanocomposite (ii) FTIR spectra of (a) polyaniline, (b) PANI-nMn_3O_4/ITO electrode and (c) Tyrs-PANI-nMn_3O_4/ITO bioelectrode.

Fig. 4 (a) Wide-scan spectra for various fabricated films in the energy region of 0-1100 eV. (b) The XPS core-level spectra of Mn 2P and (c) core-level spectra of O 1s for Mn_3O_4 film.

Fig. 5 XPS core-level spectra of C 1s for the PANI NF (a), PANI-nMn_3O_4 NF (b) and Tyrs/PANI-nMn_3O_4 NF (c) electrodes. Core-level spectra of N 1s for the PANI NF (a), PANI-nMn_3O_4 NF (b) and Tyrs/PANI-nMn_3O_4 NF (c) electrodes.

Fig. 6 (i and ii) TEM images of spherical Mn_3O_4 nanoparticles, inset images are HRTEM and SAED pattern, (iii and iv) TEM images of PANI-nMn_3O_4 nanofibers, inset zoom image of PANI-nMn_3O_4 nanofiber, inset images are HRTEM and SAED pattern, (v and vi) TEM images of Tyrs-PANI-nMn_3O_4/ITO bioelectrode after Tyrs immobilization.

Fig. 7 (i) SEM image of spherical Mn_3O_4 nanoparticles, inset zoom image of spherical Mn_3O_4 nanoparticles, (ii) Elemental analysis (EDAX) image of spherical Mn_3O_4 nanoparticles, (iii and iv) FESEM images of spherical Mn_3O_4 nanoparticles, (v) FESEM image of PANI-nMn_3O_4 nanofibers, and (vi) FESEM image of Tyrs-PANI-nMn_3O_4/ITO bioelectrode after Tyrs immobilization.

Fig. 8 (i) Electrochemical impedance spectroscopy (EIS) spectra of (a) ITO electrode, (b) PANI-nMn_3O_4/ITO electrode, and (c) Tyrs-PANI-nMn_3O_4/ITO bioelectrode in PBS (50 mM, pH 7.4) solution containing 5 mM $[Fe(CN)_6]^{3-/4-}$. (ii) The cyclic voltammogram of, (a) ITO electrode, (b) PANI-nMn_3O_4/ITO electrode, and (c)Tyrs-PANI-nMn_3O_4/ITO bioelectrode. (iii) The reproducibility of Tyrs-PANI-nMn_3O_4/ITO bioelectrode, and (iv) Repeatability of Tyrs-PANI-nMn_3O_4/ITO bioelectrode.

ACCEPTED MANUSCRIPT

Fig. 9 (i) Control study of Tyrs-PANI-nMn_3O_4/ITO bioelectrode, (ii) Cyclic voltammogram of Tyrs-PANI-nMn_3O_4/ITO bioelectrode as a function of BPA concentration (0.004 – 0.8μM) in PBS (50 mM, pH 7.4) solution containing 5 mM $[Fe(CN)_6]^{3-/4-,}$ (iii) Calibration curve between oxidation current and BPA concentration (μM), and (iv) The selectivity of Tyrs-PANI-nMn_3O_4/ITO bioelectrode.

Fig. 10 (i) Cyclic voltammogram comparison study of Tyrs-PANI-nMn_3O_4/ITO bioelectrode as a function of synthetic BPA and real sample BPA concentration (0.001-0.008 μM) in PBS (50 mM, pH 7.4) solution containing 5 mM $[Fe(CN)_6]^{3-/4-}$.

ACCEPTED MANUSCRIPT

Table. Comparison table for various biosensors characteristics with the fabricated Tyrs-PANI-nMn_3O_4NF/ITO bioelectrode

Electrodes	Techniques	Linear range (µM)	LOD (µM)	Sensitivity	References
Molecular Imprinted polymer film	EIS	0 – 12,000	420	0.00411 Ω $mM^{-1}L$	Apodaca *et al.*[37]
TyrsAPTES/nTiO_2/Ti	EIS	0.01-1.0	0.01	361.9kΩ $mM^{-1}L$	Singh *et al.*[3]
Pt/Gr-CNTs	CV/DPV	0.06 – 10	0.042		Zheng *et al.*[31]
Polypyridyl ruthenium(II)	CV/DPV	5 – 120	0.29	0.22 µA $µM^{-1}L$	Li *et al.*[38]
Tyrs MWNTs-CoPc-SF	CV	0.05–3.0	0.03		Yin *et al.*[39]
Tyrs/Thionine-carbon	CV	0.15- 45	0.15	85.4±1.5 nA $µM^{-1}L$	Portaccio *et al.* [40]
MIP Au	CV	8 – 60	13.8	--	Huang *et al.*[41]
Tyrs@PANI-Mn_3O_4/ITO	CV	0.004 – 0.8	0.004	0.776 mA $µM^{-1}L$ cm^{-2}	Present Work

ACCEPTED MANUSCRIPT

Biographies

Nawab Singh

Nawab Singh is doing PhD at the Indian Institute of Technology Hyderabad Telangana, India, in the Department of Biomedical Engineering. He received his MSc from Chaudhary Charan Singh University, Meerut, India (2010). Nawab's research interests are in micro/nano fabrication of functional nanomaterials, self and directed assembly, microfluidics based biochips for biomolecules detection, polymer thin-films, biomaterials for biosensing application. He has published 4 papers in peer-reviewed journals.

Md. Azahar Ali

Md. Azahar Ali received his PhD degree from Biomedical Engineering Department at Indian Institute of Technology Hyderabad, India in collaboration with Biomedical Instrumentation Section at National Physical Laboratory, New Delhi, India. He also received his Master of Technology degree from Department of Electronics Engineering, Tezpur University, Assam in 2009. Currently, he is doing Post-Doctoral Associate at Electrical and Computer Engineering, Iowa State University, USA. He is actively engaged in the area of microfluidic based multiplex biochips for biomolecules detection.

Kali Suresh

Kali Suresh is doing Project Officer at the Indian Institute of Technology Hyderabad Telangana, India, in the Department of Chemical Engineering. He received his MSc from National Institute of Technology Warangal, Telangana, India (2010). Kali research interests are in Carbon based hierarchical structures. He has published 2 papers in peer-reviewed journals.

Ved Varun Agrawal

Ved Varun Agrawal earned his PhD degree from the Jawaharlal Nehru Center for Advanced Scientific Research in 2008. He now works as a Scientist in the Department of Science & Technology of Biomolecular Electronics, Biomedical Instrumentation Section at National Physical Laboratory (CSIR), New Delhi, India. His current research focuses on utilizing the properties of nanomaterials to improve biosensing characteristics.

Prabhakar Rai

Prabhakar Rai is working as INSPIRE Faculty in the Department of Chemical Engineering at Indian Institute of Technology Kanpur, India. He received his Ph.D. degree in Informatic Electronics Materials Engineering in 2012 from Chonbuk National University, South Korea. He was appointed as Research Professor in the Department of Materials Science and Engineering at

ACCEPTED MANUSCRIPT

Korea University, South Korea in 2013. His research is mainly focused on synthesis of nanoscale metals and metal oxides for energy and chemical sensing applications.

Ashutosh Sharma

Ashutosh Sharma is a Chair Professor in Chemical Engineering at the Indian Institute of Technology at Kanpur (IITK). Ashutosh received his Ph.D. from the State University of New York at Buffalo (1987), MS from the Pennsylvania State University (1984) and B. Tech. from IITK(1982).Ashutosh's research interests are in soft functional interfaces, micro/nano-mechanics of confined soft matter, self-organized patterning, soft nanofabrication, colloid and interfacial engineering, carbon nanocomposites and carbon MEMS/NEMS in energy, health and environmental applications, and membranes. He is currently Secretary to the Government of India, Department of Science and Technology starting January 2015

B. D. Malhotra

B. D. Malhotra received his Ph.D. degree from the University of Delhi, Delhi, India in 1980. He has published more than 270 papers in peer-reviewed journals, filed 10 patents, and edited/co-edited books on biosensors and polymer electronics. After his stint as Chief Scientist and Head of the DST Centre on Biomolecular Electronics at the CSIR-National Physical Laboratory, New Delhi, India, he moved to Delhi Technological University (DTU), India. He has nearly 30 years of research experience in the field of biomolecular electronics and has guided 25 Ph.D. students to date. His current activities include biosensors, nanobiomaterials, conducting polymers, and ordered molecular assemblies including Langmuir–Blodgett films and self-assembled monolayers among others. Dr. Malhotra is a Fellow of the Indian National Science Academy (INSA), the National Academy of Sciences, India (NASI) and an Academician of the Asia-Pacific Academy of Materials (APAM).

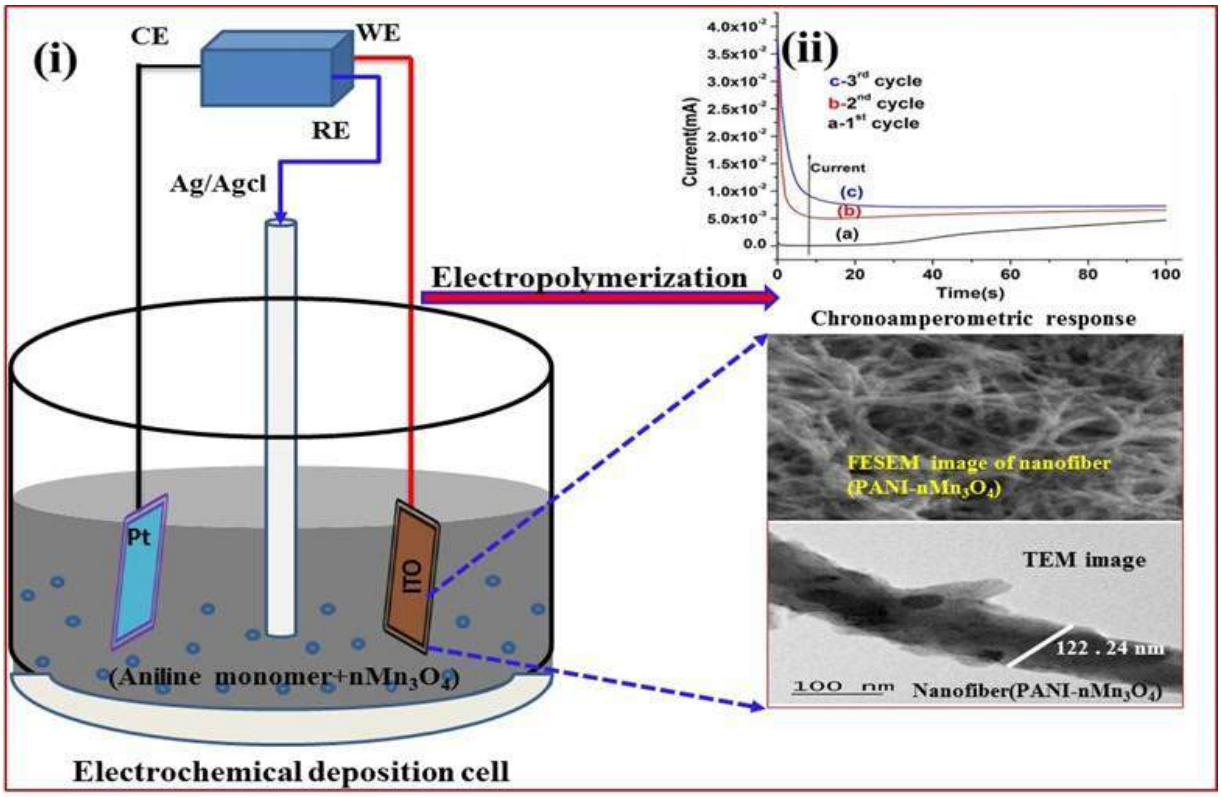
Renu John

Renu John is currently an Associate Professor and Head of the Department of Biomedical Engineering, Indian Institute of Technology Hyderabad. He received his PhD degree from Indian Institute of Technology Delhi in 2006. He carried out his post-doctoral research at Fitzpatrick center for Photonics, Duke University, Durham, NC, USA and Biophotonics Imaging Laboratory, University of Illinois, Urbana-Champaign, USA. His research interests include Nano-Biophotonics, non-invasive NIR bio-imaging, 3-D phase microscopy Optical coherence tomography (OCT), Chemical and optical Biosensors.

ACCEPTED MANUSCRIPT

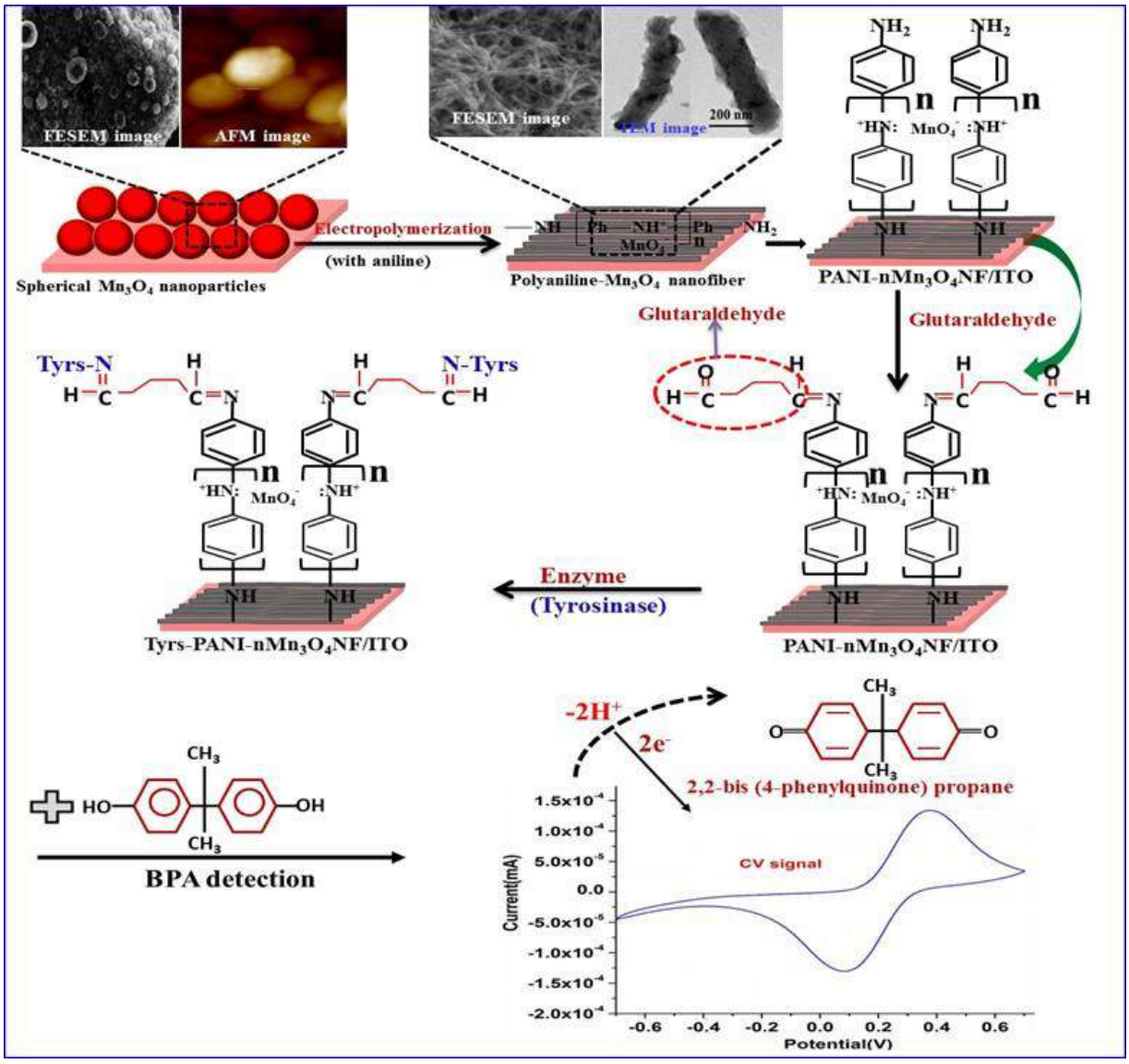
Figures

Fig. 1



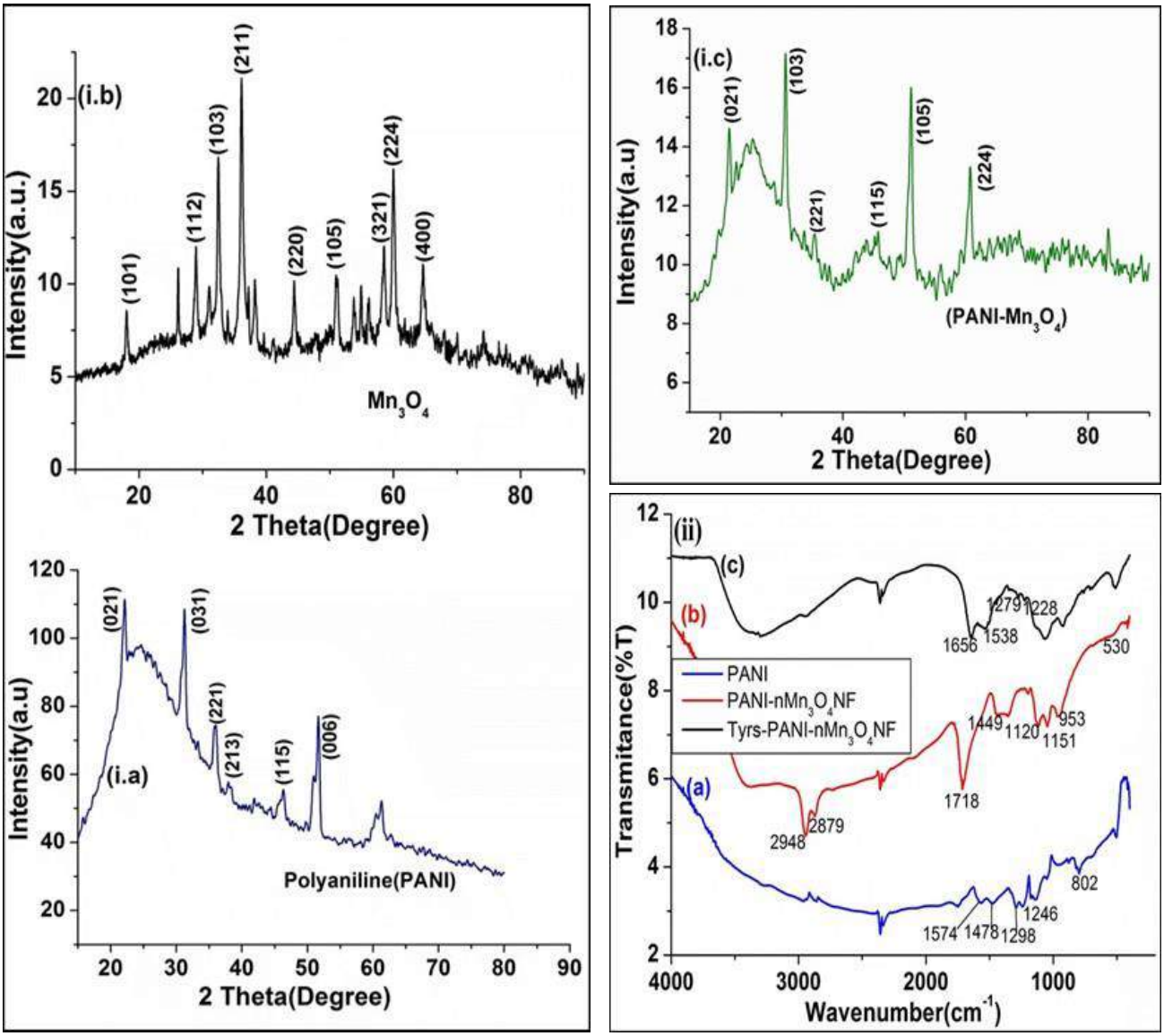
ACCEPTED MANUSCRIPT

Fig. 2



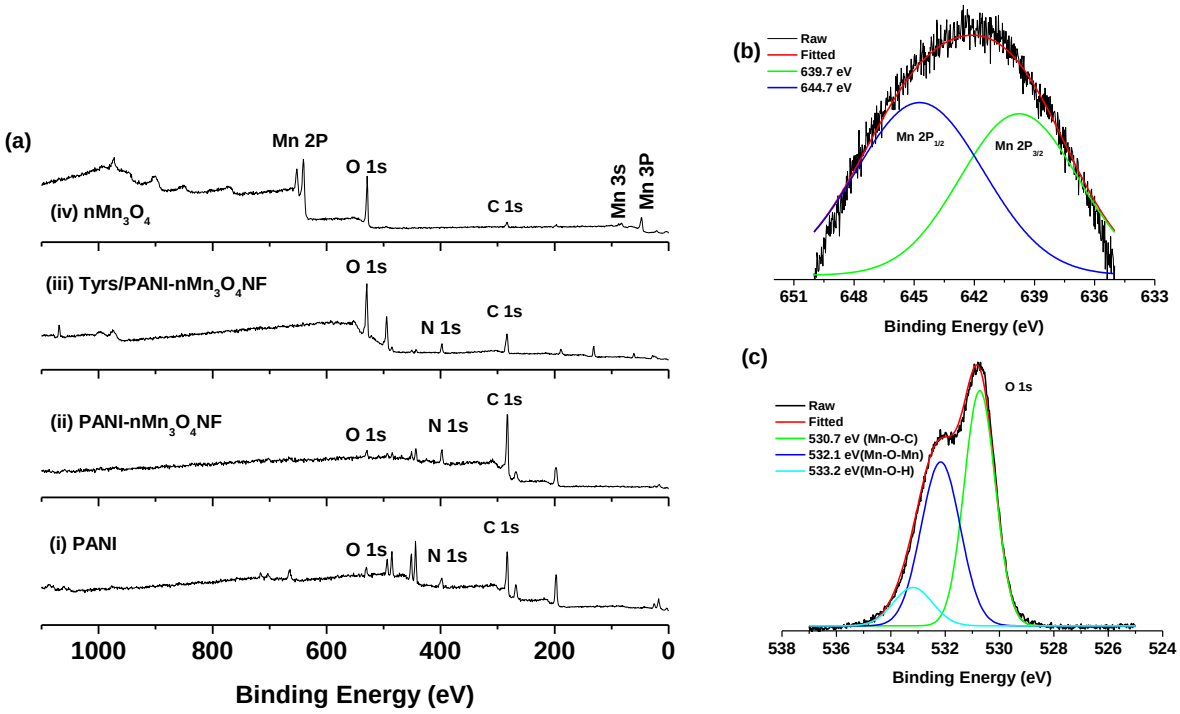
ACCEPTED MANUSCRIPT

Fig. 3



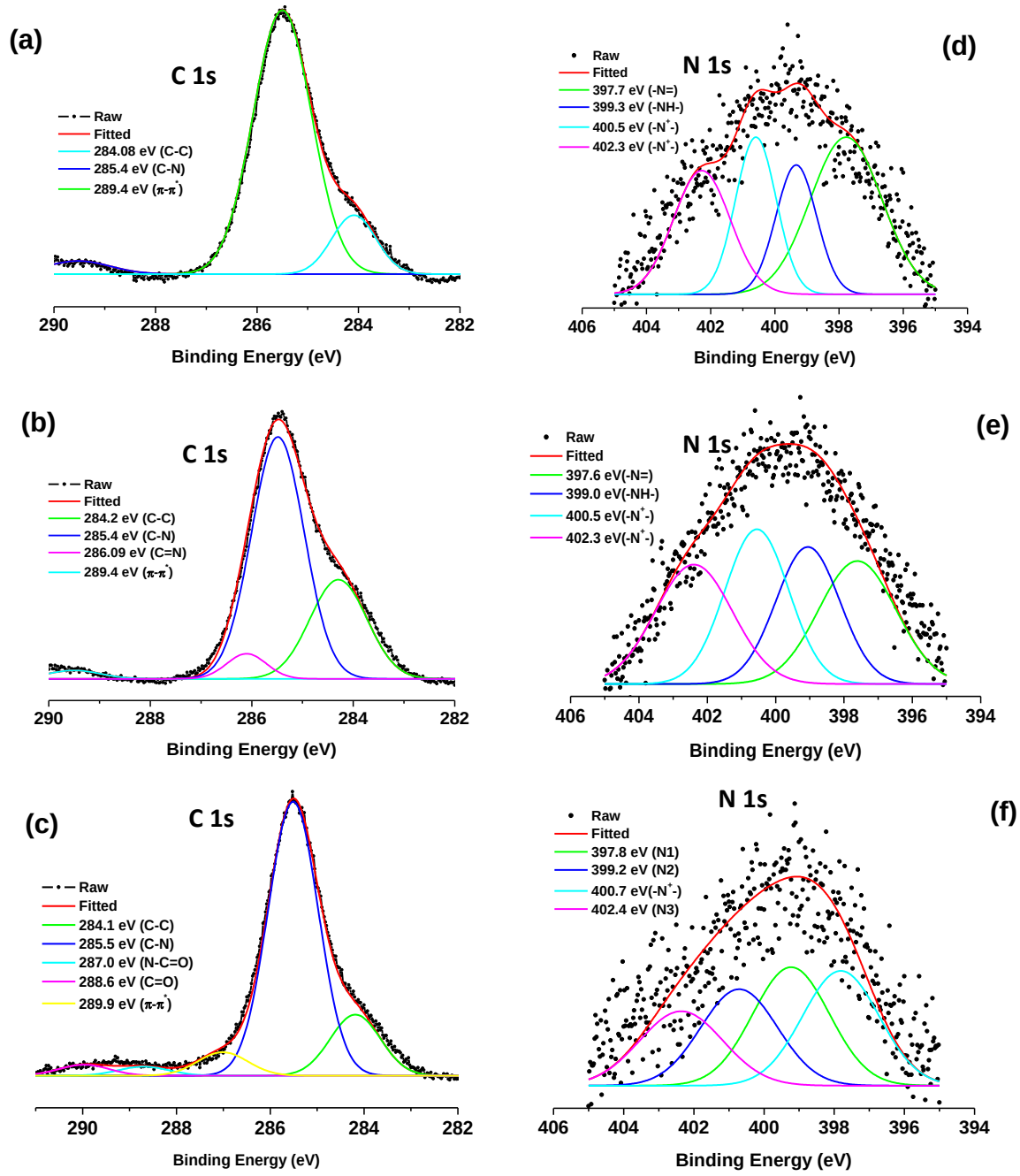
ACCEPTED MANUSCRIPT

Fig. 4



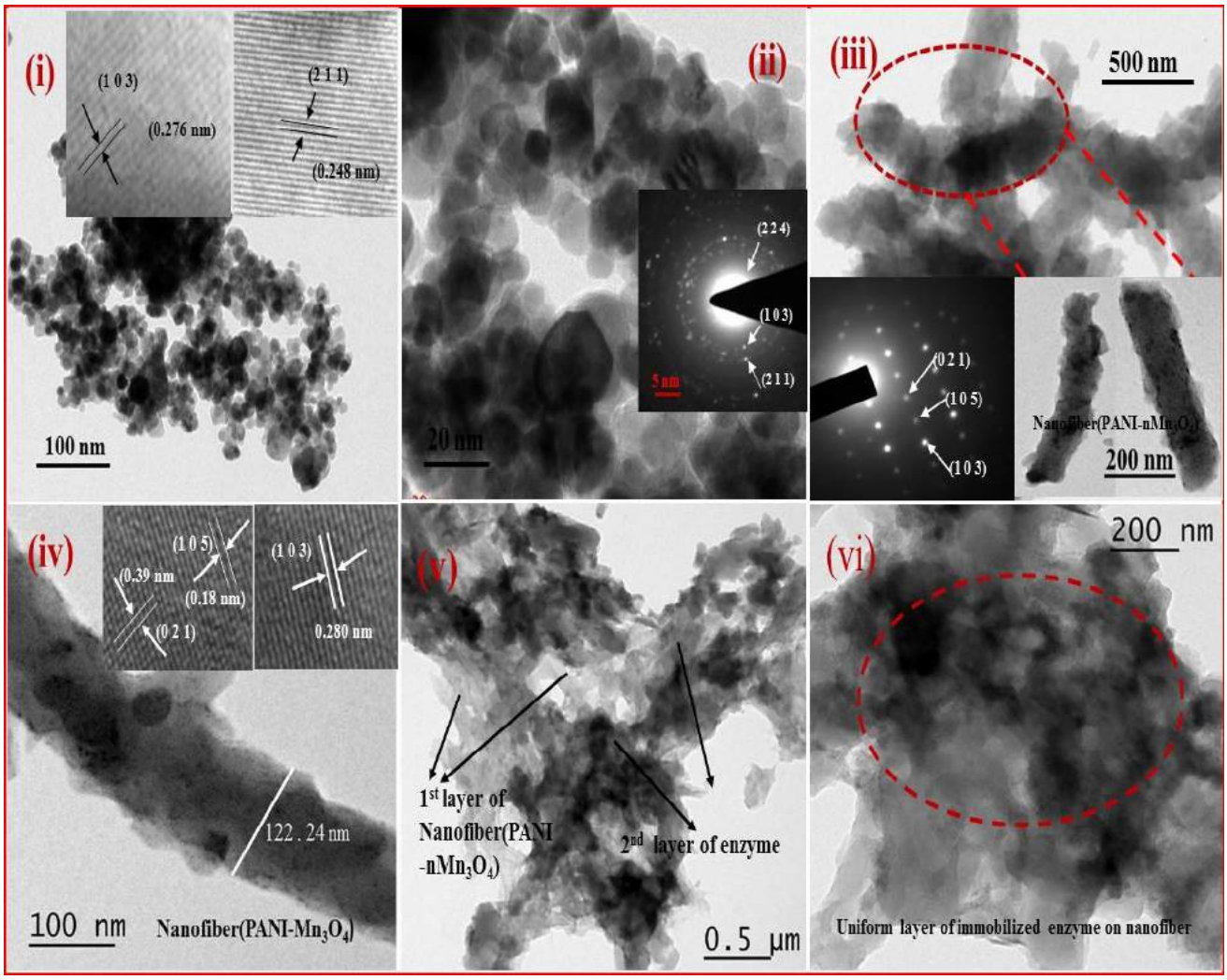
ACCEPTED MANUSCRIPT

Fig. 5



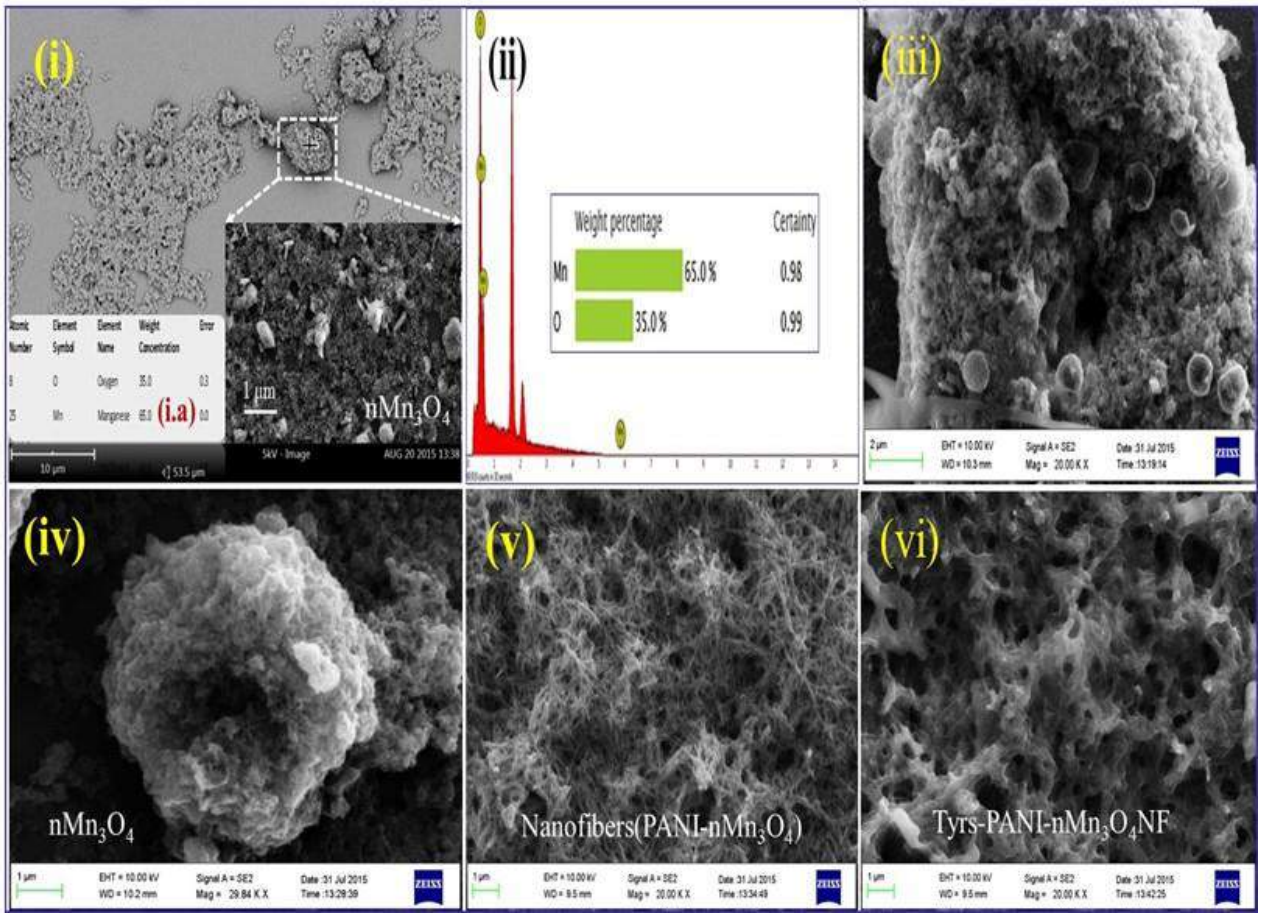
ACCEPTED MANUSCRIPT

Fig. 6



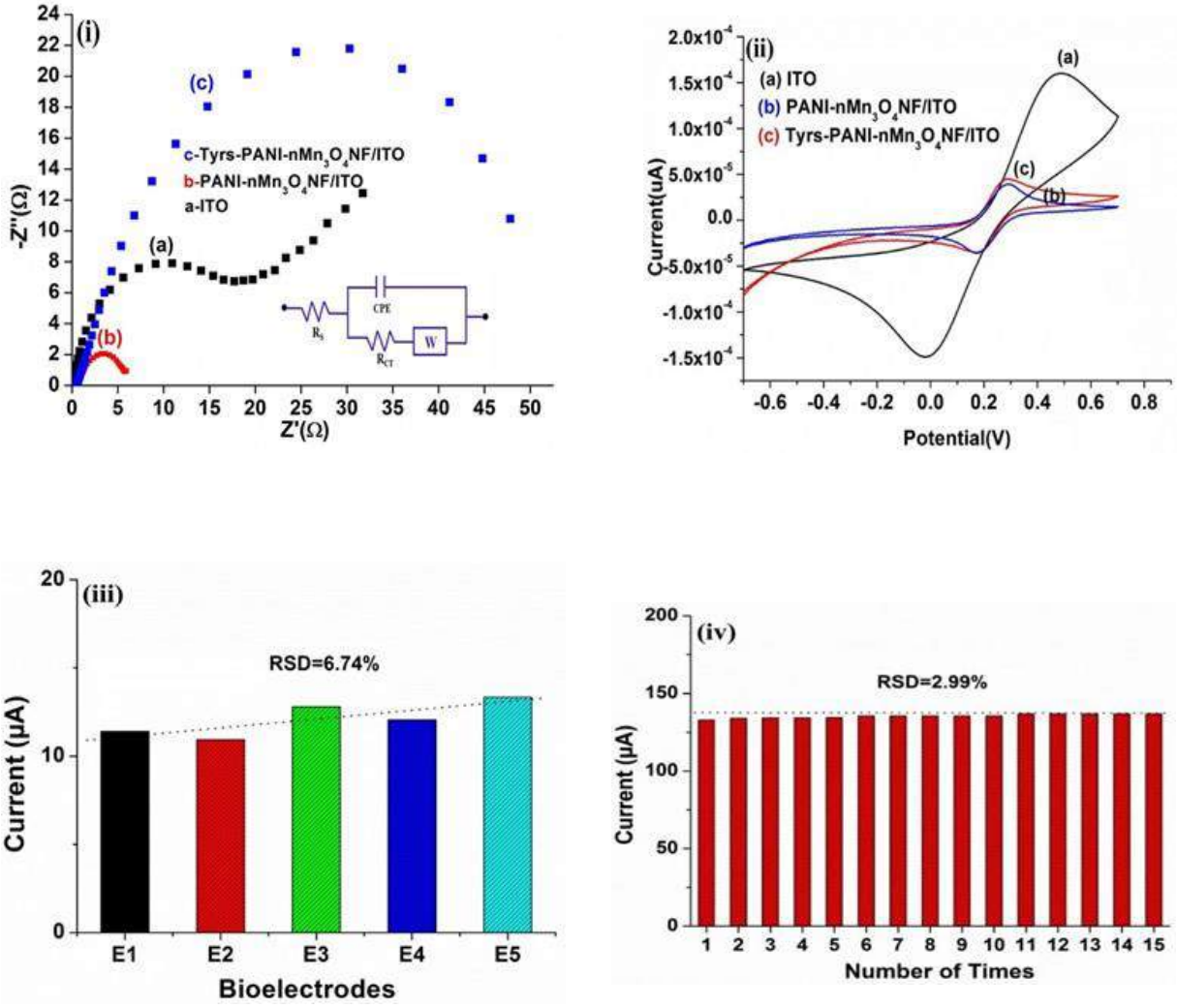
ACCEPTED MANUSCRIPT

Fig. 7



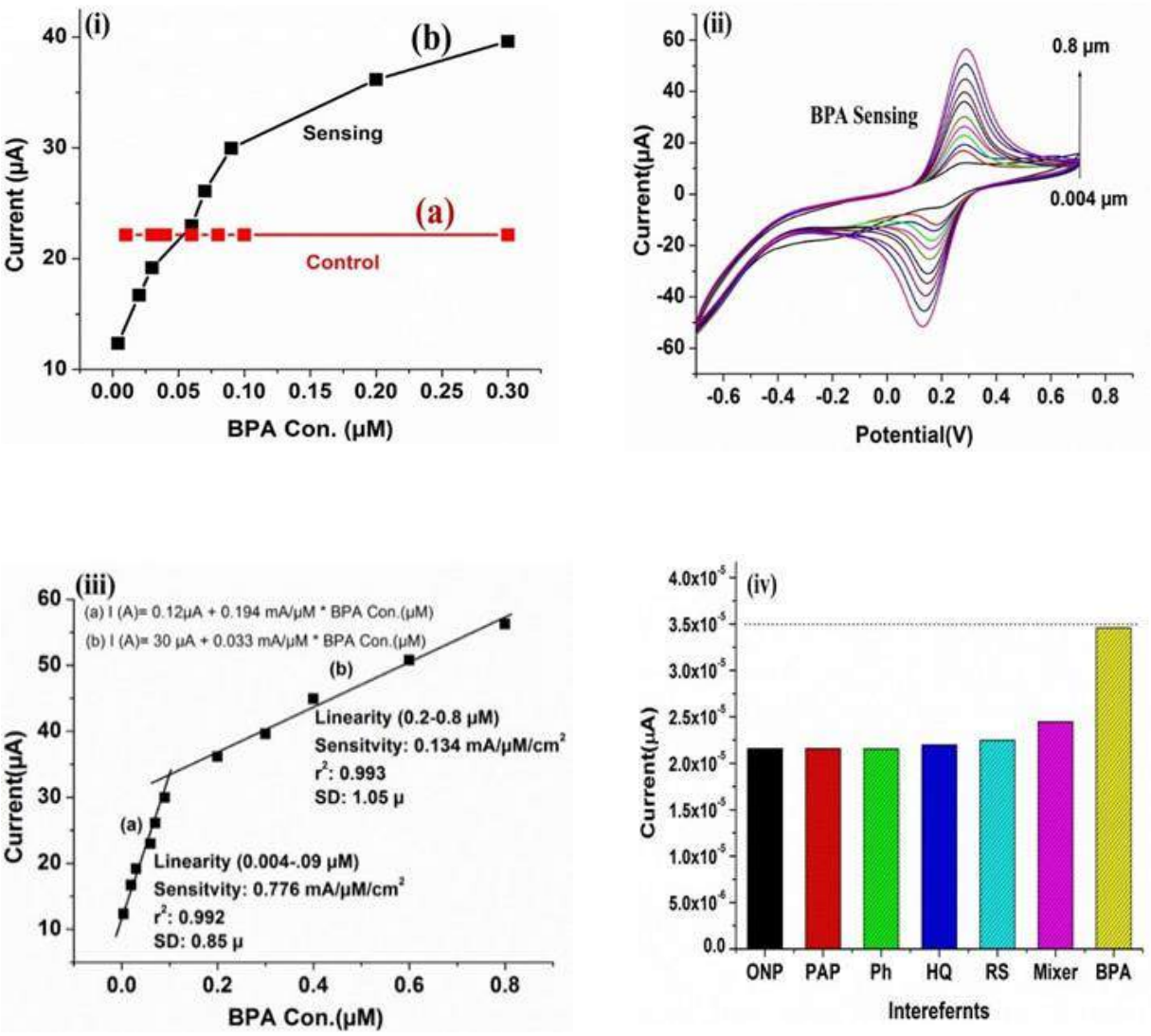
ACCEPTED MANUSCRIPT

Fig. 8



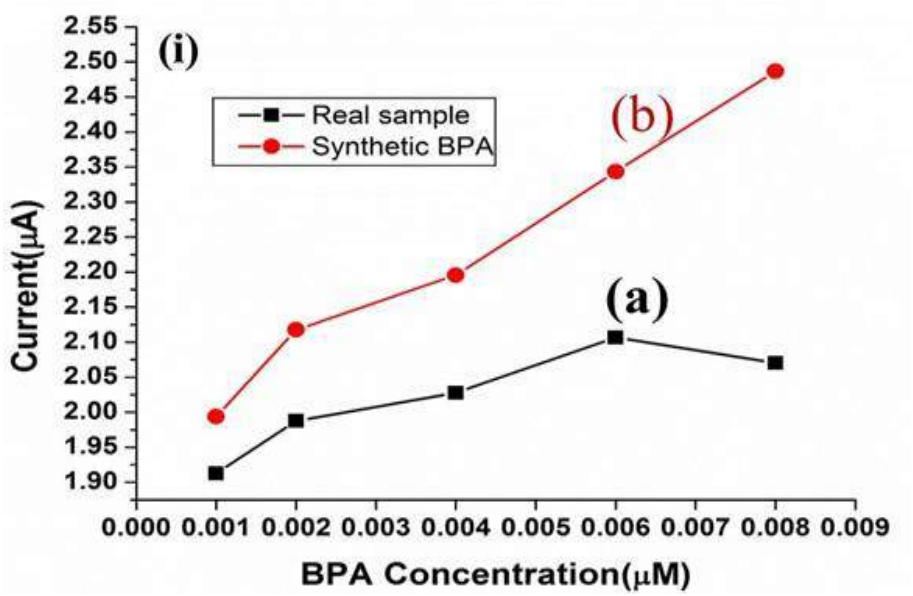
ACCEPTED MANUSCRIPT

Fig. 9



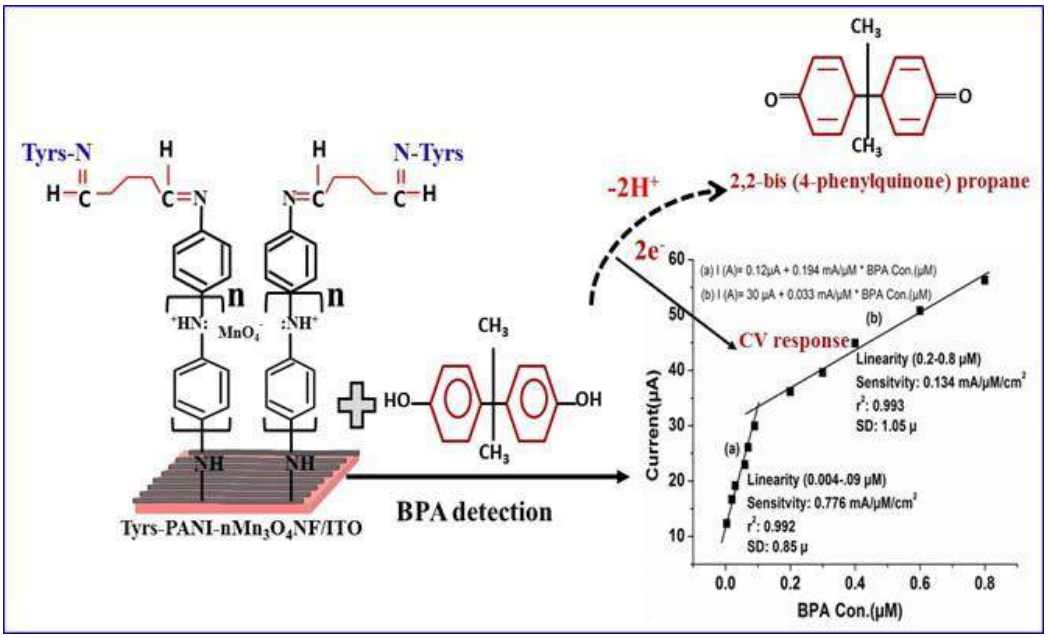
ACCEPTED MANUSCRIPT

Fig. 10



ACCEPTED MANUSCRIPT

Schematic 1. Graphical abstract



Research Article Vol. 55, No. 19 / July 1 2016 / Applied Optics 4995



Large-mode-area single-polarization single-mode photonic crystal fiber: design and analysis

Ajeet Kumar,[1,*] Than Singh Saini,[1] Kishor Dinkar Naik,[1] and Ravindra Kumar Sinha[2]

[1]Advanced Photonics Simulation Research Laboratory, Department of Applied Physics, Delhi Technological University, Delhi-110 042, India
[2]CSIR-Central Scientific Instruments Organization, Chandigarh 160030, India
*Corresponding author: ajeetdph@gmail.com

Received 2 May 2016; revised 30 May 2016; accepted 30 May 2016; posted 31 May 2016 (Doc. ID 264424); published 22 June 2016

A rectangular core photonic crystal fiber structure has been presented and analyzed for single-polarization single-mode operation. Single-polarization is obtained with asymmetric design and by introducing different loss for *x*-polarization and *y*-polarization of fundamental modes. Single-polarization single-mode operation of the proposed photonic crystal fiber is investigated in detail by using a full vector finite element method with an anisotropic perfectly matched layer. The variations of the confinement loss and effective mode area of *x*-polarization and *y*-polarization of fundamental modes have been simulated by varying the structural parameters of the proposed photonic crystal fiber. At the optimized parameters, confinement loss and effective mode area is obtained as 0.94 dB/m and 60.67 μm^2 for *y*-polarization as well as 26.67 dB/m and 67.23 μm^2 for *x*-polarization of fundamental modes, respectively, at 1.55 μm. Therefore simulation results confirmed that, 0.75 m length of fiber will be sufficient to get a *y*-polarized fundamental mode with an effective mode area as large as 60.67 μm^2. © 2016 Optical Society of America

OCIS codes: (060.5295) Photonic crystal fibers; (260.1440) Birefringence; (260.5430) Polarization; (060.2430) Fibers, single-mode; (060.2330) Fiber optics communications.

http://dx.doi.org/10.1364/AO.55.004995

1. INTRODUCTION

In recent years, photonic crystal fibers (PCFs) have been attracting a lot of attention and becoming an exciting research topic for their applications in optical fiber communication systems [1–4]. PCFs have unique light-guiding properties, such as endlessly single-mode (SM) operation, dispersion tailoring, high birefringence (HB), large mode area (LMA), high nonlinearity, and supercontinuum generation [5–15]. PCFs consist of a periodic array of air holes around a central core of solid silica or air, the air holes running along its length. Various light-guiding properties of the PCF are effectively controlled by manipulating the geometrical parameters such as lattice of air holes, diameters of air holes, and center-to-center distance of holes (i.e., pitch).

Polarization maintaining fibers (PMFs), which stabilize the state of polarization, are widely used in coherent optical communication systems and fiber sensor systems [16]. PMFs are made up of conventional HB fibers; thus, birefringence becomes one of the important characteristics of fibers. Conventional HB fibers are designed to operate in the single-polarization single-mode (SPSM) regime in which only one linearly polarized mode is guided, while the other orthogonal polarization mode is suppressed. It is difficult to eliminate the influence of polarization mode dispersion and polarization-mode coupling on system performance, even with PMFs [17–19]. Now, it has been shown that HB PCFs have the potential to realize better SPSM fibers; that is why many SPSM fibers based on PCF structures have been proposed. PCFs have higher model birefringence than conventional HB fibers because the large index contrast and the stack-and-draw fabrication process allow HB to be realized on PCFs. PCFs are made HB by designing them with different air hole diameters along the two orthogonal axes or by designing an asymmetric core of PCF or by modifying the shapes of air holes near the core of PCF. As compared to conventional HB fibers, SPSM PCFs allows the propagation of only one polarization state of the fundamental mode; thus they not only eliminate the polarization-mode coupling but also the polarization-mode dispersion [20–25].

Wideband SPSM propagation can be realized due to higher index contrast. SPSM PCF with a confinement loss of less than 0.1 dB/km from 1.48 to 1.6 μm was proposed and analyzed in [26]. Kubota *et al.* reported a PCF-based absolutely single polarization fiber with a polarization-dependent loss of 196 dB/km with a transmission loss of 28 dB/km at 1.55 μm [27]. A single-mode PCF has been demonstrated that guides only one polarization state in a 220 mm-wide spectral region centered at 727 nm [28]. Schmidt *et al.* reported an ytterbium-doped single-mode rod-type PCF structure for the spectral

range from 1030–1080 nm [29]. Numbers of designs were focused on SPSMs with LMAs that are useful in high-power systems [30–32]. Many novel optical fiber communication applications, such as wavelength multicasting, parametric amplification, and wavelength conversion utilize fiber nonlinearity and prefer low-loss nonlinear SPSM fibers [33]. Polarization-dependent noises are eliminated by nonlinear low-loss SPSM fiber, and interaction efficiency is enhanced by aligning the polarization of the interacting waves in the same direction. Near-zero dispersion with small dispersion slopes would benefit applications like polarized supercontinuum generation [34]. In [35] SPSM PCFs are designed at 1.33 and 1.55 μm, but the effective mode area (EMA) is below 40 μm^2.

In this paper, we have designed a rectangular core (RC) PCF structure which offers effective single-polarization SM operation with an EMA as large as 60.67 μm^2. SM operation has been achieved by suppressing higher-order modes, while single polarization operation has been achieved by means of high differential confinement loss between the two polarizations of fundamental modes. The PCF is designed in such a way that initially it supports both polarizations of the fundamental mode, out of which only x-polarization of the fundamental mode is perfectly guiding and y-polarization is leaky in nature. The effects of varying geometrical parameters of PCF on the characteristics of SPSM operation are discussed. A full vector finite element method (FEM) with perfectly matched layers (PMLs) as absorbing boundary conditions is used to analyze the polarization-dependent loss at 1.55 μm.

2. DESIGN OF RC SPSM PCF

The transverse cross-section view of a proposed RC SPSM PCF structure is shown in Fig. 1, in which the rectangular arrays of air holes are drawn in the fused silica along the length of the fiber. In the proposed structure, the central air hole has been removed to create the RC of the PCF.

As illustrated in Fig. 1, there are two types of air holes (having radius r_1 and r_2) arranged in four complete rectangular rings and two incomplete rectangular rings. The radius of the smaller air holes is represented by r_1. The remaining larger air holes have radius r_2. The hole-to-hole distance (i.e., pitch) is taken as Λ. The birefringence can be enlarged by making the design asymmetric; the asymmetric arrangement of the air holes shown in the rectangle gives the different effective index characteristics to the x-axis (x-polarization) and the y-axis (y-polarization).

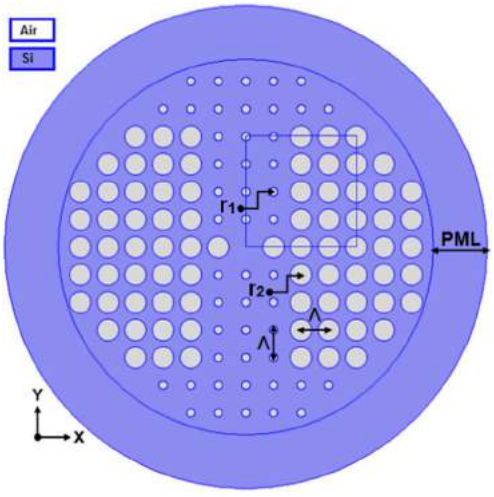


Fig. 1. Schematic cross section of proposed RC SPSM PCF.

3. METHOD OF ANALYSIS

To simulate the effective index of fundamental mode propagating though PCF, we have used the full vectorial FEM-based software COMSOL Multiphysics. For calculating the wavelength-dependent refractive index of fused silica, the Sellmeier equation has been used [36,37]:

$$n^2(\lambda) - 1 = \sum_{i=1}^{j} \frac{B_i \lambda^2}{\lambda^2 - l_i^2}, \tag{1}$$

where $j = 3$, $B_1 = 0.6961663$, $B_2 = 0.4079426$, $B_3 = 0.8974794$, $l_1 = 0.0684043$, $l_2 = 0.1162414$, and $l_3 = 9.896161$ are Sellmeier coefficients, λ is the operating wavelength, and $n(\lambda)$ is the wavelength-dependent refractive index.

In the finite-element scheme, software solves the following Maxwell vector Eq. (2):

$$\nabla \times ([s]^{-1} \nabla \times E) - k_0^2 n^2 [s] E = 0, \tag{2}$$

$$[s] = \begin{pmatrix} \frac{s_y}{s_x} & 0 & 0 \\ 0 & \frac{s_x}{s_y} & 0 \\ 0 & 0 & s_x s_y \end{pmatrix}, \tag{3}$$

where E is the electric field vector, $\mathbf{k}_0 = \frac{2\pi}{\lambda}$ is the wave number in the vacuum, λ is the operating wavelength, n is the refractive index, $[s]$ is the PML matrix, and s_x and s_y are the PML parameters.

When we solve Eq. (2) for the proposed structure, the propagation constants of modes become complex. The real part of the propagation constant gives the effective indices of modes, while the imaginary part of the propagation constant gives the confinement losses of the modes. The following, Eq. (4), gives the effective refractive index of the mode:

$$n_{\text{eff}} = \text{Re}\left(\frac{\beta}{k_0}\right), \tag{4}$$

where, β is the propagation constant obtained by solving the eigen value equation. In the PCF, by reducing the index contrast or reducing the air hole sizes, the effective area of mode can be improved. But by reducing the index contrast, there is an increment in confinement loss of the modes propagating through the PCF structure. The confinement loss arises due to the leakage of power through the air holes of the PCF. Confinement loss can be calculated using the imaginary part of effective refractive indices of modes by the following relation [38]:

$$L\left(\frac{\text{dB}}{\text{m}}\right) = \frac{40\pi}{\ln(10)\lambda} \text{Im}(n_{\text{eff}}) = 8.686 k_0 \text{Im}(n_{\text{eff}}), \tag{5}$$

where $\mathrm{Im}(n_{\mathrm{eff}})$ is the imaginary part of the refractive index of the propagating mode and λ is the free-space wavelength in μm.

A circular PML is implemented at the fiber surface to simulate the effect of an infinite domain in the FEM. With the PML, the propagation constant of modes becomes complex. The real part of the propagation constant is related to the effective index of mode, and the imaginary part is related to the confinement loss, which can be calculated by Eqs. (4) and (5).

The EMA of the fundamental mode of structure can be calculated by a transverse electric field, E of mode using Eq. (6) [39]:

$$A_{\mathrm{eff}} = \frac{\left(\iint |E|^2 \mathrm{d}x\mathrm{d}y\right)^2}{\left(\iint |E|^4 \mathrm{d}x\mathrm{d}y\right)}. \tag{6}$$

4. NUMERICAL RESULTS AND DISCUSSION

For the proposed structure, we have investigated the confinement loss and EMA using the full vectorial FEM with a perfectly matched layer absorbing boundary conditions. The refractive index of fused silica has been taken as 1.444 at 1.55 μm wavelength.

A. Effect of Geometrical Parameters on Confinement Losses

Figure 2 shows the variation of confinement losses of the fundamental mode with x-polarization (i.e., HE_{11}^{x}) and fundamental mode with y-polarization (i.e., HE_{11}^{y}) of the proposed RC SPSM PCF structure. Initially, the confinement losses of both polarizations of the fundamental mode are very high and then start to decrease on increasing r_1. A small peak is observed around $r_1 = 0.77$ μm; this is due to the resonance effect of the HE_{11}^{x} mode to the cladding at this value of r_1. The resonance effect is high when $r_1 = 0.77$ μm with confinement loss of 26.67 dB/m of x-polarization and 0.94 dB/m of y-polarization. At lower values of r_1, both polarizations have high losses. The confinement loss of the HE_{11}^{y} mode is much less as compared to the HE_{11}^{x} mode, so the HE_{11}^{x} mode filters it out from the core region after the small distance of the PCF.

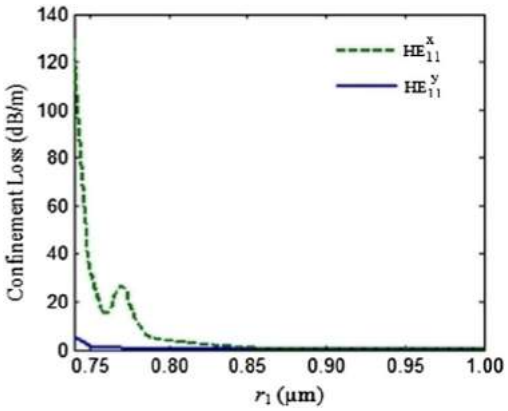


Fig. 2. Variation of the confinement loss of HE_{11}^{x} and HE_{11}^{y} of the fundamental mode with r_1 when $r_2 = 2$ μm, $\Lambda = 5$ μm, and $\lambda = 1.55$ μm.

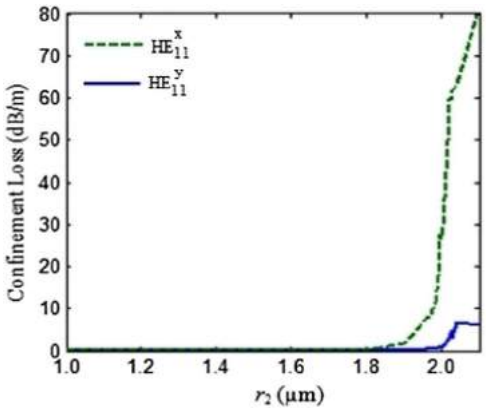


Fig. 3. Variation of the confinement loss of HE_{11}^{x} and HE_{11}^{y} of the fundamental mode with r_2 when $r_1 = 0.77$ μm, $\Lambda = 5$ μm, and $\lambda = 1.55$ μm.

The variation of confinement loss of HE_{11}^{x} and HE_{11}^{y} of the fundamental mode on r_2 has been shown in Fig. 3. The confinement loss of the HE_{11}^{y} mode is much less than that of the HE_{11}^{x} mode. At $r_2 = 2$ μm, the confinement loss of the HE_{11}^{y} mode is 0.94 dB/m, and the confinement loss of the HE_{11}^{x} mode is 26.67 dB/m. The confinement losses of both polarizations increase with r_2 due to a decrease in the core size.

The effects on confinement loss of HE_{11}^{x} and HE_{11}^{y} of the fundamental mode of the proposed structure due to pitch has been investigated in Fig. 4. The confinement loss of the HE_{11}^{y} mode is always very much less than that of the HE_{11}^{x} mode. There is a significant decrease in the confinement loss of the HE_{11}^{x} mode on increasing pitch. This is due to an increase in core size on increasing pitch. At $\Lambda = 4.5$ μm, the confinement loss of the HE_{11}^{y} mode is 8.44 dB/m, and that of the HE_{11}^{x} mode is 37.52 dB/m; at $\Lambda = 5.5$ μm the confinement loss of the HE_{11}^{y} mode is 0.34 dB/m, and that of the HE_{11}^{x} mode is 3.38 dB/m. Thus, we can state that the differential loss between the x-polarization and y-polarization reduces as pitch increases.

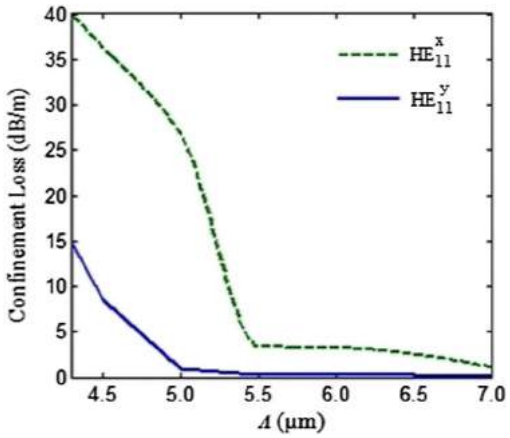


Fig. 4. Variation of the confinement loss of HE_{11}^{x} and HE_{11}^{y} of the fundamental mode with pitch when $r_1 = 0.77$ μm, $r_2 = 2$ μm, and $\lambda = 1.55$ μm.

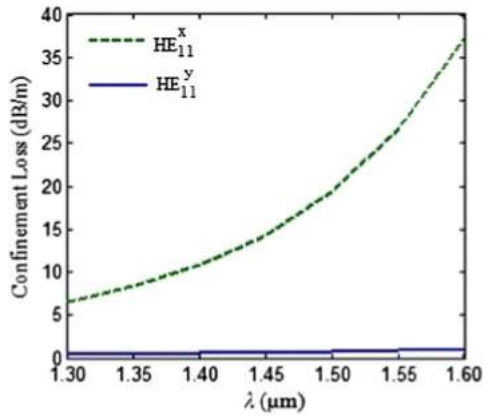


Fig. 5. Spectral variation of the confinement loss of HE_{11}^{x} and HE_{11}^{y} of the fundamental mode with $r_1 = 0.77$ μm, $r_2 = 2$ μm, $\Lambda = 5$ μm.

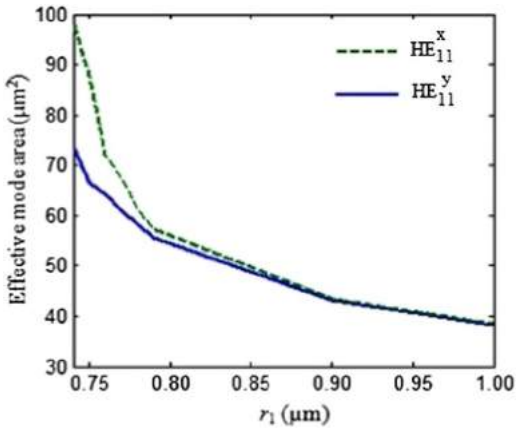


Fig. 6. Variation of the EMA of HE_{11}^{x} and HE_{11}^{y} of the fundamental mode with r_1 when $r_2 = 2$ μm, $\Lambda = 5$ μm, and $\lambda = 1.55$ μm.

B. Effect of Spectral Variation on Confinement Losses

The spectral dependence of the confinement loss of HE_{11}^{x} and HE_{11}^{y} of the fundamental mode for the proposed SPSM PCF structure is shown in Fig. 5. The confinement loss of the HE_{11}^{y} mode is always very much less than that of the HE_{11}^{x} mode within the spectral range of 1.3–1.6 μm. The confinement losses for both polarizations of the fundamental mode increase with wavelength. At 1.30 μm, the confinement loss of HE_{11}^{y} mode is 0.41 dB/m and that of the HE_{11}^{x} mode is 6.51 dB/m. Therefore, after 3.07 m length of fiber the confinement loss of the HE_{11}^{x} mode exceeds 20 dB, while the confinement loss of the HE_{11}^{y} mode would only be 1.25 dB. Thus, the SPSM operation is possible after 3.07 m length of PCF for wavelength of 1.3 μm. At 1.60 μm, the confinement loss of the HE_{11}^{y} mode is 1.14 dB/m and that of the HE_{11}^{x} mode is 37.19 dB/m, so after only 0.54 m length of the PCF, the confinement loss of the HE_{11}^{x} mode becomes more than 20 dB, while the confinement loss of the HE_{11}^{y} mode would only be 0.68 dB. For the wavelength of 1.6 μm, only a 0.54 m long PCF structure is able to offer SPSM operation.

At 1.55 μm, the confinement loss of the HE_{11}^{y} mode is 0.94 dB/m and the loss of the HE_{11}^{x} mode is 26.67 dB/m. So, traveling to 0.75 m along the length of PCF, the confinement loss of the HE_{11}^{x} mode becomes more than 20 dB, while the confinement loss of the HE_{11}^{y} mode would only be 0.75 dB. Therefore at 1.55 μm, only 0.70 m length of PCF is enough to achieve SPSM operation.

C. Effect of Geometrical Parameters on Effective Mode Area

Figure 6 illustrates the variation of EMA of *x*-polarization and *y*-polarization of the fundamental mode with structural parameter r_1 of the proposed PCF. The EMA decreases with r_1. At $r_1 = 0.77$ μm the EMA of the *y*-polarized mode is 60.77 μm^2 and that of the *x*-polarized mode is 67.23 μm^2.

In Fig. 7, we have shown the effect of r_2 on the EMA of *x*-polarization and *y*-polarization of the fundamental mode. Initially, the EMA of the *x*-polarized fundamental mode as well as the *y*-polarized fundamental mode decreases with r_2; the

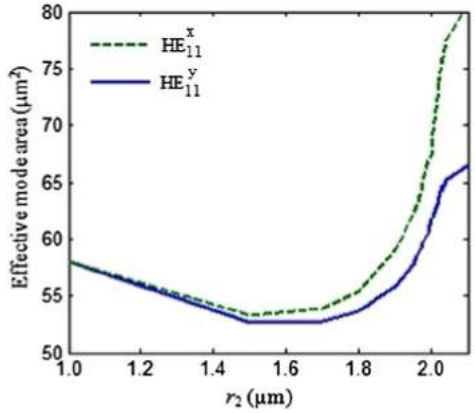


Fig. 7. Variation of the EMA of HE_{11}^{x} and HE_{11}^{y} of the fundamental mode with r_2 when $r_1 = 0.77$ μm, $\Lambda = 5$ μm, and $\lambda = 1.55$ μm.

EMA of *y*-polarization is 60.67 μm^2 and that of the *x*-polarization is 67.23 μm^2 at the value of r_2 around 2 μm and later EMA increases with r_2. It is due to the effect of the increase in index contrast between core and holey cladding on increasing the radius of air holes in the cladding region.

The EMA of the *x*- and *y*-polarized fundamental mode of the proposed RC SPSM PCF structure with pitch is illustrated in Fig. 8. This shows that the EMA of the fundamental mode with *x*-polarization and *y*-polarization increases with pitch. This is because of the increment in the core size on increasing the value of the pitch. When the pitch is 5 μm, the EMA of the *y*-polarization is 60.67 μm^2 and that of the *x*-polarization is 67.23 μm^2.

D. Effect of Spectral Variation on EMA

Figure 9 depicts the dependence of the EMA of the *x*- and *y*-polarization of the fundamental mode at different values of wavelength. The EMA of both polarizations increases with wavelength. At 1.30 μm wavelength, the confinement loss and EMA are obtained as 0.41 dB/m and 55.14 μm^2 for the *y*-polarization as well as 6.51 dB/m and 59.03 μm^2 for the *x*-polarization of fundamental mode, respectively.

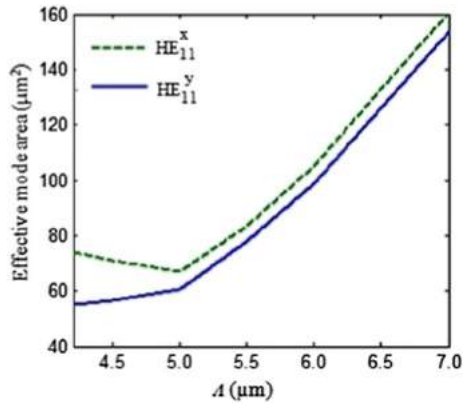


Fig. 8. Variation of the EMA of HE_{11}^{x} and HE_{11}^{y} of the fundamental mode with pitch when $r_1 = 0.77$ μm, $r_2 = 2$ μm, and $\lambda = 1.55$ μm.

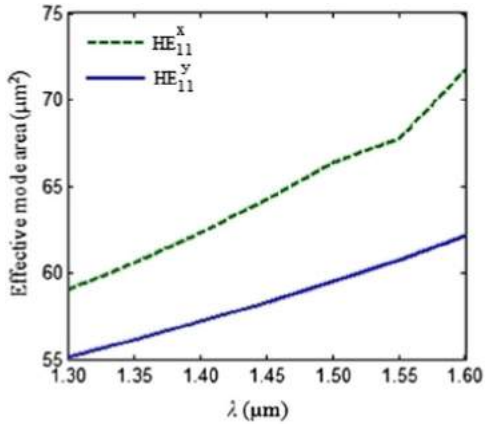


Fig. 9. Spectral variation of the EMA of HE_{11}^{x} modes with $r_1 = 0.77$ μm, $r_2 = 2$ μm, $\Lambda = 5$ μm.

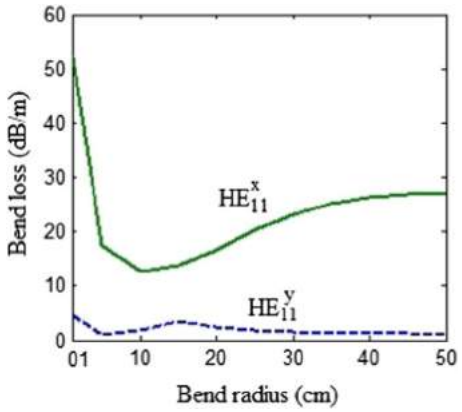


Fig. 10. Variation of the bend losses of the HE_{11}^{x} and HE_{11}^{y} modes with $r_1 = 0.77$ μm, $r_2 = 2$ μm, $\Lambda = 5$ μm, and $\lambda = 1.55$ μm.

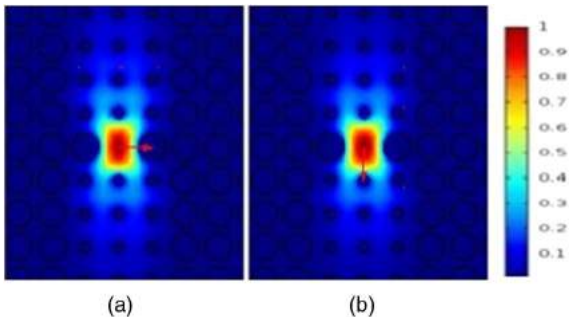


Fig. 11. Contour plot of field intensity of (a) HE_{11}^{x}; and (b) HE_{11}^{y} modes at optimized parameters with $r_1 = 0.77$ μm, $r_2 = 2$ μm, $\Lambda = 5$ μm, and $\lambda = 1.55$ μm.

At 1.6 μm, the confinement loss and EMA is obtained as 1.15 dB/m and 62.18 μm^2 for the *y*-polarization, as well as 37.19 dB/m and 71.72 μm^2 for the *x*-polarization of the fundamental mode, respectively.

The difference between the loss of *x*-polarization and *y*-polarization is very high, which indicates the SPSM operation in this wavelength range. SPSM PCF with significantly high EMA is possible within the spectral range of 1.3–1.6 μm.

The investigation of the bending performance of the proposed RC SPSM PCM is very important. As shown in Fig. 10, when we bend the PCF in *x*-direction, the bend loss of HE_{11}^{y} mode varies between ~1 dB/m and 4.6 dB/m for the bend radius spanning 1–50 cm. In case of the HE_{11}^{x}, the bend loss varies between 12.7 dB/m and 52.2 dB/m for the bend radius spanning 1–50 cm. To offer low bend loss for HE_{11}^{y} mode and large bend loss for HE_{11}^{x}, the minimum bend radius should be 20 cm. This will also help in filtering the HE_{11}^{x} mode.

Finally, the contour plots of *x*-polarization and *y*-polarization of the fundamental mode have been shown in Fig. 11 at wavelength, $\lambda = 1.55$ μm, $r_1 = 0.77$ μm, $r_2 = 2$ μm, and $\Lambda = 5$ μm. It can be observed from the figure that the HE_{11}^{y} mode is well confined within the core, while the HE_{11}^{x} mode is leaking out from the core.

5. CONCLUSION

We have designed and analyzed a RC PCF structure for SPSM operation by using the full vector FEM. By choosing proper structural parameters, we can tune the confinement loss of *x*-polarized and *y*-polarized fundamental modes of the proposed PCF structure. The proposed photonic crystal structure offers the single-polarization single-mode operation within the spectral range of 1.3–1.6 μm. The proposed structure possesses the confinement loss of 0.94 dB/m and EMA of 60.67 μm^2 for *y*-polarization of the fundamental mode while the confinement loss of 26.67 dB/m and EMA of 67.23 μm^2 for *x*-polarization of the fundamental mode at 1.55 μm. The confinement loss of the HE_{11}^{y} mode is very low, which is the propagating mode, and the confinement loss of HE_{11}^{x} is sufficiently high to leak it out from the core of the proposed PCF structure. Simulation results show that, after traveling approximately 0.75 m distance through a PCF, the HE_{11}^{x} mode offers more than 20 dB loss, while the HE_{11}^{y} mode offers only 0.70 dB loss. Therefore, the proposed PCF structure offers effective SPSM operation after 0.75 m distance of the proposed PCF with an EMA as large as 60.67 μm^2. Such a PCF structure has potential applications in

the area of compact optical devices and high-power optical communication systems.

Funding. Science and Engineering Research Board (SERB).

REFERENCES

1. J. C. Knight and P. St. J. Russell, "Photonic crystal fibers: new way to guide light," Science **296**, 276–277 (2002).
2. J. C. Knight, T. A. Birks, P. St.J. Russell, and D. M. Atkin, "All-silica single-mode optical fiber with photonic crystal cladding," Opt. Lett. **21**, 1547–1549 (1996).
3. T. A. Birks, J. C. Knight, and P. St. J. Russell, "Endlessly single-mode photonic crystal fiber," Opt. Lett. **22**, 961–963 (1997).
4. J. C. Knight, J. Broeng, T. A. Birks, and P. St. J. Russell, "Photonic band gap guidance in optical fibers," Science **282**, 1476–1478 (1998).
5. W. H. Reeves, D. V. Skryabin, F. Biancalana, J. C. Knight, P. St.J. Russell, F. G. Omenetto, A. Efimov, and A. J. Taylor, "Transformation and control of ultra-short pulses in dispersion-engineered photonic crystal fibers," Nature **424**, 511–515 (2003).
6. J. Wang, C. Jiang, W. Hu, and M. Gao, "Modified design of photonic crystal fibers with flattened dispersion," Opt. Laser Technol. **38**, 169–172 (2006).
7. P. Morin, B. Kibler, J. Fatome, C. Finot, and G. Millot, "Group modal birefringence inversion in a highly birefringent nonlinear photonic crystal fibre at telecommunication wavelengths," Electron. Lett./IEE Electron. Lett. **46**, 525–526 (2010).
8. J. Liao and J. Sun, "High birefringent rectangular-lattice photonic crystal fibers with low confinement loss employing different sizes of elliptical air holes in the cladding and the core," Opt. Fiber Technol. **18**, 457–461 (2012).
9. I. Abdelaziz, H. Ademgil, F. AbdelMalek, S. Haxha, T. Gorman, and H. Bouchriha, "Design of a large effective- mode-area photonic crystal fiber with modified rings," Opt. Commun. **283**, 5218–5223 (2010).
10. K. Kishor, R. K. Sinha, and A. D. Varshney, "Experimental verification of improved effective index method for endlessly single mode photonic crystal fiber," Opt. Lasers Eng. **50**, 182–186 (2012).
11. T. S. Saini, A. Kumar, and R. K. Sinha, "Triangular-core large-mode-area photonic crystal fiber with low bending loss for high power applications," Appl. Opt. **53**, 4251–7246 (2014).
12. T. S. Saini, A. Kumar, and R. K. Sinha, "Broadband mid-IR supercontinuum generation in As_2Se_3 based chalcogenide photonic crystal fiber: a new design and analysis," Opt. Commun. **347**, 13–19 (2015).
13. J. M. Dudley, "Supercontinuum generation in photonic crystal fiber," Rev. Mod. Phys. **78**, 1135–1184 (2006).
14. M. Napierala, T. Nasilowski, E. B. Pawlik, P. Mergo, F. Berghmans, and H. Thienpont, "Large-mode-area photonic crystal fiber with double lattice constant structure and low bending loss," Opt. Express **19**, 22628–22636 (2011).
15. M. Y. Chen, Y. R. Li, J. Zhou, and Y. K. Zhang, "Design of asymmetric large-mode area optical fiber with low-bending loss," J. Lightwave Technol. **31**, 476–481 (2013).
16. X. Dong, H. Tam, and P. Shum, "Temperature-insensitive strain sensor with polarization-maintaining photonic crystal fiber based Sagnac interferometer," Appl. Phys. Lett. **90**, 151113 (2007).
17. J. R. Simpson, R. H. Stolen, F. M. Sears, W. Pleibel, J. B. Macchesney, and R. E. Howard, "A single-polarization fiber," J. Lightwave Technol. **1**, 370–374 (1983).
18. M. J. Messerly, J. R. Onstott, and R. C. Mikkelson, "A broad-band single polarization optical fiber," J. Lightwave Technol. **9**, 817–820 (1991).
19. K. Okamoto, "Single-polarization operation in highly birefringent optical fibers," Appl. Opt. **23**, 2638–2642 (1984).
20. A. Ortigosa-Blanch, J. C. Knight, W. J. Wadsworth, J. Arriaga, B. J. Mangan, T. A. Birks, and P. St.J. Russell, "Highly birefringent photonic crystal fibers," Opt. Lett. **25**, 1325–1327 (2000).
21. K. Suzuki, H. Kubota, S. Kawanishi, M. Tanaka, and M. Fujita, "High speed bi-directional polarization division multiplexed optical transmission in ultra low-loss (1.3 dB/km) polarization-maintaining photonic crystal fiber," Electron. Lett. **37**, 1399–1401 (2001).
22. P. Pual, "Optical properties of a low-loss polarization-maintaining photonic crystal fiber," Opt. Express **9**, 676–680 (2001).
23. T. P. Hansen, J. Broeng, S. E. B. Libori, E. Knuders, A. Bjarklev, J. R. Jensen, and H. Simonsen, "Highly birefringent index-guiding photonic crystal fibers," IEEE Photon. Technol. Lett. **13**, 588–590 (2001).
24. K. Saitoh and M. Koshiba, "Photonic bandgap fibers with high birefringence," IEEE Photon. Technol. Lett. **14**, 1291–1293 (2002).
25. P. R. Chaudhuri, V. Paulose, C. Zhao, and C. Lu, "Near-elliptic core polarization-maintaining photonic crystal fiber: modeling birefringence characteristics and realization," IEEE Photon. Technol. Lett. **16**, 1301–1303 (2004).
26. K. Saitoh and M. Koshiba, "Single-polarization single-mode photonic crystal fibers," IEEE Photon. Technol. Lett. **15**, 1384–1386 (2003).
27. H. Kubota, S. Kawanishi, S. Koyanagi, M. Tanaka, and S. Yamaguchi, "Absolutely single polarization photonic crystal fiber," IEEE Photon. Technol. Lett. **16**, 182–184 (2004).
28. J. R. Folkenberg, M. D. Nielsen, and C. Jakobsen, "Broadband single-polarization photonic crystal fiber," Opt. Lett. **30**, 1446–1448 (2005).
29. O. Schmidt, J. Rothhardt, T. Eidam, F. Roser, J. Limpert, and A. Tunnermann, "Single-polarization ultra-large-mode-area Yb-doped photonic crystal fiber," Opt. Express **16**, 3918–3923 (2008).
30. M. Li, "High bandwidth single polarization fiber with elliptical central air hole," J. Lightwave Technol. **23**, 3454–3460 (2005).
31. T. Schreiber, F. Röser, O. Schmidt, J. Limpert, R. Iliew, F. Lederer, A. Petersson, C. Jacobsen, K. P. Hansen, J. Broeng, and A. Tünnermann, "Stress-induced single-polarization single-transverse mode photonic crystal fiber with low nonlinearity," Opt. Express **13**, 7621–7630 (2005).
32. X. Chen, M.-J. Li, J. Koh, and D. A. Nolan, "Wide band single polarization and polarization maintaining fibers using stress rods and air holes," Opt. Express **16**, 12060–12068 (2008).
33. F. Zhang, M. Zhang, X. Liu, and Y. Peida, "Design of wideband single-polarization single-mode photonic crystal fiber," J. Lightwave Technol. **25**, 1184–1189 (2007).
34. C. Xiong and W. J. Wadsworth, "Polarized supercontinuum in birefringent photonic crystal fibre pumped at 1064 nm and application to tunable visible/UV generation," Opt. Express **16**, 2438–2445 (2008).
35. J. Ju, W. Jin, and M. S. Demokan, "Design of single-polarization photonic crystal fiber at 1.30 and 1.55 um," J. Lightwave Technol. **24**, 825–830 (2006).
36. I. H. Malitson, "Interspecimen comparison of the refractive index of fused silica," J. Opt. Soc. Am. **55**, 1205 (1965).
37. G. P. Agrawal, *Fiber-Optic Communication Systems*, 3rd ed. (Wiley, 2002).
38. S. Haxha and H. Ademgil, "Novel design of photonic crystal fibers with low confinement losses near zero ultra-flatted chromatic dispersion, negative chromatic dispersion and improved effective mode area," Opt. Commun. **281**, 278–286 (2008).
39. T. S. Saini, A. Kumar, V. Rastogi, and R. K. Sinha, "Selectively filled large-mode-area photonic crystal fiber for high power applications," Proc. SPIE **8847**, 88471Q (2013).

Accepted Manuscript



Linking mitochondrial dysfunction, metabolic syndrome and stress signaling in Neurodegeneration

Saurabh Kumar Jha, Niraj Kumar Jha, Dhiraj Kumar, Rashmi K. Ambasta, Pravir Kumar

PII: S0925-4439(16)30157-0
DOI: doi: 10.1016/j.bbadis.2016.06.015
Reference: BBADIS 64501

To appear in: *BBA - Molecular Basis of Disease*

Received date: 19 May 2016
Revised date: 16 June 2016
Accepted date: 17 June 2016

Please cite this article as: Saurabh Kumar Jha, Niraj Kumar Jha, Dhiraj Kumar, Rashmi K. Ambasta, Pravir Kumar, Linking mitochondrial dysfunction, metabolic syndrome and stress signaling in Neurodegeneration, *BBA - Molecular Basis of Disease* (2016), doi: 10.1016/j.bbadis.2016.06.015

This is a PDF file of an unedited manuscript that has been accepted for publication. As a service to our customers we are providing this early version of the manuscript. The manuscript will undergo copyediting, typesetting, and review of the resulting proof before it is published in its final form. Please note that during the production process errors may be discovered which could affect the content, and all legal disclaimers that apply to the journal pertain.

Special issue on "*Oxidative Stress and Mitochondrial Quality in Diabetes/Obesity and Critical Illness Spectrum of Diseases*" for BBA - Molecular Basis of Disease.

Invited Manuscript

Linking mitochondrial dysfunction, metabolic syndrome and stress signaling in Neurodegeneration

Saurabh Kumar Jha[1,*], Niraj Kumar Jha[1,*], Dhiraj Kumar[1], Rashmi K Ambasta[1] and Pravir Kumar[1,†]

[1]Molecular Neuroscience and Functional Genomics Laboratory, Department of Biotechnology, Delhi Technological University (Formerly DCE), Delhi 110042

*: SKJ and NKJ contributed equally to this work

† Author to whom correspondence should be addressed:
Dr. Pravir Kumar, PhD
Associate Professor
Department of Biotechnology
Delhi Technological University (Formerly Delhi college of engineering)
Room # FW4TF3, Mechanical Engineering Building
Shahbad Daulatpur, Bawana Road, Delhi 110042
Phone: +91- 9818898622
Email: pravirkumar@dce.edu; kpravir@gmail.com

Abstract:

Mounting evidence suggests a link between metabolic syndrome (MetS) such as diabetes, obesity, non-alcoholic fatty liver disease in the progression of Alzheimer's disease (AD), Parkinson's disease (PD) and other neurodegenerative diseases (NDDs). For instance, accumulated Aβ oligomer is enhancing neuronal Ca^{2+} release and neural NO where increased NO level in the brain through post translational modification is modulating the level of insulin production. It has been further confirmed that irrespective of origin; brain insulin resistance triggers a cascade of the neurodegeneration phenomenon which can be aggravated by free reactive oxygen species burden, ER stress, metabolic dysfunction, neuorinflammation, reduced cell survival and altered lipid metabolism. Moreover, several studies confirmed that MetS and diabetic sharing common mechanisms in the progression of AD and NDDs where mitochondrial dynamics playing a critical role. Any mutation in mitochondrial DNA, exposure of environmental toxin, high-calorie intake, homeostasis imbalance, glucolipotoxicity is causative factors for mitochondrial dysfunction. These cumulative pleiotropic burdens in mitochondria

leads to insulin resistance, increased ROS production; enhanced stress-related enzymes that is directly linked MetS and diabetes in neurodegeneration. Since, the linkup mechanism between mitochondrial dysfunction and disease phenomenon of both MetS and NDDs is quite intriguing, therefore, it is pertinent for the researchers to identify and implement the therapeutic interventions for targeting MetS and NDDs. Herein, we elucidated the pertinent role of MetS induced mitochondrial dysfunction in neurons and their consequences in NDDs. Further, therapeutic potential of well-known biomolecules and chaperones to target altered mitochondria has been comprehensively documented.

***Keywords*:** Mitochondrial dysfunction, Metabolic syndrome (MetS), Neurodegenerative disorders (NDDs), Therapeutics, Biomolecules, Chaperones

1. Introduction

For the maintenance of energy metabolism and cellular homeostasis mitochondria is an important organelle which is also known as the power house of cells and predominantly required for determining many cellular functions ranging from metabolic to catabolic activities. Mitochondria performs numerous crucial functions within the cell, which include cellular ATP production, Ca^{2+} buffering, regulation of apoptotic process and involvement in the synthesis of key metabolites. Nevertheless, it also acts as a primary source of endogenous reactive oxygen species (ROS) under oxidative stress. Additionally, mitochondria provides most of the ATP for the metabolic and cellular reaction within the cell, which is mainly coupled with electron transport system (ETS) [1,2]. However, research in the past few decades has recognized various factors, such as mutations in mitochondrial DNA and environmental toxins causing homeostatic imbalances, consequently leading to the damage of normal mitochondrial dynamics. Such alterations include altered mitophagy, decelerated ATP production, disturbed Ca^{2+} homeostasis,

reduced mitochondrial membrane potential and compromised mitochondrial respiration [3]. Since, the potential mechanistic role played by altered mitochondria and their associated risk factors in MetS and NDDs remain unsettled, and their possible interlinking is still needed to be investigated. This review extensively covers the involvement of mitochondrial dysfunction in both MetS and neuronal dysfunction. Further, implementation of several biomolecules and chaperones for targeting MetS and NDDs induced by mitochondrial dysfunction has also been elaborated.

2. Metabolic syndrome and mitochondrial dysfunction: A complex interplay

Metabolic syndrome (MetS) is a cluster of aberrations of metabolic origin that augments the risk for cardiovascular disease, stroke, morbidity and mortality from type-2 diabetes (T2D) [4]. Characteristic features of these complex pathological aberrations include lipid accumulation, impaired glucose metabolism and hypertension [5]. Furthermore, obesity is also one of the most critical factors that have been linked with metabolic disturbances to facilitate tissue stress and dysfunction [6]. The obese individuals are having a greater risk for prolonged diseases and usually manifest clinical features of MetS including hypertension, insulin resistance (IR), hyperglycemia and systemic markers of chronic low-grade inflammation [7]. The central pathophysiological mechanism behind MetS is IR, which is closely related to mitochondrial dysfunctioning. However, mitochondrial dysfunction is a complicated process, but it is known to be triggered by genetic factors from both mitochondrial and nuclear genome. Additionally, mitochondrial DNA polymorphisms are also associated with the components of MetS [8]. Further, environmental risk factors, for instance, life style (food intake and physical activity), various chemicals and drugs, glucolipotoxicity, and homeostatic imbalances are also responsible for MetS associated with mitochondrial dysfunctioning and IR as well **(Figure 1) [**3**]**. Recently,

it has been reported that serum levels of many mitochondrial toxins, for instance, persistent organic pollutants (POPs) are associated with MetS. However, further investigation to reveal its precise mechanism is still unclear [9]. Likewise, deficiency of Co-enzyme Q10 (Co-Q10), an important element of the mitochondrial electron transport chain has been reported in a couple of clinical outcomes, including hypertension, heart failure, obesity, which all together leads to MetS [10]. Increasing evidence suggests that an altered or excessive glucocorticoid secretion and oxidative stress strongly lead to IR associated with MetS [11]. Furthermore, oxidative stress is also a key player in the progression of MetS, which is caused due to the loss of redox homeostasis which leads to pro-inflammatory and profibrotic pathways. These events enhance the destructions in insulin signaling, diminished endothelial-mediated vaso-relaxation and associated renal and cardiovascular risks [12]. Similarly, acute hypoxia in the body is accumulating extracellular and cytosolic irons that damage the cardiovascular tissue which is also a reason of redox homeostatic imbalance that leads to hypertension and progression of metabolic dysregulation [13].

Since, regulation of cellular energy depends on complex signaling networks that act in response to fuel availability and metabolic demands. Any imbalance in the cellular energy network also paves the way for metabolic diseases, including obesity and MetS [14]. Currently, chronic sympathetic nerve activation has been reported to promote MetS and raised levels of plasma hormone, including glucocorticoids, noradrenaline, leptin, insulin and angiotensin-II (Ang-II). This sympatho-excitatory response is primarily triggered by the activation of the paraventricular nucleus (PVN) of the hypothalamus which leads to increase in circulating Ang-II levels and further, activates Angiotensin 1 (AT1) receptors in the circumventricular organs (CVOs), mainly in the subfornical organ (SFO). Activation of AT1 receptors thereafter induces an intracellular increase in reactive oxygen species (ROS) that leads to the pathogenesis of MetS [15]. Mutation

is another causative factor for MetS progression, for example, inactivation or deficiency of Ataxia telangiectasia mutated (ATM), a cardinal multifunctional serine/threonine protein kinase due to mutation lead to the pathological hallmark for DNA damage, mitochondrial dysfunction, oxidative stress and neurodegeneration [16]. Furthermore, high-fructose/sucrose and high-fat diets have also been reported to induce MetS *in vitro*, through a HepG2 cells' model [17]. Similarly, cells of immune system such as activated leukocytes and dysfunctional metabolic tissues have been found to be associated with the clinical symptoms of obesity and MetS related chronic diseases. Conversely, it is also reported that obesity and MetS is involved in numerous immune related processes, including alterations in leukocyte activity, disruption of lymphoid tissue integrity and the coordination of innate and adaptive immune responses which, all together lead to cause chronic disease progression, altered vaccine efficacy and impaired immunity [18]. Moreover, in various studies, it has been reported that any alteration in the normal functioning of endothelial cells (ECs) due to metabolic imbalances, hyperglycemia, oxidative stress and environmental stimuli caused endothelial inflammation, compromised vascular tone, boosted permeability, advanced cell proliferation and finally cell death. These promising features lead to aggravate cardio metabolic risk factors responsible for MetS and also involved in pathologies like ischemia [19]. In a similar fashion, substantial evidence shows the role of oxidative stress and mitochondrial dysfunction not only in MetS but also in the neurodegenerative disorders (NDDs) associated with aging.

PLEASE INSERT FIGURE 1 HERE

Figure 1: Schematic illustration showing the association of mitochondrial dysfunction with clinical symptoms of metabolic syndrome as well as its associated factors.

3. Intervening role of stress and mitochondrial dysfunction in neurodegenerative disorders

In order to maintain the normal brain function, the immense amount of energy (ATP) is required. Among all the essential tissues of the body, including, brain, heart and skeletal muscle, brain is the most energy-dependent tissue. The main source of energy which is predominantly required for the normal functioning of the brain is mainly produced by normal activity of mitochondrial cells. In mitochondria, ATP production is mainly associated with an ETS where, the passage of electrons through diverse electron carriers is coupled with the transport of protons from the mitochondrial matrix into the inner-membrane space, and thereafter these protons re-enter into the mitochondrial matrix by dint of ATP synthase for the generation of ATP [1,2]. However, mitochondrial metabolism is also accountable for the ROS production in cells when unpaired electrons leave the ETS and react with molecular oxygen and thus generate superoxide. This superoxide further interacts with lipids, DNA and proteins and plays a crucial role in numerous signaling processes, which is associated with the disease phenomenon of both aging and NDDs [20]. Moreover, ROS can also react with nitric oxide (NO) to produce reactive nitrogen species (RNS) [21]. Furthermore, apart from altered energy and increased ROS production, mitochondrial dysfunction is also responsible for altered Ca^{2+} buffering, apoptosis and senescence that may lead to the progressive decline of post mitotic cells and consequently, results into aging and NDDs [22]. There are numerous NDDs identified so far, that have been reported to be associated with stress and mitochondrial dysfunctioning, which include

Alzheimer's disease (AD), Parkinson's disease (PD), Huntington's disease (HD) and Amyotrophic Lateral Sclerosis (ALS), and their underlying mechanism is depicted in **Figure 2.**

3.1 Alzheimer's disease

AD is an irreversible, progressive brain disorder that is primarily characterized by the presence of extracellular Aβ accumulations as senile plaques and intracellular tau-containing neurofibrillary tangles (NFTs) in the brain, which contribute to the progressive neuronal loss and cognitive decline. A growing body of evidence has reported that mutations in Aβ precursor protein (AβPP), presenilin 1 and 2 are the main causative factor for the early-onset of familial form of AD [23,24]. However, any damage to both the structure and components of mitochondria, increased oxidative stress and diverse other stresses are also accountable for AD pathophysiology. For instance, deficiency in various key enzymes of the tricarboxylic acid cycle (TCA) that are involved in oxidative metabolism, such as pyruvate dehydrogenase complex (PDHC) and α-ketoglutarate dehydrogenase complex (KGDHC) and enzymes involved in the rate-limiting step of the TCA cycle are accountable for reducing molecular oxygen and are responsible for consistent defect in mitochondrial components in AD brain [25]. Likewise, impairment in the functional expression of Peroxisome proliferator-activated receptor gamma co-activator 1-alpha (PGC-1α), a master regulator of mitochondrial biogenesis is also involved in AD progression [26]. Furthermore, mitochondrial axonal transport is profoundly affected by mutations in Presenilin 1, most likely by affecting phosphorylation of kinesin light chain through effects on GSK3β [27]. Moreover, accumulation of Aβ in the protein import channels of mitochondria has currently been reported in AD brains that are responsible for mitochondrial dysfunction that potentiate neuronal and synaptic stress thereby increasing the severity of disease [28]. Altered cytochrome oxidase activity is another cause of AD, which is associated with

altered mitochondrial dynamics [29]. Further, altered Ca^{2+} homeostasis, another causative factor for AD is also reported in AD cybrids made from mtDNA of AD subject [30]. It has been reported that sporadic mtDNA rearrangement and other sporadic mutation in the mtDNA control region is considerably raised in AD brains [31]. Moreover, oxidative stress and mitochondrial dysfunction involved in early onset of AD have been confirmed by using *in vivo* electron paramagnetic resonance (EPR) imaging where methoxycarbamyl-proxyl (MCP) is used as a redox-sensitive probe [32]. Mutations in presenilin (PS1 or PS2) gene have also been reported to cause mitochondrial dysfunction in the familial form of AD. Since, PS mutants cause altered intracellular Ca^{2+} homeostasis by increasing the gating of inositol trisphosphate (IP_3) receptor (IP_3R) Ca^{2+} release channel on the endoplasmic reticulum thereby leading to cause excessive Ca^{2+} release into the cytoplasm. This excessive Ca^{2+} release or altered Ca^{2+} signaling to contribute to the mitochondrial dysfunction and neuronal death [33]. Similarly, glutamate-induced calcium signaling is also accountable for altered mitochondrial dynamics and their associated neuronal death [34]. Recently, white matter degeneration in aging brain has found to be associated with mitochondrial dysfunction, underlying the greatest risk of AD. Moreover, it also causes reduced mitochondrial respiration and increased mitochondrial H_2O_2 productions [35]. In the same way, accumulation of discriminant metabolites such as acylcarnitines has also reported to involve in impaired mitochondrial function [36]. Additionally, toxic Aβ associated with over-expressed voltage-dependent anion channel 1 (VDAC1) has also involved in altered mitochondrial function and apoptosis induction [37]. Growing evidence suggests that AD neurons are having a considerably lower percentage of normal mitochondria with significant changes in their size depicting that a likely change in mitochondrial dynamics is involved in disease progression, while normal neurons contain a significantly higher percentage of the

mitochondria with broken cristae [1]. These all findings suggest the involvement of mitochondrial dynamics in AD pathogenesis.

3.2 Parkinson's disease

Parkinson's disease (PD) is one of the most common progressive disorders of the nervous system characterized by rigidity, resting tremor, postural instability and bradykinesia [38]. Its cause remained mysterious, although numerous evidences support mitochondrial dysfunctions and oxidative stress to be associated with the disease pathophysiology. For instance, mitochondrial DNA damage in dopaminergic neurons has been reported as one of the causing factors of striatal dysfunctions in a PD mouse model [39]. However, Glucocerebrosidase 1 (GBA1) gene mutations are identified as another causative factor responsible for perturbing normal mitochondrial function by increasing ROS production and by decreasing oxygen consumption, adenosine triphosphate (ATP) production and membrane potential. GBA1 mutations are also accountable for agglomerating dysfunctional and fragmented mitochondria [40]. Furthermore, quinine oxidation products responsible for ROS production have also been evidenced to be associated with mitochondrial dysfunction and dopamine cytotoxicity [41]. Similarly, the selective loss of alpha-ketoglutarate dehydrogenase complex (KGDHC) and mitochondrial complex I in the nigral neurons is another reason of PD pathogenesis. Such selective loss causes mitochondrial respiratory system failure and lead to cause oxidative damage in neurons. These abnormalities can trigger apoptotic cell death as well [42]. Further, the pesticide rotenone which is known to inhibit mitochondrial complex I in PD is also responsible for microtubule (MT) destabilization that contributes to the blockage of mitochondrial voltage-dependent anions channels (VDACs) by tubulin and thus leads to PD [43]. Upcoming research identified hepatic mitochondrial dysfunctions in a rodent model of PD that arise as a result of nigrostriatal

degeneration and interference in CNS-liver interaction due to thyroid hormone [44]. Likewise, deficiency in Phosphatase and tensin homolog (PTEN) induced putative kinase 1 causes Ca^{2+} accumulation in mitochondria that lead to both ROS production and intrinsic cell death in PD. It has revealed that mutations in PTEN-induced putative kinase 1 (PINK1) lead to a recessive form of PD. Since, PINK1 is responsible for mitochondrial quality control and its partial knock-down provokes numerous mitochondrial dysfunctions, including reduced membrane potential, decreased cellular ATP levels and enhanced susceptibility against mitochondrial toxins [45]. Apart from PINK1, mutations in numerous other PD associated genes have also been reported to be involved in impaired mitochondrial dynamics. Such genes include DJ-1, α-Synuclein, parkin and LRRK2, which caused several defects in mitochondrial dynamics, such as altered fission/fusion, biogenesis, trafficking in retrograde and anterograde directions and impaired mitophagy process [46]. Impairment in the function and expression of PGC-1α, a key regulator of mitochondrial biogenesis is also responsible for PD [47]. Further, mitochondrial transcription termination factor 2 and 4 (MTERF2 and MTERF4) has been identified in 1-methyl-4-phenylpyridinium (MPP+)-induced PD brain that is responsible for mitochondrial dysfunction [48,49]. Recently, SUMOylation, an epigenetic modification has also been found to be involved in mitochondrial dysfunction associated with PD progression [50]. Numerous studies have reported that the brain of PD patients manifests similar cellular and functional changes with signs of reduced mitochondrial function, increased oxidative stress, reduced glucose uptake and augmented peroxidation of cellular membranes [51].

3.3 Huntington's disease

Huntington's disease is a genetic neurodegenerative disorder manifested by emotional imbalance, cognitive decline and loss of movement co-ordination caused due to an autosomal

dominant mutation in huntingtin gene (Htt), which is accountable for CAG repeat expansion thereby causing the synthesis of polyglutamine tract [52]. The CAG repeat expansion is mainly caused due to mitochondrial dysfunctions, oxidative and metabolic stress and altered ion-channels. Several evidence reports that any alteration in mitochondrial activity propels the pathogenesis of HD; for instance, mtDNA damage and deletion have been reported in HD brains [53]. Significant defects in the enzymes associated with mitochondrial respiratory chain and glucose metabolism, including pyruvate dehydrogenase complex (PDHC), aconitase and succinate dehydrogenase (SDH) have been reported in HD patients [54]. Furthermore, SDH inhibitions by malonate and 3-nitropropionic acid have also reported to cause excessive mitochondrial fission and neuronal death associated with clinical and pathological features of HD [55]. Recently, an altered activity of PGC1α protein due to mHtt has been observed that resulted in an overall reduction of acetyl-CoA and ATP synthesis, thus contribute to impaired cholesterol metabolism associated with HD [56]. Further, mutant Htt agglomerates associated with mitochondria that directly affect mitochondrial trafficking in axon, calcium handling and mitochondrial membrane potential as well. It is also found to be associated with mitochondrial fragmentation along with reduced ATP levels that mediates neuronal dysfunction and leads to motility deficit [57]. mHtt is also reported to cause altered Ca^{2+} homeostasis associated with mitochondrial dysfunction [58]. Exclusively, mHtt directly inhibits mitochondrial protein import complex TIM23 *in vitro*, signifying that deficient protein import is an early event in HD [59]. Moreover, altered mitophagy process has also been reported in the presence of mHtt. Since, mitophagy is accountable for maintaining the healthy population of functional mitochondria by eliminating defective mitochondria with the help of lysosomal machinery. This process is mainly triggered by glyceraldehyde-3-phosphate dehydrogenase (GAPDH), that gets inactivated by mHtt and thus losses its selective association with damaged mitochondria. Further, abnormal

interaction of mitochondrial GAPDH with mHtt impeded GAPDH-mediated mitophagy, contributing to accumulation of damaged mitochondria and increased cell death [60]. Recent studies have reported that mHtt also curtails the maturation of SREBP and up regulates the expression of LXR and LXR-targeted genes (ABCG1, ABCG4, SREBP, ApoE and HMGCoA reductase) which further lowers both the synthesis and transport of cholesterol from astrocytes to neurons via ApoE [56]. Similarly, impaired Rhes/mTORC1 activity underlies numerous metabolic phenotypes including; mitochondrial dysfunction, striatal atrophy, aberrant cholesterol homeostasis and impaired dopamine signaling have also been reported in HD [61]. Furthermore, increased levels of protein carbonyls, malondialdehyde ($C_3H_4O_2$) and nitrite (NO^{2-}) along with reduced Mn-superoxide dismutase (Mn-SOD) and catalase activity is involved in impaired mitochondrial dynamics associated with altered cytochrome C levels and reduced mRNA expression of respiratory chain complexes in HD brain [62]. In addition, caspase-3 and -9 activity coupled with altered expression of apoptotic proteins such as Bim, AIF, Bad and Bax has also been reported to be involved in cognitive impairment leading to HD [63].

3.4 Amyotrophic lateral sclerosis

Amyotrophic lateral sclerosis (ALS) is a chronic motor neurodegenerative disorder, manifested by a substantial collapse of the large pyramidal neurons in the motor cortex, spinal cord and brain stem resulting in fasciculation, gradual muscle weakness, speech deficit and paralysis that eventually leads to neuronal death [64]. However, the precise mechanism for ALS is still unknown, but numerous mechanisms have been identified that is associated with motor neuronal death in ALS. These include mitochondrial dysfunction, metabolic dysfunction, protein aggregation, astrocyte- and microglial toxicity, glutamate-mediated excitotoxicity, oxidative stress and transition-metal-induced toxicity. Mitochondrial defects associated with decreased

complex IV activity in the spinal cord and motor neurons have been reported in ALS pathology. Such defects have also been observed in peripheral tissues from ALS brains [65]. In mutant SOD1 transgenic mice of ALS, the aberrancy in mitochondrial functions have been observed, which is associated with respiratory deficits of mitochondrial subunits [66]. Most importantly, increased levels of mitochondrial base deletion (common 5- kb deletion) have also been observed in the skeletal muscle and motor cortex of ALS patients [67]. The presence of mitochondrial morphological abnormalities in animal models of ALS and ALS patients has also been reported by several lines of studies. Previous studies revealed the appearance of heavy mitochondrial conglomerates in neurons of the lumbar spinal cord, and the occurrence of mitochondria agglomerates in the subsarcolemmal region of muscles of ALS patients. Moreover, in ALS mutant SOD1 transgenic mice, dilated and vacuolated mitochondria with unorganized cristae has been observed in the motor neurons lacking any apoptotic features. This in turn suggests that excessive mitochondrial fission is responsible for selective susceptibility of motoneuronal mitochondria to SOD1 mutation [68-70]. Further, mitochondrial dependent cell apoptosis has been reported due to accumulation of mutant SOD1 inside the intermembrane space and deposition of misfolded SOD1 onto the outer mitochondrial membrane, leading to cluster the transport across mitochondrial membranes. Substantial *in vivo* and *in vitro* evidence has also demonstrated that localization of mutant SOD1 in mitochondrial intermembrane space inevitably contributes to impaired mitochondrial functions [71]. Currently, ALS associated optineurin (OPTN) mutants (Q398X and E478G) have been found to be associated with severe mitochondrial dysfunction and neuronal injury due to increased oxidative stress and reduced antioxidase activity in SH-SY5Y cells [72]. Similarly, mutations in OPTN have also been reported to associate with the altered mitophagy process in ALS. Mitophagy is responsible

for degradation of damaged mitochondria by autophagosomes thereby leading to maintain the normal functioning of mitochondria [73]. Another cause of mitochondrial dysfunctioning in ALS is the administration of 3-nitropropionic acid (3-NP). Systemic administration of 3-NP is sufficient to change neurotrophin levels in the brain, leading to damage striatal neurons [74]. Recently, missense mutation in SIGMAR1 (c.304G > C), which encodes sigma-1 receptor (Sig-1R) has been reported in familial ALS where, mutant Sig-1R(E102Q) protein has found to be linked with reduced mitochondrial ATP production, altered proteasome activity coupled with mitochondrial injury and aggravating ER stress-induced neuronal death in neuro2A cells [75]. Likewise, impairment in the expression levels of fused in sarcoma (FUS) protein has been observed to cause ALS in gain-of-function/loss-of-function manners. Overexpression of FUS protein provokes death in primary cortical neurons and motor neuronal NSC34 cells via the mitochondrial apoptotic pathway which is independent of transactive response DNA-binding protein-43 [76]. Recently, sALS-CSF induced overexpression of the pro-apoptotic mitochondrial protein BNIP3L has also been reported to be associated with induced neurotoxicity, elevated ROS and lowered mitochondrial membrane potential, which collectively contribute to the pathogenesis of ALS [77].

PLEASE INSERT FIGURE 2 HERE

Figure 2: Molecular mechanism involved in mitochondrial dysfunction mediated pathophysiology of neurodegenerative disorders. PDHC, pyruvate dehydrogenase complex; KGDHC, ketoglutarate dehydrogenase complex; PGC1α, Peroxisome proliferator-activated receptor gamma coactivator 1-alpha; PSN-1 & PSN-2, Presenilin-1 & Presenilin-2; VDAC1, voltage dependent anion channel 1; GBA1, glucocerebrosidase 1; GAPDH, glyceraldehyde-3-phosphate dehydrogenase; PINK1, PTEN-induced putative kinase 1; TIM23, translocase of the inner membrane 23; SDH, succinate dehydrogenase; 3-NP, 3-Nitropropionic Acid; SOD1, superoxide dismutase; OPTN, optineurin; SIGMAR1, sigma-1 receptor (Sig-1R); BNIP3L, pro-apoptotic mitochondrial proteins; CSF, cerebrospinal fluid.

4. How metabolic syndrome is a causative agent for neuronal dysfunction?

Metabolic syndrome, an alliance of medical disorders that greatly increase the risk for developing metabolic and neurodegenerative disorders, has reached epidemic levels in various areas of today's world. In spite of this alarming situation, previous studies have uncovered the root mechanisms of MetS associated with neuronal dysfunction are still limited, therefore, exploring the associated mechanisms behind such an aberrancy has become essentially needed nowadays. A growing body of evidence reported that multiple targets and signaling pathways are involved in metabolic abnormalities/syndromes associated with neurodegeneration (**Figure 3**). Meanwhile, recent studies have indicated that MetS is linked with an increased risk of type-2 diabetes (T2D) and cardiovascular disease, which have been found to be associated with AD [78]. It is also ascertained that insulin resistance (IR) is one of the possible reasons for linkup between AD and MetS, since it modulates Aβ aggregation, i.e. the primary constituent of senile plaques. Moreover, insulin also inhibits the activity of glycogen synthase kinase-3β (GSK-3β) and thus tau phosphorylation thereby inhibiting the formation of neurofibrillary tangles (NFTs) in AD [79]. It has been proposed that Ca^{2+} dysregulation is another factor for metabolic alterations of glucose and insulin that establishes the association between T2D and AD [80]. Further, elevated glucose as evidenced in MetS/T2D and Aβ peptide coordinately enhanced neuronal Ca^{2+} and nitric oxide (NO) in an NMDA receptor-dependent manner in AD brain. Thus, elevated NO level in AD causes S-nitrosylation of dynamin-related protein 1 (Drp1) and insulin-degrading enzyme (IDE), thus inhibits insulin and Aβ catabolism and hyperactivating mitochondrial fission machinery. These alterations subsequently result into compromised mitochondrial dynamics and elevated oligomeric Aβ that lead to synaptic loss and dysfunctional synaptic plasticity in cortical and hippocampal neurons [81]. Interestingly, both T2D and AD

exhibit similar defects in mitochondria that impair their ability to modulate oxidation in the neuronal cell. Compelling evidence has reported about the involvement of mammalian target of rapamycin (mTOR) signaling axis in cellular senescence and age-related NDDs. Indeed, this signaling is a downstream signal of insulin signaling and regulating insulin signaling by a negative feedback mechanism that shows a valid linkup between MetS and pathogenesis of NDDs. mTOR modulates cell growth and cellular metabolism in response to growth factors, nutrients and cellular energy conditions. However, Loss of mTOR signaling in the brain disrupts multiple downstream signaling associated with glucose metabolism (insulin signaling), energy production, mitochondrial dynamics/function, cell growth and mitophagy/autophagy. These all crucial events thereafter lead to the pathogenesis of NDDs [82,83]. Further, plasma triglycerides and HDL cholesterol is found to be another possible reason for the association between AD and MetS. Since, HDL cholesterol act as a focal transporter of cholesterol in the neuronal cell, and it has been evidenced that any drop in the HDL cholesterol level causes impairment of cholesterol release in neurons thereby leading to the formation of NFTs and senile plaques [84]. Moreover, it is also reported that a low plasma HDL concentration and a high plasma triglyceride concentration cause vascular changes in the brains of AD patients [85]. Not only that, currently, the renin angiotensin system (RAS) which is crucial for fluid and blood pressure regulation has found to be associated with both MetS and AD. At one hand, genetic alterations of the RAS affect cardiovascular and metabolic phenotypes causing hypertension and cerebrovascular diseases while at another hand sustained activation of RAS augments age-related organ injury and results in cognitive impairment and dementia. Similarly, the higher levels of angiotensin-converting enzyme (ACE) confer increased risk of diseases such as congestive heart failure, diabetic nephropathy and AD [86].

A growing number of studies have been completed to confirm that the components of MetS also act as a risk factor for PD etiology. For instance, hyperglycemia exacerbates PD pathogenesis in aging brain via neuronal cell damage. It is also reported that hyperglycemia induced cell death is sustained through oxidative stress and mitochondrial superoxide generation [87]. Some evidence shows that the PD associated genes are also found to be associated with alter the insulin level through ATP-sensitive potassium ion channels (KATP channels) and extracellular kinases signaling to boost glucose level [88]. Like hyperglycemia, hyperhomocysteinemia is a risk factor for endothelial dysfunction has currently been reported in both AD and PD. Many studies have been carried out and revealed that high homocysteine associated with endothelial dysfunction is responsible for hydrogen peroxide release that caused cellular oxidative stress and inflammations mediated *in vitro* cell injury [89]. Further, it has been established that activated microglia is an important key mediator of proinflammatory and neurotoxic factors involved in advancement of PD. These proinflammatory and neurotoxic factors include cytokines such as, interleukin-6 (IL-6) and interleukin-1β (IL-1β), tumor-necrosis factor-α (TNF-α) and reactive oxygen species (ROS) [90]. Moreover, evidence indicates that both ER stress and inflammation coordinate the etiology of PD [91]. Many studies have shown that metabolic stress also causes dopamine-releasing neurons to prematurely die along with the cell death, leading to neuronal toxicity and subsequent onset of Parkinson's symptoms [92]. Further, a growing number of studies revealed that MetS like obesity in middle age individuals also augment the risk of PD and decrease life expectancy [93]. Additionally, adiposity and body mass index along with other risk factors also lead in the advancement of PD [94]. On the contrary, it has been reported that high-fat diet can also lower the risk for advancing PD via decreasing HSP27 phosphorylation, affecting glucose transport and degradation of IκBα in the nigrostriatal system. Moreover, increasing inflammatory molecules, mitochondrial dysfunction, oxidative stress and lipid metabolism has all been shown

to occur due to high-fat feeding. Most importantly, hypertension as a component of MetS is less frequent in PD, suggesting the need for exploring the possible link between PD and hypertension [93]. Furthermore, abnormalities in cholesterol homeostasis or lipid metabolism have also been associated with the neurodegenerative process of PD, and such abnormalities are occurred due to metabolic imbalances, injuries, therapeutics and autoimmune diseases [95].

An additional research which focuses on the extremely important aberrancy associated with lipid metabolism or altered cholesterol metabolism has been reported to cause neuronal dysfunction and degeneration in HD. This alteration has been attributed to the pertinent action of mHtt on sterol regulatory element binding proteins that cause a reduction to the level of active sterol regulatory element response protein-2 (SREBP-2) and such depletion are pathogenic to the brain [96]. Moreover, insulin resistance (IR) appears to act as a metabolic stressor, which is critical for advancement in disease progression. An association between HD and reduced insulin secretion has also been suggested by the R6/2 transgenic mouse model characterized by CAG repeats and this pattern of IR such as catabolic state results in weight loss and in lowering body mass index in case of HD patients. Further, this state of IR is manifested by abnormal lipid metabolism, elevated concentrations of circulating free fatty acids and high blood-glucose levels in peripheral tissues and contribute to an increased risk for developing T2D [97]. Currently, the polymorphic variants of apolipoprotein E (APOE) have also been found to be associated with pathophysiology of several NDDs including, AD, PD, HD, vascular dementia, cerebrovascular diseases and lewy body dementia. Since, APOE is a multifunctional protein of a lipoprotein transport system often involved in metabolism of dietary lipids, therefore, any metabolic imbalances due to improper nutrient and fluid supply are accountable for etiology for such abnormalities [98]. Some evidence shows that, glucose intolerance, growth hormone deficiency, IR, hyperlipidemia, reduced body

mass index (BMI), both hypometabolism and hypermetabolism are signs of the progressive dysregulated metabolic homeostasis in ALS [99]. Further, altered expression of ALS associated genes, including, C9 or f72, SOD1, FUS and TARDBP in humans and mice are often coupled with metabolic imbalances [100]. It is reported that familial mouse model of ALS goes through a progressive state of acidosis that is linked to several metabolic abnormalities. For instance, the acidosis process causes changes in glycogen, glucose and α-glucosidase activity in the spinal cord of ALS patients and is responsible for lipolysis [101]. Further, the altered levels of IL-6, IL-8, TNF-α, lipocalin-2, plasminogen activator inhibitor-1 (PAI-1), ghrelin, gastric inhibitory peptide (GIP) and pancreatic polypeptide (PP) that is associated with metabolic syndrome, have also been reported in the plasma of ALS patients [102]. It is also revealed that proteins which are responsible for disturbing carbohydrate metabolism are associated with altered glucose homeostasis, that link HD and ALS to T2D. Moreover, numerous other stresses apart from oxidative and ER stress like mitochondrial dysfunctions and microRNAs (miRNA29a/b and miRNA-9) interconnect these NDDs with T2D [103].

PLEASE INSERT FIGURE 3 HERE

Figure 3: Interlink between metabolic syndrome and pathophysiology of neurodegenerative disorders. AD, Alzheimer's disease; PD, Parkinson's disease; HD, Huntington's disease; ALS, Amyotrophic lateral sclerosis; RAS, Ranin-angiotensin system; ACE, angiotensin converting enzyme; APOE, apolipoprotein E; NO, nitric oxide; SREBP-2, sterol regulatory element binding protein -2; IL, interlukin; TNF-α, tumor necrosis factor-α; PAI-1, plasminogen activator inhibitor-1 ; GIP, gastric inhibitory peptide; PP, pancreatic polypeptide ; SOD1, superoxide dismutase 1; FUS, fused in sarcoma; TARDBP, transactive response DNA binding protein; ROS, reactive oxygen species.

5. Therapeutics approaches for targeting mitochondrial dysfunction

Nowadays, treatment against mitochondrial mediated neuronal dysfunctions and metabolic syndromes emerges as a challenging mission for the neurobiologists. Till date, numerous factors

associated with multiple targets and signaling pathways of altered mitochondrial dynamics have been reported, which include deficient mitochondrial enzymes, certain chemicals and drugs, genetic factors (mitochondrial DNA polymorphisms) and environmental risk factors. Thus, altered mitochondrial dynamics subsequently, causes compromised mitochondrial respiration, limited ATP production, disturbed Ca^{2+} homeostasis and altered mitophagy [104]. In order to overcome such challenges numerous therapeutic strategies are currently being devised to slow down or alleviate the toxicity associated with defective mitochondrial activity. For instance, numerous biomolecules based therapy has been designed to overcome the problem associated with metabolic syndromes and associated neurodegenerative disorders. Similarly, molecular chaperones are also being implicated these days to reverse the disease pathology associated with altered mitochondrial dynamics. Moreover, various other therapeutic approaches have also been formulated recently to slow down the pathophysiology behind defective mitochondria mediated neuronal dysfunction and metabolic syndrome that have been discussed here.

5.1 Biomolecules mediated therapy for altered mitochondrial dynamics

Since, there is not a single cause responsible for such alterations but diverse factors are conducing to such abnormalities. Therefore, it is decisive to implicate different biomolecules in multiple conditions in order to regain the normal function against altered mitochondrial dynamics. For this reason, these days, several biomolecules are being utilized for targeting defective mitochondria and its associated disease phenomenon in NDDs and MetS. For instance, vitamin Co-Q10 supplementation is used during the treatment of obesity, oxidative stress (T2DM) and the inflammatory process in MetS. Co-Q10 served as an antioxidant by acting as a cofactor and activator of mitochondrial uncoupling proteins, responsible for the reduction in ROS production, endothelial dysfunction and hypertension [105,106]. Similarly, numerous other

vitamins with antioxidant properties have also been developed to treat MetS induced by oxidative stress and mitochondrial dysfunctions. These vitamins are α-lipoic acid, vitamin E, vitamin C, N-acetylcysteine (NAC) and inducers of the heme oxygenase, which are responsible for reduced ROS production [107]. Further, treatment with antiepileptic drug, Levetiracetam has been found to be associated with ameliorating numerous aspects of mitochondrial dysfunction such as alterations of fission-fusion balance in a cell model for aging and early/late-onset AD [108]. Likewise, another biomolecule Icariin has also benefitted against mitochondrial fragmentation associated with $A\beta_{1-42}$ accumulation in 3×Tg-AD neurons [109]. Similarly, Salicylic acid has currently reported to provide neuroprotection against mitochondrial dysfunction, oxidative stress and apoptosis in PD brain due to its antioxidant and anti-inflammatory effects on neuronal cell [110]. Further, potential protective effect of Succinobucol against mitochondrial metabolic impairment and oxidative stress induced by 3-NP has been reported in HD brain [111]. Another biomolecule, N-acetyl-l-tryptophan (L-NAT) has been presently reported as an inhibitor of mitochondrial cytochrome c release and thereby acting as a possible neuroprotective agent for ALS [112]. Similarly, many other biomolecules have been identified and implicated so far to target altered mitochondrial dynamics in the brain which have been outlined in **Table 1**. These biomolecules act by binding to their specific targets and reduce the severity of neurological outcomes associated with altered mitochondrial dynamics.

Table 1 list of biomolecules, mitigating the effect of mitochondrial dysfunctions in both metabolic syndrome and neurodegenerative disorders

5.2 Chaperones mediated therapy for altered mitochondrial dynamics

It is another worthwhile proposal besides using distinct biomolecules to target mitochondrial dysfunction. For this purpose, nowadays different chaperones are identified and implicated against such alterations. For instance, HSP60 along with HSP10 has been reported to provide protection against intracellular Aβ aggregation through the maintenance of mitochondrial oxidative phosphorylation and functionality of TCA enzymes. Notably, both alone and combined effect of HSPs such as HSP90, HSP70, HSP60 and HSP10 has also been studied and found to be associated with reduced ROS production, preserved ATP production, reduced cytochrome C release and lowered caspase-9 activity, which all together contribute towards protection against Aβ induced neuronal dysfunction in AD. Further, HSP60 also neutralizes the toxic effect of Aβ associated with altered complex IV activity and thereby maintaining the integrity of ETS [169]. Moreover, HSPs have also been reported to protect against increased oxidative stress and apoptosis caused by mitochondrial dysfunction in PD. For instance, in PC12 cell lines of PD, α-synuclein at nanomolar concentration is associated with increased HSP70 expression that curtails α-synuclein accumulation and toxicity. Since, inducible expression of mutant α-synuclein in PC12 cell lines can result in greater sensitivity to proteasomal alteration, leading to altered mitochondrial dynamics and neuronal cell death [170]. Interestingly, mitochondrial HSP70 is also known to play a crucial role in the mitochondrial import complex and in the mitochondrial biogenesis, which is induced in response to stimuli such as glucose deprivation and oxidative injury [171]. Similarly, mitochondrial HSP90 has also been reported to mitigate α-synuclein toxicity associated with mitochondrial dysfunction. Since, serum levels of HSP90 are raised in

the brain of PD patients, and HSP90 is also found in Lewy bodies in this case. However, serum levels of HSP90 have been spotted to be decreased in AD patients and also reported to be downregulated in the temporal lobe of AD brain [171]. Recently, the mitochondrial chaperone protein, tumor necrosis factor receptor associated protein-1 (TRAP1) has also been found to be associated with reduce α-synuclein toxicity [172]. Another important chaperone, HSP27 has been currently reported to target mitochondrial pathway leading to inhibition of apoptosis. HSP27 inhibits apoptosis through blocking the entry of tBID into the mitochondria and curtails second mitochondria-derived activator of caspase (SMAC) and cytochrome C release from mitochondria [170]. Likewise, HSP40/Hdj-1, HSP70/Hsc70 and HSP27 have also been suggested to reduce poly(Q)-mediated cell death either by binding to cytochrome C and thus inhibiting the mitochondrial death pathway or by protecting against ROS [173]. Moreover, HSP40/Hdj-1 has also been proposed to have a protective role against obesity, IR and maintenance of pancreatic β-cell functions by stopping the accumulation of β-cell peptide (human amylin) [174]. Further, overexpression of the molecular chaperone regulator-1 (BAG-1) has also been identified to protect against poly(Q) induced cell death in HD. Interestingly, overexpression of BAG1 also improves the effects of HSP70 by reducing the accumulation of mHtt in cultured cells and consequently, leads to recuperate neurite outgrowth in Htt-transfected PC12 cells [175]. In case of ALS, Macrophage migration inhibitory factor (MIF) as a chaperone has been found to prevent the accumulation of misfolded SOD1 thereby leading to protect against altered mitochondrial dynamics. On the contrary, other chaperones such as HSP70/Hsc70, cyclophilin-A, aB-crystallin and glutathione peroxidase have no effect in blocking SOD1 misplacing onto the mitochondrial outer membrane which consequently, leads to damaged mitochondrial integrity [176]. Recently, reduced expression of HSP60 has exhibited the protective role against mitochondrial damage in ALS because interaction between mitochondrial

chaperonin, HSP60 and FUS protein causes its translocation to mitochondria and leads to cell damage [177]. Further, it has been reported that small HSPs, including the HSP27, HSP25 and α-crystallin family also impart neuroprotective and cardioprotective effect against secondary complications of T2D [178]. Nevertheless, more research is required to explore the potential therapeutic role of chaperones against altered mitochondrial dynamics in both NDDs and MetS.

Moreover, potential protective mechanisms of numerous chaperones against altered mitochondrial dynamics in both NDDs and MetS have been summarized in **Table 2**.

Table 2 list of chaperones, mitigating the effect of mitochondrial dysfunctions in both metabolic syndrome and neurodegenerative disorders

5.3 Emerging therapies for altered mitochondrial dynamics

However, the crucial role of biomolecules and chaperones has been addressed extensively for altered mitochondrial dynamics but there are numerous other emerging therapeutic strategies that have been identified currently to target such alterations. For instance, a neuroprotective effect of Lithium has been reported via modulation of mitochondrial dysfunction, which is likely achieved by impeding GSK-3 and inositol-145 triphosphate (IP_3) in AD [183]. Similarly, Acupuncture combined with moxibustion has benefited the hippocampal neurons in AD rats presumably via the regulation of altered mitochondrial dynamics (imbalance between fission and fusion proteins) and improvement in the mitochondrial damage in the hippocampus [184]. Further, GAPDH-siRNA treatment has also benefited against Aβ induced mitochondrial dysfunction in AD [185]. Not only that, Cocaine- and amphetamine-regulated transcript (Exogenous CART treatment) in APP/PS1 mice has obstructed depolarization of the mitochondrial membrane and provoke mitochondrial complex, I and II activities, thereby leading to an increase in ATP levels. Further, CART treatment also reduces ROS and 4-HNE level that mitigate oxidative DNA damage in AD

brain [186]. In case of PD, MicroRNA-7 (miR-7) has been found to elicit a protective role in cellular models of PD. Moreover, miR-7 overexpression inhibits mitochondrial depolarization, mitochondrial fragmentation, cytochrome C release, ROS production and release of mitochondrial Ca^{2+} in response to MPP+ in SH-SY5Y cells. Similarly knockdown of VDAC1 also led to a decrease in intracellular ROS production and subsequent cellular protection against MPP+. Thus, the protective effect of miR-7 is partly influenced through provoking mitochondrial function by targeting VDAC1 expression [187]. Further, a Parkin-AMPK alliance has recently been reported to be involved in neuroprotection against mitochondrial dysfunction. Since, Parkin along with energy sensor AMP-activated protein kinase (AMPK) critically involved in all stages of the mitochondrial life cycle (i.e., from biogenesis to its exit from the cell via mitophagy), advocating that these two proteins might act in a functionally convergent manner to preserve the quality of cellular mitochondria [188]. Recently, the gene transfer-based experiments have led to the finding of potential therapeutic targets that could ameliorate mitochondria in HD (such as mitochondrial complex II or the PGC-1α). However, preclinical studies are yet required to deduce whether it is feasible to regulate these systems *in vivo* or not [159]. Further, using RNA interference (RNAi) and the p53 inhibitor pifithrin-α is another strategy to mitigate the mitochondrial dysfunction in HD [159]. Recently, Lentiviral vector delivery of antioxidant gene such as PRDX3/NRF2 has been found to be an important approach for targeting mitochondrial dysfunction in NSC34 cells expressing the human $SOD1^{G93A}$ in ALS [189]. Similarly, stem cell therapy has identified as another possible therapeutic approach for targeting altered mitochondria dynamics in ALS [190]. Additionally, lifestyle modification, such as exercise and diet has been currently reported to decrease the risk for developing T2D, whilst physical activity has found to be associated with improve glucose tolerance. Indeed, exercise helps in improving ETS, increasing mitochondrial biogenesis through PGC-1α activity and

improving sensitivity to insulin. Moreover, it has also been observed to be involved in activating AMPK, which ameliorates both glucose and fat oxidation [191,192]. Nonetheless, more approaches are needed to be devised soon for effective treatments against both MetS and NDDs induced by altered mitochondrial dynamics.

5.4. Metabolic compounds mediated attenuation in neurodegeneration: current therapies

Albeit, the involved therapeutics for treatment of both MetS and NDDs have been discussed extensively, but there are numerous metabolic compounds have been currently identified, that have been used to attenuate the pathological atmosphere of both MetS and NDDs. For instance, increasing brain insulin levels have been reported to ameliorate cognitive function and reduce cognitive decline. Further, increased insulin signaling inhibits the kinases activity associated with tau hyperphosphorylation and also triggers downstream signaling crucial for neuronal plasticity. On the contrary, any malfunctioning in this signaling cascade or declines in insulin levels lead to the pathogenesis of both MetS and NDDs [193]. Similarly, nowadays both metformin (anti-diabetic drug) and lovastatin (cholesterol lowering drug) are being used in treating Multiple Sclerosis (MS). Treatment with these drugs in combination attenuates demyelination and axonal loss as evident from decreased levels of myelin and neurofilament proteins in the spinal cords of autoimmune encephalomyelitis (EAE) animals [194]. Further, separately and synergistically administration of metformin and thymoquinone has also been shown the protective role against ethanol-induced neuronal apoptosis in primary rat cortical neurons. Since, ethanol exposure significantly reduces mitochondrial membrane potential and increases the levels of free cytosolic Ca^{2+}, which further stimulates the release of cytochrome C from mitochondria thereby causing neurotoxicity [195]. Likewise, treatment with fat-derived hormone leptin has currently been shown to minimize neuronal damage induced by both

neurotoxins and pro-apoptotic factors. It also protects against obesity and MetS via regulation of glucose homeostasis and energy intake. Leptin administration has also been reported to modulate synaptic plasticity via increasing N-Methyl-D-aspartate (NMDA) receptor function in AD. Further, neuroprotective roles for leptin have been identified in experimental models of stroke where leptin administration protects against both middle cerebral artery occlusion and oxygen-glucose deprivation. Similarly, it also shows protective role in both *in vitro* and *in vivo* models of PD [196,197]. Recently, the protective role of another anti-diabetes drug pioglitazone (actos) has been reported in case of AD via inhibiting the Cdk5 activity. More importantly, pioglitazone treatment also corrects impaired long-term potentiation (LTP) induced by Aβ exposure [198]. Additionally, pioglitazone administration is also found to ameliorate cognitive performance in a rodent dementia model induced by intracerebroventricular (ICV) injection of streptozotocin. Similar to pioglitazone, numerous other anti-diabetes drugs including, rosiglitazone (avandia) and troglitazone (rezulin) which are also known as TZDs have also been involved in delaying of neurodegenerative process. Since, these drugs are having anti-inflammatory, anti-amyloidogenic and insulin sensitizing role as well. Troglitazone are believed to have their connection in rescuing memory loss and decreasing plasma $A\beta_{40-42}$ levels but the exact mechanisms are still needs to be investigated further. Similarly, Rosiglitazone is reported to attenuate neuronal IR induced by Aβ oligomers. It is also reported to ameliorate cognitive function in mild to moderate AD patients. Moreover, chronic administration of TZDs, in general has no effect on risk of developing AD [80]. Despite these all findings, there are huge gaps which are still required to be investigated in order to identify the proper treatments for both MetS and NDDs.

6. Conclusion

In this review, we have addressed the pertinent role of altered mitochondrial dynamics in the pathogenesis of MetS and NDDs. Moreover, the intricate interplay between mitochondrial dysfunction and disease phenomenon of MetS has been elucidated in order to identify the linkup between MetS and NDDs. Furthermore, an interlink between MetS viz. obesity, hypertension, cardiovascular risk factors and T2D in the exacerbation of NDDs has also been extensively shed light on. The disease pathology of AD, PD, HD and ALS has also been addressed with respect to altered mitochondrial dynamics. The environmental toxins, high caloric intake, homeostatic imbalances and mutations in mtDNA are causatives for mitochondrial dysfunction, which consequently leads to decelerate ATP production, altered mitophagy, disturbed Ca^{2+} homeostasis, reduced mitochondrial membrane potential and mitochondrial respiration. These pathological changes are amenable for perturbations in the normal physiological processes and brain homeostasis thereby, resulting into fatal complications linked with neuronal dysfunction and metabolic syndromes. Additionally, in order to target the malfunctioning mitochondria or reverse the chronic effects of altered mitochondrial dynamics, numerous biomolecules and chaperones mediated therapeutic strategies have also been discussed to obviate the disease symptoms of both MetS and NDDs. Further, it is reasonable to enunciate that the current knowledge's on the involvement of altered mitochondrial dynamics in the pathogenesis of both MetS and NDDs are still at an elementary stage. However, in light of its significant advancement from both clinical research and therapeutic application perspectives, we look ahead major research efforts being drawn to this field and more approaches being formulated soon. We also presume that finally these findings will be translated into effective and novel treatments against both MetS and NDDs induced by mitochondrial dysfunctions.

Acknowledgments

We would like to thanks the senior management of Delhi Technological University for constant support and encouragement. There is no conflict or competing interest declared by

References

[1] B. Su, X. Wang, L. Zheng, G. Perry, M.A. Smith, X. Zhu, Abnormal mitochondrial dynamics and neurodegenerative diseases, Biochim Biophys Acta. 1802 (2010) 135-42.

[2] I.G. Onyango, J. Lu, M. Rodova, E. Lezi, A.B. Crafter, R.H. Swerdlow, Regulation of neuron mitochondrial biogenesis and relevance to brain health, Biochim Biophys Acta. 1802 (2010) 228-34.

[3] S.R. Subramaniam, M.F. Chesselet, Mitochondrial dysfunction and oxidative stress in Parkinson's disease, Prog Neurobiol. 106-107 (2013) 17-32.

[4] L.S. Sperling, J.I. Mechanick, I.J. Neeland, C.J. Herrick, J.P. Després, C.E. Ndumele, K. Vijayaraghavan, Y. Handelsman, G.A. Puckrein, M.R. Araneta, Q.K. Blum, K.K. Collins, S. Cook, N.V. Dhurandhar, D.L. Dixon, B.M. Egan, D.P. Ferdinand, L.M. Herman, S.E. Hessen, T.A. Jacobson, R.R. Pate, R.E. Ratner, E.A. Brinton, A.D. Forker, L.L. Ritzenthaler, S.M. Grundy , The ardioMetabolic Health Alliance: Working Toward a New Care Model for the Metabolic Syndrome, J Am Coll Cardiol. 66 (2015) 1050-67.

[5] L. Lee, R.A. Sanders, Metabolic syndrome, Pediatr Rev. 33 (2012) 459-66.

[6] P. Holvoet, Stress in obesity and associated metabolic and cardiovascular disorders, Scientifica (Cairo). (2012) 205027.

[7] C.K. Roberts, A.L. Hevener, R.J. Barnard, Metabolic syndrome and insulin resistance: underlying causes and modification by exercise training, Compr Physiol. 3 (2013) 1-58.

[8] H.K. Lee, Y.M. Cho, S.H Kwak, S. Lim, K.S Park, E.B. Shim, Mitochondrial dysfunction and metabolic syndrome-looking for environmental factors, Biochim Biophys Acta. 3 (2010) 282-9.

[9] H.K. Lee, E.B. Shim, Extension of the mitochondria dysfunction hypothesis of metabolic syndrome to atherosclerosis with emphasis on the endocrine-disrupting chemicals and biophysical laws, J Diabetes Investig. 4 (2013) 19-33.

[10] S.Tangvarasittichai, Oxidative stress, insulin resistance, dyslipidemia and type 2 diabetes mellitus, World J Diabetes. 6 (2015) 456-80.

[11] J.W. Eriksson, Metabolic stress in insulin's target cells leads to ROS accumulation - a hypothetical common pathway causing insulin resistance, FEBS Lett. 581 (2007) 3734-42.

[12] M.R. Hayden, S.C. Tyagi, Intimal redox stress: accelerated atherosclerosis in metabolic syndrome and type 2 diabetes mellitus, Atheroscleropathy. Cardiovasc Diabetol. 27 (2002) 1:3.

[13] E. Gammella, S. Recalcati, I. Rybinska, P. Buratti, G. Cairo, Iron-induced damage in cardiomyopathy: oxidative-dependent and independent mechanisms, Oxid Med Cell Longev. (2015) 230182.

[14] U.J. Jung, M.S. Choi, Obesity and its metabolic complications: the role of adipokines and the relationship between obesity, inflammation, insulin resistance, dyslipidemia and nonalcoholic fatty liver disease, Int J Mol Sci. 15 (2014) 6184-223.

[15] J.C. Cruz, A.F. Flôr, M.S. França-Silva, C.M. Balarini, V.A. Braga, Reactive Oxygen Species in the Paraventricular Nucleus of the Hypothalamus Alter Sympathetic Activity During Metabolic Syndrome, Front Physiol. 6 (2015) 384.

[16] A. Guleria, S. Chandna, ATM kinase: Much more than a DNA damage responsive protein, DNA Repair (Amst). 39 (2016) 1-20.

[17] L. Zhao, X. Guo, O. Wang, H. Zhang, Y. Wang, F. Zhou, J. Liu, B. Ji, Fructose and glucose combined with free fatty acids induce metabolic disorders in HepG2 cell: A new model to study the impacts of high-fructose/sucrose and high-fat diets in vitro, Mol Nutr Food Res. 60 (2016) 909-21.

[18] C.J. Andersen, K.E. Murphy, M.L. Fernandez, Impact of Obesity and Metabolic Syndrome on Immunity, Adv Nutr. 7 (2016) 66-75.

[19] H.A. Hadi, J.A. Suwaidi, Endothelial dysfunction in diabetes mellitus, Vasc Health Risk Manag. 3 (2007) 853-76.

[20] B. Uttara, A.V. Singh, P. Zamboni, R.T. Mahajan, Oxidative stress and neurodegenerative diseases: a review of upstream and downstream antioxidant therapeutic options, Curr Neuropharmacol. 1 (2009) 65-74.

[21] R.P. Patel, J. M.c.Andrew, H. Sellak, C.R. White, H. Jo, B.A. Freeman, V.M. Darley-Usmar, Biological aspects of reactive nitrogen species, Biochim Biophys Acta. 1411 (1999) 385-400.

[22] A.Y. Seo, A.M. Joseph, D. Dutta, J.C. Hwang, J.P. Aris, C. Leeuwenburgh, New insights into the role of mitochondria in aging: mitochondrial dynamics and more, J Cell Sci. 123 (2010) 2533-42.

[23] P. Kumar, N.K. Jha, S.K. Jha, K. Ramani, R.K. Ambasta, Tau phosphorylation, molecular chaperones, and ubiquitin E3 ligase: clinical relevance in Alzheimer's disease, J Alzheimers Dis. 43 (2015) 341-61.

[24] N.K. Jha, S.K. Jha, D. Kumar, N. Kejriwal, R. Sharma, R.K. Ambasta, P. Kumar, Impact of Insulin Degrading Enzyme and Neprilysin in Alzheimer's Disease Biology:

Characterization of Putative Cognates for Therapeutic Applications, J Alzheimers Dis. 48 (2015) 891-917.

[25] P.I. Moreira, C. Carvalho, X. Zhu, M.A. Smith, G. Perry, Mitochondrial dysfunction is a trigger of Alzheimer's disease pathophysiology, Biochim Biophys Acta. 1802 (2010) 2-10.

[26] G. Sweeney, J. Song, The association between PGC-1α and Alzheimer's disease, Anat Cell Biol. 49 (2016) 1-6.

[27] K. Dolma, G.J. Iacobucci, K. Hong Zheng, J. Shandilya, E. Toska, J.A. White 2nd, E. Spina, S. Gunawardena, Presenilin influences glycogen synthase kinase-3 β (GSK-3β) for kinesin-1 and dynein function during axonal transport, Hum Mol Genet. 23 (2014) 1121-33.

[28] L. Pagani, A. Eckert, Amyloid-Beta interaction with mitochondria, Int J Alzheimers Dis. (2011) 925050.

[29] S. Sekar, J. McDonald, L. Cuyugan, J. Aldrich, A. Kurdoglu, J. Adkins, G. Serrano, T.G. Beach, D.W. Craig, J. Valla, E.M. Reiman, W.S. Liang, Alzheimer's disease is associated with altered expression of genes involved in immune response and mitochondrial processes in astrocytes, Neurobiol Aging. 36 (2015) 583-91.

[30] S.M. Khan, D.S. Cassarino, N.N. Abramova, P.M. Keeney, M.K. Borland, P.A. Trimmer, C.T. Krebs, J.C. Bennett, J.K. Parks, R.H. Swerdlow, W.D. Parker Jr, JP.Jr. Bennett, Alzheimer's disease cybrids replicate beta-amyloid abnormalities through cell death pathways, Ann Neurol. 48 (2000) 148-55.

[31] K. Hirai, G. Aliev, A. Nunomura, H. Fujioka, R.L. Russell, C.S. Atwood, A.B. Johnson, Y. Kress, H.V. Vinters, M. Tabaton, S. Shimohama, A.D. Cash, S.L. Siedlak,

P.L. Harris, P.K. Jones, R.B. Petersen, G. Perry, M.A. Smith, Mitochondrial abnormalities in Alzheimer's disease, J Neurosci. 9 (2001) 3017-23.

[32] D. Fang, Z. Zhang, H. Li, Q. Yu, J.T. Douglas, A. Bratasz, P. Kuppusamy, S.S. Yan, Increased Electron Paramagnetic Resonance Signal Correlates with Mitochondrial Dysfunction and Oxidative Stress in an Alzheimer's disease Mouse Brain, J Alzheimers Dis. 51 (2016) 80.

[33] P. Mao, P.H. Reddy, Aging and amyloid beta-induced oxidative DNA damage and mitochondrial dysfunction in Alzheimer's disease: implications for early intervention and therapeutics, Biochim Biophys Acta. 1812 (2011) 1359-70.

[34] H. Prentice, J.P. Modi, J.Y. Wu, Mechanisms of Neuronal Protection against Excitotoxicity, Endoplasmic Reticulum Stress, and Mitochondrial Dysfunction in Stroke and Neurodegenerative Diseases, Oxid Med Cell Longev. (2015) 964518.

[35] L.P. Klosinski, J. Yao, F. Yin, A.N. Fonteh, M.G. Harrington, T.A. Christensen, E. Trushina, R.D. Brinton, White Matter Lipids as a Ketogenic Fuel Supply in Aging Female Brain: Implications for Alzheimer's Disease, EBioMedicine. 2 (2015) 1888-904.

[36] M.G. Chooneman, F.M. Vaz, S.M. Houten, M.R. Soeters, Acylcarnitines: reflecting or inflicting insulin resistance? Diabetes, 62 (2013) 1-8.

[37] P.H. Reddy, Is the mitochondrial outermembrane protein VDAC1 therapeutic target for Alzheimer's disease? Biochim Biophys Acta, 1832 (2013) 67-75.

[38] P. Kumar, D. Kumar, S.K. Jha, K, N.K. Jha, R.K. Ambasta, Ion Channels in Neurological Disorders, Adv Protein Chem Struct Biol. 103 (2016) 97-136.

[39] A.M. Pickrell, M. Pinto, A. Hida, C.T. Moraes, Striatal dysfunctions associated with mitochondrial DNA damage in dopaminergic neurons in a mouse model of Parkinson's disease, J Neurosci. 31 (2011) 17649-58.

[40] A. Migdalska-Richards, A.H. Schapira, The relationship between glucocerebrosidase mutations and Parkinson disease, J Neurochem. (2016).

[41] S. Jana, M. Sinha, D. Chanda, T. Roy, K. Banerjee, S. Munshi, B.S. Patro, S. Chakrabarti, Mitochondrial dysfunction mediated by quinone oxidation products of dopamine: Implications in dopamine cytotoxicity and pathogenesis of Parkinson's disease, Biochim Biophys Acta. 1812 (2011) 663-73.

[42] G.E. Gibson, A. Starkov, J.P. Blass, R.R. Ratan, M.F. Beal, Cause and consequence: mitochondrial dysfunction initiates and propagates neuronal dysfunction, neuronal death and behavioral abnormalities in age-associated neurodegenerative diseases, Biochim Biophys Acta. 1802 (2010) 122-34.

[43] Y. Cabeza-Arvelaiz, R.H. Schiestl, Transcriptome analysis of a rotenone model of parkinsonism reveals complex I-tied and -untied toxicity mechanisms common to neurodegenerative diseases, PLoS One. 7 (2012) e44700.

[44] M. Vairetti, A. Ferrigno, V. Rizzo, G. Ambrosi, A. Bianchi, P. Richelmi, F. Blandini, M.T, Armentero, Impaired hepatic function and central dopaminergic denervation in a rodent model of Parkinson's disease: a self-perpetuating crosstalk?, Biochim Biophys Acta. 1822 (2012) 176-84.

[45] K.J. Thomas, M.R. Cookson, The role of PTEN-induced kinase 1 in mitochondrial dysfunction and dynamics, Int J Biochem Cell Biol. 41 (2009) 2025-35.

[46] V.S. Van Laar, S.B. Berman, The interplay of neuronal mitochondrial dynamics and bioenergetics: implications for Parkinson's disease, Neurobiol Dis. 51 (2013) 43-55.

[47] C. Pacelli, D. De Rasmo, A. Signorile, I. Grattagliano, G. di Tullio, A. D'Orazio, B. Nico, G.P. Comi, D. Ronchi, E. Ferranini, D. Pirolo, P. Seibel, S. Schubert, A. Gaballo,

G. Villani, T. Cocco, Mitochondrial defect and PGC-1α dysfunction in parkin-associated familial Parkinson's disease, Biochim Biophys Acta. 1812 (2011) 1041-53.

[48] Y. Han, P. Gao, S. Qiu, L. Zhang, L. Yang, J. Zuo, C. Zhong, S. Zhu, W. Liu, MTERF2 contributes to MPP(+)-induced mitochondrial dysfunction and cell damage, Biochem Biophys Res Commun. 471 (2016) 177-83.

[49] X. Ye, Y. Han, L. Zhang, W. Liu, J. Zuo, MTERF4 regulates the mitochondrial dysfunction induced by MPP(+) in SH-SY5Y cells, Biochem Biophys Res Commun. 464 (2015) 214-20.

[50] A.C. Guerra de Souza, R.D. Prediger, H. Cimarosti, Mitochondrial dysfunction and SUMOylation targets in Parkinson's disease, J Neurochem. (2016) 13599.

[51] V. Dias, E. Junn, M.M. Mouradian, The role of oxidative stress in Parkinson's disease, J Parkinsons Dis. 3 (2013) 461-91.

[52] J. Labbadia, R.I. Morimoto, Huntington's disease: underlying molecular mechanisms and emerging concepts, Trends Biochem Sci. 38 (2013) 378-85.

[53] P.H. Reddy, P. Mao, M. Manczak, Mitochondrial structural and functional dynamics in Huntington's disease, Brain Res Rev. 61 (2009) 33-48.

[54] N.N. Naseri, H. Xu, J. Bonica, J.P. Vonsattel, E.P. Cortes, L.C. Park, J. Arjomand, G.E. Gibson, Abnormalities in the tricarboxylic Acid cycle in Huntington disease and in a Huntington disease mouse model, J Neuropathol Exp Neurol. 74 (2015) 527-37.

[55] M. Corrado, L. Scorrano, S. Campello, Mitochondrial dynamics in cancer and neurodegenerative and neuroinflammatory diseases, Int J Cell Biol. (2012) 729290.

[56] V. Leoni, C. Caccia, The impairment of cholesterol metabolism in Huntington disease, Biochim Biophys Acta. 1851 (2015) 1095-105.

[57] I.P. De Castro, L.M. Martins, Tufi R. Mitochondrial quality control and neurological disease: an emerging connection, Expert Rev Mol Med. 12 (2010) e12.

[58] P.H. Reddy, U.P. Shirendeb, Mutant huntingtin, abnormal mitochondrial dynamics, defective axonal transport of mitochondria, and selective synaptic degeneration in Huntington's disease, Biochim Biophys Acta. 1822 (2012) 101-10.

[59] H. Yano, S.V. Baranov, O.V. Baranova, J. Kim, Y. Pan, S. Yablonska, D.L. Carlisle, R.J. Ferrante, A.H. Kim, R.M. Friedlander, Inhibition of mitochondrial protein import by mutant huntingtin, Nat Neurosci. 17 (2014) 822-31.

[60] S. Hwang, M.H. Disatnik, D. Mochly-Rosen, Impaired GAPDH-induced mitophagy contributes to the pathology of Huntington's disease, EMBO Mol Med. 7 (2015) 1307-26.

[61] J.H. Lee, L. Tecedor, Y.H. Chen, A.M. Monteys, M.J. Sowada, L.M. Thompson, B.L. Davidson, Reinstating aberrant mTORC1 activity in Huntington's disease mice improves disease phenotypes, Neuron. 85 (2015) 303-15.

[62] A. Mehrotra, A. Kanwal, S.K. Banerjee, R. Sandhir, Mitochondrial modulators in experimental Huntington's disease: reversal of mitochondrial dysfunctions and cognitive deficits, Neurobiol Aging. 36 (2015) 2186-200.

[63] I.L. Ferreira, M.V. Nascimento, M. Ribeiro, S. Almeida, S.M. Cardoso, M. Grazina, J. Pratas, M.J. Santos, C. Januário, C.R. Oliveira, A.C. Rego, Mitochondrial-dependent apoptosis in Huntington's disease human cybrids, Exp Neurol. 222 (2010) 243-55.

[64] M. Orsini, A.B. Oliveira, O.J. Nascimento, C.H. Reis, M.A. Leite, J.A. De Souza, C. Pupe, O.G. De Souza, V.H. Bastos, M.R. De Freitas, S. Teixeira, C. Bruno, E. Davidovich, B. Smidt, Amyotrophic Lateral Sclerosis: New Perpectives and Update, Neurol Int. 7 (2015) 5885.

[65] H. Muyderman, T. Chen, Mitochondrial dysfunction in amyotrophic lateral sclerosis - a valid pharmacological target?, Br J Pharmacol. 171 (2014) 2191-205.

[66] M. Mattiazzi, M. D'Aurelio, C.D. Gajewski, K. Martushova, M. Kiaei, M.F. Beal, G. Manfredi, Mutated human SOD1 causes dysfunction of oxidative phosphorylation in mitochondria of transgenic mice, J Biol Chem. 277 (2002) 29626-33.

[67] L.J. Martin, Mitochondrial pathobiology in ALS, J Bioenerg Biomembr. 43 (2011) 569-79.

[68] C.M. Higgins, C. Jung, Z. Xu, ALS-associated mutant SOD1G93A causes mitochondrial vacuolation by expansion of the intermembrane space and by involvement of SOD1 aggregation and peroxisomes, BMC Neurosci. 4 (2003) 16.

[69] P.C. Wong, C.A. Pardo, D.R. Borchelt, M.K. Lee, N.G. Copeland, N.A. Jenkins, S.S. Sisodia, D.W. Cleveland, D.L. Price, An adverse property of a familial ALS-linked SOD1 mutation causes motor neuron disease characterized by vacuolar degeneration of mitochondria, Neuron. 14 (1995) 1105-16.

[70] S. Sasaki, M. Iwata, Dendritic synapses of anterior horn neurons in amyotrophic lateral sclerosis: an ultrastructural study, Acta Neuropathol. 91 (1996) 278-83.

[71] F. Tafuri, D. Ronchi, F. Magri, G.P. Comi, S. Corti, SOD1 misplacing and mitochondrial dysfunction in amyotrophic lateral sclerosis pathogenesis, Front Cell Neurosci. 9 (2015) 336.

[72] M. Zhu, A. Li, J. Chen, S. Zhang, J. Wu, Effects of optineurin mutants on SH-SY5Y cell survival, Mol Cell Neurosci. 74 (2016) 18-24.

[73] Z. Jiang, W. Wang, G. Perry, X. Zhu, X. Wang, Mitochondrial dynamic abnormalities in amyotrophic lateral sclerosis, Transl Neurodegener. 4 (2015) 14.

[74] E. Mendoza, J.A. Miranda-Barrientos, R.A. Vázquez-Roque, E. Morales-Herrera, Ruelas. A, G. De la Rosa, G. Flores, E. Hernández-Echeagaray, In vivo mitochondrial inhibition alters corticostriatal synaptic function and the modulatory effects of neurotrophins, Neuroscience. 280 (2014) 156-70.

[75] K. Fukunaga, Y. Shinoda, H. Tagashira, The role of SIGMAR1 gene mutation and mitochondrial dysfunction in amyotrophic lateral sclerosis, J Pharmacol Sci. 127 (2015) 36-41.

[76] H. Suzuki, M. Matsuoka, Overexpression of nuclear FUS induces neuronal cell death, Neuroscience. 287 (2015) 113-24.

[77] A. Sharma, A.M. Varghese, K. Vijaylakshmi, R. Sumitha, V.K. Prasanna, S. Shruthi, B.K. Chandrasekhar Sagar, K.K. Datta, H. Gowda, A. Nalini, P.A. Alladi, R. Christopher, T.N. Sathyaprabha, T.R. Raju, M.M. Srinivas Bharath, Cerebrospinal Fluid from Sporadic Amyotrophic Lateral Sclerosis Patients Induces Mitochondrial and Lysosomal Dysfunction, Neurochem Res. 41 (2016) 965-84.

[78] E. Grünblatt, J. Bartl, P. Riederer, The link between iron, metabolic syndrome,and Alzheimer's disease, J Neural Transm (Vienna). 118 (2011) 371-9.

[79] SM. de la Monte, M. Tong, Brain metabolic dysfunction at the core of Alzheimer'sdisease, Biochem Pharmacol. 88 (2014) 548-59.

[80] R. Sandhir, S. Gupta, Molecular and biochemical trajectories from diabetes to Alzheimer's disease: A critical appraisal, World J Diabetes. 6 (2015) 1223-42.

[81] M.W. Akhtar, S. Sanz-Blasco, N. Dolatabadi, J. Parker, K. Chon, M.S. Lee, W. Soussou, S.R. McKercher, R. Ambasudhan, T. Nakamura, S.A. Lipton, Elevated glucose and oligomeric β-amyloid disrupt synapses via a common pathway of aberrant protein S-nitrosylation, Nat Commun. 7 (2016) 10242.

[82] K. Maiese, Z.Z. Chong, S. Wang, Y.C. Shang, Oxidant stress and signal transduction in the nervous system with the PI 3-K, Akt, and mTOR cascade, Int J Mol Sci. 13 (2012) 13830-66.

[83] M. Wong, Mammalian target of rapamycin (mTOR) pathways in neurological diseases, Biomed J. 36 (2013) 40-50.

[84] G. Razay, A. Vreugdenhil, G. Wilcock, The metabolic syndrome and Alzheimer disease, Arch Neurol. 64 (2007) 93-6.

[85] G. Zuliani, M. Cavalieri, M. Galvani, S. Volpato, A. Cherubini, S. Bandinelli, A.M. Corsi, F. Lauretani, J.M. Guralnik, R. Fellin, L. Ferrucci, Relationship between low levels of high-density lipoprotein cholesterol and dementia in the elderly, The InChianti study. J Gerontol A Biol Sci Med Sci. 65 (2010) 559-64.

[86] A.D. De Kloet, E.G. Krause, S.C. Woods, The renin angiotensin system and the metabolic syndrome, Physiol Behav. 100 (2010) 525-34.

[87] R. Tsuruta, M. Fujita, T. Ono, Y. Koda, Y. Koga, T. Yamamoto, M. Nanba, M. Shitara, S. Kasaoka, I. Maruyama, M. Yuasa, T. Maekawa, Hyperglycemia enhances excessive superoxide anion radical generation, oxidative stress, early inflammation, and endothelial injury in forebrain ischemia/reperfusion rats, Brain Res. 1309 (2010) 155-63.

[88] M. Hassan, S.A. Sehgal, S. Rashid, Regulatory cascade of neuronal loss and glucose metabolism, CNS Neurol Disord Drug Targets. 13 (2014) 1232-45.

[89] A. Rozycka, P.P. Jagodzinski, W. Kozubski, M. Lianeri, J. Dorszewska, Homocysteine Level and Mechanisms of Injury in Parkinson's Disease as Related to MTHFR, MTR, and MTHFD1 Genes Polymorphisms and L-Dopa Treatment, Curr Genomics. 14 (2013) 534-42.

[90] M.E. Lull, M.L. Block, Microglial activation and chronic neurodegeneration, Neurotherapeutics. 7 (2010) 354-65.

[91] N. Chaudhari, P. Talwar, A. Parimisetty, C. Lefebvre d'Hellencourt, P. Ravanan, A molecular web: endoplasmic reticulum stress, inflammation, and oxidative stress, Front Cell Neurosci. 8 (2014) 213.

[92] W. Dauer, S. Przedborski, Parkinson's disease: mechanisms and models, Neuron. 39 (2003) 889-909.

[93] P. Zhang, B. Tian, Metabolic syndrome: an important risk factor for Parkinson's disease, Oxid Med Cell Longev. (2014) 729194.

[94] Y.L. Wang, Y.T. Wang, J.F. Li, Y.Z. Zhang, H.L. Yin, B. Han, Body Mass Index and Risk of Parkinson's Disease: A Dose-Response Meta-Analysis of Prospective Studies, PLoS One. 10 (2015) e0131778.

[95] J.E. Vance, Dysregulation of cholesterol balance in the brain: contribution to neurodegenerative diseases, Dis Model Mech. 5 (2012) 746-55.

[96] J.M. Karasinska, M.R. Hayden, Cholesterol metabolism in Huntington disease, Nat Rev Neurol. 7 (2011) 561-72.

[97] R.C. Block, E.R. Dorsey, C.A. Beck, J.T. Brenna, I. Shoulson, Altered cholesterol and fatty acid metabolism in Huntington disease, J Clin Lipidol. 4 (2010) 17-23.

[98] P.B. Verghese, J.M. Castellano, D.M. Holtzman, Apolipoprotein E in Alzheimer's disease and other neurological disorders, Lancet Neurol. 10 (2011) 241-52.

[99] S.T. Ngo, F.J. Steyn, The interplay between metabolic homeostasis and neurodegeneration: insights into the neurometabolic nature of amyotrophic lateral sclerosis, Cell Regen (Lond). 4 (2015) 5.

[100] S.T. Ngo, F.J. Steyn, The interplay between metabolic homeostasis and neurodegeneration: insights into the neurometabolic nature of amyotrophic lateral sclerosis, Cell Regen (Lond). 4 (2015) 5.

[101] J.C. Dodge, C.M. Treleaven, J.A. Fidler, T.J. Tamsett, C. Bao, M. Searles, T.V. Taksir, K. Misra, R.L. Sidman, S.H. Cheng, L.S. Shihabuddin, Metabolic signatures of amyotrophic lateral sclerosis reveal insights into disease pathogenesis, Proc Natl Acad Sci U S A. 110 (2013) 10812-7.

[102] S.T. Ngo, F.J. Steyn, L. Huang, S. Mantovani, C.M. Pfluger, T.M. Woodruff, J.D. O'Sullivan, R.D. Henderson, P.A. McCombe, Altered expression of metabolic proteins and adipokines in patients with amyotrophic lateral sclerosis, J Neurol Sci. 357 (2015) 22-7.

[103] M. Hassan, S.A. Sehgal, S. Rashid, Regulatory cascade of neuronal loss and glucose metabolism, CNS Neurol Disord Drug Targets. 13 (2014) 1232-45.

[104] P.H. Reddy, Inhibitors of mitochondrial fission as a therapeutic strategy for diseases with oxidative stress and mitochondrial dysfunction, J Alzheimers Dis. 40 (2014) 245-56.

[105] S. Tangvarasittichai, Oxidative stress, insulin resistance, dyslipidemia and type 2 diabetes mellitus, World J Diabetes. 6 (2015) 456-80.

[106] M.A. Alam, M.M. Rahman, Mitochondrial dysfunction in obesity: potential benefit and mechanism of Co-enzyme Q10 supplementation in metabolic syndrome, J Diabetes Metab Disord. 13 (2014) 60.

[107] W.I. Sivitz, M.A. Yorek, Mitochondrial dysfunction in diabetes: from molecular mechanisms to functional significance and therapeutic opportunities, Antioxid Redox Signal. (2010) 537-77.

[108] C. Stockburger, D. Miano, M. Baeumlisberger, T. Pallas, T.N. Arrey, M. Karas, K. Friedland, W.E. Müller, A Mitochondrial Role of SV2a Protein in Aging and Alzheimer's Disease: Studies with Levetiracetam, J Alzheimers Dis. 50 (2015) 201-15.

[109] Y.J. Chen, H.Y. Zheng, X.X. Huang, S.X. Han, D.S. Zhang, J.Z. Ni, X.Y. He, Neuroprotective Effects of Icariin on Brain Metabolism, Mitochondrial Functions, and Cognition in Triple-Transgenic Alzheimer's Disease Mice, CNS Neurosci Ther. 22 (2016) 63-73.

[110] B. Thrash-Williams, S.S. Karuppagounder, D. Bhattacharya, M. Ahuja, V. Suppiramaniam, M. Dhanasekaran, Methamphetamine-induced dopaminergic toxicity prevented owing to the neuroprotective effects of salicylic acid, Life Sci. (2016) 30122-9.

[111] D. Colle, D.B. Santos, J.M. Hartwig, M. Godoi, D.F. Engel, A.F. De Bem, A.L. Braga, M. Farina Succinobucol, A Lipid-Lowering Drug, Protects Against 3-Nitropropionic Acid-Induced Mitochondrial Dysfunction and Oxidative Stress in SH-SY5Y Cells via Upregulation of Glutathione Levels and Glutamate Cysteine Ligase Activity, Mol Neurobiol. 53 (2016) 1280-95.

[112] A.C. Sirianni, J. Jiang, J. Zeng, L.L. Mao, S. Zhou, P. Sugarbaker, X. Zhang, W. Li, R.M. Friedlander, X. Wang, N-acetyl-l-tryptophan, but not N-acetyl-d-tryptophan,rescues neuronal cell death in models of amyotrophic lateral sclerosis, J Neurochem. 134 (2015) 956-68.

[113] B. Kim, J. Park, K.T. Chang, D.S. Lee, Peroxiredoxin 5 prevents amyloid-beta oligomer-induced neuronal cell death by inhibiting ERK-Drp1-mediated mitochondrial fragmentation, Free Radic Biol Med. 90 (2016) 184-94.

[114] S. Fossati, P. Giannoni, M.E. Solesio, S.L. Cocklin, E. Cabrera, J. Ghiso, A. Rostagno, The carbonic anhydrase inhibitor methazolamide prevents amyloid beta-induced

mitochondrial dysfunction and caspase activation protecting neuronal and glial cells in vitro and in the mouse brain, Neurobiol Dis. 86 (2016) 29-40.

[115] E.A. Rudnitskaya, N.A. Muraleva, K.Y. Maksimova, E. Kiseleva, N.G. Kolosova, N.A. Stefanova, Melatonin Attenuates Memory Impairment, Amyloid-β Accumulation, and Neurodegeneration in a Rat Model of Sporadic Alzheimer's Disease, J Alzheimers Dis. 47 (2015) 103-16.

[116] H.G. Kim, G. Park, S. Lim, H. Park, J.G. Choi, H.U. Jeong, M.S. Kang, M.K. Lee, M.S. Oh, Mori Fructus improves cognitive and neuronal dysfunction induced by beta-amyloid toxicity through the GSK-3β pathway in vitro and in vivo, J Ethnopharmacol. 171 (2015) 196-204.

[117] Y.P. Li, G.J. Yang, L. Jin, H.M. Yang, J. Chen, G.S. Chai, L. Wang, Erythropoietin attenuates Alzheimer-like memory impairments and pathological changes induced by amyloid β42 in mice, Brain Res 1618 (2015) 159-67.

[118] E. Kornelius, C.L. Lin, H.H. Chang, H.H. Li, W.N. Huang, Y.S. Yang, Y.L. Lu, C.H. Peng, C.N. Huang, DPP-4 Inhibitor Linagliptin Attenuates Aβ-induced Cytotoxicity through Activation of AMPK in Neuronal Cells, CNS Neurosci Ther. 21 (2015) 549-57.

[119] S. Sarkar, S. Jun, J.W. Simpkins, Estrogen amelioration of Aβ-induced defects in mitochondria is mediated by mitochondrial signaling pathway involving ERβ, AKAP and Drp1, Brain Res. 1616 (2015) 101-11.

[120] E. Kim, M. Park, J. Jeong, H. Kim, S.K. Lee, E. Lee, B.H. Oh, K. Namkoong, Cholinesterase Inhibitor Donepezil Increases Mitochondrial Biogenesis through AMP-Activated Protein Kinase in the Hippocampus, Neuropsychobiology. 73 (2016) 81-91.

[121] M. Leirós, E. Alonso, M.E. Rateb, W.E. Houssen, R. Ebel, M. Jaspars, A. Alfonso, L.M. Botana , Gracilins: Spongionella-derived promising compounds for Alzheimer disease, Neuropharmacology. 93 (2015) 285-93.

[122] L. Yu, S. Wang, X. Chen, H. Yang, X. Li, Y. Xu, Zhu X. Zhu, Orientin alleviates cognitive deficits and oxidative stress in Aβ1-42-induced mouse model of Alzheimer's disease, Life Sci. 121 (2015) 104-9.

[123] D. Pinkaew, C. Changtam, C. Tocharus, S. Thummayot, A. Suksamrarn, J. Tocharus, Di-O-demethylcurcumin protects SK-N-SH cells against mitochondrial and endoplasmic reticulum-mediated apoptotic cell death induced by Aβ25-35, Neurochem Int. 80 (2015) 110-9.

[124] A.K. Sachdeva, A. Kuhad, K. Chopra, Naringin ameliorates memory deficits in experimental paradigm of Alzheimer's disease by attenuating mitochondrial dysfunction, Pharmacol Biochem Behav. 127 (2014) 101-10.

[125] G. Kulasekaran, S. Ganapasam, Neuroprotective efficacy of naringin on 3-nitropropionic acid-induced mitochondrial dysfunction through the modulation of Nrf2 signaling pathway in PC12 cells, Mol Cell Biochem. 409 (2015) 199-211.

[126] J. Li, X. Ji, J. Zhang, G. Shi, X. Zhu, Wang K. Paeoniflorin attenuates Aβ25-35-induced neurotoxicity in PC12 cells by preventing mitochondrial dysfunction, Folia Neuropathol. 52 (2014) 285-90.

[127] X.F. Ji, T.Y. Chi, Q. Xu, X.L. He, X.Y. Zhou, R. Zhang, L.B. Zou, Xanthoceraside ameliorates mitochondrial dysfunction contributing to the improvement of learning and memory impairment in mice with intracerebroventricular injection of aβ1-42, Evid Based Complement Alternat Med. (2014) 969342.

[128] H. Lei, C.Y. Zhao, D.M. Liu, Y. Zhang, L. Li, X.L. Wang, Y. Peng, l-3-n-Butylphthalide attenuates β-amyloid-induced toxicity in neuroblastoma SH-SY5Y cells through regulating mitochondrion-mediated apoptosis and MAPK signaling, J Asian Nat Prod Res. (16) 854-64.

[129] D. Wang, L. Liu, X. Zhu, W. Wu, Y. Wang, Hesperidin alleviates cognitive impairment, mitochondrial dysfunction and oxidative stress in a mouse model of Alzheimer's disease, Cell Mol Neurobiol. 34 (2014) 1209-21.

[130] E.T. Bayrakdar, G. Armagan, Y. Uyanikgil, L. Kanit, E. Koylu, A. Yalcin, Ex vivo protective effects of nicotinamide and 3-aminobenzamide on rat synaptosomes treated with Abeta(1–42). Cell biochemistry and function, 32 (2014) 557–64.

[131] A. Prakash, A. Kumar, Implicating the role of lycopene in restoration of mitochondrial enzymes and BDNF levels in β-amyloid induced Alzheimer′s disease, Eur J Pharmacol. 741 (2014) 104-11.

[132] C. Lv, X. Liu, H. Liu, T. Chen, W. Zhang, Geniposide attenuates mitochondrial dysfunction and memory deficits in APP/PS1 transgenic mice, Curr Alzheimer Res. 11 (2014) 580-7.

[133] I.G. Onyango, J. Lu, M. Rodova, E. Lezi, A.B. Crafter, R.H. Swerdlow, Regulation of neuron mitochondrial biogenesis and relevance to brain health, Biochim Biophys Acta. 1802 (2010) 228-34.

[134] M. Lagouge, C. Argmann, Z. Gerhart-Hines, H. Meziane, C. Lerin, F. Daussin, N. Messadeq, J. Milne, P. Lambert, P. Elliott, B. Geny, M. Laakso, P. Puigserver, J. Auwerx, Resveratrol improves mitochondrial function and protects against metabolic disease by activating SIRT1 and PGC-1alpha, Cell. 127 (2006) 1109-22.

[135] D.M. Wang, S.Q. Li, W.L. Wu, X.Y. Zhu, Y. Wang, H.Y. Yuan, Effects of long-term treatment with quercetin on cognition and mitochondrial function in a mouse model of Alzheimer's disease, Neurochem Res. 39 (2014) 1533-43.

[136] D.L. Chen, P. Zhang, L. Lin, H.M. Zhang, S.D. Deng, Z.Q. Wu, S. Ou, S.H. Liu, J.Y. Wang, Protective effects of bajijiasu in a rat model of $A\beta_{25-35}$-induced neurotoxicity, J Ethnopharmacol. 154 (2014) 206-17.

[137] Q. Sun, H. Hu, W. Wang, H. Jin, G. Feng, N. Jia, Taurine attenuates amyloid β 1-42-induced mitochondrial dysfunction by activating of SIRT1 in SK-N-SH cells, Biochem Biophys Res Commun. 447 (2014) 485-9.

[138] Y.L. Jia, S.J. Sun, J.H. Chen, Q. Jia, T.T. Huo, L.F. Chu, J.T. Bai, Y.J. Yu, X.X. Yan, J.H. Wang, SS31, a Small Molecule Antioxidant Peptide, Attenuates β-Amyloid Elevation, Mitochondrial/Synaptic Deterioration and Cognitive Deficit in SAMP8 Mice, Curr Alzheimer Res. 13 (2016) 297-306.

[139] N.E. Gray, J.A. Zweig, C. Kawamoto, J.F. Quinn, P.F. Copenhaver, STX a Novel Membrane Estrogen Receptor Ligand, Protects Against Amyloid-β Toxicity, J Alzheimers Dis. 51 (2016) 391-403.

[140] M.J. McManus, M.P. Murphy, J.L. Franklin, The mitochondria-targeted antioxidant MitoQ prevents loss of spatial memory retention and early neuropathology in a transgenic mouse model of Alzheimer's disease, J Neurosci. 31 (2011) 15703-15.

[141] C. Feillet-Coudray, G. Fouret, R. Ebabe Elle, J. Rieusset, B. Bonafos, B. Chabi, D. Crouzier, K. Zarkovic, N. Zarkovic, J. Ramos, E. Badia, M.P. Murphy, J.P. Cristol, C. Coudray, The mitochondrial-targeted antioxidant MitoQ ameliorates metabolic syndrome

features in obesogenic diet-fed rats better than Apocynin or Allopurinol, Free Radic Res. 48 (2014) 1232-46.

[142] S. Hagl, R. Grewal, I. Ciobanu, A. Helal, M.T. Khayyal, W.E. Muller, G.P. Eckert, Rice bran extract compensates mitochondrial dysfunction in a cellular model of early Alzheimer's disease, J Alzheimers Dis. 43 (2015) 927-38.

[143] Q. Sun, N. Jia, W. Wang, H. Jin, J. Xu, H. Hu, Protective effects of astragaloside IV against amyloid beta1-42 neurotoxicity by inhibiting the mitochondrial permeability transition pore opening, PLoS One. 9 (2014) e98866.

[144] J. Nataraj, T. Manivasagam, A. Justin Thenmozhi, M.M. Essa, Neuroprotective effect of asiatic acid on rotenone-induced mitochondrial dysfunction and oxidative stress-mediated apoptosis in differentiated SH-SYS5Y cells, Nutr Neurosci. (2016).

[145] J.A. Bayliss, Z.B. Andrews, Ghrelin is neuroprotective in Parkinson's disease: molecular mechanisms of metabolic neuroprotection, Ther Adv Endocrinol Metab. 4 (2013) 25-36.

[146] H. Mortiboys, R. Furmston, G. Bronstad, J. Aasly, C. Elliott, O. Bandmann, UDCA exerts beneficial effect on mitochondrial dysfunction in LRRK2(G2019S) carriers and in vivo, Neurology. 85 (2015) 846-52.

[147] T. Chen, Y. Deng, X. Liao, J. Zhao, G. Wen, G. Weng, F. Ma, Y. Zheng, Effect of curcumin on oligomer formation and mitochondrial ATP-sensitive potassium channels induced by overexpression or mutation of α-synuclein, Zhonghua Yi Xue Yi Chuan Xue Za Zhi. 32 (2015) 462-7.

[148] G.F. Zhang, Y. Zhang, G. Zhao, Crocin protects PC12 cells against MPP(+)-induced injury through inhibition of mitochondrial dysfunction and ER stress, Neurochem Int. 89 (2015) 101-10.

[149] H. Liu, P. Mao, J. Wang, T. Wang, C.H. Xie, Allicin Protects PC12 Cells Against 6-OHDA-Induced Oxidative Stress and Mitochondrial Dysfunction via Regulating Mitochondrial Dynamics, Cell Physiol Biochem. 36 (2015) 966-79.

[150] N.P. Mena, O. García-Beltrán, F. Lourido, P.J. Urrutia, R. Mena, V. Castro-Castillo, B.K. Cassels, M.T. Núñez, The novel mitochondrial iron chelator 5-((methylamino)methyl)-8-hydroxyquinoline protects against mitochondrial-induced oxidative damage and neuronal death, Biochem Biophys Res Commun. 463 (2015) 787-92.

[151] Z. Tan, H. Xu, X. Shen, H. Jiang, Nesfatin-1 antagonized rotenone-induced neurotoxicity in MES23.5 dopaminergic cells, Peptides. 69 (2015) 109-14.

[152] S. Srivastav, S.K. Singh, A.K. Yadav, S. Srikrishna, Folic acid supplementation rescues anomalies associated with knockdown of parkin in dopaminergic and serotonergic neurons in Drosophila model of Parkinson's disease, Biochem Biophys Res Commun. 460 (2015) 780-5.

[153] Y. Binawade, A. Jagtap, Neuroprotective effect of lutein against 3-nitropropionic acid-induced Huntington's disease-like symptoms: possible behavioral, biochemical, and cellular alterations, J Med Food. 16 (2013) 934-43.

[154] J. Nataraj, T. Manivasagam, A.J. Thenmozhi, M.M. Essa, Lutein protects dopaminergic neurons against MPTP-induced apoptotic death and motor dysfunction by ameliorating mitochondrial disruption and oxidative stress, Nutr Neurosci. (2015).

[155] Y. Lee, H.R. Park, H.J. Chun, J. Lee, Silibinin prevents dopaminergic neuronal loss in a mouse model of Parkinson's disease via mitochondrial stabilization, J Neurosci Res. 93 (2015) 755-65.

[156] Z. Cai, W. Zeng, K. Tao, F. Lu, G. Gao, Q. Yang, Myricitrin alleviates MPP^+-induced mitochondrial dysfunction in a DJ-1-dependent manner in SN4741 cells, Biochem Biophys Res Commun. 458 (2015) 227-33.

[157] W.N. Cong, W. Chadwick, R. Wang, C.M. Daimon, H. Cai, J. Amma, W.H. Wood, 3rd, Becker KG, Martin B, Maudsley S. Amitriptyline improves motor function via enhanced neurotrophin signaling and mitochondrial functions in the murine N171-82Q Huntington disease model, J Biol Chem. 290 (2015) 2728-43.

[158] S. Gupta, B. Sharma, Pharmacological benefits of agomelatine and vanillin in experimental model of Huntington's disease, Pharmacol Biochem Behav. 122 (2014) 122-35.

[159] M. Damiano, L. Galvan, N. Déglon, E. Brouillet, Mitochondria in Huntington's disease, Biochim Biophys Acta. 1802 (2010) 52-61.

[160] S. Shetty, A. Hariharan, T. Shirole, A.G. Jagtap, Neuroprotective potential of escitalopram against behavioral, mitochondrial and oxidative dysfunction induced by 3-nitropropionic acid, Ann Neurosci. 22 (2015) 11-8.

[161] J. Mishra, A. Kumar, Improvement of mitochondrial function by paliperidone attenuates quinolinic acid-induced behavioural and neurochemical alterations in rats: implications in Huntington's disease, Neurotox Res. 26 (2014) 363-81.

[162] J. Mishra, T. Chaudhary, A Kumar, Rosiglitazone synergizes the neuroprotective effects of valproic acid against quinolinic acid-induced neurotoxicity in rats: targeting PPARγ and HDAC pathways, Neurotox Res. 26 (2014) 130-51.

[163] S. Gupta, B. Sharma, Protective effects of phosphodiesterase-1 (PDE1) and ATP sensitive potassium (KATP) channel modulators against 3-nitropropionic acid induced

behavioral and biochemical toxicities in experimental Huntington′s disease, Eur J Pharmacol. 732 (2014) 111-22.

[164] J. Mishra, A. Kumar, Improvement of mitochondrial NAD(+)/FAD(+)-linked state-3 respiration by caffeine attenuates quinolinic acid induced motor impairment in rats: implications in Huntington's disease, Pharmacol Rep. 66 (2014) 1148-55.

[165] D.J. Wright, T. Renoir, Z.M. Smith, A.E. Frazier, P.S. Francis, D.R. Thorburn, S.L. McGee, A.J. Hannan, L.J. Gray, N-Acetylcysteine improves mitochondrial function and ameliorates behavioral deficits in the R6/1 mouse model of Huntington's disease, Transl Psychiatry. 5 (2015) e492.

[166] V. Srinivasan, D.W. Spence, S.R. Pandi-Perumal, G.M. Brown, D.P. Cardinali, Melatonin in mitochondrial dysfunction and related disorders, Int J Alzheimers Dis. (2011) 326320.

[167] L. Palamiuc, A. Schlagowski, S.T. Ngo, A. Vernay, S. Dirrig-Grosch, A. Henriques, A.L. Boutillier, J. Zoll, A. Echaniz-Laguna, J.P. Loeffler, F. René, A metabolic switch toward lipid use in glycolytic muscle is an early pathologic event in a mouse model of amyotrophic lateral sclerosis, EMBO Mol Med. 7 (2015) 526-46.

[168] R.S. Pandya, H. Zhu, W. Li, R. Bowser, R.M. Friedlander, X. Wang, Therapeutic neuroprotective agents for amyotrophic lateral sclerosis, Cell Mol Life Sci. 70 (2013) 4729-45.

[169] V. Veereshwarayya, P. Kumar, K.M. Rosen, R. Mestril, H.W. Querfurth, Differential effects of mitochondrial heat shock protein 60 and related molecular chaperones to prevent intracellular beta-amyloid-induced inhibition of complex IV and limit apoptosis, J Biol Chem. 281 (2006) 29468-78.

[170] G.R. Luo, S. Chen, W.D. Le, Are heat shock proteins therapeutic target for Parkinson's disease?, Int J Biol Sci. 3 (2006) 20-6.

[171] R.K. Leak, Heat shock proteins in neurodegenerative disorders and aging. J Cell Commun Signal, 8 (2014) 293-310.

[172] E.K. Butler, A. Voigt, A.K. Lutz, J.P. Toegel, E. Gerhardt, P. Karsten, B., Reinartz A. Falkenburger, K.F. Winklhofer, J.B. Schulz, The mitochondrial chaperone protein TRAP1 mitigates α-Synuclein toxicity, PLoS Genet. 8 (2012) e1002488.

[173] A. Wyttenbach, O. Sauvageot, J. Carmichael, C. Diaz-Latoud, A.P. Arrigo, D.C. Rubinsztein, Heat shock protein 27 prevents cellular polyglutamine toxicity and suppresses the increase of reactive oxygen species caused by huntingtin, Hum Mol Genet. 11 (2002) 1137-51.

[174] J. Abubaker, A. Tiss, M. Abu-Farha, F. Al-Ghimlas, I. Al-Khairi, E. Baturcam, P. Cherian, N. Elkum, M. Hammad, J. John, S. Kavalakatt, A. Khadir, S. Warsame, S. Dermime, K. Behbehani, M. Dehbi, DNAJB3/HSP-40 cochaperone is downregulated in obese humans and is restored by physical exercise, PLoS One. 8 (2013) e69217.

[175] A.L. Orr, S. Huang, M.A. Roberts, J.C. Reed, S. Li, X.J. Li, Sex-dependent effect of BAG1 in ameliorating motor deficits of Huntington disease transgenic mice, J Biol Chem. 283 (2008) 16027-36.

[176] A. Israelson, D. Ditsworth, S. Sun, S. Song, J. Liang, M. Hruska-Plochan, M. McAlonis-Downes, S. Abu-Hamad, G. Zoltsman, T. Shani, M. Maldonado, A. Bui, M. Navarro, H. Zhou, M. Marsala, B.K. Kaspar, S. Da Cruz, D.W. Cleveland, Macrophage migration inhibitory factor as a chaperone inhibiting accumulation of misfolded SOD1, Neuron. 89 (2015) 218-32.

[177] J. Deng, M. Yang, Y. Chen, X. Chen, J. Liu, S. Sun, H. Cheng, Y. Li, E.H. Bigio, M. Mesulam, Q. Xu, S. Du, K. Fushimi, L. Zhu, J.Y. Wu, FUS Interacts with HSP60 to Promote Mitochondrial Damage, PLoS Genet. 11 (2015) e1005357.

[178] I. Padmalayam, The heat shock response: its role in pathogenesis of type 2 diabetes and its complications, and implications for therapeutic intervention, Discov Med. 18 (2014) 29-39.

[179] C.W. Zhang, H.B. Adeline, B.H. Chai, E.T. Hong, C.H. Ng, K.L. Lim, Pharmacological or Genetic Activation of Hsp70 Protects against Loss of Parkin Function, Neurodegener Dis. (2016).

[180] L.F. Burbulla, C. Schelling, H. Kato, D. Rapaport, D. Woitalla, C. Schiesling, C. Schulte, M. Sharma, T. Illig, P. Bauer, S. Jung, A. Nordheim, L. Schöls, O. Riess, R. Krüger, Dissecting the role of the mitochondrial chaperone mortalin in Parkinson's disease: functional impact of disease-related variants on mitochondrial homeostasis, Hum Mol Genet. 19 (2010) 4437-52.

[181] A.C. Costa, S.H. Loh, Martins LM. Drosophila Trap1 protects against mitochondrial dysfunction in a PINK1/parkin model of Parkinson's disease, Cell Death Dis. 4 (2013) e467.

[182] H.Q. Wang, Y.X. Xu, X.Y. Zhao, H. Zhao, J. Yan, X.B. Sun, J.C. Guo, C.Q. Zhu, Overexpression of F(0)F(1)-ATP synthase alpha suppresses mutant huntingtin aggregation and toxicity in vitro, Biochem Biophys Res Commun. 390 (2009) 1294-8.

[183] O.V. Forlenza, V.J. De-Paula, B.S. Diniz, Neuroprotective effects of lithium: implications for the treatment of Alzheimer's disease and related neurodegenerative disorders, ACS Chem Neurosci. 5 (2014) 443-50.

[184] L. Luo, G.J. Sun, Y.J. Du, Effect of "Kidney-reinforcing and Govenor Vessel-regulating" of Acupuncture plus Moxibustion on Mitochondrial Dynamics-related Proteins in Hippocampal Neurons of Rats with Alzheimer's Disease, Zhen Ci Yan Jiu. 40 (2015) 270-4.

[185] M. Itakura, H. Nakajima, T. Kubo, Y. Semi, S. Kume, S. Higashida, A. Kaneshige, M. Kuwamura, N. Harada, A. Kita, Y.T. Azuma, R. Yamaji, T. Inui, T. Takeuchi, Glyceraldehyde-3-phosphate Dehydrogenase Aggregates Accelerate Amyloid-β Amyloidogenesis in Alzheimer Disease, J Biol Chem. 290 (2015) 26072-87.

[186] J.L. Jin, A.K. Liou, Y. Shi, K.L. Yin, L. Chen, L.L. Li, X.L. Zhu, L. Qian, R. Yang, J. Chen, Y. Xu, CART treatment improves memory and synaptic structure in APP/PS1 mice, Sci Rep. 5 (2015) 10224.

[187] A.D. Chaudhuri, D.C. Choi, S. Kabaria, A. Tran, E. Junn, MicroRNA-7 Regulates the Function of Mitochondrial Permeability Transition Pore by Targeting VDAC1 Expression, J Biol Chem. 291 (2016) 6483-93.

[188] L. Hang, J. Thundyil, K.L. Lim, Mitochondrial dysfunction and Parkinson disease: a Parkin-AMPK alliance in neuroprotection, Ann N Y Acad Sci. 1350 (2015) 37-47.

[189] A. Nanou, A. Higginbottom, C.F. Valori, M. Wyles, K. Ning, P. Shaw, M. Azzouz, Viral delivery of antioxidant genes as a therapeutic strategy in experimental models of amyotrophic lateral sclerosis, Mol Ther. 21 (2013) 1486-96.

[190] Z. Mao, S. Zhang, H. Chen, Stem cell therapy for amyotrophic lateral sclerosis, Cell Regen (Lond). 4 (2015) 11.

[191] S.R. Colberg, R.J. Sigal, B. Fernhall, J.G. Regensteiner, B.J. Blissmer, R.R. Rubin, L. Chasan-Taber, A.L. Albright, B. Braun, Exercise and type 2 diabetes: the American

College of Sports Medicine and the American Diabetes Association: joint position statement, Diabetes Care. 33 (2010) e147-67.

[192] E.A. Richter, N.B. Ruderman, AMPK and the biochemistry of exercise: implications for human health and disease, Biochem J. 418 (2009) 261-75.

[193] S.M. de la Monte, Intranasal insulin therapy for cognitive impairment and neurodegeneration: current state of the art, Expert Opin Drug Deliv. 10 (2013) 1699-709.

[194] A.S. Paintlia, S. Mohan, I. Singh, Combinatorial Effect of Metformin and Lovastatin Impedes T-cell Autoimmunity and Neurodegeneration in Experimental Autoimmune Encephalomyelitis, J Clin Cell Immunol. 30 (2013) 4.

[195] I. Ullah, N. Ullah, M.I. Naseer, H.Y. Lee, M.O. Kim, Neuroprotection with metformin and thymoquinone against ethanol-induced apoptotic neurodegeneration in prenatal rat cortical neurons, BMC Neurosci. 19 (2012) 13:11.

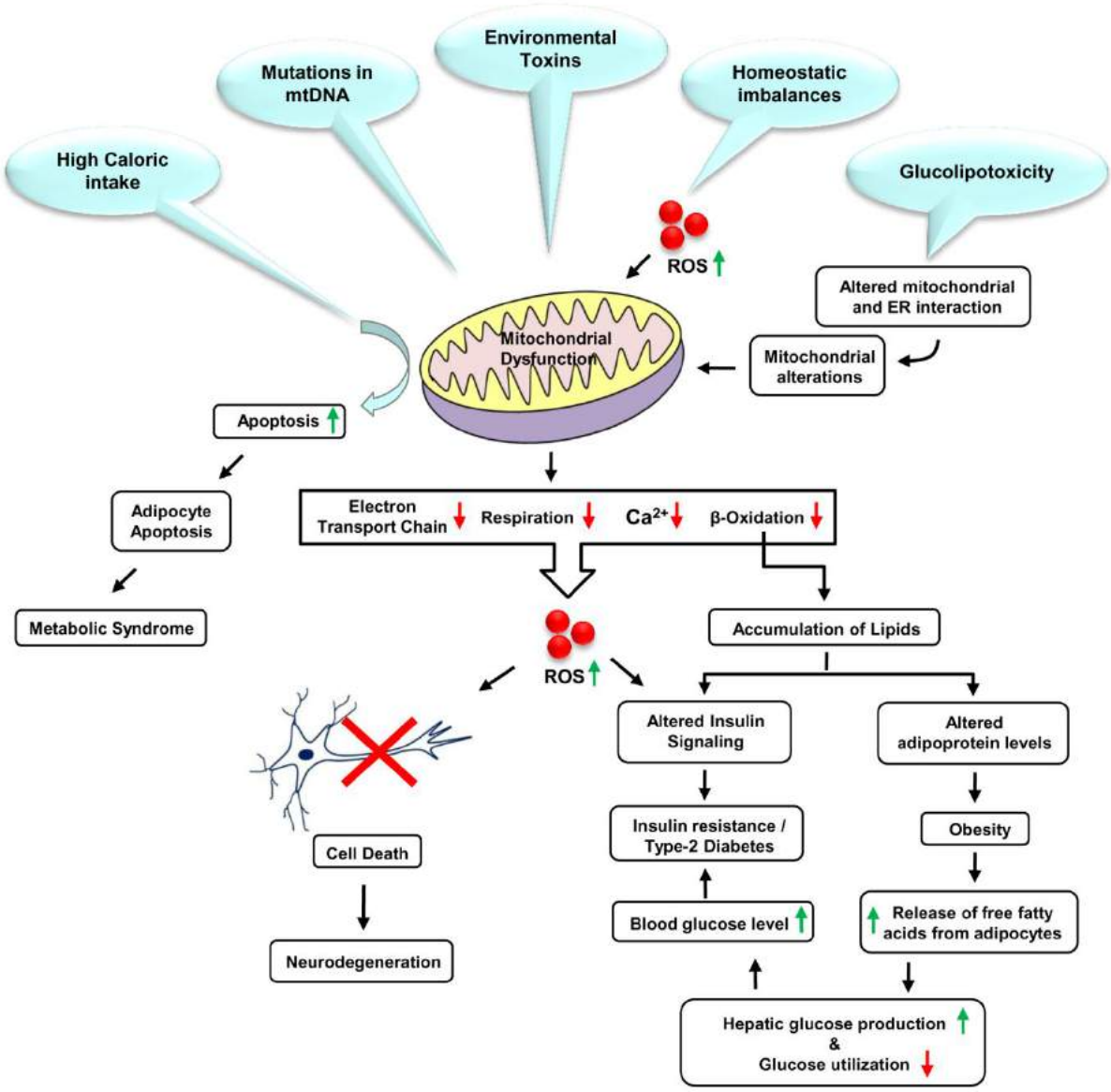
[196] C. Davis, J. Mudd, M. Hawkins, Neuroprotective effects of leptin in the context of obesity and metabolic disorders, Neurobiol Dis. 72 (2014) 61-71.

[197] A.P. Signore, F. Zhang, Z. Weng, Y. Gao, J. Chen, Leptin neuroprotection in the CNS: mechanisms and therapeutic potentials, J Neurochem. 106 (2008) 1977-90.

[198] J. Chen, S. Li, W. Sun, J. Li, Anti-diabetes drug pioglitazone ameliorates synaptic defects in AD transgenic mice by inhibiting cyclin-dependent kinase5 activity, PLoS One. 10 (2015) e0123864.

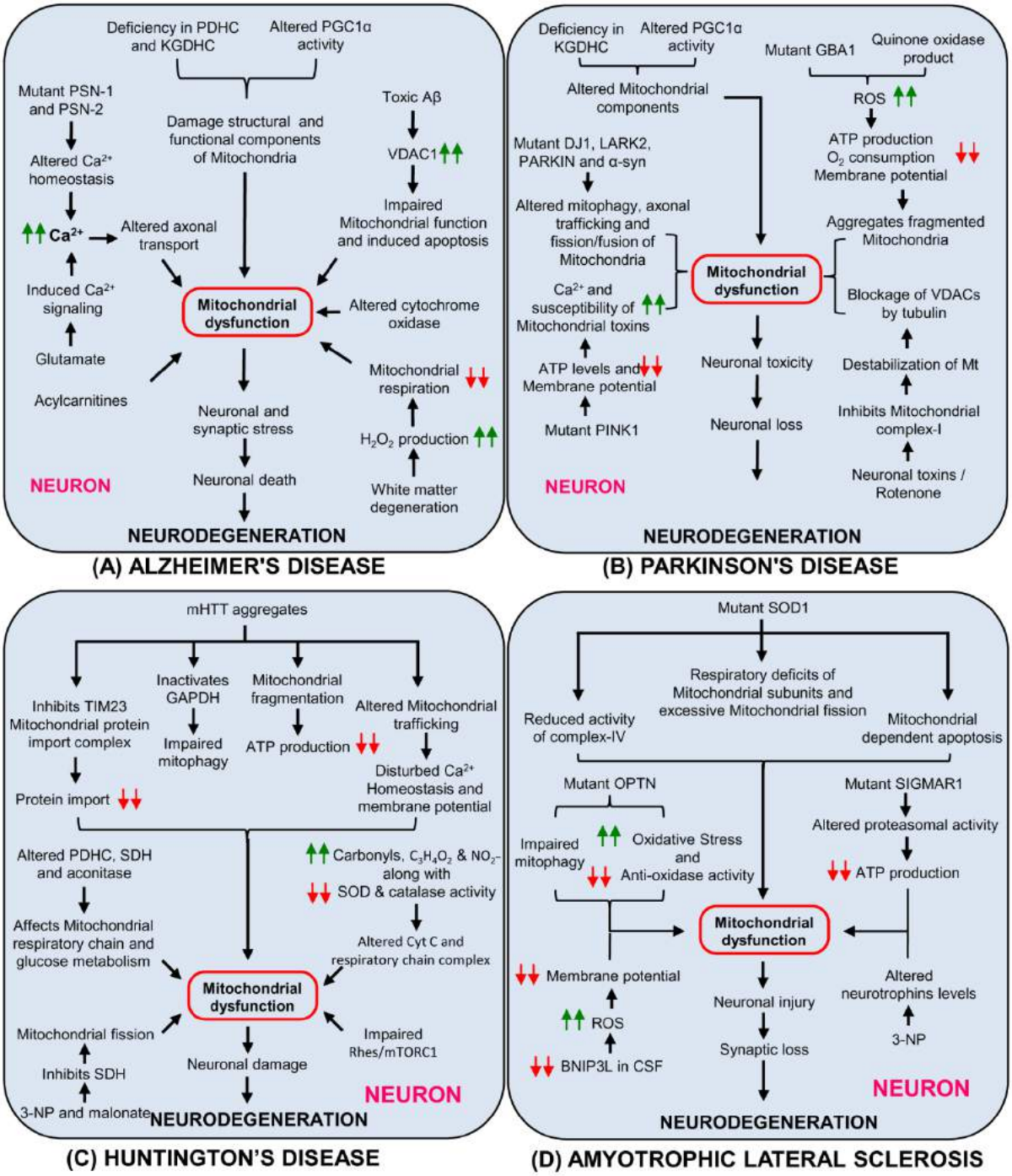
Special issue on "*Oxidative Stress and Mitochondrial Quality in Diabetes/Obesity and Critical Illness Spectrum of Diseases*" for BBA - Molecular Basis of Disease.

Figure 1



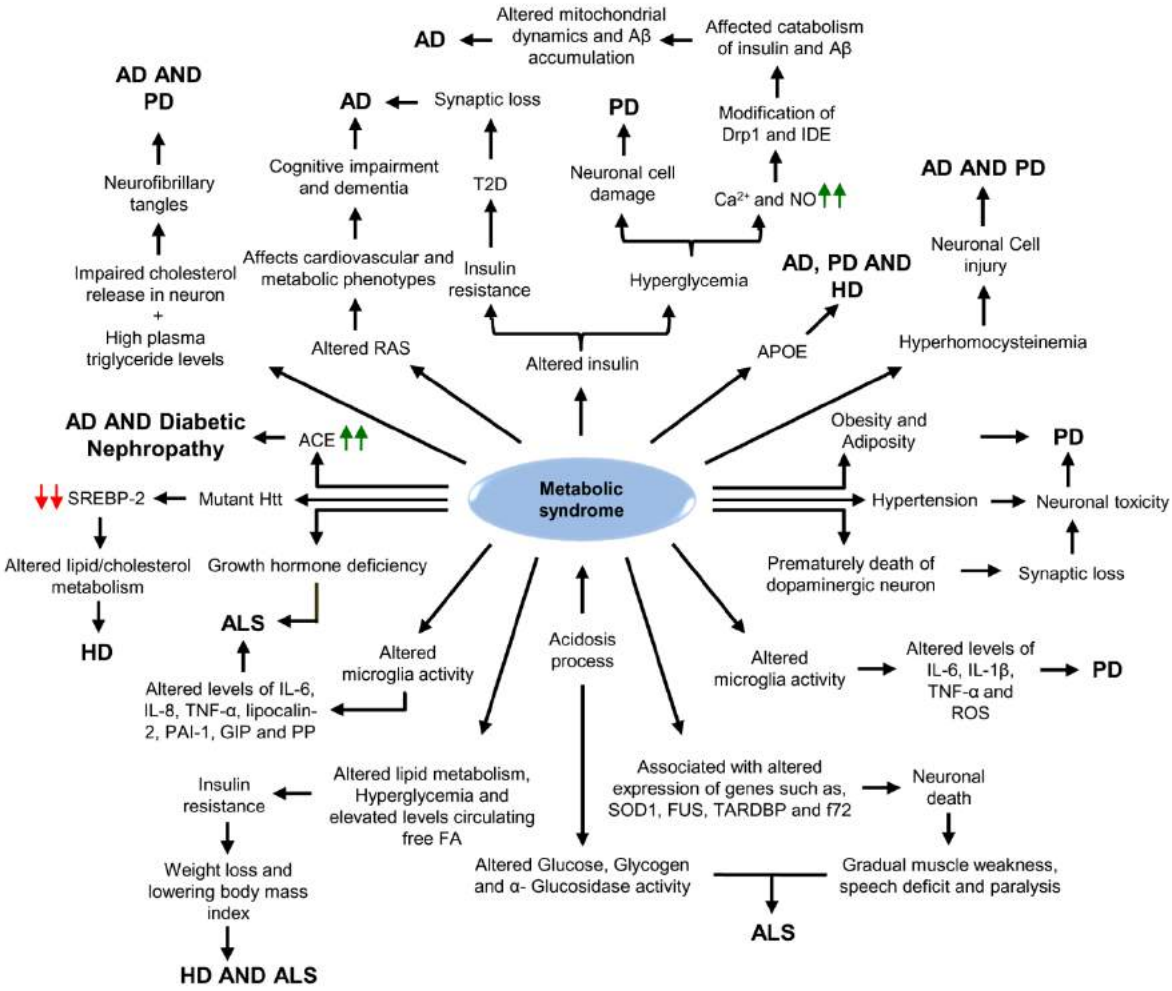
Special issue on "*Oxidative Stress and Mitochondrial Quality in Diabetes/Obesity and Critical Illness Spectrum of Diseases*" for BBA - Molecular Basis of Disease.

Figure 2



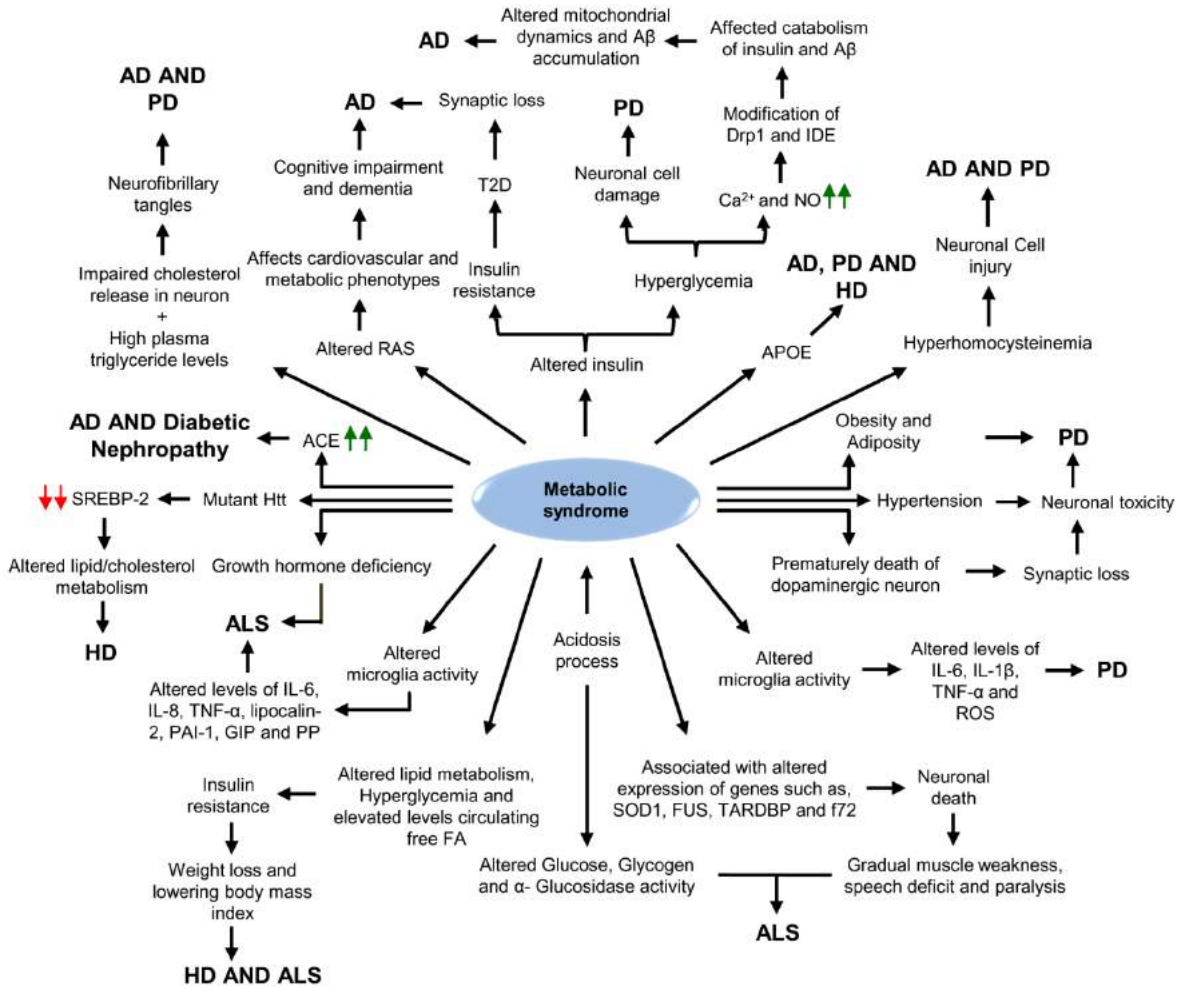
Special issue on "*Oxidative Stress and Mitochondrial Quality in Diabetes/Obesity and Critical Illness Spectrum of Diseases*" for BBA - Molecular Basis of Disease.

Figure 3



Special issue on "*Oxidative Stress and Mitochondrial Quality in Diabetes/Obesity and Critical Illness Spectrum of Diseases*" for BBA - Molecular Basis of Disease.

GRAPHICAL ABSTRACT: METABOLIC SYNDROME ASSOCIATED NEURODEGENERATION



Special issue on "*Oxidative Stress and Mitochondrial Quality in Diabetes/Obesity and Critical Illness Spectrum of Diseases*" for BBA - Molecular Basis of Disease.

HIGHLIGHTS

- Establishing a link between altered mitochondrial, metabolic syndrome and stress signaling
- Altered mitochondrial dynamics related to metabolic syndrome and neurodegenerative disorders.
- Consequences of mitochondrial dysfunction in AD, PD, HD and ALS
- Application of biomolecules and chaperones as therapeutic molecules

Research Article Adv. Mater. Lett. 2016, **7**(7), 567-572 Advanced Materials *Letters*

www.vbripress.com/aml, DOI: 10.5185/amlett.2016.6172 Published online by the VBRI Press in 2016

Microstructural and dielectric investigations of vanadium substituted barium titanate ceramics

Aditya Jain[1], Neelam Maikhuri[1], Rakesh Saroha[1], Mukul Pastor[2], A. K. Jha[3], A. K. Panwar[1*]

[1]*Department of Applied Physics, Delhi Technological University, Delhi 110042, India*

[2]*Department of Physics, Bundelkhand University, Jhansi 284002, Uttar Pradesh, India*

[3]*Department of Applied Science, A.I.A.C.T.R, Delhi 110031, India*

*Corresponding author: Tel: (+91) 9891778307; E-mail: amrish.phy@dce.edu and panwaramar@gmail.com

Received: 15 September 2015, Revised: 19 February 2016 and Accepted: 20 May 2016

ABSTRACT

In this investigation, the microstructural and dielectric properties of pure $BaTiO_3$ and vanadium (V^{5+}) substituted on Ba^{2+} site (A-site) and Ti^{4+} site (B-site) in $BaTiO_3$ ceramic have been studied. The three compositions of $BaTiO_3$ (BT), $Ba_{0.9}V_{0.1}TiO_3$ (BTA) and $BaTi_{0.9}V_{0.1}O_3$ (BTB) were synthesized using solid-state reaction route. The XRD analysis of all three compositions has been carried out at room temperature and proper phase formation for BT, BTA and BTB are confirmed. However, compositions BTA and BTB indicate the presence of secondary phases, and it may be due to higher amount of vanadium substitution at A and B sites. Addition of vanadium inhibited the grain growth of $BaTiO_3$ ceramic. Vanadium substitution on A- and B-site have resulted in decrease of Curie temperature as well as dielectric loss compared to pure BT. A more diffused behavior is observed in vanadium substituted samples as compare to pure BT which shows a sharp transition and lower value of diffuseness parameter. Impedance study shows that substitution of vanadium on A- as well as B-site results in decrease of AC conductivity. These properties of vanadium substituted samples can be utilized to reduce the dielectric loss in capacitors and in radio frequency applications. Copyright © 2016 VBRI Press.

Keywords: Barium titanate; conductivity; dielectric constant; sintering.

Introduction

Lead-based oxide materials such as lead titanate ($PbTiO_3$), lead zirconate ($PbZrO_3$), lead strontium titanate ($PbSrTiO_3$) etc. are dominant ferroelectric materials due to their extraordinary dielectric properties. Due to their inherent dielectric properties, they are widely used in sensors, actuators and multi-layered ceramic capacitor (MLCC) applications [**1**]. Although, Lead based materials contains a higher amount of lead oxide which is highly toxic and causes various environmental problems and health risks [**2-4**]. Hence, for environmental safety issues and technological advancement, research work is explored in lead-free materials such as $BaTiO_3$, $SrTiO_3$, etc. [**5**]. Barium titanate has attracted a lot of attention because of its high dielectric constant and excellent piezoelectric and pyro-electric properties. Generally, barium titanate based ceramics show sharp peak transitions, due to this reason barium titanate based materials have higher ferroelectricity compared to other perovskite structure based materials [**6-8**]. Also barium titanate based ceramics have the advantage of better electrical properties at room temperature including good chemical and mechanical stability. Pure barium titanate and its doping with certain dopants exhibit positive temperature coefficient of resistivity (PTCR) properties. This suggests that at Curie temperature it will exhibit an increase in resistance. This increase in resistance may be of several orders of magnitude. This property of barium titanate based materials can be used in sensing applications [**9**].

Barium strontium titanate is one of the preferred materials for tunable applications, but due to its high dielectric loss, it has limited applicability. In general, the substitution of transition metals and rare earths has been widely explored to improve the dielectric and microstructural properties of barium titanate ceramics [**10-11**]. It has also been observed that the substitution of non-ferroelectric material may result in decrease in dielectric constant as well as the dielectric loss [**12, 13**]. Nagao *et al.* [**14**] have synthesized Eu-doped $BaTiO_3$ nanoparticles by hydrolysis and found an enhancement in luminescent properties and dielectric properties. Nath *et al.* [**15**] prepared bismuth doped $BaTiO_3$ by solid state reaction and found an enhancement in piezoelectric properties. Petrovic *et al.* [**16**] found the addition of La results in increase of dielectric constant and appearance of PTCR effect in barium titanate ceramic. Liu *et al.* [**17**] showed that cobalt doping in barium titanate may results in better ferromagnetic properties and can be used for multiferroic applications. It is implied that proper doping or substitution can improve microstructural, electrical and magnetic properties of $BaTiO_3$ ceramics. Vanadium is one of the most important dopant and have resulted in modifying microstructural and dielectric properties of various

 Copyright © 2016 VBRI Press

ceramics. Moreover, it is well reported that electrical behavior of barium titanate based ceramics is related to chemical state of the constituent materials [**18**]. In recent years, most studies are concentrated on temperature dependence of the dielectric properties, magnetic, optical, relaxor behavior and domain structure of barium titanate based materials. Zheng *et al*. [**19**] reported that vanadium substitution at B-site could enhance ferroelectric properties of $CaBi_4Ti_4O_{15}$ ceramic. Effects of vanadium doping on dielectric properties in barium strontium titanate and strontium bismuth niobate have been investigated by Bandyopadhyay et al. [**20**] and Wu *et al*. [**21**]. However, there is no information on the microstructure and electrical properties of higher amount of vanadium doping in barium titanate ceramics, which prompted the authors to investigate the present composition.

The objective of this research is to investigate the effect of higher amount of vanadium substitution on A- and B-site of $BaTiO_3$ ceramic and analyze their microstructural, dielectric and impedance properties. In addition, the temperature dependence of the dielectric constant was used to evaluate the diffuseness parameter for comprehending the modulation in ferroelectric transition characteristics due to the vanadium substitution on A- and B-site.

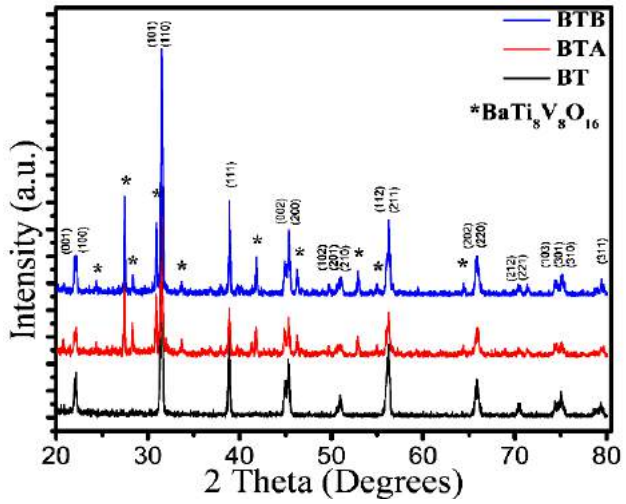


Fig. 1. XRD patterns of BT1260, BTA1200 and BTB1200 ceramics pellets sintered for 4 hours.

Experimental

Synthesis of ceramics

$BaTiO_3$ (BT), $Ba_{0.9}V_{0.1}TiO_3$ (BTA) and $BaTi_{0.9}V_{0.1}O_3$(BTB) were synthesized using solid-state reaction route. The starting materials barium carbonate ($BaCO_3$, 99.0%, Sigma-Aldrich), titanium oxide (TiO_2, 99.9%, Sigma-Aldrich) and vanadium pentoxide (V_2O_5, 99.9%, Merck Millipore) were used to synthesize the desired compositions. These precursors were thoroughly mixed and grounded in mortar-pestle for approximately 5 hours and then all the three compositions were calcined at 1100°C for 4 hours to remove volatile impurities. The calcined powders were mixed with 2.5 wt.% poly-vinyl alcohol and then they were pressed into pellets at 50 MPa pressure. These pellets were kept at 220°C for 40 min to eliminate the solvent and binder after that these pellets were sintered at different temperatures. The pure barium titanate (BT) powder was sintered at 1225°C and 1260 °C for 4 hours. While vanadium substituted compositions, BTA and BTB were sintered at 1150 °C and 1200 °C for 4 hours.

Characterization

Phase formation of pure BT, BTA and BTB were analyzed using X-ray diffractogram recorded by Bruker D8 Advance X-ray diffractometer using $CuK_{\alpha 1}$ radiation of wavelength, 1.540 Å in conjunction with Ni filter. Microstructural analysis of the specimens was done by using Hitachi S-3700 scanning electron microscope. Dielectric measurements were performed to observe the effect of variation of dielectric constant and dielectric loss with temperature and frequency using Agilent 4284A precision LCR meter on a polished and silver coated pellets of size 10 mm diameter and 1 mm thickness. The measurements were performed in the temperature range of 27° C to 190° C.

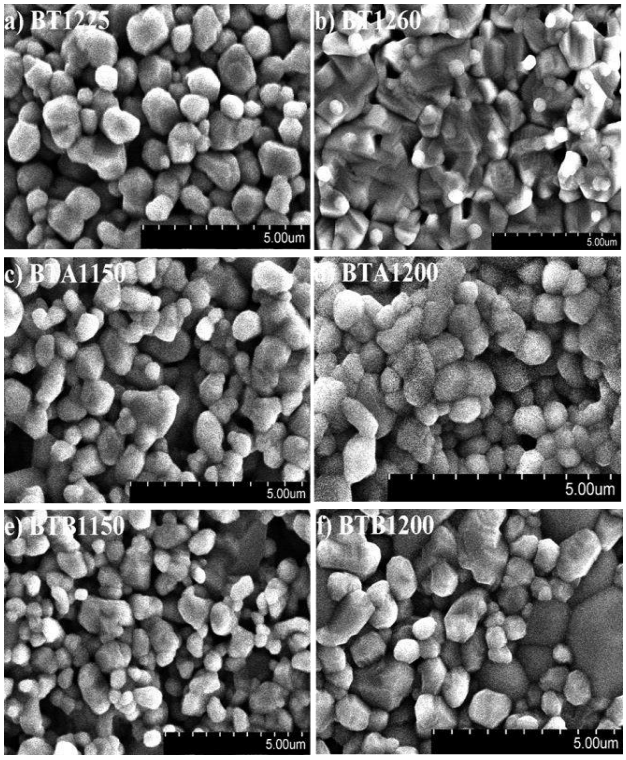


Fig. 2. SEM micrograph of compositions of ceramics sintered at different temperatures for 4 hours: (i) pure BT (a): 1225°C and (b): 1260°C; (ii) BTA (c): 1150 °C and (d): 1200 °C; (iii) BTB (e): 1150 °C and (f): 1200 °C.

Results and discussion

Crystal structure

X-ray diffraction pattern of pure BT specimen sintered at 1260 °C for 4 hours (BT1260), BTA and BTB both sintered at 1200 °C for 4 hours (BTA1200 and BTB1200) ceramics are shown in **Fig. 1**. These XRD patterns were indexed with standard barium titanate compound (JCPDS no. – 01-075-0462) using X'pert highscore software, which

Copyright © 2016 VBRI Press

confirms the formation of tetragonal phase with P4mm space group for pure BT. However, some extra peaks (marked as *) are also observed in the patterns of BTA and BTB. Peaks marked as * are identified as secondary phase, possibly due to higher amount of substitution of vanadium in BTA and BTB and they belong to $BaTi_8V_8O_{16}$ having tetragonal phase with I4/m space group. The XRD patterns also indicate that irrespective of vanadium substitution on A site or B site, the vanadium ion might have gone to the same site in both the compositions. The presence of non-ferroelectric secondary phases in XRD pattern of BTA and BTB may lead to a decrease in dielectric constant [**22-25**].

Microstructural analysis

Fig. 2 shows the SEM images of all the three samples sintered at different temperatures. To see the effect of sintering temperature on the microstructural properties of ceramics, all the three compositions were sintered at two different temperatures. The pellets of pure barium titanate composition were sintered at 1225 °C and 1260 °C. It is observed that BT sample sintered at 1225°C (BT1225) possess a uniform distribution of grains with clearly visible grain boundaries. While the BT sample sintered at 1260 °C (BT1260) shows some agglomeration in grains. The average grain size of BT1225 sample is observed to be in the range of 750 to 780 nm as calculated from Image J software. The vanadium substituted compositions BTA and BTB were sintered at three different sintering temperatures: 1150°C, 1200°C and 1225°C. The reason for low-temperature synthesis of vanadium substituted samples is the lower melting point of vanadium precursor (V_2O_5), which results in melting of overall composition [**26**].

It is observed that up to sintering temperature of 1200 °C vanadium substituted samples BTA1200 and BTB1200 retain the visible grains and grain boundaries, while for sintering temperature above 1200 °C both vanadium substituted compositions have started melting. The average grain size of BTA1150, BTB1150, BTA1200 and BTB1200 were found to be in the range of 510-530 nm, 535-550 nm, 490-515 nm and 570-590 nm, respectively. Hence, the average grain size of both the vanadium substituted compositions decreases as compare to pure BT. These results also suggest that the decrease in average grain size of vanadium substituted compositions may lead to decrease in dielectric constant [**27**].

Dielectric study

Dielectric measurements of all three compositions BT1260, BTA1200 and BTB1200 were performed. The temperature dependence of dielectric constant and dielectric loss of these three compositions at three frequencies measured in the temperature range of 27 to 200 °C are shown in **Fig. 3(a)-(c)**. It can be seen from **Fig. 3** that at lower temperature the dielectric constant decreases gradually and near the Curie temperature the dielectric constant increases abruptly and then decreases indicating the phase transition from ferroelectric state to paraelectric state [**28, 29**]. The decrease in dielectric constant above T_c is due to the structural transition from tetragonal to cubic phase. Moreover, there is an increase in thermal oscillations of the molecules and degree of disorder in dipoles in cubic phase, which results in decrease of dielectric constant [**30**]. It is observed that as frequency increases dielectric constant decreases, this may be because the increase in frequency leads to a drop in net polarization of the material. Overall the magnitude of dielectric constant decreases in vanadium substituted compositions BTA and BTB. The higher value of dielectric constant for pure BT as compare to vanadium substituted samples may be due to well-developed grains which result in the easier motion of the domain walls [**31**].

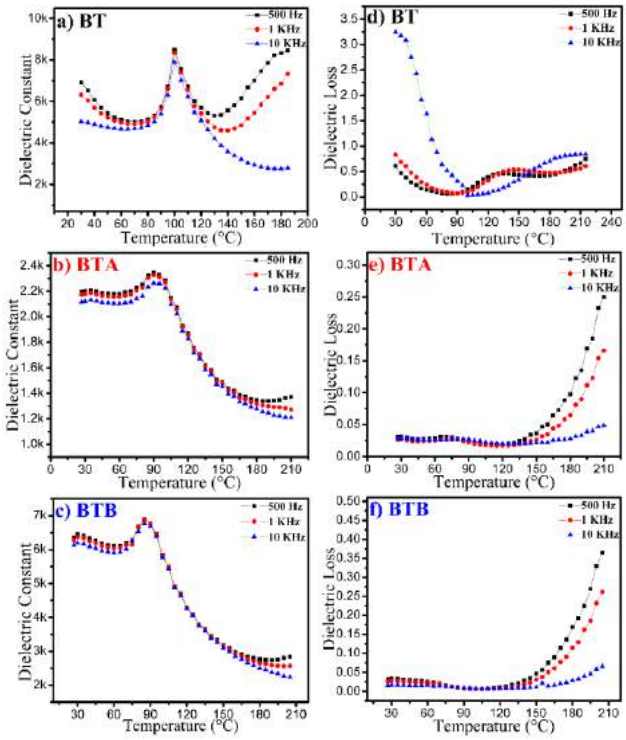


Fig. 3. Variation of dielectric constant and dielectric loss with temperature: (a) and (d) for BT1260; (b) and (e) BTA1200; (c) and (f) BTB1200 at three different frequencies of 500Hz, 1KHz and 10KHz.

Dielectric loss of all three compositions, BT1260, BTA1200 and BTB1200 at different frequencies, 500 Hz, 1 kHz, and 10 kHz are shown in **Fig. 3(d)-(f)**. It has been observed that the dielectric loss of pure BT is much higher at lower temperature (room temperature), as the temperature increases the dielectric loss decreases upto 100°C and again increases further after crossing dielectric transition temperature. It can be seen that the magnitude of dielectric loss in the observed temperature range of 27 °C to 210 °C is lower in BTA and BTB compared to that in BT. The dielectric loss remains almost constant in the vanadium substituted compositions BTA and BTB from room temperature to 150 °C temperature at different frequencies of 500 Hz, 1 kHz and 10 kHz. A sharp increase in the dielectric loss is observed at higher temperatures in BTA and BTB specimens. The increase in dielectric loss at higher temperature and high frequencies may be due to the increase in the mobility of charge carriers arises from the vacancies or defects in of BTA and BTB compositions [**32**]. A decrease in dielectric loss in BTA and BTB specimen compared to pure BT is observed which may be attributed to charge compensation effect caused by the substitution of V^{5+} on A and B site of $BaTiO_3$ structure. The

Copyright © 2016 VBRI Press

variation of dielectric constant and dielectric loss is also observed in a wide range of frequency range of 20 Hz to 1 MHz, as shown in **Fig. 4**. The measurements were taken at three different temperatures of 30 °C, 100 °C and 175 °C. It is observed that vanadium substituted BTA and BTB samples show almost similar behavior for dielectric constant and dielectric loss except that BTA has lower value of both the dielectric constant and dielectric loss. Overall on comparing both the dielectric constant and dielectric loss with frequency in BT, BTA and BTB for different temperatures, it is observed that BTA has lower dielectric loss compared to BT and BTB. Similar behavior is noticed in case of dielectric constant in terms of overall magnitude.

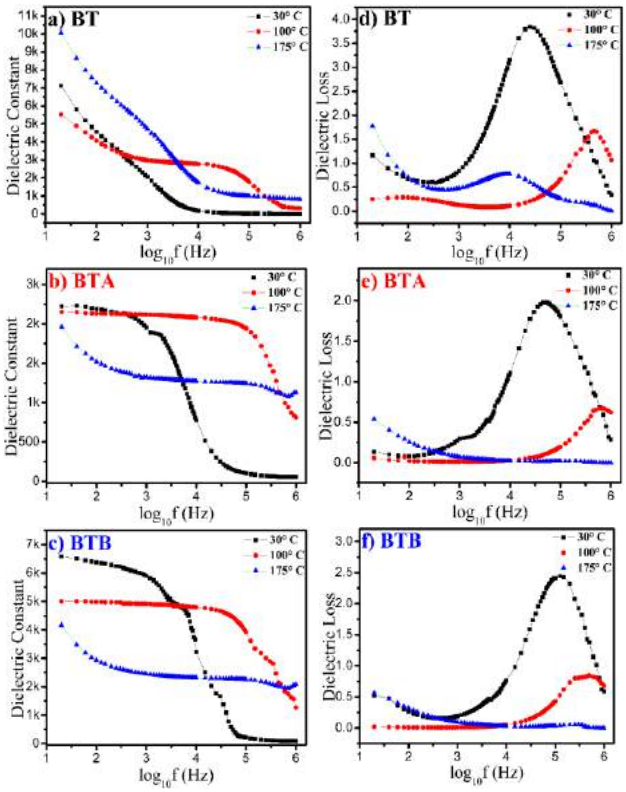


Fig. 4. Variation of dielectric constant and dielectric loss with frequency: (a) and (d) BT1260; (b) and (e) BTA1200; (c) and (f) BTB1200 at three different temperatures of 30 °C, 100 °C and 175 °C.

The variation of dielectric constant with temperature is also related to the tolerance factor of perovskite materials. The tolerance factor can be calculated from the following equation [33-35]:

$$t = \frac{R_O + R_A}{\sqrt{2}(R_B + R_O)} \quad (1)$$

where, R_A is the ionic radius of A site atom, R_B is ionic radius of B site atom and R_O ionic radius of the oxygen atom. But above equation is modified for the compositions of BTA and BTB of vanadium substituted compositions in this investigation and it may be rewritten as:

For A site:

$$t = \frac{R_O + (0.9R_{Ba^{2+}} + 0.1R_{V^{5+}}}{\sqrt{2}(R_{Ti^{4+}} + R_O)} \quad (2)$$

For B site:

$$t = \frac{R_O + R_{Ba^{2+}}}{\sqrt{2}(0.9R_{Ti^{4+}} + 0.1R_{V^{5+}} + R_O)} \quad (3)$$

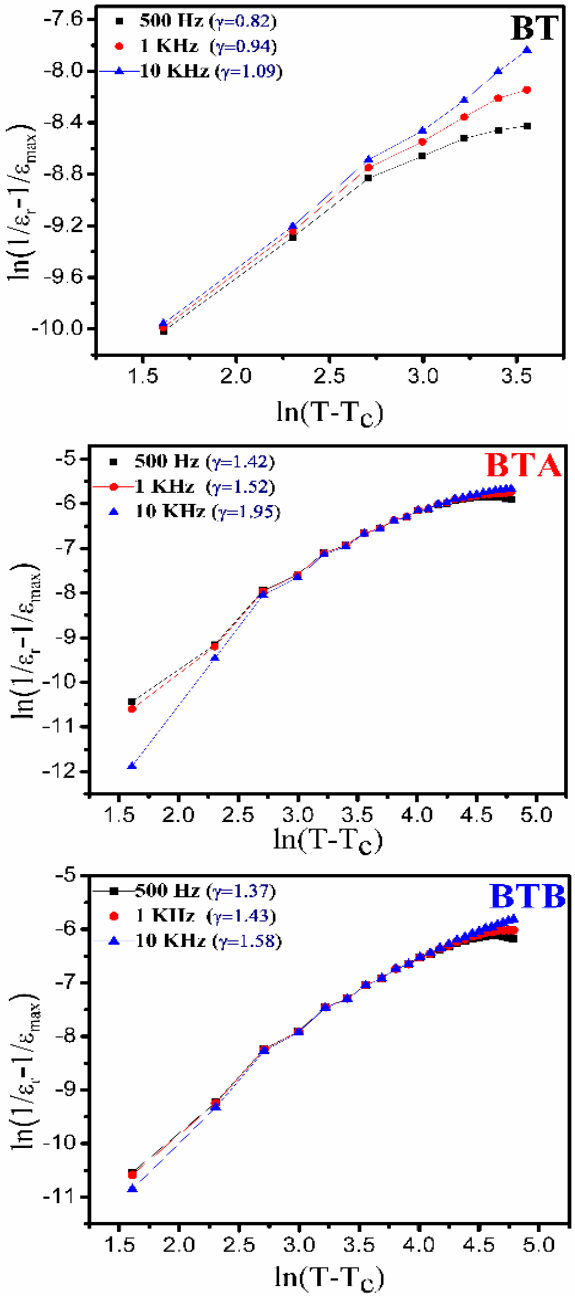


Fig. 5. Diffuseness parameter for BT1260, BTA1200 and BTB1200 at 500Hz, 1KHz and 10KHz.

For stable perovskite structure, value of t should be close to unity. The value of tolerance factor for BTA and BTB were found to be 1.023 and 1.065 compared to 1.061 for pure BT. Pure BT possesses a stable ferroelectric phase with sharp phase transition while a little deviation from its tolerance value has resulted in disorderedness in the

Copyright © 2016 VBRI Press

material leading to diffuse transition as observed in BTA and BTB. The diffuseness of phase transition γ was calculated for all the three compositions and is shown in **Fig. 5**. The empirical relation of diffuseness parameter is given by following equation for a modified Curie-Weiss law [**36-38**].

$$\frac{1}{\varepsilon} - \frac{1}{\varepsilon_m} = \frac{(T-T_c)^{\gamma}}{C'} \quad (4)$$

where, ε is the dielectric constant, ε_m is the dielectric constant at temperature T_c, c' is the curie constant and γ represents the diffuseness parameter.

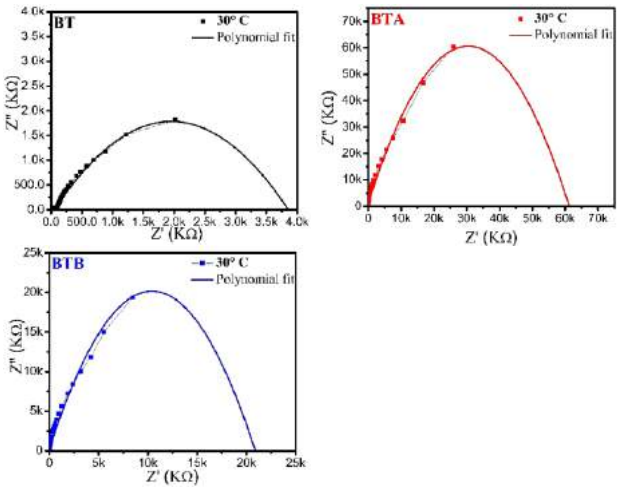


Fig. 6. Estimation of AC resistance of BT1260, BTA1200 and BTB1200 using Nyquist plot.

The diffuseness parameter, γ = 1corresponds to normal ferroelectric behavior while 1< γ<2 correspond to diffused phase transition [**39-41**]. The value of diffuseness parameter was calculated for BT, BTA and BTB compositions at three different frequencies 500 Hz, 1 kHz and 10 kHz. A higher value of diffusivity was observed for BTA and BTB leading to lower ferroelectricity compared to that in BT. A higher value of diffusivity also suggests that on substitution of vanadium ion on A and B site of BT lattice have resulted in the lowering of long range ordering and crystallinity of the material [**42**]. The ionic radii of Ti^{4+} and V^{5+} in six coordination no. are 60.5 and 54 pm, respectively as compare 135 pm for Ba^{2+}. This suggest the higher probability of vanadium ion to go on to Ti site rather than at Ba site, also a much higher charge compensation is required at Ba site rather than at Ti site for vanadium substitution.

Impedance study

Impedance measurement was carried out at room temperature in the frequency range 20 Hz-1 MHz. Fig. 6 shows the Nyquist plot between real (Z') and imaginary (Z'') parts of the impedance for the synthesized specimens BT, BTA and BTB. Nyquist plots for BT, BTA and BTB indicate generation of only one semicircle which corresponds to the grain boundary resistance. However, grain boundary resistance is maximum in BTA while minimum in pure BT suggesting that there is decrease in conductivity when vanadium is substituted either at A-site or B-site while for BTB it is lower than BTA means vanadium substitution is more favorable at B-site rather than A-site. It is found that AC conductivity decreases with vanadium substitution in BTA and BTB compositions. The obtained value of conductivity for BT, BTA and BTB are 5.07, 0.34 and 0.95 μS/m, respectively. The decrease in conductivity of BTA and BTB compared to that in pure BT may be due to the higher number of grain boundaries in vanadium substituted samples because higher no. of grain boundaries contributes to grain boundary resistance which further result in the form of overall resistance [**43**].

Conclusion

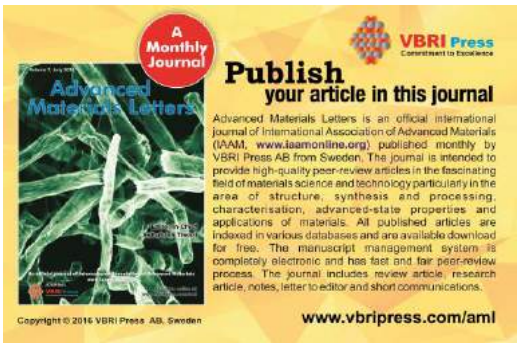
$BaTiO_3$(BT), $Ba_{0.9}V_{0.1}TiO_3$(BTA) and $BaTi_{0.9}V_{0.1}O_3$(BTB) were synthesized by solid state reaction route. X-ray diffraction pattern confirms the tetragonal phase for all the three samples BT, BTA and BTB while secondary peaks of $BaTi_8V_8O_{16}$ for BTA and BTB was also observed, which suggests the limited solubility of vanadium in barium titanatelattice. Micro structural investigation indicates that addition of vanadium has inhibited the grain growth and results in decrease of grain size compared to pure BT. The sintering temperature of pure BT was reduced by approximately 60-80 °C with vanadium substitution. The addition +of vanadium causes the lowering in the Curie temperature. The dielectric constant of the ceramic was found to decrease, which is due to decrease in crystallinity and presence of non-ferroelectric secondary phase with vanadium substitution. The diffuseness of phase transition enhances with vanadium substitution on A- and B-site of $BaTiO_3$. The substitution of higher concentration of vanadium on Ba^{2+} and Ti^{4+} results in decrease of dielectric constant which may be attributed to decreased leakage current inside the material. AC conductivity results shows that vanadium substituted samples possesses a lower value of conductivity that can be correlated to grain boundary effect which is dominating in BTA and BTB as compared to BT. The lowering of dielectric loss and conductivity of the material can be utilized in fabricating the multi-layered ceramic capacitors (MLCC), radio frequency applications and in reducing dielectric materials losses.

Reference

1. Moulson, A. J. and Herbert, J. M., *Electroceramics:* Dielectrics and Insulators; *Wiley*, **2003**, *pp.* 243. **DOI:** 10.1002/0470867965.ch5
2. K. Takeda, T. Muraishi, T. Hoshina, H. Takeda, and T. Tsurumi, *J. Appl. Phys.***2010,** *107*, 074105. **DOI:** 10.1063/1.3371679
3. L.G.A. Marques, L.S. Cavalcante , A.Z. Sim˜oes , F.M. Pontes , L.S. Santos-J´unior, M.R.M.C. Santos, I.L.V. Rosa , J.A. Varela , E. Longo, *Mater. Chem. Phys.***2007,** *105* 293. **DOI:** 10.1016/j.matchemphys.2007.04.065
4. X.G. Tang, R.K. Zheng, Y.P. Jiang, H.L.W. Chan, *J. Appl. Phys.* **2006**, *39*, 3394. **DOI:** 10.1088/0022-3727/39/15/026
5. W. Wang, W.L. Li, D. Xu, W.P. Cao, Y.F. Hou, W.D. Fei, *Ceramic. Inter.***2014,** *40* 3933. **DOI:** 10.1016/j.ceramint.2013.08.037
6. John Bechhoefer, Yi Deng, Joel Zylberberg, Chao Lei, and Zuo-Guang Ye, *Am J Phys.***2007,** *75*, 1046. **DOI:** 10.1119/1.2723801

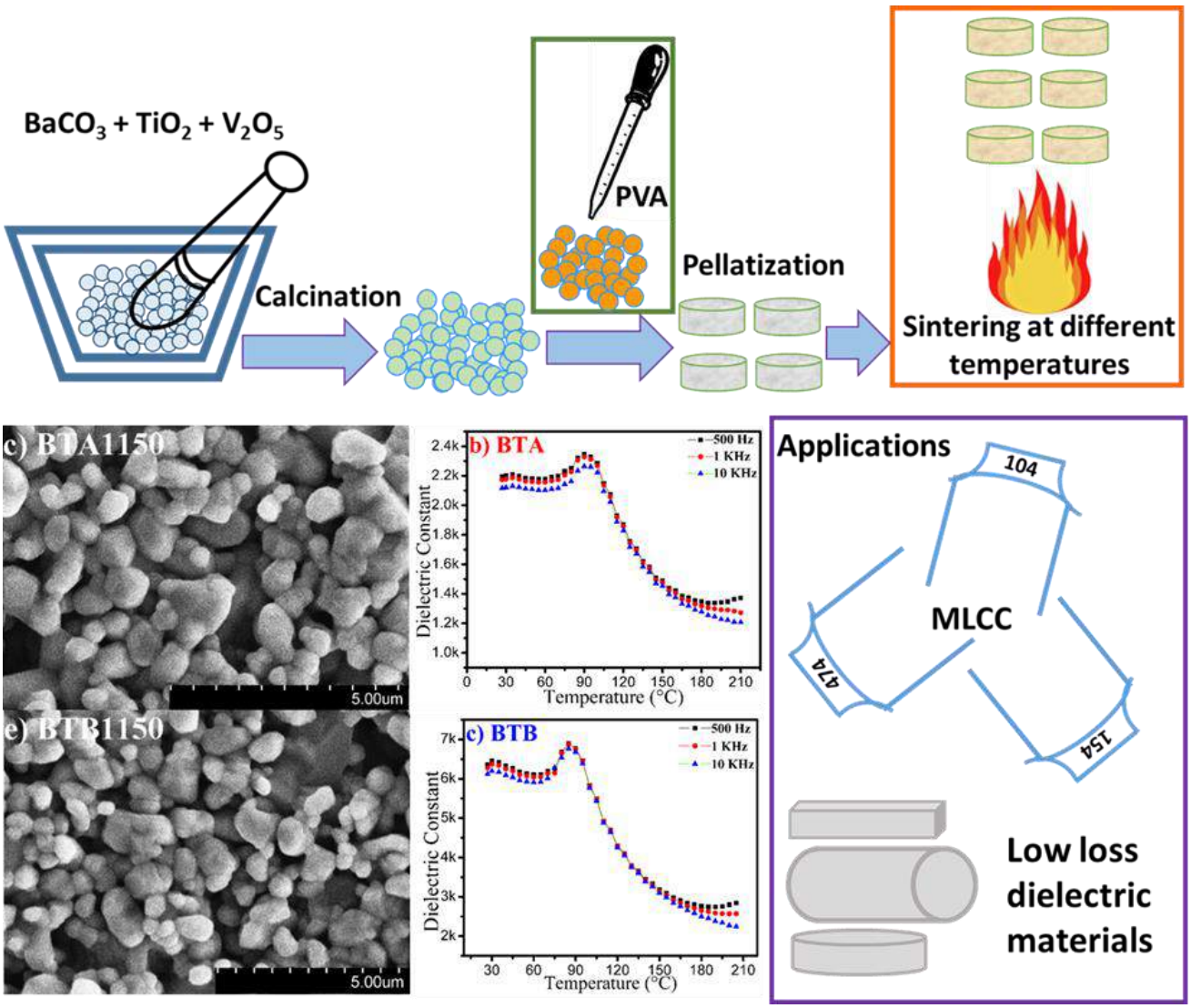
 Copyright © 2016 VBRI Press

7. LaviniaCurecheriu, Maria Teresa Buscaglia, Vincenzo Buscaglia, Zhe Zhao, and Liliana Mitoseriu, *Appl. Phys. Lett.* **2010,** *97*, 242909.
DOI: 10.1063/1.3526375
8. J. Zhang, M. W. Cole, and S. P. Alpay, *J. Appl. Phys.* **2010,** *108*, 054103.
DOI: 10.1063/1.3475482
9. Wei Cai, Chunlin Fu, JiachengGao, Xiaoling Deng, Weihai Jiang and Zebin Lin, *Mater. Sci. Forum* **2011,** *687*, 263.
DOI: 10.4028/www.scientific.net/MSF.687.263
10. Ansu Kumar Roy, K. Amar Nath, K. Prasad, Ashutosh Prasad, *Adv. Mater. Lett.* **2014,** *5(2)*,100.
DOI: 10.5185/amlett.2013.fdm.77
11. Neelam Maikhuri, Amrish K. Panwar, A. K. Jha, *J. Appl. Phys*. 2013, 113, 17D915.
DOI: 10.1063/1.4796193
12. Su-E Hao, Liang Sun, Jin-Xiang Huang, *Mater. Chem. Phys.* **2008,** *109*, 45.
DOI: 10.1016/j.matchemphys.2007.10.041
13. Wei Cai, Chunlin Fu, Zebin Lin, Xiaoling Deng, *Ceram. Int.* **2011**, 37, 3643.
DOI: 10.1016/j.ceramint.2011.06.024
14. Daisuke Nagao, Hirobumi Saito, Haruyuki Ishii, Yoshio Kobayashi, Mikio Konno, *Colloids Surf. A* **2012**, 409, 94.
DOI: 10.1016/j.colsurfa.2012.05.042
15. A.K. Nath, Nirmali Medhi, *Mater. Lett.***2012**, 73, 75.
DOI: 10.1016/j.matlet.2011.12.113
16. M.M. VijatovićPetrović, J.D. Bobić, T. Ramoška, J. Banys, B.D. Stojanović, *Mater. Charact.* **2011**, 62, 1000.
DOI: 10.1016/j.matchar.2011.07.013
17. Hongxue Liu, Baobao Cao, Charles J. O'Connor, *J. Magn. Magn. Mater.***2010**, 322, 790.
DOI: 10.1016/j.jmmm.2009.11.004
18. Chunlin Fu, Jingnan Liang, Wei Cai, Gang Chen, Xiaoling Deng, *J. Mater. Sci. - Mater. Electron.***2013**, 24, 2438.
DOI: 10.1007/s10854-013-1115-4
19. Jiangtao Zeng, Yongxiang Li, Qunbao Yang, Qingrui Yin, Mater. Sci. Eng., B **2005**, 117, 241-245.
DOI: 10.1016/j.mseb.2004.11.015
20. S. Bandyopadhyay, S.J. Liu, Z.Z. Tang, R.K. Singh, N. Newman, *Acta Mater.* **2009**, 57, 4935–4947.
DOI: 10.1016/j.actamat.2009.06.063
21. Yun Wu, Chau Nguyen, SeanaSeraji, Mike J. Forbess, Steven J. Limmer, Tammy Chou, Guozhong Cao, *J. Am. Ceram. Soc.* **2001**, 84, 2882-88.
DOI: 10.1111/j.1151-2916.2001.tb01109.x
22. Xiujian Chou, Jiwei Zhai, W and Xi Yao, *J. Am. Ceram. Soc.***2007,** *90*, 2799–2801.
DOI: 10.1111/j.1551-2916.2007.01825.x
23. Kumari, M.; Prakash, C.; and Chatterjee, R.; *J. Appl. Phys.* **2013,** *113*, 17D918.
DOI: 10.1063/1.4795425
24. Daniel J. R. Appleby, Nikhil K. Ponon, Kelvin S. K. Kwa, SrinivasGanti, UllrichHannemann, Peter K. Petrov, Neil M. Alford, and Anthony O'Neill, *J. Appl. Phys.* **2014,** *116*, 124105.
DOI: 10.1063/1.4895050
25. Wei Cai, Jiacheng Gao, Chunlin Fu, Liwen Tang, *J. Alloy. Comp.* **2009,** *487*, 668–674.
DOI: 10.1016/j.jallcom.2009.08.034
26. Lai, George Y.; *High-Temperature Corrosion and Materials Applications ASM International*, **2007**.
ISBN: 978-0-87170-853-3
27. S. Bhaskar Reddy, K. Prasad Rao, M.S. Ramachandra Rao," *J. Alloy. Comp.* **2014,** *509*, 1266.
DOI: 10.1016/j.jallcom.2010.09.211
28. Yuanliang Li, Ranran Wang, Xuegang Ma, Zhongqiu Li, Rongli Sang, Yuanfang Qu, *Mater. Res. Bull.***2014,** *49*, 601.
DOI: 10.1016/j.materresbull.2013.10.001
29. P. Mishra a, Sonia b, P. Kumar, *J. Alloy. Comp.* **2012,** *545*, 210.
DOI: 10.1016/j.jallcom.2012.08.017
30. Kumar, N.; Tirupathi, P.; Kumar, B.; Pastor, M.; Pandey, A. C.; Choudhary, R. N. P.; *Adv. Mater. Lett.* **2015,** *6(4)*, 284**.**
DOI: 10.5185/amlett.2015.6618
31. Wei Han, Zhu, J.; Sijia Zhang, Zhang Hui, Xiaohui Wang, Qinglin Wang, ChunxiaoGao, and Changqing Jin, *J. Appl. Phys.* **2013,** *113*, 193513.
DOI: 10.1063/1.4806996
32. Priyanka Arora Jha, A.K. Jha, *J. Alloy. Comp.* **2012,** *513*, 580.
DOI: 10.1016/j.jallcom.2011.11.012
33. Priyanka A. Jha, A.K. Jha, *Ceramic. Inter.* **2014,** *40*, 5209.
DOI: 10.1016/j.ceramint.2013.10.087
34. M. Ganguly, S.K. Rout, C.W. Ahn , I.W. Kim, ManoranjanKar, Structural, *Ceramic. Inter.* **2013,***39*, 9511-9524.
DOI: 10.1016/j.ceramint.2013.05.070
35. T. Limboeck and E. Soergel, *Appl. Phys. Lett.***2014,** *105*, 152901.
DOI:10.1063/1.4897361
36. Xia Huang, Jingji Zhang, LudongJi, Hongfang Qi, Jiangying Wang, *J. Alloy. Comp.* **2014,** *592*, 105–108.
DOI: 10.1016/j.jallcom.2014.01.015
37. P. A Jha and A K Jha, *Indian J. Phys.***2014,** *88(5)*, 489-496.
DOI: 10.1007/s12648-014-0445-2
38. E. Antonelli, M. Letonturier, J.-C. M'Peko , A.C. Hernandes, *J. Eur. Ceram. Soc.***2009,** *29*, 1449–1455.
DOI: 10.1016/j.jeurceramsoc.2008.09.009
39. PatriTirupathi, Nawnit Kumar, Mukul Pastor, A. C. Pandey and R. N. P. Choudhary*J. Appl. Phys*. **2015**, *117* , 074105.
DOI: 10.1063/1.4908222
40. JianQuan Qi , Bai Bo Liu , Hu Yong Tian , Han Zou , Zhen Xing Yue, Long Tu Li, *Solid State Sci***.2012,** *14*, 1520-1524.
DOI:10.1016/j.solidstatesciences.2012.08.009
41. Andreas Leschhorn, StephaneDjoumbou, and Herbert Kliem, *J. Appl. Phys.* **2014,** *115*, 114106.
DOI:10.1063/1.4868901
42. S. Bhagat, K. Amar Nath, K.P. Chandra, R.K. Singh, A.R. Kulkarni, K. Prasad, *Adv. Mater. Lett.* **2014**, *5(3)*, 117-121.
DOI:10.5185/amlett.2013.fdm.28
43. DevidasGulwade, Prakash Gopalan, *Physica B***2009**, *404*, 1799-1805.
DOI: 10.1016/j.physb.2009.02.026



Copyright © 2016 VBRI Press

Graphical abstract



Copyright © 2016 VBRI Press

Review

Wiley Online Library

ELECTROANALYSIS

DOI: 10.1002/elan.201600173

Nanocarbon-based Electrochemical Detection of Heavy Metals

Shailendra Kumar Pandey,[a] Priti Singh,[b] Jyoti Singh,[b] Sadhana Sachan,[a] Sameer Srivastava,[b] and Sunil Kumar Singh*[b]

Abstract: Heavy metal species are toxic, non-decomposable molecules which exist in our ecological systems and food chains, eventually exposing us to serious health hazards and economic damage. In this context, various attempts have been made for sensitive detection of heavy metal ions through electrochemical sensor. Carbon nanomaterials endowed with unique physiochemical properties were found to be most suitable for electrochemical detection of heavy metal due to their ease to modify, high sensitivity, good selectivity and high reproducibility. Here, we present a critical review about detection of heavy metals using nanocarbon with focus on graphene and carbon nanotubes in various sources of water, soil, and foods for fast and sensitive detection of heavy metal ions. We have evaluated the current trends and discussed the major challenges associated with electrode modification and electrochemical analysis with the aim to achieve the best sensing performance.

Keywords: Electrochemical sensor · Graphene · Heavy metals · Nanocarbon · Voltammetry

1 Introduction

Heavy metals (HMs) are the elements having metallic nature and belong to the family of transition metals, metalloids, lanthanides, and actinides. According to Srivastava and Majumder (2008), HMs are elements having atomic weights between 63.5 and 200.6, and a specific gravity greater than 5 [1]. Some HMs such as iron, copper, cobalt, manganese, molybdenum, and zinc are required for proper growth of plants and animals. But excessive levels of these essential metals could also lead to detrimental effect on living organisms. Other HMs like mercury, chromium, cadmium, arsenic and lead are poisonous and highly undesirable even at low concentrations (<2 ppb). Short-term damage of HMs on human includes skin discoloration, stomach pain, nausea, vomiting, and diarrhea whereas long-term exposure leads to serious illness and cancer.

HMs naturally occur in the earth's crust and contaminate the waste water through various channels. The deposition and erosion of HMs are naturally occurring phenomena which are difficult to control. The runoff of water from different sources such as landfill, manufacturing process of glass, electronic parts, paints and used batteries are the main cause of HMs pollution [2–4]. Waste residues and sludge from electroplating industries, wood processing units, printed circuit board (PCB) manufacturing and petroleum refining are the primary generators of HMs contamination in surface and ground water [5–7]. HMs bioaccumulation in the soil reduced the crop yield and may cause risk to human health when transferred to the food chain (Fig. 1) [3,8]. These effects comply with the requirement for efficient monitoring of toxic metal by rapid and simple analytical methods. Challenged to a greater extent of stringent regulations, nowadays regular monitoring of HMs in both water and soil has become the most critical issue across the world. The standard guidelines of these metal ion concentrations in drinking water by the US Environmental Protection Agency (US EPA) and Central Pollution Control Board (CPCB) India are shown in Table 1. The Indian standard for industrial waste water effluent discharge into inland surface and public sewer has also been tabulated. Exposure to these toxic metal ion leads to various health problems in human and causes detrimental loss in economy.

The composite materials based on the different metal alloy were also implanted on biomedical devices that are being converted by a redox process into its ionic form. This provides their indirect response to toxicity and inflammation [9]. Advanced techniques for analysis of HMs employed are the essential prerequisite at all stages from its sources of contamination to the final usage for safety of human health. Various types of analytical techniques in recent years are in convention, including atomic absorption spectroscopy (AAS) [3] inductively coupled plasma-mass spectrometry (ICP-MS) [10], ion chromatography [11] for determination of HMs. The conventional analysis for regular monitoring of HMs is time consuming and involves complex procedures and bulky instruments. The regular, on-site controlled monitoring of HMs needs

[a] S. K. Pandey, S. Sachan
Department of Chemical Engineering, Motilal Nehru National Institute of Technology Allahabad, Allahabad-211004, India

[b] P. Singh, J. Singh, S. Srivastava, S. K. Singh
Department of Biotechnology, Motilal Nehru National Institute of Technology Allahabad, Allahabad- 211004, India
*e-mail: singh.sunil06@gmail.com

© 2016 Wiley-VCH Verlag GmbH & Co. KGaA, Weinheim

rapid and reliable sensor system with a lower limit of detection. For the last fifteen years many research articles have been published for the electrochemical detection of HMs, however in last five years reports have been increased drastically due to exploitation of variety of nanomaterials-based electrochemical techniques for the analysis of HMs (see Fig. 2). Nanosensors have been developed for HMs detection at different sources of industrial wastewater and drinking water [12,13] soil [14–16]; food [17–19]; milk [20] and herbal drugs [21–22]. In the recent studies, carbon-based nanomaterials (nanocarbons) have been widely explored for the metal ion sensing. The present review mainly focuses on the recent developments in the nanocarbon-based electrochemical detection of HMs.

2 Electrochemical Sensor in HMs Detection

In recent years, research has been focused on developing chemical sensor for analysis of metal ions at very low molar concentration. Chemical sensors cover all-encompassing devices employed to monitor, measure and analyze chemical signal as generated due to changes in ana-

Shailendra Kumar Pandey received his Master of Technology degree in Chemical Engineering from the National Institute of Technology Rourkela, India, in 2010. He is pursuing PhD from the Motilal Nehru National Institute of Technology (MNNIT) Allahabad. His current research interest focus on the graphene based materials and polymerized composites for chemical sensors.



Priti Singh received her Master of Technology degree in Nanoscience and Technology from the Delhi Technological University in 2013. She is a PhD scholar at the Department of Biotechnology, Motilal Nehru National Institute of Technology (MNNIT) Allahabad. Her current research is focused on prospective biomedical nanomaterials.



Jyoti Singh received her Bachelor degree in Science from the Allahabad University and Post Graduate degree in Biotechnology from the Amity University in 2011. She is a PhD student at the Department of Biotechnology of the Motilal Nehru National Institute of Technology (MNNIT) Allahabad. Her current research is focused on the development of diagnostic tools for the detection of pathogenic bacteria.



Dr. Sadhana Sachan is currently an Associate Professor at the Motilal Nehru National Institute of Technology (MNNIT) Allahabad. She received her PhD degree in Chemical Engineering from the Indian Institute of Technology Kanpur in 2005. Her research interest is focused on the synthesis and development of carbon composite materials for environmental applications.



Dr. Sameer Srivastava is currently working as an Assistant Professor at Motilal Nehru National Institute of Technology (MNNIT) Allahabad. He received his PhD degree in Biotechnology from the National Chemical Laboratory (NCL) Pune in 2009. He received the Endeavour Award from the Australian Government and DBT Research Associate Fellowship from the Department of Biotechnology, India. His main research interest is focused on biochemistry including molecular biology.



Dr. Sunil Kumar Singh is currently an Assistant Professor (INSPIRE Faculty) at the Motilal Nehru National Institute of Technology (MNNIT) Allahabad. He received his PhD in Biotechnology from the Institute of Medical Science, Banaras Hindu University in 2012. He received the DST-INSPIRE Faculty Award from the Department of Science and Technology (DST) India. He is also awarded with the NASI-Young Scientist Platinum Jubilee Award from The National Academy of Sciences Allahabad, India, INSA Medal for Young Scientists from the Indian National Science Academy, India and Foundation of Science and Technology (FCT) Postdoctoral Fellowship, Portugal. His main research interests include the application of nanomaterials in electrochemistry, nanomaterials-cell interactions and biomedical applications of nanomaterials.



© 2016 Wiley-VCH Verlag GmbH & Co. KGaA, Weinheim

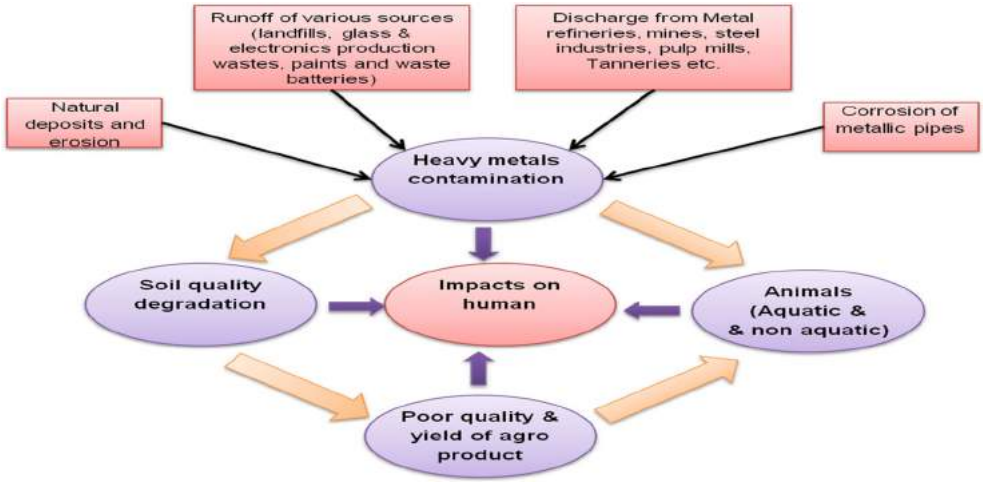


Fig. 1. Heavy metal contamination from its sources to final impact on human.

Table 1. Standards for heavy metal concentration in drinking water and industrial effluent discharge.

Heavy metals	Drinking water Standard (mg/L)		Maximum permissible limit for industrial effluent discharges in India (mg/L) [25,26].		Health Effects from Long-Term Exposure Above the permissible limit
	US EPA (MCL)[23]	*Indian standard (IS:10500)** [24]	*Into inland surface IS-2490*	*Into Public sewers IS-3306*	
Arsenic	0.010	0.01–0.05	0.2	0.2	Skin damage, carcinogenic, problems with circulatory systems, hyperkeratosis. [27,28]
Cadmium	0.005	0.003-NR	2.0	1.0	Liver damage, renal dysfunction cardio vascular system affected lung emphysema. [2,29]
Chromium	0.1	0.05-NR	0.1	2.0	Lung and stomach cancer, increased risk of bone, prostate, lymphomas. [28,30]
Copper	1.3	0.05–1.5	3.0	3.0	Gastrointestinal distress, nausea, abdominal pain, kidney disorders. [31]
Lead	0.015	0.01-NR	0.1	1.0	Risk for Alzheimer, mutagenic, anemia, abdominal pain, gradual paralysis in the muscles, convulsions, coma, renal failure, cancer [32,33]
Mercury	0.002	0.001-NR	0.01	0.01	Lung damage, paresthesia, malaise, severe kidney and nervous system disorder, coma [2,34]
Iron	0.3	0.3-NR	3.0	3.0	Haemochromatosis [35]
zinc	5.0	5.0–15.0	5.0	15.0	Gastro intestinal irritation; leukopenia, neutropenia, hypoferraemia, abdominal pain, chest pain, cough and dizziness [36,37]

* Lower limit is the desirable value and upper limit is permissible only in the absence of alternate source, NR – No relaxation

lyte concentration [38]. Electrochemical Sensor (ECS) provides low detection limit, high sensitivity, high surface area, good reproducibility, better signal-to noise ratio and selective sensing of more than one metal ion [12,39]. It is a tool that adapts the chemical information of sample and converts it into an analytical signal. The chemical information originated by the physical property of the system or by the reaction of the species present in the analyte was utilized in the receptor unit (working electrode), which further transformed in electrical signal by the potentiostat/galvanostat based electrochemical workstation as transducer system. The final analytical useful results can be deliberated by applying various modes of signal amplifications techniques such as potentiometry, voltammetry, conductommetry and electrochemical impedance spectroscopy. Different modification of working electrode can be carried out for enhancing the sensitivity, selectivity and reproducibility of the electrochemical sensor. A schematic view of ECS has been shown in Fig 3A, with scope of utilizing various working electrodes. The cyclic voltammetry (CV) method is widely used for understanding the redox processes and reaction intermediate comparatively less sensitive for quantification. The square wave voltammetry (SWV) method has been proved to be more sensitive and faster than the CV and differential pulse voltammetry (DPV) methods for determination of trace metal ions. In common SWV voltammetry, the accumulation of metal ions is mainly due to sorption of complexes at the

© 2016 Wiley-VCH Verlag GmbH & Co. KGaA, Weinheim

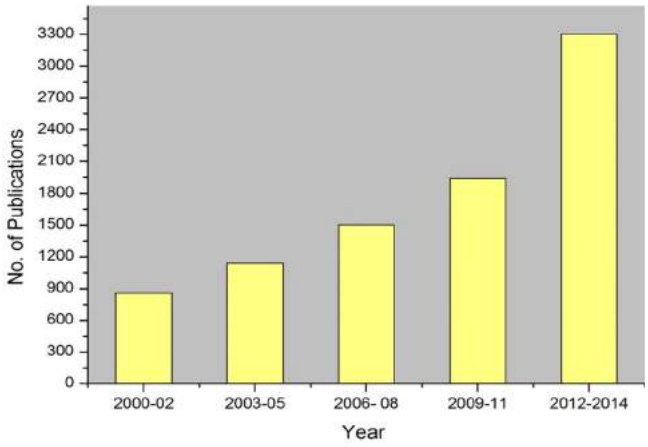


Fig. 2. Number of articles published during the last fifteen years for electrochemical based detection of heavy metal. Data were taken on April 15, 2015 from www.sciencedirect.com using "heavy metal" and "electrochemical detection" in the advanced search option.

surface of the electrode in open circuit condition. Metal ions like Cr and Al were quantified by adsorptive stripping voltammetry after complexation with cupferron [40,41] and Ni and Co were detected after complexation with dimethylglyoxime [42]. In general, SWV involved single step for metal detection in which the metal ion is interacted with active sites of electrodes *via* sorption while sensitivity in metal ion quantification is significantly increased by involving two step stripping voltammetry methods.

This is attributed to more effective accumulation of metal ion by applying potential (anodic and cathodic) over the electrode for certain duration. This method is capable of determining five to six analyte samples simultaneously at below sub-ppb levels. In anodic stripping voltammetry (Fig. 3B), the accumulated metal ion (M^{n+}) reduced to M^0 on applying negative potential. In stripping step, the metal ion is stripped back to the electrolytic solution towards positive potential scanning (M^0 to M^{n+}). The stripping peak current is directly proportional to the quantity of accumulated metal ion and selectivity of the metal ion is determined with the peak potential [43]. Traditionally, the stripping voltammetry method is employed with hanging mercury drop electrodes (HMDE) due to more clean surface regeneration with new drop. Mercury thin film electrodes are more advanced and could be an alternative to HMDE. But both these electrodes are now strictly limited due to obvious toxicity concerns. Alternatives to mercury based electrodes bismuth-film electrodes (BFEs) were introduced in year 2000 which are more environmentally friendly with negligible toxicity [44].

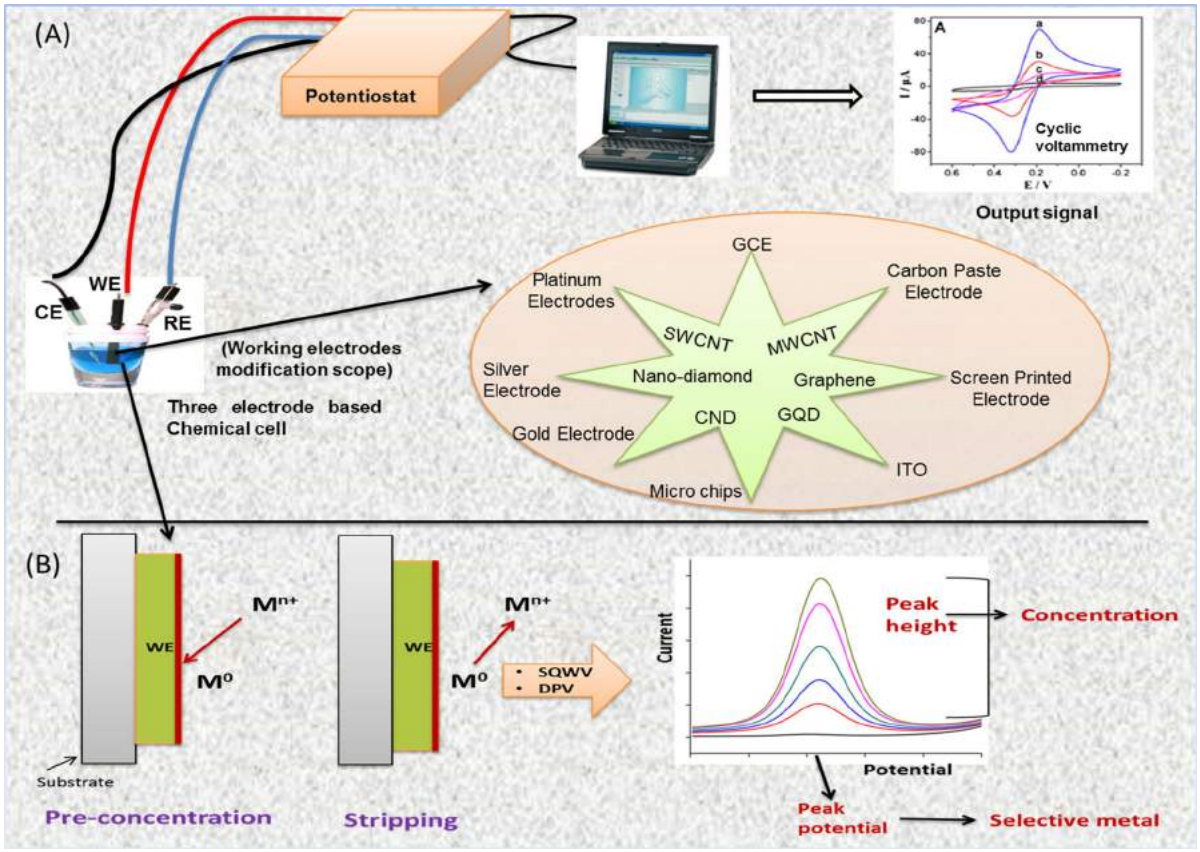


Fig. 3. (A) Schematic representation of ECS working platform and scope of utilizing different modified working electrodes (B) Principle of anodic stripping voltammetry for metal ion detection.

© 2016 Wiley-VCH Verlag GmbH & Co. KGaA, Weinheim

The higher homogeneity of bismuth film offers improved analytical performances for lead detection [45]. The two main strategies of including bismuth modified electrodes for heavy-metal ion sensing: (1) Ex-situ, preplating of bismuth, (2) In situ, bismuth precursor added directly into the solution to be analyzed, and the analyte is incorporated as the Bi film is formed. The detection of lead at the surface of a Bi electrode is due to the capacity of Bi to form a fused alloy and thus easier to get reduced. Effect of bismuth microstructures for Sn(II) sensing ability was investigated by Lien et al. (2013) [46]. A synergistic effect between bismuth grain size and preferred orientation ratio, *i.e.* diffraction intensity ratio of facets Bi (1 1 0) and Bi (0 1 2) leads to enhancement in Sn(II) sensing ability with concentration varying from 0.2 to 95 ppm. Antimony film electrodes was also utilized by Hocevar et al. (2007) for metal ion detection and found similar stripping behavior to bismuth film electrodes [47]. In current years, nanomaterials-based ECS has become the most vibrant field in environmental analysis [48]. Compared with the traditional macroelectrodes, the nanomodified electrodes have big mass sensitivity, an increased mass-transport rate, a decreased influence of the solution resistance, and a higher signal-to-noise ratio [49,50]. Due to unique physiochemical properties, nanomaterials are now being widely explored for electrochemical sensing [51–53]. Metal oxide based nanomaterials such as TiO_2, zirconium and cobalt oxide are widely used in modifying the electrodes [54,55]. Gold modified electrodes which is widely been explored in the area of bioagents and DNA sensing [56,57] has also been used for HMs detection [58]. Screen-printed gold electrode was employed by Wan et al. (2015) for analysis of lead and copper [59]. Gold nanoparticles electrodeposited over the spin coated nafion/GCE electrode through cyclic voltammetry were used by Huang et. al (2013) for the selective detection of arsenic(III) with LOD ~ 0.047 μg/L [53]. Mercury electrodes were previously applied but its applicability may be limited due to its toxicity [60,61]. In electrochemical sensing, from last one decade, carbon material based electrodes like glassy carbon electrode (GCE), screen printed carbon electrode (SPCE) and electrodes prepared from graphite carbon pastes is widely been utilized for HMs detection [62–64]. Shams and Torabi (2006) used the carbon paste electrode modified with inorganic zirconium for determination of cadmium [65]. Zeolite modified carbon paste over ITO were exploited for making the sensing platform for Cd(II) and Pb(II) ions in groundwater and industrial effluents [66]. Several attempts for utilizing carbon paste and screen printed electrodes modified with other non nanocarbon based compound are presented in Table 2. Nanocarbon materials are proven better for electrode modification in ECS due to its good conductivity and organic nature. Due to unique electronic properties, these carbon based nanomaterials are of great concern in the area of chemical sensing including detec-

Table 2. Carbon paste and screen printed electrodes modified with non- nanocarbon composites for metal ion sensing.

Electrode fabricated	Metal ion	Detection limit	Linear range	Method	Matrix Applied	Ref.
CP/Bismuth/OPFP	Cd(II)	0.10 μg/L0.12 μg/L	1–100 μg/L	SWASV	Soil	[16]
	Pb(II)		1–100 μg/L			
SPC/Hg	Cd(II)		5–100 μg/L	CV	Herbal drugs	[22]
	Pb(II)		5–100 μg/L			
Graphite/epoxy/DPC CP/DPC	Cr(VI)	6.3×10^{-7} M	10^{-6}–10^{-2} M	CV	River	[48]
	Cr(VI)	9×10^{-7} M	10^{-6}–10^{-2} M	CV		
CP/TiO_2/ZrO_2	Cd(II)	7.6×10^{-6} M	10^{-2}–5×10^{-5} M	CV		[55]
	Pb(II)	1.1×10^{-5} M	10^{-2}–10^{-5} M			
CP/SBA-15 silica/IL	$Cd^{(I}I)$	8.0×10^{-8} M	0.6–30 μM	DPASV	Tap, River, Hair	[62]
	Pb(II)	4.0×10^{-8} M	0.4–90 μM			
	$Cu^{(I}I)$	6.0×10^{-8} M	0.3–100 μM			
	$Hg^{(I}I)$	1.0×10^{-8} M	0.08–50 μM			
CP/N-BDMP	Cd(II)	6.6 μg/L	10–2000 μg/L	SWASV	Tap, Fish, Plant food stuff	[63]
	Hg(II)	8.2 μg/L	10–2000 μg/L			
CP/SBA-15 silica	Pb(II)	4.0×10^{-8} M	0.3–7.0 μM	DPASV	Well, sugar caIvane spirit	[64]
	Cu(II)	2.0×10^{-7} M	0.8–10.0 μM			
	Hg(II)	4.0×10^{-7} M	0.2–10.0 μM			
CP/SH-SAMMS	Pb(II)	0.5 ppb	10–1500 ppb	SWASV		[77]
	Hg(II)	3.0 ppb	20–1600 ppb			
CP/Sb	Cd(II)	0.8 μg/L	5–50 μg/L	SWASV	Lake	[78]
	Pb(II)	0.2 μg/L	5–50 μg/L			
CP/Poly(1,8-DAN)	Pb(II)	30.0 μg/L	0.2–10 μM/L	DPV	Tap and seawater	[79]
CP/Bi-zeolite	Cd(II)	0.08 μg/L	1–20 μg/L	DPSV	Tap and sewage	[80]
	Pb(II)	0.10 μg/L	1–20 μg/L			
SPC/EAG	Hg(II)	4.6 ppb	0.05–14.7 ppm	CV, DPV	River	[81]
SPC/Au	Hg(II)	3.3 μg/L	5–100 μg/L	SWASV	Tap, River	[82]

CP – Carbon paste, SPC – Screen printed carbon, DPC – Diphenylcarbazide, IL – Ionic liquid, N-BDMP – Nitro benzoyl diphenylmethylenphosphorane, DAN – Diaminonaphthalene, SH-SAMMS – Thiol terminated self-assembled monolayer on mesoporous silica, EAG – Electrochemically activated graphite, OPFP – n-octylpyridinium hexafluorophosphate (Ionic liquid).

© 2016 Wiley-VCH Verlag GmbH & Co. KGaA, Weinheim

tion of wide categories of organic chemicals, bio-agents, blood glucose, cholesterol and DNA detection [57,67–69]. Nanocarbon modified electrodes are being successfully employed for the sensitive and selective detection of HMs ion (Fig. 3A) [70–73].

3 Nanocarbon in Electrochemical Sensing

Nanocarbon materials include single walled carbon nanotubes (SWNTs), multiwalled carbon nanotubes (MWNTs), graphene, nanodiamonds, fullerenes and graphene quantum dots (Figure 4). The most widely explored nanocarbon derivatives in electrochemical sensing are CNTs and graphene. Thin gap between the electronic shells makes the carbon into three different (sp, sp^2, sp^3) hybridized forms. These forms are exploited for the formation of different organic compounds and nano-carbon materials. The allotropes of carbon with cylindrical nanostructure like carbon nanotubes (CNTs) are a member of the fullerene structural family. They exhibit extraordinary strength and unique electrical properties. CNTs normally, act as preconcentrator agent and transducer platform having numerous advantage such as large effective detection surface, fast electron transfer rate compared to bulk carbon electrodes, high electrocatalytic activity and low electrode fouling [74,75]. CNTs are attached to electrode surface either by functionalization or by incorporation on polymeric film and exhibit low background current, chemical inertness with wide potential window [76].

Graphene is merely one of many parallel sheets constituting graphite of sp^2-bonded carbon with a honeycomb structure. Graphene has high mechanical strength [83,84], thermal conductivity, optical properties [85] tunable band gap [86] and electron transport capabilities [87]. The transfer of electrons between graphene and the molecule in the aqueous solution occurs at the edges of the graphene or at defects in the basal plane. Graphene is endowed with high surface area (theoretically 2630 m^2/g for single-layer graphene) that enables large amounts of defects and thus generates more electro-active sites [88,89] on graphene surface providing great potential in the development of sensing materials. It is an ideal material for the construction of sensor devices in various transduction modes, from electrical and electrochemical transduction to optical transduction [90]. Other known carbon material used for HMs detection is fullerenes which were mostly applied for chromatographic speciation of metal ions. Some attempts have been done in metal detection based on fullerenes and carbon nano dots [91–93]. Functionalized nanocarbon provides the perfect scaling of anodic and cathodic currents and proved to be promising materials as transducer for chemical sensing. The output signal response of these materials is found to be stable with good reproducibility. Depending upon the characteristics of analytes various types of electrodes and their modification with carbon nanomaterials has been carried out for their respective identification in different matrixes. CNTs, graphene, nanodiamond and other carbon based sensor platform for detection of HMs were discussed in details in the classified section.

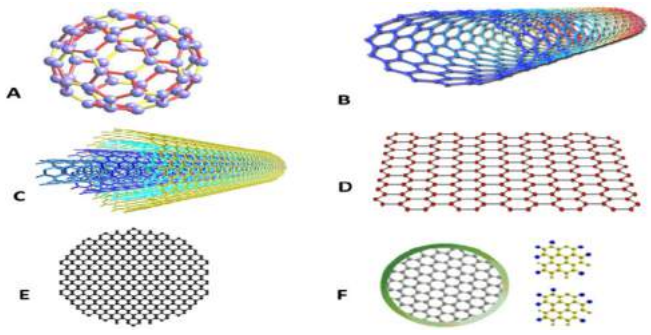


Fig. 4. Structures of Nanocarbon (A) Fullerene (B) SWCNT (C) MWCNT (D) Graphene (E) nano-diamond (F) Graphene quantum dots.

3.1 CNTs Based Sensor for Metal Ion Detection

Numerous attempts have been carried out to explore the sensing potential of CNTs (utilized in different platform) towards HMs detection (see Table 3). MWCNTs modified gold electrode exploited for trace detection of As(III) and Bi(III) and found acceptable for HMs detection in saline water without desalting the sample [76]. Hwang et al. (2008) reported preparation of bismuth film by in situ plating of bismuth onto the screen-printed CNTs electrode [84]. The electrodes provide well-defined, sharp stripping and reproducible signals for lead, cadmium and zinc simultaneously. The more evidently enhanced performance for lead detection comparing with bare electrodes have been done using CNT/Bi-modified GCE [94], screen-printed CNTs with plated bismuth film [95] and a CNT/Bi nanoelectrode array [96].

Bagheri et al. (2013) utilized MWCNTs with triphenylphosphine and ionic liquid for sensitive and real-time analysis of Cd(II), Pb(II) and Hg(II) [52]. Fig. 5A shows the nyquist plots of the bare CPE and other modified electrodes. The equivalent circuit can be described as solution resistance (R_s) in series with the parallel circuit of double layer capacitance (C_{dl}) and faradic impedance (Z_f). Faradic impedance is composed of charge-transfer resistance (R_{ct}) and Warburg impedance (Z_w) which accounts for the Nernstian diffusion. There have been non-significant changes in value of Rs and Zw on modification of electrodes, so it is concluded that they were not affected by the modification on the electrode surface. But the R_{ct} value of MWCNT/PPh3/IL/CPE electrodes has remarkably decreased to about 72%, of the unmodified electrodes (421.6 Ω). Also the comparable SWV of these electrodes for cadmium, lead and mercury ions (40 nM) have been shown in Fig. 5B. The more intense peak for MWCNT/PPh3/IL/CPE electrodes shown that more target metal ions were attached on the surface of electrode when MWCNTs was modified with the ionic liquid as compared to PPh3/IL/CPE electrodes. The MWCNT

© 2016 Wiley-VCH Verlag GmbH & Co. KGaA, Weinheim

Table 3. CNTs based detection of metal ion. Electrode fabricated

	Metal ions	Detection limit	Linear range	Method	Matrix applied	Ref.
MWCNTs/peptide	Cd(II)	2.749×10^{-8} M	0.1–50.5 ppm	CV	Waste water	[12]
	Hg(II)	9.068×10^{-10} M	0.1–50.5 ppm			
MWCNTs/PPh3/IL	Cd(II)	7.4×10^{-5} μM	10^{-4}–0.15 μM	SWASV	Soil, tap and waste water	[52]
	Pb(II)					
	Hg(II)	6.0×10^{-5} μM	10^{-4}–0.15 μM			
		9.2×10^{-5} μM	10^{-}–0.15 μM			
MWCNTs/nanoPt-Fe(III)/GCE	As(III)	10 nM	0.01–0.3 μM	ASLSV		[72]
SWCNT-PhSH/Au	Hg(II)	3 nM	5–90 nM	SWASV	Tap and river water	[73]
MWCNTs/Au	As(III)		0.3–50 μg/L	DPV	Tap and Sea water	[76]
SPCNT/Au	Hg(II)	0.2 μg/L	0.5–50 μg/L	SWASV	Tap and river water	[82]
CNTs/Bi	Cd(II)	0.7 μg/L	20–100.0 μg/L	SWASV	River water	[95]
	Pb(II)	1.3 μg/L	20–100.0 μg/L			
	Zn(II)	12 μg/L	20–100.0 μg/L			
MWCNTs/Chit-SH/GCE	Hg(II)	3 nM	10–140 nM	SWASV	River water	[98]
CNTs tower	Cd(II)	2.5×10^{-2} μM	1.0–4.0 μM	ASV,		[99]
	Pb(II)	1.2×10^{-2} μM	0.5–3.0 μM	OSWSV		
	Cu(II)	4.4×10^{-2} μM	1.5–6.0 μM			
	Zn(II)	6.7×10^{-2} μM	2.0–8.0 μM			
Cu-IIP-CNT-MCPE	Cu(II)	0.34 μg/L	2–120 μg/L	DPASV	Tap, well, river, human hair	[100]
$Zn_3(PO_4)_2$@MWCNTs-DNA	Hg(II)	0.071 nM	0.1–50 nM	EIS	Tap and river wate	[101]
MWCNTs/Schiff base	Pb(II)	6.00×10^{-4} μM	2×10^{-3}–0.7 μM	SWASV	Sea water, tobacco, marine and human teeth	[102]
	Hg(II)	9.00×10^{-4} μM	2×10^{-3}–0.7 μM			
L/MWCNTs/CPE(IL)	Cd(II)	0.070 μg/L	0.2–23 μg/L	DPASV	Tobacco, hair, milk powder, Edible fungi	[105]
MWCNTs/NA/Bi/SPE	Pb(II)	0.01 μg/L	0.05–100 μg/L	DPASV		[106]
	Zn(II)					
	Cd(II)		0.5–100 μg/L			
			0.5–80 μg/L			

PPh3 – Triphenyl phosphine, Chit-SH – Thiol functionalized chitosan, PhSH – thio phenol, SPCNT-screen-printed carbon nanotubes, SWASV – Square wave anodic stripping voltammetry, OSWSV – Osteryoung Square Wave Stripping Voltammetry, ASLSV – Anodic stripping-linear sweep voltammetry, Cu-IIP-CNT-MCPE – Cu(II)-ion imprinted polymer-carbon nanotube-modified carbon paste electrode, NA – Nafion

provides large surface area and the special surface characteristic like unsaturated suspending bonds, pentagons carbon loops, pentagon-heptagon defect pairs can cause interactions between carboxylate and the analytes at the electrode interface. This interaction leads to pose effective chelation which may provide lower detection limits.

Shin & Hong (2010) has exploit Pt-Fe(III) electrodeposited MWCNTs-Nafion nanocomposites film for the sensitive determination of As(III) [72]. Ashrafi et al. (2014) fabricated electrode from MWCNT modified with antimony nanoparticles (SbNPs) using carbon paste and found to me more sensitive and enhanced peak signal than the Sb film carbon paste electrode [97]. Besides, MWCNT electrode containing Sb showed the enhanced analytical signal (more than double) as compared with MWCNT alone for detection of Cd^{2+} and Pb(II). Authors proposed that Sb particles size on the coated layer influenced the oxidation current and analytical signal and it decreased in order of Sb-nanoparticle > Sb-film > Sb-microsphere. This might be due to larger quantities of active sites formation on increased large surface area of electrodes that leads to more accumulation and deposition of metals at the electrode surface. Thiol functionalized chitosan films with MWCNTs showed the strong adsorption ability of Hg(II) with a well-defined stripping response [98]. Osteryoung square wave stripping voltammetry (OSWSV) was applied with a new type of highly aligned MWCNTs tower electrode for trace analysis of Pb(II), Cd(II), Cu(II) and Zn(II) [99].

Ashkenani and Taher (2012) have selectively detected copper using Cu(II)-ion imprinted polymer-carbon nanotube film through formation of 1-(2-pyridylazo)-2-naphthol complex [100]. In this stripping voltammetry method, accumulation of ions using both with and without an applied potential (closed or open circuit condition) is compared and revealed that the open circuit condition is more selective than closed circuit condition.

He et al. (2016) recently developed new strategy through electrochemical impedence spectroscopy (EIS) for the detection of mercury using multifunctional $Zn_3(PO_4)^{2-}$ based nanocomposites containing Hg(II) - targeted DNA strands [$Zn_3(PO_4)^{2-}$@DNA] and MWCNTs immobilized with Hg(II)-targeted DNA strands [$Zn_3(PO_4)^{2-}$@MWCNT-DNA] (See Figure 6). The formation of T-Hg(II)-T coordination between DNA and Hg(II) ions provides more advantages including high ad-

© 2016 Wiley-VCH Verlag GmbH & Co. KGaA, Weinheim

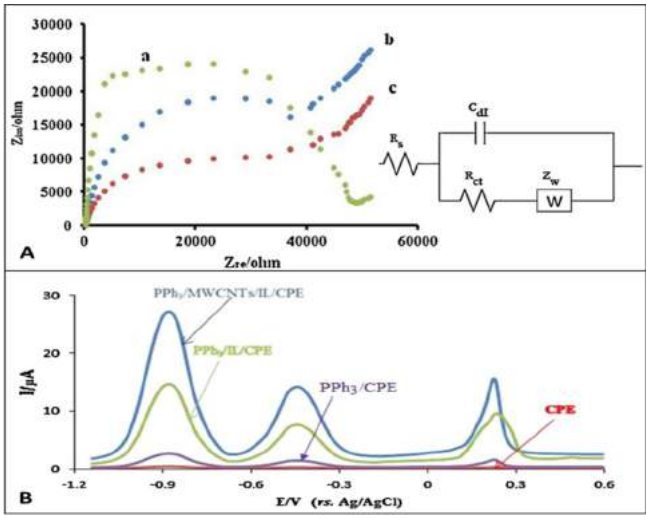


Fig. 5. (A) Nyquist plots for different electrodes in $Fe(CN)_6^{3-/4-}$ containing 0.1 M KNO_3: (a) unmodified CPE, (b) IL/CPE, (c) PPh_3/MWCNT/IL/CPE. Inset shows the equivalent circuit compatible with the nyquist diagram for this system. (B) Square wave anodic stripping voltammograms of cadmium, lead and mercury ions (40 nM) using various electrodes in 0.1 M KNO_3/ 0.1 M HCl solution of pH 3.0. Accumulation time = 75 s. Preconcentration potential = −1.2 V. [Reproduced with permission from [52] © Elsevier 2013].

sorption amounts of Hg(II) originated from hollow nanostructure of $Zn_3(PO_4)^{2-}$ and direct selective detection of Hg(II) because of immobilized T-rich DNA strands [101]. MWCNTs immobilized biosensor showed enhanced electrochemical activity with a detection limit of 0.071 nM as compared to non-MWCNTs biosensor due to more improved crystallization degree. Rahman et al. (2012) utilized the cyclic dipeptide modified MWCNTs gold electrode for simultaneous analysis of Cd(II) and Hg(II) [12]. The results were ascertained to be highly sensitive, stable and convenient for analysis of electroplating and wood treatment industry wastewater sample comparable with ICP-OES conventional method. Wei and his group confirmed strong chelation strength towards the mercury ion through thiol groups with the detection limit of 3.0 nM using SWCNT film-gold electrode [73]. 4-methoxybenzylideneamino-2-thioxothiazolodin-4-one as a newly synthesized Schiff base with MWCNTs was constructed and suitably performs the accurate detection of Pb(II) and Hg(II) ions in various real samples up to nano-molar levels [102].

Besides above discussed direct determination of metal ions, few attempts based on enzymatic based indirect HMs detection has also been done. Recently Moyo and Okonkwo (2014) utilized maize tassel (MT)-MWCNT composite for the detection of cadmium using hydrogen peroxide (H_2O_2) biosensor through inhibitive measure-

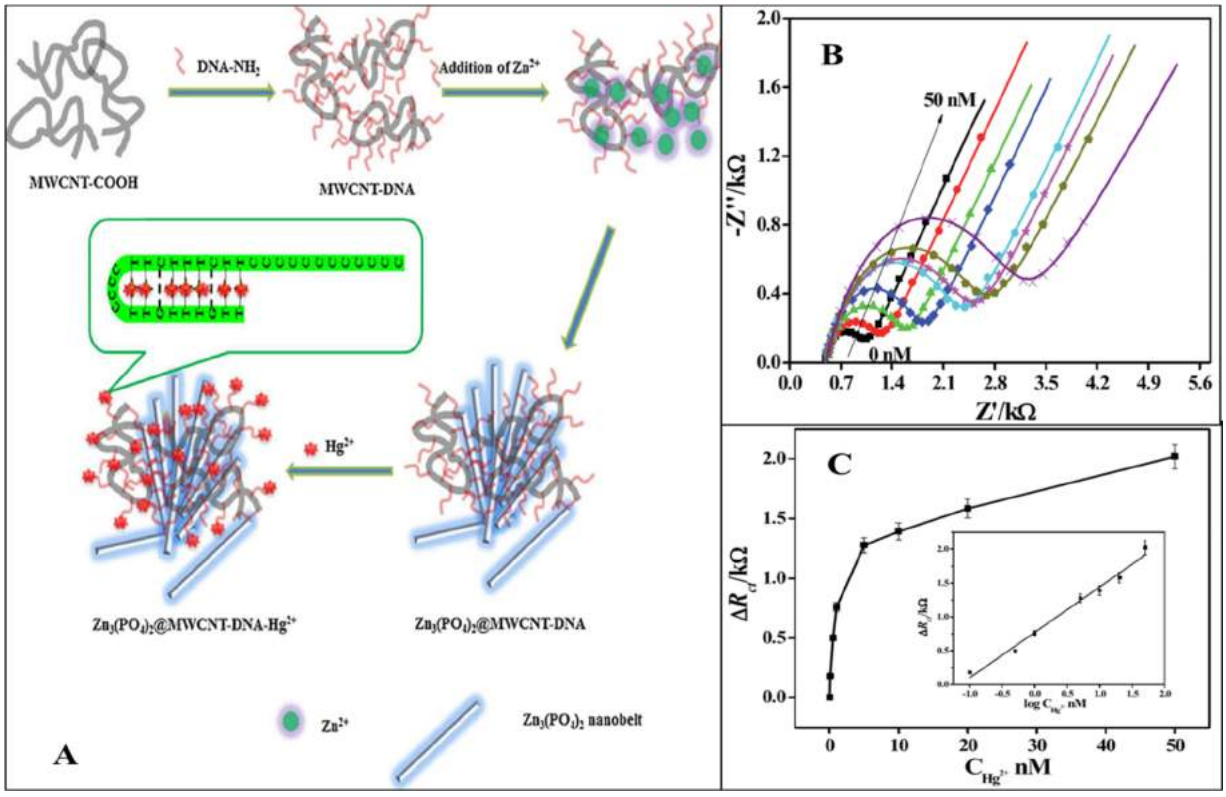


Fig. 6. (A) Schematic diagram of the Hg(II) detection using the electrochemical biosensor based on $Zn_3(PO_4)^{2-}$@MWCNTs-DNA nanoblet. (B) EIS Nyquist plots for the detection of different concentrations of Hg(II) ions. The concentrations are of 0, 0.1, 0.5, 1, 5, 10, 20 and 50 nM. (C) The linear fit plots ΔR_{ct} as function of the logarithm of Hg(II) concentration (inset). Error bar represents the standard deviation of three parallel experiments. [Reproduced with permission from [101] © Elsevier 2016].

© 2016 Wiley-VCH Verlag GmbH & Co. KGaA, Weinheim

ment [103]. The schematic representation of stepwise biosensor fabrication process and inhibitive measurement of immobilized HRP activity in Cd^{2+} ion solution were shown in figure 7A. The determination of Cd(II) was performed based on inhibition of electrocatalytic HRP enzyme activity to reduce H_2O_2. The decrease in the reduction current found to be proportional to the concentration of the trace metal ion inhibited the enzyme activity (linear range 5 to 30 $\mu g L^{-1}$; LOD 0.51 $\mu g L^{-1}$) (Figure 7C).

The CV response of the HRP/MT-MWCNT/GCE biosensor with different concentration of Cd(II) has been shown in Fig. 7B. This similar maize tassel-MWCNT electrode was also utilized in another work for inhibitive determination of Pb(II) and Cu(II) with LOD of 2.5 $\mu g L^{-1}$ 4.2 $\mu g L^{-1}$ respectively [104]. This inhibition was determined to be reversible with mixed mechanism (competitive and non-competitive) for both metal cations.

3.2 Graphene Based Sensor for Metal Ion Detection

The sensitivity and selectivity of metal ion detection using graphene could be enhanced by differential functionalization. Sahoo and co-workers deposited bismuth nanoparticles by in situ modified Hummers method on the surface of reduced graphene oxide (RGO) for simultaneous analysis of Cd(II), Pb(II), Cu(II) and Zn(II) [39]. Fig. 8 shows DPASV and linear calibration plot across the concentration range from 20 to 120 mg/L with lower detection limit of 0.55 µg/L for Pb(II). Bismuth nanoparticles forbid the reloading of graphene and hence provide the good dispersion. TEM image in Fig. 8b shows bismuth nanoparticles as dark dots ranging from size 40 to 100 nm with uniform spreading without any conglomeration. Few attempts have been done with metals NPs based graphene nanocomposites for sensing the analyte metal ion. Prakash et al. (2012) employed super paramagnetic Fe_3O_4 nanoparticles on RGO for chromium detection [70]. Conventional mercury based electrode are known to be controversial due to its toxicity and volatile nature that leads to a serious environmental impact. But recently, Zhao and his group established the Hg-graphene oxide (GO) modified glassy carbon electrode with improved stripping performance and very promising hands-on applications for lead detection [13]. Mercury was anchored after casting Hg/GO electrode which is difficult for Hg leakage that reduced the toxic nature of mercury. Besides, Hg(II) sensing platform was constructed by homogenously distributing Au nanoparticles (AuNPs) onto graphene nanosheet matrix using chitosan as a stabilizer showing remarkably enhanced sensitivity with a lower detection limit of 6 ppt for river water monitoring due to better electron-transfer process facility [71].

The effect of interfering species of metal ions like Cu(II), Cr(III), Co(II), Fe(III), Zn(II) and I- found to be insignificant and difference of 6.7 % with ICP-MS. The

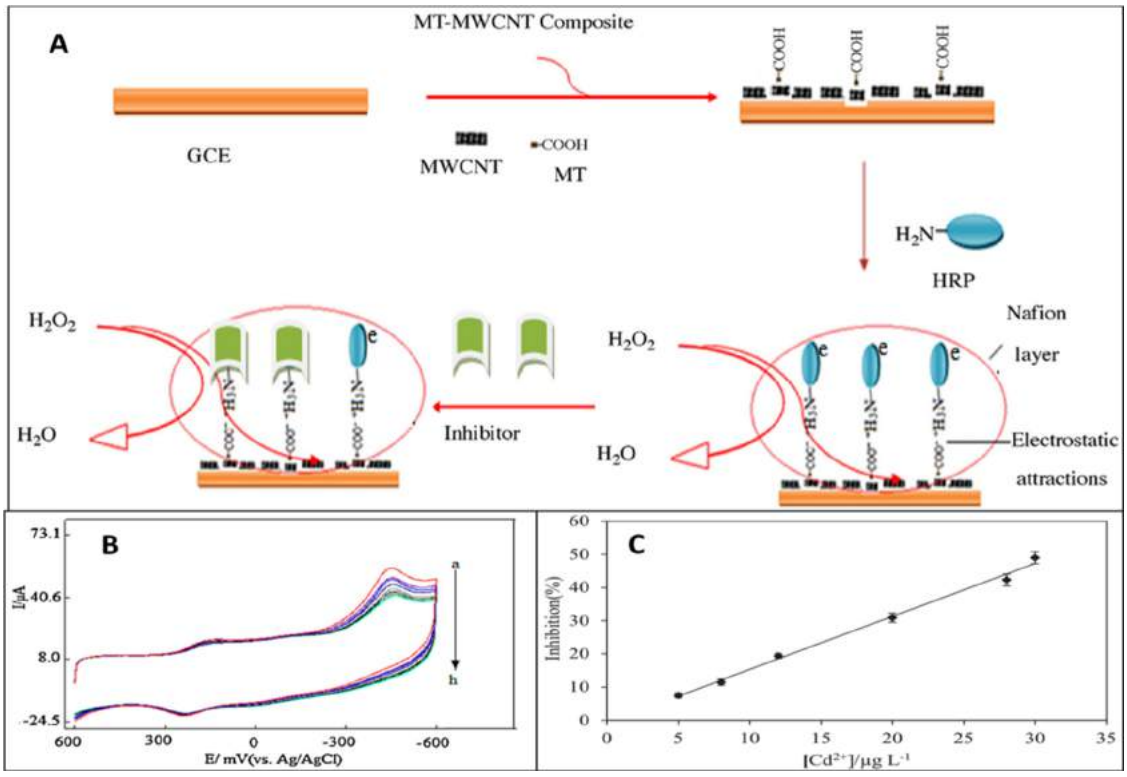


Fig. 7. (A) Stepwise biosensor fabrication process and immobilized HRP inhibition in Cd(II) ion solution. (B) CVs for the HRP/MT-MWCNT/GCE biosensor in 0.1 M PBS (pH 7.0) in presence of 0.1 mM H_2O_2 after incubation for 20 min in 0, 5.0, 10.0, 20.0, 25.0, 35.0, 45.0 and 65.0 $\mu g L^{-1}$ Cd(II) (a–h). Scan rate of 100 $mV s^{-1}$. (C) Caliberation of inhibition plot for the HRP/MT-MWCNT/GCE biosensor. Error bar = ± S. D. and n = 3. [Reproduced with permission from [103] © Elsevier 2013].

© 2016 Wiley-VCH Verlag GmbH & Co. KGaA, Weinheim

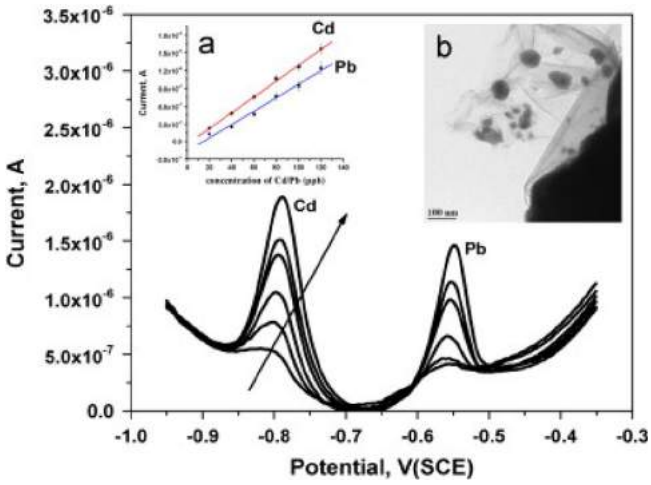


Fig. 8. Differential pulse anodic stripping voltammetry Cd(II) and Pb(II) using RGO/Bi composite modified carbon paste electrode. Solution concentrations of Cd(II) and Pb(II) were increased by 20 µg/L (ppb) in every addition. Inset (a) shows corresponding calibration plot and inset (b) is the TEM image of RGO/Bi nanocomposite. [Reproduced with permission from [39] © Elsevier 2013].

covalent bindings of graphene usually destroy some of the graphene's structure and compromise its excellent properties. But the interactions of non-covalent modifications are usually weaker. Kong et al. (2013) reported the modification of gold electrodes with functional aryl diazonium salt by covalent attachment of pyrene, through which graphene nanosheets were then immobilized via non-covalent π-π stacking interaction [58]. Here, OSWV method was proved to be more sensitive than DPV for electroanalysis of copper and lead ion. Exfoliated graphene oxide (EGO) accompanied with electrochemically deposited lead oxide revealed superior material for analysing of arsenic at a concentration of $\geq$10 nM [107]. Metal ion analysis through various graphene based electrochemical sensor is discussed in Table 4.

Ruecha and co-workers (2015) was recently developed a more cost effective graphene based sensor using transparent plastic film and filter paper as potential low-cost substrates for measurement of Zn(II), Cd(II), and Pb(II) having LOD below 1 ppb [108]. The preparation of the graphene/PANI nanocomposite and the screen printing of the modified film over paper and plastic substrate have been schematically shown in figure 9A and 9B respectively. Two deposition methods (drop-casting and electrospray) were employed to successfully deposit the graphene/PANI nanocomposite as shown in Fig. 9C.

In very recent studies Zhou et al. (2016) have developed more biocompatible graphene-chitosan film using

Table 4. Graphene based detection of metal ion.

Electrode fabricated	Metal ion	Detection limit	Linear range	Method	Matrix Applied	Ref.
GO/Hg	Pb(II)	0.13 ng/L	5 to 70 ng/L	SWASV	River, lake, Tap water	[13]
RGO/Bi/SPE	Cd(II)	0.5 µg/L	1–60 µg/L	SWASV	Milk	[20]
	Pb(II)	0.8 µg/L	1–60 µg/L			
RGO/Bi	Cd(II)	2.8 µg/L	20–120 µg/L	DPASV	Ground and lake water	[39]
	Pb(II)	0.55 µg/L	20–120 µg/L			
	Cu(II)	26 µg/L	20–100 µg/L			
	Zn(II)	17 µg/L	100–400 µg/L			
GR/Au	Cu(II)	1.5 nM	1.5–20 nM	OSWSV		[58]
	Pb(II)	0.4 nM	0.4–20 nM			
RGO/Fe_3O_4	Cr(III)	-	0.2–2 nM	CV		[70]
GR/Au	Hg(II)	6 ppt	0.025–60 ppb	SWASV	River water	[71]
GO/Cysteamine	Hg(II)	3 nM	5–40 nM	ASV		[81]
SPGO/Au	Hg(II)	1.9 µg/L	2–50 µg/L	SWASV	Tap and River	[82]
RGO/PbO	As(III)	10 nM		SWASV		[106]
GR/Nafion/PANI	Zn(II)	1.0 µg/L	1–300 µg/L	SWASV	Human serum	[107]
	Cd(II)	0.1 µg/L	1–300 µg/L			
	Pb(II)	0.1 µg/L	1–300 µg/L			
L-cystine/GR-CS/GCE	Cd(II)	0.45 µg/L	0.56–67.2 µg/L	DPASV	Honey, rice	[108]
	Pb(II)	0.12 µg/L	1.04–62.1 µg/L			
Nitrogen-GR/GCE	Cd(II)	0.05 µM	0.05–1008	DPASV	Tap water	[112]
	Pb(II)	0.005 µM	0.01–9			
	Cu(II)	0.005 µM	0.01–5			
	Hg(II)	0.05 µM	0.2–9			
L-cystine-rGO/GCE	Cd(II)	0.03 µM	0.4–2 µM	DPASV	Industrial effluents, lake	[119]
	Pb(II)	0.02 µM	0.4–1.2 µM			
	Cu(II)	0.04 µM	0.4–2 µM			
	Hg(II)	0.01 µM	0.4–2 µM			
GR/BiF/Nafion/IL/ SPCE	Zn(II)	0.09 µg/L	0.1–100 µg/L	SWASV	Drinking water	[120]
	Cd(II)	0.06 µg/L	0.1–100 µg/L			
	Pb(II)	0.08 µg/L	0.1–100 µg/L			

GR – Graphene, SPGO – screen-printed graphene oxide, IL – 1-butyl-2,3-dimethylimidazolium tetrafluoroborate (Ionic liquid).

© 2016 Wiley-VCH Verlag GmbH & Co. KGaA, Weinheim

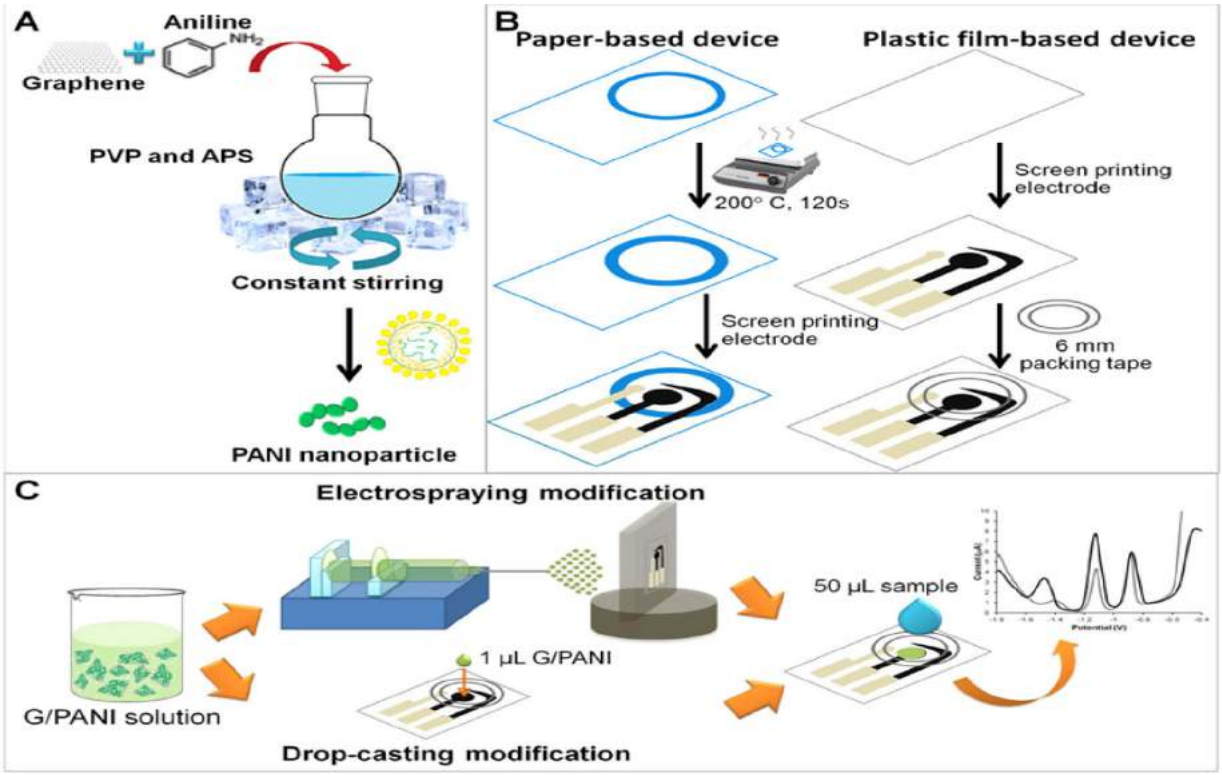


Fig. 9. Schematic drawing of (A) the preparation of the graphene/PANI nanocomposite, (B) electrochemical sensor fabrication on plastic film or paper, and (C) drop-casting and electrospraying processes. [Reproduced with permission from [108] © Elsevier 2015].

L-cysteine based amino acid for Cd(II) and Pb(II) detection [109]. A strongly adsorbed polymer film of L- cysteine based graphene-chitosan film has better sensing performance than mercury, bismuth and gold modified graphene films. The electrochemical properties of nanocarbon materials can be intrinsically modified by doping with foreign atoms such as boron [110], and nitrogen [111,112]. Xing et al. (2016) have firstly applied the nitrogen doped graphene electrodes for high selectivity and a long-term usage possibility for determination of Cd(II), Pb(II), Cu(II), and Hg(II) [113]. Nitrogen doping plays a crucial role in fascinating the electronic properties and enhancing the electrocatalytic activity of carbon materials [114]. Yang et al. (2015) developed nano-rod structured of RGO and polyaniline synthesized *via* in situ chemical oxidative polymerization method. The developed sensitive layer used as DNA adsorbent for detecting Hg(II) showed high selectivity and sensitivity within a concentration range from 0.1 nM to 100 nM with LOD of 0.035 nM [115].

Apart from the above discussed sensors, 3D Graphene-MWCNTs based electrochemical sensor was also been successfully utilized for the first time for the detection of Cd(II), Pb(II), Zn(II) and Cu(II) using simple and green electrochemical reduction method [116] (see Figure 10). A good synergistic effect between MWCNTs and graphene is observed having combined conductivity of CNTs with the partial hydrophilicity of GO that possess the strong ability to catch metal ions through coordination reactions. The 2D GO sheets and 1D MWCNTs creates an interconnected framework, in which the aggregation tendency between MWCNTs is effectively inhibited. On comparison of graphene with CNT based electrodes, the large specific surface area of graphene could greatly enhanced the electroactive sites and increased the electrical conductivity of graphene which improved the electron transfer rate between the electrode surface and metal ion. Wu et al. (2014) has systematically compared the performance of the graphene based sensor with MWCNTs-modified sensor and illustrated better sensing performance of Cd(II) concentrations from 0.25 mg/L to 5 mg/L with a LOD of 3.5 ng/L using graphene sheet based sensor with relative standard deviation (RSD) of 0.29 % as compared to MWCNT-Nafion/GCE (LOD 25 ng/L) having RSD of 12 % for MWCNTs based sensor [117]. Owing to better electronic behavior of graphene, 2D nanostructure with a single atomic layer of carbon could provide a very broad space for the easy transfer of cadmium ions (diameter 0.316 nm) as compared to MWCNTs having small specific surface area resulted in poor LOD Due to the close interlayer distance between MWCNTs (0.34 nm, slightly greater than the diameter of cadmium ions (0.316 nm) [118], cadmium ions were adsorbed continuously, causing the MWCNTs to become enriched with cadmium ions (Figure 11). This adsorption ultimately resulted in the poor reproducibility of the MWCNT-Nafion/GC electrode. Martín-Yerga et al. (2012) also compared the performance CNTs and GO modified with gold nano-

 © 2016 Wiley-VCH Verlag GmbH & Co. KGaA, Weinheim

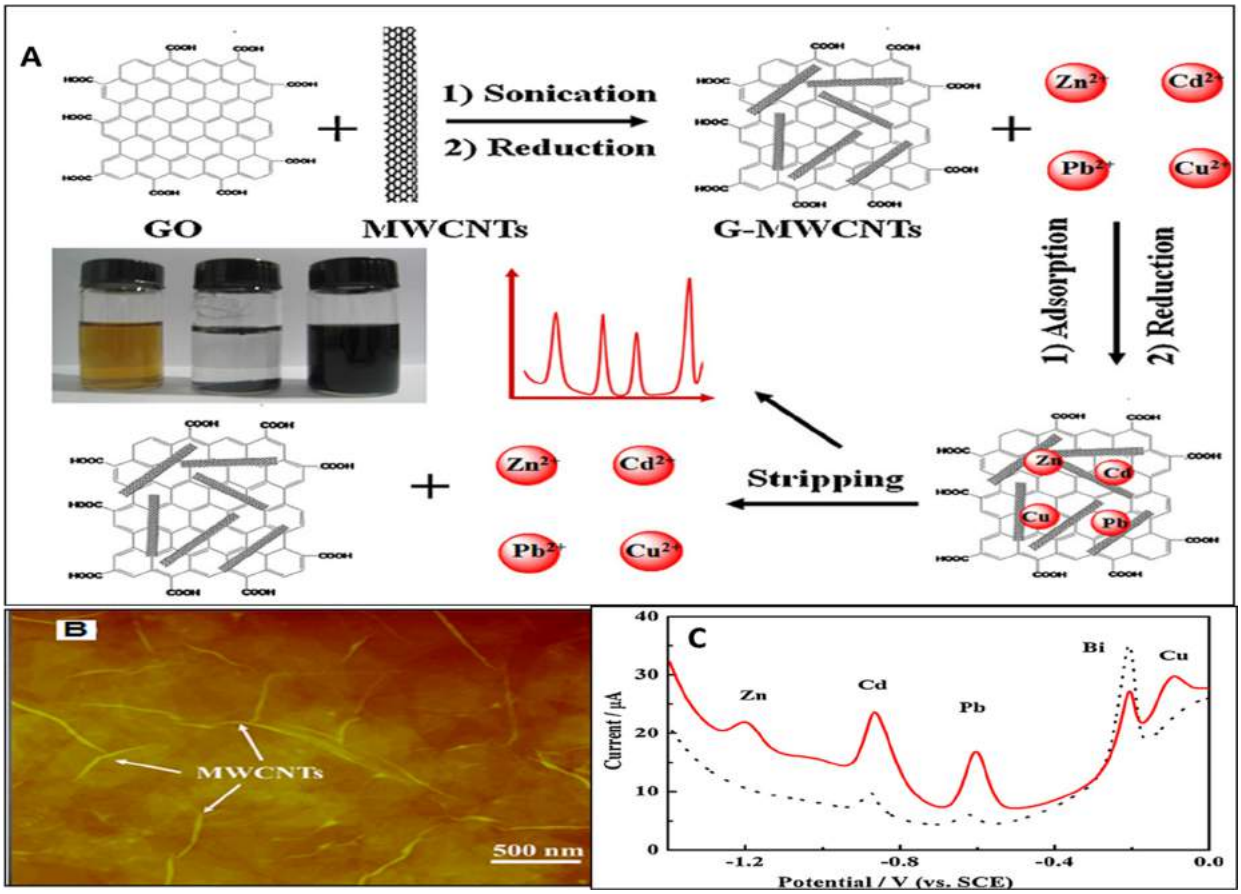


Fig. 10. (A) Schematic diagram for the synthesis of G-MWCNTs hybrid nanomaterials and their application as novel electrode materials which are applicable to the electrochemical detection of heavy metal ions by means of ASV method. Inset shows the digital photos for the GO, MWCNTs and GO-MWCNTs solutions, respectively. **(B)** AFM images of GO-MWCNTs nanocomposites. Here the arrows point to the MWCNTs. **(C)** DPASV stripping signals for Zn^{2+}, Cd^{2+}, Pb(II) and Cu^{2+} ions with the same concentration (15 $\mu g L^{-1}$) on bismuth film modified bare GCE and Graphene/MWCNTs/GCE. [Reproduced with permission from [116] © Elsevier 2014].

hybrid screen-printed electrodes for Hg(II) analysis. CNTs modified screen-printed electrodes showed higher sensitivity (LOD 0.2 μg/L) than GO based electrodes (LOD 1.9 μg/L) and gold modified screen-printed electrodes (LOD of 3.3 μg/L). This is due to more loading of nano-gold particle with higher amount in CNTs [82].

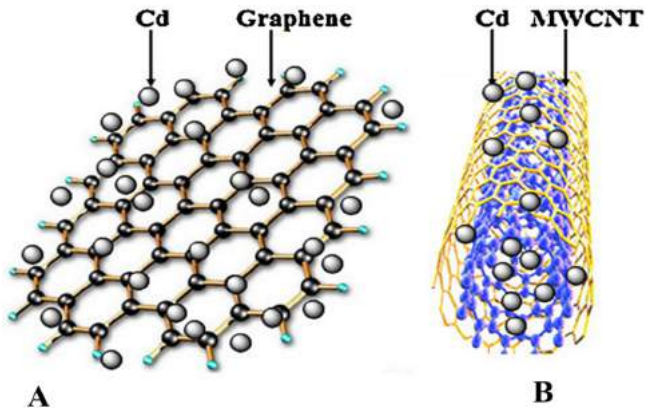


Fig. 11. Schematic diagram of cadmium ion absorption on (A) nanographene and (B) MWCNT [Reproduced with permission from [117] © Elsevier 2014].

3.3 Nano-diamonds Based Sensor for Metal Ion Detection

The intrinsic electrochemical properties of diamond that differs from other commonly used sp^2-bonded carbon electrodes includes excellent structural and morphological stability at high temperatures and current density, low and stable background current, long-term response stability and good optical behavior in UV/Vis and IR regions for spectroelectrochemical analysis [121,122]. The nano-diamond films doped with boron have proved the more excellent response accuracy, reduced over potential of certain redox reactions electrocatalytic behavior, low limit of detection by several studies [123–125]. The properties which preferred the use of boron doped diamond over other electrodes for HMs detection includes chemical inertness, non-toxicity, high thermal conductivity, wide electrochemical potential window, low capacitance and good electrochemical stability [126,127]. Recently, Nur-

© 2016 Wiley-VCH Verlag GmbH & Co. KGaA, Weinheim

hayati et al. (2015) firstly explored the capability of boron-doped nanocrystalline diamond (BD-NCD) fabricated via hot filament chemical vapor deposition for determination of Cu(II), Pb(II) and Hg(II) ions without pre-concentration step using linear sweep voltammetry technique [128]. The enhanced surface properties obtained through dynamic polarization possess minimum adventitious carbon content on its surface leads to an increase of electrode kinetic. The detection limit of electrodes is 0.102, 1.339 and 0.666 μM whereas sensitivity is 0.104, 0.014 and 0.057 $\mu A\,\mu M^{-1}mm^2$ for Cu(II), Pb(II) and Hg(II) respectively.

Recent research proposed biocompatible property of boron-doped nano-diamond electrode and compared the performance of nano crystalline boron-doped diamond film over Hg-coated glassy carbon electrode (Hg-GCE) for trace metal ions [127,129]. They concluded that even though higher sensitivity found in Hg-GC due to greater amount of metal deposited but the lower background current enabled nano crystalline diamond with superior LOD values. Recently, Honório et al. (2014) used nanocrystalline boron-doped diamond electrode and found detection limits of 1.28, 0.37, 0.40 and 0.16 mg/L for Cd(II), Cu(II), Pb(II) and Zn(II) in honey respectively using DPASV [17]. The film morphology characteristics and conductivity along with the doping level on nanocrystalline diamond films has also been studied. May et al. (2008) have suggested that electrodes fabricated with controlled roughness and conductivity considered as excellent for electrochemical applications [130]. The lead ion detected in the range from 1 to 10 μg/L using square-wave anodic stripping voltammetry (SWASV) technique found good reproducibility and lowest detection limit for BDND doped with 2000 mg/L in B/C ratio [131].

3.4 Other Nanocarbons for Metal Ion Detection

Other nanocarbon like carbon nanodots (CNDs), fullerene and GQDs based electrodes has also been used for heavy metal detection but their applicability for electrochemical approach in sensing metal ion is however found to be limited. Mercury and tin compounds was analysed in water and sediments using C_{60} fullerenes based on gas chromatography-mass spectrometry (GC-MS) technique [132]. Fluorescence-based copper ion sensor has been developed by novel fullerene-ferrocene based donor-bridge-acceptor dyad [133]. Another fluorescence based detection of Hg(II) by carbon nano dots (CNDs) synthesized from green microwave-assisted method using flour as the carbon source. High sensitivity and selectivity toward Hg(II) with very low detection limit of 0.5 nM have been obtained that can be practically utilized for determination of Hg(II) in real lake water successfully [93] Based on electrochemical strategy, TPEA (N-(2-aminoethyl)-N, N′,N′-Tris(pyridine-2-yl-methyl)ethane-1,2-diamine) functionalized carbon dots (C-Dot-TPEA) have been exploit for Cu(II) ion sensor[134]. Recently graphene quantum dots have been exploited as electrochemical sensor for sensitive detection of metal ions [135,136]. GQDs are a zero dimensional material having characteristics of both graphene and carbon Dots [137]. It exhibit new phenomena due to edge effects and quantum confinement, which are similar to carbon dots [138]. GQDs are superior in terms of their excellent properties, such as high photostability against photo bleaching and blinking, biocompatibility, and low toxicity [139]. Graphene nanodots-encaged porous gold electrode were fabricated via ion beam sputtering deposition for electrochemical sensing used for the analysis of Cu(II) and Pb(II).Owing to the entrapped graphene nanodots in 3-D porous structure the developed platform exhibited enhanced detection range of 0.009–4 μM for Cu(II) and 0.006–2.5 μM for Pb(II) with good reusability and repeatability [135]. More recently Ting et al. (2015) employed the novel conjugates of GQDs and gold nanoparticles for Hg(II) and Cu(II) detection having ultralow detection limit of 0.02 nM with S/N = 6.25 and 0.05 nM with S/N = 4.81 respectively [140] (Figure 12). SEM image revealed that the individual particle size however is not significantly increased because of the very small size of GQDs on comparing with that of nano-gold electrode, but the response of nano-gold modified electrode is much weaker on comparison with the GQD-AuNP modified electrodes for Hg(II) detection. (Figure 12B and 12C). Zhou and co-worker developed an effective approach to produce GQDs based on the cutting of GO powder into smaller using sodium polystyrene sulfonated as a dispersant and L-ascorbic acid as the reducing agent The modified GQDs/GCE electrodes has shown better solubility in water and more biocompatibility than GO having remarkably low detection limit of 7×10^{-9} M for Pb(II) [136].

4 Challenges and Future Prospective

The HMs detection in different sources of raw water, soil and food materials is a highly prerequisite for regular on-site monitoring and control. In ECS, the role of nano-structured film plays the key role in sensing the metal ion. The significance of electrochemical sensors belongs to their high sensitivity, selectivity, low detection limit and good reproducible results. The electrochemical sensing performance of the nanocarbon is highly dependent upon on its unique electronic and structural properties. Nanocarbon modified electrode transduce the chemical interaction of metal ion analytes into the well-developed redox peak with applying stripping voltammetry of appropriate accumulation and potential. In spite of various electrodes modifications process, the specificity with higher reproducibility is the key challenges associated with the discussed nanocarbon sensor for long term usability. The increase in preconcentration efficiency of selective metal ions with accelerated electron transfer rate demands more effective chelating agents with stable configuration. Occurrence of modifier oxidation earlier before the metal ion stripping must be resolved. Uncontrolled modification sometimes leads to large background

 © 2016 Wiley-VCH Verlag GmbH & Co. KGaA, Weinheim

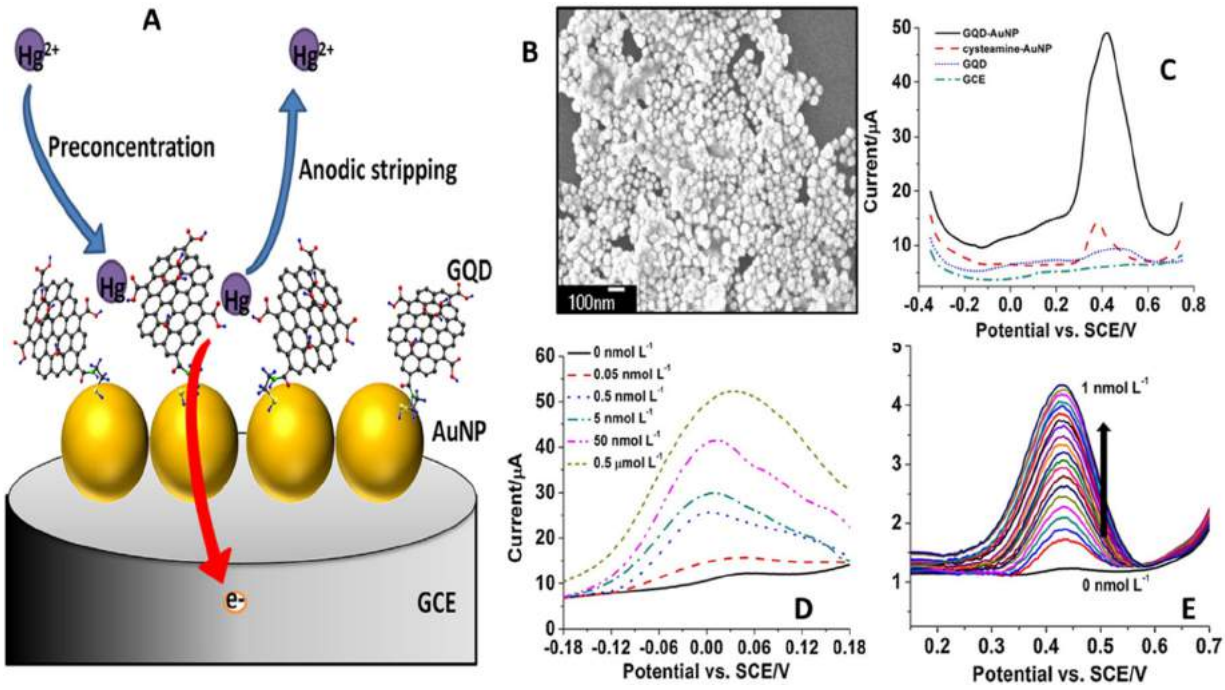


Fig. 12. (A) Schematic illustration of GQD modified electrode for Hg(II) detection. (B) SEM of GQD-AuNPs on GCE (C) SQASV response in the presence of 0.1 mM of Hg(II). (D) & (E) SWASV curves for Cu(II) and Hg(II) respectively. [Reproduced with permission from [140]© Elsevier 2015].

current or noise and non-reproducible response. The better performance of the sensor platform depends on a process of modification with other chemical species, so the controlled morphologies of the nanostructured film with optimized functionalization parameter must have been performed. Electrochemical properties of nanocarbon are highly dependent on its controlled high surface area architecture which will serve as a conductive support for further modification that can be used in electroanalysis. The major challenges are to achieve the metal sensing with selective sensing of multiple metal ions simultaneously with maintaining effect of interference as low as possible. The applicability of ECS narrowed because of the declination in its accuracy after employing it certain duration. Graphene and CNTs have proved its distinctiveness in sensing of HMs in various matrixes but maintaining the stability of the electrode film for a long duration to meet the cost effective sensor is a major challenges. So to use nanocarbon electrode for daily applications, good sensing platform with low material cost is required. The operational parameters for achieving selectivity and sensitivity for metal analysis are not constant with different functionalized layer of same nanocarbon materials. So the parameters like pH, deposition potential, time and concentration of electrode functionalized material must be carefully evaluated for optimized results. Enzymatic based sensor based on inhibition mechanism only provides the total toxicity of the sample rather than the specific metal ions. Also the activity of the enzyme is decreased after longer duration of uses. So to overcome these issues appropriate regeneration of enzymatic biosensor is required without affecting modified surface for every new analysis. Biomolecules based sensors have been proved to be highly specific towards various types of biomarkers and diseases. But combinations of bioagents utilized with nanocarbon very rarely have been done for HMs detection and not yet available for on-field detection. Sometimes the complex synthesis procedures are restricting its applicability with nanocarbon materials for convenient sensor fabrication. The enhanced nano modified film must be resistant against fouling agents present in waste water which degrades the sensor performance. Recently the researchers are more focussed on the microchip based devices. Graphene appears to be highly promising towards the construction of nanostructured devices such as FET sensors because of the possibility of lithographically controlling the transfer or growth of high quality graphene. Demands for applying flexible plastic based substrate of potentially low cost to be anticipated in coming future for regular on field monitoring of HMs just like reliable glucometers are available commercially. The future perspective in the development of HMs sensor is towards the manufacture of miniaturized devices employing as hand held tools for day-to-day on-site monitoring with a nano-molar range of the detection limit. In spite of obtaining prominent achievements, the complicated procedures and inconvenience in the fabrication of platform apparently hindered their sensing applications. Therefore, new fabrication materials and technologies are anticipated in the future in response to these prospects.

© 2016 Wiley-VCH Verlag GmbH & Co. KGaA, Weinheim

Acknowledgements

S. K. Singh would like to sincerely thank DST-INSPIRE faculty fellowship grant (No. IFA-LSBM-31) received from the Department of Science and Technology (DST), New Delhi. The authors also would like to acknowledge TEQIP-II, Motilal Nehru National Institute of technology (MNNIT) Allahabad India for the research support.

References

[1] N. K. Srivastava, C. B. Majumder, *J. Hazard. Mater.* **2008**, *151*, 1–8.
[2] S. Clemens, J. F. Ma, *Annu. Rev. Plant Biol* **2016**, *67*, 489–512.
[3] O. B. Olafisoye, T. Adefioye, O. A. Osibote, *Pol. J. Environ Stud.* **2013**, *22*, 1431–1439.
[4] G. Ebong, J. Essien, C. Ekong, S. Eduok, *Int. J. Chem., Environ. Pharm. Res* **2012**, *3*, 152–157.
[5] J. Liu, X. H. Zhang, H. Tran, D. Q. Wang, Y. N. Zhu, *Environ. Sci. Pollut. Res.* **2011**, *18*, 1623–1632.
[6] J. Mohmand, S. A. M. A. S. Eqani, M. Fasola, A. Alamdar, I. Mustafa, N. Ali, H. Shen, *Chemosphere* **2015**, *132*, 142–151.
[7] M. A. Barakat, *Arabian J. Chem.* **2011**, *4*, 361–377.
[8] X. X. Long, X. E. Yang, W. Z. Ni, *J Appl Ecol.* **2002**, *13*, 757–62.
[9] J. M. Anderson, *Annu. Rev. Mater. Res.* **2001**, *31*, 81–110.
[10] H. Malassa, M. Al-Qutob, M. Al-Khatib, F. Al-Rimawi, *J. Environ. Prot.* **2013**, *4*, 818.
[11] M. J. Shaw, P. R. Haddad, *Environ. Int.* **2004**, *30*, 403–431.
[12] N. A. Rahman, N. A. Yusof, N. A. M. Maamor, S. M. M. Noor, *Int. J. Electrochem. Sci.* **2012**, *7*, 186–196.
[13] Q. Zhao, Y. Chai, R. Yuan, J. Luo, *Sens. Actuators B.* **2013**, *178*, 379–384.
[14] Z. Q. Wang, G. Liu, L. N. Zhang, H. Wang, *Int. J. Electrochem. Sci.* **2012**, *7*, 12326–12339.
[15] K. Christidis, P. Robertson, K. Gow, P. Pollard, *Measurement.* **2007**, *40*, 960–967.
[16] J. Ping, J. Wu, Y. Ying, M. Wang, G. Liu, M Zhan, *J. Agric. Food Chem.* **2011**, *59*, 4418–4423.
[17] G. G. Honório, G. C. Azevedo, M. A. C Matos, M. A. L. de Oliveira, R. C. Matos, *Food Control.* **2014**, *36*, 42–48.
[18] O. Chailapakul, S. Korsrisakul, W. Siangproh, K. Grudpan, *Talanta.* **2008**, *74*, 683–689.
[19] K. Keawkim, S. Chuanuwatanakul, O. Chailapakul S. Motomizu, *Food Control.* **2013**, *31*, 14–21.
[20] J. Ping, Y. Wang, J. Wu, Y. Ying, *Food Chem.* **2014**, *151*, 65–71.
[21] S. Ramezani, M. Ghobadi, B. N. Bideh, *Sens. Actuators, B.* **2014**, *192*, 648–657.
[22] I. Palchetti, M. Mascini, M. Minunni, A. R. Bilia, F. F. Vincieri, *J. Pharm. Biomed. Anal.* **2003**, *32*, 251–256.
[23] http://water.epa.gov/drink/contaminants/index.cfm (accessed March 15, 2015).
[24] *Indian standard Drinking water-specification* (Second revision), IS-10500:2012, ICS 13.060.20, Bureau of Indian Standards, New Delhi, **2012**.
[25] http://iasri.res.in/agridata/02data%5Cchapter%202%5Cdb2002tb2_7.htm (accessed March 15, 2015).
[26] http://hppcb.gov.in/eiasorang/spec.pdf (accessed March 21, 2015).
[27] D. Das, A. Chatterjee, B. K. Mandal, G. Samanta, D. Chakraborti, B. Chanda, *Analyst.* **1995**, *120(3)*, 917–924.
[28] A. H. Smith, C. M. Steinmaus, *Annu. Rev. Public Health.* **2009**, *30*, 107.
[29] R. G. Walker, T. D. Hewitson, G. J. Becker in *Core Concepts in Parenchymal Kidney Disease (Eds*: F. C. Fervenza, J. Lin, S. Sethi, A. K. Singh) Springer, New York, **2014**, pp. 341–360.
[30] Y. Chervona, A. Arita, M. Costa, *Metallomics* **2012**, *4*, 619–627.
[31] M. Seeley, C. S. Wells, E. J. Wannamaker, R. L. Mattuck, S. Ren, B. D. Beck, *Regul. Toxicol. Pharmacol* **2013**, *65*, 47–59.
[32] L. Patrick, *Altern Med Rev.* **2006**, *11*, 114–127.
[33] Y. H. Li, Z. Di, J. Ding, D. Wu, Z. Luan Y. Zhu, *Water Res.* **2005**, *39*, 605–609.
[34] Z. V. P. Murthy, P. A. Parikh, N. B. Patel, *J. Dispersion Sci. Technol* **2013**, *34*, 747–755.
[35] Guidelines for drinking water quality, 2nd edn, vol 2: health criteria and other supporting information, 1996 (pp. 940–949) and Addendum to vol 2. 1998 (pp. 281–283). World Health Organization, Geneva **1996**.
[36] J. D. Deshpande, M. M. Joshi P. A. Giri, *Int J Med Sci Public Health.* **2013**, *2*, 1–6.
[37] A. K. Geletzke, J. M. Rinaldi, B. E. Phillips, S. B. Mobley, J. Miller, T. Dykes, D. I. Soybel, *Journal of Gastrointestinal Surgery* **2014**, *18*, 646–655.
[38] A. Hulanicki, S. Glab, F. Ingman, *Pure Appl. Chem.* **1991**, *63*, 1247–1250.
[39] P. K. Sahoo, B. Panigrahy, S. Sahoo, A. K. Satpati, D. Li, D. Bahadur, *Biosens. Bioelectron.* **2013**, *43*, 293–296.
[40] E. Chatzitheodorou, A. Economou, A. Voulgaropoulos, *Electroanalysis* **2004**, *16*, 1745–1754.
[41] G. Kefala, A. Economou, M. Sofoniou, *Talanta* **2006**, *68*, 1013–1019.
[42] E. A. Hutton, J. T. van Elteren, B. Ogorevc, M. R. Smyth, *Talanta* **2004**, *63*, 849–855.
[43] G. March, T. D. Nguyen, B. Piro, *Biosensors* **2015**, *5*, 241–275.
[44] J. Wang, J. Lu, S. B. Hocevar, P. A. Farias, B. Ogorevc, *Anal. Chem* **2000**, *72*, 3218–3222.
[45] L. Nunes, R. Faria, *Electroanalysis* **2008**, *20*, 2259–2263.
[46] C. H. Lien, C. C. Hu, K. H. Chang, Y. D. Tsai, D. S. H. Wang, *Electrochim. Acta* **2013**, *105*, 665–670.
[47] S. B. Hocevar, I. Švancara, B. Ogorevc, K. Vytras, *Anal. Chem* **2007**, *79*, 8639–8643.
[48] R. A. Sánchez-Moreno, M. J. Gismera, M. T. Sevilla, J. R. Procopio, *Sens. Actuators, B.* **2010**, *143*, 716–723.
[49] A. Merkoçi, M. Pumera, X. Llopis, B. Pérez, M. Del Valle, S. Alegret, *TrAC, Trends Anal. Chem.* **2005**, *24*, 826–838.
[50] A. Merkoçi, *Microchim. Acta.* **2006**, *152*, 157–174.
[51] M. A. El Mhammedi, M. Achak, M. Bakasse, *Arabian J. Chem.* **2013**, *6*, 299–305.
[52] H. Bagheri, A. Afkhami, H. Khoshsafar, M. Rezaei, A. Shirzadmehr, *Sens. Actuators, B.* **2013**, *186*, 451–460.
[53] J. F. Huang, H. H. Chen, *Talanta.* **2013**, *116*, 852–859.
[54] A. Salimi, H. Mamkhezri, R. Hallaj, S. Soltanian, *Sens. Actuators, B* **2008**, *129*, 246–254.
[55] P. K. Q. Nguyen, S. K. Lunsford, *Talanta.* **2012**, *101*, 110–121.
[56] Q. Wang, F. Gao, X. Zhang, B. Zhang, S. Li, Z. Hu, F. Gao , *Electrochim. Acta.* **2012**, *62*, 250–255.
[57] S. Wang, L. Li, H. Jin, T. Yang, W. Bao, S. Huang, J. Wang, *Biosens. Bioelectron.* **2013**, *41*, 205–210.
[58] N. Kong, J. Liu, Q. Kong, R. Wang, C. J. Barrow, W. Yang, *Sens. Actuators, B.* **2013**, *178*, 426–433.
[59] H. Wan, Q. Sun, H. Li, F . Sun, N. Hu, P. Wang, *Sens. Actuators, B.* **2015**, *209*, 336–342.

 © 2016 Wiley-VCH Verlag GmbH & Co. KGaA, Weinheim

[60] E. Shams, A. Babaei, M. Soltaninezhad, *Anal. Chim. Acta.* **2004**, *501*, 119–124.
[61] A. A. Ensafi, T. Khayamian, S. S. Khaloo, *Anal. Chim. Acta.* **2004**, *505*, 201–207.
[62] P. Zhang, S. Dong, G. Gu, T. Huang, *Bull. Korean Chem .Soc.* **2010**, *31*, 2949–2954.
[63] A. Afkhami, T. Madrakian, S. J. Sabounchei, M. Rezaei, S. Samiee, M. Pourshahbaz, *Sens. Actuators, B*, **2012**, *161*, 542–548.
[64] I. Cesarino, G. Marino, J. do Rosário Matos, E. T. G. Cavalheiro, *Talanta.* **2008**, *75*, 15–21.
[65] E. Shams, R. Torabi, *Sens. Actuators, B.* **2006**, *117*, 86–92.
[66] S. Senthilkumar, R Saraswathi, *Sens. Actuators B.* **2009**, *141*, 65–75.
[67] K. A. Mahmoud, S. Hrapovic, J. H. Luong, *ACS Nano.* **2008**, *2*, 1051–1057.
[68] J. Kailashiya, N. Singh, S. K. Singh, V. Agrawal, D. Dash, *Biosens. Bioelectron.* **2015**, *65*, 274–280.
[69] X. Cai, X. Gao, L. Wang, Q. Wu, X. Lin, *Sens. Actuators, B.* **2013**, *181,* 575–583.
[70] A. Prakash, S. Chandra, D. Bahadur, *Carbon* **2012**, *50*, 4209–4219.
[71] J. Gong, T. Zhou, D. Song, L. Zhang, *Sens. Actuators B.* **2010**, *150*, 491–497.
[72] S. H. Shin, H. G. Hong, *Bull. Korean Chem. Soc.* **2010**, *31*, 3077–3083.
[73] J. Wei, D. Yang, H. Chen, Y. Gao H. Li, *Sens. Actuators, B.* **2014**, *190*, 968–974.
[74] G. Aragay, J. Pons, A. Merkoçi, *Chem. Rev.* **2011**, *111*, 3433–3458.
[75] L. Cui, J. Wu, H. Ju, *Biosens. Bioelectron.* **2015**, *63*, 276–286.
[76] A. Profumo, M. Fagnoni, D. Merli, E. Quartarone, S. Protti, D. Dondi, A. Albini, *Anal. Chem.* **2006**, *78*, 4194–4199.
[77] W. Yantasee, Y. Lin, T. S. Zemanian, G. E. Fryxell, *Analyst.* **2003**. *128*, 467–472.
[78] E. Tesarova, L. Baldrianova, S. B. Hocevar, I. Svancara, K. Vytras, B. Ogorevc, *Electrochim. Acta* **2009**, *54*, 1506–1510.
[79] S. Majid, M. El Rhazi, A. Amine, A. Curulli, G. Palleschi, *Microchim. Acta* **2003**, *143*, 195–204.
[80] L. Cao, J. Jia, Z. Wang, *Electrochim. Acta* **2008**, *53*, 2177–2182.
[81] H. Zhou, X. Wang, P. Yu, X. Chen, L. Mao, *Analyst.* **2012**, *137*, 305–308.
[82] D. Martín-Yerga, M. B. González-García, A. Costa-García, *Sens. Actuators, B.* **2012**, *165*, 143–150.
[83] J. S. Bunch, A. M. Van Der Zande, S. S. Verbridge, I. W. Frank, D. M. Tanenbaum, J. M. Parpia, H. G. Craighead, P. L. McEuen, *Science.* **2007**, *315*, 490–493.
[84] C. Lee, X. Wei, J. W. Kysar, J. Hone, *Science.* **2008**, *321*, 385–388.
[85] R. R. Nair, P. Blake, A. N. Grigorenko, K. S. Novoselov, T. J. Booth, T. Stauber, A. K. Geim, *Science.* **2008**, *320*, 1308–1308.
[86] A. K. Geim, K. S. Novoselov, *Nat. Mater.* **2007**, *6*, 183–191.
[87] Y. Zhang, Y. W. Tan, H. L. Stormer, P. Kim, *Nature.* **2005**, *438*, 201–204.
[88] M. D. Stoller, S. Park, Y. Zhu, J. An, R. S. Ruoff, *Nano Lett.* **2008**, *8*, 3498–3502.
[89] M. Pumera, *Chem. Soc. Rev.* **2010**, *39*, 4146–4157.
[90] M. Pumera, *Mater. Today.* **2011**, *14*, 308–315.
[91] B. A. Leśniewska, I. Godlewska, B. Godlewska-Żyłkiewicz, *Spectrochim. Acta, Part B.* **2005**, *60*, 377–384.
[92] Y. Liu, Y. Zhao, Y. Zhang, *Sens. Actuators, B.* **2014**, *196*, 647–652.
[93] X. Qin, W. Lu, A. M. Asiri, A. O. Al-Youbi, X. Sun, *Sens. Actuators, B.* **2013**, *184*, 156–162.
[94] N. Wang, X. Dong, *Anal. Lett* **2008**, *41*, 1267–1278.
[95] G. H. Hwang, W. K. Han, J. S. Park, S. G. Kang, *Talanta* **2008**, *76*, 301–308.
[96] G. Liu, Y. Lin, Y. Tu, Z. Ren, *Analyst* **2005**, *130*, 1098–1101.
[97] A. M. Ashrafi, S. Cerovac, S. Mudrić, V. Guzsvány, L. Husáková, I. Urbanová, K. Vytřas, *Sens. Actuators, B* **2014**, *191*, 320–325.
[98] W. Deng, Y. Tan, Y. Li, Y. Wen, Z. Su, Z. Huang, S. Yao, *Microchim. Acta.* **2010**, *169*, 367–373.
[99] X. Guo, Y. Yun, V. N. Shanov, H. B. Halsall, W. R. Heineman, *Electroanalysis.* **2011**, *23*, 1252–1259.
[100] H. Ashkenani, M. A. Taher, *J. Electroanal. Chem* **2012**, *683*, 80–87
[101] L. He, S. Zhang, M. Wang, D. Peng, F. Yan, Z. Zhang, L. Zhou, *Sens. Actuators, B,* **2016**. doi:10.1016/j.snb.2016.01.004.
[102] A. Afkhami, H. Bagheri, H. Khoshsafar, M. Saber-Tehrani, M. Tabatabaee, A. Shirzadmehr, *Anal. Chim. Acta.* **2012**, *746*, 98–106.
[103] M. Moyo, J. O. Okonkwo, *Sens. Actuators, B* **2014**, *193*, 515–521.
[104] M. Moyo, J. O. Okonkwo, N. M. Agyei, *Enzyme Microb. Technol* **2014**, *56*, 28–34.
[105] A. Afkhami, H. Khoshsafar, H. Bagheri, T. Madrakian, *Mater. Sci. Eng., C* **2014**, *35*, 8–14.
[106] L. Fu, X. Li, J. Yu, J. Ye, *Electroanalysis* **2013**, *25,* 567–572.
[107] G. K. Ramesha, S. Sampath, *Sens. Actuators, B.* **2011**, *160*, 306–311.
[108] N. Ruecha, N. Rodthongkum, D. M. Cate, J. Volckens, O. Chailapakul, C. S. Henry, *Anal. Chim. Acta* **2015**, *874*, 40–48.
[109] W. Zhou, C. Li, C. Sun, X. Yang, *Food Chem* **2016**, *192*, 351–357.
[110] R. P. Hardikar, D. Das, S. S. Han, K. R. Lee, A. K. Singh, *Phys. Chem. Chem. Phys* **2014**, *16*, 16502–16508.
[111] F. X. Ma, J. Wang, F. B. Wang, X. H. Xia, *Chem. Commun* **2015**, *51*, 1198–1201.
[112] A. L. M. Reddy, A. Srivastava, S. R. Gowda, H. Gullapalli, M. Dubey, P. M. Ajayan, *ACS Nano* **2010**, *4*, 6337–6342.
[113] H. Xing, J. Xu, X. Zhu, X. Duan, L. Lu, W. Wang, Y. Zhang, T. Yang, *J. Electroanal. Chem* **2016**, *760*, 52–58.
[114] Y. Y. Shao, J. H. Sui, G. P. Yin, Y. Z. Gao, *Appl. Catal. B* **2008**, *79*, 89–99.
[115] Y. Yang, M. Kang, S. Fang, M. Wang, L. He, J. Zhao, Z. Zhang, *Sens. Actuators, B* **2015**, *214*, 63–69.
[116] H. Huang, T. Chen, X. Liu, H. Ma, *Anal. Chim. Acta* **2014**, *852*, 45–54.
[117] L. Wu, X. Fu, H. Liu, J. Li, Y. Song, *Anal. Chim. Acta* **2014**, *851*, 43–48.
[118] M. D. Ma, L. M. Shen, L. F. Wang, Q. S. Zheng, *Int. J. Multiscale Comput*, **2013**.*11*, 17–26.
[119] S. Muralikrishna, K. Sureshkumar, T. S. Varley, D. H. Nagaraju, T. Ramakrishnappa, *Anal. Methods* **2014**, *6*, 8698–8705.
[120] S. Chaiyo, E. Mehmeti, K. Žagar, W. Siangproh, O. Chailapakul, K. Kalcher, *Anal. Chim. Acta* **2016**, *918*, 26–34.
[121] R. F. Brocenschi, R. C. Rocha-Filho, L. Li, G. M. Swain, *J. Electroanal. Chem* **2014**, *712*, 207–214.
[122] A. F. Azevedo, M. R. Baldan, N. G. Ferreira. *Int. J. Electrochem*. **2012**, doi:10.1155/2012/508453
[123] S. Wang, V. M. Swope, J. E. Butler, T. Feygelson, G. M. Swain, *Diamond Relat. Mater.* **2009**, *18*, 669–677.

 © 2016 Wiley-VCH Verlag GmbH & Co. KGaA, Weinheim *Electroanalysis* **2016**, *28, 1 – 18* ▮16▮

These are not the final page numbers! ↗↗

[124] A. F. Azevedo, N. A. Braga, F. A. Souza, J. T. Matsushima, M. R. Baldan, N. G. Ferreira, *Diamond Relat. Mater.* **2010**, *19*, 462–465.
[125] A. E. Fischer, Y. Show, G. M. Swain, *Anal. Chem.* **2004**, *76*, 2553–2560.
[126] A. Manivannan, R. Kawasaki, D. A. Tryk, A. Fujishima, *Electrochim. Acta* **2004**, *49*, 3313–3318.
[127] E.A McGaw, G. M. Swain, *Anal. Chim. Acta.* **2006**, *575*, 180–189.
[128] E. Nurhayati, Y. Juang, M. Rajkumar, C. Huang, C. C. Hu, *Sep. Purif. Technol.* **2015**, *156*, 1047–1056.
[129] P. Sonthalia, E. McGaw, Y. Show, G. M. Swain, *Anal. Chim. Acta.* **2004**, *522*, 35–44.
[130] P. W. May, W. J. Ludlow, M. Hannaway, P. J. Heard, J. A. Smith, K. N. Rosser, *Diamond Relat. Mater.* **2008**, *17*, 105–117.
[131] T. M. Arantes, A. Sardinha, M. R. Baldan, F. H. Cristovan, N. G. Ferreira, *Talanta* **2014**, *128*, 132–140.
[132] J. Munoz, M. Gallego, M. Valcárcel, *Anal. Chim. Acta* **2005**, *548*, 66–72.
[133] A. Kumar, S. K. Menon, *J. Phys. Org. Chem.* **2009**, *22*, 661–669.
[134] X. Shao, H. Gu, Z. Wang, X. Chai, Y. Tian, G. Shi, *Anal. Chem* **2012**, *85*, 418–425.
[135] H. Zhu, Y. Xu, A. Liu, N. Kong, F. Shan, W. Yang, C. J. Barrow, J. Liu, *Sens. Actuators, B.* **2015**, *206*, 592–600.
[136] C. Zhou, W. Jiang, B. K. Via, *Colloids Surf, B.* **2014**, *118*, 72–76.
[137] J. Shen, Y. Zhu, X. Yang, C. Li, *Chem. Commun.* **2012**, *48*, 3686–3699.
[138] L. Li, G. Wu, G. Yang, J. Peng, J. Zhao, J. J. Zhu, *Nanoscale.* **2013**, *5*, 4015–4039.
[139] S. Zhu, S. Tang, J. Zhang, B. Yang, *Chem. Commun.* **2012**, *48*, 4527–4539.
[140] S. L. Ting, S. J. Ee, A. Ananthanarayanan, K. C. Leong, P. Chen, *Electrochim. Acta* **2015**, *172*, 7–11.

Received: March 17, 2016
Accepted: May 7, 2016
Published online: ■■ ▮▮, 0000

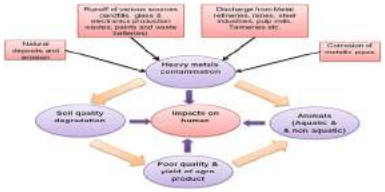
 © 2016 Wiley-VCH Verlag GmbH & Co. KGaA, Weinheim

REVIEWS

S. K. Pandey, P. Singh, J. Singh,
*S. Sachan, S. Srivastava, S. K. Singh**

■■–■■

Nanocarbon-based Electrochemical Detection of Heavy Metals



© 2016 Wiley-VCH Verlag GmbH & Co. KGaA, Weinheim

ResearchGate

See discussions, stats, and author profiles for this publication at: https://www.researchgate.net/publication/291019783

Pilot based Channel Estimation and SCGNN based Equalization for MIMO-OFDM System

Article · December 2015

DOI: 10.5120/ijca2015907205

READS

14

2 authors, including:



Zainul Abdin Jaffery

Jamia Millia Islamia

33 PUBLICATIONS **76** CITATIONS

SEE PROFILE

All in-text references underlined in blue are linked to publications on ResearchGate, letting you access and read them immediately.

Available from: Zainul Abdin Jaffery
Retrieved on: 08 June 2016

Pilot based Channel Estimation and SCGNN based Equalization for MIMO-OFDM System

Zeeshan A. Abbasi
Assistant Professor
University Polytechnic
Jamia Millia Islamia, New Delhi

Zainul Abdin Jaffery
Professor
Dept. of Electrical Engineering
Jamia Millia Islamia, New Delhi

ABSTRACT
In this paper a new channel equalization technique is described based on Scaled Conjugate Gradient Neural Network (SCGNN) for Multiple Input Multiple Output (MIMO) Orthogonal Frequency Division Multiplexing (OFDM). To estimate the channel in frequency domain, Space Time Block Code (STBC) is used. At the beginning of each transmitted OFDM block the pilot sequence is inserted to estimate the channel. In the transmitter the 16-QAM modulation is used as it is efficient in conserving bandwidth. The performance is evaluated using MATLAB and various results are plotted at different values of SNR. It is observed from the simulation that the proposed channel estimation and equalization method greatly reduced the Symbol Error Rate. We are able to achieve the SER as low as 0.01at a very low value of SNR. The MMSE is also greatly reduced and the system converges very fast.

General Terms
ISI (Inter-symbol Interference), BER (Bit Error Rate), SNR (Signal to Noise Ratio)

Keywords
Scaled Conjugate Gradient Network, MIMO, OFDM, Equalization

1. INTRODUCTION
For wireless mobile communication the OFDM gained a lot of attention of the researchers as it fulfill the needs of high data transmission rates. OFDM gives huge channel capacity gain but the multipath effect is more severe as compare to the Single Input Single Output (SISO) system [1-4]. OFDM technology for wireless communication is becoming popular due to its advantages such as the high spectral efficiency, robustness to frequency selective fading and the feasibility of low cost transceiver implementations [5].OFDM is considered one of the most promising technology for present and future wireless communication used in 3G or WiMex [6].

To improve the performance of the OFDM system, channel estimation and equalization plays an important role. For OFDM over fast varying fading channels the channel estimation is carried out by transmitting known pilot symbols in given position. The equalization is to reduce the channel distortion causing Inter Symbol Interference (ISI). The circuit or equipment used to achieve equalization is called an equalizer. The equalizer strengthen or weaken the energy of specific frequency band [7]. In this paper the channel estimation is done using pilot based approach and equalization using SCGNN.

There are many pilot design techniques exist for I/Q imbalance estimation in Quadrature modulation.. The work in [8] explain the I/Q imbalance for SISO system. IT applies two OFDM training symbols per-subcarrier to perform estimation. The first training symbol has null tones at all negative subcarrier indexes. The drawback of this method is that it neither optimizes the pilot overhead (large overhead).It also does not considers the complex problem of pilot-data-multiplexed symbols, MIMO-OFDM, and exploitation of frequency-domain correlation. Similar drawbacks apply to [9] with only the difference that it considers (mainly frequency independent (FI)) transmitter I/Q imbalance only, and uses a different pilot design. It uses an even number of OFDM training symbols with non-zero pilots where the pilots at the negative (positive) subcarrier indexes of the even symbols are the same as (negatives of) the corresponding pilots at the odd training symbols. The same pilot design using two OFDM training symbols is applied in [10] but one extra symbol is added for channel estimation for the FI receiver I/Q imbalance, resulting in a larger overhead. It considers pilot-data-multiplexed symbols, but the other drawbacks still hold. [11] applies a pilot design (a combination of the designs in [8] and [9] which uses an even number of OFDM training symbols with null pilots at the negative subcarrier indexes of the first half of OFDM training symbols and at the positive subcarrier indexes of the second half of OFDM training symbols. It considers FI receiver I/Q imbalance only, and is also associated with the above drawbacks. In this paper comb type pilot based channel estimation is used in which we have inserted Np pilot symbol in the series of Z(k) OFDM symbols as per the following equation:

$$Z(k)=Z(mL+l)$$

Where L=number of sub carriers with respect to N_p, m is the pilot carrier index [12].

Several adaptive learning algorithms for feed-forward neural networks has already been discovered and implemented in equalizers. Many of these uses gradient decent algorithm but it suffers poor convergence rate and depends on parameters which have to be specified by the users because there is still no theoretical basis exist for choosing them. The value of these parameters are often crucial for the success of the algorithm e.g. back-propagation algorithm [13].The problem of optimizing the weight adjustment of neural network cab be effectively solve by Conjugate Gradient method.

2. OFDM SYSTEM MODEL
OFDM can be assumed as the special case of multicarrier wireless transmission. In OFDM a single data stream is transmitted over a number of low rate subcarriers. The idea of OFDM is to split the total bandwidth into a number of orthogonal subcarriers in order to transmit symbols using these sub carriers in parallel.

Figure 1 describe OFDM transmitter with two transmitting TX antenna and Figure 2 describe the OFDM receiver for two receive Rx antenna However, the idea can be applied to any number of Tx and Rx antennas. It can be seen from the

figure 1 that pilots are inserted at the beginning of the data and then the data is modulated by any of the modulating scheme but here 16-QAM modulation is used as it is bandwidth conserving. The modulated data is then encoded using the space time encoder. The output of the encoder is then split into two path, one for each antenna as described for the simple case of MIMO space-time coding in [14]. From [14] as it is applied for the OFDM system, we can have the following vectors for TX antennas 1 and 2:

T_{x_1} =[S_1 - $\hat{S_2}$ S_3 -$\hat{S_4}$ S_{N-1}-$\hat{S_N}$] .....(1)

T_{x_2} =[S_2 $\hat{S_1}$ S_4 $\hat{S_3}$ … S_N $\hat{S_{N-1}}$] .....(2)

where T_{x_1}, T_{x_2} are the vectors of the output of two Tx

antennas 1 and 2 respectively.

S_1 , S_2 are the pilot symbols and S_3 , S_4 ……. S_N are the message symbols. The total symbols will be double of the number of subcarrier. The encoded data is then passed through the serial to parallel converter which regroup the data as per the table 1:

Time	Carrier		
	1	2	k
T	S_1	S_3	S_{N-1}
t+T	$\hat{S_2}$	$-\hat{S_4}$	$\hat{-S_N}$

Before transmitting the signal to each antenna, a cyclic prefix is added to the message signal of each Tx antenna and then the signal is transmitted through the frequency selective channel. The cyclic prefix is assumed to be longer than the largest delay spread.The channel is assumed as the Rayleigh fading channel which is widely used as the channel in urban areas. Assuming CH1 and CH2 are the two channels from Tx antennas 1 and 2 respectively to the receiver.

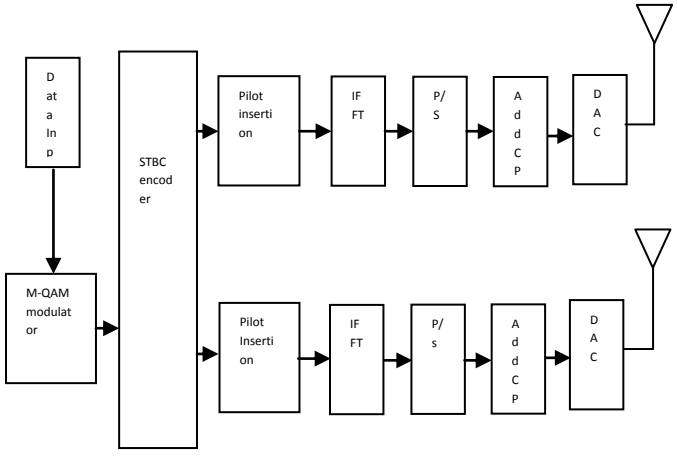


Figure 1. OFDM Transmitter with Two Transmitting Antennas

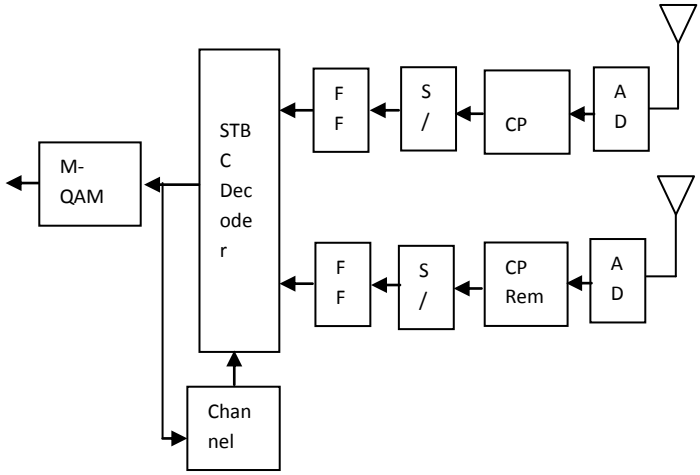


Figure 2. OFDM Receiver with Two Receiving Antennas

During transmission, noise also effect the transmitted signal and added to it thus by assuming CH [n,k]=CH[n+1,k], the received signal can be expressed as:

$$r[n,k] = CH_1[n,k]S_1[n,k] + CH_2[n,k]S_2[n,k] + \eta[n,k] \quad (3)$$

where

$r[n,k]$ = Received Symbols

$S[n,k]$ =Transmitted Symbols

$\eta[n,k]$ =White Gaussian Noise (AWGN)

$[n,k]$ = n-th OFDM block and k-th sub-carrier

S_1, S_2 = symbols transmitted from the Tx antennas 1 and 2 respectively and are given by

$$S_1 = [s_1 \; s_3 \; s_{N-1} \quad -\hat{s}_2 \; -\hat{s}_4 \; -\hat{s}_N \;] \quad \text{.....(4)}$$

$$S_2 = [s_2 \; s_4 \; s_N \quad \hat{s}_1 \; \hat{s}_3 \; \hat{s}_{N-1}] \quad \text{.....(5)}$$

Finally the received signal is decoded as given by [14] and the result is given by

$$\hat{S}_{i+1}[n,k] = CH_1^*[n,k]r[n,k] + CH_2[n,k]r^*[n,k+1] \quad (6)$$

$$\hat{S}_{i+1}[n,k] = CH_2^*[n,k]r[n,k] - CH_1[n,k]r^*[n,k+1] \quad (7)$$

Where $i = 1,3,5.....N-1$ representing the symbol and $\hat{S}$ representing the decoded data.

3. PROPOSED CHANNEL ESTIMATION METHOD

There are several techniques discussed in [15] to estimate the radio channel in OFDM system. In propose system we have

used pilot aided channel estimation technique. In order to estimate the channel first a pilot symbol is transmitted. In OFDM system the pilot is transmitted in the beginning of each OFDM block. Once the channel is estimated, equation (6) & (7) are used to decode the transmitted symbol by replacing CH_1 and CH_2 by the estimated ones. Thus, the two received symbols and the first symbol of each block of each antenna are used to estimated CH_1 and CH_2.

The estimated equation for CH_1 and CH_2 can be expressed as:

$$\hat{CH}_1[n,k] = \frac{r[n,k]S_1^*[n,k] - r[n,k+1]S_2[n,k]}{|S_1[n,k]|^2 + |S_2[n.k]|^2} \quad (8)$$

$$\hat{CH}_2[n,k] = \frac{r[n,k]S_2^*[n,k] - r[n,k+1]S_1[n,k]}{|S_1[n,k]|^2 + |S_2[n.k]|^2} \quad (9)$$

Therefore simply by replacing CH_1 and CH_2 in equation (6) and (7) by $\hat{CH}_1$, $\hat{CH}_2$ in equation (8) and (9) it can be deduced :

$$\hat{S}_{i+2}[n,k] = \hat{CH}_1[n,k]\, r[n,k+2] + \hat{CH}_2[n,k]\, r^*[n,k+3] \quad (10)$$

$$\hat{S}_{i+3}[n,k] = \hat{CH}2[n,k]\, r[n,k+2] - \hat{CH}_1[n,k]\, r^*[n,k+3] \quad (11)$$

Where $i = 1,3,5.....N-4$

The propose method is simple and cost , computation effective.

4. PROPOSED CHANNEL EQUALIZATION METHOD

The channel equalization is the most important part as it reduces the ISI affect and improve the BER of the system. In this paper the channel equalization is done using Scale Conjugate Gradient Method . SCG is used to train the feed forward neural network. The neural network used in our system Consist of three layers: input ,hidden and output. The number of nodes used in input layer are three, hidden Layer are ten and in the output layer the nodes are two. The transfer function used for input is Logistic Sigmoidal and for hidden layer is purelin. Linear is selected for the output. Figure 2 shows the model of the Neural Network Used for simulation.

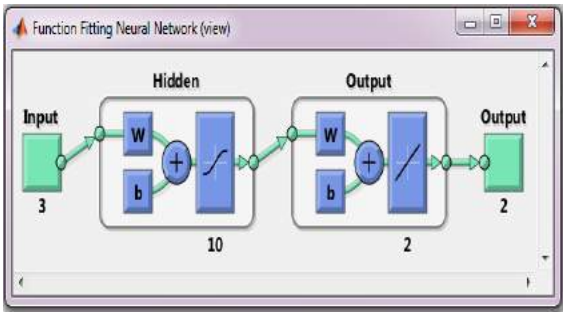


Figure 2: NN based Channel Equalizer

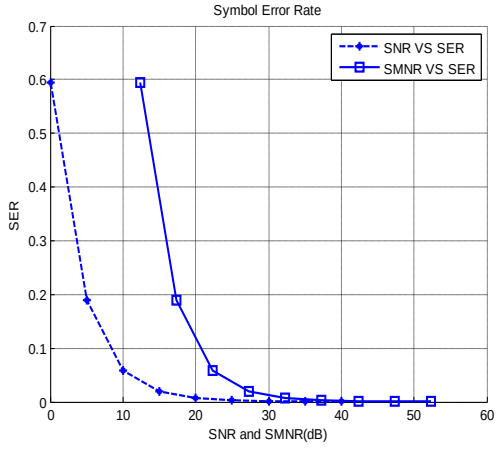
5. SIMULATION RESULTS

After the network is trained using the SCG method three parameters Such as channel length, signal length and channel noise are inputted to the network. For our simulation we have used signal length as 500, channel length as 20 and channel noise as 5. The simulation is done on MATLAB R2013a.Three different parameters Symbol Error Rate (SER),Bit Error Rate (BER) and Minimum mean square error (MMSE) are plotted against different values of Signal to noise ratio (SNR).

The results are tabulated in Table 2 and plotted in figure 3.

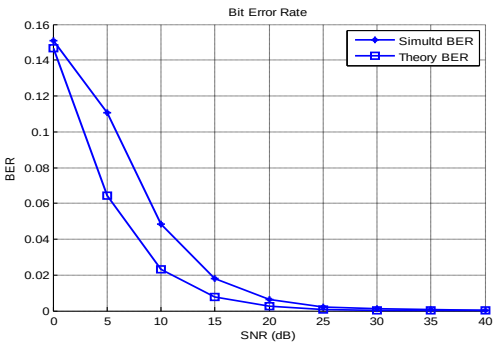
Table 2 : SNR VS BER/SER/MMSE

SNR	BER	SER	MMSE
0	0.1519	0.5964	0.1484
5	0.1078	0.1858	0.0769
10	0.0488	0.0589	0.0377
15	0.0181	0.0193	0.0188
20	0.0061	0.0062	0.0054
25	0.0022	0.0023	0.0021
30	0.001	0.001	0.0006
35	0.0006	0.0006	0.0005
40	0.0005	0.0005	0.0003



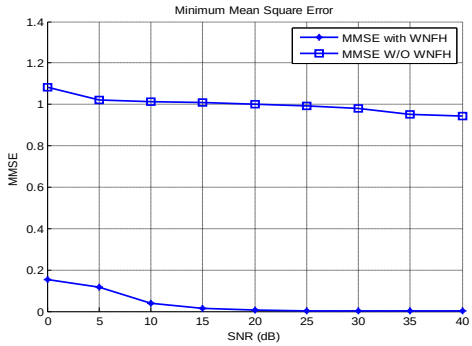
Graph 1. SNR/SNER VS SER

In Graph 1 the Symbol error rate (SER) are plotted against the two quantities signal to noise ratio (SNR) and Symbol to noise ratio (SMNR).Initially both behaves in the same manner but the slope of SMNR are more steep and both are coincide at the higher values.



Graph 2. SNR VS BER

In graph 2 the BER at different values of SNR are plotted. It is clear from the graph that the proposed SCGNN algorithm are performing very good as the simulated BER are very close to theoretical BER at very low values of SNR and as the SNR are increased up to 25 the two response become coincide i.e. simulated result catches the theoretical values.



Graph 3. SNR VS MMSE

In Graph 3 we have plotted minimum mean square error (MMSE) with and without equalization. It is very clear that the MMSE with equalization are far better which shows the effectiveness of our proposed SCGNN algorithm for equalization.

6. CONCLUSION

Wireless transmission of digital signals through multipath frequency selective channels can be done in perfect way using OFDM technique. OFDM can mitigate distortion caused by frequency selective fast fading channels as in OFDM the same copy of the data message can be obtained at the receiving end each experience different fading conditions (impossible to have deep fading at all the links) so the reception process can be performed in better manner as evident from graph 2.

The performance of the STBC-OFDM receiver depends mainly on the channel equalization stage. It has proven that NN based equalizers are very effective in dealing this kind of problem which is true from the graph 3.

7. REFERENCES

[1] Sanjana T and Suma M N, "Comparison of Channel

[2] Estimation and Equalization Techniques for OFDMSystems", *Circuits and Systems: Aninternationaljournal (CSIJ),* Vol 1,No 1, January 2014. Yi-Sheng Chen, "Semi-Blind Channel Estimation for

[3] MIMO Single Carrier With Frequency Domain Equalization Systems." *IEEE Transaction on VehicularTechnology,* Vol 59.No 1, pp 53-63, January 2010.Delestre F and Sum Y, "Pilot Added Channel Estimation for MIMO-OFDM System", *London Communication Symposium* 2009.

[4] Osvaldo Simeone and Umberto Spagnolini, "Pilot Based Channel Estimation for OFDM Systems by Tracking the Delay Subspace", *IEEE Transaction on Wireless Communications,* vol. 3, NO 1, January 2004.

[5] Tian-Ming Ma,Yu-Song Shi and Tying-Guan Wang, "A Low Complexity MMSE for OFDM Systems Over Frequency Selective Fading Channels", *IEEE Communication Letters,* Vol. 16. No 3, March 2012.

[6] D. Gesbert, M. Shafi, S. Da-shan, P. J. Smith, and A. Naguib, "From theory to practice: an overview of MIMO space-time coded wireless systems," *IEEE Journal on Selected Areas in Communications,* vol. 21, pp. 281-302, 2003.

[7] Xiang Li, Wen-De Zhong, Arokiaswami Alphones and Changyuan Yu, "Channel Equalization Using Independent

[8] Component Analysis in PDM-CO-OFDM",*IEEE Photonics Technology Letters*,Vol 26,No 5,pp 497 501,March 2014.W. Kirkland and K. Teo, "I/Q distortion correction for OFDM direct conversion receiver" *Electron. Lett.*, vol. 39, pp. 131-133, 2003.

[9] L. Brotje, S. Vogeler, and K-D. Kammeyer, "Estimation and correction of transmitter-caused I/Q imbalance in OFDM systems," in *Proc. 7thIntl. OFDM Workshop, ,* pp. 178–182. Sep. 2002

[10] Y. Egashira, Y. Tanabe, and K. Sato, "A novel IQ imbalance compensation method with pilot-signals for OFDM system," in *Proc. IEEE VTC Fall,* pp. 1–5,2006.

[11] A. Tarighat, R. Bagheri, and A. Sayed, "Compensation schemes and performance analysis of IQ imbalances in OFDM receivers," *IEEE Trans. Signal Process.*, vol. 53, pp. 3257–3268, 2005.

[12] Saroj K. Meher, Ashish Ghosh*, B. Uma Shankar and Lorenzo Bruzzone, "Neuro-Fuzzy Fusion: A New Approach to Multiple Classifier System" , 9th IEEE International Conference on Information Technology (ICIT'06),2005.

[13] Ibnkahla,M, "Application for Neural Networks to Digital Communications-A survey", Signal Processing,80,pp 1185- 1215, 2000.

[14] S. M. Alamouti, "A simple transmit diversity technique for wireless communications," *IEEE Journal on Selected Areas in Communications,* vol. 16, pp. 1451-1458, 1998.

[15] Mehmat Kemal Ozdemir and Huseyin Arslan, " Channel Estimation For Wireless OFDM System", IEEE Communication Surveys,Vol.9,No.2 pp 18-42,2007.

8. AUTHOR PROFILE

Prof. Zainul Abdin Jaffery obtained his B. Tech and M. Tech. in Electronics and Communication Engineering from Aligarh Muslim University, Aligarh, India in 1987 and 1989 respectively. He obtained his PhD degree from Jamia Millia Islamia (a central Govt. of India University) in 2004. Dr. Jaffery started his carrier as lecturer at Jamia Millia Islamia in 1990. Presently he is working as Professor in the Department of Electrical Engineering, Faculty of Engineering and

Technology, Jamia Millia Islamia, New Delhi, since 2010. Prof. Jaffery has published more than fifty research papers in the area of Electronics and communication engineering in refereed international /national journals and conferences. His research area includes applications of soft computing techniques in signal and image processing. Prof. Jaffery is a member of various academic societies of national and international repute

Zeeshan Ahmad Abbasi obtained his Bachelor's degree in Electronics and Communication with Honors from Jamia Millia Islamia, Delhi India. Then he obtained his Master's degree in Communication from Delhi College of Engineering, University of Delhi.He is pursuing his Ph.D from JMI Delhi. He has worked for 20 years in Police Communication, Ministry of Home affairs, Government of India on VSAT Networks and HF, VHF Communication. He has taught various Electronics and Communication Engineering papers at many reputed Universities like Jamia Millia Islamia, Hamdard University, Delhi University, Maharishi Dayanand University, IGNOU etc.

Question Answering over Knowledge Base using Factual Memory Networks

Sarthak Jain
Department of Computer Engineering
Delhi Technological University
DL, India
successar@gmail.com

Abstract

In the task of question answering, Memory Networks have recently shown to be quite effective towards complex reasoning as well as scalability, in spite of limited range of topics covered in training data. In this paper, we introduce Factual Memory Network, which learns to answer questions by extracting and reasoning over relevant facts from a Knowledge Base. Our system generate distributed representation of questions and KB in same word vector space, extract a subset of initial candidate facts, then try to find a path to answer entity using multi-hop reasoning and refinement. Additionally, we also improve the run-time efficiency of our model using various computational heuristics.

1 Introduction

Open-domain question answering (Open QA) is a longstanding problem that has been studied for decades. Early systems took an information retrieval approach, where question answering is reduced to returning passages of text containing an answer as a substring. Recent advances in constructing large-scale knowledge bases (KBs) have enabled new systems that return an exact answer from a KB.

A key challenge in Open QA is to be robust to the high variability found in natural language and the many ways of expressing knowledge in large-scale KBs. Another challenge is to link the natural language of questions with structured semantics of KBs. In this paper, we present a novel architecture based on memory networks (Bordes et al., 2015) that can be trained end-to-end using (question, answer) pairs as training set, instead of strong supervision in the form of (question, associated facts in KB) pairs.

The major contributions of this paper are two-fold: first, we introduce factual memory networks, which are used to answer questions in natural language (e.g *"Where was Bill Gates born?"*) using facts stored in the form of (subject, predicate, object) triplets in a KB (e.g *('Bill Gates', 'place of birth', 'Seattle')*). We evaluate our system against current baselines on various benchmark datasets. Since KBs can be extremely large, making it computationally inefficient to search over all entities and paths, our second goal of this paper is to increase the efficiency of our model in terms of various performance measures and provide better coverage of relevant facts, by intelligently selecting which nodes to expand.

2 Related Work

The state-of-the-art methods for QA over a knowledge base can be classified into three classes: semantic parsing, information retrieval and embedding based.

Semantic parsing (Cai and Yates, 2013; Berant et al., 2013; Kwiatkowski et al., 2013; Berant and Liang, 2014; Fader et al., 2014) based approaches aim to learn semantic parsers which parse natural language questions into logical forms and then query knowledge base to lookup answers. Even though these approaches are difficult to train at scale because of the complexity of their inference, they tend to provide a deep interpretation of the question.

Information retrieval based systems retrieve a set of candidate answers and then conduct further analysis to rank them. Their main difference lies in select-

Proceedings of NAACL-HLT 2016, pages 109–115,
San Diego, California, June 12-17, 2016. ©2016 Association for Computational Linguistics

ing correct answers from the candidate set. Yao and Van Durme (2014) used rules to extract question features from dependency parse of questions, and used relations and properties in the retrieved topic graph as knowledge base features.

Embedding based approaches (Bordes et al., 2014b; Bordes et al., 2014a) learn low-dimensional vectors for words and knowledge base constitutes, and use the sum of these vectors to represent questions and candidate answers. However, simple vector addition ignores word order information and higher order n-grams. For example, the question representations of *"who killed A?"* and *"who A killed?"* are same in the vector addition model. (Bordes et al., 2015) used strong supervision signal in form of supporting facts for a question during training to improve their performance.

3 Preprocessing KB and Questions

3.1 Processing FREEBASE

Freebase : Freebase (Bollacker et al., 2008) is a huge and freely available database of factual information, organized as triplets (subject Entity, Relationship, object Entity). All Freebase entities and relationships are typed and the lexicon for types and relationships is closed. Each entity has an internal id and a set of alternative names (called aliases, e.g. JFK for John Kennedy) that can refer to that entity in text.

The overall structure of Freebase is a hypergraph, in which more than two entities can be linked together in a n-ary fact. The underlying triple storage involves dummy entities to represent such facts, effectively making actual entities involved linked through paths of length 2, instead of 1. For example, a statement like *"A starred as character B in movie C"* is represented in Freebase as (A, 'starring', dummy entity), (dummy entity, 'movie', C), (dummy entity, 'character', B), where dummy entity has same internal id in all three facts.

To obtain direct links between entities in such cases, we modify these facts by removing the dummy entities and using the second relationship as the relationship for the new condensed facts. In our example, we condense aforementioned facts into two : (A, 'character', B) and (A, 'movie', C). Also, we label these condensed facts as siblings of each other. Therefore, (A, 'character', B) is **sibling** of (A, 'movie', C) and vice versa. Moving forward, we use the term 'fact' to refer to a triplet in Freebase, containing actual entities only (no dummy entities).

After above preprocessing, we represent each entity and relationship in KB as a vector $\in \mathbb{R}^d$. Each such entity/relationship vector is computed as the average of its word vectors, where each word vector $\in \mathbb{R}^d$. In case of entities, we also include word vectors of all its aliases when calculating the average. Such a scheme has the additional advantage that we can benefit from pre-trained unsupervised word vectors (e.g. from Word2Vec), which in general capture some distributional syntactic and semantic information.

3.2 Processing Question

Let a question be given as sequence of words $(x_1, x_2, \ldots, x_{|q|})$. Each word x_i mapped to its word vector. We experimented with two different ways to compose the question embedding q out of these word-vectors:

Bag-of-words (BOW): It is sum of individual word vectors i.e. $q = \sum_{i=1}^{|q|} x_i$.

Position Encoding (PE): This heuristic take in account order of words in the question. The embedding is of form $q = \sum_{i=1}^{|q|} l_i \odot x_i$ where $\odot$ is an element-wise multiplication. For each i, l_i is a column vector $\in \mathbb{R}^d$ with the structure $l_{ij} = \min(\frac{i \times d}{j \times |q|}, \frac{j \times |q|}{i \times d})$, where d is the dimension of the embedding and j runs from 1 to d. This type of function ensures that initial part of summed vector is weighed higher for initial word vectors and vice versa. Thus, a statement like 'Who is parent of Darth Vader?' will map to a different embedding than statement like 'Who is Darth Vader parent of?'.

4 Model Description

4.1 Fact Extraction

To begin, we generate an initial list of facts (called candidate fact list) which is fed as input to our network. To generate this list, we match all possible n-grams of words of the question to aliases of Freebase entities and discard all n-grams (and their matched entities) that are a subsequence of another n-gram. All facts having one of the remaining entities as subject are added to candidate fact list.

4.2 Factual Memory Network

A L-Hop Factual Memory Network consists of L Computation Layers $C_1 \dots C_L$ connected one after another in a linear chain, and an Output Function. The initial Computation Layer C_1 takes as input the candidate fact list (from previous step) and the initial question embedding (from Section 3.2). The Output Function takes as input the output of final Computation Layer C_L and generates a list of answers (in form of Freebase entities). Layer C_i takes as input the output of layer C_{i-1}.

4.2.1 Computation Layer

A Computation layer accesses two inputs : 1) a fact list (our 'memory') $F = \{f_1 \dots f_{|F|}\}$, where each fact f is of form (s, R, o), s and o being the entity vectors and R the relationship vector, 2) a question embedding $q \in \mathbb{R}^d$. For each fact $f \in F$, we calculate an unnormalised score $g(f)$ and a normalized score $h(f)$.

We visualize a fact $f = (s, R, o)$ as a question-answer pair with (s, R) forming the question and o the answer. Therefore, $g(f)$ calculates similarity between the given question embedding and a hypothetical question of form $q' = (s, R)$.

$$g(f) = q^T(s + R) \tag{1}$$

For example, given a question q = *"Where was Bill Gates born?"* and a fact f = ('Bill Gates', 'place of birth', 'Seattle'), $g(f)$ will compute similarity between the question q and a hypothetical question q' of form *"Bill Gates place of birth?"*.

In case a fact f has some siblings $b_1, b_2, \dots, b_k$ (Section 3.1), we re-calculate its $g(f)$ as follows:

$$g(f) = \text{average}(g(f), g(b_1), g(b_2), \dots, g(b_k)) \tag{2}$$

where $g(f)$ on RHS is calculated using Eq.(1). For each sibling b_i, we calculate $g(b_i)$ using Eq.(1), but with b_i's subject replaced by its object in the formula.

Continuing with example in Section 3.1, if f = (A,'character',B) and b_1 = (A,'movie',C) is sibling of f, then this kind of processing is helpful in answering questions like *"What character does A play in movie C?"*, where fact f alone would not be enough to answer the question. Thus, above processing corresponds to a hypothetical question of form *"A character C movie ?"* for the fact f.

The normalized score $h(f)$ for a fact f is calculated using softmax function over all facts to determine their relative importance.

$$h(f) = \frac{exp(g(f))}{\sum_{f' \in F} exp(g(f'))} \tag{3}$$

Next we modify the fact list and the question embedding on basis of above calculated scores.

Step 1. Fact Pruning: We choose a threshold value ϵ and remove facts from fact list with $h(f) < \epsilon$. We found in our experiments that setting $\epsilon = \frac{\max_{f' \in F} h(f)}{2}$ gives best results. Performing pruning seems to remove non-relevant facts from subsequent computation, significantly improving our response time and allowing us to explore larger search space around the subgraphs of our question entities.

Step 2. The question embedding is modified as follows:

$$q' = q + \sum_{f \in F} h(f)(s + R) \tag{4}$$

Each such modification allows us to incorporate knowledge gathered (in form of hypothetical questions (s, R), weighted by their relevance h) at a particular layer about the question and pass it on to subsequent layer.

Step 3. Fact Addition: For each object entity o belonging to a fact f, we find all the facts (o, R', o') connected to it in KB and assign a score $h(f)q'^T(o + R')$ to each of them. If the new fact's score is $> \epsilon$, it is added to the fact list, effectively increasing path-length of our search space by 1.

The modified fact list along with the new question embedding(q') form the outputs of this layer, which are fed as input to next Computation Layer or the Output function.

4.2.2 Output Function

Output Function takes as input the output of final Computation Layer C_L (i.e. its output fact list and q') and calculate scores $h(f)$. The answer set is formed by the object entity of highest scoring fact as well as object entities of all those facts that have same s **and** R **as the highest scoring fact**.

This simple heuristic can increase utility of our model when there are multiple correct answers for a question. For example, a question like *'Who is*

Anakin Skywalker father of?' has more than one answer entities i.e. [*'Leia Organa'*, *'Luke Skywalker'*], and they are all linked by same s ('Anakin Skywalker') and R ('children') in Freebase. Of course, this follows the assumption that all such facts survive till this stage and atleast one of them is highest scoring fact.

4.3 Training Objectives

Let the QA training set $\mathcal{D}$ be set of question-answer pairs (q, A), where q is the question with list of correct answers A, e.g. (q = *'Who is Anakin Skywalker father of?'*, A = [*'Leia Organa'*, *'Luke Skywalker'*]). To train our parameters, we minimize the following loss function:

$$L_{QA} = \sum_{(q,A)} \sum_{n=1}^{L} \frac{n}{L} \| |F_n| \sum_{a \in A} a - |A| \sum_{f \in F_n} h(f).o \|^2 \quad (5)$$

Here n refers to n-th Computation Layer in our network (with F_n as its input fact list) and L is total number of Computation layers/hops in the network. This loss function defines the degree to which the object entities in fact list of a given layer are near to given answer list, weighted by $h(f)$, by taking pairwise difference between entities in answer list and objects in fact list. It was observed that minimizing this function gives higher weights to facts in which object entities are similar to answer entities as well as allow our network to generate shorter paths to reach answers from the question.

Paraphrasing Loss: Following previous work such as (Fader et al., 2013; Bordes et al., 2015), we also use the question paraphrases dataset **WikiAnswers**[1] to generalize for words and question patterns which are unseen in the training set of question-answer pairs. We minimize hinge loss so that a question and its paraphrases should map to similar representations. For the paraphrase dataset $\mathcal{P}$ of set of tuples (p, p') where p and p' are paraphrases of each other, the loss is defined as:

$$L_{PP} = \sum_{(p,p')} max\{0, 0.1 - p^T p' + p^T p''\} \quad (6)$$

where p'' is random example in $\mathcal{P}$ that is not a paraphrase of p and 0.1 is the margin hyper-parameter.

[1] http://knowitall.cs.washington.edu/paralex/

Backpropagation is used to calculate gradients while Adagrad was used to perform optimisation using max-norm regularisation. At each time step, a sample is drawn from either $\mathcal{P}$ with probability 0.25 or $\mathcal{D}$ with probability 0.75. If sample from $\mathcal{P}$ is chosen, gradient of L_{PP} is calculated. Otherwise, gradient of L_{QA} is calculated. The only parameters optimised in our model are the word vectors.

5 Experimental Setup

5.1 Baselines

We evaluate our model on following datasets:

WebQuestions[2]: This dataset, introduced in (Berant et al., 2013), contains 5,810 question-answer pairs where answer can be a list of entities, similar to (q, A) pairs described before. It was created by crawling questions through the Google Suggest API, and then obtaining answers using Amazon Mechanical Turk. WebQuestions is built on Freebase since all answers are defined as Freebase entities.

On **WebQuestions**, we evaluate against following baselines : (Berant et al., 2013; Berant and Liang, 2014; Yih et al., 2015) (semantic parsing based methods), (Fader et al., 2013) (uses a pattern matching scheme), (Bordes et al., 2014b; Bordes et al., 2014a; Bordes et al., 2015) (Embedding based approaches). Results of the baselines have been extracted from respective papers, except for (Berant et al., 2013; Berant and Liang, 2014) where we use the code provided by the author to replicate the results[2].

We compare our system in terms of F1 score as computed by the official evaluation script [2] (Berant et al., 2013), which is the average, over all test questions, of the F1-score of the sets of predicted answers.

SimpleQuestions[3]: The SimpleQuestions dataset, introduced in (Bordes et al., 2015), consists of a total of 108,442 questions written in natural language by human English-speaking annotators each paired with a corresponding Freebase fact. Our model only use the answer entity during the training, instead of whole fact. For example, {q = *'Which forest is Fires Creek in?'*, *Fact = '(fires creek, contained by, nantahala national forest)'*} could be data point in SimpleQuestions but we only use {q = *'Which forest is*

[2] www-nlp.stanford.edu/software/sempre/

[3] fb.ai/babi

Fires Creek in?', A = ['nantahala national forest']} for training.

On **SimpleQuestions**, we evaluate against previous result (Bordes et al., 2015) in terms of path-level accuracy, in which a prediction is correct if the subject and the relationship of highest scoring fact were correctly retrieved by the system.

5.2 Experimental Setup

The current dump of Freebase data was downloaded[4] and processed as described before. Our data contained 1.9B triplets. We used following splits of each evaluation dataset for training, validation and testing, same as (Bordes et al., 2015).
WebQuestions (WQ) : [3000, 778, 2032]
SimpleQuestions (SQ) : [75910, 10845, 21687]
We also train on automatic questions generated from the KB, which are essential to learn embeddings for the entities not appearing in either WebQuestions or SimpleQuestions. We generated one training question per fact following the same process as that used in (Bordes et al., 2014a).

The embedding dimension d was chosen 64 and max-norm cutoff was chosen as 4 using validation dataset. We pre-train our word vectors using method described by (Wang et al., 2014) to initialize our embeddings.

We experimented with variations of our model on both test sets. Specifically, we analyze the effect of question encoding **(PE vs BOW)**, number of Hops and inclusion of pruning/fact-additions **(P/FA)** in our model. In subsequent section, the word 'significant' implies that the results were statistically significant ($p < 0.05$) with paired T-test

6 Results

The results of our experiments are presented in Table 1. It shows that our best model outperforms considered baselines by about 3% in case of WebQuestions and even comparable to previous results in case of SimpleQuestions. Note that the best performing system for SimpleQuestions used strong supervision (question with supporting fact) while our model used only answer entities associated with a question for training.

[4]https://developers.google.com/freebase/data

Setup	WQ F1	SQ Acc
Random Guess	1.9	4.9
(Berant et al., 2013)	31.3	n/a
(Bordes et al., 2014a)	39.2	n/a
(Berant and Liang, 2014)	39.9	n/a
(Yih et al., 2015)	52.5	n/a
(Bordes et al., 2015)	42.2	**63.9**
PE + 3-Hop	**55.6**	59.7
BOW + 3-Hop	48.5	54.6
PE + 2-Hop	53.8	57.3
PE + 1-Hop	47.9	55.2
without P/FA	44.3	53.8

Table 1: Results on Evaluation datasets. Acc = Accuracy

We also give the performance for the variations of our model. Position Encoding improves our performance by 7% on WQ and by 5% on SQ, validating our choice of heuristic. Also, most answers in both datasets can be found within path length of two from candidate fact list, thus a 3-Hop network shows only 2% improvement over 2-Hop network.

	WQ	SQ
Top-2	70.1	68.7
Top-3	76.4	74.5
Top-5	80.3	77.6
Top-10	88.9	85.2

Table 2: Top-K results of our best model on each test set

Top-K Performance: In Table 2, we present the top-k results on both datasets. A large majority of questions can be answered from the top two or three candidates. By providing these alternative results (in addition to the top-ranked candidate) to the user, many questions can be answered correctly.

6.1 Efficiency and Error Analysis

Efficiency: All experiments for this paper were done on an Intel Core i5 CPU @ 2.60GHz, 8GB RAM with average HDD Access time of 12.3 ms. We calculated the Average Response time / Query (ART/Q), defined as average time taken by the system from input of query till the generation of answer list, including both computational and search-and-access time for KB. ART/Q for 1, 2 and 3 Hop Networks was 200, 350 and 505 ms respectively. Also the training time (including time to search for

hyper-parameters) for each of these networks was 740, 1360 and 2480 min respectively.

The major bottleneck in ART/Query for our network was the search-and-access of large amount of KB Data, therefore we implemented efficient search procedures using Prefix Trees for String Matching and pipelined different stages of the model using multi-threading (i.e. Fact Extraction, Computation and Back-Propagation were performed on individual threads) to improve our response and training time.

Effect of Pruning/Fact-Additions : From Table 1, we can see that pruning and fact-additions have significantly improved scores on all datasets. We analyzed 200 random data points from set of examples that were correctly answered only when P/FA was used (for each test set). In 97.5% of these samples, we observed that pruning allowed our model to remove spurious facts generated during initial fact extraction, making soft-max calculation in Eq. (3) more robust.

We also observed that the set of correctly answered questions using model without P/FA was proper subset of one with P/FA on each evaluation dataset, signifying that if relevant facts were scored higher in previous Computation layers, their scores are not reduced as more facts are added in subsequent layers. Removing pruning alone didn't improve our performance by more than 0.4% on any dataset while exponentially increasing the response time, signifying that pruning itself didn't remove relevant/correct fact in majority of examples.

On the computational end, we tried to determine the effect of pruning on our model response time (excluding search and access time). Including pruning improved our ART/Q by approximately 44% during test phase and by 21% during training phase for our 3 Hop network.

Manual Error Analysis : We sampled 100 examples from each test set to identify major sources of errors made by our model. Following classes of errors were determined :

Complex Questions (55%) : These types of questions involved temporal or superlative qualifier like 'first', 'after', 'largest', etc. This problem occurred in both test sets. We may be able to solve this problem using small set of rules for comparison on final answer set or better semantic representations for numerical values and qualifiers.

Question Ambiguity (20%) : This error class contains those questions that may have ambiguity in their interpretation. For example, a question like 'Where is shakira from?' generated answer as 'place_of_birth' (Baranquilla) while ground truth is 'nationality' (Colombia). This occurred mostly in WebQuestions dataset.

Ground truth Inconsistency (10%) : This type of error occurred when ground truth differed from correct entity present in Freebase KB (even though both are correct in many cases). For example, the question 'Where did eleanor roosevelt died?' have ground truth as 'New York City' whereas KB delivers the entity 'Manhattan', even though both are entities in Freebase. It occurred only in WebQuestions dataset.

Miscellaneous (15%) : This error class contains bad entity/relationship extraction (for example, mapping Anakin Skywalker to Darth Vader), bad question/answer pairs (e.g. q = "what time does american horror story air?" A = [Tom Selleck]), Typos in Question, etc.

7 Conclusion

This paper presents a Factual Memory Network model that aims to perform question-answering using facts from Knowledge bases like Freebase. The system uses a multi-hop neural network that can perform reasoning over facts generated from named entities in a given question as well as traverse the knowledge graph to include more information.

In future, we hope to extend our system so that it can work better with n-ary relations present in Freebase to deal with qualifiers, improve entity disambiguation mechanism in our model as well as include a mechanism to involve user interaction with system to improve our rates. Another goal is to add support for KBs with noisy data generated through automated relation extraction from unstructured data (for example OLLIE, etc) as well as for unstructured sources of knowledge (like Wikipedia) in our model, to extend and improve its utility.

References

Hannah Bast and Elmar Haussmann. 2015. More accurate question answering on freebase. In *Proceedings*

of the 24th ACM International on Conference on Information and Knowledge Management, pages 1431–1440.

Jonathan Berant and Percy Liang. 2014. Semantic parsing via paraphrasing. In *Proceedings of the 52nd Annual Meeting of the Association for Computational Linguistics*, pages 1415–1425.

Jonathan Berant, Andrew Chou, Roy Frostig, and Percy Liang. 2013. Semantic parsing on freebase from question-answer pairs. In *Proceedings of the 2013 Conference on Empirical Methods in Natural Language Processing*, pages 1533–1544.

Kurt Bollacker, Colin Evans, Praveen Paritosh, Tim Sturge, and Jamie Taylor. 2008. Freebase: a collaboratively created graph database for structuring human knowledge. In *Proceedings of the 2008 ACM SIGMOD international conference on Management of data*, pages 1247–1250.

Antoine Bordes, Sumit Chopra, and Jason Weston. 2014a. Question answering with subgraph embeddings. In *Proceedings of the 2014 Conference on Empirical Methods in Natural Language Processing*, pages 615–620.

Antoine Bordes, Jason Weston, and Nicolas Usunier. 2014b. Open question answering with weakly supervised embedding models. In *Machine Learning and Knowledge Discovery in Databases*, pages 165–180. Springer.

Antoine Bordes, Nicolas Usunier, Sumit Chopra, and Jason Weston. 2015. Large-scale simple question answering with memory networks. *arXiv preprint arXiv:1506.02075*.

Qingqing Cai and Alexander Yates. 2013. Semantic parsing freebase: Towards open-domain semantic parsing. In *Second Joint Conference on Lexical and Computational Semantics (*SEM), Volume 1: Proceedings of the Main Conference and the Shared Task: Semantic Textual Similarity*, pages 328–338.

Li Dong, Furu Wei, Ming Zhou, and Ke Xu. 2015. Question answering over freebase with multi-column convolutional neural networks. In *Proceedings of the 53rd Annual Meeting of the Association for Computational Linguistics*, pages 260–269.

Anthony Fader, Stephen Soderland, and Oren Etzioni. 2011. Identifying relations for open information extraction. In *Proceedings of the Conference on Empirical Methods in Natural Language Processing*, pages 1535–1545.

Anthony Fader, Luke Zettlemoyer, and Oren Etzioni. 2013. Paraphrase-driven learning for open question answering. In *Proceedings of the 51st Annual Meeting of the Association for Computational Linguistics*, pages 1608–1618.

Anthony Fader, Luke Zettlemoyer, and Oren Etzioni. 2014. Open question answering over curated and extracted knowledge bases. In *Proceedings of the 20th ACM SIGKDD international conference on Knowledge discovery and data mining*, pages 1156–1165.

Tom Kwiatkowski, Eunsol Choi, Yoav Artzi, and Luke Zettlemoyer. 2013. Scaling semantic parsers with on-the-fly ontology matching. In *Proceedings of the 2013 Conference on Empirical Methods in Natural Language Processing*, pages 1545–1556.

Thomas Lin, Oren Etzioni, et al. 2012. Entity linking at web scale. In *Proceedings of the Joint Workshop on Automatic Knowledge Base Construction and Web-scale Knowledge Extraction*, pages 84–88.

Siva Reddy, Mirella Lapata, and Mark Steedman. 2014. Large-scale semantic parsing without question-answer pairs. *Transactions of the Association for Computational Linguistics*, 2:377–392.

Richard Socher, Danqi Chen, Christopher D Manning, and Andrew Ng. 2013. Reasoning with neural tensor networks for knowledge base completion. In *Advances in Neural Information Processing Systems*, pages 926–934.

Sainbayar Sukhbaatar, Jason Weston, Rob Fergus, et al. 2015. End-to-end memory networks. In *Advances in Neural Information Processing Systems*, pages 2431–2439.

Zhen Wang, Jianwen Zhang, Jianlin Feng, and Zheng Chen. 2014. Knowledge graph and text jointly embedding. In *Proceedings of the Conference on Empirical Methods in Natural Language Processing*.

Jason Weston, Sumit Chopra, and Antoine Bordes. 2014. Memory networks. *arXiv preprint arXiv:1410.3916*.

Min-Chul Yang, Nan Duan, Ming Zhou, and Hae-Chang Rim. 2014. Joint relational embeddings for knowledge-based question answering. In *Proceedings of the 2014 Conference on Empirical Methods in Natural Language Processing*, pages 645–650.

Wen-tau Yih, Ming-Wei Chang, Xiaodong He, and Jianfeng Gao. 2015. Semantic parsing via staged query graph generation: Question answering with knowledge base. In *Association for Computational Linguistics (ACL)*.

Solar Energy 135 (2016) 242–252

Contents lists available at ScienceDirect

Solar Energy

journal homepage: www.elsevier.com/locate/solener

Rear contact SiGe solar cell with SiC passivated front surface for >90-percent external quantum efficiency and improved power conversion efficiency

Rahul Pandey, Rishu Chaujar *

Department of Engineering Physics, Delhi Technological University, Shahbad Daulatpur, Main Bawana Road, New Delhi, Delhi 110042, India

ARTICLE INFO

Article history:
Received 4 November 2015
Received in revised form 26 April 2016
Accepted 31 May 2016

Keywords:
ATLAS
Rear contact
Power conversion efficiency
Recombination
SiGe
Solar cell

ABSTRACT

In this effort, 10 μm thick rear contact (RC) silicon–germanium (SiGe) based solar cell device has been discussed with SiC (20 nm)-based front surface passivation for the suppression of interface recombination as well as improvement of short circuit current density (J_{SC}) and open-circuit voltage (V_{OC}). The design principles presented here balance the electronic and photonic effects together and is a significant step to design highly efficient thin solar cells. Photo reflectance is significantly reduced in the UV/visible spectral region due to the presence of SiC. This results in external quantum efficiency (EQE) >90% in the spectrum range of 400–650 nm wavelength. Also, at wavelengths equivalent to 300 nm, SiC passivated device shows record EQE of 85%. The presence of SiC as a surface passivating layer shows enhanced surface characteristics in terms of reduced surface recombination and higher photon absorption rate. This results in 15.4% power conversion efficiency (PCE) under standard air mass 1.5 illuminations. Further, the proposed device has also been analyzed for concentrator photovoltaics (CPV) applications, resulting in 18.4% and 19.3% efficiencies at 1 W/cm^2 (10 suns, 27 °C) and 2 W/cm^2 (20 suns, 27 °C) respectively. Till date, the proposed design proves to be highly efficient in the sub 10 μm regime. All the simulations have been done using DEVEDIT and ATLAS device simulator

© 2016 Elsevier Ltd. All rights reserved.

1. Introduction

Environment-friendly energy source has emerged as a great alternative for the grievous conventional energy source. Solar energy has been discovered to be the most eye-catching energy source because of its environment-friendly nature. In order to use this energy, it must be converted into the desired form of energy. Solar photovoltaic (PV) system is used to convert solar energy into electricity. The growing research topic in the field of PV is the development of low-cost and high-efficiency silicon solar cell. To maximize solar cell efficiency, it is necessary to optimize both the electrical characteristics and the optical absorption of the device (Green, 2003).

Systems based on silicon wafers are currently the dominant technology in PV market. Silicon is widely used material for PV due to its reliability, abundance, and mature fabrication process. In Silicon PV technology, to absorb the solar spectrum the thickness of conventional silicon cell typically more than 100 μm is required (Deinega et al., 2013). Since the absorption coefficient of silicon is small. The requirement of large volume and high-quality silicon significantly increases the module cost. Further, to make PV system feasible at large scale, it should be cost effective, with module cost to be <$0.5/W.

One promising high-efficiency solar cell concept is the back-contact back-junction (BC-BJ) solar cell, having both, junction and the electrodes are at the back side of the device. Now, since the junction and contacts are on the back side, front surface can be designed for optimum optical performance (Kerschaver and Beaucarne, 2006; Diouf et al., 2009). It has the advantages, such as prevention of optical shading losses at the front side and higher absorption and current density. The first 17% efficient under 50 sun condition BC-BJ solar cell was presented by Schwartz and Lammert (1975). It was designed as a cell for concentrator applications. The back diffusion, contact opening, and contacts were implemented using photolithography, about six lithography steps is required to produce the cell. This fabrication technique is not compatible with the cost-effective production of the solar cell. Further, a simplified processing of BC-BJ solar cell was introduced (Sinton and Swanson, 1990; Sinton et al., 1998). This was a major step toward the cost-effective BC-BJ solar cell and commercialized with Sunpower Corporation (Sinton et al., 1993). Today, Sunpower is the world leading

* Corresponding author.
E-mail address: Rishu.phy@dce.edu (R. Chaujar).

http://dx.doi.org/10.1016/j.solener.2016.05.056
0038-092X/© 2016 Elsevier Ltd. All rights reserved.

manufacturer of BC-BJ solar cell. Sunpower Corp. showed in 2007 that it is possible to achieve an average cell efficiency of 22% in the mass production of BC-BJ silicon solar cell (Ceuster et al., 2007). In year 2014, independently confirmed conversion efficiency of 23.0% for *N*-type RC cells has also been reported, at the end of the year, the interdigitated back contact (IBC) solar cells developed which resulted in an independently confirmed designated-area efficiency of 24.4%. The cell was fabricated on a 230 μm thick 1.5 Ω cm *N*-type CZ wafer (Feldmann et al., 2014; Franklin et al., 2014). The conventional RC solar cell has a large area which results in the higher material cost.

Further, nanostructuring has been projected as an appropriate method to make thin silicon an efficient absorber. However, these cells are not efficient due to Auger and surface recombination as the surface to volume ratio of the cells is large. However, a recent method to minimize the surface recombination for nanostructured based ~300 μm thick devices has been presented which results in 20% and 22% efficient cells (Ingenito et al., 2015; Savin et al., 2015). These cells have higher thickness, require high-quality materials, to have higher minority carrier lifetime: order of magnitude 10 ms. This kind of c-Si is very expensive, resulting in increased module cost. Conventional Si-based devices have 30 times higher thickness compared to the (15.4% efficient RC-SiGe) device proposed in this work. Some of the thin c-Si silicon-based solar cells are also available in the literature such as microsystem enabled 14 μm thick, 250 μm wide solar cell, with 14.9% efficiency is reported, and effort shows that the ultrathin wafer handling problem can be avoided by using low-cost microsystem techniques (Cruz-Campa et al., 2011). In the year 2013, an all-back-contact ultra-thin i.e. 10 μm thick silicon nanocone solar cell with 13.7% power conversion efficiency is reported (Jeong et al., 2013). A Si/Organic hybrid heterojunction solar cell has also been reported with PCE of 13.6% (He et al., 2015).

In our previous work, thin defect free SiC-based anti-reflection passivation layer has been designed for *N*-type wafer based RC Si and intrinsic wafer based SiGe solar cells (Pandey and Chaujar, 2015a,b). The SiC-based coaxial silicon nanowire solar cell has also been designed for optimal photovoltaic performance (Pandey and Chaujar, 2015c). Here, 10 μm thick SiC passivated *N*-type wafer based RC SiGe solar cell device has been designed and simulated which overcomes the critical problems associated with thin devices such as Auger, surface recombination and lower absorption at a higher wavelength. Present work shows superior EQE compared to Si cell, at higher wavelengths, since absorption coefficient of SiGe is higher as compared to Si in the higher wavelength regime. SiGe is used because the energy of the visible part of the spectrum used by the solar cell is less than 50% and to increase the absorption of sunlight, the low bandgap (<1.1 eV) material is required. Using low bandgap material in the solar cell makes the conversion efficiency of the cell effective. Nowadays, SiGe is used for high-frequency transistors as well as potential has been explored for solar cells also. In SiGe technology, the electrical properties of silicon are modified with germanium the number of free electrons in germanium is higher than silicon at a given temperature, which results in higher conductivity of Ge. SiGe processing is simple, the physical and electrical properties of silicon and germanium are similar (Ouellette, 2002; Kasap and Capper, 2007). Also, SiGe possesses higher mechanical strength and suppresses the high-intensity degradation of the solar cell under illumination (Yang et al., 2010). The band gap of SiGe can be modified by changing the Ge content, alternatively the optical absorption (Povolny et al., 2011; Wang et al., 2012). However, the cost of germanium doped wafer is higher compared to a silicon wafer, though present work shows it can be a good candidate for energy efficient applications. In future, development of novel cost effective energy efficient methode may reduce the overall dollar per watt ($/W) of the device. The discussed device shows superior EQE compared to silicon cell. Also, previous work shows that the photovoltaic parameters of 5 μm thick SiGe cell and 10 μm thick silicon cell are approximately same (Pandey and Chaujar, 2015d). This indicates that the proposed device significantly saves the material. In our previous work calibrated software program has been written in Silvaco ATLAS device simulator for 10 μm thick RC contact silicon cell (Pandey and Chaujar, 2015e). Therefore, 10 μm thick RC SiGe device has been simulated with the help of calibrated software program by changing the material parameters, since experimental results are not available for 10 μm thick RC SiGe solar cell.

2. Device structure and model description

Silvaco ATLAS has been used to simulate the device optoelectronic characteristics. In the simulation, we assume a two-dimensional structure i.e. RC SiGe solar cell as shown in Fig. 1(a). Also, the width is set so that the cell has an area of 1 cm^2. The $Si_{0.9}$ $Ge_{0.1}$ was used, with a very small Ge content. Since increasing the Ge content, decreases the band gap of SiGe, which further results in lower open circuit voltage. The bandgap 1.08 eV is used for SiGe. All the material parameters for SiGe including band gap have been obtained from experimentally available data (NSM Archive, 2016a), and the same has been used in the simulation. The substrate was *N*-type, with a doping density of 3×10^{15} cm^{-3}, whereas *N*+/*P*+ region has the doping density of 4×10^{20} cm^{-3}. The depth of *P*+ and *N*+ region was 3 μm and 2.5 μm, respectively, whereas the width was 45 μm and 30 μm, respectively and centre-to-centre distance (pitch) between the *N*+ and *P*+ regions is 52 μm. In a standard solar cell, *P*-type wafer has been preferred, so hence the diffusion length of minority carrier (electrons) in *P*-type wafer is higher than the diffusion length of minority carrier (holes) in *N*-type wafer. However, in large-scale production, it is difficult to avoid chemical and mechanical imperfection to the wafer. Here, lies the big advantage of *N*-type wafer solar cells. The performance of *N*-type cell is less vulnerable by chemical and mechanical imperfections. The *N*-type cell have several advantages over *P*-type cells. They are not prone to light-induced degradation due to the splitting of boron-oxygen complexes (Glunz et al., 1999; Tjahjono and Cotter, 2005). Further, 70 nm thick Nitride (Si_3N_4) is used as anti-reflecting front surface passivation, and modeled as an optical layer. The oxide (SiO_2) is used for back surface passivation with a thickness of 50 nm. Also, as the contact interface between metal and semiconductor is highly doped both for the emitter and back surface field (BSF) i.e. ~10^{20} cm^{-3}, we have defined our contacts as ohmic. This is done to avoid Schottky barriers, and thus unnecessarily higher computation time. The contact width of 6 μm has been used for both *P*+ and *N*+ regions with the thickness of 700 nm as shown in Fig. 1(a).

Further, in the presence of heavy doping, (>10^{18} cm^{-3}), experimental work has shown that the *PN* product turns out to be doping dependent (Slotboom, 1977). As the doping level rises, a decrease in the bandgap occurs, where the valence band raises by an approximately same amount as the conduction band is lowered. Discussed structure has heavily doped *P* and *N* regions, and so bandgap narrowing effects are enabled. These effects can be described by an analytic expression relating the variation in the bandgap, ΔEg to the doping concentration, *n* (Slotboom and de Graaff, 1977). Furthermore, the solar cell is carrier recombination affected device. Therefore, Auger and Shockley–Read–Hall (SRH) recombination models are selected during the simulation. Phonon transitions occur in the presence of trap or defect within the forbidden gap of the semiconductor (Shockley and Read, 1952; Hall, 1952), and Auger recombination occurs through a three particle transition whereby a mobile carrier is either captured or emitted.

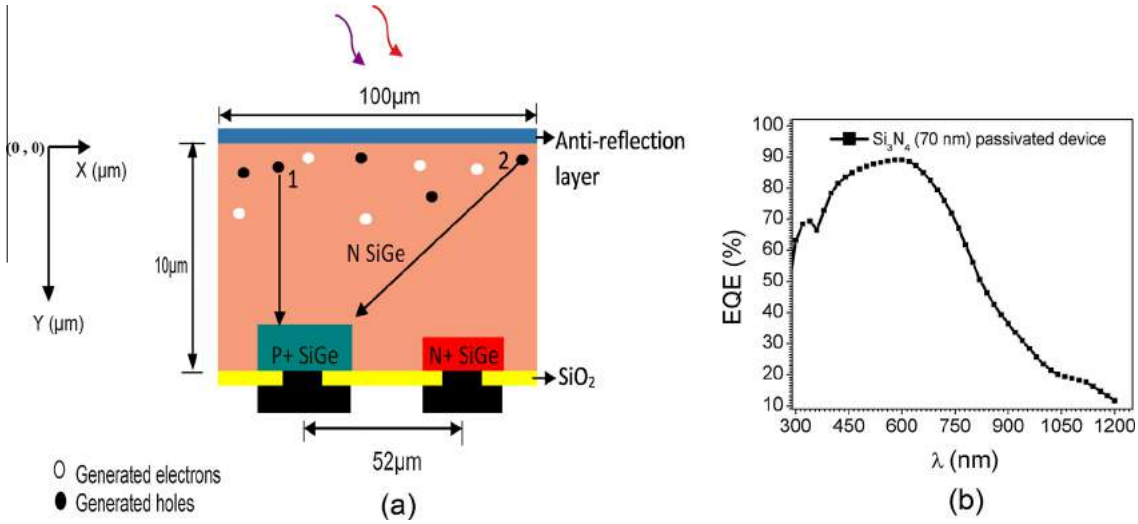


Fig. 1. (a) 10 μm RC-SiGe solar cell with 70 nm thick antireflection (AR) layer on top, 50 nm thick oxide layer has been used for back surface passivation. The region denoted by black color shows the ohmic contact to *N*+ and *P*+ regions. Pitch of the device is 52 μm, and (b) EQE of the device as shown in figure (a).

The underlying physics of such processes is unclear, and normally a more qualitative understanding is sufficient (Selberherr, 2012; Dziewior and Schmid, 1977). The concentration dependent mobility and field dependent mobility models have also been selected during simulation. The standard air mass 1.5G spectrum has been used for illumination and ray tracing algorithm is used to obtain the optical interaction. The complex reflective indices of all the materials as a function of wavelength and temperature have been obtained from sopra database (Atlas, 2014). Poisson's equation together with the continuity equation for electrons and holes are solved simultaneously by the software to obtain the current density–voltage (*J*–*V*) characteristics.

3. Results and discussions

3.1. Recombination rate and EQE of RC SiGe solar cell

In this section, 10 μm thick SiGe-based RC solar cell has been simulated as shown in Fig. 1(a). The EQE and recombination rate contour of proposed device have been presented in Figs. 1b and 2, respectively. In silicon-based cell, thickness more than 100 μm is required to absorb the solar spectrum (Deinega et al., 2013). Thinning the Si wafer, results in absorption loss, particularly at higher wavelengths, since the absorption coefficient (α) is small (Green and Keevers, 1995; Green, 2008). Therefore, use of SiGe instead of Si is a possible solution to minimize the absorption loss at higher wavelengths. The experimentally available data shows, the absorption coefficient (α) of SiGe is greater than Si in higher wavelength regime (NSM Archive, 2016b). The complex refractive index data of SiGe is obtained from software library and shown in Fig. 6(a) and (b), and the same have been used in the simulation. The proposed device shows superior EQE, and remarkably it achieved EQE > 76% in the spectrum range of 400–700 nm wavelength, shown in Fig. 1(b). At wavelength equivalent to 400 nm, proposed device shows EQE of the order of 78% that is at least 12% higher than of other Si nanostructured solar cells (Oh et al., 2012) and 18% greater than that of planar 10 μm thick Si cell with anti-reflection coating (Jeong et al., 2013).

Further, at the interface, the holes that are generated at point 1 need to travel the shorter diffusion length, to arrive at *N* – *P*+ junction compared to holes that are generated at point 2 shown in Fig. 1(a). This results in decreased collection probability in region II, therefore, higher recombination rate is observed in region II compared to the region I, as shown in Fig. 2(a) and (b). Region I and region II is defined in *N*-type region only, they do not includes the *P*+ and *N*+ regions. Further, the maximum recombination rate has been observed in *N*+ type and *P*+ type region due to heavy dop-

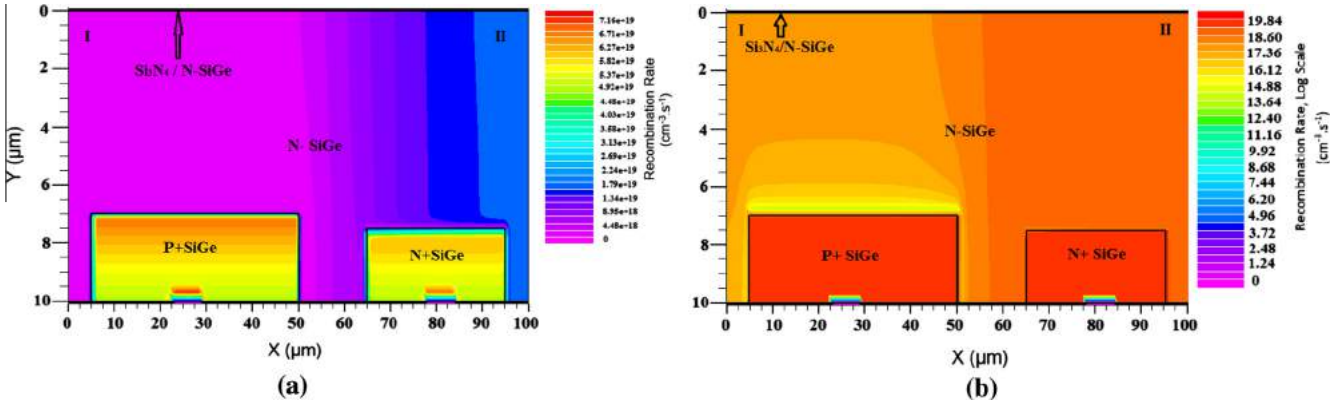


Fig. 2. Recombination rate contour (cm^{-3} s^{-1}) of illuminated, 10 μm thick RC SiGe solar cell under short circuit condition. Consisting 70 nm thick AR layer on top: (a) linear scale, and (b) log scale.

ing profile. Previous result shows, the recombination rate in region II of the 10 μm thick silicon-based RC solar cells is in the order of $\sim 10^{20}$ cm^{-3} s^{-1} (Pandey and Chaujar, 2015d), whereas in proposed device it is in the order of $\sim 10^{18}$ cm^{-3} s^{-1} shown in Fig. 2, suppressed minority carrier recombination has been observed in proposed device. In the case of back contact design, most of the carriers are generated near the front surface while the junction is far at the back surface. Lower recombination ensures higher carrier collection efficiency in proposed device.

3.2. Impact of front surface passivation on proposed device

In this section, different front surface passivation schemes have been discussed on proposed device i.e. 10 μm RC-RJ SiGe solar cell. The crystalline materials have the discontinuity of the crystal arrangement at the surface, which creates the dangling bond. Further, these dangling bonds at the interface create energy states within the forbidden energy band gap, which acts as a good recombination center. The recombination phenomena that arise from these states are known as Shockley–Read–Hall (SRH) recombination (Aberle et al., 1992). The front surface of most of the solar cell normally consists of well – passivated antireflective coating of thermal SiO_2 or Si_3N_4 layers (Diouf et al., 2010). In another technique, surface passivation is achieved by creating the front surface field using the high level of doping in low doped semiconductors of similar impurity. In this way, *P+*/*P* or *N+*/*N* regions are formed at the interface, which gives rise to an electric field at the junction. The electric field repels desired minority carriers from the interface and reduces the recombination at the surface. However, Auger recombination is increased due to the heavily doped region at the front surface.

Here, thin defect free SiC-based surface passivation scheme has been discussed with proposed device and results are compared with conventional insulators based passivation. The bandgap 2.2 eV has been used for SiC during simulation. Result shows, minority carrier concentration, is drastically reduced at the SiC/*N*-SiGe interface. This type of passivation prevents the minority carrier (holes) to reach the SiC/*N*-SiGe interface. The impact of three different front surface passivation (FSP) schemes has been obtained: single SiO_2 termed as FSP1, Si_3N_4 termed as FSP2, and SiC termed as FSP3.

Further, some useful parameters are plotted in Figs. 3 and 4, which shows that superior surface passivation has been achieved in the FSP3 layered device. The distribution of electric field near

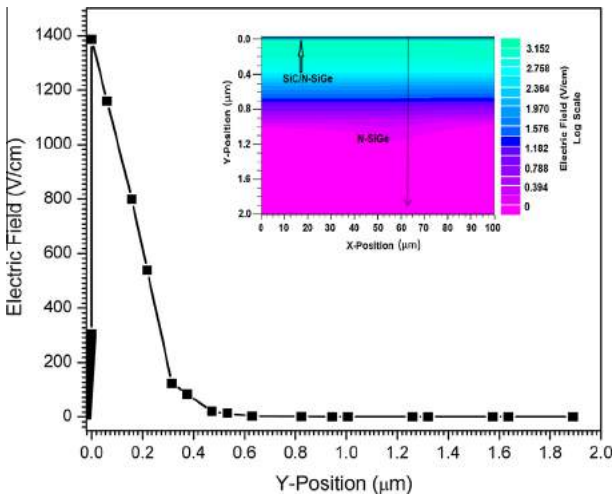


Fig. 3. The distribution of electric field near the (SiC/*N*-SiGe) interface. Inset shows the contour representation of electric field. Data is obtained under illumination with zero-bias voltage.

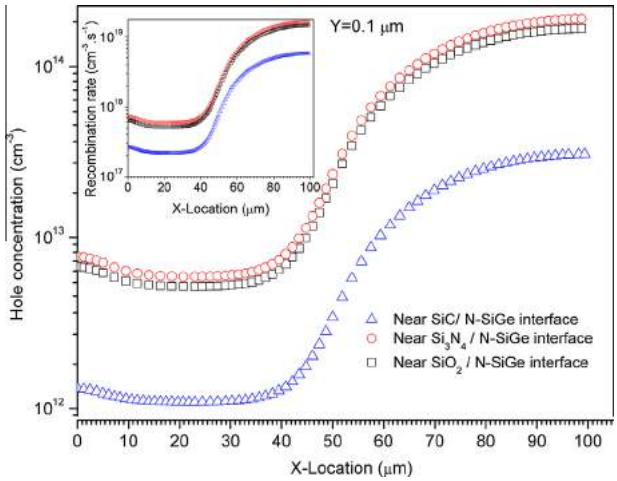


Fig. 4. Hole concentration near the interface of SiC, Si_3N_4 and SiO_2 passivated devices, respectively. Inset shows the recombination rate near the interface of SiC, Si_3N_4 and SiO_2 passivated devices, respectively. Data has been obtained from location (0, 0.1) to (100, 0.1) under illumination with short circuit condition.

the passivating interface has been presented in Fig. 3. The electric field direction is directed from SiC to SiGe, rendering it energetically unfavourable for hole transport to SiC/*N*-SiGe interface, resulting in a low concentration of holes at the passivating interface. In surface recombination process, an electron from conduction band recombines with the hole in the valence band via a defect level within the bandgap. If the concentration of one comrade electrons or holes is drastically reduced, then recombination rate reduces strongly (Aberle, 2000). Therefore, higher the concentration difference between electron and hole, lower is the recombination. The concentration of electron in the *N*-SiGe region is $\sim 10^{15}$ cm^{-3}. Therefore, sinking the hole concertation at the interface will produce higher concentration difference between electrons and holes, and thus results in lower surface recombination rate, as shown in Fig. 4. Results shows, the concentration difference between electron and hole is higher in SiC passivated device compared to SiO_2 and Si_3N_4 devices. Thus, results in lower surface recombination rate, as shown in the inset of Fig. 4. In FSP3 layered device, ten times lower minority carrier concentration is obtained near the interface (SiC/*N*-SiGe), compared to minority carrier concentration in the bulk (*N*-SiGe) region of the device, this shows the presence of SiC reduces the concentration of minority carriers only at the interface. In region II, at the interface, the hole concentration of $\sim 10^{13}$ cm^{-3} has been observed in FSP3 layer device, whereas the concentration of $\sim 10^{14}$ cm^{-3} observed in FSP1 as well as FSP2 layer devices, shown in Fig. 4. The hole concentration as well as recombination rate is low in region I compared to region II, as shown in Figs. 2 and 4. It is a typical distribution in the case of a short-circuiting. Under short-circuit condition, a space charge region is formed around the junction having an associated electric field that collects the generated electron-hole pairs, and the collection is complete in near *P+* region. However, outside the *P+* region, the substrate is neutral, and the collection will be by diffusion of electrons and holes toward the field region where they will be collected and separated. So, the regions nearer to the junction will have lower hole concentration since its holes will diffuse to the collecting field regions. The electrons and holes generated in a region greater than the diffusion length will never reach the junction, and the recombination process will balance them. As there is a lateral hole concentration gradient showing lateral hole flow to the junction. This concentration gradient decreases with the distance from the *P+*—*N* junction region. Furthermore, Fig. 5 shows the contour plot of recombination rate in the devices. At the interface, the

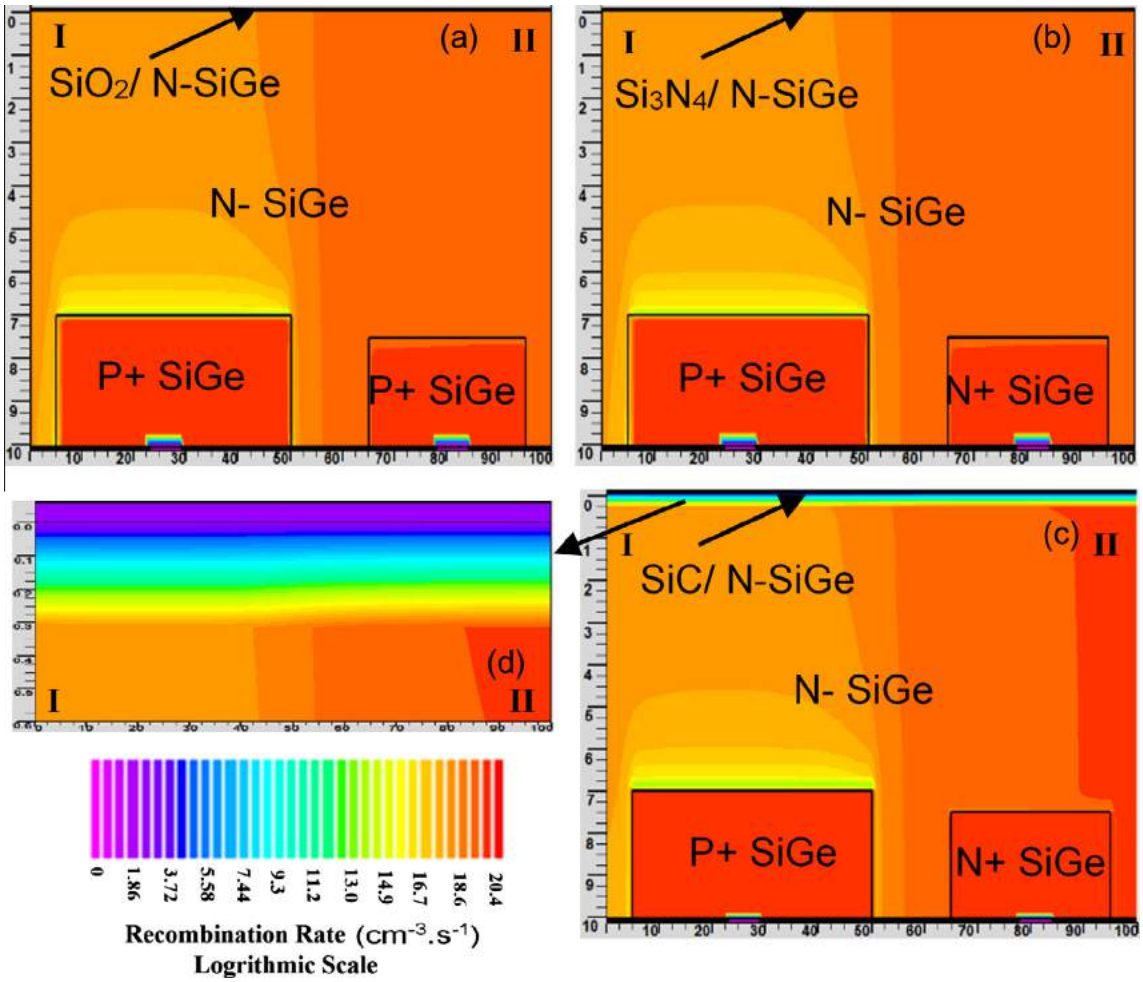


Fig. 5. Contour plot of recombination rate ($cm^{-3}\ s^{-1}$) in the log scale, (a) SiO_2 passivated RC-SiGe solar cell, (b) Si_3N_4 passivated RC-SiGe solar cell, (c) SiC passivated RC- SiGe solar cell and (d) Magnified view of (SiC/*N*-SiGe) interface in case of SiC passivated device. Data has been obtained under illumination with zero-bias voltage.

magnitude of recombination rate in the FSP3 layered device is of the order of 10^5–$10^{14}\ cm^{-3}\ s^{-1}$ from the location ($Y = 0.05$ to $Y = 0.03$) shown in Fig. 5(c) and (d). Whereas in the FSP1 and FSP2 devices it is around 10^{18}–$10^{19}\ cm^{-3}\ s^{-1}$. This shows SiC layer is much better for surface passivation as compared to conventional SiO_2 or Si_3N_4 layers. Lower recombination ensures that generated carrier will contribute more in external current and recombination current density will be suppressed.

Moreover, the spectrum response has been obtained for SiO_2, Si_3N_4, and SiC passivated devices, respectively. The optical properties of material used in the simulation are shown in Fig. 6(a)–(c) and EQE with different front surface passivation layers are shown in Fig. 6(d). Normally, the blue response of solar cell is reduced due to front surface recombination, whereas the midway response is reduced due to lower diffusion length and the red response is reduced due to transmitted photons and the back surface recombination. Result shows, significant improvement in blue response, as well as midway response, in FSP3 layer device compared to FSP1 and FSP2 layer devices shown in Fig. 6(d). The SiC-based device achieved EQE > 80% in the wavelength range of 300–720 nm. At wavelength equivalent to 550 nm, it shows EQE of the order of 95% that is 25.5% and 10.2% higher than FSP1 and FSP2 layer devices, respectively as shown in Fig. 6(d). Moreover, at smaller wavelength (300 nm) the SiC-based device shows, 35%, and 70% higher EQE compared to Si_3N_4 and SiO_2 based devices, respectively, as shown in Fig. 6(d). The performance of a solar cell is directly related to the amount of light entering the cell. The optical properties i.e. refractive index (n) and extinction coefficient (k) required for an antireflection coating (ARC) of a solar cell depend on the refractive index of the underlying substrate and, if applicable on the encapsulated cover, as well as the operating wavelength of that solar cell, in addition to the absorption of the light in the ARC film for that solar cell. Therefore, to minimise the absorption of the useful light in the ARC, a material having low absorption of useful light is needed. A low k can be equated to a low absorption, α (e.g. a k of less than 0.01 corresponds to the absorption of less than 1%), since $\alpha = 4\pi k/\lambda$. Fig. 6(a) and (c) shows that SiC has n between 2.9 and 2.5 in the spectrum range of 300–1200 nm and k of less than 0.01 for the wavelengths greater than 430 nm. In addition, thin SiO_2 based encapsulation has been assumed at the front surface of the SiC-based device, to minimize the reflectivity (Pandey and Chaujar, 2015a). Also, as per the patented work of (Allen et al., 2009), SiC film having n between 2.7 and 2.3 and k of less than 0.01 at a wavelength of 630 nm is a good candidate for antireflective coating for solar cells. Further, wavelength dependent extinction coefficient and absorption coefficient reported in Fig. 6(c) shows that SiC has higher absorption coefficient at lower wavelengths, whereas it is desired that SiC should be transparent in the simulated spectrum. The absorbance in a material is directly related to the absorption coefficient and thickness of the material used. This suggests that to minimize the absorption and increase the transparency, thinner SiC layer should be used. This phenomenon sets the limit on the thickness of SiC. The SiC layer used in the simulation is only 20 nm thick whose absorbance is

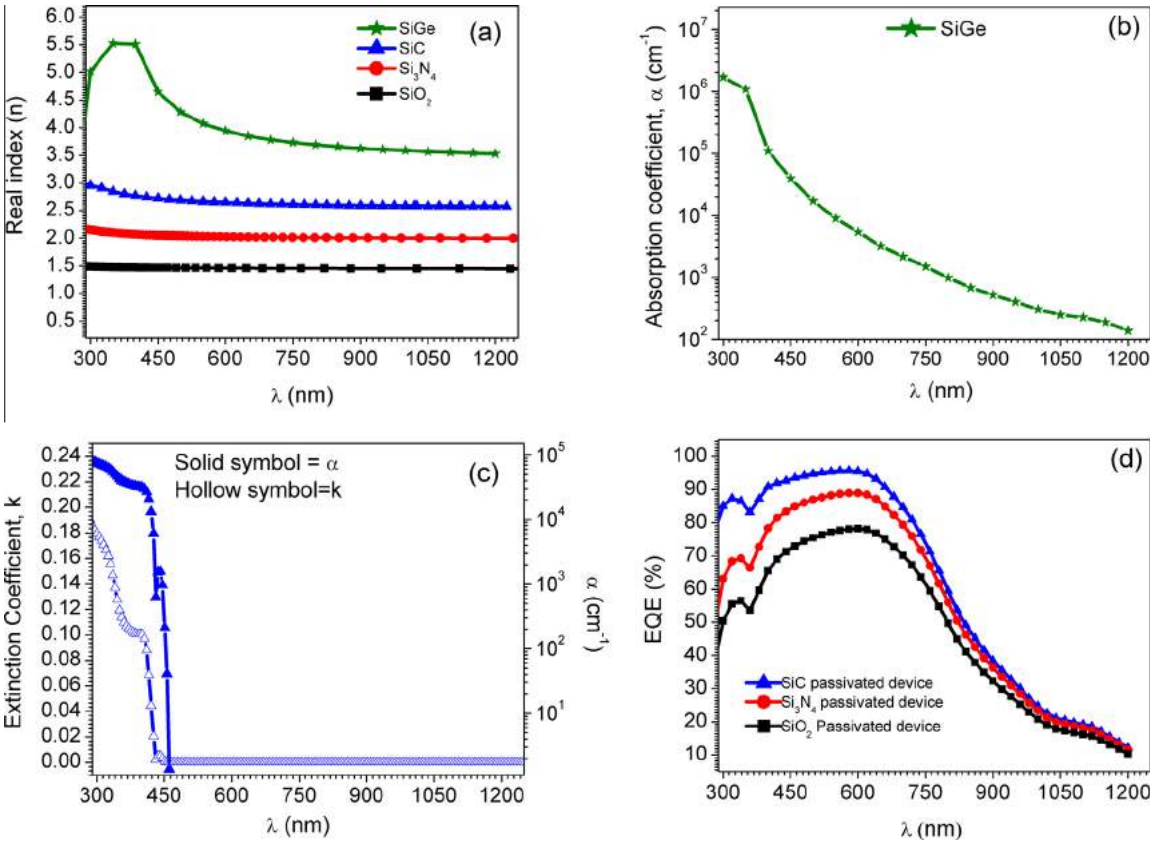


Fig. 6. Optical properties i.e. wavelength dependent (a) real index, n for the materials, (b) absorption coefficients of SiGe, (c) extinction and absorption coefficients of SiC, and (d) EQEs of SiC, Si_3N_4, and SiO_2 passivated RC-SiGe solar cells, respectively.

negligible. However, consequences of using thicker SiC layer has also been discussed. Four SiC-based *N*-type SiGe wafer has been designed with a different thickness of SiC i.e. 20 nm, 40 nm, 80 nm, and 160 nm respectively, and photon absorption rate has been obtained in underlying SiGe wafer as shown in Fig. 7(a)–(d). The contour representation shows that the photon coupling in underlying SiGe is higher for 20 nm thick SiC-based device. However, increasing the thickness results in absorbance in SiC and hence lower optical coupling in underlying SiGe. The 160 nm thick SiC-based SiGe wafer shows worst optical behavior compared to other wafers as shown in Fig. 7. Meanwhile, the photon absorption contour is also obtained for all the devices, and same has been presented in Fig. 8(a)–(f). Results reveal that higher photon absorption rate is achieved in FSP3 layer based device. FSP3 layer device

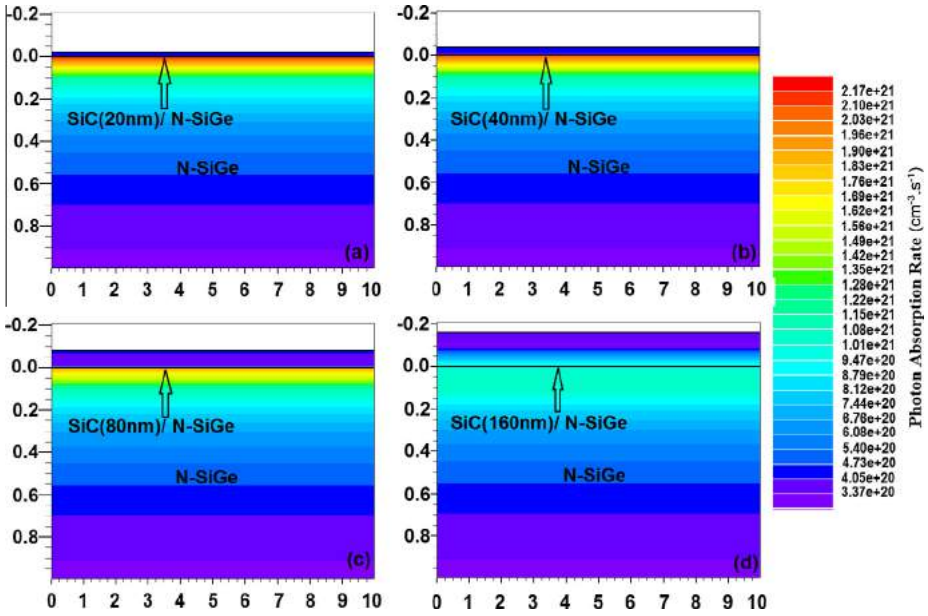


Fig. 7. The contour representation of photon absorption rate ($cm^{-3}\,s^{-1}$) in underlying SiGe with different SiC thicknesses: (a) 20 nm, (b) 40 nm, (c) 80 nm, and (d) 160 nm.

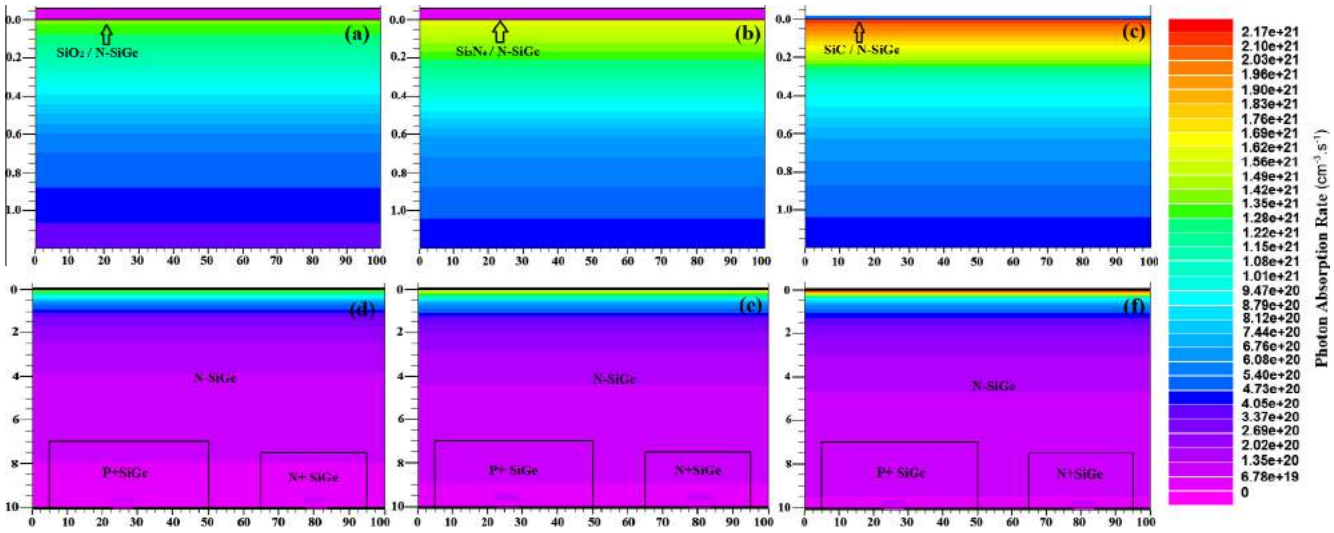


Fig. 8. The contour representation of photon absorption rate ($cm^{-3}\ s^{-1}$) in RC-SiGe solar cell: (a) magnified view near the (SiO_2/*N*-SiGe) interface in SiO_2 passivated device, (b) magnified view near the (Si_3N_4/*N*-SiGe) interface in Si_3N_4 passivated device, (c) magnified view near the (SiC/*N*-SiGe) interface in SiC passivated device, and figure (d–f) show the SiO_2, Si_3N_4, and SiC passivated device on full scale. Data has been obtained under illumination with zero-bias voltage.

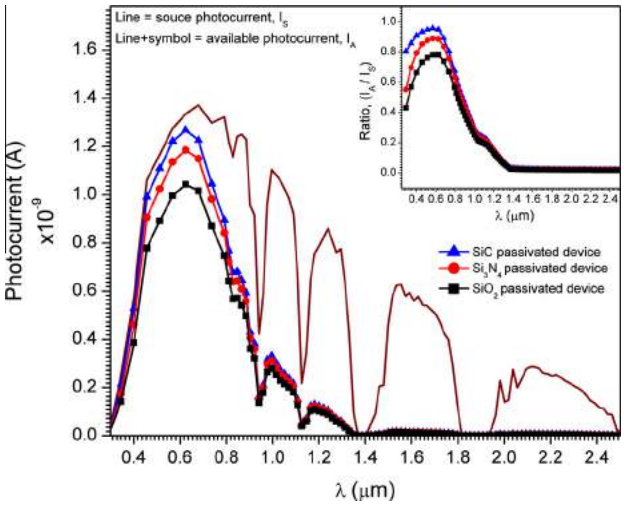


Fig. 9. Comparison of spectrum response under AM1.5 illumination for an RC-SiGe solar cell with SiC, Si_3N_4, and SiO_2 passivation layers, respectively. The inset shows the I_A/I_S ratio for all the three devices.

shows, the 12.5% and 5% higher photon absorption rate compared to FSP1 and FSP2 layer device, respectively as shown in Fig. 8(d)–(f). Also, magnified view of the interfaces shows higher photon absorption rate at the front surface, in SiC-based device, as shown in Fig. 8(a)–(c). This validates the higher optical coupling of photons with lower wavelengths. Further, Fig. 9 shows, the source photocurrent of AM1.5 spectrum, along with the ratio of available photocurrent (I_A) to the source photocurrent (I_S). The improved optical behavior of the SiC-based device results in higher available photocurrent, which further increases the I_A/I_S ratio. Result shows, >80% ratio with a maximum value of 95.7% in the spectrum range of 289–735 nm wavelengths. Thus, reflecting a superior spectrum response of SiC passivated device compared to SiO_2 and Si_3N_4 based devices. Improved optical coupling and better surface passivation, leads to superior EQE in the SiC-based device.

The most important part of the solar cell design is its current–voltage characteristics. Any design must have a higher short-circuit current density (J_{SC}) and a higher open circuit voltage (V_{OC}). The *J*–*V* characteristic of the device is simulated with ray tracing algorithm without reflection, under AM1.5 illumination with optical power 0.1 W/cm^2. Results are presented in Fig. 10 (a) and (b). In Fig. 10(a), the J_{SC} and V_{OC} in FSP3 layer device are 28 mA cm^{-2} and 668 mV, whereas J_{SC}, V_{OC} in FSP1 and FSP2 layer devices are 22.6 mA cm^{-2}, 662 mV and 25.8 mA cm^{-2}, 667 mV respectively. Thus, FSP3 layer device shows 24% and 8% higher J_{SC} compared to FSP1 and FSP2 layer devices, respectively. Also, the higher power density of 14.7 mW/cm^2 was obtained in FSP3 layer device compared to 11.7 mW/cm^2 and 13.5 mW/cm^2 in FSP1 and FSP2 layer devices, respectively. A detailed comparison of electrical parameters is shown in Table 1. Improved photovoltaic properties indicate proposed device with SiC passivation can be used in light-weight, low-cost installation of PV modules. Also, the device has RC architecture it is easier to interconnect and can be placed closer together in the modules, no need of space between cells. Also, Fig. 10(b) shows the comparison of illuminated and dark characteristics of the devices. In Fig. 10(b), the illuminated response shows sharp minima, taking intercept from this point to *x*-axis gives the V_{OC} of the respective devices.

3.3. Impact of surface recombination velocity (SRV) on the devices

Further, the impact of surface passivating layer is analyzed. The impact of surface recombination velocity on J_{SC} and PCE has been obtained which is presented Fig. 11. At, SRV equivalent to 10^2 cm s^{-1} the difference between available photocurrent and short circuit current is 2.2 mA cm^{-2} in FSP3 layered device whereas the difference of ~7 mA cm^{-2} has been observed in FSP1 and FSP2 layered devices. This shows, 7 mA cm^{-2} is lost because of the recombination and the parasitic absorption in FSP1 & FSP2 layered device, whereas only 2 mA cm^{-2} has been lost in FSP3 layered device. Also, when SRV changes from 10^1 to 10^7 cm s^{-1} the PCE and J_{SC} went down to 12.1% and 23.2 mA cm^{-2}, respectively in FSP3 device, whereas these values are 1.33% and 3.97 mA cm^{-2} and 1.5% and 4.49 mA cm^{-2} in FSP1 and FSP2 devices, respectively. Results reveal that characteristics of the FSP3 device are less affected by surface recombination velocity. Fig. 11 shows, enhanced surface characteristics has been obtained in the FSP3 layered device. Also, result reveals that new surface passivation

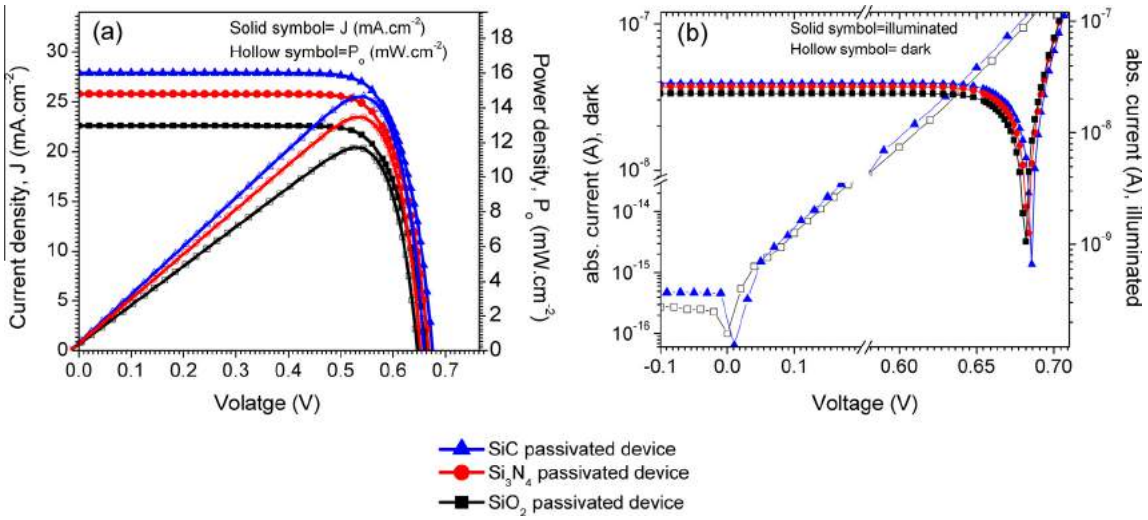


Fig. 10. Electrical characteristics i.e. current density–voltage (*J–V*) curve of RC-SiGe solar cell with different passivation layers. (a) *J–V* curve on primary axis and *P–V* curve on secondary axis, (b) *I–V* (dark and illuminated condition on primary and secondary axis, respectively).

Table 1
Comparisons of photovoltaic parameters of 10 μm thick RC-SiGe solar cell with SiO_2, Si_3N_4 and SiC based passivation layers, respectively.

Device	J_{SC} (mA cm^{-2})	V_{OC} (mV)	FF (%)	PCE (%)
FSP1 layered	22.6	662	78.2	11.7
FSP2 layered	25.8	667	78.0	13.5
FSP3 layered	28.0	668	78.6	14.7

scheme is useful when the surface to volume ratio of the device is a large i.e. thin device. Thin devices suffer from higher surface recombination.

3.4. Impact of diffusion depth of P+ and N+ regions

In this section, the impact of diffusion depth on device characteristics have been obtained. In Fig. 5, the Auger recombination rate in *P*+ and *N*+ region is higher because of the heavily doped region ($\sim 10^{20}$ cm^{-3}) and higher diffusion depth in *Y*-direction. Therefore, the diffusion depth of *P*+ and *N*+ region have been minimized to minimize the auger recombination rate in these regions. The PCE of 15.4% i.e. 4.7% higher than initial value (14.7%) is obtained by minimizing the diffusion depth of the regions. Fig. 12 shows the contour representation of recombination rate of the devices with different diffusion depth. Result reveals, carrier recombination, is reduced by reducing the diffusion depth of *P*+ and *N*+ regions. Further, the impact of depth on device characteristics is presented in Table 2.

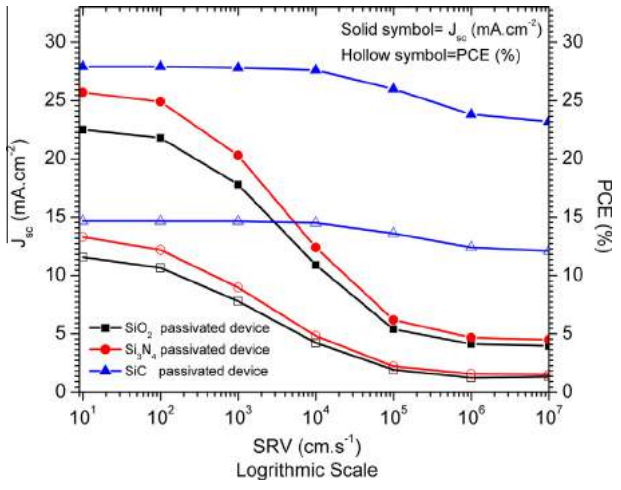


Fig. 11. Impact of surface recombination velocity on RC-SiGe solar cell with different passivation layers. J_{SC} and PCE are presented on primary and secondary axis, respectively.

3.5. Impact of Irradiance and temperature

In this section, we have discussed the application of RC SiGe solar cell for concentrator's photovoltaics (CPV) cell application. Altering the irradiance on a solar cell varies all solar cell parameters, including J_{SC}, V_{OC}, fill factor (FF), PCE, series and shunt resistances. The light intensity on a solar cell is called the number of suns, where one-sun corresponds to standard illumination at AM1.5, or 100 mW/cm^2. The PV module intended to work under one- sun is called a "flat plate" while those using more than one-sun or concentrated sunlight are called "concentrators." Further, concentrators have some advantages in terms of higher efficiency than a one-sun solar cell and the lower cost. The J_{SC} of a solar cell depends linearly on irradiance, this indicates, device operating under 10 Suns would have 10 times the J_{SC} as the same device under one sun operation. However, this will not result in increased PCE, since the incident power also increases linearly. The efficiency benefits arise from the open-circuit voltage, as V_{OC} increases logarithmically with light intensity (Würfe, 2008).

The impact of irradiance and temperature on different devices is obtained, and the results are presented in Fig. 13(a)–(c). The devices are simulated up to 20-suns (2 W/cm^2) condition at room temperature (300 K), since the temperature also increases as a function of input optical power per unit area. Further, cell operating at higher concentration levels requires complex cooling system, and overall cost of the PV module will be increased. Previously, the silicon-based concentrator solar cell with the efficiencies range of (15–27.5)% has been reported for the concentration level of (20–150) suns (Sinton et al., 1986; Cuevas et al., 1990; Lammert and Schwartz, 1977; Wenham and Green, 1995; Zhao et al., 1990). In silicon-based concentrator cells, thickness >100 μm is required to achieve high efficiency. This results in higher $/W. Further, V_{OCs} of 766 mV, 800 mV PCEs of, 18.37%, 19.32% at 10-sun and 20-sun conditions respectively have been

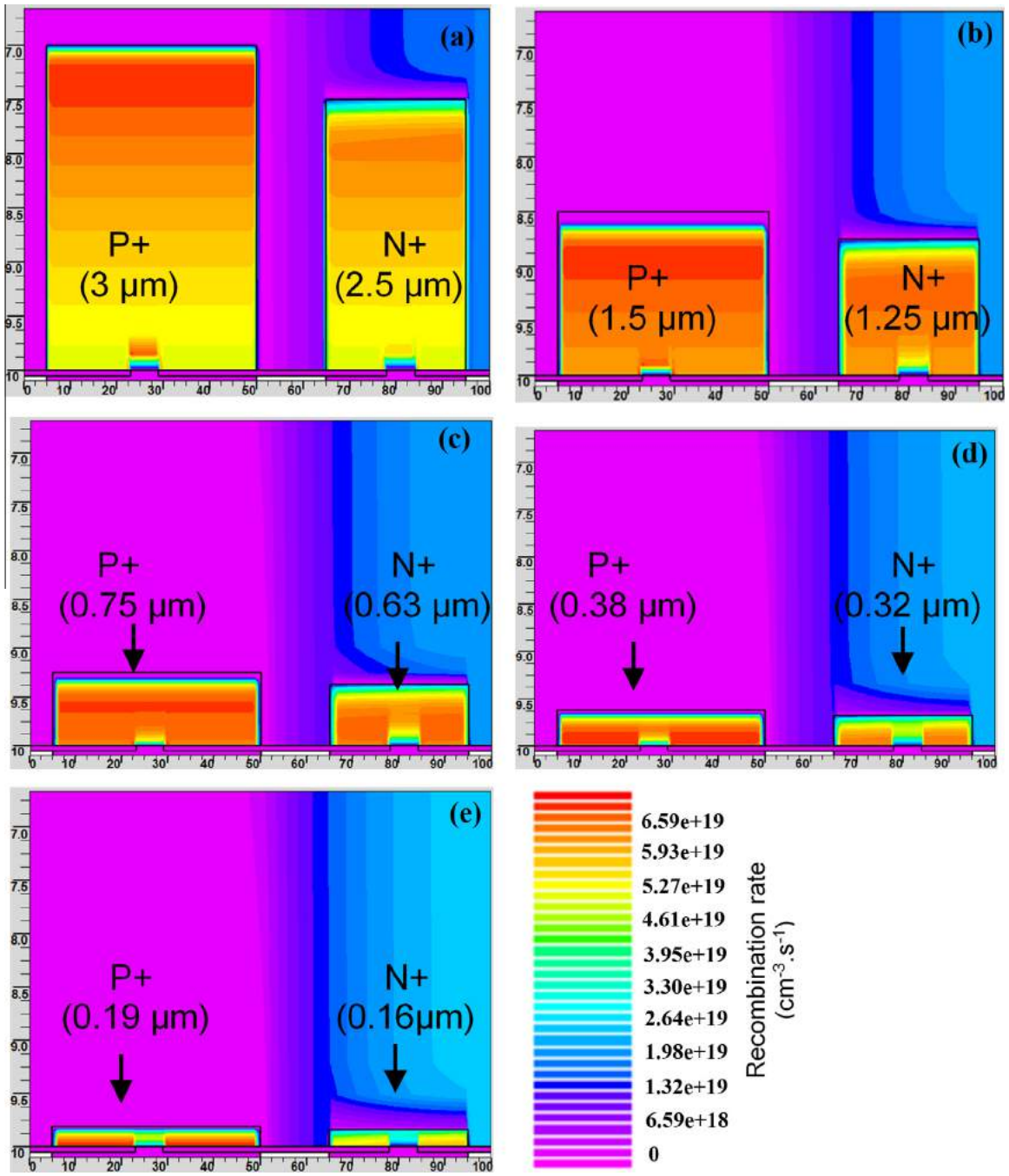


Fig. 12. Recombination rate ($cm^{-3}\ s^{-1}$) contour of SiC passivated RC-SiGe solar cell with different diffusion depth of *P+* and *N+* regions. Data has been obtained under illumination with zero-bias voltage.

Table 2
Impact of *N+* and *P+* regions diffusion depth on photovoltaic parameters of SiC passivated 10 μm thick RC-SiGe solar cell.

S. No.	Regions	Thickness (μm)	J_{SC} (mA cm^{-2})	V_{OC} (mV)	FF (%)	PCE (%)
1	*P+*	3.0	28.0	668	78.6	14.70
	N+	2.5				
2	*P+*	1.5	28.9	666	78.6	15.13
	N+	1.25				
3	*P+*	0.75	29.3	666	78.3	15.30
	N+	0.63				
4	*P+*	0.38	29.5	666	78.3	15.37
	N+	0.32				
5	*P+*	0.19	29.6	667	78.2	15.41
	N+	0.16				

obtained as shown in Fig. 13(a). Also, results show 10.2% and 13.7% higher PCE at the concentration levels of 4, 6 suns compared to 1-sun condition. Further, the desired concentration level can be selected from Fig. 13(a) depending upon the applications. Furthermore, the impact of temperature on device parameters: V_{OC}, PCE and FF for three different conditions (1-sun, 10-suns, 20-suns) has been analyzed. Since, under concentrated light device temperature increases. Although, it can be avoided by using a suitable cooling system (Royne et al., 2005). Fig. 13(b) and (c), shows that device performance degrades as the temperature increases since intrinsic carrier concentrations increase at higher temperatures. Therefore, bandgap decreases, which further results in decrease V_{OC}, as shown in Fig. 13(b). The V_{OC} values 804 mV, 778 mV,

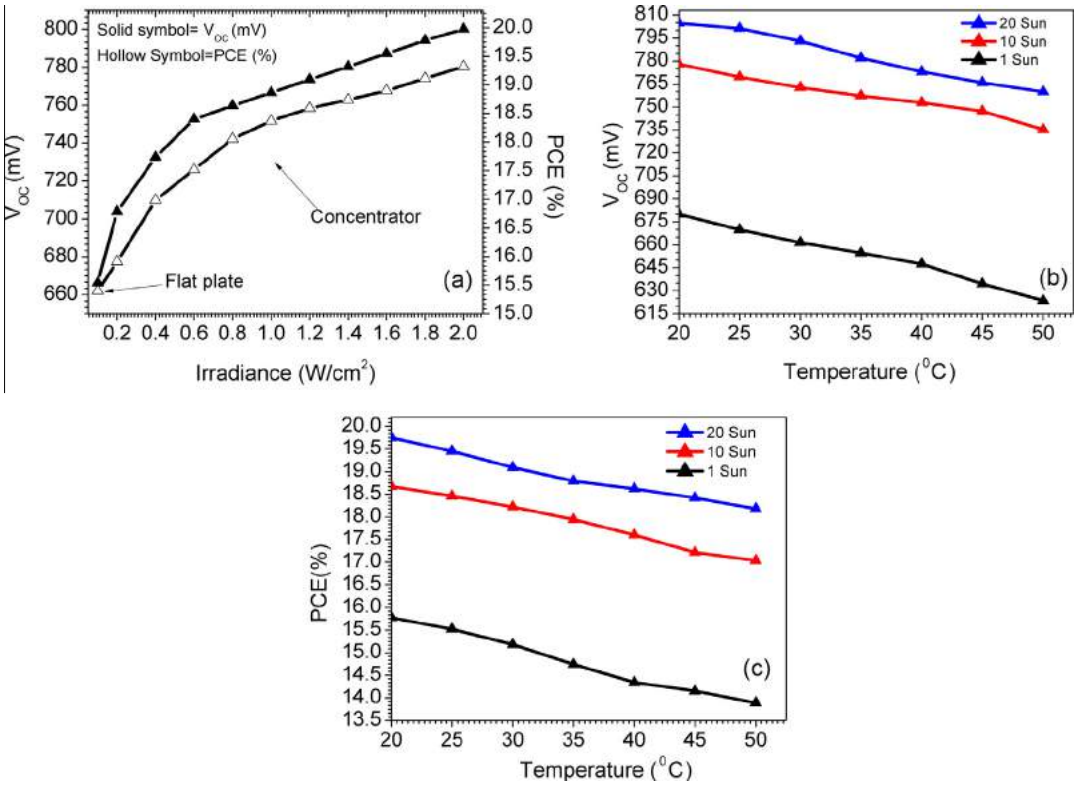


Fig. 13. Impact of irradiance and temperature on SiC passivated RC-SiGe solar cell: (a) effect of irradiance on V_{OC} and PCE, (b) effect of temperature on V_{OC} for 1 sun, 10 suns and 20 suns condition, respectively, (c) effect of temperature on PCE for 1 sun, 10 suns and 20 suns condition, respectively.

680 mV and PCE values of 19.75%, 18.67%, 15.77% is obtained at 20 °C for 20-sun, 10-sun and 1-sun conditions respectively, whereas V_{OC} values 760 mV, 735 mV, 623 mV and PCE values of 18.2%, 17%, 13.9% is obtained at 50 °C. Results show, as the temperature increases from 20 °C to 45 °C, 10.2% decrease in PCE is obtained for flat plate cell, whereas 7.8% and 6.7% decrease in PCE is obtained for the same cell operating at 10-suns and 20-suns, as shown in Fig. 13(c). Further, all the results of this section conclude that highest PCE of 19.3% is obtained at 20-suns in the sub 10 μm thick device with the cost effective material. This suggests that the proposed device can be a cost-effective candidate for the flat plate as well as low concentrator applications.

4. Conclusion

In the present work, RC SiGe solar cell with SiC-based front surface passivation has been proposed, which shows enhanced photovoltaic properties. EQE > 90% in the wavelength range of 400–650 nm has been achieved. Also, at wavelengths equivalent to 300 nm, SiC passivated device shows record EQE of 85%. The presence of SiC as a surface passivating layer shows enhanced surface characteristics. At the (SiC/*N*-SiGe) interface, the barrier height of 1.1 eV has been achieved for minority carrier (Holes) in SiC passivated device this suppresses the surface recombination. The power conversion efficiency (PCE) of 15.4% has been achieved, and the device is less affected by SRV. Further, discussed device has RC architecture it is useful in high current cells such as CPV or large areas. Therefore, device performance for concentrator application has also been discussed. We obtained 19.3% PCE at 2 W/cm^2 (20 suns, 27 °C) in 10 μm regime. This suggests, proposed device can be an energy efficient candidate for the flat plate as well as low concentrator applications. The simulation work achieved here shows that if fabricated experimentally it can prove to be a cost-effective solution for energy efficient applications. In future, thin defect free SiC-based passivation scheme can be used in nanostructured based thin devices. This can tackle the problem like auger and surface recombination by stacking a thin layer of SiC between nanostructures and the front surface of the cell.

Acknowledgements

The authors would like to thank Microelectronics Research Lab, Department of Engineering Physics, Delhi Technological University to carry out this work. Rahul Pandey (JRF) acknowledge UGC, Govt. of India for providing fellowship.

References

Aberle, A.G., Glunz, S., Warta, W., 1992. Impact of illumination level and oxide parameters on Shockley–Read–Hall recombination at the Si–SiO_2 interface. J. Appl. Phys. 71 (9), 4422 (accessed October 15, 2015) <http://scitation.aip.org/content/aip/journal/jap/71/9/10.1063/1.350782>.

Aberle, A.G., 2000. Surface passivation of crystalline silicon solar cells: a review. Prog. Photovoltaics Res. Appl. 8 (5), 473–487. http://dx.doi.org/10.1002/1099-159X(200009/10)8:5<473::AID-PIP337>3.0.CO;2-D.

Allen, S., Awad, Y., Gaumond, A., & Davies, M., 2009. U.S. Patent Application No. 12/994,973.

Atlas user manual, 2014. Silvaco, Inc. Santa Clara. pp. 481.

Ceuster, D.D., Cousins, P., Rose, D., Vicente, D., Tipones, P., Mulligam, W., 2007. Low cost, high volume production of >22% efficiency silicon solar cells. In: Proceedings of the 22nd European Photovoltaic Solar Energy Conference, pp. 816–819.

Cruz-Campa, J.L. et al., 2011. Microsystems enabled photovoltaics: 14.9% efficient 14 μm thick crystalline silicon solar cell. Sol. Energy Mater. Sol. Cells 95 (2), 551–558. http://dx.doi.org/10.1016/j.solmat.2010.09.015.

Cuevas, A. et al., 1990. 26-percent efficient point-junction concentrator solar cells with a front metal grid. IEEE Electron Device Lett. 11 (1), 6–8, <http://ieeexplore.ieee.org/lpdocs/epic03/wrapper.htm?arnumber=46913> (accessed October 15, 2015).

Deinega, A., Eyderman, S., John, S., 2013. Coupled optical and electrical modeling of solar cell based on conical pore silicon photonic crystals. J. Appl. Phys. 113 (22),

224501 (accessed October 15, 2015) <http://scitation.aip.org/content/aip/journal/jap/113/22/10.1063/1.4809982>.
Diouf, D. et al., 2009. Study of interdigitated back contact silicon heterojunctions solar cells by two-dimensional numerical simulations. Mater. Sci. Eng. B: Solid-State Mater. Adv. Technol. 159–160 (C), 291–294.
Diouf, D. et al., 2010. Effects of the front surface field in *n*-type interdigitated back contact silicon heterojunctions solar cells. Energy Procedia 2 (1), 59–64. http://dx.doi.org/10.1016/j.egypro.2010.07.011.
Dziewior, J., Schmid, W., 1977. Auger coefficients for highly doped and highly excited silicon. Appl. Phys. Lett. 31 (5), 346 (accessed October 15, 2015) <http://scitation.aip.org/content/aip/journal/apl/31/5/10.1063/1.89694>.
Feldmann, F. et al., 2014. Passivated rear contacts for high-efficiency *n*-type Si solar cells providing high interface passivation quality and excellent transport characteristics. Sol. Energy Mater. Sol. Cells 120 (PART A), 270–274.
Franklin, E. et al., 2014. Design, fabrication and characterisation of a 24.4% efficient interdigitated back contact solar cell. Progr. Photovolt.: Res. Appl. http://dx.doi.org/10.1002/pip.2556, pp. n/a–n/a. (accessed October 10, 2015).
Green, M.A., Keevers, M.J., 1995. Optical properties of intrinsic silicon at 300 K. Prog. Photovoltaics Res. Appl. 3 (3), 189–192. http://dx.doi.org/10.1002/pip.4670030303 (accessed December 7, 2015).
Green, M.A., 2003. Third Generation Photovoltaics – Advanced Solar Energy. Springer. <http://www.springer.com/jp/book/9783540401377> (accessed March 2, 2016).
Green, M.A., 2008. Self-consistent optical parameters of intrinsic silicon at 300 K including temperature coefficients. Sol. Energy Mater. Sol. Cells 92 (11), 1305–1310 (accessed December 19, 2015) <http://www.sciencedirect.com/science/article/pii/S0927024808002158>.
Glunz, S.W. et al., 1999. Comparison of boron- and gallium-doped *p*-type Czochralski silicon for photovoltaic application. Prog. Photovoltaics Res. Appl. 7 (6), 463–469. http://dx.doi.org/10.1002/%28SICI%291099-159X%28199911/12%297%3A6%3C463%3A%3AAID-PIP293%3E3.0.CO%3B2-H (accessed October 15, 2015).
Hall, R., 1952. Electron-hole recombination in Germanium. Phys. Rev. 87 (2), 387. http://dx.doi.org/10.1103/PhysRev.87.387 (accessed December 28, 2014).
He, J. et al., 2015. Realization of 13.6% efficiency on 20 μm Thick Si/Organic hybrid heterojunction solar cells via advanced nanotexturing and surface recombination suppression. ACS Nano 9 (6), 6522–6531. http://dx.doi.org/10.1021/acsnano.5b02432 (accessed February 25, 2016).
Ingenito, A., Isabella, O., Zeman, M., 2015. Nano-cones on micro-pyramids: modulated surface textures for maximal spectral response and high-efficiency solar cells. Prog. Photovoltaics Res. Appl. 20 (1), 6. http://dx.doi.org/10.1002/pip.1160, http://dx.doi.org/10.1002/pip.2606.
Jeong, S., McGehee, M.D., Cui, Y., 2013. All-back-contact ultra-thin silicon nanocone solar cells with 13.7% power conversion efficiency. Nature Commun. 4 (May), 2950 <http://www.ncbi.nlm.nih.gov/pubmed/24335845>.
Kasap, S., Capper, P. (Eds.), 2007. Springer Handbook of Electronic and Photonic Materials. Springer US, Boston, MA, pp. 481–498 (accessed February 26, 2016) <http://www.springerlink.com/index/10.1007/978-0-387-29185-7>.
Kerschaver, E.Van., Beaucarne, G., 2006. Back-contact solar cells: a review. Prog. Photovoltaics Res. Appl. 14 (2), 107–123. http://dx.doi.org/10.1002/pip.657 (accessed October 14, 2015).
Lammert, M.D., Schwartz, R.J., 1977. The interdigitated back contact solar cell: a silicon solar cell for use in concentrated sunlight. IEEE Trans. Electron Dev. 24 (4), 337–342, <http://ieeexplore.ieee.org/lpdocs/epic03/wrapper.htm?arnumber=1478930> (accessed October 15, 2015).
NSM Archive – Silicon Germanium (SiGe), 2016a. <http://www.ioffe.rssi.ru/SVA/NSM/Semicond/SiGe/> (accessed February 26, 2016).
NSM Archive – Silicon Germanium (SiGe) – Optical Properties, 2016b. <http://www.ioffe.ru/SVA/NSM/Semicond/SiGe/optic.html> (accessed February 26, 2016).
Oh, J., Yuan, H.-C., Branz, H.M., 2012. An 18.2%-efficient black-silicon solar cell achieved through control of carrier recombination in nanostructures. Nat. Nanotechnol. 7 (11), 743–748. http://dx.doi.org/10.1038/nnano.2012.166 (accessed February 26, 2016).
Ouellette, J., 2002. Silicon-germanium gives semiconductors the edge. Indust. Phys. 8 (3), 22–25.
Pandey, R., Chaujar, R., 2015a. Novel back-contact back-junction SiGe (BC-BJ SiGe) solar cell for improved power conversion efficiency. Microsyst. Technol., 1–8 http://dx.doi.org/10.1007/s00542-015-2552-1 [accessed October 15, 2015) <http://www.researchgate.net/publication/275660629_Novel_back-contact_back-junction_SiGe_(BC-BJ_SiGe)_solar_cell_for_improved_power_conversion_efficiency>.
Pandey, R., Chaujar, R., 2015b. Front Surface Passivation Scheme for Back-Contact Back-Junction (BC-BJ) Silicon Solar Cell. Adv. Sci. Lett., in press.
Pandey, R., Chaujar, R., 2015c. Novel SiC encapsulated coaxial silicon nanowire solar cell for optimal photovoltaic performance. In: 2015 IEEE 42nd Photovoltaic Specialist Conference (PVSC). IEEE, pp. 1–5, <http://ieeexplore.ieee.org/lpdocs/epic03/wrapper.htm?arnumber=7355933> (accessed January 6, 2016).
Pandey, R., Chaujar, R., 2015d. TCAD Analysis of Silicon-Germanium (SiGe) based Back-Contact Back-Junction (BC-BJ) solar cell as an alternative for silicon based cells. In: TechConnectWorld Innovation Conference and Expo, June 14–17, 2015 Washington, DC, USA, pp. 199–202. http://dx.doi.org/10.13140/RG.2.1.1008.6246.
Pandey, R., Chaujar, R., 2015e. Rear contact solar cell with ZrO_2 nano structured front surface for efficient light trapping and enhanced surface passivation. In: 2015 IEEE 42nd Photovoltaic Specialist Conference (PVSC). IEEE, pp. 1–5 (accessed February 4, 2016) <http://ieeexplore.ieee.org/lpdocs/epic03/wrapper.htm?arnumber=7356322>.
Povolny, H. et al., 2011. Comparison study of a-SiGe solar cells and materials deposited using different hydrogen dilution. MRS Proceed. 609, A30.3 (accessed October 15, 2015) <http://journals.cambridge.org/abstract_S1946427400605596>.
Royne, A., Dey, C., Mills, D., 2005. Cooling of photovoltaic cells under concentrated illumination: a critical review. Sol. Energy Mater. Sol. Cells 86 (4), 451–483 (accessed January 12, 2015) <http://www.researchgate.net/publication/223267048_Cooling_of_photovoltaic_cells_under_concentrated_illumination_A_critical_review>.
Savin, H. et al., 2015. Black silicon solar cells with interdigitated back-contacts achieve 22.1% efficiency. Nat. Nanotechnol. 10 (May), 1–6 <http://www.ncbi.nlm.nih.gov/pubmed/25984832>.
Schwartz, R.J., Lammert, M.D., 1975. Silicon solar cells for high concentration applications. In: 1975 International Electron Devices Meeting. IRE, pp. 350–352, <http://ieeexplore.ieee.org/lpdocs/epic03/wrapper.htm?arnumber=1478257> (accessed October 15, 2015).
Selberherr, S., 2012. Analysis and Simulation of Semiconductor Devices. Springer Science & Business Media.
Sinton, R.A. et al., 1986. 27.5-Percent Silicon Concentrator Solar Cells. IEEE Electron Device Lett. 7 (10), 567–569.
Sinton et al., 1998. Development efforts in silicon backside-contact solar cells. In: Eighth E.C. Photovoltaic Solar Energy Conference, vol. 2, pp. 1472–1476.
Sinton, R.A., Swanson, R.M., 1990. Simplified backside-contact solar cells. IEEE Trans. Electron Dev. 37 (2), 348–352, <http://ieeexplore.ieee.org/lpdocs/epic03/wrapper.htm?arnumber=46364> (accessed October 15, 2015).
Sinton, R.A. et al., 1993. Large-area 21% efficient Si solar cells. In: Conference Record of the Twenty Third IEEE Photovoltaic Specialists Conference - 1993 (Cat. No. 93CH3283-9). IEEE, pp. 157–161, <http://ieeexplore.ieee.org/lpdocs/epic03/wrapper.htm?arnumber=347061> (accessed October 15, 2015).
Shockley, W., Read, W., 1952. Statistics of the recombinations of holes and electrons. Phys. Rev. 87 (5), 835–842. http://dx.doi.org/10.1103/PhysRev.87.835 (accessed July 9, 2014).
Slotboom, J.W., 1977. The pn-product in silicon. Solid-State Electron. 20 (4), 279–283 (accessed August 31, 2015) <http://www.sciencedirect.com/science/article/pii/0038110177901083>.
Slotboom, J.W., de Graaff, H.C., 1977. Bandgap narrowing in silicon bipolar transistors. IEEE Trans. Electron Dev. 24 (8), 1123–1125, <http://ieeexplore.ieee.org/lpdocs/epic03/wrapper.htm?arnumber=1479081> (accessed October 15, 2015).
Tjahjono, B.S., Cotter, J.E., 2005. 19.2% efficiency *n*-type laser-grooved silicon solar cells. In: Conference Record of the Thirty-first IEEE Photovoltaic Specialists Conference, 2005. IEEE, pp. 983–986, <http://ieeexplore.ieee.org/lpdocs/epic03/wrapper.htm?arnumber=1488297> (accessed October 15, 2015).
Wang, C.C. et al., 2012. Characterization of nanocrystalline SiGe thin film solar cell with double graded-dead absorption layer. Int. J. Photoen. 2012 (1).
Wenham, S., Green, M.A., 1995. Large area, concentrator buried contact solar cells. IEEE Trans. Electron Dev. 42 (1), 144–149, <http://ieeexplore.ieee.org/lpdocs/epic03/wrapper.htm?arnumber=370024> (accessed October 15, 2015).
Würfe, 2008. Physics of Solar Cells: From Principles to New Concepts - Wiley Online Library <http://onlinelibrary.wiley.com/book/10.1002/9783527618545> (accessed February 26, 2016).
Yang, D. et al., 2010. Germanium-doped crystal silicon for solar cells. In: 2010 10th IEEE International Conference on Solid-State and Integrated Circuit Technology. IEEE, p. 1994, <http://ieeexplore.ieee.org/lpdocs/epic03/wrapper.htm?arnumber=5667855> (accessed October 15, 2015).
Zhao, J., Wang, A., Green, M.A., 1990. 24% efficient PERL structure silicon solar cells. In: IEEE Conference on Photovoltaic Specialists. IEEE, pp. 333–335, <http://ieeexplore.ieee.org/lpdocs/epic03/wrapper.htm?arnumber=111642> (accessed October 15, 2015).

Tumor Biol.
DOI 10.1007/s13277-016-5098-7

REVIEW

Role of interleukin-6 in cancer progression and therapeutic resistance

Neeraj Kumari[1,2] · B. S. Dwarakanath[3] · Asmita Das[2] · Anant Narayan Bhatt[1]

Received: 3 February 2016 / Accepted: 22 May 2016
© International Society of Oncology and BioMarkers (ISOBM) 2016

Abstract In the last several decades, the number of people dying from cancer-related deaths has not reduced significantly despite phenomenal advances in the technologies related to diagnosis and therapeutic modalities. The principal cause behind limitations in the curability of this disease is the reducing sensitivity of the cancer cells towards conventional anticancer therapeutic modalities, particularly in advance stages of the disease. Amongst several reasons, certain secretory factors released by the tumour cells into the microenvironment have been found to confer resistance towards chemo- and radiotherapy, besides promoting growth. Interleukin-6 (IL-6), one of the major cytokines in the tumour microenvironment, is an important factor which is found at high concentrations and known to be deregulated in cancer. Its overexpression has been reported in almost all types of tumours. The strong association between inflammation and cancer is reflected by the high IL-6 levels in the tumour microenvironment, where it promotes tumorigenesis by regulating all hallmarks of cancer and multiple signalling pathways, including apoptosis, survival, proliferation, angiogenesis, invasiveness and metastasis, and, most importantly, the metabolism. Moreover, IL-6 protects the cancer cells from therapy-induced DNA damage, oxidative stress and apoptosis by facilitating the repair and induction of countersignalling (antioxidant and anti-apoptotic/pro-survival) pathways. Therefore, blocking IL-6 or inhibiting its associated signalling independently or in combination with conventional anticancer therapies could be a potential therapeutic strategy for the treatment of cancers with IL-6-dominated signalling.

Keywords IL-6 · Cancer · Therapeutic resistance · STAT-3 · Chemotherapy · Radio-resistance

Introduction

Inflammation has a very strong link with various types of cancer. Malignant cells are highly proliferative in nature, which is facilitated by the inflammatory molecules that are continuously being secreted by other cells and/or tumour cells themselves in a microenvironment [1, 2]. Interleukin-6 (IL-6) is one such inflammatory molecule, which is produced and secreted by various types of cells including the tumour cells. It is involved in the proliferation and differentiation of malignant cells and found to be high in serum and tumour tissues of a majority of cancers, viz. colorectal cancer [3], breast cancer [4], prostate cancer [5], ovarian carcinoma [6], pancreatic cancer [7], lung cancer [8], renal cell carcinoma [9], cervical cancer [10] and multiple myeloma [11]. Elevated levels of IL-6 are associated with aggressive tumour growth and response to therapies in many types of cancer [12, 13]. Patients with high levels of circulating IL-6 are generally associated with poor prognosis and shorter survival, whilst a lower level of IL-6 is associated with better response to therapy [14, 15].

Anticancer drugs and ionizing radiation used during cancer therapy induce inflammatory signalling, mainly in the form of the nuclear factor-kappa B (NF-kB) pathway [16, 17]. NF-kB regulates the expression of different pro-inflammatory

✉ Anant Narayan Bhatt
anant@inmas.drdo.in; anbhatt@yahoo.com

1 Division of Metabolic Cell Signalling Research, Institute of Nuclear Medicine and Allied Sciences, Brig SK Mazumdar Road, Delhi 110 054, India

2 Department of Biotechnology, Delhi Technological University, Delhi 110042, India

3 Central Research Facility, Sri Ramachandra University, Chennai 600116, India

Published online: 03 June 2016

cytokines, chemokines and anti-apoptotic genes and acts as a key molecular link between inflammation and initiation as well as progression of oncogenesis [18]. Chemotherapeutic drugs and radiation also induce IL-6 expression in tumour and stromal cells [12, 13] through the activation of NF-kB signalling, leading to therapeutic resistance [19, 20]. These evidences suggest that blocking IL-6 or inhibiting the IL-6 downstream signalling pathways may provide therapeutic gain in those cancers which are associated with a higher level of IL-6. This review provides an insight into the current understanding of the role of IL-6 in the regulation of various hallmarks and associated signalling in cancer as well as its contribution to therapeutic resistance. It also provides an insight into how the anti-IL-6 antibody or the inhibitors of pathways downstream to IL-6 signalling can improve the effectiveness of cancer radio- and/or chemotherapy.

Interleukin-6

IL-6 is a glycosylated polypeptide chain having a molecular weight of nearly 25 kDa, depending on the glycosylation and the species. It has a characteristic structure made up of four long α-helices arranged in an up–up–down–down topology [21]. It was first discovered as a B cell differentiation factor (BSF-2) which induces the maturation of B cells into antibody-producing cells [22]. Besides its role in immune regulation, it plays an important role in the maintenance of hepatocytes, haematopoietic progenitor cells, the skeleton, the placenta, the cardiovascular system and the endocrine as well as nervous systems. In the murine haematopoietic system, IL-6 induces the expansion of progenitor cells by stimulating cells from the resting stage to enter the G1 phase [23]. IL-6 also supports various physiological functions by acting as a hepatocyte stimulatory factor and by inducing the acute-phase protein synthesis. It is also known to stimulate osteoclast formation, induce bone resorption and is responsible for neural differentiation [24]. IL-6 supports the survival of cholinergic neurons, induces adrenocorticotropic hormone synthesis, and, in placenta, causes the secretion of chorionic gonadotropin from trophoblasts [23]. IL-6 also plays a very important role in metabolism. For example, in the absence of IL-6, mice develop glucose intolerance and insulin resistance, whilst IL-$6^{-/-}$ mice exhibit signs of liver inflammation [25]. The secretion and availability of IL-6 is ubiquitous, and it can bind to various types of cells in different tissues. However, its binding on different cell types may differ, resulting in two different types of IL-6-dependent cell signalling (Fig. 1).

IL-6 binds to the IL-6 receptor (IL-6R) on the plasma membrane, and the resultant IL-6/IL-6R complex associates with gp130 and causes gp130 homodimerization to form an activated IL-6 receptor complex, which is a hexameric structure consisting of two molecules each of IL-6, IL-6R and gp130 [26, 27]. The binding of IL-6 to IL-6R occurs at three distinct receptor-binding sites of IL-6R and gp130. However, the Ig-like domain of the human IL-6R is not involved in the direct binding of IL-6 [28]. Upon binding to the receptor and gp130, IL-6 induces various functions by activating cell signalling events [24]. IL-6 triggers signal transduction via two forms of IL-6R: one a transmembrane 80-kDa receptor with a short cytoplasmic domain (mbIL-6R, also known as IL-6Rα, gp80 or CD126) and the other a small, extracellular, secretory soluble receptor (sIL-6R) [29]. Classical IL-6 signalling, which is the predominant form of IL-6 signalling, requires membrane-bound IL-6R (mbIL-6R) and is restricted to hepatocytes, some epithelial cells and certain leukocytes (Fig. 1) [26]. IL-6R contains a very short cytosolic domain that lacks the major potential motifs for transduction of intracellular cell signalling. However, gp130 (also known as IL-6Rβ or CD130) in the same hexameric complex is rich in all these potential motifs required for intracellular signalling, such as SHP-2 domain and YXXQ motif for JAK/STAT signalling. Upon binding with IL-6/IL-6R, the dimerization of gp130 leads to the activation of associated cytoplasmic tyrosine kinases, resulting in the phosphorylation of various transcription factors [24]. gp130 is expressed in almost all organs, including the brain, heart, lung, liver, kidney, spleen and placenta, where it plays an indispensable role in their development, cell survival, growth and tissue homeostasis [30]. gp130 is a common signal transducing receptor and is also used by other members of the IL-6 family cytokines, such as IL-11, IL-12, IL-27, leukaemia inhibitory factor, oncostatin M, etc. [31]. Although the expression of transmembrane IL-6R is limited to the hepatocytes and subsets of leukocytes, gp130 is expressed ubiquitously. Therefore, the IL-6/sIL-6R complex can transduce the IL-6 signal in various cells, which do not express transmembrane IL-6R but express gp130, through a trans-signalling mechanism. sIL-6R is generated by alternative splicing of IL-6R mRNA or by limited proteolysis of mbIL-6R by Zn-dependent metalloproteinase (ADAM10 and ADAM17, a disintegrin and metalloproteinases 10 and 17; Fig. 1) [29–32]. sIL-6R is devoid of the cytoplasmic and transmembrane domains and binds to IL-6 with comparable affinity as the membrane-bound form, thereby mediating gp130 activation in an autocrine or paracrine manner [21]. Consequently, by binding to sIL-6R, IL-6 increases its reach to a wide variety of cells. There is enough evidence to suggest that neural cell, neural stem cells, haematopoietic stem cells, liver progenitor cells and embryonic stem cells depend on sIL-6R in their response to IL-6 [33–36]. The level of sIL-6R present in the human sera increases during inflammation [32, 37]. Knockdown of the IL-6R gene in hepatocytes reduces the levels of sIL-6R by 32 % in the serum, whilst ablation of the IL-6R gene in haematopoietic cells reduces the sIL-6R serum levels by 60 % [38]. These observations suggest that hepatocytes and haematopoietic cells are the main sources of sIL-6R

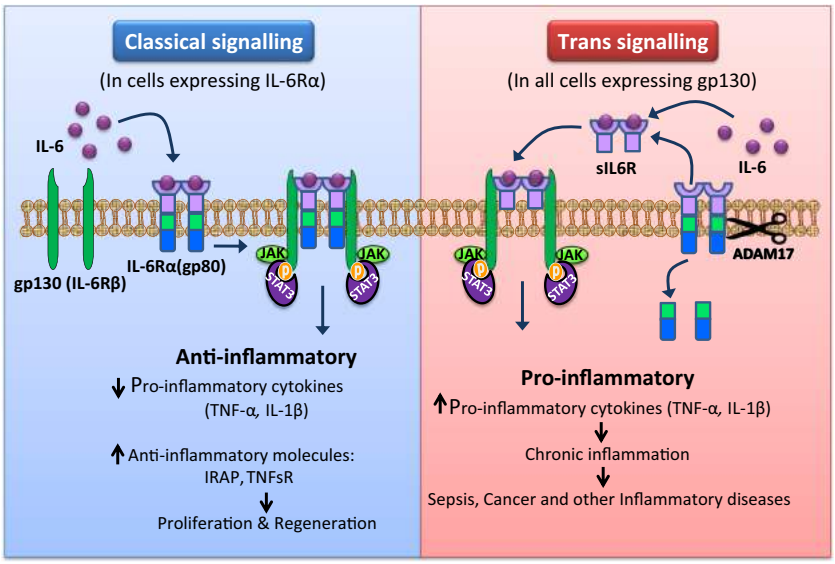


Fig. 1 Classical and trans-signalling of IL-6: In classical signalling, which occurs mainly in leukocytes and liver cells, IL-6 binds to the membrane-bound receptor mbIL-6Rα, which then forms a complex with the ubiquitously present cell receptor gp130 (*IL-6Rβ*). Trans-signalling can occur in any cell expressing gp130. In trans-signalling, IL-6 forms a complex with sIL-6R, which is a small part of mbIL-6Rα produced by either metalloproteinase or by alternative splicing. Furthermore, the IL-6–sIL-6R complex binds with gp130 on cells which do not express mbIL-6R. The inflammatory reactions induce the production of sIL-6R, which elicits response to IL-6 in cells that do not express IL-6 receptor (mbIL-6Rα) and/or remain inert to IL-6 signalling in normal physiological conditions. Classical signalling activates the anti-inflammatory pathways and promotes the regeneration of tissues, whereas trans-signalling activates pro-inflammatory pathways and is known to play a significant role in many diseases such as sepsis and cancer

found in the circulation [38]. Like sIL-6R, a soluble form of the signal transducer protein gp130 (sgp130) is also present in the circulation at relatively high concentrations during inflammation and cancer [37, 39]. sgp130 is mainly produced by alternative splicing rather than limited proteolysis, as in the case of sIL-6R generation. Since sgp130 binds to the IL-6/sIL-6R complex in the circulation, it acts as a specific inhibitor of IL-6-mediated trans-signalling [40]. Classic signalling via the mbIL-6R is not affected by sgp130. Its inhibitory action depends on the IL-6/sIL-6R ratio, with trans-signalling inhibition at low concentrations [37].

IL6 expression and secretion

The common characteristic of many of the stimuli that activate IL-6 is that they are associated with tissue damage or stress (e.g. ionizing radiation, UV, reactive oxygen species, viruses, microbial products and other pro-inflammatory cytokines) [12, 41, 42]. IL-6 production is predominantly regulated by changes in the gene expression of various transcription factors such as NF-kB, CCAAT/enhancer-binding protein a and activator protein 1, the major transcriptional regulator, although posttranscriptional modifications have also been identified [41, 43]. Though the activation of these transcription factors leads to the overexpression of this cytokine during inflammation, its expression is also known to be regulated epigenetically in breast cancer, hepatocellular carcinoma, colon cancer, prostate cancer and lung cancer through miRNAs (Lin28 and Let-7) [44].

The normal blood circulating level of IL-6 is nearly 1 pg/ml [45, 46], but an increase in its level is found under several conditions such as acute hyperglycemia [47], high-fat meal [48], normal menstrual cycle [49], physical activity [50] and during/after surgery [51]. Inconsistent levels of IL-6 have also been observed during pregnancy, with median values around 128 pg/ml registered at delivery, which drop by more than two fold (~58 pg/ml) immediately afterward [52]. Furthermore, serum IL-6 levels have been found to increase drastically during sepsis [53].

Many physiological factors such as diet, exercise and stress are known to regulate the secretion of IL-6 [47–53]. Exercise is an important stimulus for increased gene expression and production of IL-6 in skeletal muscle, and the majority of circulating IL-6 during exercise originates from contracting muscle, resulting in a 100-fold increase over the normal physiological level [50, 54]. IL-6 produced in the working muscle during physical activity acts as an energy sensor that activates AMP-activated kinase and enhances glucose uptake, metabolism, lipolysis and fat oxidation [50]. IL-6 is also known to sensitize myotubes to insulin and enhances glucose uptake in muscles for high glycogen synthesis. Moreover, the reduced level of muscle glycogen also augments IL-6 production and secretion from muscle cells [55]. In addition to exercise, the expression of IL-6 increases in skeletal muscles under other

conditions as well, such as denervation of muscles and muscular dystrophy, also resulting in the upregulated expression of muscle IL-6 [54]. The adipose tissue produces nearly 30 % of circulating systemic IL-6, where it is closely associated with obesity, impaired glucose tolerance and insulin resistance [56]. Plasma IL-6 concentrations are a predictor of the development of type 2 diabetes, and peripheral administration of IL-6 results in insulin resistance in rodents and humans by causing hyperlipidaemia and hyperglycaemia [56]. Besides muscle cells, e.g. macrophages, mast cells, dendritic cells, B cells and CD4 effector T helper cells in the immune system are amongst the major sources of IL-6 production [22, 57–59]. In addition, IL-6 is also secreted by a variety of non-haematopoietic cells such as fibroblasts, endothelial cells, epithelial cells, astrocytes and malignant cells [2, 33, 42, 60]. Enhanced levels of IL-6 have been found in many cancers, with an inverse relationship between IL-6 levels and response to chemotherapy and hormone therapy [61]. Furthermore, IL-6 expression has also been found higher in recurrent tumours as compared to primary tumours, as well as in recurrent metastatic lesion as compared to primary metastasis [15].

The primary sources of IL-6 in the tumour microenvironment are tumour cells as well as tumour-associated macrophages (TAMs), $CD4^+$ T cells, myeloid-derived suppressor cells (MDSCs) and fibroblasts [59–62]. In the tumour microenvironment, IL-6 supports tumorigenesis by directly affecting cancer cells through the modulation of both the intrinsic and extrinsic activities of tumour cells as well as by influencing stromal cells that indirectly support tumorigenesis [63]. For example, in skin and prostate cancer, the autocrine and paracrine secretion of IL-6 induces a complex of cytokine, growth factors and protease network consisting of granulocyte macrophage colony-stimulating factor (GM-CSF), IL-8, MCP-1, vascular endothelial growth factor (VEGF) and MMP-1 and stimulates malignant progression [64]. Basically, tumour cells produce IL-6 for promoting their survival and progression and do not depend on paracrine release of IL-6 by stromal cells [63]. However, both autocrine and paracrine mechanisms of IL-6 are known to influence tumour progression and metastasis through IL-6 trans-signalling [2, 64].

Pleiotropic role of IL-6

Cancer is an inflammatory disease, and the key feature of cancer-related inflammation is the expression of cytokines. Different cytokines play different roles in the onset and resolution of inflammation. However, a ubiquitous and functionally diverse cytokine, IL-6 is a pleiotropic cytokine with pro- and anti-inflammatory properties (Fig. 1). It is an important cytokine regulating the acute-phase response of inflammation [21]. During inflammatory response, tumour necrosis factor alpha (TNFα) induces the expression of IL-6 together with other inflammatory alarm cytokines, such as IL-1β, which are involved in the elicitation of acute-phase inflammatory reactions/responses (Fig. 1) [65]. Furthermore, IL-6 controls the level of acute inflammatory responses by downregulating the expression of pro-inflammatory cytokines and upregulating anti-inflammatory molecules, including IL-1 receptor antagonist protein, TNF-soluble receptor and extrahepatic protease inhibitors (Fig. 1) [66]. IL-6 has also been found to counter inflammation by inhibiting TNFα release in experimental endotoxemia [67]. This pleiotropic nature of IL-6 maintains the host–tumour homeostasis.

During switch between pro- and anti-inflammatory roles, TNFα and IL-1β negatively regulate IL-6 signalling at different levels by enhancing the IL-6-induced expression of the suppressor of cytokine signalling (SOCS3, feedback inhibitor) and/or targeting IL-6-induced gene expression via its action on target gene promoters [59, 68–70]. IL-1β also counteracts IL-6-mediated STAT-3 activation independent of SOCS3 expression [71]. IL-1β is the major regulator of the pro- and anti-inflammatory nature of IL-6; on the one hand, it reduces the pro-inflammatory activity of IL-6 that results in the inhibition of overshooting immunological reactivity, such as in inflammatory bowel disease or autoimmune arthritis, whilst on the other hand, it delays the anti-inflammatory effects of IL-6 to reinforce the pro-inflammatory processes in the initial phase of inflammation [70]. Similarly, the high concentration of IL-1β in the tumour microenvironment must maintain the chronic inflammatory environment by suppressing the anti-inflammatory processes of IL-6.

Emerging evidences suggest that IL-6 plays key roles in the acute as well as the transition (resolution) phase of inflammation [68]. Furthermore, IL-6 trans-signalling recruits T cells at the site of inflammation by triggering the expression of T cell-attracting chemokines (CCL4, CCL5, CCL17 and CXCL10) [72]. Moreover, IL-6 also rescues T cells from entering apoptosis by STAT-3-dependent upregulation of anti-apoptotic regulators (Bcl-2 and Bcl-xL) and modulation of Fas surface expression [73, 74]. IL-6 also regulates the differentiation of recruited T cells towards TH2 by inducing the expression of IL-4. Thus, IL-6 regulates some of the key steps in controlling inflammation and sets the anti-inflammatory environment by promoting TH2 response [57]. Collectively, these evidences suggest that endogenous IL-6 plays a vital anti-inflammatory role in both local and systemic acute inflammatory responses by controlling the level of pro-inflammatory cytokines, mainly. The trans-signalling of IL-6 regulates mainly the pro-inflammatory response; however, IL-6 classical signalling imparts its anti-inflammatory or regenerative activity (Fig. 1) such as regeneration [75], inhibition of epithelial apoptosis and the activation of the acute-phase response [76]. Understanding of the pleiotropic role of IL-6 in cancer

is not very clear; however, the information available from other inflammatory diseases suggest that IL-6 might play both pro- and anti-inflammatory roles in the tumour microenvironment, which is crucial for host–tumour interaction.

Role of IL-6 and associated signalling in cancer

The notion that inflammation drives cancer is now well established. One of the major drivers of this link is NF-kB, which plays a central role in the secretion and activation of numerous pro-inflammatory cytokines from multiple cell types in the tumour microenvironment, including macrophages, T cells and epithelial cells [43, 57, 58]. Several pro-inflammatory cytokines released by innate and adaptive immune cells regulate cancer cell growth and thereby contribute to tumour promotion and progression. Amongst these, IL-6 is important in the development of human cancer and activates oncogenic pathways, and it is known to be deregulated in cancer [77]. Overexpression of IL-6 in many types of tumours, such as colorectal cancer [3], prostate cancer [5], breast cancer [4], ovarian carcinoma [6], pancreatic cancer [7], lung cancer [8], renal cell carcinoma [9], cervical cancer [10], multiple myeloma [11] and lymphomas [78], suggests a strong link between this cytokine and cancer. The high susceptibility and incidence of liver cancer in males is also found to be associated with high levels of IL-6 [79]. However, in females, oestrogen steroid hormones inhibit IL-6 production and so protect female mice from cancer [79, 80]. Activation of the IL-6/STAT-3 signalling axis is an important event in cancer which promotes tumorigenesis by regulating multiple survival signalling pathways in cancer cells [24]. IL-6 regulates nearly all hallmarks of cancer, such as inhibition of apoptosis [81, 82], promotion of survival [8, 75], proliferation [35, 83], angiogenesis [10], invasiveness and metastasis [62, 84], and is also known to regulate cancer cell metabolism (Fig. 2) [85, 86]. Therefore, there exists a strong link between IL-6 and cancer, similar to the link between cancer and inflammation. Majority of the phenotypes or hallmarks of cancer which are influenced by IL-6 comprise many biological capabilities that are acquired during tumour development. The role of IL-6 in the regulation of hallmarks of cancer will be discussed in detail later.

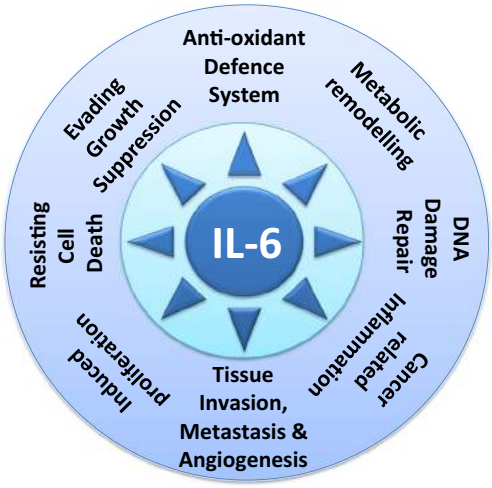


Fig. 2 IL-6 and cancer hallmarks: IL-6 plays an important role in cancer growth and progression by influencing nearly all hallmarks of cancer. The picture illustrates the contribution of IL-6 in some major characteristics of cancer, which are known as cancer hallmarks

Evasion of growth suppressors

Cancer cells evade some powerful programmes that negatively regulate cell proliferation. Many of these programmes depend on the action of tumour suppressor genes such as p53 and RB (retinoblastoma gene), which undergo either loss or gain of function, respectively, to limit cell growth and proliferation. Rb (retinoblastoma-associated) and TP53 proteins are the essential regulatory nodes within two key complementary cellular regulatory circuits that govern the decisions of cells to proliferate or activate senescence and apoptotic programmes [87]. The hypermethylation of CpG islands in the promoter regions of tumour suppressor genes has been found in many tumours, which allows cancer cells to bypass crucial checkpoints in cell cycle progression and evade apoptotic signals (Fig. 3) [88, 89]. IL-6 is known to increase both the expression of DNA methyltransferase (DNMT-1) [90] and its translocation to the nucleus by DNMT-1 nuclear localizing signal's phosphorylation via PI-3K/AKT signalling [91], thereby increasing the activity of DNMT-1, resulting in CpG island methylation of the promoter region of the p53 gene (Fig. 3) [89]. Contrary to the hypermethylation of tumour suppressor genes, IL-6 is also involved in causing global hypomethylation of retrotransposon long interspersed nuclear element-1 in oral squamous cell carcinoma cell lines, which promotes tumorigenesis in the oral cavity [92]. These epigenetic alterations in tumour cells contribute to the epigenetic silencing of tumour suppressor genes and lead to enhanced tumorigenesis.

Mutations in the RB gene contribute to cellular transformation in various types of malignancies [93]. Normal retinoblastoma protein suppresses the transition from the G1 to the S phase of the cell cycle, which is regulated by the phosphorylation of Rb protein. The active, hypo- or dephosphorylated form of Rb binds with E2F and induces G1 growth arrest. On the contrary, the phosphorylated Rb, which is inactive, cannot bind E2F and activates CDK, thereby facilitating entry of cells into the S phase [94]. In multiple myeloma (MM) cells, IL-6

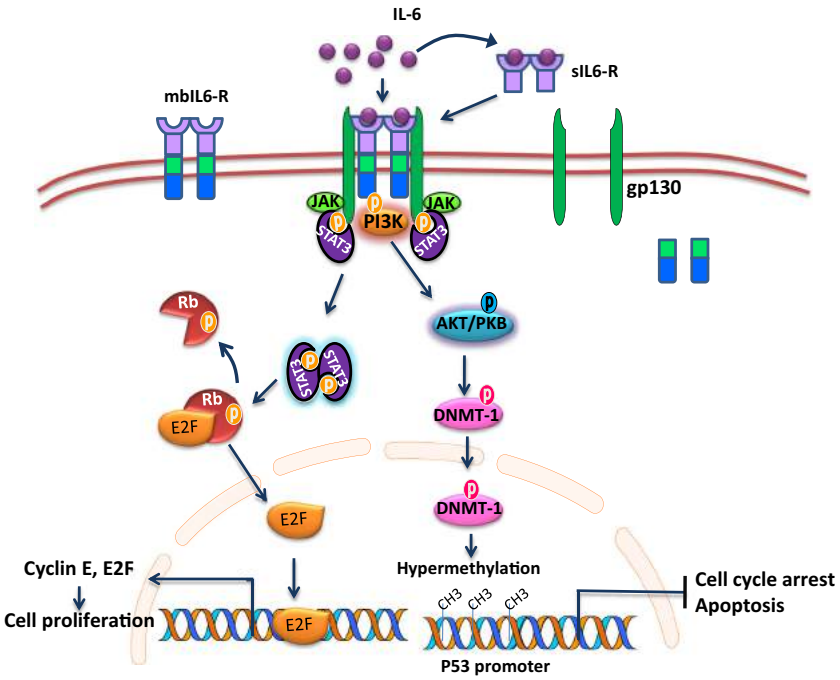


Fig. 3 Role of IL-6 in evading growth suppressors: Normally, E2F remains bound with Rb and localized to the cytosol. IL-6 signalling either induced by mbIL-6R or sIL-6R activates JAK/STAT-3 phosphorylation, which then phosphorylates Rb, resulting in the dissociation of E2F from Rb. The free E2F translocates to the nucleus, where it induces the expression of genes (cyclin E and E2F itself) responsible for the proliferation of cells. Similarly, IL-6 via PI3K/AKT signalling causes the activation of DNMT-1 by its phosphorylation. After phosphorylation, DNMT-1 translocates to the nucleus and hypermethylates the p53 promoter, resulting in silencing of tumour suppressor, pro-apoptotic and other p53 target genes

facilitates the phosphorylation of Rb and, thus, promotes cell growth (Fig. 3). Furthermore, Rb phosphorylation also upregulates IL-6 secretion by MM cells and IL-6-mediated autocrine tumour cell growth [95].

Resistance against cell death

Cancer cells evolve a variety of cytoprotective approaches to limit or circumvent cell death programmes, mainly apoptosis. Besides evading growth suppression signalling, by loss of TP53 function, tumours are also associated with an increase in the expression of anti-apoptotic regulators (Bcl-2, Bcl-xL and Mcl-1) and survival signals (Igf1/2) or downregulated pro-apoptotic factors (Bax, Bim and Puma) [96, 97]. IL-6 regulates the process of apoptosis by activating STAT-3 and NF-kB signalling (Fig. 4), which transactivates the expression of many anti-apoptotic proteins such as Bcl-2, Bcl-xL, Mcl-1, etc., in cholangiocarcinoma cells [98], cervical cancer [99], gastric cancer cells [81], myeloma cells [82], basal cell carcinoma cells [100] and esophageal carcinoma [101]. In addition, these pro-survival proteins, mainly Bcl-2, promote cell proliferation [102]. As the balance between pro-apoptotic and anti-apoptotic proteins is important for apoptotic decision, the ratio of pro-apoptotic to anti-apoptotic factors is increased with oxidative stress, but the increased levels of IL-6 may alter this ratio in favour of anti-apoptotic signalling, leading to cell survival, both in IL-6-treated cells and IL-6-expressing transgenic mice [103]. Besides this, IL-6-induced Bcl-2 regulates Bak interactions with mitofusins via inhibition of Bak dissociation from Mfn2 and also inhibits the interaction of Bak with Mfn1. These two mitochondrial events are the major determinants of cell death pathways as they prevent mitochondrial fragmentation during apoptosis [103, 104]. Therefore, Bcl-2 appears to be an essential mediator of IL-6-induced cytoprotection (Fig. 4).

Besides Bcl-2 and Bcl-xL, IL-6 also supports tumour cell survival by inducing the expression of survivin through direct binding of STAT-3 to the survivin promoter [105]. Furthermore, downregulation of survivin at the gene expression level by inhibiting STAT-3 induces apoptosis in tumour cells [105]. IL-6 triggers PI3K/Akt, NF-kB and MAPK/ERK signalling in prostate cancer cells and results in the upregulation of cyclin A1 expression that promotes tumour cell proliferation in hepatoma, prostate cancer, bladder cancer and in multiple myeloma. IL-6-induced activation of PI3K/Akt signalling further activates IkB kinase (IKK), which initiates NF-kB signalling, leading to transactivation of pro-survival and proliferation-inducing proteins (Fig. 4) [83, 106–109]. IL-6/STAT-3 signalling is also required for the survival of intestinal epithelial cells in colitis-associated cancer, where IL-6 produced from lamina propria myeloid cells protects normal and pre-malignant epithelial cells from cell death [75].

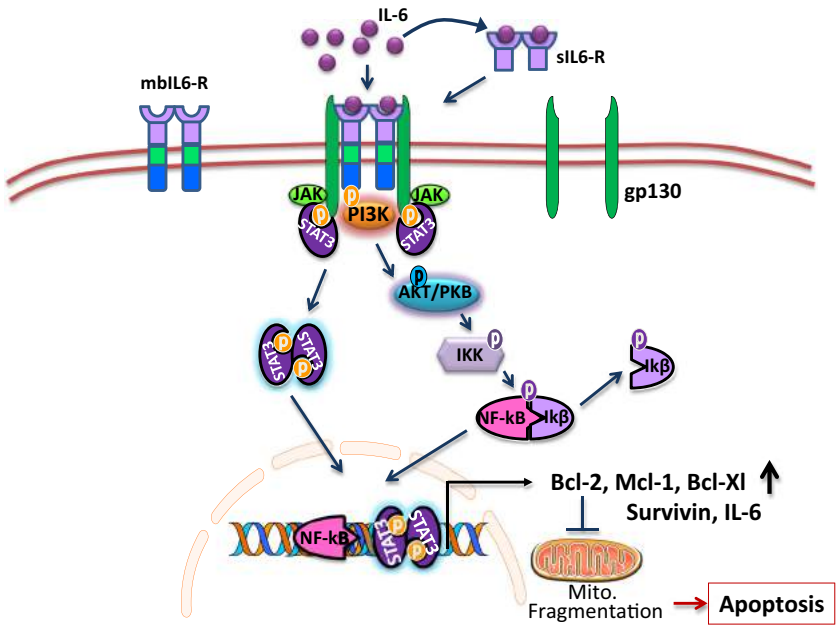


Fig. 4 IL-6 in resisting cell death: IL-6-induced JAK/STAT-3 and NF-kB signalling facilitates the translocation of STAT-3 and NF-kB in the nucleus. Activation of these signalling pathways results in the expression of anti-apoptotic genes (*Bcl-2*, *Bcl-xL*, *Mcl-1*, *survivin*, etc.) and IL-6 for the constitutive activation of IL-6-dependent signalling in cancer cells. IL-6-induced Bcl-2 expression inhibits stress (endogenous and therapeutic)-induced mitochondrial fragmentation and protects the cells from apoptosis

Collectively, it appears that IL-6 facilitates tumour growth primarily by inhibiting apoptosis and enhancing cell proliferation. Besides deriving the growth potential, cancer cells exploit IL-6 for inducing resistance towards anticancer therapy-induced death pathways. For example, IL-6 confers protection from dexamethasone-induced apoptosis by activating PI3K/AKT signalling and inactivating casapase-9, thereby inhibiting apoptosis in multiple myeloma cells [109]. It is also known to induce resistance in cisplatin-mediated cytotoxicity in prostate cancer cell lines and esophageal squamous cell carcinoma [110, 111]. Furthermore, IL-6-induced Bcl-2 confers protection against hyperoxic damage and oxidant (H_2O_2) injury [103]. Thus, enhanced IL-6 levels appear to confer resistance against chemotherapy in cancer by downregulating cell death pathways.

Induction of proliferation/replicative immortality

The potential growth stimulatory effect of IL-6 in tumour cells is due to the activation of several signalling pathways. IL-6 stimulates tumour cell proliferation and survival by activating the Ras/Raf/MEK/MAPK, PI3K/AKT and JAK/STAT pathways via gp130 tyrosine phosphorylation [83, 101, 108]. In colitis-associated cancer, IL-6 produced by myeloid cells stimulates the proliferation of malignant epithelial cells via NF-kB/IL-6/STAT-3 cascade [75]. These signalling pathways help tumours in the acquisition of unlimited replication potential, which is essentially required to generate large tumours.

Majority of the genes that regulate cell survival and proliferation, such as Bcl-2, Bcl-xL, Mcl-1, Fas, cyclin D1, cyclin E1 and p21, are direct targets of STAT-3. In addition, other transcription factors which promote proliferation, including c-Myc, c-Jun and c-Fos, are also targets of STAT-3 [112]. In tumour cells, STAT-3 activation is mediated through autocrine production and paracrine secretion of IL-6 from stroma and infiltrating inflammatory cells [58–62]. IL-6/STAT-3 signalling also functions as a transcriptional repressor of p53 expression, whilst blocking STAT-3 upregulates the expression of p53, leading to p53-mediated apoptosis [113].

IL-6 has also been found to mediate its multi-lineage haematopoietic effects by shifting stem cells from the G0 to the G1 stage of the cell cycle, thereby inducing the proliferation and making stem cells more responsive to additional haematopoietic growth factors such as IL-3, IL-4, G-CSF, M-CSF or GM-CSF [114]. The autocrine production of IL-6 by non-stem cells activates the JAK1/STAT-3 signal transduction pathway which plays an important role in the conversion of non-stem cells into stem-like cells through the upregulation of Oct-4 (a stem cell marker) [115]. Therefore, IL-6 not only induces the proliferation of cancer cells but also maintains the population of cancer stem cells that induce the reoccurrence of tumours. Since only the cancer stem cells have tumorigenic potential amongst the heterogeneous mass of tumours [116], IL-6 seems to play an important role in the maintenance of equilibrium between non-cancer and cancer stem cells, as observed in breast and prostate cancers

[44]. Thus, IL-6 has been suggested as a potential regulator of normal and tumour stem cell self-renewal.

Cancer-related inflammation

Accumulating evidences suggest that chronic inflammation predisposes cells and tissues to different forms of cancer [117]. Thus, cancer and inflammation have a strong connection, which prompted the use of anti-inflammatory drugs for cancer prevention. Cancer-related inflammation involves the infiltration of TAMs, white blood cells and inflammatory messengers like cytokines, such as TNF, IL-1 and IL-6, and chemokines (CCL2 and CXCL8), which facilitate tissue remodelling and angiogenesis [118]. IL-6 is one of the most highly expressed mediators of inflammation in the tumour microenvironment, and STAT-3-dependent tumorigenesis has been associated with the local secretion of IL-6 and its related trans-signalling within the tumour microenvironment in inflammation-induced colorectal cancer [75]. In addition, production of IL-6 by M2-type macrophages in ulcerative colitis supports the development of colon tumours [119]. These studies have identified a link between IL-6 and tumour-associated inflammation. The primary players in inflammation include transcription factors such as NF-kB, STAT-3 and primary inflammatory cytokines (IL-1b, IL-6 and TNFα) [1, 120]. NF-kB is the major regulator of inflammation which is deregulated in many cancers [120]. As a major effector molecule of NF-kB activation through the STAT-3 pathway, IL-6 appears to be an important component of the NF-kB/IL-6/STAT-3 cascade involved in tumorigenesis [75]. STAT-3 is required for the maintenance of NF-kB activation in tumours [121], whilst IL-6 promotes carcinogenesis through inflammation and cell proliferation [35, 44, 106]. Since inflammation enhances the growth and progression of gastrointestinal tumours via the activation of IL-6-mediated STAT-3 signalling, it appears that there is a strong link between IL-6, inflammation and tumour promotion [1, 117, 118].

Metabolic remodelling

Enhanced aerobic glycolysis is one of the prominent phenotypes of a majority of cancer cells which facilitate proliferation and confer protection against death, besides energy production [122, 123]. This induced glycolysis is one of the major factors that contribute to IL-6-induced therapeutic resistance in cancer. IL-6-mediated stimulation of glucose metabolism is dependent on the signal transduction involving the PI-3 kinase and JAK/STAT pathways through the enhanced expression of major glycolytic enzymes hexokinase 2 and PFKFB-3 [124]. It also enhances glucose transport by inducing the expression of glucose transporters GLUT-1 and GLUT-4, which further translocate to the plasma membrane, resulting in a higher glucose influx in cells (Fig. 5) [124]. In addition, it also increases fatty acid oxidation (Fig. 5) [85]. Furthermore, IL-6-induced p53 regulates glycolytic metabolism through NF-kB-mediated mechanism, which also increases GLUT-2 and GLUT-4 receptors on the cells to enhance glycolysis [125].

IL-6 also causes 5′ AMP-activated protein kinase (AMPK) phosphorylation, which is important for IL-6-mediated glucose uptake and lipid oxidation (Fig. 5) [126] and is known to be involved in obesity-associated cancers [127]. In sickle cell disease, elevated plasma IL-6 levels are correlated with increased rates of glycolysis in red blood cells, as evidenced by the increase in lactic acid and higher 2,3-bisphosphoglycerate levels [128]. More recently, treatment of IL-$6^{-/-}$ mice with diethylnitrosamine (a carcinogenic agent) after a high-fat diet has been shown not to support faster development of hepatocellular carcinoma (HCC) as compared to a low-fat diet, suggesting that IL-6 preferentially may render obese individuals susceptible to HCC [106]. In cachectic tumour-bearing mice, a high level of IL-6 has been found to suppress mTORC1 activity by AMPK activation, thereby rendering the mice irresponsive to glucose administration [86]. p62 is a scaffold protein that binds to the nutrient-sensing component of mTOR, crucial for metabolic reprogramming during cell transformation. Loss of p62 has been found to reduce mTOR activity, resulting in impaired metabolism and higher IL-6 release, causing tumorigenesis [129].

Maintenance of redox potential

Oxidative stress induced either by therapeutic agents or metabolic alterations induces damage to macromolecules, viz. proteins, lipids, membranes and DNA, that play a key role in the development of cancer. NF-kB is a critical transcription factor that senses redox imbalance and facilitates cytokine gene induction during cellular stress [130]. Endogenous or induced oxidative stress activates transcription factor NF-kB, which regulates the expression of IL-6 by binding to the promoter region of the IL-6 gene [131, 132]. IL-6, which is the major effector molecule of NF-kB, itself causes NF-kB activation in cancer cells, which results in more IL-6 production. Furthermore, this enhanced IL-6 concentration in the tumour microenvironment constitutively activates NF-kB signalling in the same or neighbouring cells (autocrine/paracrine) [131, 133]. Aberrant NF-kB regulation has been observed in many cancers, whose sustained activation requires STAT-3. Since NF-kB and STAT-3 are regulated by IL-6, it appears that the NF-kB/STAT-3/IL-6 signalling cascade plays an important role in oncogenesis [134]. IL-6 is known to protect cardiac myocytes from oxidative stress-induced apoptosis through STAT-3 signalling and gastric cancer cells by upregulating Mcl-1 expression [81]. In multiple myeloma cells, IL-6 causes radio-resistance by activating NF-kB in an autocrine manner, which results in the activation of antioxidant defence system

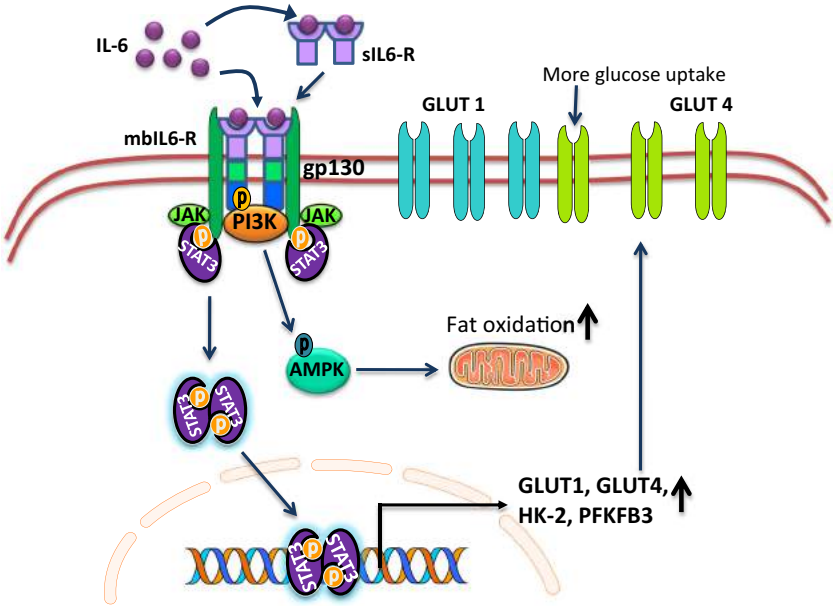


Fig. 5 IL-6 in metabolic remodelling: IL-6-induced JAK/STAT-3 signalling (both classical and trans) induces the expression of major glycolytic enzymes (*HK2* and *PFKB3*) and glucose transporters (*GLUT-1* and *GLUT-4*). The expression of these glycolytic genes ensures aerobic glycolysis in tumour cells. IL-6 also induces fatty acid oxidation in the mitochondria by activating the AMPK pathway

enzymes such as glutathione peroxidase (GPx), superoxide dismutase II (MnSOD) and catalase (Fig. 6) [135].

Apoptosis plays a very crucial role in maintaining genomic integrity by selectively removing the population of heavily damaged cells. Reactive oxygen species (ROS) and pro-inflammatory cytokines are generally elevated following exposure to ionizing radiation and during human carcinogenic processes [136]. Hydrogen peroxide (H_2O_2) is a potent reactive oxygen species that causes mitochondrial dysfunction and cell death. Preconditioning cells with IL-6 decreases H_2O_2-induced cell death by increasing the expression of prohibitin, which is involved in mitochondrial biogenesis and metabolism, apoptosis and replicative senescence [137]. In addition to signalling through STAT-3, the stress-induced activation

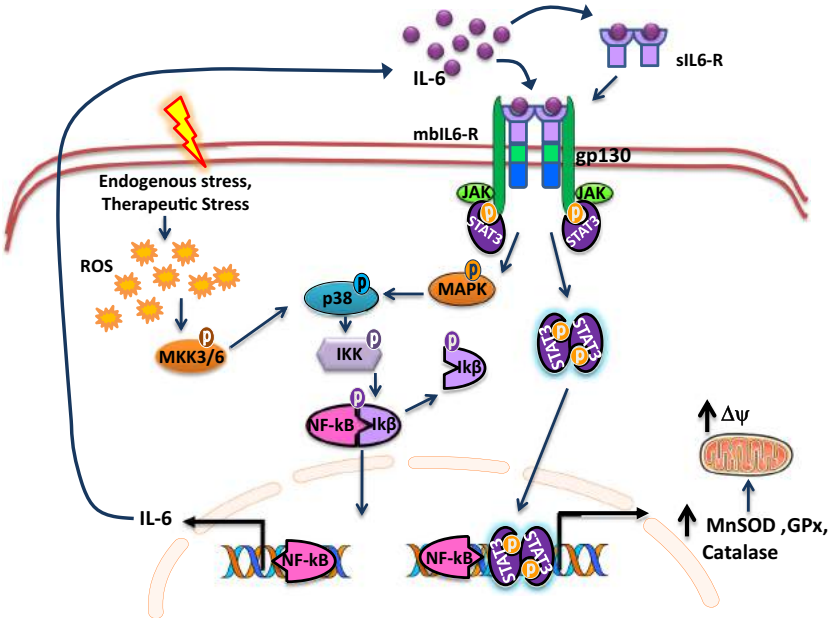


Fig. 6 IL-6 maintains redox balance: p38 senses oxidative stress through ROS-induced phosphorylation of MKK3/6. p38 activation (phosphorylation) induces NF-kB signalling, leading to the enhanced expression and secretion of IL-6 from affected cells. IL-6 (in classical/trans-signalling fashion) further activates JAK/STAT-3 signalling in both paracrine and autocrine manner, resulting in the overexpression of the antioxidant enzymes MnSOD, glutathione peroxidase (*GPx*) and catalase. Altered favourable redox balance also enhances the mitochondrial membrane potential

(phosphorylation) of p38 also induces IL-6 release from cells via the activation of NF-kB (Fig. 6) [138]. All these studies showed the antioxidant potential of IL-6.

Invasion, metastasis and angiogenesis

During tumour metastasis, cancer cells invade surrounding local tissues to migrate to distant organs by acquiring a mesenchymal phenotype that allows the metastatic cancer cells to migrate from the site of the primary tumour. Upon lodging into the new organ, tumour cells lodge themselves by switching back to an epithelial phenotype and proliferate to form metastatic tumours. The processes by which cells switch between epithelial and mesenchymal phenotypes are widely known as the epithelial-to-mesenchymal transition (EMT) and its counterpart, the mesenchymal-to-epithelial transition [139]. It is well established that inflammation promotes EMT [139, 140]. Elevated levels of IL-6 in the serum have been associated with EMT and invasion along with increased size of tumours, metastasis and decreased survival of colorectal cancer patients [60]. Available evidences suggest that IL-6 facilitates the metastasis of many tumours (e.g. breast, lung, prostate, renal carcinomas, neuroblastoma, melanoma and multiple myeloma) to the bone [141] by increasing CXCR4 expression via STAT-3 and c-Jun [142]. Furthermore, IL-6-activated STAT-3 plays a role in EMT, invasiveness and angiogenesis in bladder cancer by increasing VEGF, MMP9 and DNMT1 expressions [107]. Autocrine production of IL-6 has also been shown to enhance the capacity to invade the extracellular matrix in breast cancer [143].

Supply of nutrients and oxygen as well as the clearance of metabolic by-products required for tumour sustenance are provided by tumour-associated neovasculature. The formation and maintenance of this neovasculature remains always activated as an 'angiogenic switch' and helps tumour development [144]. STAT-3 activation by IL-6 facilitates angiogenesis in many cancers by inducing the expressions of VEGF, bFGF and MMP9 in tumour-associated endothelial cells, TAMs and MDSCs [60, 84, 143, 145]. In addition, the Notch ligand, JAG-2, has been reported to be overexpressed in malignant plasma cells from MM patients, which induces the secretion of IL-6 and VEGF [146], whilst in breast cancer, Notch-3-dependent ERK activation via IL-6 appears to activate JAG-1 (Notch ligand) and CA-IX (a hypoxia survival gene). Furthermore, this CA-IX upregulated by IL-6 has also been found to maintain the invasive potential of breast cancer cells and mammospheres [143].

DNA damage and repair

DNA is the primary target of majority of the established anticancer therapies which induce cell death processes in tumour cells. DNA damage has been shown to induce the expression and secretion of IL-6 from cancer cells, resulting in the activation of the JAK1/STAT-3 signalling pathway. STAT-3 activation not only protects tumour cells against DNA damage but also facilitates the growth of damaged cells by inhibiting induced senescence [147, 148]. Furthermore, inhibition of the IL-6/STAT-3 signalling pathway by the STAT-3 inhibitors, knockdown of gp130, or the neutralization of IL-6 impairs the growth of tumour cells exposed to DNA damage [147]. IL-6 secreted by tumour-associated endothelial cells in the tumour microenvironment has been suggested to protect lymphoma cells from genotoxic chemotherapy [149], whilst persistent DNA damage response has been shown to induce IL-6 secretion in stromal cells such as fibroblasts [148]. The ATM/NEMO/ELKS complex formed by DNA damage-induced phosphorylation of ATM promotes IKK-mediated IkBα degradation, leading to NF-kB activation, which further induces the expression of IL-6 (Fig. 7) [150]. In the partial hepatectomy (PH) model of DNA repair, wild-type mice were found to express some of the key DNA repair enzymes such as OGG-1, 8-oxo-GTP, Neil-1 and PARP, whereas these enzymes were absent in IL-6 knockout mice, suggesting a direct role of IL-6 in the repair of DNA damage [151]. Thus, in PH, it appears that IL-6 facilitates the restoration of hepatic mass by activating DNA repair enzymes, followed by accurate replication in proliferating hepatic cells [151]. Loss of Rrm2b function (a key enzyme in de novo deoxyribonucleotide synthesis) is known to cause severe numerical and structural chromosomal abnormalities, which leads to the activation of NF-kB through ATM phosphorylation and IKK activation, leading to enhanced IL-6 expression and constitutive activation of STAT-3 [152]. Since IL-6 signalling functions by the activation of transcription factors such as STAT-3 and NF-kB, inhibition of these transactivators or neutralizing the IL-6 may enhance the efficacy of DNA damage-causing chemotherapeutic drugs [153].

IL-6 induces therapeutic resistance in cancer

Accumulating evidences suggest that inflammatory signals from tumour cells and surrounding microenvironment facilitate tumour growth [63, 117]. Furthermore, most anticancer therapies induce inflammation by killing tumour cells and normal tissues [154]. Several inflammatory cytokines are believed to play key roles in therapeutic resistance and lead to tumour regrowth, invasion and angiogenesis. Anticancer therapies induce upregulation of the levels of a variety of inflammatory cytokines, including IL-6, IL-8 and TNFα [8, 12, 13]. Amongst these, IL-6 is known to contribute to poor therapeutic gain, tumour relapse and aggressive tumour growth [2, 8, 12]. IL-6 is also recognised as a key regulator of immunosuppression in patients with advanced cancer [1, 154]. Elevated IL-6 serum levels have been correlated with metastasis and

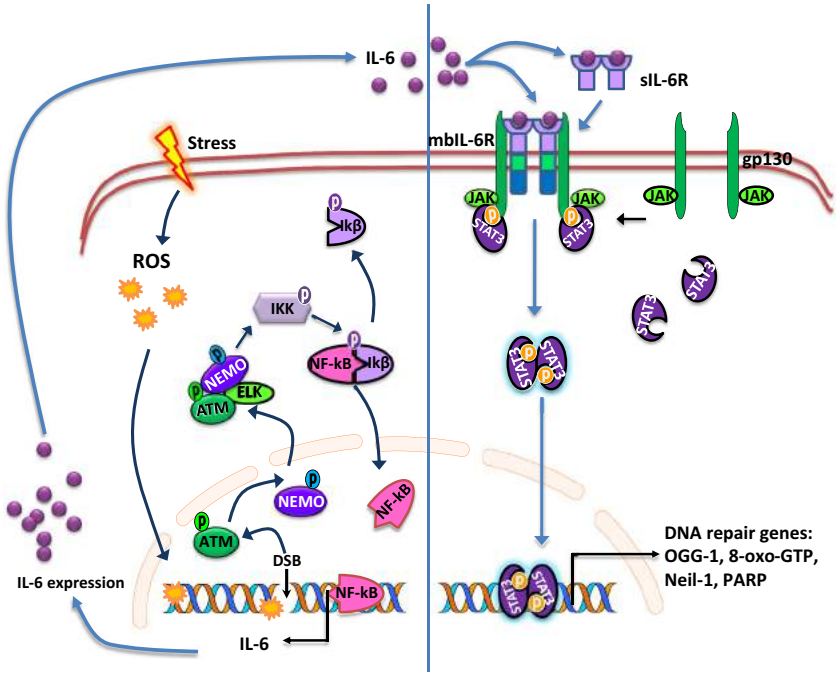


Fig. 7 Role of IL-6 in DNA repair: IL-6 facilitates DNA repair by inducing the expression of DNA repair enzymes in cancer cells. The induction of DNA damage phosphorylates the ATM, leading to the phosphorylation of IKK through the phosphorylation of various downstream kinases. IKK phosphorylation activates NF-kB signalling, resulting in sustained IL-6 expression and constitutive activation of STAT-3 signalling, which induces the expression of DNA repair enzymes

morbidity in prostate cancer and therapeutic resistance in ovarian cancer, whilst patients with reduced levels of IL-6 respond better to therapy [14, 15]. It appears that tumour cells produce IL-6 as a protective mechanism against drug-induced death, as in the case of prostate cancer where inhibition of IL-6 secretion increases the sensitivity of prostate cancer cells to anticancer drugs [12, 110]. Clinical studies on combinations of docetaxel and zolendronic acid in prostate cancer patients with bone metastasis have shown interesting data in relation to IL-6. Patients who responded to therapy had a 35 % decrease in overall serum IL-6 levels, whilst patients who did not respond had a 76 % increase in serum IL-6 levels [155], lending support to the notion that IL-6 confers therapeutic resistance in prostate cancer [5, 12]. The autocrine secretion of IL-6 by breast cancer cells is also shown to confer therapeutic resistance; however, it does not affect their growth. Further studies showed that drug-sensitive breast cancer cells do not express IL-6, whereas multidrug-resistant breast cancer cells produced high levels of IL-6 [156]. IL-6-mediated STAT3 activation has been reported to cause therapeutic resistance in tumours by inducing several pro-survival pathways [12, 105, 110]. However, IL-6-induced drug resistance is associated with increased expression of the multidrug resistance gene, *mdr1*, and upregulation of C/EBPβ and C/EBPδ (CCAAT enhancer-binding protein family of transcription factors) [156]. Moreover, in colorectal cancer, IL-6 secreted from stromal cells induces CYP2E1 and CYP1B1 expression (CYP450 enzymes have a significant role in xenobiotic activation) through the JAK/STAT and PI3K/AKT pathways, which causes tumour initiation and promotion via the activation of chemical carcinogens [157].

IL-6-induced modifications of the stromal cell function appear to be important for tumour growth and angiogenesis as an anti-IL-6 receptor antibody has been found to inhibit tumour angiogenesis and growth by blocking tumour–stroma interaction [60]. Cancer-associated adipocytes can also promote radio-resistance by secreting IL-6 [158], whilst IL-6 and IL-8 secreted by mesenchymal stem cells activate macrophages in the microenvironment of human colorectal and ovarian cancers, causing chemoresistance [159, 160]. Besides causing resistance to chemo- and radiotherapy, autocrine secretion of IL-6 (induced by therapy) also confers resistance to some targeted therapies; for example, aflibercept (anti-VEGF, inhibitor)-resistant epidermoid carcinoma cells and herceptin (trastuzumab, anti-HER2)-resistant breast cancer cells secrete a large amount of IL-6 and show hyperactivation of STAT-3 signalling, causing resistance to therapy [161, 162].

Besides therapeutic resistance, IL-6 also minimizes clinical outcome by promoting the maintenance of a highly therapeutic-resistant cancer stem cell population which is mainly responsible for tumour reoccurrence [116]. IL-6 secreted from either cancer cells or tumour microenvironment (immune cells and tumour stromal cells) not only facilitates tumour growth but also acts as a major obstacle in obtaining

therapeutic gain and tumour-free survival [163]. Therefore, targeting IL-6 and its associated signalling may hold greater promise in minimizing therapeutic resistance in cancer. IL-6 inhibition could sensitize tumour cells to anticancer drugs and radiation by increasing DNA damage and cell death, and mitigate tumour regrowth by inhibiting subsequent angiogenesis and reducing cancer stem cell population.

Targeting IL-6 for therapeutic gain

IL-6 plays an important role in tumour progression and therapeutic resistance through inhibition of cancer cell apoptosis and stimulation of tumour-promoting factors such as proliferation, angiogenesis, etc. These effects are mediated by several signalling pathways; however, STAT-3 plays a central and major role [1, 112]. Targeting the IL-6/JAK/STAT-3 pathway has shown promising results in many types of cancer and various inflammation-related diseases. The clinical correlation of increased serum IL-6 concentrations and advanced tumour stages in various malignancies, as discussed earlier in the review, makes a strong case of blocking IL-6 signalling for therapeutic gain. Therefore, inhibiting IL-6 signalling or minimizing the level of IL-6 can be a potential therapeutic strategy for those cancers which are characterized by overproduction of IL-6. IL-6 signalling can be targeted in multiple ways, such as the use of specific monoclonal antibodies against IL-6 or IL-6R [15, 19, 31], by using synthetic/semi-synthetic compounds as specific inhibitors of IL-6 downstream signalling molecules or by kinase inhibitors (like JAK inhibitor) [164]. All these approaches evaluated in experimental models and reached clinical trials are summarized in Table 1.

Table 1 Multiple therapeutic approaches for targeting IL-6, IL-6R and IL-6-associated signalling

S. no.	Target molecule	Type of cancer	Therapeutic approach	References
1	IL-6	Prostate cancer	IL-6 siRNA	[12]
			Siltuximab (CNTO328)—anti-IL-6 antibody	[165]
		Colorectal cancer	Siltuximab (CNTO328)	[3, 166]
		Ovarian cancer	Siltuximab (CNTO328)	[166]
			Lysophosphatidic acid	[167]
		Renal cancer	Siltuximab (CNTO328)	[166]
		Lung cancer	Siltuximab (CNTO328)	[166, 168]
		Multiple myeloma	Siltuximab (CNTO328)	[166, 169]
		Lymphoma	BE-8 (monoclonal antibody)	[170]
		Prostate cancer	Siltuximab, zoledronic acid	[15, 171]
		Breast cancer	Siltuximab, zoledronic acid, PMA (medroxyprogesterone acetate)	[15, 172, 173]
2	IL-6R	Colon cancer	MR16-1, tocilizumab (anti-IL-6R antibody)	[3, 60]
		Oral squamous cell carcinoma	Tocilizumab	[174]
		Lung cancer	Tocilizumab	[175]
		Multiple myeloma	Tocilizumab	[176, 177]
		Ovarian cancer	Tocilizumab	[178]
		Breast cancer	Tocilizumab	[179]
3	JAKs	Lung cancer	TG101209 (JAK inhibitor)	[180]
		Multiple myeloma	TG101209	[181]
		Ovarian cancer	AG490	[182]
		Acute myeloid leukaemia	Ruxolitinib (JAK1/JAK2 inhibitor)	[183]
		Colitis-associated cancer	CEP-33779 (JAK inhibitor)	[184]
		Acute myeloid leukaemia	SB1518 (JAK2)	[185]
4	STAT-3	Glioblastoma	Sorafenib (multiple kinase inhibitor)	[186]
		Breast cancer	SD-1029	[187]
		Ovarian cancer	SD-1029	[187]
		Lymphoma	JSI-124	[188]
		Glioblastoma	JSI-124	[189]
		Breast cancer	JSI-124	[190]
		Hepatocellular carcinoma	Sorafenib (Nexavar)	[191]
		Breast cancer	Sorafenib	[192]
		Advanced renal cell carcinoma	Sorafenib	[193]
		Colorectal cancer	Sorafenib	[194]

Antibodies targeting IL-6 or IL-6 signalling have been extensively investigated in experimental tumour models and clinical trials for a variety of cancers. Elsilimomab (BE-8), a murine monoclonal antibody, and siltuximab (CNTO 328), a chimeric antibody with strong affinity to IL-6 and licenced for the treatment of Castleman's disease, are used for the treatment of prostate cancer, ovarian cancer, renal cell carcinoma and colorectal cancer in combination with other chemotherapeutics [3, 6, 166]. In prostate cancer, siltuximab has been shown to downregulate the genes downstream of IL-6 signalling along with decreased STAT-3 expression [165]. Tocilizumab, a FDA-approved drug for rheumatoid arthritis and Crohn's disease, is the humanized antibody specific for IL-6R that recognises both soluble and membrane-bound receptors and blocks its signalling [195]. BE-8, a murine anti-IL-6 monoclonal antibody, has also been used in the treatment of lymphoma and multiple myeloma [196]. Sequestering the enhanced IL-6 showed a significant increase in the therapeutic efficacy of paclitaxel in mouse models of epithelial ovarian cancer by reducing tumour angiogenesis [197]. Tocilizumab has also been used in the treatment of oral cell carcinoma, prostate cancer, renal cancer, multiple myeloma and breast cancer [15]. It inhibits the growth of prostate and breast cancer cells by reducing STAT-3-induced VEGF expression. In addition, it reduces bone metastasis of breast cancer cells [142]. Tocilizumab has been shown to improve cachexia developed by IL-6 overexpression in lung cancer patients [175]. The combination of anti-IL-6R with herceptin and aflibercept enhances therapeutic gain, also in targeted therapy-resistant breast cancer and epidermoid carcinoma, respectively [161, 162]. However, blocking IL-6 signalling can be harmful and may result in some adverse effects, such as gastrointestinal, nasopharyngeal and upper respiratory tract infections, gastrointestinal haemorrhage, thrombocytopenia and neutropenia [198]. Therefore, selective blocking of trans-signalling (the major pathway involved in inflammation and related diseases like cancer) using sgp130Fc (a recombinant fusion protein of soluble gp130 and human IgG_1 Fc) may be useful in achieving therapeutic gain in cancer [76].

Besides antibodies, a number of other compounds are currently available that inhibit IL-6 signalling. Zoledronic acid (ZA) is the most potent nitrogen-containing bisphosphonate compound which has been used in adjuvant therapies to inhibit bone metastasis caused by multiple cancers [172]. It inhibits growth, besides inducing apoptosis by reducing IL-6 secretion in prostate cancer cell lines, which is suggestive of its use in the treatment of prostate cancer either alone or in combination with chemotherapy [171]. Radiation activates IL-6/STAT-3 signalling, which stimulates tumour invasion and EMT changes and promotes the survival of tumour cells after therapy, thereby conferring resistance to therapy [12, 84, 156]. However, use of siRNA against IL-6 inhibits tumour regrowth after radiotherapy in prostate cancer and sensitizes tumour cells to radiation by increasing cell death and DNA damage [12]. Its inhibition also mitigates tumour regrowth by eliminating radiotherapy-triggered MDSC and subsequent angiogenesis after radiation exposure [199]. Therefore, inhibition of IL-6 could be a potential therapeutic strategy for increasing the radiation response of tumours. Similarly, medroxyprogesterone acetate (MPA) is a synthetic compound used as an endocrine therapeutic agent for patients with breast cancer which is known to reduce serum IL-6 levels [173]. Several studies have shown that the use of an inhibitor for downstream targets of IL-6 signalling can also be a good approach for enhancing therapeutic gain. For example, the use of JAK inhibitor (TG101209) enhances the efficacy of radiotherapy in lung cancer [180]. Similarly, WP1066 and CEP3379, other JAK2 inhibitors, suppress the growth of gastric cancer and colorectal tumours by inhibiting IL-6/JAK2/STAT-3 signalling [184, 200]. Sorafenib, which is a multiple kinase inhibitor, causes dephosphorylation of STAT-3 and prevents AKT signalling in glioblastoma cells and prostate cancer, respectively [186]. AG490, a potent JAK inhibitor, targets STAT-3 signalling, reduces the invasion of human pancreatic cancer cells in vitro and induces apoptosis in gastric cancer cells [201, 202]. Moreover, AG490 is also effective in murine ovarian cancer, where it induces the expression of anti-tumour cytokines [182]. Another JAK inhibitor, ruxolitinib, is currently in clinical trials for leukaemia [183].

Inhibition of STAT-3 phosphorylation by the use of STAT-3 inhibitors can also be a good approach to block IL-6 signalling. JSI-124 (STAT-3 inhibitor) inhibits STAT-3 phosphorylation at serine 727 and sensitizes B-leukaemia cells to apoptosis [203]. JSI-124 suppresses breast cancer cell growth by downregulating STAT-3 activation in tumour-associated B cells. Stattic and Eriocalyxin B (a diterpenoid) also inhibit STAT-3 phosphorylation and induce apoptosis in MDA-MB-231 and HepG2 cells [204, 205]. Besides inhibiting STAT-3 phosphorylation and transcriptional activation, Decoy oligodeoxynucleotides target the DNA-binding domain of STAT-3 by competing against endogenous DNA *cis* element, which results in reduced cell growth and increased apoptosis [206]. G-quartet oligodeoxynucleotides can also be used as a STAT-3 inhibitor which suppresses the growth of prostate, breast, and head and neck cancers in nude mice [206, 207]. Instead of inhibiting STAT-3 phosphorylation, these oligodeoxynucleotides inhibit the binding of STAT-3 dimer on DNA. Moreover, small-molecule inhibitors can also be used to inhibit STAT-3. A small-molecule non-peptide STAT-3 inhibitor named S3I-201 (a.k.a. NSC74859) selectively inhibits STAT-3 DNA-binding activity in vitro and blocks the formation of STAT-3:STAT-3 dimer, which leads to the inhibition of STAT-3-dependent gene transcription and the blockade of the proliferation and survival of human breast carcinoma cells [208]. STA-21 also selectively inhibits STAT-3 DNA-binding activity in vitro, disrupts STAT-3:STAT-3

dimerization and suppresses STAT-3-mediated gene transcription along with cell growth inhibition and apoptosis through the caspase pathway in a human breast carcinoma and rhabdomyosarcoma model [209, 210]. Catechol-containing compounds, IS3 295, galiellalactone and peptide aptamers have been found to inhibit the DNA-binding ability of STAT-3 and further signalling [208, 211].

Conclusion

IL-6, which is produced by tumours and many other cells in the tumour microenvironment, facilitates tumour growth and sustenance by influencing and regulating nearly all hallmarks of cancer, besides contributing to therapeutic resistance. Recent studies have enhanced our knowledge regarding the potential role of IL-6 in the cross talk between tumour and its microenvironment. IL-6/JAK/STAT-3 appears to be the primary pathway through which IL-6 regulates majority of the tumour-promoting functions. Therefore, neutralizing IL-6 or the IL-6 receptor to prevent the initiation of signalling or inhibiting the activity of two other members, JAK and STAT-3, to prevent the execution in the end has established therapeutic efficacy in cellular and systemic models of cancer. Blocking IL-6 using monoclonal antibodies against either IL-6 or IL-6R has shown promising results in preclinical studies and clinical trials. Phase I and II clinical trials have established the efficacy of monoclonal antibodies either as a single agent or in combination with other chemotherapeutic drugs, radiation and targeted therapies in various types of cancer. Subsequently, certain synthetic molecules, such as ZA, MPA, polyphenols, etc., have also shown promising results in various cancers by regulating IL-6 levels. The use of small-molecule inhibitors of JAK and STAT-3 alone or in combination with radiation or anticancer agents has also resulted in promising anti-tumour effects in various cancers. However, undesirable effects (such as infections, gastrointestinal haemorrhage, thrombocytopenia and neutropenia) of anti-IL-6 therapy have also been reported in patients with various inflammatory diseases. Therefore, selective inhibition of IL-6 trans-signalling using molecules such as sgp130Fc in the future may result in better therapeutic gain without the side effects associated with anti-IL-6 therapy currently under evaluation.

Acknowledgments NK thanks the Defence Research and Development Organization, Government of India, for fellowship support. We acknowledge Director INMAS for constant support and encouragement.

References

1. Bromberg J, Wang TC. Inflammation and cancer: IL-6 and STAT3 complete the link. Cancer Cell. 2009;15:79–80.
2. Grivennikov S, Karin M. Autocrine IL-6 signaling: a key event in tumorigenesis? Cancer Cell. 2008;13:7–9.
3. Waldner MJ, Foersch S, Neurath MF. Interleukin-6—a key regulator of colorectal cancer development. Int J Biol Sci. 2012;8(9):1248–53.
4. Dethlefsen C, Højfeldt G, Hojman P. The role of intratumoral and systemic IL-6 in breast cancer. Breast Cancer Res Treat. 2013;138(3):657–64.
5. Culig Z, Puhr M. Interleukin-6: a multifunctional targetable cytokine in human prostate cancer. Mol Cell Endocrinol. 2012;360(1–2):52–8.
6. Macciò A, Madeddu C. The role of interleukin-6 in the evolution of ovarian cancer: clinical and prognostic implications—a review. J Mol Med. 2013;91:1355–68.
7. Miura T, Mitsunaga S, Ikeda M, Shimizu S, Ohno I, Takahashi H, et al. Characterization of patients with advanced pancreatic cancer and high serum interleukin-6 levels. Pancreas. 2015;44(5):756–63.
8. Chang CH, Hsiao CF, Yeh YM, Chang GC, Tsai YH, Chen YM, et al. Circulating interleukin-6 level is a prognostic marker for survival in advanced nonsmall cell lung cancer patients treated with chemotherapy. Int J Cancer. 2013;132(9):1977–85.
9. Altundag O, Altundag K, Gunduz E. Interleukin-6 and C-reactive protein in metastatic renal cell carcinoma. J Clin Oncol. 2005;23:1044.
10. Wei LH, Kuo ML, Chen CA, Chou CH, Lai KB, Lee CN, et al. Interleukin-6 promotes cervical tumor growth by VEGF-dependent angiogenesis via a STAT3 pathway. Oncogene. 2003;22:1517–27.
11. Singh U, Shevra CR, Singh S, Singh N, Kumar S, Rai M. Interleukin-6 and interleukin-4 levels in multiple myeloma and correlation of interleukin-6 with β2 microglobulin and serum creatinine. Clin Cancer Investig J. 2015;4:211–5.
12. Wu CT, Chen MF, Chen WC, Hsieh CC. The role of IL-6 in the radiation response of prostate cancer. Radiat Oncol. 2013;8:159.
13. Chen MF, Chen PT, Lu MS, Lin PY, Chen WC, Lee KD. IL-6 expression predicts treatment response and outcome in squamous cell carcinoma of the esophagus. Mol Cancer. 2013;12:26.
14. Shibayama O, Yoshiuchi K, Inagaki M, Matsuoka Y, Yoshikawa E, Sugawara Y, et al. Association between adjuvant regional radiotherapy and cognitive function in breast cancer patients treated with conservation therapy. Cancer Med. 2014;3(3):702–9.
15. Guo Y, Xu F, Lu T, Duan Z, Zhang Z. Interleukin-6 signaling pathway in targeted therapy for cancer. Cancer Treat Rev. 2012;38(7):904–10.
16. Veuger SJ, Hunter JE, Durkacz BW. Ionizing radiation-induced NF-kappaB activation requires PARP-1 function to confer radioresistance. Oncogene. 2009;28:832–42.
17. Kozakai N, Kikuchi E, Hasegawa M, Suzuki E, Ide H, Miyajima A, et al. Enhancement of radiosensitivity by a unique novel NF-kB inhibitor, DHMEQ, in prostate cancer. Br J Cancer. 2012;107:652–7.
18. Naugler WE, Karin M. NF-kappaB and cancer-identifying targets and mechanisms. Curr Opin Genet Dev. 2008;18(1):19–26.
19. Wolf J, Rose-John S, Garbers C. Interleukin-6 and its receptors: a highly regulated and dynamic system. Cytokine. 2014;70(1):11–20.
20. Yoon S, Woo SU, Kang JH, Kim K, Shin HJ, Gwak HS, et al. NF-kB and STAT3 cooperatively induce IL6 in starved cancer cells. Oncogene. 2012;31(29):3467–81.

21. Scheller J, Chalaris A, Schmidt-Arras D, Rose-John S. The pro- and anti-inflammatory properties of the cytokine interleukin-6. Biochim Biophys Acta. 2011;1813(5):878–88.
22. Hirano T, Taga T, Nakano N, Yasukawa K, Kashiwamura S, Shimizu K, et al. Purification to homogeneity and characterization of human B-cell differentiation factor (BCDF or BSFp-2). Proc Natl Acad Sci U S A. 1985;82(16):5490–4.
23. Kishimoto T, Akira S, Narazaki M, Taga T. Interleukin-6 family of cytokines and gp130. Blood. 1995;86:1243–54.
24. Mihara M, Hashizume M, Yoshida H, Suzuki M, Shiina M. IL-6/IL-6 receptor system and its role in physiological and pathological conditions. Clin Sci (Lond). 2012;122(4):143–59.
25. Wunderlich FT, Ströhle P, Könner AC, Gruber S, Tovar S, Brönneke HS, et al. Interleukin-6 signaling in liver-parenchymal cells suppresses hepatic inflammation and improves systemic insulin action. Cell Metab. 2010;12(3):237–49.
26. Taga T, Kishimoto T. Gp130 and the interleukin-6 family of cytokines. Annu Rev Immunol. 1997;15:797–819.
27. Hibi M, Murakami M, Saito M, Hirano T, Taga T, Kishimoto T. Molecular cloning and expression of an IL-6 signal transducer, gp130. Cell. 1990;63:1149–57.
28. Yawata H, Yasukawa K, Natsuka S, Murakami M, Yamasaki K, Hibi M, et al. Structure–function analysis of human IL-6 receptor: dissociation of amino acid residues required for IL-6-binding and for IL-6 signal transduction through gp130. EMBO J. 1993;12(4):1705–12.
29. Jones SA, Horiuchi S, Topley N, Yamamoto N, Fuller GM. The soluble interleukin 6 receptor: mechanisms of production and implications in disease. FASEB J. 2001;15(1):43–58.
30. Yoshida K, Taga T, Saito M, Suematsu S, Kumanogoh A, Tanaka T, et al. Targeted disruption of gp130, a common signal transducer for the interleukin 6 family of cytokines, leads to myocardial and hematological disorders. Proc Natl Acad Sci U S A. 1996;93(1):407–11.
31. Jones SA, Scheller J, Rose-John S. Therapeutic strategies for the clinical blockade of IL-6/gp130 signaling. J Clin Invest. 2011;121:3375–83.
32. Chalaris A, Garbers C, Rabe B, Rose-John S, Scheller J. The soluble interleukin 6 receptor: generation and role in inflammation and cancer. Eur J Cell Biol. 2011;90(6–7):484–94.
33. Islam O, Gong X, Rose-John S, Heese K. Interleukin-6 and neural stem cells: more than gliogenesis. Mol Biol Cell. 2009;20(1):188–99.
34. Peters M, Solem F, Goldschmidt J, Schirmacher P, Rose-John S. Interleukin-6 and the soluble interleukin-6 receptor induce stem cell factor and Flt-3L expression in vivo and in vitro. Exp Hematol. 2001;29(2):146–55.
35. Yeoh GC, Ernst M, Rose-John S, Akhurst B, Payne C, Long S, et al. Opposing roles of gp130-mediated STAT-3 and ERK-1/2 signaling in liver progenitor cell migration and proliferation. Hepatology. 2007;45(2):486–94.
36. Humphrey RK, Beattie GM, Lopez AD, Bucay N, King CC, Firpo MT, et al. Maintenance of pluripotency in human embryonic stem cells is STAT3 independent. Stem Cells. 2004;22(4):522–30.
37. Rose-John S. IL-6 trans-signaling via the soluble IL-6 receptor: importance for the pro-inflammatory activities of IL-6. Int J Biol Sci. 2012;8(9):1237–47.
38. McFarland-Mancini MM, Funk HM, Paluch AM, Zhou M, Giridhar PV, Mercer CA, et al. Differences in wound healing in mice with deficiency of IL-6 versus IL-6 receptor. J Immunol. 2010;184(12):7219–28.
39. Kovacs E. Investigation of interleukin-6 (IL-6), soluble IL-6 receptor (sIL-6R) and soluble gp130 (sgp130) in sera of cancer patients. Biomed Pharmacother. 2001;55(7):391–6.
40. Jostock T, Müllberg J, Ozbek S, Atreya R, Blinn G, Voltz N, et al. Soluble gp130 is the natural inhibitor of soluble interleukin-6 receptor transsignaling responses. Eur J Biochem. 2001;268(1):160–7.
41. Akira S, Kishimoto T. IL-6 and NF-IL6 in acute-phase response and viral infection. Immunol Rev. 1992;127:25–50.
42. Yang R, Lin Q, Gao HB, Zhang P. Stress-related hormone norepinephrine induces interleukin-6 expression in GES-1 cells. Braz J Med Biol Res. 2014;47(2):101–9.
43. Zhao W, Liu M, Kirkwood KL. p38alpha stabilizes interleukin-6 mRNA via multiple AU-rich elements. J Biol Chem. 2008;283(4):1778–85.
44. Iliopoulos D, Hirsch HA, Struhl K. An epigenetic switch involving NF-kappaB, Lin28, Let-7 microRNA, and IL6 links inflammation to cell transformation. Cell. 2009;139(4):693–706.
45. Narbutt J, Lukamowicz J, Bogaczewicz J, Sysa-Jedrzejowska A, Torzecka JD, Lesiak A. Serum concentration of interleukin-6 is increased both in active and remission stages of pemphigus vulgaris. Mediat Inflamm. 2008;2008:875394.
46. D'Auria L, Bonifati C, Mussi A, D'Agosto G, De Simone C, Giacalone B, et al. Cytokines in the sera of patients with pemphigus vulgaris: interleukin-6 and tumour necrosis factor-alpha levels are significantly increased as compared with healthy subjects and correlate with disease activity. Eur Cytokine Netw. 1997;8(4):383–7.
47. Devaraj S, Venugopal SK, Singh U, Jialal I. Hyperglycemia induces monocytic release of interleukin-6 via induction of protein kinase c-{alpha} and -{beta}. Diabetes. 2005;54(1):85–91.
48. Blackburn P, Després JP, Lamarche B, Tremblay A, Bergeron J, Lemieux I, et al. Postprandial variations of plasma inflammatory markers in abdominally obese men. Obesity (Silver Spring). 2006;14(10):1747–54.
49. Angstwurm MW, Gartner R, Ziegler-Heitbrock HW. Cyclic plasma IL-6 levels during normal menstrual cycle. Cytokine. 1997;9:370–4.
50. Reihmane D, Dela F. Interleukin-6: possible biological roles during exercise. Eur J Sport Sci. 2014;14(3):242–50.
51. Sakamoto K, Arakawa H, Mita S, Ishiko T, Ikei S, Egami H, et al. Elevation of circulating interleukin 6 after surgery: factors influencing the serum level. Cytokine. 1994;6:181–6.
52. Keski-Nisula L, Hirvonen MR, Roponen M, Heinonen S, Pekkanen J. Spontaneous and stimulated interleukin-6 and tumor necrosis factor-alpha production at delivery and three months after birth. Eur Cytokine Netw. 2004;15:67–72.
53. Naffaa M, Makhoul BF, Tobia A, Kaplan M, Aronson D, Saliba W, et al. Interleukin-6 at discharge predicts all-cause mortality in patients with sepsis. Am J Emerg Med. 2013;31(9):1361–4.
54. Muñoz-Cánoves P, Scheele C, Pedersen BK, Serrano AL. Interleukin-6 myokine signaling in skeletal muscle: a double-edged sword? FEBS. 2013;280(17):4131–48.
55. Steensberg A, Febbraio MA, Osada T, Schjerling P, van Hall G, Saltin B, et al. Interleukin-6 production in contracting human skeletal muscle is influenced by pre-exercise muscle glycogen content. J Physiol. 2001;537:633–9.
56. Bastard JP, Maachi M, Van Nhieu JT, Jardel C, Bruckert E, Grimaldi A, et al. Adipose tissue IL-6 content correlates with resistance to insulin activation of glucose uptake both in vivo and in vitro. J Clin Endocrinol Metab. 2002;87(5):2084–9.
57. Krishnamoorthy N, Oriss T, Pagila M, Ray A, Ray P. A critical role for IL-6 secretion by dendritic cells promoting Th2 and limiting Th1 response. J Immunol. 2007;178:S181.
58. Mitchem JB, Brennan DJ, Knolhoff BL, Belt BA, Zhu Y, Sanford DE, et al. Targeting tumor-infiltrating macrophages decreases tumor-initiating cells, relieves immunosuppression, and improves chemotherapeutic responses. Cancer Res. 2013;73(3):1128–4.
59. Bode JG, Nimmesgern A, Schmitz J, Schaper F, Schmitt M, Frisch W, et al. LPS and TNFalpha induce SOCS3 mRNA and inhibit IL-

6-induced activation of STAT3 in macrophages. FEBS Lett. 1999;463:365–70.
60. Nagasaki T, Hara M, Nakanishi H, Takahashi H, Sato M, Takeyama H. Interleukin-6 released by colon cancer-associated fibroblasts is critical for tumour angiogenesis: anti-interleukin-6 receptor antibody suppressed angiogenesis and inhibited tumour–stroma interaction. Br J Cancer. 2014;110(2):469–78.
61. Nolen BM, Marks JR, Ta'san S, Rand A, Luong TM, Wang Y, et al. Serum biomarker profiles and response to neoadjuvant chemotherapy for locally advanced breast cancer. Breast Cancer Res. 2008;10(3):R45.
62. Oh K, Lee OY, Shon SY, Nam O, Ryu PM, Seo MW, et al. A mutual activation loop between breast cancer cells and myeloid-derived suppressor cells facilitates spontaneous metastasis through IL-6 trans-signaling in a murine model. Breast Cancer Res. 2013;15(5):R79.
63. Fisher DT, Appenheimer MM, Evans SS. The two faces of IL-6 in the tumor microenvironment. Semin Immunol. 2014;26(1):38–47.
64. Lederle W, Depner S, Schnur S, Obermueller E, Catone N, Just A, et al. IL-6 promotes malignant growth of skin SCCs by regulating a network of autocrine and paracrine cytokines. Int J Cancer. 2011;128(12):2803–14.
65. Gruys E, Toussaint MJM, Niewold TA, Koopmans SJ. Acute phase reaction and acute phase proteins. J Zhejiang Univ Sci B. 2005;6(11):1045–56.
66. Tilg H, Trehu E, Atkins MB, Dinarello CA, Mier JW. Interleukin-6 (IL-6) as an anti-inflammatory cytokine: induction of circulating IL-1 receptor antagonist and soluble tumor necrosis factor receptor p55. Blood. 1994;83(1):113–8.
67. Aderka D, Le JM, Vilcek J. IL-6 inhibits lipopolysaccharide induced tumor necrosis factor production in cultured human monocytes, U937 cells and in mice. J Immunol. 1989;143:3517–23.
68. Xing Z, Gauldie J, Cox G, Baumann H, Jordana M, Lei XF, et al. IL-6 is an antiinflammatory cytokine required for controlling local or systemic acute inflammatory responses. J Clin Invest. 1998;101(2):311–20.
69. Croker BA, Krebs DL, Zhang JG, Wormald S, Willson TA, Stanley EG, et al. SOCS3 negatively regulates IL-6 signaling in vivo. Nat Immunol. 2003;4:540–5.
70. Radtke S, Wüller S, Yang XP, Lippok BE, Mütze B, Mais C, et al. Cross-regulation of cytokine signalling: pro-inflammatory cytokines restrict IL-6 signalling through receptor internalisation and degradation. J Cell Sci. 2010;123(6):947–59.
71. Ahmed ST, Mayer A, Ji JD, Ivashkiv LB. Inhibition of IL-6 signaling by a p38-dependent pathway occurs in the absence of new protein synthesis. J Leukoc Biol. 2002;72:154–62.
72. McLoughlin RM, Jenkins BJ, Grail D, Williams AS, Fielding CA, Parker CR, et al. IL-6 trans-signaling via STAT3 directs T cell infiltration in acute inflammation. Proc Natl Acad Sci U S A. 2005;102(27):9589–94.
73. Curnow SJ, Scheel-Toellner D, Jenkinson W, Raza K, Durrani OM, Faint JM, et al. Inhibition of T cell apoptosis in the aqueous humor of patients with uveitis by IL-6/soluble IL-6 receptor trans-signaling. J Immunol. 2004;173(8):5290–7.
74. Atreya R, Mudter J, Finotto S, Müllberg J, Jostock T, Wirtz S, et al. Blockade of IL-6 transsignaling abrogates established experimental colitis in mice by suppression of the antiapoptotic resistance of lamina propria T cells. Nat Med. 2000;6(5):583–8.
75. Grivennikov S, Karin E, Terzic J, Mucida D, Yu G-Y, Vallabhapurapu S, et al. IL-6 and STAT3 signaling is required for survival of intestinal epithelial cells and colitis associated cancer. Cancer Cell. 2009;16:103–13.
76. Barkhausen T, Tschernig T, Rosenstiel P, van Griensven M, Vonberg RP, Dorsch M, et al. Selective blockade of interleukin-6 trans-signaling improves survival in a murine polymicrobial sepsis model. Crit Care Med. 2011;39(6):1407–13.
77. Grivennikov SI, Karin M. Inflammatory cytokines in cancer: tumour necrosis factor and interleukin 6 take the stage. Ann Rheum Dis. 2011;70 Suppl 1:i104–8.
78. Cozen W, Gill PS, Ingles SA, Masood R, Martinez-Maza O, Cockburn MG, et al. IL-6 levels and genotype are associated with risk of young adult Hodgkin lymphoma. Blood. 2004;103:3216–21.
79. Naugler WE, Sakurai T, Kim S, Maeda S, Kim K, Elsharkawy AM, et al. Gender disparity in liver cancer due to sex differences in MyD88-dependent IL-6 production. Science. 2007;317(5834):121–4.
80. Wei Q, Guo P, Mu K, Zhang Y, Zhao W, Huai W, et al. Estrogen suppresses hepatocellular carcinoma cells through ERβ-mediated upregulation of the NLRP3 inflammasome. Lab Investig. 2015;95(7):804–16.
81. Lin MT, Juan CY, Chang KJ, Chen WJ, Kuo ML. IL-6 inhibits apoptosis and retains oxidative DNA lesions in human gastric cancer AGS cells through up-regulation of anti-apoptotic gene mcl-1. Carcinogenesis. 2001;22(12):1947–53.
82. Jourdan M, Veyrune JL, Vos JD, Redal N, Couderc G, Klein B. A major role for Mcl-1 antiapoptotic protein in the IL-6-induced survival of human myeloma cells. Oncogene. 2003;22(19):2950–9.
83. Wegiel B, Bjartell A, Culig Z, Persson JL. Interleukin-6 activates PI3K/Akt pathway and regulates cyclin A1 to promote prostate cancer cell survival. Int J Cancer. 2008;122(7):1521–9.
84. Zou M, Zhang X, Xu C. IL6-induced metastasis modulators p-STAT3, MMP-2 and MMP-9 are targets of 3,3′-diindolylmethane in ovarian cancer cells. Cell Oncol (Dordr). 2015;39:47–57.
85. Mauer J, Denson JL, Brüning JC. Versatile functions for IL-6 in metabolism and cancer. Trends Immunol. 2015;36(2):92–101.
86. White JP, Puppa MJ, Gao S, Sato S, Welle SL, Carson JA. Muscle mTORC1 suppression by IL-6 during cancer cachexia: a role for AMPK. Am J Physiol Endocrinol Metab. 2013;304(10):E1042–52.
87. Hanahan D, Weinberg RA. Hallmarks of cancer: the next generation. Cell. 2011;144(5):646–74.
88. Herman JG. Hypermethylation of tumor suppressor genes in cancer. Semin Cancer Biol. 1999;9:359–67.
89. Hodge DR, Peng B, Cherry JC, Hurt EM, Fox SD, Kelley JA, et al. Interleukin 6 supports the maintenance of p53 tumor suppressor gene promoter methylation. Cancer Res. 2005;65(11):4673–82.
90. Liu CC, Lin JH, Hsu TW, Su K, Li AF, Hsu HS, et al. IL-6 enriched lung cancer stem-like cell population by inhibition of cell cycle regulators via DNMT1 upregulation. Int J Cancer. 2015;136(3):547–59.
91. Hodge DR, Cho E, Copeland TD, Guszczynski T, Yang E, Seth AK, et al. IL-6 enhances the nuclear translocation of DNA cytosine-5-methyltransferase 1 (DNMT1) via phosphorylation of the nuclear localization sequence by the AKT kinase. Cancer Genomics Proteomics. 2007;4(6):387–98.
92. Gasche JA, Hoffmann J, Boland CR, Goel A. Interleukin-6 promotes tumorigenesis by altering DNA methylation in oral cancer cells. Int J Cancer. 2011;129(5):1053–63.
93. Nevins JR. The Rb/E2F pathway and cancer. Hum Mol Genet. 2001;10(7):699–703.
94. Giacinti C, Giordano A. RB and cell cycle progression. Oncogene. 2006;25(38):5220–7.
95. Urashima M, Ogata A, Chauhan D, Vidriales MB, Teoh G, Hoshi Y, et al. Interleukin-6 promotes multiple myeloma cell growth via phosphorylation of retinoblastoma protein. Blood. 1996;88(6):2219–27.
96. Zhuang L, Lee CS, Scolyer RA, McCarthy SW, Zhang XD, Thompson JF, et al. Mcl-1, Bcl-XL and Stat3 expression are associated with progression of melanoma whereas Bcl-2, AP-2 and

MITF levels decrease during progression of melanoma. Mod Pathol. 2007;20(4):416–26.
97. Borhani N, Manoochehri M, Saleh-Gargari S, Ghaffari Novin M, Mansouri A, Omrani MD. Decreased expression of proapoptotic genes caspase-8- and BCL2-associated agonist of cell death (BAD) in ovarian cancer. Clin Ovarian Other Gynecol Cancer. 2014;7:8–23.
98. Isomoto H, Kobayashi S, Werneburg NW, Bronk SF, Guicciardi ME, Frank DA, et al. Interleukin 6 upregulates myeloid cell leukemia-1 expression through a STAT3 pathway in cholangiocarcinoma cells. Hepatology. 2005;42:1329–38.
99. Wei LH, Kuo ML, Chen CA, Chou CH, Cheng WF, Chang MC, et al. The anti-apoptotic role of interleukin-6 in human cervical cancer is mediated by up-regulation of Mcl-1 through a PI 3-K/Akt pathway. Oncogene. 2001;20(41):5799–809.
100. Jee SH, Chiu HC, Tsai TF, Tsai WL, Liao YH, Chu CY, et al. The phosphotidyl inositol 3-kinase/Akt signal pathway is involved in interleukin-6-mediated Mcl-1 upregulation and anti-apoptosis activity in basal cell carcinoma cells. J Investig Dermatol. 2002;119(5):1121–7.
101. Leu CM, Wong FH, Chang C, Huang SF, Hu CP. Interleukin-6 acts as an antiapoptotic factor in human esophageal carcinoma cells through the activation of both STAT3 and mitogen-activated protein kinase pathways. Oncogene. 2003;22(49):7809–18.
102. Garcia-Tuñón I, Ricote M, Ruiz A, Fraile B, Paniagua R, Royuela M. IL-6, its receptors and its relationship with bcl-2 and bax proteins in infiltrating and in situ human breast carcinoma. Histopathology. 2005;47(1):82–9.
103. Waxman AB, Kolliputi N. IL-6 protects against hyperoxia-induced mitochondrial damage via Bcl-2-induced Bak interactions with mitofusions. Am J Respir Cell Mol Biol. 2009;41(4):385–96.
104. Brooks C, Wei Q, Feng L, Dong G, Tao Y, Mei L, et al. Bak regulates mitochondrial morphology and pathology during apoptosis by interacting with mitofusins. Proc Natl Acad Sci U S A. 2007;104:11649–54.
105. Gritsko T, Williams A, Turkson J, Kaneko S, Bowman T, Huang M, et al. Persistent activation of stat3 signaling induces survivin gene expression and confers resistance to apoptosis in human breast cancer cells. Clin Cancer Res. 2006;12(1):11–9.
106. Johnson C, Han YY, Nathan H, McCarra J, Alpini G, Meng F. Interleukin-6 and its receptor, key players in hepatobiliary inflammation and cancer. Transl Gastrointest Cancer. 2012;1:58–70.
107. Chen M-F, Lin P-Y, Wu C-F, Chen W-C, Wu C-T. IL-6 expression regulates tumorigenicity and correlates with prognosis in bladder cancer. PLoS ONE. 2013;8(4):e61901.
108. Hsu JH, Shi Y, Frost P, Yan H, Hoang B, Sharma S, et al. Interleukin-6 activates phosphoinositol-3′ kinase in multiple myeloma tumor cells by signaling through RAS-dependent, and separately, through p85-dependent pathways. Oncogene. 2004;23(19):3368–75.
109. Hideshima T, Nakamura N, Chauhan D, Anderson KC. Biologic sequelae of interleukin-6 induced PI3-K/Akt signaling in multiple myeloma. Oncogene. 2001;20(42):5991–6000.
110. Borsellino N, Belldegrun A, Bonavida B. Endogenous interleukin 6 is a resistance factor for *cis*-diamminedichloroplatinum and etoposide-mediated cytotoxicity of human prostate carcinoma cell lines. Cancer Res. 1995;55:4633–9.
111. Suchi K, Fujiwara H, Okamura S, Okamura H, Umehara S, Todo M, et al. Overexpression of interleukin-6 suppresses cisplatin-induced cytotoxicity in esophageal squamous cell carcinoma cells. Anticancer Res. 2011;31(1):67–75.
112. Hirano T, Ishihara K, Hibi M. Roles of STAT3 in mediating the cell growth, differentiation and survival signals relayed through the IL-6 family of cytokine receptors. Oncogene. 2000;19:2548–56.
113. Niu G, Wright KL, Ma Y, Wright GM, Huang M, Irby R, et al. Role of Stat3 in regulating p53 expression and function. Mol Cell Biol. 2005;25(17):7432–40.
114. Patchen ML, MacVittie TJ, Williams JL, Schwartz GN, Souza LM. Administration of interleukin-6 stimulates multilineage hematopoiesis and accelerates recovery from radiation-induced hematopoietic depression. Blood. 1991;77(3):472–80.
115. Kim SY, Kang JW, Song X, Kim BK, Yoo YD, Kwon YT, et al. Role of the IL-6–JAK1–STAT3–Oct-4 pathway in the conversion of non-stem cancer cells into cancer stem-like cells. Cell Signal. 2013;25(4):961–9.
116. Gupta PB, Fillmore CM, Jiang G, Shapira SD, Tao K, Kuperwasser C, et al. Stochastic state transitions give rise to phenotypic equilibrium in populations of cancer cells. Cell. 2011;146(4):633–44.
117. Landskron G, De la Fuente M, Thuwajit P, Thuwajit C, Hermoso MA. Chronic inflammation and cytokines in the tumor microenvironment. J Immunol Res. 2014;2014:149185.
118. Colotta F, Allavena P, Sica A, Garlanda C, Mantovani A. Cancer-related inflammation, the seventh hallmark of cancer: links to genetic instability. Carcinogenesis. 2009;30(7):1073–81.
119. Schiechl G, Bauer B, Fuss I, Lang SA, Moser C, Ruemmele P, et al. Tumor development in murine ulcerative colitis depends on MyD88 signaling of colonic F4/80^{+}CD11b^{high}Gr1^{low} macrophages. J Clin Invest. 2011;121(5):1692–708.
120. Karin M. Nuclear factor-kappaB in cancer development and progression. Nature. 2006;441(7092):431–6.
121. Kesanakurti D, Chetty C, Maddirela DR, Gujrati M, Rao JS. Essential role of cooperative NF-kB and Stat3 recruitment to ICAM-1 intronic consensus elements in the regulation of radiation-induced invasion and migration in glioma. Oncogene. 2013;32(43):10.
122. Warburg O. On the origin of cancer cells. Science. 1956;123:309–14.
123. Bhatt AN, Chauhan A, Khanna S, Rai Y, Singh S, Soni R, et al. Transient elevation of glycolysis confers radio-resistance by facilitating DNA repair in cells. BMC Cancer. 2015;15:335.
124. Ando M, Uehara I, Kogure K, Asano Y, Nakajima W, Abe Y, et al. Interleukin 6 enhances glycolysis through expression of the glycolytic enzymes hexokinase 2 and 6-phosphofructo-2-kinase/fructose-2,6-bisphosphatase-3. J Nippon Med Sch. 2010;77(2):97–105.
125. Kawauchi K, Araki K, Tobiume K, Tanaka N. p53 regulates glucose metabolism through an IKK–NF-kappaB pathway and inhibits cell transformation. Nat Cell Biol. 2008;10:611–8.
126. Carey AL, Steinberg GR, Macaulay SL, Thomas WG, Holmes AG, Ramm G, et al. IL-6 increases insulin-stimulated glucose disposal in humans and glucose uptake and fatty acid oxidation in vitro via AMP activated protein kinase. Diabetes. 2006;55:2688–97.
127. Ghosh S, Ashcraft K. An IL-6 link between obesity and cancer. Front Biosci. 2013;5:461–78.
128. Sarkar PD, Gopinath A, Skaria LK. Association of serum interleukin-6 and glycolysis in sickle cell disease patients. Med J DPU. 2014;7(3):317–20.
129. Valencia T, Kim JY, Abu-Baker S, Moscat-Pardos J, Ahn CS, Reina-Campos M, et al. Metabolic reprogramming of stromal fibroblasts through p62-mTORC1 signaling promotes inflammation and tumorigenesis. Cancer Cell. 2014;26(1):121–35.
130. Mercurio F, Manning AM. NF-kappaB as a primary regulator of the stress response. Oncogene. 1999;18(45):6163–71.
131. Kratsovnik E, Bromberg Y, Sperling O, Zoref-Shani E. Oxidative stress activates transcription factor NF-kB-mediated protective

signaling in primary rat neuronal cultures. J Mol Neurosci. 2005;26(1):27–32.
132. Libermann TA, Baltimore D. Activation of interleukin-6 gene expression through the NF-kappa B transcription factor. Mol Cell Biol. 1990;10(5):2327–34.
133. Wang L, Walia B, Evans J, Gewirtz AT, Merlin D, Sitaraman SV. IL-6 induces NF-kappa B activation in the intestinal epithelia. J Immunol. 2003;171(6):3194–201.
134. Grivennikov S, Karin M. Dangerous liaisons: STAT3 and NF-kB collaboration and crosstalk in cancer. Cytokine Growth Factor Rev. 2010;21(1):11–9.
135. Brown CO, Salem K, Wagner BA, Bera S, Singh N, Tiwari A, et al. Interleukin-6 counteracts therapy-induced cellular oxidative stress in multiple myeloma by up-regulating manganese superoxide dismutase. Biochem J. 2012;444(3):515–27.
136. Reuter S, Gupta SC, Chaturvedi MM, Aggarwal BB. Oxidative stress, inflammation, and cancer: how are they linked? Free Radic Biol Med. 2010;49(11):1603–16.
137. Jia Y, Zhou F, Deng P, Fan Q, Li C, Liu Y, et al. Interleukin 6 protects H(2)O(2)-induced cardiomyocytes injury through upregulation of prohibitin via STAT3 phosphorylation. Cell Biochem Funct. 2012;30(5):426–31.
138. Craig R, Larkin A, Mingo AM, Thuerauf DJ, Andrews C, McDonough PM, et al. p38 MAPK and NF-kappa B collaborate to induce interleukin-6 gene expression and release. Evidence for a cytoprotective autocrine signaling pathway in a cardiac myocyte model system. J Biol Chem. 2000;275(31):23814–24.
139. Kalluri R, Weinberg RA. The basics of epithelial–mesenchymal transition. J Clin Invest. 2009;119(6):1420–8.
140. Ricciardi M, Zanotto M, Malpeli G, Bassi G, Perbellini O, Chilosi M, et al. Epithelial-to-mesenchymal transition (EMT) induced by inflammatory priming elicits mesenchymal stromal cell-like immune-modulatory properties in cancer cells. Br J Cancer. 2015;112(6):1067–75.
141. Tawara K, Oxford JT, Jorcyk CL. Clinical significance of interleukin (IL)-6 in cancer metastasis to bone: potential of anti-IL-6 therapies. Cancer Manag Res. 2011;3:177–89.
142. Helbig G, Christopherson 2nd KW, Bhat-Nakshatri P, Kumar S, Kishimoto H, Miller KD, et al. NF-kappaB promotes breast cancer cell migration and metastasis by inducing the expression of the chemokine receptor CXCR4. J Biol Chem. 2003;278(24):21631–8.
143. Sansone P, Storci G, Tavolari S, Guarnieri T, Giovannini C, Taffurelli M, et al. IL-6 triggers malignant features in mammospheres from human ductal breast carcinoma and normal mammary gland. J Clin Invest. 2007;117(12):3988–4002.
144. Hanahan D, Folkman J. Patterns and emerging mechanisms of the angiogenic switch during tumorigenesis. Cell. 1996;86(3):353–64.
145. Kujawski M, Kortylewski M, Lee H, Herrmann A, Kay H, Yu H. Stat3 mediates myeloid cell dependent tumor angiogenesis in mice. J Clin Invest. 2008;118(10):3367–77.
146. Houde C, Li Y, Song L, Barton K, Zhang Q, Godwin J, et al. Overexpression of the NOTCH ligand JAG2 in malignant plasma cells from multiple myeloma patients and cell lines. Blood. 2004;104(12):3697–704.
147. Yun UJ, Park SE, Jo YS, Kim J, Shin DY. DNA damage induces the IL-6/STAT3 signaling pathway, which has anti-senescence and growth-promoting functions in human tumors. Cancer Lett. 2012;323(2):155–60.
148. Rodier F, Coppé JP, Patil CK, Hoeijmakers WA, Muñoz DP, Raza SR, et al. Persistent DNA damage signalling triggers senescence-associated inflammatory cytokine secretion. Nat Cell Biol. 2009;11:973–9.
149. Gilbert LA, Hemann MT. DNA damage-mediated induction of a chemoresistant niche. Cell. 2010;143:355–66.
150. Wu ZH, Wong ET, Shi Y, Niu J, Chen Z, Miyamoto S, et al. ATM- and NEMO-dependent ELKS ubiquitination coordinates TAK1-mediated IKK activation in response to genotoxic stress. Mol Cell. 2010;40:75–86.
151. Tachibana S, Zhang X, Ito K, Ota Y, Cameron AM, Williams GM, et al. Interleukin-6 is required for cell cycle arrest and activation of DNA repair enzymes after partial hepatectomy in mice. Cell Biosci. 2014;4(1):6.
152. Chang L, Guo R, Huang Q, Yen Y. Chromosomal instability triggered by Rrm2b loss leads to IL-6 secretion and plasmacytic neoplasms. Cell Rep. 2013;3(5):1389–97.
153. Deorukhkar A, Krishnan S. Targeting inflammatory pathways for tumor radiosensitization. Biochem Pharmacol. 2010;80(12):1904–14.
154. Grivennikov SI, Greten FR, Karin M. Immunity, inflammation, and cancer. Cell. 2010;140(6):883–99.
155. Woods Ignatoski KM, Friedman J, Escara-Wilke J, Zhang X, Daignault S, Dunn RL, et al. Change in markers of bone metabolism with chemotherapy for advanced prostate cancer: interleukin-6 response is a potential early indicator of response to therapy. J Interferon Cytokine Res. 2008;29(2):105–12.
156. Conze D, Weiss L, Regen PS, Bhushan A, Weaver D, Johnson P, et al. Autocrine production of interleukin 6 causes multidrug resistance in breast cancer cells. Cancer Res. 2001;61:8851–8.
157. Patel SAA, Bhambra U, Charalambous MP, David RM, Edwards RJ, Lightfoot T, et al. Interleukin-6 mediated upregulation of CYP1B1 and CYP2E1 in colorectal cancer involves DNA methylation, miR27b and STAT3. Br J Cancer. 2014;111(12):2287–96.
158. Bochet L, Meulle A, Imbert S, Salles B, Valet P, Muller C. Cancer-associated adipocytes promotes breast tumor radioresistance. Biochem Biophys Res Commun. 2011;1:102–6.
159. Xu H, Lai W, Zhang Y, Liu L, Luo X, Zeng Y, et al. Tumor-associated macrophage-derived IL-6 and IL-8 enhance invasive activity of LoVo cells induced by PRL-3 in a KCNN4 channel-dependent manner. BMC Cancer. 2014;14:330.
160. Touboul C, Lis R, Al Farsi H, Raynoud CM, Warfa M, Althawadi H, et al. Mesenchymal stem cells enhances ovarian cancer cell infiltration through IL-6 secretion in an amniochorionic membrane based 3D model. J Transl Med. 2013;11:28.
161. Eicthen A, Su J, Adler A, Zhang L, Loffe E, Parveen AA, et al. Resistance to anti-VEGF therapy mediated by autocrine IL-6/STAT3 signaling and overcome by IL-6 blockade. Cancer Res. 2016;76:2327–39.
162. Korkaya H, Kim GI, Davis A, Malik F, Henry NL, Ithimakin S, et al. Activation of IL-6 inflammatory loop mediates transtuzumab resistance in HER2+ breast cancer by expanding the cancer stem cell population. Mol Cell. 2012;47(4):570–84.
163. Chen F, Zhuang X, Lin L, Yu P, Wang Y, Shi Y, et al. New horizons in tumor microenvironment biology: challenges and opportunities. BMC Med. 2015;13:45.
164. Kontzias A, Kotlyar A, Laurence A, Changelian P, O'Shea JJ. Jakinibs: a new class of kinase inhibitors in cancer and autoimmune disease. Curr Opin Pharmacol. 2012;12(4):464–70.
165. Karkera J, Steiner H, Li W, Skradski V, Moser PL, Riethdorf S, et al. The anti-interleukin-6 antibody siltuximab down-regulates genes implicated in tumorigenesis in prostate cancer patients from a phase I study. Prostate. 2011;71(13):1455–65.
166. Chen R, Chen B. Siltuximab (CNTO 328): a promising option for human malignancies. Drug Des Devel Ther. 2015;9:3455–8.
167. Chou CH, Wei LH, Kuo ML, Huang YJ, Lai KP, Chen CA, et al. Up-regulation of interleukin-6 in human ovarian cancer cell via a Gi/PI3K-Akt/NF-kappaB pathway by lysophosphatidic acid, an ovarian cancer-activating factor. Carcinogenesis. 2005;26(1):45–52.
168. Song L, Smith MA, Doshi P, Sasser K, Fulp W, Altiok S, et al. Antitumor efficacy of the anti-interleukin-6 (IL-6) antibody

siltuximab in mouse xenograft models of lung cancer. J Thorac Oncol. 2014;9(7):974–82.
169. Bagcchi S. Siltuximab in transplant-ineligible patients with myeloma. Lancet Oncol. 2014;15(8):e309.
170. Emilie D, Wijdenes J, Gisselbrecht C, Jarrousse B, Billaud E, Blay JY, et al. Administration of an anti-interleukin-6 monoclonal antibody to patients with acquired immunodeficiency syndrome and lymphoma: effect on lymphoma growth and on B clinical symptoms. Blood. 1994;84:2472–9.
171. Asbagh LA, Uzunoglu S, Cal C. Zoledronic acid effects interleukin-6 expression in hormone findependent prostate cancer cell lines. Int Braz J Urol. 2008;34(3):355–64.
172. Gnant M. Zoledronic acid in breast cancer: latest findings and interpretations. Ther Adv Med Oncol. 2011;3(6):293–301.
173. Kurebayashi J, Yamamoto S, Otsuki T, Sonoo H. Medroxyprogesterone acetate inhibits interleukin 6 secretion from KPL-4 human breast cancer cells both in vitro and in vivo: a possible mechanism of the anticachectic effect. Br J Cancer. 1999;79(3/4):631–6.
174. Shinriki S, Jono H, Ota K, Ueda M, Kudo M, Ota T, et al. Humanized anti-interleukin-6 receptor antibody suppresses tumor angiogenesis and in vivo growth of human oral squamous cell carcinoma. Clin Cancer Res. 2009;15(17):5426–34.
175. Ando K, Takahashi F, Kato M, Kaneko N, Doi T, Ohe Y, et al. Tocilizumab, a proposed therapy for the cachexia of interleukin6-expressing lung cancer. PLoS One. 2014;9(7):e102436.
176. Moreau P, Harousseau JL, Wijdenes J, Morineau N, Milpied N, Bataille R. A combination of anti-interleukin 6 murine monoclonal antibody with dexamethasone and high-dose melphalan induces high complete response rates in advanced multiple myeloma. Br J Haematol. 2000;109:661–4.
177. Tai YT, Anderson KC. Antibody-based therapies in multiple myeloma. Bone Marrow Res. 2011;2011:924058.
178. Isobe A, Sawada K, Kinose Y, Ohyagi-Hara C, Nakatsuka E, Makino H, et al. Interleukin 6 receptor is an independent prognostic factor and a potential therapeutic target of ovarian cancer. PLoS ONE. 2015;10(2):e0118080.
179. Jiang XP, Yang DC, Elliott RL, Head JF. Down-regulation of expression of interleukin-6 and its receptor results in growth inhibition of MCF-7 breast cancer cells. Anticancer Res. 2011;31:2899–906.
180. Sun Y, Moretti L, Giacalone NJ, Schleicher S, Speirs CK, Carbone DP, et al. Inhibition of JAK2 signaling by TG101209 enhances radiotherapy in lung cancer models. J Thorac Oncol. 2011;6(4):699–706.
181. Ramakrishnan V, Kimlinger T, Haug J, Timm M, Wellik L, Halling T, et al. TG101209, a novel JAK2 inhibitor, has significant in-vitro activity in multiple myeloma and displays preferential cytotoxicity for CD45+ myeloma cells. Am J Hematol. 2010;85(9):675–86.
182. Kobayashi A, Tanizaki Y, Kimura A, Ishida Y, Nosaka M, Toujima S, et al. AG490, a Jak2 inhibitor, suppressed the progression of murine ovarian cancer. Eur J Pharmacol. 2015;766:63–75.
183. Eghtedar A, Verstovsek S, Estrov Z, Burger J, Cortes J, Bivins C, et al. Phase II study of the JAK kinase inhibitor ruxolitinib in patients with refractory leukemias, including post myeloproliferative neoplasms (MPN) acute myeloid leukemia (AML). Blood. 2012;119(20):4614–8.
184. Seavey MM, Lu LD, Stump KL, Wallace NH, Hockeimer W, O'Kane TM, et al. Therapeutic efficacy of CEP-33779, a novel selective JAK2 inhibitor, in a mouse model of colitis-induced colorectal cancer. Mol Cancer Ther. 2012;11(4):984–93.
185. Hart S, Goh KC, Novotny-Diermayr V, Tan YC, Madan B, Amalini C, et al. Pacritinib (SB1518), a JAK2/FLT3 inhibitor for the treatment of acute myeloid leukemia. Blood Cancer J. 2011;1(11):e44.
186. Yang F, Brown C, Buettner R, Hedvat M, Starr R, Scuto A, et al. Sorafenib induces growth arrest and apoptosis of human glioblastoma cells through the dephosphorylation of signal transducers and activators of transcription 3. Mol Cancer Ther. 2010;9(4):953–62.
187. Duan Z, Bradner JE, Greenberg E, Levine R, Foster R, Mahoney J, et al. SD-1029 inhibits signal transducer and activator of transcription 3 nuclear translocation. Clin Cancer Res. 2006;12(22):6844–52.
188. Shi X, Franko B, Frantz C, Amin HM, Lai R, et al. JSI-124 (cucurbitacin I) inhibits Janus kinase-3/signal transducer and activator of transcription-3 signalling, downregulates nucleophosmin-anaplastic lymphoma kinase (ALK), and induces apoptosis in ALK-positive anaplastic large cell lymphoma cells. Br J Haematol. 2006;135(1):26–32.
189. Su Y, Li G, Zhang X, Gu J, Zhang C, Tian Z, et al. JSI-124 inhibits glioblastoma multiforme cell proliferation through G2/M cell cycle arrest and apoptosis augment. Cancer Biol Ther. 2008;7(8):1243–9.
190. Blaskovich MA, Sun J, Cantor A, Turkson J, Jove R, Sebti SM. Discovery of JSI-124 (cucurbitacin I), a selective Janus kinase/signal transducer and activator of transcription 3 signaling pathway inhibitor with potent antitumor activity against human and murine cancer cells in mice. Cancer Res. 2003;63(6):1270–9.
191. Gholam P. The role of sorafenib in hepatocellular carcinoma. Clin Adv Hematol Oncol. 2015;13(4):232–4.
192. Moreno-Aspitia A. Clinical overview of sorafenib in breast cancer. Future Oncol. 2010;6(5):655–63.
193. Jäger D, Ma JH, Mardiak J, Ye DW, Korbenfeld E, Zemanova M, et al. Sorafenib treatment of advanced renal cell carcinoma patients in daily practice: the large international PREDICT Study. Clin Genitourin Cancer. 2015;13(2):156–64.e1.
194. Moreira RB, Peixoto RD, de Sousa Cruz MR. Clinical response to sorafenib in a patient with metastatic colorectal cancer and FLT3 amplification. Case Rep Oncol. 2015;8(1):83–7.
195. Tanaka T, Narazaki M, Kishimoto T. Anti-interleukin-6 receptor antibody, tocilizumab, for the treatment of autoimmune diseases. FEBS Lett. 2011;585(23):3699–709.
196. Trikha M, Corringham R, Klein B, Rossi J-F. Targeted anti-interleukin-6 monoclonal antibody therapy for cancer: a review of the rationale and clinical evidence. Clin Cancer Res. 2003;9(13):4653–65.
197. Coward J, Kulbe H, Chakravarty P, Leader D, Vassileva V, Leinster DA, et al. Interleukin-6 as a therapeutic target in human ovarian cancer. Clin Cancer Res. 2011;17(18):6083–96.
198. Guan M, Zhou YP, Sun JL, Chen SC. Adverse events of monoclonal antibodies used for cancer therapy. Biomed Res Int. 2015;2015:428169.
199. Chen MF, Hsieh CC, Chen WC, Lai CH. Role of interleukin-6 in the radiation response of liver tumors. Int J Radiat Oncol Biol Phys. 2012;84(5):e621–30.
200. Judd LM, Menheniott TR, Ling H, Jackson CB, Howlett M, Kalantzis A, et al. Inhibition of the JAK2/STAT3 pathway reduces gastric cancer growth in vitro and in vivo. PLoS One. 2014;9(5):e95993.
201. Huang C, Yang G, Jiang T, Huang K, Cao J, Qiu Z. Effects of IL-6 and AG490 on regulation of Stat3 signaling pathway and invasion of human pancreatic cancer cells in vitro. J Exp Clin Cancer Res. 2010;29(1):51.
202. Xiong A, Yang Z, Shen Y, Zhou J, Shen Q. Transcription factor STAT3 as a novel molecular target for cancer prevention. Cancers. 2014;6(2):926–57.
203. Ishdorj G, Johnston JB, Gibson SB. Inhibition of constitutive activation of STAT3 by curcurbitacin-I (JSI-124) sensitized human B-leukemia cells to apoptosis. Mol Cancer Ther. 2010;9(12):3302–14.
204. Schust J, Sperl B, Hollis A, Mayer TU, Berg T. Stattic: a small-molecule inhibitor of STAT3 activation and dimerization. Chem Biol. 2006;13(11):1235–42.

205. Yu X, He L, Cao P, Yu Q. Eriocalyxin B inhibits STAT3 signaling by covalently targeting STAT3 and blocking phosphorylation and activation of STAT3. PLoS ONE. 2015;10(5):e0128406.
206. Jing N, Li Y, Xiong W, Sha W, Jing L, Tweardy DJ. G-quartet oligonucleotides: a new class of signal transducer and activator of transcription 3 inhibitors that suppresses growth of prostate and breast tumors through induction of apoptosis. Cancer Res. 2004;64(18):6603–9.
207. Jing N, Zhu Q, Yuan P, Li Y, Mao L, Tweardy DJ. Targeting signal transducer and activator of transcription 3 with G-quartet oligonucleotides: a potential novel therapy for head and neck cancer. Mol Cancer Ther. 2006;5(2):279–86.
208. Yue P, Turkson J. Targeting STAT3 in cancer: how successful are we? Expert Opin Investig Drugs. 2009;18(1):45–56.
209. Chen CL, Loy A, Cen L, Chan C, Hsieh FC, Cheng G, et al. Signal transducer and activator of transcription 3 is involved in cell growth and survival of human rhabdomyosarcoma and osteosarcoma cells. BMC Cancer. 2007;7:111.
210. Song H, Wang R, Wang S, Lin J. A low-molecular-weight compound discovered through virtual database screening inhibits Stat3 function in breast cancer cells. Proc Natl Acad Sci U S A. 2005;102(13):4700–5.
211. Weidler M, Rether J, Anke T, Erkel G. Inhibition of interleukin-6 signaling by galiellalactone. FEBS Lett. 2000;484(1):1–6.

Rural Empowerment in India through Small scale Power generation using Vegetable oil based Fuels

Rajiv Chaudhary*, P B Sharma, S. Maji, Naveen Kumar & R C Singh
Department of Mechanical Engineering, Delhi Technological University, Delhi
*Email ID: rch_dce@rediffmail.com

Abstract. Every Energy options would be a matter of great interest for Electrical power generation too. Also there are several related issues of the fuels used for power generation. The high energy demand, and the derived problems of the widespread use of fossil fuels make increasingly necessary the development of renewable energy sources. The diesel engine dominates in the field of technology because they can be easily operated and are more fuel efficient. In recent years systematic efforts have been undertaken by many researchers to determine the suitability of vegetable oil, animal oil fats and their derivatives as fuel or additives to diesel. The Government of India also has approved the National Policy on Biofuels on December 24, 2009, encouraging use of renewable energy resources as alternative fuels. 2017.

Under the observation, two oilseeds Jatropha and Karanja have been found very suitable to Indian conditions, which can be used as straight vegetable oil and for producing Biodiesel. The biodiesel as a substitute to diesel can be used in automobiles also. There is a large junk of degraded forest land unutilized public land fallow lands of farmers and lands in the rural areas. So by planning a widespread plantation of these oilseeds of Jatropha and Karanja under the National Policy on Biofuels, great achievements can be made through establishing smaller power plants run by vegetable oil based fuels at rural level, which will bring energy independence, employment generation, prosperity, rural development as well as overall economic growth to the country.

I-INTRODUCTION

Energy is essential for the development of the human society. Energy is a basic necessity for socio-economic upliftment that leads to sustainable development. The goal of energy depends upon: Availability, Accessibility and Acceptability (3A strategy) for both developed and under-developed countries. During the last decade, India has maintained a high growth rate in accepting the improved technological challenges in the global scenario, and ranked sixth in the world in terms of energy demand, accounting for 3.5% of the world commercial energy demand in 2001. This high energy demand, and the derived problems of the widespread use of fossil fuels make increasingly necessary the development of renewable energy sources.

Electricity has emerged as the most popular form of energy. Apart from the various conventional sources of energy, in producing electricity, renewable energy sources are also suitable for off-grid electricity supply and has been successfully introduced in countless cases in developing countries. Several research institutions and international agencies rate biomass as one of the cheapest available renewable energy sources for power generation. Furthermore, the conversion of biomass into electricity is a low-carbon process as the resulting CO2 can be captured by plant regrowth. Although the application of biomass as a sustainable electricity source seems promising, it is still seldom perceived as an option for providing electricity and prosperity to the rural people of India, and ultimately the growth and development of our country.

To generate electricity, from various such sources of biomass which can be either through combustion, gasification, biological digestion, fermentation or ultimately converting it into liquid fuels propelling a generator. The diesel engine dominates in the field of technology because they can be easily operated and are more fuel efficient. The consumption of diesel is much higher than that of petrol.

In contrast to solar PV or wind power, biomass power technology can generate electricity on demand at any time, as long as a sufficient supply of biomass stocks is assured. Many agricultural and forest product residues can provide feedstock for energy conversion without increasing land requirements. Local farmers can generate additional

income by providing biomass fuels to small local power plants.

In recent years systematic efforts have been undertaken by many researchers to determine the suitability of vegetable oil, animal oil fats and their derivatives as fuel or additives to diesel. The Government of India (GOI) also has approved the National Policy on Biofuels on December 24, 2009. The biofuel policy encourages use of renewable energy resources as alternative fuels to supplement transport fuel (gasoline and diesel for vehicles) and proposes a target of 20 percent biofuel blending (bio-diesel and bio-ethanol) by 2017.

As raw materials for these biofuels there are many tree species, bearing seeds available in India, which are rich in non-edible vegetable oil, like from Jatropha and Karanja seeds. But surprisingly these are not being used as per their potential. Therefore in India the feasibility of producing and using vegetable oils and their derivatives as biodiesel, as a diesel substitute can be considered alongwith the unutilization of the available potential of non-edible oil sources. There is a large junk of degraded forest land, unutilized public land, fallow lands of farmers and lands in the rural areas, which can be utilized for this purpose, ensuring overall economic growth of the country.

II-FEEDSTOCKS OF VEGETABLE BASED OILS FOR INDIA

The countries like USA and EU, can afford using edible oil as the feedstock for biodiesel production, because of it's overproduction. But, it would be not acceptable to India due to scarcity of edible oils. In this context, it is relevant to use other multi feedstocks (Vegetable oils or animal fats) available in India and assess their suitability for biodiesel production. Several Non-edible oils, such as Jatropha Curcas, Pongamia Pinnata ('Honge' or 'Karanja') are suitable for biodiesel production in Indian conditions. However, the potential availability of these oils is not very attractive and efforts are underway for large scale cultivation of these species all over India. It is also relevant to mention that 80-85% of the cost of the biodiesel is attributed to the cost of the feedstock.

The much required green energy revolution would provide India an opportunity o change it's standing from a fuel importing nation to one that generates clean affordable energy. Among various alternatives to diesel . Planning Commission of India has identified Jatropha, a non-edible oil bearing tree capable of producing oil that is easily convertible in to biodiesel with properties almost to diesel [1].

Jatropha curcas plant is a drought-resistant, perennial, plant living upto 50 years and has the capability to grow on marginal soils. It requires very little irrigation and grows in all types of soils, thus making Jatropha a more sustainable choice than other vegetable oils [2,3,4,5]. Jatropha and Karanja Biodiesel can be used for small scale power generation at rural level and as a replacement for diesel fuel in irrigation pumping sets, diesel operated power generating sets and other equipments. Thus Jatropha and Karanja can be seen as a phenomenon, having economic, social, environmental as well as political dimensions.

Self-sustainable energy sources are likely to hold the key to economic development of India in future. India should not look towards a certain group of countries to meet its ever growing needs, but it is mandatory to seriously implement bioenergy development programs as a part of environmental sustainability in the form of clean development mechanism CDM [6].

III – GOVERNMENT INITIATIVES : NATIONAL POLICY ON BIO-FUELS

With the general scenario of renewable energy resources for developing countries, we can now attempt to estimate some economics of the more important renewable energies, with special reference to the global situation, as well as that in the Third-World countries. Reliable data is not available in most of the cases, and its projections even to the year 2020 A.D. are brought with numerous uncertainties. Nevertheless, it is not difficult to see that at least four types of Renewable Energies, namely hydro-electricity, biomass, wind and direct solar energy, deserve immediate attention. From 1980 onwards, there are several sources of techno-economic data on renewable energy, possessing a fair degree of reliability, which are:

1. Renewable Energy Conference at Rio de Janeiro in 1992.
2. World Renewable Energy Conference VI, 2000
3. Kyoto Protocol, 2001
4. World Summit on Sustainable Development (WSSD), Johannesburg 2002.
5. World Energy Assessment - 2001 UNDP.

Bio-fuels provide a strategic advantage to promote sustainable development and to supplement conventional energy sources in meeting the rapidly increasing requirements for transportation fuels associated with high economic growth, as well as in meeting the energy needs of India's vast rural population. Bio-fuels can increasingly satisfy these

energy needs in an environmentally benign and cost-effective manner while reducing dependence on import of fossil fuels and thereby providing a higher degree of National Energy Security. The Indian approach to bio-fuels is based solely on non-food feedstocks to be raised on degraded or wastelands that are not suited to agriculture, thus avoiding a possible conflict of fuel vs. food security.

With this viewpoint the National Policy on Bio-fuels and its implementation has been approved by the Union Cabinet on December 24, 2009. The Policy endeavors to facilitate and bring about optimal development and utilization of indigenous biomass feed stocks for production of bio-fuels. [7].

The salient features of the National Policy on Bio-fuels are:-

1–Bio-diesel production will be taken up from non-edible oil seeds in waste/degraded/marginal lands.

2–An indicative target of 20% blending of bio-fuels, both for bio-diesel and bio-ethanol, by 2017 has been proposed.

3–Minimum Support Price (MSP) for non-edible oil seeds would be announced with periodic revision to provide fair price to the growers.

4 – Minimum Purchase Price (MPP) for purchase of bio-ethanol and bio-diesel would be announced with periodic revision.

5 – Major thrust will be given to research, development and demonstration with focus on plantations, processing and production of bio-fuels, including Second Generation Bio-fuels.

6 – Financial incentives, including subsidies and grants, may be considered for second generation bio-fuels. If it becomes necessary, a National Bio-fuel Fund could be considered.

7 – A National Biofuel Coordination Committee, headed by the Prime Minister, will be set up to provide policy guidance and coordination.

8 – A Biofuel Steering Committee, chaired by Cabinet Secretary, will be set up to oversee implementation of the Policy.

The Ministry of New & Renewable Energy has been designated as the co-ordinating Ministry for biofuel development and utilization while specific roles have been assigned to other concerned Ministries. MNRE has taken several initiatives on various aspects of biofuel development. An exercise has been initiated with scientific agencies – ICAR, CSIR, DBT, DRDO, NOVOD Board on collection, screening and identification of elite germplasms of jatropha and on processing and end use technologies. The objective is to generate and make available elite planting materials for plantations. The scientific agencies and the private sector have identified 25 superior genotypes/accessions of jatropha for further multiplication for demonstration at various sites in potential States. Another exercise has been taken up on realistic costing of biodiesel which will provide guidance on review and revision of the purchase price for biodiesel. A survey has been undertaken to assess the status of Jatropha plantations in nine States. Major thrust is being given to development of second generation biofuels. An Indo-US MoU has been signed on biofuels with focus on joint R&D, particularly on second generation biofuels such as, cellulosic ethanol and algal biodiesel. Another initiative with research institutes and industry is on for development of high efficiency engines for use of SVO for stationary applications.

IV-GLOBAL EXPERIENCE OF BIODIESEL

Biodiesel production rapidly expanded from about 5 million gallons in 2001 to 250 million gallons in 2006[8] Even though high oil prices have lately tended to reduce biodiesel production, several forces may contribute to long-term expansion in the biodiesel industry.

High petroleum prices are raising diesel prices and the likely increasing costs of future oil production. [9]. Government mandates, such as the provisions of the Energy Independence and Security Act of 2007, that includes mandates of up to 36 million gallons of biofuels [10]. The public and government's concern over global warming may provide a value for biodiesels CO2 recycling characteristics. The U.S. government has discussed the use of GHG emission price in a cap and trade system, such as in the Lieberman-Warner Climate Security Act of 2008 [11]

Biomass resources are very abundant in China, with great energy potential. Energy utilization from biomass is an important way to national economic sustainable development on renewable energy, as we as reducing population to environment. Due to gradual depletion, of the world petroleum reserve, rising petroleum reserve rising petroleum prices, increasing threat to the environment from exhaust emission and global warming have generated an intense international interest in developing alternative, non-petroleum fuels for long or partial replacement. Availability relates to reliable source available and it's security. Accessibility means providing clean-energy at affordable prices for all people. Acceptability of an energy-source relates to public attitude, social and cultural circumstances.

Keeping in view the 3A principle, the policy of renewable-energy may be designed for each country to satisfy the basic needs of their people and to achieve the target growth-rate in their economies. The overall aim should be to provide sustainable

modern energy for all the segments of population, at the latest by 2020 (goal set by WEC) or 2030, with special focus on the developing world (targeting 2 billion poor people currently without light). The energy-policy would naturally vary from country to country, but general guidelines needs to be drawn.

V-TECHNICAL ASPECTS OF THE BIO OIL (VEGETABLE OIL / BIODIESEL)

V.I Vegetable Oil

Vegetable oil can be used to fuel diesel engines as straight vegetable oil (SVO) or by converting it to Biodiesel. The more advanced the engine technology, the more complicated or limited the use of SVO. Hence for use in modern cars with direct injection engines the conversion of SVO to biodiesel is mandatory. However SVO can be directly used as fuel for most simple stationary diesel engines used in generator sets or pump stations. Special SVO engines are also available.

For robust stationary (non-vehicle) engines, the use of pure SVO is the most attractive option. This way the additional and somewhat dangerous biodiesel conversion process (due to some highly inflammable components) can be avoided; furthermore the energy yield per gallon of vegetable oil is higher when using SVO directly. This paper will in general focus on the direct use of SVOs only.

V.II Benefits of Vegetable oil.

Listed below are the potential benefits of SVOs as fuel for power generation in rural areas: [12]

-SVOs are a renewable energy source low in greenhouse gas (GHG) emissions.
-Local production is possible and can contribute to value generation in rural areas.
-SVOs are liquid, hardly evaporate and are thus easily handled, stored and transported.
-SVOs are neither flammable nor explosive and do not release toxic gases.
-SVOs can be burnt in a relatively clean manner.
-SVOs do not cause major damage if accidentally spilt.

Almost all vegetable oils have a calorific value that is very similar to that of diesel fuel. However vegetable oil differs from diesel considerably with regard to viscosity, which is 10 - 20 times higher for SVOs. Furthermore, the solidification points of SVOs can be rather high. Coconut oil for example solidifies at temperatures below 22°C. This can cause major problems particularly in cold regions.

Oil characteristics can differ considerably between different types of SVOs as their composition of fatty acids varies. This can lead to plugging and gumming of lines, filters and injectors, as well as cause deposits inside the motor or excessive engine wear.

There is long-term experience particularly with rapeseed oil, which has been used in Germany and other countries as fuel for cars, trucks and tractor engines for several years. There is no doubt that rapeseed oil is relatively easy and reliable to use in diesel engines.

Other oils like palm oil, sunflower, soybean, coconut, jatropha and cotton oil have also been used to fuel motors. Many examples are regularly presented at conferences and can be found in publications. However there does not yet seem to be much large-scale and long-term practical experience regarding the proper and economic long-term functioning of such plant oil motor-generator systems.

For economic long-term use all machines need clean homogenous oil with specific characteristics. Elsbett, a German company that specialises in the construction of motors for plant oil fuel states, 'Standardising of the fuel is a must.' (Elsbett, 2003)

Some engines are specially designed to operate with vegetable oils. Elsbett produces vegetable oil engines and provides sets for the conversion of tractor or truck engines to be fuelled by SVOs. Small (< 20 kW) Lister type diesel engines produced in England or India are also appropriate for SVOs as fuel; they are very common worldwide.

A how-to guide for small stationary engines' published by the world bank (2009) gives a good overview of the technical details for quality SVO production and the necessary properties for engine modifications.

There are several companies offering small generator sets especially for SVO use.

V.III Biodiesel

Based on some differences in the properties of Diesel and Biodiesel, it can be said that Biodiesel is not a perfect substitute for diesel fuel. However, Diesel fuel can be taken as the base fuel, and comparison of various properties have been made by different researchers.

hence this section examines the compatibility between these fuels using #2 diesel as the basis. This discussion of fuel properties is based on using methanol as an input, because methanol is the cheapest alcohol and the most widely researched. The fuel properties change if other alcohols are used [13,14,15,16]

The most important property of diesel fuel is the cetane number. Diesel engines do not have spark plugs. The engine's piston compresses the fuel and air mixture until heat and pressure ignite the mixture.

This ignition point is identified by the cetane number. Cetane numbers for several fuels are listed in Table 1. Conventional diesel fuel generally has cetane numbers ranging between 40 and 50, with higher quality diesel fuels having higher cetane numbers [7,26]. Biodiesel made from unsaturated oils like soybean oil has comparable cetane numbers to conventional diesel while biodiesel made from saturated oils like tallow have higher cetane numbers [17,13].

Table 1. Biodiesel and diesel fuel properties

Characteristics	Units	Diesel Fuel #2	Soybean Oil Biodiesel	Tallow Biodiesel
Cetane Number	100%	40 to 52	45 to 56.9	58.8 to 70
Flash Point	^{0}C	60 to 72	131	117
Cloud Point	^{0}C	-15 to 5	-3 to 3	12 to 16
Pour Point	^{0}C	-35 to 15	-7 to 19	6 to 13
Higher Heating Value	BTU / Gal.	138,700	130,995	129,022
Lower Heating Value	BTU / Gal.	128,700	120,201	-

Sources: Barnwal and Sharma [19]. Davis and Diegel [20]; Graboski and McCormick [21] ; Shay [22]

Biodiesel has three benefits when compared to #2 diesel. First, biodiesel can be blended with diesel fuel up to 100%. Second, biodiesel has a higher flash point. The flash point is the minimum temperature the fuel must be heated to ignite the vapor and air mixture. The U.S. Department of Transportation defines a nonhazardous fuel as one with a flash point higher than 90 0C [17,13,21,23].

As shown in Table 1, #2 diesel is considered hazardous while soydiesel and tallow diesel are not. Finally, pure biodiesel has better lubrication properties than #2 diesel. Biodiesel helps to lubricate the fuel pump and fuel injectors, which could extend engine life [17,13,21]. The lubrication properties may become more important because the EPA mandated a reduction in the sulfur content of diesel fuel in 2007. Sulfur acts as a lubricant, but contributes to SOX emissions.

Biodiesel has unfavorable cold fuel properties as measured by the cloud and pour points. Cloud point is the temperature that causes the fuel to form wax on the fuel filter, thus clogging it, whereas pour point is the temperature the fuel turns into a gel, impeding fuel flow. The cloud point and pour point for soy
biodiesel (Table 1) are approximately 0°C and -5°C, while tallow biodiesel has much higher cloud and pour points. Number 2 diesel can have a cloud point as low -15° C and a pour point as low as -35°C. Thus, biodiesel may not be usable during winter where temperatures dip below freezing, preventing large-scale market penetration [17,21]. Biodiesel contains lower energy than diesel. The lower energy content of biodiesel reduces torque, acceleration, and miles per gallon rating of the vehicle [7,8,24].

Researchers use two measures of energy content. The higher heating value (HHV) is the combustion energy plus the energy to vaporize water, while the lower heating value (LHV) only includes the combustion energy [13,25]. Researchers use LHV, because vaporized water does not contribute to an engine's power. Thus, biodiesel contains approximately 93.40% the energy as diesel fuel when measure in gallons and using the LHV. Biodiesel has more potential problems such as oxidation [3,17,21,14], microbial growth from dissolved water [13,21,22], deposit accumulation in tanks [17,21] , and degradation of engine gaskets and seals [21,24,22].

VI- CONCLUSION

As per the current practice most of the world's electricity generation is based on fossil fuels such as coal, natural gas and petroleum fuel oil, which is the most cost effective way of producing electricity at least for now. In the U.S., fossil fuels account for about 70% of the fuels used for electricity generation, while biofuel only accounts for about 1%. There are many reasons why biofuel is not economically competitive with conventional fossil fuel-based energy. Biofuels are bulky often with high water content. Fuel quality may not be predictable. Physical handling of the material can be challenging. Hauling can be expensive. These characteristics drive up the cost of biofuel energy, as additional land, labor and equipment is required for feedstock planting, harvesting, transport, storage and processing compared to conventional fuels. Moreover, biofuel-fired power plants are relatively small in size and capacity, thus they tend to have a high fixed capital cost to generated electricity ratio.

On the other hand, the electric power sector, based on fossil fuel, is a major source of CO2 emissions which contribute to global climate change. A substantial amount of CO2 emissions could be reduced if the electric sector uses biofuels rather than fossil fuels to generate electricity. However, electricity producers do not have incentives to switch from fossil fuels to biofuels simply because biofuels are not cost competitive, as mentioned above.

Growing experience with vegetable oil technologies in India suggests that technology push policies need to be substituted or augmented by market pull policies. The Govt also has framed policies in this regard. So, many scientists, politicians, and the public believe biodiesel is the cure for a dependence on petroleum fuels. Various properties of vegetable oil based fuels are quite comparable to diesel and it can be used in diesel engine without any trouble. The cold fuel properties of biodiesel have to improve for large-scale penetration of biodiesel, by making it usable in winter conditions.

So if the vegetable oil based fuels are used in electricity generation, it will be very suitable; technically, economically, socially as well as politically. Looking into it's multifaceted prospects, the Government is also promoting it's use, as it has potential to lead the country new heights of economic growth.

REFERENCES.

[1]-Planning Commission of India, Report of the Committee on Development of Biofuel, 2003.

[2] B. Reubens et al., W.J.Maes et al., Journal of Arid Environments, 2011, 75,2,201-05.

[3]-NOVOD, 2007, www./http://www.novodboard.com/Jartopha-english.pdf. [4]-NOVOD,2008 , www./http://www.novodboard.com/3rd%20R&D-Report.pdf.

[5]-[T. Altenburg et al., H. Dietz et al., M. Hahl et al., N. Nikolidakis et al., German Development Institute, Bonn, 2009]

[6] S. Kumar, A. Chaube, S K Jain, Journal of Environmental Research and Development, 2010, 4,3,877-84

[7]-The Policy at the Ministry's Website www.mnre.gov.in.

[8]-National Biodiesel Board. March 17, 2006. Estimated US Biodiesel Production by Fiscal Year. http://www.biodiesel.org/pdf_files/fuelfactsheets/Production_graph_slide. pdf

[9] - Hotelling, Harold. April 1931. "The Economics of Exhaustible Resources." The Journal of Political Economy 39(2):137-75. The prices in the long run and tend to increase over time, as petroleum is depleted.

[10] - U.S. Government Printing Office. 2007. Energy Independence and Security Act of 2007. Washington, DC: http://purl.access.gpo.gov/GPO/LPS94451.

[11] The Library of Congress. 2008. Lieberman-Warner Climate Security Act of 2008 (S 3036). Washington, DC: http://thomas.loc.gov/cgi-bin/query/D?c110:4:./temp/~c1106UdsR6.

[12] [Elmar Dimpl, 'Small-scale Electricity Generation from Biomass : Experience with Small-scale Technologies for Basic Energy Supply Part III: Vegetable Oil'. Ist edition, GIZ-HERA, January 2011]

[13]-Gerpen, J. Van, B. Shanks, R. Pruszko, D. Clements, and G. Knothe. July 2004. Biodiesel Analytical Methods: August 2002-January 2004. Golden, CO: National Renewable Energy Laboratory, NREL/SR-510-36240.

[14] Sheehan, John, Vince Camobreco, James Duffield, Michael Graboski, and Housein Shapouri. May 1998. An Overview of Biodiesel and Petroleum Diesel Life Cycles. Golden, CO: National Renewable Energy Laboratory, Report NREL/TP- 580-24772.

[15] Zhang, Y., M.A. Dube, D.D. McLean, and M. Kates. August 2003. "Biodiesel Production from waste Cooking Oil: 1. Process Design and Technological Assessment." Bioresource Technology 89(1):1-16.

[16] Encinar, J.M., J.F. Gonzalez, J.J. Rodriguez, and A. Tejedor. March 2002. "Biodiesel Fuels from Vegetable Oils: Transesterification of Cynara Cardunculus L. Oils with Ethanol." Energy & Fuels 16(2):443-50.

[17]-Duffield, James, Hosein Shapouri, Michael Graboski, Robert McCormick, and Richard Wilson. September 1998. U.S. Biodiesel development: New markets for conventional and geneticallymodified agricultural products. Washington, DC: U.S. Department of Agriculture, Economic Research Service, Agriculture Economic Report 770.

[18]-Leffler, William L. 1985. Petroleum Refining for the Non-Technical Person. Tulsa, OK: PennWell Publishing Company, pp.104-106.

[19] Barnwal, B.K. and M. P. Sharma. August 2005. "Prospects of Biodiesel Production from Vegetable Oils in India." Renewable and Sustainable Energy Reviews 9(4):363-78.

[20] Davis, Stacy C. and Susan W. Diegel. 2006. Transportation Energy Data Book: Edition 25, Oakridge, TN: Center for Transportation Analysis, Oak Ridge National Laboratory, Report;

[21] Graboski, Michael S. and Robert L. McCormick. 1998. "Combustion of Fat and

Vegetable Oil Derived Fuels in Diesel Engines." Prog. Energy Combustion Science 24:125-64.
[22] Shay, E. Griffin. 1993. "Diesel Fuel from Vegetable Oils: Status and Opportunities." Biomass and Bioenergy 4(4):227-42.
[23] Srivastava, Anjana and Ram Prasad. 2000. "Triglycerides-Based Diesel Fuels." Renewable and Sustainable Energy Reviews 4:111-33.
[24] Tyson, K. Shaine, Joseph Bozell, Robert Wallace, Eugene Peterson, and Luc Moens. June 2004. Biomass Oil Analysis: Research Needs and Recommendations. Golden, CO: National Renewacble Energy Laboratory, Report NREL/TP-510-34796.
[25] Hammerschlag, Roel. 2006. "Ethanol's Energy Return on Investment: A Survey of the Literature, 1990-Present." Environmental Science & Technology 40(6):1744-50.
[26] Leffler, William L. 1985. Petroleum Refining for the Non-Technical Person. Tulsa, OK: PennWell Publishing Company, pp.104-106.

J Mater Sci: Mater Electron
DOI 10.1007/s10854-016-5060-x

Structural, dielectric and ferroelectric studies of $Ba_{1-x}Sr_xTiO_3$ ceramics prepared by mechanochemical activation technique

Aditya Jain[1] · A. K. Panwar[1] · A. K. Jha[2]

Received: 1 April 2016 / Accepted: 22 May 2016
© Springer Science+Business Media New York 2016

Abstract In the present study, specimens of composition $Ba_{1-x}Sr_xTiO_3$ (x = 0.0, 0.05, 0.075, 0.10 & 0.15) were synthesized using mechanochemical activation technique and their structural, dielectric and ferroelectric characteristics were investigated for the major applications such as a multi-layered ceramic capacitor (MLCC) and microwave tunable devices. Structural analysis using X-ray diffraction pattern of the systems by Rietveld refinement confirms the formation of tetragonal phase with *P4 mm* space group. The intensity ratio of bonds and wave number shift in Raman spectra suggests little structural changes with strontium content. Microstructural investigation reveals that there is no appreciable change in grain size with increasing strontium concentration. The results on the variation of dielectric constant with temperature suggest the shifting of Curie temperature to lower temperature side with increasing strontium concentration. Current–voltage characteristics reveal that with increasing strontium content current increases which can be correlated with the observed variation of activation energy of the studied samples, which also decreases with the increasing concentration of strontium.

✉ A. K. Jha
prof.akjha@gmail.com

[1] Department of Applied Physics, Delhi Technological University (Formerly Delhi College of Engineering), Bawana Road, New Delhi 110042, India

[2] Department of Applied Science, A.I.A.C.T.R, New Delhi 110042, India

1 Introduction

Barium titanate is known to be one of the most potentially useful ferroelectric material of perovskite family. The electrical, microstructural and optical properties of $BaTiO_3$ can be tailored by substituting the A-site and B-site atoms, which results in diverse applications in electro-optical systems, electromechanical systems, piezoelectric transducers, pyroelectric sensors, ceramic industry, etc. Many commercial applications like pyroelectric sensors require the ferroelectric Curie temperature of $BaTiO_3$ based materials to be close to room temperature, which can be achieved by substituting various transition metals and rare earths on A-site and B-site depending on the solubility [1, 2]. Barium strontium titanate is one of the promising material for tunable microwave devices and dynamic random access memory applications [3, 4]. It has been observed that materials which have high dielectric constant also possess high dielectric loss and high dielectric constant with high loss in a material can cause substantial impedance mismatch problems. So to overcome these issues it is necessary to lower both dielectric constant and dielectric loss, which can be achieved to a certain extent by substituting Ba site in $BaTiO_3$ by Sr. The solid solution range in any material depends mainly on three factors: ionic radii, charge neutrality and tolerance factor (which should be close to unity) [5].

In the present study, Sr-substituted barium titanate ceramics of the compositional formula $Ba_{1-x}Sr_xTiO_3$ (x = 0.0, 0.05, 0.075, 0.10 and 0.15) were synthesized using mechanochemical activation technique (Planetary ball milling). An extensive literature survey shows that ball milling has been used to synthesize several ferroelectric and multiferroic materials [6–9]. However, very few reports are available on the synthesis and extensive characterization of

Published online: 30 May 2016

$Ba_{1-x}Sr_xTiO_3$ via ball milling. This prompted the authors to synthesize the present composition using planetary ball milling. The phase, microstructure and electrical properties of these compositions were investigated. The main objective of the present work is to investigate the effect of Sr substitution and ball milling on the nature of transition temperature, microstructure and electrical properties.

2 Experimental

$Ba_{1-x}Sr_xTiO_3$ (x = 0.0, 0.05, 0.075, 0.10 & 0.15) were synthesized using mechanochemical activation technique. Reagents grade $BaCO_3$ (99.9 %), $SrCO_3$ (99.9 %) and TiO_2 (99.8 %) of *Sigma-Aldrich* make were used as the starting materials. All precursor materials were taken in stoichiometric amount and milled in air at 450 rpm for effective 30 h. Ball milling was carried out using a *Retsch PM100* planetary ball mill. A zirconia vial with a diameter of 45 mm and 30 zirconia balls with a diameter of 10 mm were used as milling medium. The milled powders were calcined at 1100 °C for 4 h to form the desired phase. Then these obtained solid solutions were subsequently mixed with polyvinyl alcohol and compacted into pellets of approximately 10 mm diameter and 1 mm thickness at a pressure of 100 kN. The pellets were then sintered at 1250 °C for 4 h.

The phase and crystallographic structure of as-prepared samples were examined by X-ray diffractometer (*Bruker D8 Advance*) using $CuK_{\alpha 1}$ radiation having the wavelength of 1.540 Å. Raman measurement was performed using *Horiba Jobin–Yvon LabRAM HR* model equipped with a laser of 488 nm wavelength in the scan range of 100–1000 cm^{-1}. The microstructural features and surface morphology of sintered pellets were analyzed using scanning electron microscope (*Hitachi S-3700 N*). The sintered pellets were polished to 1 mm thickness and silver paste was applied on both sides of pellets to form electrodes, the pellets were then cured at 150 °C for 30 min. Further, these pellets were used to perform dielectric measurement by an LCR meter (*Agilent 4284A*) at 1, 10, 100 kHz and 1 MHz frequencies. Temperature dependent dielectric measurement was carried out within the temperature range of 27–250 °C. The hysteresis loops of the samples were analyzed using a P–E loop tracer (*M/s Marine India*). DC resistance and I–V measurement were performed using *Keithley 6517A*.

3 Results and discussion

3.1 X-ray diffraction (XRD)

In order to understand the structural modification on the substitution of strontium in barium titanate, the structural refinement has been carried out for observed XRD patterns by Rietveld method using *X'Pert Highscore Plus* software. All the synthesized samples of $Ba_{1-x}Sr_xTiO_3$ (x = 0.0, 0.05, 0.075, 0.10, 0.15) abbreviated as BT for x = 0.0, BST05 for x = 0.05, BST075 for x = 0.075, BST10 for x = 0.10 and BST15 for x = 0.15, respectively have shown single phase formation as shown in Fig. 1a–e along with the Rietveld analysis. The well fitted refined profile of all the samples with their experimental profile in *P4 mm* space group with tetragonal phase clearly suggests the validity of Rietveld parameters and the refined model. In the refinement of observed XRD patterns of all the samples, barium titanate (JCPDS no. 01-074-1957) has been taken as the reference pattern and the peaks were refined using the Pseudo-Voigt function. Table 1 shows the comparison of different Rietveld parameters. The diffraction peaks indicate excellent homogeneity and no secondary phase is seen due to complete solid solubility of strontium in barium titanate unit cell up to 15 % of substitution at A-site. The refined lattice parameters, c/a ratio and unit cell volume are compared and shown in Table 2. The lattice parameters are found to decrease with increasing strontium concentration which is possibly due to smaller ionic radii

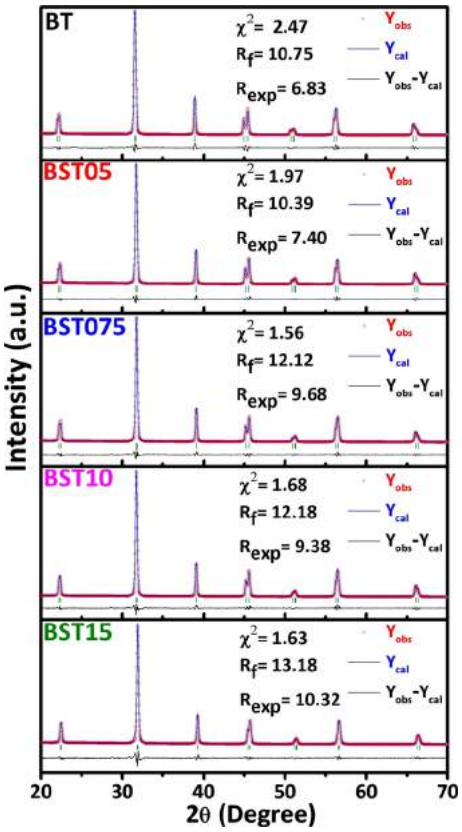


Fig. 1 Rietveld refined X-ray diffraction (XRD) patterns of pure and Sr-substituted $BaTiO_3$ ceramic samples at room temperature

Table 1 Comparison of Rietveld refined parameters for BT, BST05, BST075, BST10 and BST15

Sample	χ^2	R_{exp}	R_f	R_{Bragg}
BT	2.47	6.83	10.75	1.46
BST05	1.97	7.40	10.39	1.48
BST075	1.56	9.68	12.12	0.95
BST10	1.68	9.38	12.18	2.07
BST15	1.63	10.32	13.18	1.34

of Sr^{2+} (1.44 Å) atom compared to that of Ba^{2+} (1.61 Å) in 12 coordination [10].

3.2 Raman spectroscopy

Raman spectroscopy is known to be a powerful nondestructive tool for investigating the onset of ferroelectric order in the polar disordered system and for the study of local structure in crystalline, non-crystalline and quasicrystalline materials that can be used in identifying the atomic and nano-scale structural information of the materials [11]. Raman spectroscopy provides necessary information about the variation in lattice vibrations, which is a collection of different entities that directly control the macroscopic ferroelectricity [12]. Recently Raman spectroscopy has been broadly used for the study of multiferroic materials. The local variation in A–O bonds changes the macroscopic ferroelectricity by altering the fluctuations in octahedral rotation modes [13].

In both, the paraelectric as well as ferroelectric phase, $BaTiO_3$ has one molecule (5 atoms/molecule) per unit cell, which leads to 12 ($3 \times 5 - 3$) long wavelength optical modes. In the paraelectric phase (above 120 °C), the optical modes in Raman spectra transform according to the triply degenerate irreducible representation, $3F_{1u} + F_{2u}$ of the *Pm3 m* symmetry [14]. Here the F_{1u} mode is only infrared active and the F_{2u} mode is silent, which suggest that there is no Raman-active mode in paraelectric phase of barium titanate. In case of ferroelectric phase with tetragonal structure and *P4 mm* symmetry, the F_{1u} splits into nondegenerate A_1 mode and doubly degenerate E mode which further splits into transverse optic (TO) and longitudinal optic (LO) modes, this is due to the association of long-range electrostatic force with lattice iconicity. The F_{2u} mode splits into B_1 and E modes. Tetragonal $BaTiO_3$ possess C_{4v} symmetry at room temperature and permits 3 (A_1) + 1 (E + B_1) Raman active optical modes and 1 (E + A_1) acoustic mode [3]. Figure 2a shows the Raman spectra of the BT sample that depicts the A_1 (TO_1), A_1 (TO_2), A_1 (TO_3) and A_1 (LO_3) modes located at ~164, 256, 509 and 714 cm^{-1}, respectively. The sharp A_1 (TO_1) mode at 164 cm^{-1} corresponds to vibration of Ba ions against TiO_6 octahedra. The interference of A_1 (TO_1) with the broad A_1 (TO_2) at 256 cm^{-1} results in anti-resonance effect in the form of a dip at 179 cm^{-1}. The A_1 (TO_3) mode at 509 cm^{-1} arises from the motion of Ti and O_1 ions against O_2 and O_3 ions located in the plane perpendicular to it. The A_1 (LO_3) mode appearing at 714 cm^{-1} arises due to phonon propagating along the c axis, which is a feature of tetragonal structure in $BaTiO_3$. The E (LO) mode arises simultaneously with A_1 (LO_3) at 714 cm^{-1} indicates the propagation of phonon along the a–b axis. The E (TO_2) mode was found at 299 cm^{-1}, which is related to tetragonal to cubic phase transition [15]. The modes at 164, 299 and 714 cm^{-1} signifies long-range ferroelectric ordering.

Figure 2b–e shows the room temperature Raman spectra of strontium substituted ceramics with phonon mode assignment. As the strontium concentration is increased from $x = 0$ to $x = 0.15$ in $BaTiO_3$, an intense peak at 256 cm^{-1} get shifted towards lower wave number as compared to pure $BaTiO_3$, which is possibly due to complete incorporation of Sr^{2+} on Ba^{2+} site [12]. It has also been known that mode frequency of this mode changes with the change in perovskite unit cell and ionic radii of substituent atom [15]. An increase in intensity and decrease in the broadening of A_1 (TO_3) mode is observed with subsequent increase in Sr content. The changes in A_1 (TO_3)

Table 2 Lattice parameters, cell volume, type of structure, saturation polarization (P_s), remanent polarization ($2P_r$) and coercive field ($2E_c$) of pure and Sr substituted BT samples

Sample	a (Å)	b (Å)	c (Å)	c/a	Cell volume (Å^3)	Density (gm/cm^3)	Structure	Saturation polarization ($2P_s$) (μC/cm^2)	Remanent polarization ($2P_r$) (μC/cm^2)	Coercive field ($2E_c$) (kV/cm)
BT	3.9913	3.9913	4.0283	1.0092	64.1727	5.95	Tetragonal	28.98	3.56	1.96
BST05	3.9885	3.9885	4.0236	1.0088	64.0079	5.99	Tetragonal	31.70	3.27	1.62
BST075	3.9872	3.9872	4.0187	1.0079	63.8883	5.92	Tetragonal	28.10	2.76	1.65
BST10	3.9850	3.9850	4.0136	1.0071	63.7368	5.86	Tetragonal	24.50	2.02	1.69
BST15	3.9822	3.9822	4.0044	1.0055	63.5014	5.84	Tetragonal	18.40	1.83	2.04

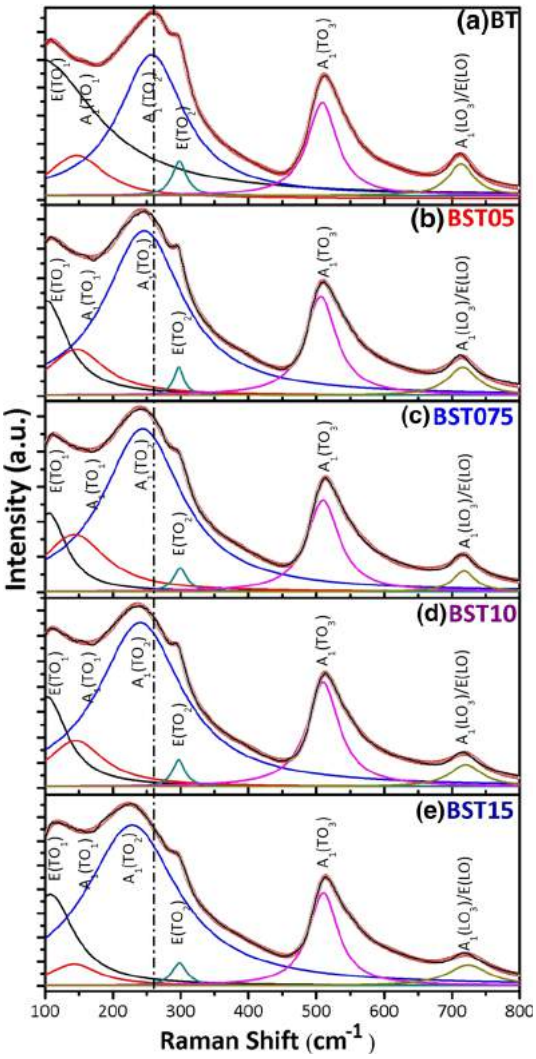


Fig. 2 Raman spectra of pure and Sr substituted $BaTiO_3$ ceramic samples at room temperature: **a** BT, **b** BST05, **c** BST075, **d** BST10 and **e** BST15

mode may be attributed to changes in Ti–O–Ti bond, which is affected by Sr substitution.

3.3 Microstructural studies

Figure 3a–e shows the SEM micrographs of pellets sintered at 1250 °C for 4 h. From the SEM micrographs, it can be observed that the grains are well grown with regular shape in all the five compositions. The average grain size calculated from *ImageJ* software for specimens BT, BST05, BST075, BST10 and BST15 were observed to be 262, 283, 273, 261 and 257 nm, respectively. Therefore, it can be concluded that, Sr substitution do not significantly affect the grain size and lies approximately in the same range. For all the compositions, the grains have distinct grain boundaries and they are densely packed without many cracks or pores. SEM micrographs depict that the grains are nearly crystal shape and their connectivity with neighboring grain indicate the grain growth by diffusion. It has been observed that, the density of the material increases with increase in strontium concentration up to $x = 0.05$ and then decreases on further increasing the strontium content. The density of all the five synthesized composition is listed in Table 2. The change in density is attributed to change in mass and unit cell volume of the compositions under study and hence, it is not remarkably affected by grain size of the materials. By observing at the grain morphology and grain size, it can be inferred that Sr^{2+} shows a good solubility up to 15 % of barium substitution.

3.4 Dielectric studies

The dielectric properties of sintered pellets were measured as a function of temperature up to well above the Curie temperature T_c for all the five studied specimens at different frequencies (1, 10, 100 kHz and 1 MHz). The dielectric constant of all the samples was found to increase with increasing temperature and after attaining maximum, it starts decreasing sharply showing the characteristic of typical ferroelectric-paraelectric transition. Figure 4a–e demonstrates the variation of dielectric constant and dielectric loss at the four selected frequencies. The phase transition from ferroelectric to paraelectric of BT, BST05, BST075, BST10 and BST15 are observed to occur at 126, 109, 105, 95 and 81 °C respectively, which clearly indicates the continuous reduction in Curie temperature of BT after substitution of Sr. This phase transition in these materials can be described on the basis of increase of domain wall mobility with the increasing temperature. The ferroelectric to paraelectric transition in perovskites generally occur because of the instability of temperature dependent low frequency optical soft mode [16, 17]. At phase transition temperature, frequency of the soft mode tends to decrease and lattice displacement associated with this soft mode becomes unstable and therefore results in phase transition [18]. From Fig. 4a–e, it can be seen that the value of dielectric constant is maximum at lower frequency which may be attributed to the higher contribution of space charge polarization at lower frequency [19]. It can be observed that at first dielectric constant increases for $x = 0.05$ and then it decreases with further increase in strontium content. It is a well-known fact that dielectric constant is directly proportional to tetragonality, grain size and density of the material [3]. The slight increase in dielectric constant in BST05 may be attributed to the small increase in grain size and density. On further increasing the Sr content beyond $x = 0.05$ both grain size and density decreases which leads to decrease in dielectric constant of the samples. In addition to this, tetragonality may also

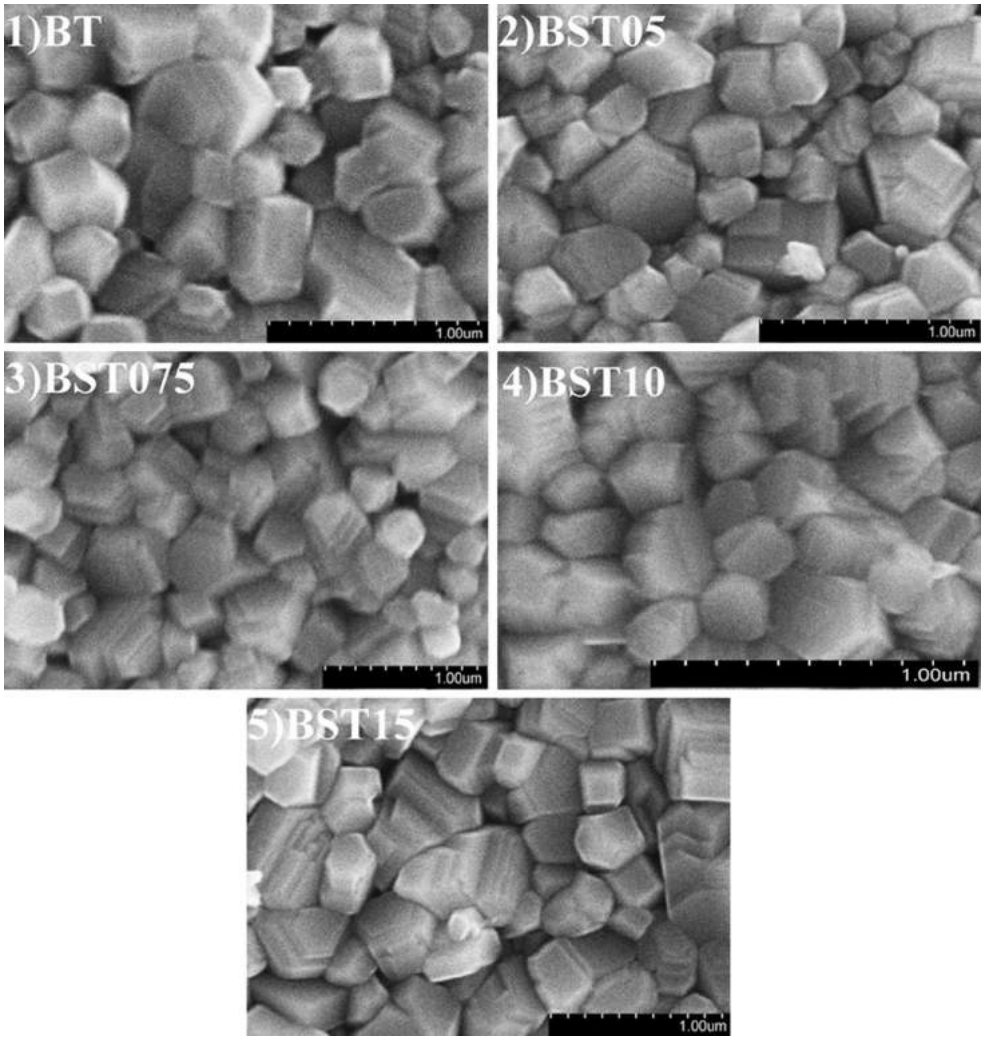


Fig. 3 SEM micrograph of pure and Sr substituted $BaTiO_3$ ceramic samples sintered at 1250 °C for 4 h: **a** BT, **b** BST05, **c** BST075, **d** BST10 and **e** BST15

contribute in the reduction of dielectric constant. A slow phase transition from tetragonal to cubic can be understood by observing the c/a ratio listed in Table 2. This tetragonal to cubic transition has also been confirmed by Raman spectroscopy described above. It can be seen that BT, BST05, BST075 and BST10 are showing a sharp transition as compared to a relatively broad transition for BST15 exhibiting dispersion in T_c corresponding to the ε-T maximum.

It is clearly observed that dielectric loss increases at higher temperature, which may be attributed to the increase in the mobility of charge carriers and defects or imperfection in the material [18]. Also, dielectric loss is found to decrease with increasing strontium concentration. By observing dielectric loss curves, it can be concluded that dielectric loss values remain at low values within a wide temperature range (30–170 °C), showing potential for practical application as low-loss dielectric materials.

In view of phase transition temperature, the dielectric constant (ε) and Curie temperature (T_c) of normal ferroelectric materials can be explained by Curie–Weiss law expressed as [20, 21]:

$$\varepsilon = \frac{C}{T - T_c}(T > T_C) \tag{1}$$

where c represents the Curie constant and T_c is the Curie–Weiss temperature. Figure 5 shows the inverse of dielectric constant as a function of temperature at 10 kHz for all the synthesized compositions. The experimental data obtained from dielectric measurement were fitted by Eq. (1) and the obtained parameters (T_c, T_o, T_{dev}, δT_m) are summarized in Table 3. The parameter δT_m, which

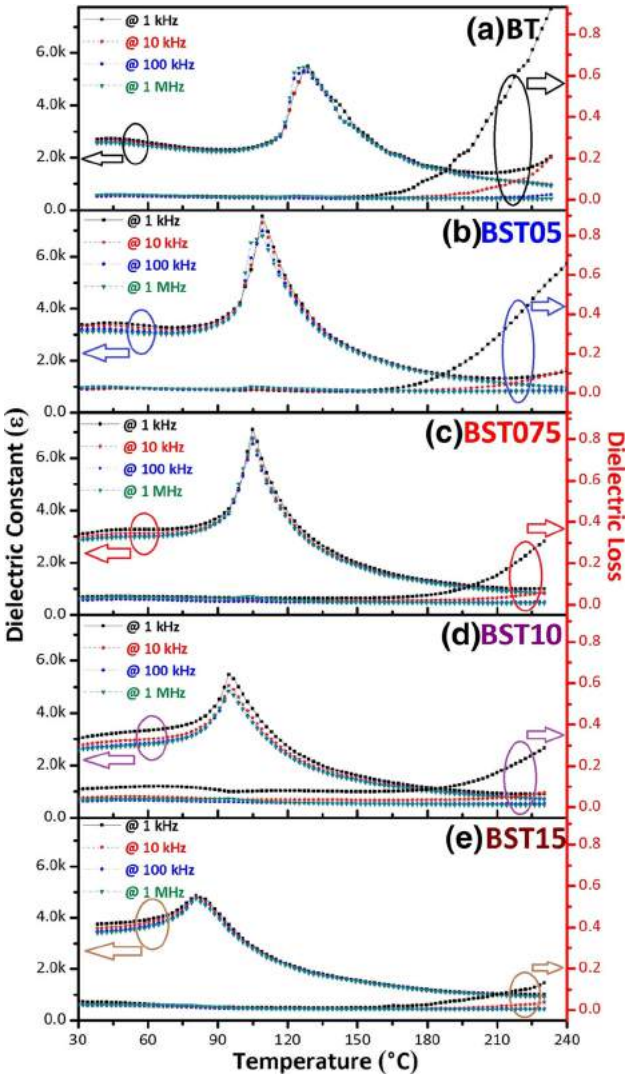


Fig. 4 Temperature dependent dielectric constant and loss tangent of pure and Sr-substituted $BaTiO_3$ ceramic samples at 1, 10, 100 kHz and 1 MHz within a temperature range of 30–240 °C: **a** BT, **b** BST05, **c** BST075, **d** BST10 and **e** BST15

describes the degree of deviation from the Curie–Weiss law is defined as [22].

$$\delta T_{\mathrm{m}} = T_{\mathrm{dev}} - T_{\mathrm{m}} \tag{2}$$

where T_{dev} indicates the temperature at which the dielectric constant starts to deviate from Curie–Weiss law and T_{m} is the temperature corresponding to the maximum dielectric constant. It can be seen from Table 3 that the value of T_o and δT_m reduces with increasing strontium substitution. In order to further investigate the dielectric dispersion and diffuseness of phase transition, a modified Curie–Weiss law is proposed [23]:

$$\frac{1}{\varepsilon} - \frac{1}{\varepsilon_m} = \frac{(T - T_c)^{\gamma}}{C'} \tag{3}$$

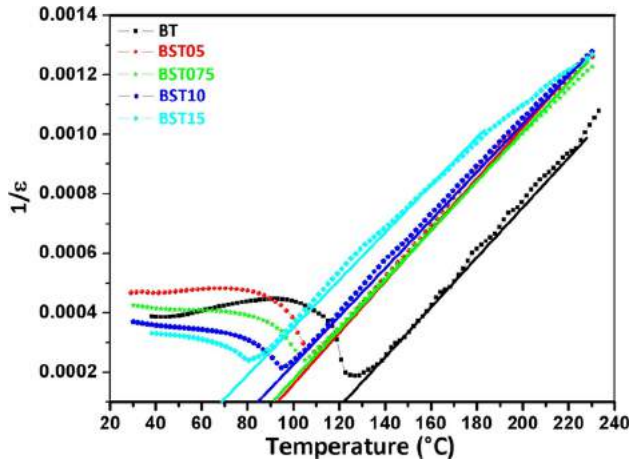


Fig. 5 Temperature dependence of inverse dielectric constant for pure and Sr substituted $BaTiO_3$ ceramic samples at 100 kHz

where γ represents the diffuseness of phase transition and C' is a constant. The parameter γ indicates the phase transition character of any material. The limiting value $\gamma = 1$ corresponds to classical ferroelectric behavior, while $1 < \gamma < 2$ describes a diffuse phase transition. Typical fitting curves obtained from Eq. (3) are plotted in the Fig. 6 and the parameter γ obtained from these curves are listed in Table 3. It can be observed that the fitted values of γ for strontium substituted compositions increases gradually. For sample BST15, the value of γ is obtained to be 1.16, which reveals that as strontium concentration increases, the sample becomes more diffused. These results suggest that the degree of diffuseness of phase transition and relaxor ferroelectric behavior are enhanced with increasing strontium concentration.

A dimensionless quantity known as the Goldschmidt tolerance factor (t) is used to define the strain in a crystal structure; also this parameter is an indicator of stability and distortion in any crystal structure [24, 25]. For perovskite type structures, the following formula is used to calculate tolerance factor, t:

$$t = \frac{R_O + R_A}{\sqrt{2}(R_B + R_O)} \tag{4}$$

where R_A, R_B and R_o represents the ionic radii of the A-site, B-site and oxygen atoms respectively. For the composition in the present work, Eq. (4) can be rewritten as:

$$t = \frac{R_O + ((1-x)R_{Ba^{2+}} + xR_{Sr^{2+}})}{\sqrt{2}(R_B + R_O)} \tag{5}$$

For a stable perovskite structure, the value of tolerance factor (t) should be close to unity. The calculated values of tolerance factor (t) are listed in Table 3, which shows that with increasing strontium substitution, the tolerance factor

Table 3 The temperature of the dielectric constant maximum (T_c), the Curie–Weiss temperature (T_o), the temperature above which dielectric constant deviates from Curie–Weiss law (T_{dev}), degree of deviation from Curie–Weiss law (δT_m), degree of relaxation (γ), tolerance factor (t) and resistance (R) of pure and Sr-substituted BT samples

Sample	T_c (°C)	T_o (°C)	T_{dev} (°C)	δT_m (°C)	γ	t	Resistance R ($\times 10^9$ Ohm)
BT	126	121	136	10	1.03	1.061	12.9
BST05	109	93	118	9	1.05	1.058	11.0
BST075	105	91	112	7	1.06	1.057	9.71
BST10	95	84	100	5	1.14	1.055	9.60
BST15	81	68	86	5	1.16	1.052	7.44

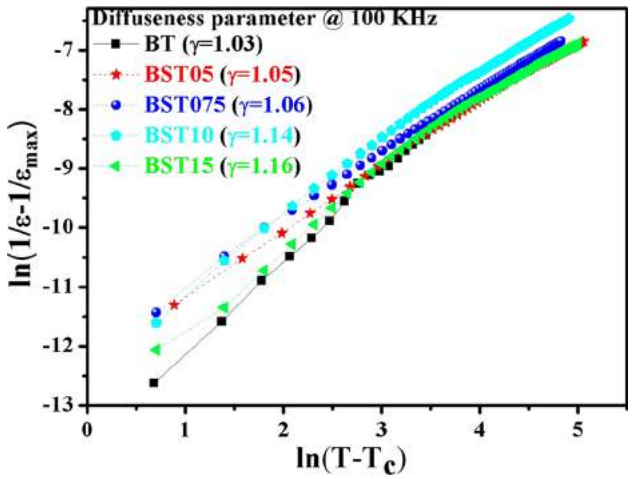


Fig. 6 The plot of ln ($1/\varepsilon - 1/\varepsilon_m$) as a function of ln ($T - T_c$) for pure and Sr-substituted $BaTiO_3$ ceramic samples at 100 kHz

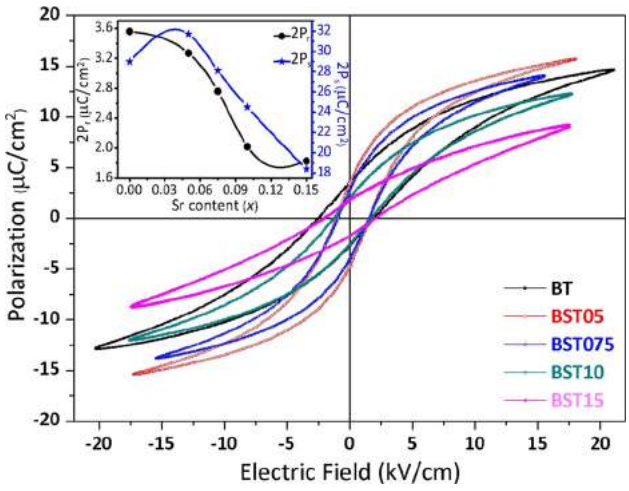


Fig. 7 Ferroelectric hysteresis loops of pure and Sr-substituted $BaTiO_3$ ceramic samples at room temperature and inset shows the variation of remanent polarization ($2P_r$) and saturation polarization with strontium content (x)

decreases. The decrease in tolerance factor may be attributed to lower ionic radii of Sr^{2+} (1.44 Å) compared to Ba^{2+} (1.61 Å) in 12 coordination [26].

3.5 Ferroelectric studies

The P–E hysteresis loops of pure and Sr-substituted BT samples at room temperature are shown in Fig. 7. The hysteresis loops were recorded at a frequency of 50 Hz and an applied field of up to 21 kV/cm. It can be seen that S-shaped loops with high remanent polarization (P_r) are observed for all the samples. The shapes of hysteresis P–E loop are related to the crystalline structure of the materials. The saturation polarization ($2P_s$), remanent polarization ($2P_r$) and coercive field ($2E_c$) values for the studied samples are listed in Table 2. As Sr content increases, the saturation polarization (P_s) increases up to x = 0.05 and then decreases continuously at higher concentration of strontium. However, remanent polarization (P_r) of the samples was found to decrease with increasing strontium concentration because Sr^{2+} (1.44 Å) substitution at Ba^{2+} (1.61 Å) site results in lattice shrinkage, which reduces interspace of oxygen octahedron inside the unit cell, resulting in the decrease of remanent polarization. In addition, the large grain size corresponds to better ferroelectricity because reversal of polarization of ferroelectric domain is much easier inside a large grain as compare to that of smaller grains [18]. The polarization and coercive field values are very much dependent on the exact nature of the sample under study. Also, the coercive field rely strongly on the crystal perfection and the time duration of the applied electric field [27]. It has been observed that the coercive field ($2E_c$) of BST ceramics initially decreases to minimum and then increases with the increasing Sr content. These results may be attributed to slight variation in grain size of the pure and Sr substituted BT ceramics.

3.6 Conductivity studies

The effect of temperature on the DC electrical conductivity for pure and Sr-substituted BT samples was investigated. The measurement of conductivity was carried out from 27

to 200 °C. In all the samples, the increase in conductivity was gradual up to 90 °C, and it increases rapidly with further increase in temperature. Figure 8a shows the variation of conductivity in the temperature range of 27–90 °C and Fig. 8b from 90 to 200 °C, respectively. Activation energy of all the samples was calculated using the plot in Fig. 8a–b and Arrhenius equation, which is expressed as:

$$\sigma_{dc} = \sigma_o \exp \frac{-E_a}{K_B T} \tag{6}$$

where K_B is the Boltzmann constant, E_a is the activation energy and T is the temperature. The temperature dependent conductivity in ceramics is attributed to both hopping mechanism of electrons and charge transfer via excited state [28]. The increase in conductivity with temperature suggests the semiconducting behavior of ceramics. The change in slope around Curie temperature indicates a change in activation energy E_a. This explains that different conduction mechanism is in play in different temperature region [29]. In low-temperature region, the extrinsic defects are responsible for the conduction, while in the high-temperature region, the thermally active oxygen vacancies are responsible for conduction mechanism.

3.7 I–V measurement

The DC I–V characteristics of all the samples, measured at room temperature in the applied DC voltage range of 0–2 V, are shown in Fig. 9. Here, it is observed that pure BT and strontium substituted samples shows a linear dependence of the current in 0–2 V range. In ceramics, the

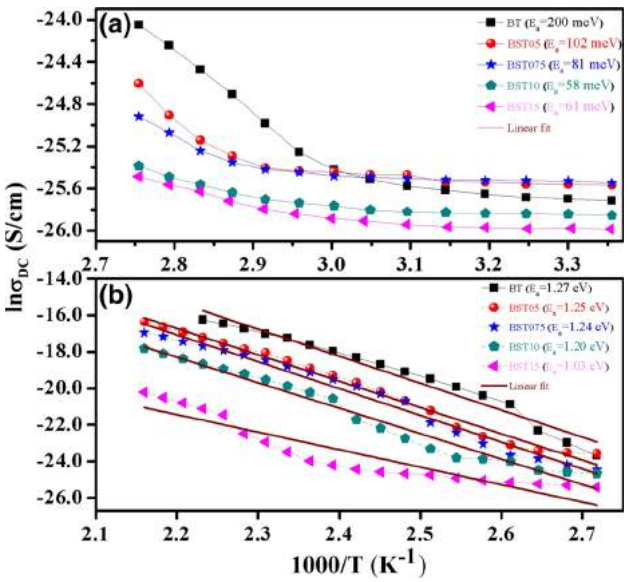


Fig. 8 Variation of DC electrical conductivity, σ with temperature: **a** temperature range of 27–90 °C and **b** variation from 90–200 °C for pure and Sr-substituted $BaTiO_3$ ceramic samples

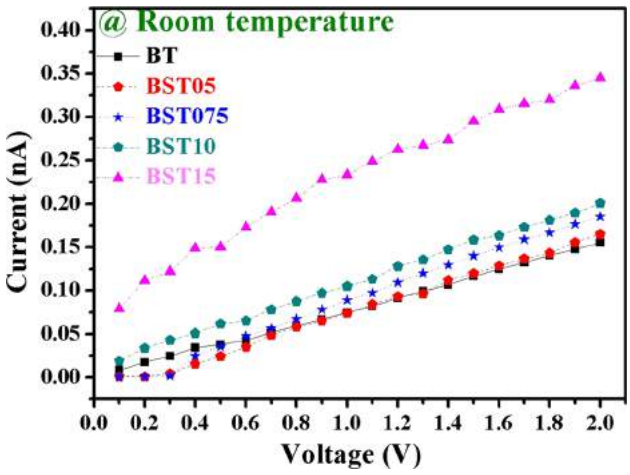


Fig. 9 I–V characteristics of pure and Sr-substituted $BaTiO_3$ ceramic samples measured at room temperature

charging current flows through the material during polarization, such current results from the movement of free charges from the inside of the material, changes in domain structure and charges injected from the electrodes [30]. The distinctly seen portion of I–V characteristics where Ohm's law is satisfied is used to calculate the material resistance.

When the applied voltage is small, a relatively weak electric field appears at the grain boundaries. Also nonlinear effects occurring in the material are weak, which results in lower value of current. When the concentration of equilibrium charges is more than injected ones, a linear dependence between voltage and current is noticed. The electric field that disturbs the charges inside the grain is feeble because it is additionally lowered by the depolarizing field [31]. The calculated value of resistance for all the synthesized samples are listed in Table 3. It has been observed that BT sample has the highest ohmic resistance that is found to decrease with increasing strontium content. These results are in good agreement with the results obtained from conductivity studies, where also the activation energy is observed to decrease with increasing strontium content.

4 Conclusion

In this study, series of $Ba_{1-x}Sr_xTiO_3$ (x = 0.0, 0.05, 0.075, 0.10 & 0.15) were synthesized using mechanochemical activation technique. Detailed X-ray diffraction structural analysis by Rietveld analysis and Raman spectra measured at room temperature reveals the formation of tetragonal phase with *P4 mm* space group for all the samples. Microstructural investigation shows the formation of well-developed grains with clearly distinguishable grain boundaries. The substitution of Sr on A-site in $BaTiO_3$

increases the dielectric constant for substitution up to $x = 0.05$; however, on further increase in the Sr content dielectric constant decreases. Dielectric loss of the materials decreases on Sr substitution. Sr substitution on A-site has resulted in the decrease of long-range polar ordering which subsequently decreases tetragonality as well as Curie temperature. Ferroelectric hysteresis loops measured at room temperature shows decrease in remanent polarization with Sr substitution. The activation energy of the materials is observed to decrease with Sr substitution which is in conformity with I–V characteristics where resistance decreases with Sr substitution. Overall the $Ba_{1-x}Sr_xTiO_3$ ceramics with suitable dielectric constant, lower dielectric loss and good ferroelectric properties could be a potential ceramic material for microwave devices and multi-layer ceramic capacitor (MLCC) applications.

Acknowledgments Authors are thankful for the support of DST-SERB, India to carry out this research work.

References

1. N. Sawangwan, J. Barrel, K. Mackenzie, T. Tunkasiri, Appl. Phys. A **90**, 723–727 (2008)
2. N. Maikhuri, A.K. Panwar, A. Jha, J. Appl. Phys. **113**, 17D915 (2013)
3. M. Ganguly, S. Rout, C. Ahn, I. Kim, M. Kar, Ceram. Int. **39**, 9511–9524 (2013)
4. X. Wang, R. Huang, Y. Zhao, Y. Zhao, H. Zhou, Z. Jia, J. Alloy. Compd. **533**, 25–28 (2012)
5. U. Mizutani, MRS Bull. **37**, 169 (2012)
6. C. Liu, P. Liu, X.-G. Lu, C.-J. Gao, G.-Q. Zhu, X.-M. Chen, Powder Technol. **212**, 299–302 (2011)
7. P.K. Jha, P.A. Jha, G. Srivastava, A. Jha, R. Kotnala, R. Dwivedi, J. Magn. Magn. Mater. **349**, 95–99 (2014)
8. R. Rani, S. Singh, J. Juneja, K. Raina, C. Prakash, Ceram. Int. **37**, 3755–3758 (2011)
9. C. Liu, P. Liu, J. Alloy. Compd. **584**, 114–118 (2014)
10. R.T. Shannon, Acta crystallographica section A: crystal physics, diffraction, theoretical and general crystallography **32**, 751–767 (1976)
11. P.A. Jha, P.K. Jha, A. Jha, R. Kotnala, R. Dwivedi, J. Alloy. Compd. **600**, 186–192 (2014)
12. V.S. Puli, D.K. Pradhan, W. Pérez, R. Katiyar, J. Phys. Chem. Solids **74**, 466–475 (2013)
13. D. Maurya, A. Kumar, V. Petkov, J.E. Mahaney, R.S. Katiyar, S. Priya, RSC Adv. **4**, 1283–1292 (2014)
14. Z. Yao, H. Liu, Y. Liu, Z. Wu, Z. Shen, Y. Liu, M. Cao, Mater. Chem. Phys. **109**, 475–481 (2008)
15. N. Karan, R. Katiyar, T. Maiti, R. Guo, A. Bhalla, J. Raman Spectrosc. **40**, 370–375 (2009)
16. E. Tasarkuyu, A. Coskun, A. Irmak, S. Aktürk, G. Ünlü, Y. Samancioglu, A. Yücel, C. Sankürkcü, S. Aksoy, M. Acet, J. Alloy. Compd. **509**, 3717–3722 (2011)
17. K. Prasad, A. Raju, K. Varma, J. Mater. Sci. **29**, 2691–2696 (1994)
18. P. Mishra, P. Kumar, J. Alloy. Compd. **545**, 210–215 (2012)
19. Y. Wang, L. Li, J. Qi, Z. Gui, Mater. Chem. Phys. **76**, 250–254 (2002)
20. X. Tang, K.-H. Chew, H. Chan, Acta Mater. **52**, 5177–5183 (2004)
21. Y. Li, R. Wang, X. Ma, Z. Li, R. Sang, Y. Qu, Mater. Res. Bull. **49**, 601–607 (2014)
22. X. Chou, J. Zhai, X. Yao, Mater. Chem. Phys. **109**, 125–130 (2008)
23. S. Anwar, P. Sagdeo, N. Lalla, Solid State Commun. **138**, 331–336 (2006)
24. V. Goldschmidt, Die Naturwissenschaften **14**, 477–485 (1928)
25. S. Švarcová, K. Wiik, J. Tolchard, H.J. Bouwmeester, T. Grande, Solid State Ionics **178**, 1787–1791 (2008)
26. R. Haire, R. Baybarz, J. Inorg. Nucl. Chem. **35**, 489–496 (1973)
27. H.B. Sharma, H. Sarma, A. Mansingh, J. Mater. Sci. **34**, 1385–1390 (1999)
28. M.T. Rahman, C. Ramana, Ceram. Int. **40**, 14533–14536 (2014)
29. N. Kumar, P. Tirupathi, B. Kumar, M. Pastor, A. Pandey, R. Choudhary, Adv. Mater. Lett. **6**, 284–289 (2015)
30. A. Dedyk, A. Kanareykin, E. Nenasheva, J.V. Pavlova, S. Karmanenko, Tech. Phys. **51**, 1168–1173 (2006)
31. W. Osak, K. Tkacz, J. Phys. D Appl. Phys. **22**, 1746 (1989)

SUPPLEMENTARY MATERIALS: SYMPY: SYMBOLIC COMPUTING IN PYTHON

AARON MEURER*, CHRISTOPHER P. SMITH†, MATEUSZ PAPROCKI‡, ONDŘEJ ČERTÍK§, MATTHEW ROCKLIN¶, AMIT KUMAR‖, SERGIU IVANOV#, JASON K. MOORE††, SARTAJ SINGH‡‡, THILINA RATHNAYAKE§§, SEAN VIG¶¶, BRIAN E. GRANGER‖‖, RICHARD P. MULLER##, FRANCESCO BONAZZI[1], HARSH GUPTA[2], SHIVAM VATS[3], FREDRIK JOHANSSON[4], FABIAN PEDREGOSA[5], MATTHEW J. CURRY[6], ASHUTOSH SABOO[7], ISURU FERNANDO[8], SUMITH[9], ROBERT CIMRMAN[10], AND ANTHONY SCOPATZ[11]

As in the paper, all examples in the supplement assume that the following has been run:

```
>>> from sympy import *
>>> x, y, z = symbols('x y z')
```

SM1. Limits: The Gruntz Algorithm. SymPy calculates limits using the Gruntz algorithm, as described in [SM7]. The basic idea is as follows: any limit can

*University of South Carolina, Columbia, SC 29201 (asmeurer@gmail.com).
†Polar Semiconductor, Inc., Bloomington, MN 55425 (smichr@gmail.com).
‡Continuum Analytics, Inc., Austin, TX 78701 (mattpap@gmail.com).
§Los Alamos National Laboratory, Los Alamos, NM 87545 (certik@lanl.gov).
¶Continuum Analytics, Inc., Austin, TX 78701 (mrocklin@gmail.com).
‖Delhi Technological University, Shahbad Daulatpur, Bawana Road, New Delhi 110042, India (dtu.amit@gmail.com).
#Université Paris Est Créteil, 61 av. Général de Gaulle, 94010 Créteil, France (sergiu.ivanov@u-pec.fr).
††University of California, Davis, Davis, CA 95616 (jkm@ucdavis.edu).
‡‡Indian Institute of Technology (BHU), Varanasi, Uttar Pradesh 221005, India (singhsartaj94@gmail.com).
§§University of Moratuwa, Bandaranayake Mawatha, Katubedda, Moratuwa 10400, Sri Lanka (thilinarmtb.10@cse.mrt.ac.lk).
¶¶University of Illinois at Urbana-Champaign, Urbana, IL 61801 (sean.v.775@gmail.com).
‖‖California Polytechnic State University, San Luis Obispo, CA 93407 (ellisonbg@gmail.com).
##Center for Computing Research, Sandia National Laboratories, Albuquerque, NM 87185 (rmuller@sandia.gov).
[1]Max Planck Institute of Colloids and Interfaces, Department of Theory and Bio-Systems, Am Mühlenberg 1, 14424 Potsdam, Germany (francesco.bonazzi@mpikg.mpg.de).
[2]Indian Institute of Technology Kharagpur, Kharagpur, West Bengal 721302, India (hargup@protonmail.com).
[3]Indian Institute of Technology Kharagpur, Kharagpur, West Bengal 721302, India (shivamvats.iitkgp@gmail.com).
[4]INRIA Bordeaux-Sud-Ouest – LFANT project-team, 200 Avenue de la Vieille Tour, 33405 Talence, France (fredrik.johansson@gmail.com).
[5]INRIA – SIERRA project-team, 2 Rue Simone IFF, 75012 Paris, France (f@bianp.net).
[6]Department of Physics and Astronomy, University of New Mexico, Albuquerque, NM 87131 (mattjcurry@gmail.com).
[7]Birla Institute of Technology and Science, Pilani, K.K. Birla Goa Campus, NH 17B Bypass Road, Zuarinagar, Sancoale, Goa 403726, India (ashutosh.saboo@gmail.com).
[8]University of Moratuwa, Bandaranayake Mawatha, Katubedda, Moratuwa 10400, Sri Lanka (isuru.11@cse.mrt.ac.lk).
[9]Indian Institute of Technology Bombay, Powai, Mumbai, Maharashtra 400076, India (sumith@cse.iitb.ac.in).
[10]New Technologies – Research Centre, University of West Bohemia, Univerzitní 8, 306 14 Plzeň, Czech Republic (cimrman3@ntc.zcu.cz).
[11]University of South Carolina, Columbia, SC 29201 (scopatz@cec.sc.edu).

be converted to a limit $\lim_{x\to\infty} f(x)$ by substitutions like $x \to \frac{1}{x}$. Then the subexpression ω (that converges to zero as $x \to \infty$ faster than all other subexpressions) is identified in $f(x)$, and $f(x)$ is expanded into a series with respect to ω. Any positive powers of ω converge to zero (while negative powers indicate an infinite limit) and any constant term independent of ω determines the limit. When a constant term still dependends on x the Gruntz algorithm is applied again until a final numerical value is obtained as the limit.

To determine the most rapidly varying subexpression, the comparability classes must first be defined, by calculating L:

$$L \equiv \lim_{x\to\infty} \frac{\log|f(x)|}{\log|g(x)|} \tag{SM1}$$

The relations $<$, $>$, and $\sim$ are defined as follows: $f > g$ when $L = \pm\infty$ (it is said that f is more rapidly varying than g, i.e., f goes to ∞ or 0 faster than g), $f < g$ when $L = 0$ (f is less rapidly varying than g) and $f \sim g$ when $L \neq 0, \pm\infty$ (both f and g are bounded from above and below by suitable integral powers of the other). Note that if $f > g$, then $f > g^n$ for any n. Here are some examples of comparability classes:

$$2 < x < e^x < e^{x^2} < e^{e^x}$$

$$2 \sim 3 \sim -5$$

$$x \sim x^2 \sim x^3 \sim \frac{1}{x} \sim x^m \sim -x$$

$$e^x \sim e^{-x} \sim e^{2x} \sim e^{x+e^{-x}}$$

$$f(x) \sim \frac{1}{f(x)}$$

The Gruntz algorithm is now illustrated with the following example:

$$f(x) = e^{x+2e^{-x}} - e^x + \frac{1}{x}\,. \tag{SM2}$$

The goal is to calculate $\lim_{x\to\infty} f(x)$. First, the set of most rapidly varying subexpressions is determined—the so-called *mrv set*. For (SM2), the mrv set $\{e^x, e^{-x}, e^{x+2e^{-x}}\}$ is obtained. These are all subexpressions of (SM2) and they all belong to the same comparability class. This calculation can be done using SymPy as follows:

```
>>> from sympy.series.gruntz import mrv
>>> mrv(exp(x+2*exp(-x))-exp(x) + 1/x, x)[0].keys()
dict_keys([exp(x + 2*exp(-x)), exp(x), exp(-x)])
```

Next, an arbitrary item ω is taken from mrv that converges to zero for $x \to \infty$. The item $\omega = e^{-x}$ is obtained. If such a term is not present in the mrv set (i.e., all terms converge to infinity instead of zero), the relation $f(x) \sim \frac{1}{f(x)}$ can be used.

The next step is to rewrite the mrv set in terms of ω: $\{\frac{1}{\omega}, \omega, \frac{1}{\omega}e^{2\omega}\}$. Then the original subexpressions are substituted back into $f(x)$ and expanded with respect to ω:

$$f(x) = \frac{1}{x} - \frac{1}{\omega} + \frac{1}{\omega}e^{2\omega} = 2 + \frac{1}{x} + 2\omega + O(\omega^2) \tag{SM3}$$

Since ω is from the mrv set, then in the limit as $x \to \infty$, $\omega \to 0$, and so $2\omega + O(\omega^2) \to 0$ in (SM3):

$$f(x) = \frac{1}{x} - \frac{1}{\omega} + \frac{1}{\omega}e^{2\omega} = 2 + \frac{1}{x} + 2\omega + O(\omega^2) \to 2 + \frac{1}{x} \tag{SM4}$$

Since the result $(2 + \frac{1}{x})$ still depends on x, the above procedure is repeated until just a value independent of x is obtained. This is the final limit. In the above case the limit is 2, as can be verified by SymPy:

```
>>> limit(exp(x+2*exp(-x))-exp(x) + 1/x, x, oo)
2
```

In general, when $f(x)$ is expanded in terms of ω, the following is obtained:

$$f(x) = \underbrace{O\left(\frac{1}{\omega^3}\right)}_{\infty} + \underbrace{\frac{C_{-2}(x)}{\omega^2}}_{\infty} + \underbrace{\frac{C_{-1}(x)}{\omega}}_{\infty} + C_0(x) + \underbrace{C_1(x)\omega}_{0} + \underbrace{O(\omega^2)}_{0} \tag{SM5}$$

The positive powers of ω are zero. If there are any negative powers of ω, then the result of the limit is infinity, otherwise the limit is equal to $\lim_{x\to\infty} C_0(x)$. The expression $C_0(x)$ is simpler than $f(x)$ and so the algorithm always converges. A proof of this and further details on the algorithm are given in Gruntz's PhD thesis [SM7].

SM2. Series.

SM2.1. Series Expansion. SymPy is able to calculate the symbolic series expansion of an arbitrary series or expression involving elementary and special functions and multiple variables. For this it has two different implementations: the `series` method and Ring Series.

The first approach stores a series as an instance of the `Expr` class. Each function has its specific implementation of its expansion, which is able to evaluate the Puiseux series expansion about a specified point. For example, consider a Taylor expansion about 0:

```
>>> from sympy import symbols, series
>>> x, y = symbols('x, y')
>>> series(sin(x+y) + cos(x*y), x, 0, 2)
1 + sin(y) + x*cos(y) + O(x**2)
```

The newer and much faster approach called Ring Series makes use of the fact that a truncated Taylor series is simply a polynomial. Correspondingly, they may be represented by sparse polynomials which perform well in a under a wide range of cases. Ring Series also gives the user the freedom to choose the type of coefficients to use, resulting in faster operations on certain types.

For this, several low-level methods for expansion of trigonometric, hyperbolic and other elementary operations (like series inversion, calculating the nth root, etc.) are implemented using variants of the Newton Method [SM2]. All these support Puiseux series expansion. The following example demonstrates the use of an elementary function that calculates the Taylor expansion of the sine of a series.

```
>>> from sympy import ring
>>> from sympy.polys.ring_series import rs_sin
>>> R, t = ring('t', QQ)
>>> rs_sin(t**2 + t, t, 5)
-1/2*t**4 - 1/6*t**3 + t**2 + t
```

The function `sympy.polys.rs_series` makes use of these elementary functions to expand an arbitrary SymPy expression. It does so by following a recursive strategy of expanding the lowermost functions first and then composing them recursively to calculate the desired expansion. Currently, it only supports expansion about 0 and is under active development. Ring Series is several times faster than the default implementation with the speed difference increasing with the size of the series. The `sympy.polys.rs_series` takes as input any SymPy expression and hence there is no need to explicitly create a polynomial `ring`. An example demonstrating its use:

```
>>> from sympy.polys.ring_series import rs_series
>>> from sympy.abc import a, b
>>> from sympy import sin, cos
>>> rs_series(sin(a + b), a, 4)
-1/2*(sin(b))*a**2 + (sin(b)) - 1/6*a**3*(cos(b)) + a*(cos(b))
```

SM2.2. Formal Power Series. SymPy can be used for computing the formal power series of a function. The implementation is based on the algorithm described in the paper on formal power series [SM8]. The advantage of this approach is that an explicit formula for the coefficients of the series expansion is generated rather than just computing a few terms.

The following example shows how to use `fps`:

```
>>> f = fps(sin(x), x, x0=0)
>>> f.truncate(6)
x - x**3/6 + x**5/120 + O(x**6)
>>> f[15]
-x**15/1307674368000
```

SM2.3. Fourier Series. SymPy provides functionality to compute Fourier series of a function using the `fourier_series` function:

```
>>> L = symbols('L')
>>> expr = 2 * (Heaviside(x/L) - Heaviside(x/L - 1)) - 1
>>> f = fourier_series(expr, (x, 0, 2*L))
>>> f.truncate(3)
4*sin(pi*x/L)/pi + 4*sin(3*pi*x/L)/(3*pi) + 4*sin(5*pi*x/L)/(5*pi)
```

SM3. Logic. SymPy supports construction and manipulation of boolean expressions through the `sympy.logic` module. SymPy symbols can be used as propositional variables and subsequently be replaced with `True` or `False` values. Many functions for manipulating boolean expressions have been implemented in the `logic` module.

SM3.1. Constructing boolean expressions. A boolean variable can be declared as a SymPy `Symbol`. Python operators `&`, `|` and `~` are overridden when using SymPy objects to use the SymPy functionality for logical `And`, `Or`, and `Not`. Other logic functions are also integrated into SymPy, including `Xor` and `Implies`, which are constructed with `^` and `>>`, respectively. Expressions can therefore be constructed either by using the shortcut operator notation or by directly creating the relevant objects: `And()`, `Or()`, `Not()`, `Xor()`, `Implies()`, `Nand()`, `Nor()`, etc. »»»> reviews

```
>>> e = (x & y) | z
>>> e.subs({x: True, y: True, z: False})
True
```

SM3.2. CNF and DNF. Any boolean expression can be converted to conjunctive normal form, disjunctive normal form, or negation normal form. The API also

exposes methods to check if a boolean expression is in any of the aforementioned forms.

```
>>> from sympy.logic.boolalg import is_dnf, is_cnf
>>> to_cnf((x & y) | z)
And(Or(x, z), Or(y, z))
>>> to_dnf(x & (y | z))
Or(And(x, y), And(x, z))
>>> is_cnf((x | y) & z)
True
>>> is_dnf((x & y) | z)
True
```

SM3.3. Simplification and Equivalence. The `sympy.logic` module supports simplification of given boolean expression by making deductions from the expression. Equivalence of two logical expressions can also be checked. In the case of equivalence, the function `bool_map` can be used to show which variables of the first expression correspond to which variables of the second one.

```
>>> a, b, c = symbols('a b c')
>>> e = a & (~a | ~b) & (a | c)
>>> simplify(e)
And(Not(b), a)
>>> e1 = a & (b | c)
>>> e2 = (x & y) | (x & z)
>>> bool_map(e1, e2)
(And(Or(b, c), a), {a: x, b: y, c: z})
```

SM3.4. SAT solving. The module also supports satisfiability (SAT) checking of a given boolean expression. If an expression is satisfiable, it is possible to return a variable assignment which satisfies it. The API also supports listing all possible assignments. The SAT solver has a clause learning DPLL algorithm implemented with a watch literal scheme and VSIDS heuristic [SM11].

```
>>> satisfiable(a & (~a | b) & (~b | c) & ~c)
False
>>> satisfiable(a & (~a | b) & (~b | c) & c)
{a: True, b: True, c: True}
```

SM4. Diophantine Equations. Diophantine equations play a central role in number theory. A Diophantine equation has the form, $f(x_1, x_2, \ldots, x_n) = 0$ where $n \geq 2$ and $x_1, x_2, \ldots, x_n$ are integer variables. If there are n integers $a_1, a_2, \ldots, a_n$ such that $x_1 = a_1, x_2 = a_2, \ldots, x_n = a_n$ satisfies the above equation, the equation is said to be solvable.

Currently, the following five types of Diophantine equations can be solved using SymPy's Diophantine module ($a_1, \ldots, a_{n+1}$, a, b, c, d, e, f, and k are explicitly given rational constants):

- Linear Diophantine equations: $a_1x_1 + a_2x_2 + \cdots + a_nx_n = b$
- General binary quadratic equation: $ax^2 + bxy + cy^2 + dx + ey + f = 0$
- Homogeneous ternary quadratic equation: $ax^2+by^2+cz^2+dxy+eyz+fzx = 0$
- Extended Pythagorean equation: $a_1x_1^2 + a_2x_2^2 + \cdots + a_nx_n^2 = a_{n+1}x_{n+1}^2$
- General sum of squares: $x_1^2 + x_2^2 + \cdots + x_n^2 = k$

The `diophantine` function factors the equation it is given (if possible), solves each factor separately, and combines the results to give a final solution set. The following

examples illustrate some of the basic functionalities of the Diophantine module.

```
>>> from sympy.solvers.diophantine import *
>>> diophantine(2*x + 3*y - 5)
set([(3*t_0 - 5, -2*t_0 + 5)])

>>> diophantine(2*x + 4*y - 3)
set()

>>> diophantine(x**2 - 4*x*y + 8*y**2 - 3*x + 7*y - 5)
set([(2, 1), (5, 1)])

>>> diophantine(x**2 - 4*x*y + 4*y**2 - 3*x + 7*y - 5)
set([(-2*t**2 - 7*t + 10, -t**2 - 3*t + 5)])

>>> diophantine(3*x**2 + 4*y**2 - 5*z**2 + 4*x*y - 7*y*z + 7*z*x)
set([(-16*p**2 + 28*p*q + 20*q**2,
3*p**2 + 38*p*q - 25*q**2,
4*p**2 - 24*p*q + 68*q**2)])

>>> x1, x2, x3, x4, x5, x6 = symbols('x1, x2, x3, x4, x5, x6')
>>> diophantine(9*x1**2 + 16*x2**2 + x3**2 + 49*x4**2 + 4*x5**2 - 25*x6**2)
set([(70*t1**2 + 70*t2**2 + 70*t3**2 + 70*t4**2 - 70*t5**2, 105*t1*t5,
420*t2*t5, 60*t3*t5, 210*t4*t5,
42*t1**2 + 42*t2**2 + 42*t3**2 + 42*t4**2 + 42*t5**2)])

>>> a, b, c, d = symbols('a:d')
>>> diophantine(a**2 + b**2 + c**2 + d**2 - 23)
set([(2, 3, 3, 1)])
```

SM5. Sets. SymPy supports representation of a wide variety of mathematical sets. This is achieved by first defining abstract representations of atomic set classes and then combining and transforming them using various set operations.

Each of the set classes inherits from the base class `Set` and defines methods to check membership and calculate unions, intersections, and set differences. When these methods are not able to evaluate to atomic set classes, they are represented as abstract unevaluated objects.

SymPy has the following atomic set classes:

- `EmptySet` represents the empty set $\emptyset$.
- `UniversalSet` is an abstract "universal set" of which everything is a member. The union of the universal set with any set gives the universal set and the intersection gives the other set itself.
- `FiniteSet` is functionally equivalent to Python's built in `set` object. Its members can be any SymPy object including other sets.
- `Integers` represents the set of integers $\mathbb{Z}$.
- `Naturals` represents the set of natural numbers $\mathbb{N}$, i.e., the set of positive integers.
- `Naturals0` represents the set of whole numbers $\mathbb{N}_0$, which are all the non-negative integers.
- `Range` represents a range of integers. A range is defined by specifying a start value, an end value, and a step size. The enumeration of a `Range` object

is functionally equivalent to Python's `range` except it supports infinite endpoints, allowing the representation of infinite ranges.
- `Interval` represents an interval of real numbers. It is defined by giving the start and the end points and by specifying if the interval is open or closed on the respective ends.

Other than unevaluated classes of `Union`, `Intersection`, and `Complement` operations, SymPy has the following set classes.

- `ProductSet` defines the Cartesian product of two or more sets. The product set is useful when representing higher dimensional spaces. For example, to represent a three-dimensional space, SymPy uses the Cartesian product of three real sets.
- `ImageSet` represents the image of a function when applied to a particular set. The image set of a function F with respect to a set S is $\{F(x) \mid x \in S\}$. SymPy uses image sets to represent sets of infinite solutions of equations such as $\sin(x) = 0$.
- `ConditionSet` represents a subset of a set whose members satisfy a particular condition. The subset of set S given by the condition H is $\{x \mid H(x), x \in S\}$. SymPy uses condition sets to represent the set of solutions of equations and inequalities, where the equation or the inequality is the condition and the set is the domain over which it is being solved.

A few other classes are implemented as special cases of the classes described above. The set of real numbers, `Reals`, is implemented as a special case of `Interval`. `ComplexRegion` is implemented as a special case of `ImageSet`. `ComplexRegion` supports both polar and rectangular representation of regions on the complex plane.

SM6. Category Theory. SymPy includes a module for dealing with categories—abstract mathematical objects representing classes of structures as classes of objects (points) and morphisms (arrows) between the objects. The module was designed with the following two goals in mind:

1. automatic typesetting of diagrams given by a collection of objects and of morphisms between them, and
2. specification and semi-automatic derivation of properties using commutative diagrams.

As of version 1.0, SymPy only implements the first goal, while a partially working draft of implementation of the second goal is available at https://github.com/scolobb/sympy/tree/ct4-commutativity.

In order to achieve the two goals, the module `sympy.categories` defines several classes representing some of the essential concepts: objects, morphisms, categories, and diagrams. In category theory, the inner structure of objects is often discarded in the favor of studying the properties of morphisms, so the class `Object` is essentially a synonym of the class `Symbol`. There are several morphism classes which do not have a particular internal structure either, though an exception is `CompositeMorphism`, which essentially stores a list of morphisms.

The class `Diagram` captures the properties of morphisms. This class stores a family of morphisms, the corresponding source and target objects, and, possibly, some properties of the morphisms. Generally, no restrictions are imposed on what the properties may be—for example, one might use strings of the form "forall", "exists", "unique", etc. Furthermore, the morphisms of a diagram are grouped into *premises* and *conclusions* in order to be able to represent logical implications of the form "for a collection of morphisms P with properties $p : P \to \Omega$ (the premises), there exists a

collection of morphisms C with properties $c : C \to \Omega$ (the conclusions)", where Ω is the universal collection of properties. Finally, the class `Category` includes a collection of diagrams which are deemed commutative and which therefore define the properties of this category.

Automatic typesetting of diagrams takes a `Diagram` and produces LaTeX code using the `Xy-pic` package. Typesetting is done in two stages: layout and generation of `Xy-pic` code. The layout stage is taken care of by the class `DiagramGrid`, which takes a `Diagram` and lays out the objects in a grid, trying to reduce the average length of the arrows in the final picture. By default, `DiagramGrid` uses a series of triangle-based heuristics to produce a rectangular grid. A linear layout can also be imposed. Furthermore, groups of objects can be given; in this case, the groups will be treated as atomic cells, and the member objects will be typeset independently of the other objects.

The second phase of diagram typesetting consists in actually drawing the picture and is carried out by the class `XypicDiagramDrawer`. An example of a diagram automatically typeset by `DiagramgGrid` and `XypicDiagramDrawer` in given in Figure SM1.

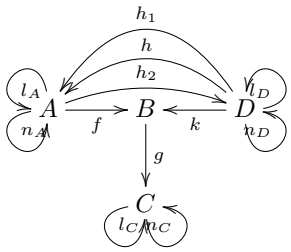


Fig. SM1: An automatically typeset commutative diagram

As far as the second main goal of the module is concerned, the principal idea consists in automatically deciding whether a diagram is commutative or not, given a collection of "axioms": diagrams known to be commutative. The implementation is based on graph embeddings (injective maps): whenever an embedding of a commutative diagram into a given diagram is found, one concludes that the subdiagram is commutative. Deciding commutativity of the whole diagram is therefore based (theoretically) on finding a "cover" of the target diagram by embeddings of the axioms. The naïve implementation proved to be prohibitively slow; a better optimized version is therefore in order, as well as application of heuristics.

SM7. SymPy Gamma. SymPy Gamma is a simple web application that runs on Google App Engine. It executes and displays the results of SymPy expressions as well as additional related computations, in a fashion similar to that of Wolfram|Alpha. For instance, entering an integer will display its prime factors, digits in the base-10 expansion, and a factorization diagram. Entering a function will display its docstring; in general, entering an arbitrary expression will display its derivative, integral, series expansion, plot, and roots.

SymPy Gamma also has several features beyond just computing the results using SymPy.

- SymPy Gamma displays integration and differentiation steps in detail, which can be viewed in Figure SM2:

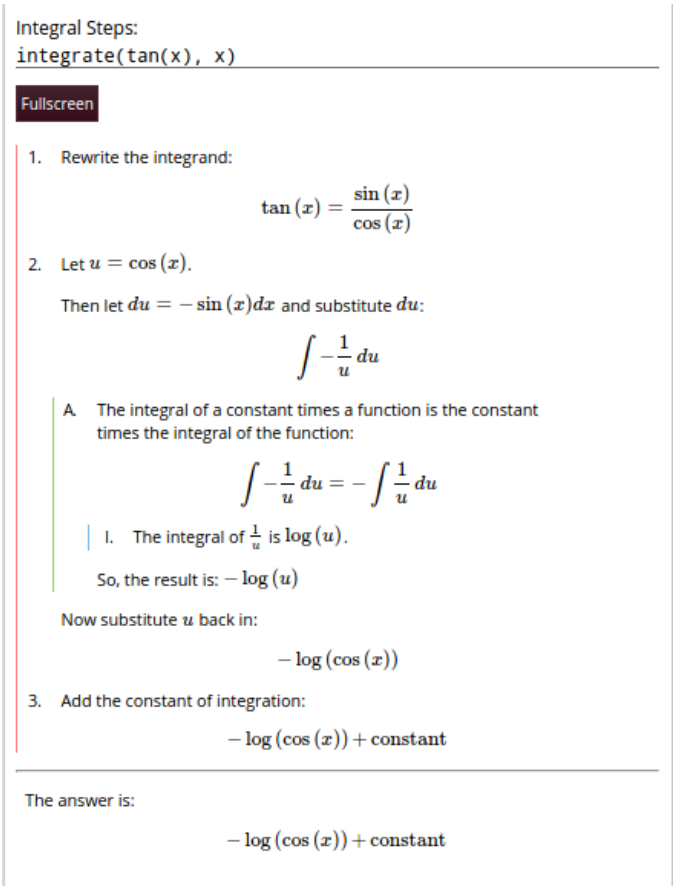


Fig. SM2: Integral steps of $\tan(x)$

- SymPy Gamma displays the factor tree diagrams for different numbers.
- SymPy Gamma saves user search queries, and offers many such similar features for free, which Wolfram|Alpha only offers to its paid users.

Every input query from the user on SymPy Gamma is first parsed by its own parser capable of handling several different forms of function names which SymPy as a library does not support. For instance, SymPy Gamma supports queries like `sin x`, whereas SymPy will only recognise `sin(x)`.

This parser converts the input query to the equivalent SymPy readable code, which is then processed by SymPy, and the result is finally printed with the built-in LaTeX output and rendered by the SymPy Gamma web application.

SM8. SymPy Live. SymPy Live is an online Python shell, which uses the Google App Engine to executes SymPy code. It is integrated in the SymPy documentation examples at http://docs.sympy.org.

This is accomplished by providing a HTML/JavaScript GUI for entering source code and visualization of output, and a server that evaluates the requested source code. It is an interactive AJAX shell that runs SymPy code using Python on the server.

SM9. Comparison with Mathematica. Wolfram Mathematica is a popular proprietary CAS that features highly advanced algorithms, has a core written in C++ [SM15], and interprets its own programming language, Wolfram Language.

Analogous to Lisp S-expressions, Mathematica uses its own style of M-expressions, which are arrays of either atoms or other M-expressions. The first element of the expression identifies the type of the expression and is indexed by zero, and the first argument is indexed starting with one. In SymPy, expression arguments are stored in a Python tuple (that is, an immutable array), while the expression type is identified by the type of the object storing the expression.

Mathematica can associate attributes to its atoms. Attributes may define mathematical properties and behavior of the nodes associated to the atom. In SymPy, the usage of static class fields is roughly similar to Mathematica's attributes, though other programming patterns may also be used to achieve an equivalent behavior such as class inheritance.

Unlike SymPy, Mathematica's expressions are mutable: one can change parts of the expression tree without the need of creating a new object. The mutability of Mathematica expressions allows for a lazy updating of any references to a given data structure.

Products in Mathematica are determined by some built in node types, such as `Times`, `Dot`, and others. `Times` is a representation of the `*` operator, and is always meant to represent a commutative product operator. The other notable product is `Dot`, which represents the `.` operator. This product represents matrix multiplication. It is not commutative. Unlike Mathematica, SymPy determines commutativity with respect to multiplication from the expression type of the factors. Mathematica puts the `Orderless` attribute on the expression type.

Regarding associative expressions, SymPy handles associativity of sums and products by automatically flattening them, Mathematica specifies the `Flat` attribute on the expression type.

Mathematica relies heavily on pattern matching—even the so-called equivalent of function declaration is in reality the definition of a pattern generating an expression tree transformation on input expressions. Mathematica's pattern matching is sensitive to associative, commutative, and one-identity properties of its expression tree nodes. SymPy has various ways to perform pattern matching. All of them play a lesser role in the CAS than in Mathematica and are basically available as a tool to rewrite expressions. The differential equation solver in SymPy somewhat relies on pattern matching to identify differential equation types, but it is envisaged to replace that strategy with analysis of Lie symmetries in the future. Mathematica's real advantage is the ability to add (at runtime) new overloading to the expression builder or specific subnodes. Consider for example:

```
In[1]:= Unprotect[Plus]
Out[1]= {Plus}

In[2]:= Sin[x_]^2 + Cos[y_]^2 := 1

In[3]:= x + Sin[t]^2 + y + Cos[t]^2
Out[3]= 1 + x + y
```

This expression in Mathematica defines a substitution rule that overloads the functionality of the `Plus` node (the node for additions in Mathematica). A symbol with a trailing underscore is treated as a wildcard. Although one may wish to keep this identity unevaluated, this example clearly illustrates the potential to define one's own

immediate transformation rules. In SymPy, the operations constructing the addition node in the expression tree are Python class constructors and cannot be modified at runtime.[1] The way SymPy deals with extending the missing runtime overloadability functionality is by subclassing the node types: subclasses may redefine the class constructor to yield the proper extended functionality.

Unlike SymPy, Mathematica does not support type inheritance or polymorphism [SM4]. SymPy relies heavily on class inheritance, but for the most part, class inheritance is used to make sure that SymPy objects inherit the proper methods and implement the basic hashing system.

While Mathematica interprets nested lists as matrices whenever the sublists have the same length, matrices in SymPy are a type in their own right, allowing ordinary operators and functions (like multiplication and exponentiation) to be used as they traditionally are in mathematics.

```
>>> exp(Matrix([[1, 1],[0, 2]])) * Matrix([a, b])
Matrix([
[E*a + b*(-E + exp(2))],
[             b*exp(2)]])
```

Using the standard multiplication in Mathematica performs an element-wise product and calling the exponential function `Exp` on a matrix returns an element-wise exponentiation of its elements.

Unevaluated expressions in Mathematica can be achieved in various ways, most commonly with the `HoldForm` or `Hold` nodes, that block the evaluation of subnodes by the parser. Such a node cannot be expressed in Python because of greedy evaluation. Whenever needed in SymPy, it is necessary to add the parameter `evaluate=False` to all subnodes.

In Mathematica, the operator `==` returns a boolean whenever it is able to immediately evaluate the truth of the equality, otherwise it returns an `Equal` expression. In SymPy, `==` means structural equality and is always guaranteed to return a boolean expression. To express a mathematical equality in SymPy it is necessary to explicitly construct an instance of the `Equality` class.

SymPy, in accordance with Python (and unlike the usual programming convention), uses ** to express the power operator, while Mathematica uses the more common `^`.

SymPy's use of floating-point numbers is similar to that of most other CASs, including Maple and Maxima. By contrast, Mathematica uses a form of significance arithmetic [SM13] for approximate numbers. This offers further protection against numerical errors, although it comes with its own set of problems (for a critique of significance arithmetic, see Fateman [SM4]). Internally, SymPy's `evalf` method works similarly to Mathematica's significance arithmetic, but the semantics are isolated from the rest of the system.

SM10. Other Projects that use SymPy. There are several projects that use SymPy as a library for implementing a part of their functionality. Some of them are listed below:

- **Cadabra**: Cadabra is a CAS designed specifically for the resolution of problems encountered in field theory.
- **Octave Symbolic**: The Octave-Forge Symbolic package adds symbolic calculation features to GNU Octave. These include common CAS tools such as

[1] Nonetheless, Python supports monkey patching but it is a discouraged programming pattern.

algebraic operations, calculus, equation solving, Fourier and Laplace transforms, variable precision arithmetic, and other features.
- **SymPy.jl**: Provides a Julia interface to SymPy using PyCall.
- **Mathics**: Mathics is a free, general-purpose online CAS featuring Mathematica compatible syntax and functions. It is backed by highly extensible Python code, relying on SymPy for most mathematical tasks.
- **Mathpix**: An iOS App, that detects handwritten math as input, and uses SymPy Gamma to evaluate the math input and generate the relevant steps to solve the problem.
- **IKFast**: IKFast is a robot kinematics compiler provided by OpenRAVE. It analytically solves robot inverse kinematics equations and generates optimized C++ files. It uses SymPy for its internal symbolic mathematics.
- **Sage**: A CAS, visioned to be a viable free open source alternative to Magma, Maple, Mathematica and MATLAB. Sage includes many open source mathematical libraries, including SymPy.
- **SageMathCloud**: SageMathCloud is a web-based cloud computing and course management platform for computational mathematics.
- **PyDy**: Multibody Dynamics with Python.
- **galgebra**: Geometric algebra (previously `sympy.galgebra`).
- **yt**: Python package for analyzing and visualizing volumetric data (`yt.units` uses SymPy).
- **SfePy**: Simple finite elements in Python, see section SM10.1.
- **Quameon**: Quantum Monte Carlo in Python.
- **Lcapy**: Experimental Python package for teaching linear circuit analysis.
- **Quantum Programming in Python**: Quantum 1D Simple Harmonic Oscillator and Quantum Mapping Gate.
- **LaTeX Expression project**: Easy LaTeX typesetting of algebraic expressions in symbolic form with automatic substitution and result computation.
- **Symbolic statistical modeling**: Adding statistical operations to complex physical models.

SM10.1. SfePy. **SfePy** (Simple finite elements in Python), cf. [SM3], is a Python package for solving partial differential equations (PDEs) in 1D, 2D and 3D by the finite element (FE) method [SM16]. SymPy is used within this package mostly for code generation and testing, namely:

- generation of the hierarchical FE basis module, involving generation and symbolic differentiation of 1D Legendre and Lobatto polynomials, constructing the FE basis polynomials [SM14] and generating the C code;
- generation of symbolic conversion formulas for various groups of elastic constants [SM6]: provide any two of the Young's modulus, Poisson's ratio, bulk modulus, Lamé's first parameter, shear modulus (Lamé's second parameter) or longitudinal wave modulus and get the other ones;
- simple physical unit conversions, generation of consistent unit sets;
- testing FE solutions using method of manufactured (analytical) solutions: the differential operator of a PDE is symbolically applied and a symbolic right-hand side is created, evaluated in quadrature points, and subsequently used to obtain a numerical solution that is then compared to the analytical one;
- testing accuracy of 1D, 2D and 3D numerical quadrature formulas (cf. [SM1]) by generating polynomials of suitable orders, integrating them, and comparing the results with those obtained by the numerical quadrature.

SM11. Tensors. Ongoing work to provide the capabilities of tensor computer algebra has so far produced the `tensor` module. It comprises three submodules whose purposes are quite different: `sympy.tensor.indexed` and `sympy.tensor.indexed_methods` support indexed symbols, `sympy.tensor.array` contains facilities to operate on symbolic N-dimensional arrays, and finally `sympy.tensor.tensor` is used to define abstract tensors. The abstract tensors submodule is inspired by xAct [SM10] and Cadabra [SM12]. Canonicalization based on the Butler-Portugal [SM9] algorithm is supported in SymPy. Tensor support in SymPy is currently limited to polynomial tensor expressions.

SM12. Numerical simplification. The `nsimplify` function in SymPy (a wrapper of `identify` in mpmath) attempts to find a simple symbolic expression that evaluates to the same numerical value as the given input. It works by applying a few simple transformations (including square roots, reciprocals, logarithms and exponentials) to the input and, for each transformed value, using the PSLQ algorithm [SM5] to search for a matching algebraic number or optionally a linear combination of user-provided base constants (such as π).

```
>>> t = 1 / (sin(pi/5)+sin(2*pi/5)+sin(3*pi/5)+sin(4*pi/5))**2
>>> nsimplify(t)
-2*sqrt(5)/5 + 1
>>> nsimplify(pi, tolerance=0.01)
22/7
>>> nsimplify(1.783919626661888, [pi], tolerance=1e-12)
pi/(-1/3 + 2*pi/3)
```

SM13. Examples.

SM13.1. Simplification.

- `expand`:
  ```
  >>> expand((x + y)**3)
  x**3 + 3*x**2*y + 3*x*y**2 + y**3
  ```
- `factor`:
  ```
  >>> factor(x**3 + 3*x**2*y + 3*x*y**2 + y**3)
  (x + y)**3
  ```
- `collect`:
  ```
  >>> collect(y*x**2 + 3*x**2 - x*y + x - 1, x)
  x**2*(y + 3) + x*(-y + 1) - 1
  ```
- `cancel`:
  ```
  >>> cancel((x**2 + 2*x + 1)/(x**2 - 1))
  (x + 1)/(x - 1)
  ```
- `apart`:
  ```
  >>> apart((x**3 + 4*x - 1)/(x**2 - 1))
  x + 3/(x + 1) + 2/(x - 1)
  ```
- `trigsimp`:
  ```
  >>> trigsimp(cos(x)**2*tan(x) - sin(2*x))
  -sin(2*x)/2
  ```

SM13.2. Polynomials.

- Factorization:
  ```
  >>> t = symbols("t")
  >>> f = (2115*x**4*y + 45*x**3*z**3*t**2 - 45*x**3*t**2 -
  ...      423*x*y**4 - 47*x*y**3 + 141*x*y*z**3 + 94*x*y*z*t -
  ```

```
...      9*y**3*z**3*t**2 + 9*y**3*t**2 - y**2*z**3*t**2 +
...      y**2*t**2 + 3*z**6*t**2 +  2*z**4*t**3 - 3*z**3*t**2 -
...      2*z*t**3)
>>> factor(f)
(t**2*z**3 - t**2 + 47*x*y)*(2*t*z + 45*x**3 - 9*y**3 - y**2 +
 3*z**3)
```

- Gröbner bases:

```
>>> x0, x1, x2 = symbols('x:3')
>>> I = [x0 + 2*x1 + 2*x2 - 1,
...      x0**2 + 2*x1**2 + 2*x2**2 - x0,
...      2*x0*x1 + 2*x1*x2 - x1]
>>> groebner(I, order='lex')
GroebnerBasis([7*x0 - 420*x2**3 + 158*x2**2 + 8*x2 - 7,
7*x1 + 210*x2**3 - 79*x2**2 + 3*x2,
84*x2**4 - 40*x2**3 + x2**2 + x2], x0, x1, x2, domain='ZZ',
order='lex')
```

- Root isolation:

```
>>> f = 7*z**4 - 19*z**3 + 20*z**2 + 17*z + 20
>>> intervals(f, all=True, eps=0.001)
([],
 [((-425/1024 - 625*I/1024, -1485/3584 - 2185*I/3584), 1),
  ((-425/1024 + 2185*I/3584, -1485/3584 + 625*I/1024), 1),
  ((3175/1792 - 2605*I/1792, 1815/1024 - 10415*I/7168), 1),
  ((3175/1792 + 10415*I/7168, 1815/1024 + 2605*I/1792), 1)])
```

SM13.3. Solvers.

- Single solution:

```
>>> solveset(x - 1, x)
{1}
```

- Finite solution set, quadratic equation:

```
>>> solveset(x**2 - pi**2, x)
{-pi, pi}
```

- No solution:

```
>>> solveset(1, x)
EmptySet()
```

- Interval solution:

```
>>> solveset(x**2 - 3 > 0, x, domain=S.Reals)
(-oo, -sqrt(3)) U (sqrt(3), oo)
```

- Infinitely many solutions:

```
>>> solveset(x - x, x, domain=S.Reals)
(-oo, oo)
>>> solveset(x - x, x, domain=S.Complexes)
S.Complexes
```

- Linear systems (`linsolve`)

```
>>> A = Matrix([[1, 2, 3], [4, 5, 6], [7, 8, 10]])
>>> b = Matrix([3, 6, 9])
>>> linsolve((A, b), x, y, z)
{(-1, 2, 0)}
>>> linsolve(Matrix(([1, 1, 1, 1], [1, 1, 2, 3])), (x, y, z))
{(-y - 1, y, 2)}
```

Below are examples of `solve` applied to problems not yet handled by `solveset`.

- Nonlinear (multivariate) system of equations (the intersection of a circle and a parabola):

```
>>> solve([x**2 + y**2 - 16, 4*x - y**2 + 6], x, y)
[(-2 + sqrt(14), -sqrt(-2 + 4*sqrt(14))),
 (-2 + sqrt(14), sqrt(-2 + 4*sqrt(14))),
 (-sqrt(14) - 2, -I*sqrt(2 + 4*sqrt(14))),
 (-sqrt(14) - 2, I*sqrt(2 + 4*sqrt(14)))]
```

- Transcendental equations:

```
>>> solve((x + log(x))**2 - 5*(x + log(x)) + 6, x)
[LambertW(exp(2)), LambertW(exp(3))]
>>> solve(x**3 + exp(x))
[-3*LambertW((-1)**(2/3)/3)]
```

SM13.4. Matrices.

- Matrix expressions

```
>>> m, n, p = symbols("m, n, p", integer=True)
>>> R = MatrixSymbol("R", m, n)
>>> S = MatrixSymbol("S", n, p)
>>> T = MatrixSymbol("T", m, p)
>>> U = R*S + 2*T
>>> U.shape
(m, p)
>>> U[0, 1]
2*T[0, 1] + Sum(R[0, _k]*S[_k, 1], (_k, 0, n - 1))
```

- Block Matrices

```
>>> n, m, l = symbols('n m l')
>>> X = MatrixSymbol('X', n, n)
>>> Y = MatrixSymbol('Y', m ,m)
>>> Z = MatrixSymbol('Z', n, m)
>>> B = BlockMatrix([[X, Z], [ZeroMatrix(m, n), Y]])
>>> B
Matrix([
[X, Z],
[0, Y]])
>>> B[0, 0]
X[0, 0]
>>> B.shape
(m + n, m + n)
```

SM14. References.

REFERENCES

[SM1] M. Abramowitz and I. A. Stegun, *Handbook of Mathematical Functions with Formulas, Graphs, and Mathematical Tables*, Dover Publications, New York, NY, USA, ninth printing ed., 1964, http://www.math.ucla.edu/~cbm/aands/.

[SM2] R. P. Brent and P. Zimmermann, *Modern Computer Arithmetic*, Cambridge University Press, version 0.5.1 ed.

[SM3] R. Cimrman, *SfePy - write your own FE application*, in Proceedings of the 6th European Conference on Python in Science (EuroSciPy 2013), P. de Buyl and N. Varoquaux, eds., 2014, pp. 65–70. http://arxiv.org/abs/1404.6391.

[SM4] R. J. Fateman, *A review of Mathematica*, Journal of Symbolic Computation, 13 (1992),

pp. 545–579, http://dx.doi.org/DOI:10.1016/S0747-7171(10)80011-2.
[SM5] H. R. P. Ferguson, D. H. Bailey, and S. Arno, *Analysis of PSLQ, an integer relation finding algorithm*, Mathematics of Computation, 68 (1999), pp. 351–369.
[SM6] Y. C. Fung, *A first course in continuum mechanics*, Pearson, third edition ed., 1993.
[SM7] D. Gruntz, *On Computing Limits in a Symbolic Manipulation System*, PhD thesis, Swiss Federal Institute of Technology, Zürich, Switzerland, 1996.
[SM8] D. Gruntz and W. Koepf, *Formal power series*, (1993).
[SM9] L. R. U. Manssur, R. Portugal, and B. F. Svaiter, *Group-theoretic approach for symbolic tensor manipulation*, International Journal of Modern Physics C, 13 (2002), http://dx.doi.org/http://dx.doi.org/10.1142/S0129183102004571.
[SM10] J. Martín-García, *xAct, efficient tensor computer algebra*, 2002-2016, http://metric.iem.csic.es/Martin-Garcia/xAct/.
[SM11] M. Moskewicz, C. Madigan, and S. Malik, *Method and system for efficient implementation of boolean satisfiability*, Aug. 26 2008, http://www.google.co.in/patents/US7418369. US Patent 7,418,369.
[SM12] K. Peeters, *Cadabra: a field-theory motivated symbolic computer algebra system*, Computer Physics Communications, (2007).
[SM13] M. Sofroniou and G. Spaletta, *Precise numerical computation*, Journal of Logic and Algebraic Programming, 64 (2005), pp. 113–134.
[SM14] P. Solin, K. Segeth, and I. Dolezel, *Higher-Order Finite Element Methods*, Chapman & Hall / CRC Press, 2003.
[SM15] S. Wolfram, *The Mathematica Book*, Wolfram Media, Champaign, IL, USA, fifth ed., 2003.
[SM16] O. Zienkiewicz, R. Taylor, and J. Zhu, *The Finite Element Method: Its Basis and Fundamentals*, Butterworth-Heinemann, seventh edition ed., 2013, http://dx.doi.org/http://dx.doi.org/10.1016/B978-1-85617-633-0.00019-8.

PeerJ Preprints NOT PEER-REVIEWED

SYMPY: SYMBOLIC COMPUTING IN PYTHON

AARON MEURER*, CHRISTOPHER P. SMITH†, MATEUSZ PAPROCKI‡, ONDŘEJ ČERTÍK§, MATTHEW ROCKLIN¶, AMIT KUMAR‖, SERGIU IVANOV#, JASON K. MOORE††, SARTAJ SINGH‡‡, THILINA RATHNAYAKE§§, SEAN VIG¶¶, BRIAN E. GRANGER‖‖, RICHARD P. MULLER##, FRANCESCO BONAZZI[1], HARSH GUPTA[2], SHIVAM VATS[3], FREDRIK JOHANSSON[4], FABIAN PEDREGOSA[5], MATTHEW J. CURRY[6], ASHUTOSH SABOO[7], ISURU FERNANDO[8], SUMITH KULAL[9], ROBERT CIMRMAN[10], AND ANTHONY SCOPATZ[11]

Abstract. SymPy is an open source computer algebra system written in pure Python. It is built with a focus on extensibility and ease of use, through both interactive and programmatic applications. These characteristics have led SymPy to become the standard symbolic library for the scientific Python ecosystem. This paper presents the architecture of SymPy, a description of its features, and a discussion of select domain specific submodules.

1. Introduction.

SymPy is a full featured computer algebra system (CAS) written in the Python programming language [24]. It is free and open source software, being licensed under the 3-clause BSD license [36]. The SymPy project was started

*University of South Carolina, Columbia, SC 29201 (asmeurer@gmail.com).
†Polar Semiconductor, Inc., Bloomington, MN 55425 (smichr@gmail.com).
‡Continuum Analytics, Inc., Austin, TX 78701 (mattpap@gmail.com).
§Los Alamos National Laboratory, Los Alamos, NM 87545 (certik@lanl.gov).
¶Continuum Analytics, Inc., Austin, TX 78701 (mrocklin@gmail.com).
‖Delhi Technological University, Shahbad Daulatpur, Bawana Road, New Delhi 110042, India (dtu.amit@gmail.com).
#Université Paris Est Créteil, 61 av. Général de Gaulle, 94010 Créteil, France (sergiu.ivanov@u-pec.fr).
††University of California, Davis, Davis, CA 95616 (jkm@ucdavis.edu).
‡‡Indian Institute of Technology (BHU), Varanasi, Uttar Pradesh 221005, India (singhsartaj94@gmail.com).
§§University of Moratuwa, Bandaranayake Mawatha, Katubedda, Moratuwa 10400, Sri Lanka (thilinarmtb.10@cse.mrt.ac.lk).
¶¶University of Illinois at Urbana-Champaign, Urbana, IL 61801 (sean.v.775@gmail.com).
‖‖California Polytechnic State University, San Luis Obispo, CA 93407 (ellisonbg@gmail.com).
##Center for Computing Research, Sandia National Laboratories, Albuquerque, NM 87185 (rmuller@sandia.gov).
[1]Max Planck Institute of Colloids and Interfaces, Department of Theory and Bio-Systems, Am Mühlenberg 1, 14424 Potsdam, Germany (francesco.bonazzi@mpikg.mpg.de).
[2]Indian Institute of Technology Kharagpur, Kharagpur, West Bengal 721302, India (hargup@protonmail.com).
[3]Indian Institute of Technology Kharagpur, Kharagpur, West Bengal 721302, India (shivamvats.iitkgp@gmail.com).
[4]INRIA Bordeaux-Sud-Ouest – LFANT project-team, 200 Avenue de la Vieille Tour, 33405 Talence, France (fredrik.johansson@gmail.com).
[5]INRIA – SIERRA project-team, 2 Rue Simone IFF, 75012 Paris, France (f@bianp.net).
[6]Department of Physics and Astronomy, University of New Mexico, Albuquerque, NM 87131 (mattjcurry@gmail.com).
[7]Birla Institute of Technology and Science, Pilani, K.K. Birla Goa Campus, NH 17B Bypass Road, Zuarinagar, Sancoale, Goa 403726, India (ashutosh.saboo@gmail.com).
[8]University of Moratuwa, Bandaranayake Mawatha, Katubedda, Moratuwa 10400, Sri Lanka (isuru.11@cse.mrt.ac.lk).
[9]Indian Institute of Technology Bombay, Powai, Mumbai, Maharashtra 400076, India (sumith@cse.iitb.ac.in).
[10]New Technologies – Research Centre, University of West Bohemia, Univerzitní 8, 306 14 Plzeň, Czech Republic (cimrman3@ntc.zcu.cz).
[11]University of South Carolina, Columbia, SC 29201 (scopatz@cec.sc.edu).

PeerJ Preprints | https://doi.org/10.7287/peerj.preprints.2083v2 | CC-BY 4.0 Open Access | rec: 30 May 2016, publ: 30 May 2016

PeerJ Preprints NOT PEER-REVIEWED

by Ondřej Čertík in 2005, and it has since grown to over 500 contributors. Currently, SymPy is developed on GitHub using a bazaar community model [32]. The accessibility of the codebase and the open community model allow SymPy to rapidly respond to the needs of users and developers.

Python is a dynamically typed programming language that has a focus on ease of use and readability. Due in part to this focus, it has become a popular language for scientific computing and data science, with a broad ecosystem of libraries [27]. SymPy is itself used by many libraries and tools to support research within a variety of domains, such as Sage [39] (pure mathematics), yt [44] (astronomy and astrophysics), PyDy [15] (multibody dynamics), and SfePy [10] (finite elements).

Unlike many CASs, SymPy does not invent its own programming language. Python itself is used both for the internal implementation and end user interaction. The exclusive usage of a single programming language makes it easier for people already familiar with that language to use or develop SymPy. Simultaneously, it enables developers to focus on mathematics, rather than language design.

SymPy is designed with a strong focus on usability as a library. Extensibility is important in its application program interface (API) design. Thus, SymPy makes no attempt to extend the Python language itself. The goal is for users of SymPy to be able to include SymPy alongside other Python libraries in their workflow, whether that be in an interactive environment or as a programmatic part in a larger system.

As a library, SymPy does not have a built-in graphical user interface (GUI). However, SymPy exposes a rich interactive display system, including registering printers with Jupyter [29] frontends, including the Notebook and Qt Console, which will render SymPy expressions using MathJax [9] or LaTeX.

The remainder of this paper discusses key components of the SymPy software. Section 2 discusses the architecture of SymPy. Section 3 enumerates the features of SymPy and takes a closer look at some of the important ones. The section 4 looks at the numerical features of SymPy and its dependency library, mpmath. Section 5 looks at the domain specific physics submodules for performing symbolic and numerical calculations in classical mechanics and quantum mechanics. Conclusions and future directions for SymPy are given in section 6.

2. Architecture.

Software architecture is of central importance in any large software project because it establishes predictable patterns of usage and development [38]. This section describes the essential structural components of SymPy, provides justifications for the design decisions that have been made, and gives example user-facing code as appropriate.

2.1. Basic Usage.

The following statement imports all SymPy functions into the global Python namespace. From here on, all examples in this paper assume that this statement has been executed.

```
>>> from sympy import *
```

Symbolic variables, called symbols, must be defined and assigned to Python variables before they can be used. This is typically done through the `symbols` function, which may create multiple symbols in a single function call. For instance,

```
>>> x, y, z = symbols('x y z')
```

creates three symbols representing variables named x, y, and z. In this particular instance, these symbols are all assigned to Python variables of the same name. However, the user is free to assign them to different Python variables, while representing the same symbol, such as `a, b, c = symbols('x y z')`. In order to minimize potential confusion, though, all examples in this paper will assume that the symbols `x`, `y`, and

PeerJ Preprints | https://doi.org/10.7287/peerj.preprints.2083v2 | CC-BY 4.0 Open Access | rec: 30 May 2016, publ: 30 May 2016

PeerJ Preprints NOT PEER-REVIEWED

`z` have been assigned to Python variables identical to their symbolic names.

Expressions are created from symbols using Python's mathematical syntax. Note that in Python, exponentiation is represented by the `**` binary infix operator. For instance, the following Python code creates the expression $(x^2 - 2x + 3)/y$.

```
>>> (x**2 - 2*x + 3)/y
(x**2 - 2*x + 3)/y
```

Importantly, SymPy expressions are immutable. This simplifies the design of SymPy by allowing expression interning. It also enables expressions to be hashed and stored in Python dictionaries, thereby permitting features such as caching.

2.2. The Core. A computer algebra system (CAS) represents mathematical expressions as data structures. For example, the mathematical expression $x + y$ is represented as a tree with three nodes, $+$, x, and y, where x and y are ordered children of $+$. As users manipulate mathematical expressions with traditional mathematical syntax, the CAS manipulates the underlying data structures. Automated optimizations and computations such as integration, simplification, etc. are all functions that consume and produce expression trees.

In SymPy every symbolic expression is an instance of a Python `Basic` class, a superclass of all SymPy types providing common methods to all SymPy tree-elements, such as traversals. The children of a node in the tree are held in the `args` attribute. A terminal or leaf node in the expression tree has empty `args`.

For example, consider the expression $xy + 2$:

```
>>> expr = x*y + 2
```

By order of operations, the parent of the expression tree for `expr` is an addition, so it is of type `Add`. The child nodes of `expr` are `2` and `x*y`.

```
>>> type(expr)
<class 'sympy.core.add.Add'>
>>> expr.args
(2, x*y)
```

Descending further down into the expression tree yields the full expression. For example, the next child node (given by `expr.args[0]`) is `2`. Its class is `Integer`, and it has an empty `args` tuple, indicating that it is a leaf node.

```
>>> expr.args[0]
2
>>> type(expr.args[0])
<class 'sympy.core.numbers.Integer'>
>>> expr.args[0].args
()
```

A useful way to view an expression tree is using the `srepr` function, which returns a string representation of an expression as valid Python code with all the nested class constructor calls to create the given expression.

```
>>> srepr(expr)
"Add(Mul(Symbol('x'), Symbol('y')), Integer(2))"
```

Every SymPy expression satisfies a key identity invariant:

```
expr.func(*expr.args) == expr
```

This means that expressions are rebuildable from their `args`.[1] Note that in SymPy the `==` operator represents exact structural equality, not mathematical equality. This allows testing if any two expressions are equal to one another as expression trees. For

[1] `expr.func` is used instead of `type(expr)` to allow the function of an expression to be distinct from its actual Python class. In most cases the two are the same.

PeerJ Preprints | https://doi.org/10.7287/peerj.preprints.2083v2 | CC-BY 4.0 Open Access | rec: 30 May 2016, publ: 30 May 2016

PeerJ Preprints NOT PEER-REVIEWED

example, even though $(x+1)^2$ and x^2+2x+1 are equal mathematically, SymPy gives

```
>>> (x + 1)**2 == x**2 + 2*x + 1
False
```

because they are different as expression trees (the former is a `Pow` object and the latter is an `Add` object).

Python allows classes to override mathematical operators. The Python interpreter translates the above `x*y + 2` to, roughly, `(x.__mul__(y)).__add__(2)`. Both `x` and `y`, returned from the `symbols` function, are `Symbol` instances. The `2` in the expression is processed by Python as a literal, and is stored as Python's built in `int` type. When `2` is passed to the `__add__` method of `Symbol`, it is converted to the SymPy type `Integer(2)` before being stored in the resulting expression tree. In this way, SymPy expressions can be built in the natural way using Python operators and numeric literals.

2.3. Assumptions. SymPy performs logical inference through its assumptions system. The assumptions system allows users to specify that symbols have certain common mathematical properties, such as being positive, imaginary, or integral. SymPy is careful to never perform simplifications on an expression unless the assumptions allow them. For instance, the identity $\sqrt{t^2} = t$ holds if t is nonnegative ($t \geq 0$). If t is real, the identity $\sqrt{t^2} = |t|$ holds. However, for general complex t, no such identity holds.

By default, SymPy performs all calculations assuming that symbols are complex valued. This assumption makes it easier to treat mathematical problems in full generality.

```
>>> t = Symbol('t')
>>> sqrt(t**2)
sqrt(t**2)
```

By assuming the most general case, that symbols are complex by default, SymPy avoids performing mathematically invalid operations. However, in many cases users will wish to simplify expressions containing terms like $\sqrt{t^2}$.

Assumptions are set on `Symbol` objects when they are created. For instance `Symbol('t', positive=True)` will create a symbol named `t` that is assumed to be positive.

```
>>> t = Symbol('t', positive=True)
>>> sqrt(t**2)
t
```

Some of the common assumptions that SymPy allows are `positive`, `negative`, `real`, `nonpositive`, `nonnegative`, `real`, `integer`, and `commutative`.[2] Assumptions on any object can be checked with the `is_`*`assumption`* attributes, like `t.is_positive`.

Assumptions are only needed to restrict a domain so that certain simplifications can be performed. They are not required to make the domain match the input of a function. For instance, one can create the object $\sum_{n=0}^{m} f(n)$ as `Sum(f(n), (n, 0, m))` without setting `integer=True` when creating the Symbol object `n`.

The assumptions system additionally has deductive capabilities. The assumptions use a three-valued logic using the Python built in objects `True`, `False`, and `None`. `None` represents the "unknown" case. This could mean that given assumptions do not unambiguously specify the truth of an attribute. For instance, `Symbol('x', real=True).is_positive` will give `None` because a real symbol might be positive or negative. The `None` could also mean that not enough is known or implemented to compute

[2] If A and B are Symbols created with `commutative=False` then SymPy will keep $A \cdot B$ and $B \cdot A$ distinct.

PeerJ Preprints | https://doi.org/10.7287/peerj.preprints.2083v2 | CC-BY 4.0 Open Access | rec: 30 May 2016, publ: 30 May 2016

PeerJ Preprints NOT PEER-REVIEWED

the given fact. For instance, `(pi + E).is_irrational` gives `None`, because determining whether $\pi + e$ is rational or irrational is an open problem in mathematics [23].

Basic implications between the facts are used to deduce assumptions. For instance, the assumptions system knows that being an integer implies being rational, so `Symbol('x', integer=True).is_rational` returns `True`. Furthermore, expressions compute the assumptions on themselves based on the assumptions of their arguments. For instance, if `x` and `y` are both created with `positive=True`, then `(x + y).is_positive` will be `True` whereas `(x - y).is_positive` will be `None`.

2.4. Extensibility. While the core of SymPy is relatively small, it has been extended to a wide variety of domains by a broad range of contributors. This is due in part because the same language, Python, is used both for the internal implementation and the external usage by users. All of the extensibility capabilities available to users are also utilized by SymPy itself. This eases the transition pathway from SymPy user to SymPy developer.

The typical way to create a custom SymPy object is to subclass an existing SymPy class, usually `Basic`, `Expr`, or `Function`. All SymPy classes used for expression trees[3] should be subclasses of the base class `Basic`, which defines some basic methods for symbolic expression trees. `Expr` is the subclass for mathematical expressions that can be added and multiplied together. Instances of `Expr` typically represent complex numbers, but may also include other "rings" like matrix expressions. Not all SymPy classes are subclasses of `Expr`. For instance, logic expressions such as `And(x, y)` are subclasses of `Basic` but not of `Expr`.

The `Function` class is a subclass of `Expr` which makes it easier to define mathematical functions called with arguments. This includes named functions like $\sin(x)$ and $\log(x)$ as well as undefined functions like $f(x)$. Subclasses of `Function` should define a class method `eval`, which returns values for which the function should be automatically evaluated, and `None` for arguments that should not be automatically evaluated.

Many SymPy functions perform various evaluations down the expression tree. Classes define their behavior in such functions by defining a relevant `_eval_*` method. For instance, an object can indicate to the `diff` function how to take the derivative of itself by defining the `_eval_derivative(self, x)` method, which may in turn call `diff` on its `args`. The most common `_eval_*` methods relate to the assumptions. `_eval_is_`*`assumption`* defines the assumptions for *assumption*.

As an example of the notions presented in this section, Listing 1 presents a minimal version of the gamma function $\Gamma(x)$ from SymPy, which evaluates itself on positive integer arguments, has the positive and real assumptions defined, can be rewritten in terms of factorial with `gamma(x).rewrite(factorial)`, and can be differentiated. `fdiff` is a convenience method for subclasses of `Function`. `fdiff` returns the derivative of the function without considering the chain rule. `self.func` is used throughout instead of referencing `gamma` explicitly so that potential subclasses of `gamma` can reuse the methods.

Listing 1: A minimal implementation of `sympy.gamma`.

```
from sympy import Integer, Function, floor, factorial, polygamma

class gamma(Function)
```

[3]Some internal classes, such as those used in the polynomial module, do not follow this rule for efficiency reasons.

PeerJ Preprints | https://doi.org/10.7287/peerj.preprints.2083v2 | CC-BY 4.0 Open Access | rec: 30 May 2016, publ: 30 May 2016

PeerJ Preprints NOT PEER-REVIEWED

```
    @classmethod
    def eval(cls, arg):
        if isinstance(arg, Integer) and arg.is_positive:
            return factorial(arg - 1)

    def _eval_is_positive(self):
        x = self.args[0]
        if x.is_positive:
            return True
        elif x.is_noninteger:
            return floor(x).is_even

    def _eval_is_real(self):
        x = self.args[0]
        # noninteger means real and not integer
        if x.is_positive or x.is_noninteger:
            return True

    def _eval_rewrite_as_factorial(self, z):
        return factorial(z - 1)

    def fdiff(self, argindex=1):
        from sympy.core.function import ArgumentIndexError
        if argindex == 1:
            return self.func(self.args[0])*polygamma(0, self.args[0])
        else:
            raise ArgumentIndexError(self, argindex)
```

The gamma function implemented in SymPy has many more capabilities than the above listing, such as evaluation at rational points and series expansion.

3. Features. Although SymPy's extensive feature set cannot be covered in-depth in this paper, calculus and other bedrock areas are discussed in their own subsections. Additionally, Table 1 gives a compact listing of all major capabilities present in the SymPy codebase. This grants a sampling from the breadth of topics and application domains that SymPy services. Unless stated otherwise, all features noted in Table 1 are symbolic in nature. Numeric features are discussed in Section 4.

Table 1: SymPy Features and Descriptions

Feature	Description
Calculus	Algorithms for computing derivatives, integrals, and limits.
Category Theory	Representation of objects, morphisms, and diagrams. Tools for drawing diagrams with Xy-pic.
Code Generation	Generation of compilable and executable code in a variety of different programming languages from expressions directly. Target languages include C, Fortran, Julia, JavaScript, Mathematica, MATLAB and Octave, Python, and Theano.

PeerJ Preprints | https://doi.org/10.7287/peerj.preprints.2083v2 | CC-BY 4.0 Open Access | rec: 30 May 2016, publ: 30 May 2016

PeerJ Preprints NOT PEER-REVIEWED

Combinatorics & Group Theory	Permutations, combinations, partitions, subsets, various permutation groups (such as polyhedral, Rubik, symmetric, and others), Gray codes [26], and Prufer sequences [4].
Concrete Math	Summation, products, tools for determining whether summation and product expressions are convergent, absolutely convergent, hypergeometric, and for determining other properties; computation of Gosper's normal form [31] for two univariate polynomials.
Cryptography	Block and stream ciphers, including shift, Affine, substitution, Vigenère's, Hill's, bifid, RSA, Kid RSA, linear-feedback shift registers, and Elgamal encryption.
Differential Geometry	Representations of manifolds, metrics, tensor products, and coordinate systems in Riemannian and pseudo-Riemannian geometries [40].
Geometry	Representations of 2D geometrical entities, such as lines and circles. Enables queries on these entities, such as asking the area of an ellipse, checking for collinearity of a set of points, or finding the intersection between objects.
Lie Algebras	Representations of Lie algebras and root systems.
Logic	Boolean expressions, equivalence testing, satisfiability, and normal forms.
Matrices	Tools for creating matrices of symbols and expressions. Both sparse and dense representations, as well as symbolic linear algebraic operations (e.g., inversion and factorization), are supported.
Matrix Expressions	Matrices with symbolic dimensions (unspecified entries). Block matrices.
Number Theory	Prime number generation, primality testing, integer factorization, continued fractions, Egyptian fractions, modular arithmetic, quadratic residues, partitions, binomial and multinomial coefficients, prime number tools, hexidecimal digits of pi, and integer factorization.
Plotting	Hooks for visualizing expressions via matplotlib [20] or as text drawings when lacking a graphical back-end. 2D function plotting, 3D function plotting, and 2D implicit function plotting are supported.
Polynomials	Polynomial algebras over various coefficient domains. Functionality ranges from simple operations (e.g., polynomial division) to advanced computations (e.g., Gröbner bases [1] and multivariate factorization over algebraic number domains).
Printing	Functions for printing SymPy expressions in the terminal with ASCII or Unicode characters and converting SymPy expressions to LaTeX and MathML.
Quantum Mechanics	Quantum states, bra–ket notation, operators, basis sets, representations, tensor products, inner products, outer products, commutators, anticommutators, and specific quantum system implementations.
Series	Series expansion, sequences, and limits of sequences. This includes Taylor, Laurent, and Puiseux series as well as special series, such as Fourier and formal power series.

PeerJ Preprints | https://doi.org/10.7287/peerj.preprints.2083v2 | CC-BY 4.0 Open Access | rec: 30 May 2016, publ: 30 May 2016

PeerJ Preprints NOT PEER-REVIEWED

Sets	Representations of empty, finite, and infinite sets. This includes special sets such as for all natural, integer, and complex numbers. Operations on sets such as union, intersection, Cartesian product, and building sets from other sets are supported.
Simplification	Functions for manipulating and simplifying expressions. Includes algorithms for simplifying hypergeometric functions, trigonometric expressions, rational functions, combinatorial functions, square root denesting, and common subexpression elimination.
Solvers	Functions for symbolically solving equations, systems of equations, both linear and non-linear, inequalities, ordinary differential equations, partial differential equations, Diophantine equations, and recurrence relations.
Special Functions	Implementations of a number of well known special functions, including Dirac delta, Gamma, Beta, Gauss error functions, Fresnel integrals, Exponential integrals, Logarithmic integrals, Trigonometric integrals, Bessel, Hankel, Airy, B-spline, Riemann Zeta, Dirichlet eta, polylogarithm, Lerch transcendent, hypergeometric, elliptic integrals, Mathieu, Jacobi polynomials, Gegenbauer polynomial, Chebyshev polynomial, Legendre polynomial, Hermite polynomial, Laguerre polynomial, and spherical harmonic functions.
Statistics	Support for a random variable type as well as the ability to declare this variable from prebuilt distribution functions such as Normal, Exponential, Coin, Die, and other custom distributions [35].
Tensors	Symbolic manipulation of indexed objects.
Vectors	Basic operations on vectors and differential calculus with respect to 3D Cartesian coordinate systems.

3.1. Simplification. The generic way to simplify an expression is by calling the `simplify` function. It must be emphasized that simplification is not an unambiguously defined mathematical operation [8]. The `simplify` function applies several simplification routines along with heuristics to make the output expression as "simple" as possible.

It is often preferable to apply more directed simplification functions. These apply very specific rules to the input expression and are typically able to make guarantees about the output. For instance, the `factor` function, given a polynomial with rational coefficients in several variables, is guaranteed to produce a factorization into irreducible factors. Table 2 lists common simplification functions.

Table 2: Some SymPy Simplification Functions

`expand`	expand the expression
`factor`	factor a polynomial into irreducibles
`collect`	collect polynomial coefficients
`cancel`	rewrite a rational function as p/q with common factors canceled
`apart`	compute the partial fraction decomposition of a rational function

PeerJ Preprints | https://doi.org/10.7287/peerj.preprints.2083v2 | CC-BY 4.0 Open Access | rec: 30 May 2016, publ: 30 May 2016

PeerJ Preprints NOT PEER-REVIEWED

Substitutions are performed using the `.subs` method.

```
>>> (sin(x) + x**2 + 1).subs(x, y + 1)
(y + 1)**2 + sin(y + 1) + 1
```

3.2. Calculus. Integrals are calculated with the `integrate` function. SymPy implements a combination of the Risch algorithm [6], table lookups, a reimplementation of Manuel Bronstein's "Poor Man's Integrator" [5], and an algorithm for computing integrals based on Meijer G-functions [33, 34]. These allow SymPy to compute a wide variety of indefinite and definite integrals. The Meijer G-function algorithm and the Risch algorithm are respectively demonstrated below by the computation of

$$\int_0^\infty e^{-st} \log(t)\, dt = -\frac{\log(s) + \gamma}{s}$$

and

$$\int \frac{-2x^2 (\log(x) + 1) e^{x^2} + \left(e^{x^2} + 1\right)^2}{x(e^{x^2} + 1)^2 (\log(x) + 1)}\, dx = \log(\log(x) + 1) + \frac{1}{e^{x^2} + 1}.$$

```
>>> s, t = symbols('s t', positive=True)
>>> integrate(exp(-s*t)*log(t), (t, 0, oo)).simplify()
-(log(s) + EulerGamma)/s
>>> integrate((-2*x**2*(log(x) + 1)*exp(x**2) +
... (exp(x**2) + 1)**2)/(x*(exp(x**2) + 1)**2*(log(x) + 1)), x)
log(log(x) + 1) + 1/(exp(x**2) + 1)
```

Derivatives are computed with the `diff` function, which recursively uses the various differentiation rules.

```
>>> diff(sin(x)*exp(x), x)
exp(x)*sin(x) + exp(x)*cos(x)
```

Summations and products are computed with `summation` and `product`, respectively. Summations are computed using a combination of Gosper's algorithm [17], an algorithm that uses Meijer G-functions [33, 34], and heuristics. Products are computed via a suite of heuristics.

```
>>> i, n = symbols('i n')
>>> summation(2**i, (i, 0, n - 1))
2**n - 1
>>> summation(i*factorial(i), (i, 1, n))
n*factorial(n) + factorial(n) - 1
```

Limits are computed with the `limit` function. The limit module implements the Gruntz algorithm [18] for computing symbolic limits. For example, the following computes $\lim_{x\to\infty} x\sin(\frac{1}{x}) = 1$. Note that SymPy denotes ∞ as `oo`.

```
>>> limit(x*sin(1/x), x, oo)
1
```

As a more complex example, SymPy computes

$$\lim_{x\to 0} \left(2e^{\frac{1-\cos(x)}{\sin(x)}} - 1\right)^{\frac{\sinh(x)}{\operatorname{atan}^2(x)}} = e.$$

```
>>> limit((2*E**((1-cos(x))/sin(x))-1)**(sinh(x)/atan(x)**2), x, 0)
E
```


PeerJ Preprints | https://doi.org/10.7287/peerj.preprints.2083v2 | CC-BY 4.0 Open Access | rec: 30 May 2016, publ: 30 May 2016

PeerJ Preprints NOT PEER-REVIEWED

Integrals, derivatives, summations, products, and limits that cannot be computed return unevaluated objects. These can also be created directly if the user chooses.

```
>>> integrate(x**x, x)
Integral(x**x, x)
>>> Sum(2**i, (i, 0, n - 1))
Sum(2**i, (i, 0, n - 1))
```

3.3. Polynomials. SymPy implements a suite of algorithms for polynomial manipulation, which ranges from relatively simple algorithms for doing arithmetic of polynomials, to advanced methods for factoring multivariate polynomials into irreducibles, symbolically determining real and complex root isolation intervals, or computing Gröbner bases.

Polynomial manipulation is useful in its own right. Within SymPy, though, it is mostly used indirectly as a tool in other areas of the library. In fact, many mathematical problems in symbolic computing are first expressed using entities from the symbolic core, preprocessed, and then transformed into a problem in the polynomial algebra, where generic and efficient algorithms are used to solve the problem. The solutions to the original problem are subsequently recovered from the results. This is a common scheme in symbolic integration or summation algorithms.

SymPy implements dense and sparse polynomial representations.[4] Both are used in the univariate and multivariate cases. The dense representation is the default for univariate polynomials. For multivariate polynomials, the choice of representation is based on the application. The most common case for the sparse representation is algorithms for computing Gröbner bases (Buchberger, F4, and F5) [7, 11, 12]. This is because different monomial orderings can be expressed easily in this representation. However, algorithms for computing multivariate GCDs or factorizations, at least those currently implemented in SymPy [28], are better expressed when the representation is dense. The dense multivariate representation is specifically a recursively-dense representation, where polynomials in $K[x_0, x_1, \ldots, x_n]$ are viewed as a polynomials in $K[x_0][x_1]\ldots[x_n]$. Note that despite this, the coefficient domain K, can be a multivariate polynomial domain as well. The dense recursive representation in Python gets inefficient as the number of variables increases.

3.4. Printers. SymPy has a rich collection of expression printers. By default, an interactive Python session will render the `str` form of an expression, which has been used in all the examples in this paper so far. The `str` form of an expression is valid Python and roughly matches what a user would type to enter the expression.

```
>>> phi0 = Symbol('phi0')
>>> str(Integral(sqrt(phi0), phi0))
'Integral(sqrt(phi0), phi0)'
```

Expressions can be printed with 2D, monospace fonts via `pprint`. Unicode characters are used for rendering mathematical symbols such as integral signs, square roots, and parentheses. Greek letters and subscripts in symbol names that have Unicode code points associated are also rendered automatically.

```
>>> pprint(Integral(sqrt(phi0 + 1), phi0))
⌠
⎮  ╱ φ₀ + 1  d(φ₀)
⌡
```

[4] In a dense representation, the coefficients for all terms up to the degree of each variable are stored in memory. In a sparse representation, only the nonzero coefficients are stored.

PeerJ Preprints | https://doi.org/10.7287/peerj.preprints.2083v2 | CC-BY 4.0 Open Access | rec: 30 May 2016, publ: 30 May 2016

PeerJ Preprints NOT PEER-REVIEWED

Alternately, the `use_unicode=False` flag can be set, which causes the expression to be printed using only ASCII characters.

```
>>> pprint(Integral(sqrt(phi0 + 1), phi0), use_unicode=False)
  /
 |
 |   __________
 | \/ phi0 + 1  d(phi0)
 |
/
```

The function `latex` returns a LaTeX representation of an expression.

```
>>> print(latex(Integral(sqrt(phi0 + 1), phi0)))
\int \sqrt{\phi_{0} + 1}\, d\phi_{0}
```

Users are encouraged to run the `init_printing` function at the beginning of interactive sessions, which automatically enables the best pretty printing supported by their environment. In the Jupyter Notebook or Qt Console [29], the LaTeX printer is used to render expressions using MathJax or LaTeX, if it is installed on the system. The 2D text representation is used otherwise.

Other printers such as MathML are also available. SymPy uses an extensible printer subsystem for customizing any given printer, and allows custom objects to define their printing behavior for any printer. The code generation functionality of SymPy relies on this subsystem to convert expressions into code in various target programming languages.

3.5. Solvers. SymPy has a module of equation solvers that can handle ordinary differential equations, recurrence relationships, Diophantine equations, and algebraic equations. There is also rudimentary support for simple partial differential equations.

There are two functions for solving algebraic equations in SymPy: `solve` and `solveset`. `solveset` has several design changes with respect to the older `solve` function. This distinction is present in order to resolve the usability issues with the previous `solve` function API while maintaining backward compatibility with earlier versions of SymPy. `solveset` only requires essential input information from the user. The function signatures of `solve` and `solveset` are

```
solve(f, *symbols, **flags)
solveset(f, symbol, domain=S.Complexes)
```

The `domain` parameter is typically either `S.Complexes` (the default) or `S.Reals`; the latter causes `solveset` to only return real solutions.

An important difference between the two functions is that the output API of `solve` varies with input (sometimes returning a Python list and sometimes a Python dictionary) whereas `solveset` always returns a SymPy set object.

Both functions implicitly assume that expressions are equal to 0. For instance, `solveset(x - 1, x)` solves $x - 1 = 0$ for x.

`solveset` is under active development as a planned replacement for `solve`. There are certain features which are implemented in `solve` that are not yet implemented in `solveset`. Notably, these include nonlinear multivariate system and transcendental equations.

3.6. Matrices. Besides being an important feature in its own right, computations on matrices with symbolic entries are important for many algorithms within SymPy. The following code shows some basic usage of the `Matrix` class.

```
>>> A = Matrix(2, 2, [x, x + y, y, x])
>>> A
```


PeerJ Preprints | https://doi.org/10.7287/peerj.preprints.2083v2 | CC-BY 4.0 Open Access | rec: 30 May 2016, publ: 30 May 2016

PeerJ Preprints NOT PEER-REVIEWED

```
Matrix([
[x, x + y],
[y,     x]])
```

SymPy matrices support common symbolic linear algebra manipulations, including matrix addition, multiplication, exponentiation, computing determinants, solving linear systems, and computing inverses using LU decomposition, LDL decomposition, Gauss-Jordan elimination, Cholesky decomposition, Moore-Penrose pseudoinverse, and adjugate matrix.

All operations are performed symbolically. For instance, eigenvalues are computed by generating the characteristic polynomial using the Berkowitz algorithm and then solving it using polynomial routines.

```
>>> A.eigenvals()
{x - sqrt(y*(x + y)): 1, x + sqrt(y*(x + y)): 1}
```

Internally these matrices store the elements as lists of lists, making it a dense representation.[5] For storing sparse matrices, the `SparseMatrix` class can be used. Sparse matrices store their elements as a dictionary of keys.

SymPy also supports matrices with symbolic dimension values. `MatrixSymbol` represents a matrix with dimensions $m \times n$, where m and n can be symbolic. Matrix addition and multiplication, scalar operations, matrix inverse, and transpose are stored symbolically as matrix expressions.

Block matrices are also implemented in SymPy. `BlockMatrix` elements can be any matrix expression, including explicit matrices, matrix symbols, and other block matrices. All functionalities of matrix expressions are also present in `BlockMatrix`.

When symbolic matrices are combined with the assumptions module for logical inference, they provide powerful reasoning over invertibility, semi-definiteness, orthogonality, etc., which are valuable in the construction of numerical linear algebra systems.

4. Numerics. Floating point numbers in SymPy are implemented by the `Float` class, which represents an arbitrary-precision binary floating-point number by storing its value and precision (in bits). This representation is distinct from the Python built-in `float` type, which is a wrapper around machine `double` types and uses a fixed precision (53-bit).

Because Python `float` literals are limited in precision, strings should be used to input precise decimal values:

```
>>> Float(1.1)
1.10000000000000
>>> Float(1.1, 30)   # precision equivalent to 30 digits
1.10000000000000008881784197001
>>> Float("1.1", 30)
1.10000000000000000000000000000
```

The `evalf` method converts a constant symbolic expression to a `Float` with the specified precision, here 25 digits:

```
>>> (pi + 1).evalf(25)
4.1415926535897932384626433
```

`Float` numbers do not track their accuracy, and should be used with caution within symbolic expressions since familiar dangers of floating-point arithmetic apply [16]. A notorious case is that of catastrophic cancellation:

[5] Similar to the polynomials module, dense here means that all entries are stored in memory, contrasted with a sparse representation where only nonzero entries are stored.

PeerJ Preprints | https://doi.org/10.7287/peerj.preprints.2083v2 | CC-BY 4.0 Open Access | rec: 30 May 2016, publ: 30 May 2016

PeerJ Preprints NOT PEER-REVIEWED

```
>>> cos(exp(-100)).evalf(25) - 1
0
```

Applying the `evalf` method to the whole expression solves this problem. Internally, `evalf` estimates the number of accurate bits of the floating-point approximation for each sub-expression, and adaptively increases the working precision until the estimated accuracy of the final result matches the sought number of decimal digits:

```
>>> (cos(exp(-100)) - 1).evalf(25)
-6.91948263368368765324340 7e-88
```

The `evalf` method works with complex numbers and supports more complicated expressions, such as special functions, infinite series, and integrals. The internal error tracking does not provide rigorous error bounds (in the sense of interval arithmetic) and cannot be used to accurately track uncertainty in measurement data; the sole purpose is to mitigate loss of accuracy that typically occurs when converting symbolic expressions to numerical values.

4.1. The mpmath library. The implementation of arbitrary-precision floating-point arithmetic is supplied by the mpmath library. Originally, it was developed as a SymPy module but has subsequently been moved to a standalone pure-Python package. The basic datatypes in mpmath are `mpf` and `mpc`, which respectively act as multiprecision substitutes for Python's `float` and `complex`. The floating-point precision is controlled by a global context:

```
>>> import mpmath
>>> mpmath.mp.dps = 30    # 30 digits of precision
>>> mpmath.mpf("0.1") + mpmath.exp(-50)
mpf('0.10000000000000000000192874984794')
>>> print(_)   # pretty-printed
0.10000000000000000000192874985
```

For pure numerical computing, it is convenient to use mpmath directly with `from mpmath import *`. Nevertheless, it is best to avoid such an import statement when using SymPy simultaneously, since the names of numerical functions such as `exp` will collide the symbolic counterparts in SymPy.

Like SymPy, mpmath is a pure Python library. Internally, mpmath represents a floating-point number $(-1)^s x \cdot 2^y$ by a tuple (s, x, y, b) where x and y are arbitrary-size Python integers and the redundant integer b stores the bit length of x for quick access. If GMPY [19] is installed, mpmath automatically uses the `gmpy.mpz` type for x, and GMPY methods for rounding-related operations, improving performance.

The mpmath library supports special functions, root-finding, linear algebra, polynomial approximation, and numerical computation of limits, derivatives, integrals, infinite series, and ODE solutions. All features work in arbitrary precision and use algorithms that allow computing hundreds of digits rapidly (except in degenerate cases).

The double exponential (tanh-sinh) quadrature is used for numerical integration by default. For smooth integrands, this algorithm usually converges extremely rapidly, even when the integration interval is infinite or singularities are present at the endpoints [42, 2]. However, for good performance, singularities in the middle of the interval must be specified by the user. To evaluate slowly converging limits and infinite series, mpmath automatically tries Richardson extrapolation and the Shanks transformation (Euler-Maclaurin summation can also be used) [3]. A function to evaluate oscillatory integrals by means of convergence acceleration is also available.

A wide array of higher mathematical functions are implemented with full support

PeerJ Preprints | https://doi.org/10.7287/peerj.preprints.2083v2 | CC-BY 4.0 Open Access | rec: 30 May 2016, publ: 30 May 2016

PeerJ Preprints NOT PEER-REVIEWED

for complex values of all parameters and arguments, including complete and incomplete gamma functions, Bessel functions, orthogonal polynomials, elliptic functions and integrals, zeta and polylogarithm functions, the generalized hypergeometric function, and the Meijer G-function. The Meijer G-function instance $G^{3,0}_{1,3}\left(0; \frac{1}{2}, -1, -\frac{3}{2}|x\right)$ is a good test case [43]; past versions of both Maple and Mathematica produced incorrect numerical values for large $x > 0$. Here, mpmath automatically removes an internal singularity and compensates for cancellations (amounting to 656 bits of precision when $x = 10000$), giving correct values:

```
>>> mpmath.mp.dps = 15
>>> mpmath.meijerg([[],[0]],[[-0.5,-1,-1.5],[]],10000)
mpf('2.4392576907199564e-94')
```

Equivalently, with SymPy's interface this function can be evaluated as:

```
>>> meijerg([[],[0]],[[-S(1)/2,-1,-S(3)/2],[]],10000).evalf()
2.43925769071996e-94
```

Symbolic integration and summation often produces hypergeometric and Meijer G-function closed forms (see Subsection 3.2); numerical evaluation of such special functions is a useful complement to direct numerical integration and summation.

5. Domain Specific Submodules. SymPy includes several packages that allow users to solve domain specific problems. For example, a comprehensive physics package is included that is useful for solving problems in mechanics, optics, and quantum mechanics along with support for manipulating physical quantities with units.

5.1. Classical Mechanics. One of the core domains that SymPy suports is the physics of classical mechanics. This is in turn separated into two distinct components: vector algebra symbolics and mechanics.

5.1.1. Vector Algebra. The `sympy.physics.vector` package provides reference frame-, time-, and space-aware vector and dyadic objects that allow for three-dimensional operations such as addition, subtraction, scalar multiplication, inner and outer products, and cross products. Both of these objects can be written in very compact notation that make it easy to express the vectors and dyadics in terms of multiple reference frames with arbitrarily defined relative orientations. The vectors are used to specify the positions, velocities, and accelerations of points; orientations, angular velocities, and angular accelerations of reference frames; and forces and torques. The dyadics are essentially reference frame-aware 3×3 tensors [41]. The vector and dyadic objects can be used for any one-, two-, or three-dimensional vector algebra, and they provide a strong framework for building physics and engineering tools.

The following Python code demonstrates how a vector is created using the orthogonal unit vectors of three reference frames that are oriented with respect to each other, and the result of expressing the vector in the A frame. The B frame is oriented with respect to the A frame using Z-X-Z Euler Angles of magnitude π, $\frac{\pi}{2}$, and $\frac{\pi}{3}$rad, respectively, whereas the C frame is oriented with respect to the B frame through a simple rotation about the B frame's X unit vector through $\frac{\pi}{2}$rad.

```
>>> from sympy.physics.vector import ReferenceFrame
>>> A = ReferenceFrame('A')
>>> B = ReferenceFrame('B')
>>> C = ReferenceFrame('C')
>>> B.orient(A, 'body', (pi, pi/3, pi/4), 'zxz')
>>> C.orient(B, 'axis', (pi/2, B.x))
>>> v = 1*A.x + 2*B.z + 3*C.y
```


PeerJ Preprints | https://doi.org/10.7287/peerj.preprints.2083v2 | CC-BY 4.0 Open Access | rec: 30 May 2016, publ: 30 May 2016

PeerJ Preprints NOT PEER-REVIEWED

```
>>> v
A.x + 2*B.z + 3*C.y
>>> v.express(A)
A.x + 5*sqrt(3)/2*A.y + 5/2*A.z
```

5.1.2. Mechanics. The `sympy.physics.mechanics` package utilizes the `sympy.physics.vector` package to populate time-aware particle and rigid-body objects to fully describe the kinematics and kinetics of a rigid multi-body system. These objects store all of the information needed to derive the ordinary differential or differential algebraic equations that govern the motion of the system, i.e., the equations of motion. These equations of motion abide by Newton's laws of motion and can handle arbitrary kinematic constraints or complex loads. The package offers two automated methods for formulating the equations of motion based on Lagrangian Dynamics [22] and Kane's Method [21]. Lastly, there are automated linearization routines for constrained dynamical systems [30].

5.2. Quantum Mechanics. The `sympy.physics.quantum` package has extensive capabilities for performing symbolic quantum mechanics, using Python objects to represent the different mathematical objects relevant in quantum theory [37]: states (bras and kets), operators (unitary, Hermitian, etc.), and basis sets, as well as operations on these objects such as representations, tensor products, inner products, outer products, commutators, and anticommutators. The base objects are designed in the most general way possible to enable any particular quantum system to be implemented by subclassing the base operators and defining the relevant class methods to provide system-specific logic.

Symbolic quantum operators and states may be defined, and one can perform a full range of operations with them.

```
>>> from sympy.physics.quantum import Commutator, Dagger, Operator
>>> from sympy.physics.quantum import Ket, qapply
>>> A = Operator('A')
>>> B = Operator('B')
>>> C = Operator('C')
>>> D = Operator('D')
>>> a = Ket('a')
>>> comm = Commutator(A, B)
>>> comm
[A,B]
>>> qapply(Dagger(comm*a)).doit()
-<a|*(Dagger(A)*Dagger(B) - Dagger(B)*Dagger(A))
```

Commutators can be expanded using common commutator identities:

```
>>> Commutator(C+B, A*D).expand(commutator=True)
-[A,B]*D - [A,C]*D + A*[B,D] + A*[C,D]
```

On top of this set of base objects, a number of specific quantum systems have been implemented in a fully symbolic framework. These include:

- Many of the exactly solvable quantum systems, including simple harmonic oscillator states and raising/lowering operators, infinite square well states, and 3D position and momentum operators and states.
- Second quantized formalism of non-relativistic many-body quantum mechanics [13].
- Quantum angular momentum [45]. Spin operators and their eigenstates can be represented in any basis and for any quantum numbers. A rotation opera-

PeerJ Preprints | https://doi.org/10.7287/peerj.preprints.2083v2 | CC-BY 4.0 Open Access | rec: 30 May 2016, publ: 30 May 2016

tor representing the Wigner-D matrix, which may be defined symbolically or numerically, is also implemented to rotate spin eigenstates. Functionality for coupling and uncoupling of arbitrary spin eigenstates is provided, including symbolic representations of Clebsch-Gordon coefficients and Wigner symbols.

- Quantum information and computing [25]. Multidimensional qubit states, and a full set of one- and two-qubit gates are provided and can be represented symbolically or as matrices/vectors. With these building blocks, it is possible to implement a number of basic quantum algorithms including the quantum Fourier transform, quantum error correction, quantum teleportation, Grover's algorithm, dense coding, etc. In addition, any quantum circuit may be plotted using the `circuit_plot` function (Figure 1).

Here are a few short examples of the quantum information and computing capabilities in `sympy.physics.quantum`. Start with a simple four-qubit state and flip the second qubit from the right using a Pauli-X gate:

```
>>> from sympy.physics.quantum.qubit import Qubit
>>> from sympy.physics.quantum.gate import XGate
>>> q = Qubit('0101')
>>> q
|0101>
>>> X = XGate(1)
>>> qapply(X*q)
|0111>
```

Qubit states can also be used in adjoint operations, tensor products, inner/outer products:

```
>>> Dagger(q)
<0101|
>>> ip = Dagger(q)*q
>>> ip
<0101|0101>
>>> ip.doit()
1
```

Quantum gates (unitary operators) can be applied to transform these states and then classical measurements can be performed on the results:

```
>>> from sympy.physics.quantum.qubit import measure_all
>>> from sympy.physics.quantum.gate import H, X, Y, Z
>>> c = H(0)*H(1)*Qubit('00')
>>> c
H(0)*H(1)*|00>
>>> q = qapply(c)
>>> measure_all(q)
[(|00>, 1/4), (|01>, 1/4), (|10>, 1/4), (|11>, 1/4)]
```

Lastly, the following example demonstrates creating a three-qubit quantum Fourier transform, decomposing it into one- and two-qubit gates, and then generating a circuit plot for the sequence of gates (see Figure 1).

```
>>> from sympy.physics.quantum.qft import QFT
>>> from sympy.physics.quantum.circuitplot import circuit_plot
>>> fourier = QFT(0,3).decompose()
>>> fourier
SWAP(0,2)*H(0)*C((0),S(1))*H(1)*C((0),T(2))*C((1),S(2))*H(2)
>>> c = circuit_plot(fourier, nqubits=3)
```


PeerJ Preprints | https://doi.org/10.7287/peerj.preprints.2083v2 | CC-BY 4.0 Open Access | rec: 30 May 2016, publ: 30 May 2016

PeerJ Preprints NOT PEER-REVIEWED

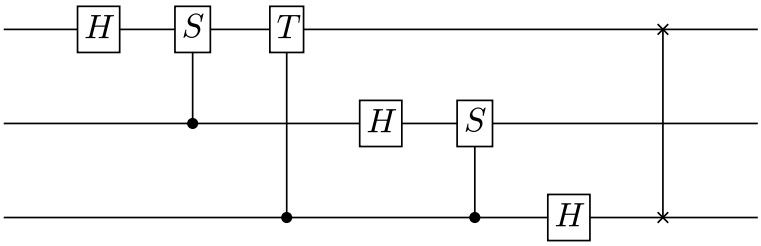


Fig. 1: The circuit diagram for a three-qubit quantum Fourier transform generated by SymPy.

6. Conclusion and future work. SymPy is a robust computer algebra system that provides a wide spectrum of features both in traditional computer algebra and in a plethora of scientific disciplines. This allows SymPy to be used in a first-class way with other Python projects, including the scientific Python stack. Unlike many other CASs, SymPy is designed to be used in an extensible way: both as an end-user application and as a library.

SymPy expressions are immutable trees of Python objects. SymPy uses Python both as the internal language and the user language. This permits users to access to the same methods that the library implements in order to extend it for their needs. Additionally, SymPy has a powerful assumptions system for declaring and deducing mathematical properties of expressions.

SymPy has submodules for many areas of mathematics. This includes functions for simplifying expressions, performing common calculus operations, pretty printing expressions, solving equations, and representing symbolic matrices. Other included areas are discrete math, concrete math, plotting, geometry, statistics, polynomials, sets, series, vectors, combinatorics, group theory, code generation, tensors, Lie algebras, cryptography, and special functions. Additionally, SymPy contains submodules targeting certain specific domains, such as classical mechanics and quantum mechanics. This breadth of domains has been engendered by a strong and vibrant user community. Anecdotally, these users likely chose SymPy because of its ease of access.

Some of the planned future work for SymPy includes work on improving code generation, improvements to the speed of SymPy (one area of work in this direction is SymEngine, a C++ symbolic manipulation library that is planned to be usable as a alternative core for SymPy), improving the assumptions system, and improving the solvers module.

7. Acknowledgements. The Los Alamos National Laboratory is operated by Los Alamos National Security, LLC, for the National Nuclear Security Administration of the U.S. Department of Energy under Contract No. DE-AC52-06NA25396.

Sandia is a multiprogram laboratory operated by Sandia Corporation, a Lockheed Martin Company, for the United States Department of Energy's National Nuclear Security Administration under Contract DE-AC04-94AL85000.

Google Summer of Code is an international annual program in which Google

PeerJ Preprints | https://doi.org/10.7287/peerj.preprints.2083v2 | CC-BY 4.0 Open Access | rec: 30 May 2016, publ: 30 May 2016

PeerJ Preprints NOT PEER-REVIEWED

awards stipends to all students who successfully complete a requested free and open-source software coding project during the summer.

The author of this paper Francesco Bonazzi thanks the Deutsche Forschungsgemeinschaft (DFG) for its financial support via the International Research Training Group 1524 "Self-Assembled Soft Matter Nano-Structures at Interfaces."

8. References.

REFERENCES

[1] W. W. Adams and P. Loustaunau, *An introduction to Gröbner bases*, no. 3, American Mathematical Society, 1994.

[2] D. H. Bailey, K. Jeyabalan, and X. S. Li, *A comparison of three high-precision quadrature schemes*, Experimental Mathematics, 14 (2005), pp. 317–329.

[3] C. M. Bender and S. A. Orszag, *Advanced Mathematical Methods for Scientists and Engineers*, Springer, 1st ed., October 1999.

[4] N. Biggs, E. K. Lloyd, and R. J. Wilson, *Graph Theory, 1736-1936*, Oxford University Press, 1976.

[5] M. Bronstein, *Poor Man's Integrator*, http://www-sop.inria.fr/cafe/Manuel.Bronstein/pmint.

[6] M. Bronstein, *Symbolic Integration I: Transcendental Functions*, Springer–Verlag, New York, NY, USA, 2005.

[7] B. Buchberger, *Ein Algorithmus zum Auffinden der Basis Elemente des Restklassenrings nach einem nulldimensionalen Polynomideal*, PhD thesis, University of Innsbruck, Innsbruck, Austria, 1965.

[8] J. Carette, *Understanding Expression Simplification*, in ISSAC '04: Proceedings of the 2004 International Symposium on Symbolic and Algebraic Computation, New York, NY, USA, 2004, ACM Press, pp. 72–79, http://dx.doi.org/http://doi.acm.org/10.1145/1005285.1005298.

[9] D. Cervone, *Mathjax: a platform for mathematics on the web*, Notices of the AMS, 59 (2012), pp. 312–316.

[10] R. Cimrman, *SfePy - write your own FE application*, in Proceedings of the 6th European Conference on Python in Science (EuroSciPy 2013), P. de Buyl and N. Varoquaux, eds., 2014, pp. 65–70. http://arxiv.org/abs/1404.6391.

[11] J. C. Faugère, *A New Efficient Algorithm for Computing Gröbner Bases (F4)*, Journal of Pure and Applied Algebra, 139 (1999), pp. 61–88, http://www-calfor.lip6.fr/~jcf/Papers/F99a.pdf.

[12] J. C. Faugère, *A New Efficient Algorithm for Computing Gröbner Bases Without Reduction To Zero (F5)*, in ISSAC '02: Proceedings of the 2002 International Symposium on Symbolic and Algebraic Computation, New York, NY, USA, 2002, ACM Press, pp. 75–83, http://dx.doi.org/http://doi.acm.org/10.1145/780506.780516, http://www-calfor.lip6.fr/~jcf/Papers/F02a.pdf.

[13] A. Fetter and J. Walecka, *Quantum Theory of Many-Particle Systems*, Dover Publications, 2003.

[14] H. Fu, X. Zhong, and Z. Zeng, *Automated and Readable Simplification of Trigonometric Expressions*, Mathematical and Computer Modelling, 55 (2006), pp. 1169–1177.

[15] G. Gede, D. L. Peterson, A. S. Nanjangud, J. K. Moore, and M. Hubbard, *Constrained multibody dynamics with Python: From symbolic equation generation to publication*, in ASME 2013 International Design Engineering Technical Conferences and Computers and Information in Engineering Conference, American Society of Mechanical Engineers, 2013, pp. V07BT10A051–V07BT10A051.

[16] D. Goldberg, *What every computer scientist should know about floating-point arithmetic*, ACM Computing Surveys (CSUR), 23 (1991), pp. 5–48.

[17] R. W. Gosper, *Decision procedure for indefinite hypergeometric summation*, Proceedings of the National Academy of Sciences, 75 (1978), pp. 40–42.

[18] D. Gruntz, *On Computing Limits in a Symbolic Manipulation System*, PhD thesis, Swiss Federal Institute of Technology, Zürich, Switzerland, 1996.

[19] C. V. Horsen, *GMPY*. https://pypi.python.org/pypi/gmpy2, 2015.

[20] J. D. Hunter, *Matplotlib: A 2d graphics environment*, Computing In Science & Engineering, 9 (2007), pp. 90–95.

[21] T. R. Kane and D. A. Levinson, *Dynamics, Theory and Applications*, McGraw Hill, 1985.

[22] J. Lagrange, *Mécanique analytique*, no. v. 1 in Mécanique analytique, Ve Courcier, 1811.

PeerJ Preprints | https://doi.org/10.7287/peerj.preprints.2083v2 | CC-BY 4.0 Open Access | rec: 30 May 2016, publ: 30 May 2016

PeerJ Preprints NOT PEER-REVIEWED

[23] S. Lang, *Introduction to transcendental numbers*, Reading, Mass, (1966).

[24] M. Lutz, *Learning Python*, O'Reilly Media, Inc., 2013.

[25] M. Nielsen and I. Chuang, *Quantum Computation and Quantum Information*, Cambridge University Press, 2011.

[26] A. Nijenhuis and H. S. Wilf, *Combinatorial Algorithms: For Computers and Calculators*, Academic Press, New York, NY, USA, second ed., 1978.

[27] T. E. Oliphant, *Python for scientific computing*, Computing in Science & Engineering, 9 (2007), pp. 10–20.

[28] M. Paprocki, *Design and implementation issues of a computer algebra system in an interpreted, dynamically typed programming language*, master's thesis, University of Technology of Wrocław, Poland, 2010.

[29] F. Pérez and B. E. Granger, *IPython: a system for interactive scientific computing*, Computing in Science & Engineering, 9 (2007), pp. 21–29.

[30] D. L. Peterson, G. Gede, and M. Hubbard, *Symbolic linearization of equations of motion of constrained multibody systems*, Multibody System Dynamics, 33 (2014), pp. 143–161, http://dx.doi.org/10.1007/s11044-014-9436-5.

[31] M. Petkovšek, H. S. Wilf, and D. Zeilberger, *A= BAK peters*, Wellesley, MA, (1996).

[32] E. Raymond, *The cathedral and the bazaar*, Knowledge, Technology & Policy, 12 (1999), pp. 23–49.

[33] K. Roach, *Hypergeometric function representations*, in ISSAC '96: Proceedings of the 1996 International Symposium on Symbolic and Algebraic Computation, New York, NY, USA, 1996, ACM Press, pp. 301–308, http://dx.doi.org/http://doi.acm.org/10.1145/236869.237088, http://www.planetquantum.com/TheMission/Papers/Issac96.pdf.

[34] K. Roach, *Meijer G function representations*, in ISSAC '97: Proceedings of the 1997 international symposium on Symbolic and algebraic computation, New York, NY, USA, 1997, ACM, pp. 205–211, http://dx.doi.org/http://doi.acm.org/10.1145/258726.258784.

[35] M. Rocklin and A. R. Terrel, *Symbolic statistics with SymPy*, Computing in Science and Engineering, 14 (2012), http://dx.doi.org/10.1109/MCSE.2012.56.

[36] L. Rosen, *Open source licensing*, vol. 692, Prentice Hall, 2005.

[37] J. Sakurai and J. Napolitano, *Modern Quantum Mechanics*, Addison-Wesley, 2010.

[38] M. Shaw and D. Garlan, *Software Architecture: Perspectives on an Emerging Discipline*, Prentice Hall, 1996. Prentice Hall Ordering Information.

[39] W. Stein and D. Joyner, *SAGE: System for Algebra and Geometry Experimentation*, Communications in Computer Algebra, 39 (2005).

[40] G. J. Sussman and J. Wisdom, *Functional Differential Geometry*, Massachusetts Institute of Technology Press, 2013.

[41] C.-T. Tai, *Generalized vector and dyadic analysis: applied mathematics in field theory*, vol. 9, Wiley-IEEE Press, 1997.

[42] H. Takahasi and M. Mori, *Double exponential formulas for numerical integration*, Publications of the Research Institute for Mathematical Sciences, 9 (1974), pp. 721–741.

[43] V. T. Toth, *Maple and Meijer's G-function: a numerical instability and a cure*. http://www.vttoth.com/CMS/index.php/technical-notes/67, 2007.

[44] M. J. Turk, B. D. Smith, J. S. Oishi, S. Skory, S. W. Skillman, T. Abel, and M. L. Norman, *yt: A Multi-code Analysis Toolkit for Astrophysical Simulation Data*, The Astrophysical Journal Supplement Series, 192 (2011), pp. 9–+, http://dx.doi.org/10.1088/0067-0049/192/1/9, arXiv:1011.3514.

[45] R. Zare, *Angular Momentum: Understanding Spatial Aspects in Chemistry and Physics*, Wiley, 1991.

PeerJ Preprints | https://doi.org/10.7287/peerj.preprints.2083v2 | CC-BY 4.0 Open Access | rec: 30 May 2016, publ: 30 May 2016

Accepted Manuscript



Synthesis, characterization and fluorescence turn-on behavior of new porphyrin analogue: meta-benziporphodimethenes

Ravi Kumar Sharma, Lale Kiran Gajanan, Mohan Singh Mehata, Firasat Hussain, Anil Kumar

PII: S1386-1425(16)30334-1
DOI: doi: 10.1016/j.saa.2016.06.020
Reference: SAA 14497

To appear in:

Received date: 24 April 2016
Revised date: 9 June 2016
Accepted date: 11 June 2016

Please cite this article as: Ravi Kumar Sharma, Lale Kiran Gajanan, Mohan Singh Mehata, Firasat Hussain, Anil Kumar, Synthesis, characterization and fluorescence turn-on behavior of new porphyrin analogue: meta-benziporphodimethenes, (2016), doi: 10.1016/j.saa.2016.06.020

This is a PDF file of an unedited manuscript that has been accepted for publication. As a service to our customers we are providing this early version of the manuscript. The manuscript will undergo copyediting, typesetting, and review of the resulting proof before it is published in its final form. Please note that during the production process errors may be discovered which could affect the content, and all legal disclaimers that apply to the journal pertain.

ACCEPTED MANUSCRIPT

Synthesis, characterization and fluorescence *turn-on* behavior of new porphyrin analogue: *meta*-benziporphodimethenes

Ravi Kumar Sharma[a], Lale Kiran Gajanan[a], Mohan Singh Mehata[b], Firasat Hussain[c] and Anil Kumar[a]*

[a]*Department of Applied Chemistry, Delhi Technological University, Bawana Road, Delhi, India.*

[b]*Department of Applied Physics, Delhi Technological University, Bawana Road, Delhi, India.*

[c] *Department of Chemistry, University of Delhi, India*.

*Corresponding author E-mail: anil_kumar@dce.ac.in

Abstract

New fluorescence *switch-on meso*-substituted free base *meta*-benziporphodimethenes were synthesized, characterized via acid catalyzed condensation reaction and metallated with Zn^{2+}.Their photophysical properties were also studied. The fluorescence spectra analysis demonstrates substituent's independent behaviour on emitting λ_{max}. The average Stokes shift of 33 nm was observed. Crystal structure of **8** was obtained and gave expected perturbed geometry.

Keywords: Fluorescence, cell imaging, quantum yield, porphyrinoid

ACCEPTED MANUSCRIPT

Introduction

Fluorescent molecules for the recognition of metal ions are of great interest for chemist as well as biologist because of their significant role in biological and environmental process.[1-18] Bioimaging with the help of these fluorescent molecules is an important and powerful approach to achieve target specific information which paves the way to understand the structural and functional properties of cells, organs, and living organism in the context of molecular biology, diagnostics and therapeutics.[19-26] The fluorescent techniques are always promising and better tool for analysis because of its high resolution; ease of use and cheaper than other analytical techniques.[27] Different kind of fluorescent sensor have been developed and synthesized like fluorescent proteins,[28-29] dyes,[30] metal complexes,[31] and nanoparticles.[32] The coordination of metal ion with fluorophore increases the fluorescence intensity of chromophore, called chelation-enhanced fluorescence, CHEF. Mostly sensors like fluorescein,[33-34] dansyl,[35-38] anthracene,[11,13] and BIODPY[39] shows CHEF. These CHEF based sensors emit lower than 600 nm and constitute background fluorescence. Still, there is a crunch and in need of development of sensors emitting above 600 nm or even low and zero background fluorescence, high penetration and lesser scattering in optically diffuse samples which in turn may induce lesser tissue damage.[40-42] Deficiency of Zn, Cd, Cu or other transition metals in trace amount can lead to human or animal diseases.[27,43] So, sincere efforts of environmental, biological scientist and chemist in this direction need to be required for the development of fluorescent molecular sensor for the detection of these trace metals. Out of these trace elements, Zinc is the most abundant transition elements after iron in human body.[44] Zinc plays various important roles in several biological processes such as neurotransmission, signal transduction and gene expression.[45] Literature on homeostasis of zinc is lesser known but structural chemistry explored greatly by chemist because of the spectroscopically silent nature of d^{10} Zn^{2+}.[46]Zn^{2+} fluorescent probes are of three main

ACCEPTED MANUSCRIPT

categories small-molecules, genetically encoded, and hybrid probes. But out of these three classes small-molecule sensors are of higher choice. Again small molecules sensors were further divided into two systems: intensity based and ratiometric probes. Intensity base probes undergo a change in fluorescence intensity upon binding with Zn^{2+}.[46] Bruckner and co-workers showed 300 fold enhancements in fluorescence intensity after Zn^{2+} binding with quinoline based moiety.[47] Varieties of fluorophores have been developed with low background and turn-on fluorescence suitable for biological imaging like proteins[48-49] and peptides based.[50] Other approaches have also been implemented like fluoroscein,[33-34]Zincpyr family and their modified derivatives,[51] ZnAF probes,[52] coumarin,[53] rhodamine,[54] tricarbocyanine,[55] 4-aminophthalimide.[56] Li, Lin and their co-workers recently developed ZNBR1-3 probes based on benzoresorufin and ZIMIR, respectively.[57] LuoZin-3 probe was recently used by Kornfeld for imaging Zn^{2+} in an optically transparent living organism and later for time lapse imaging and revealed exqusite Zn^{2+} transients.[58] Lippard and Chyan laboratory recently used fluorescent probes, Znpyr modified family, for Zn^{2+} levels in prostate cancer.[59] Large number of fluorescent probes have been developed and used in biological imaging but almost all suffer from high background fluorescence and low CHEF. In this direction, Hung and co-workers developed a fluorescence probe, *meta*-benziporphodimethene, had no background emission and upon binding with Zn^{2+} shows tremendous increase in fluorescence intensity and represented turn-on probe for Zn^{2+} sensor.[60-61] The change in magnitude of fluorescence intensity with binding of Zn^{2+} with fluorophore can be tuned on manipulation of fluorophore. This can be accomplished in two different ways, first on changing *meso* substituent's or modification on pyrrole β-carbon atoms to tune the electron density. In this paper, we report on the extension of the synthesis of *meta*-benziporphodimethenes, with various *meso*-substitutents and their effects on photophysical properties upon binding with Zn^{2+} have been studied.

ACCEPTED MANUSCRIPT

Experimental Section

Reagents

Pyrrole and substituted aldehydes (liquid) were distilled prior to use. α, α-dihydroxy-1, 3-diisopropylbenzene (TCI) and boron trifluoride ethyl ether complex, 2,3-dichloro-5,6-dicyano-*p*-benzoquinone were used as supplied. Solvents and all other reagents were used as such without purification. $CDCl_3$ was used as supplied. Basic alumina oxide and silica gel were obtained from Merck.

General Information

Absorption spectra were recorded with Shimadzu UV-1800 at room temperature. Fluorescence spectra were recorded by JobinYyon Horiba Fluorolog-3 spectrofluorometer equipped with double-grating at excitation and emission monochromators and an R928P photomultiplier tube (PMT). The excitation source was a 450 Watt CW xenon lamp. Fluorescence decay profiles were recorded using time-correlated single photon counting (TCSPC) system (DeltaFlex-01-DD, Horiba JobinYvon IBH Ltd) coupled with Delta Diode Laser. NMR spectra were recorded on Bruker and Jeol Delta. Fourier transform infrared (FTIR) spectra were obtained in the wavenumber range of 4000-400 cm^{-1} by using a Nicolet 380 FTIR spectrometer with the KBr pellet technique. NMR spectra were referenced to residual solvent signals. ESI-mass spectra were recorded on Waters Synapt G2 HDMS. Column chromatography was carried out on Merck silica gel with gravity-feel-column technique. Thin-layer chromatographies were performed on Merck silica gel 60 F254 precoated aluminium sheets.

ACCEPTED MANUSCRIPT

*Synthesis of **1-8***:

A solution of α, α'-dihydroxy-1, 3-diisopropylbenzene (98 mg, 0.50 mmol), substituted aldehyde (102 mL, 1.01 mmol), and pyrrole (104 mL, 1.51 mmol) were dissolved in CH_2Cl_2 (150 mL). The resulted solution was treated with $BF_3{\cdot}OEt_2$ (13 µL, 0.10 mmol) and stirred at room temperature. DDQ (374 mg, 1.65 mmol) was added into the reaction mixture after 2 h and continuously stirred for another 2 h at room temperature. The reaction mixture was quenched with triethylamine and the solvent was removed in vacuo. The crude mixture was dissolved in a minimum amount of CH_2Cl_2 and was purified using silica gel column chromatography (450 mL) eluting with mixture of CH_2Cl_2 and n-hexane to give **1- 8** as a red powder. The yields obtained for compound (% yield) are as follows: **1** (17%), **2**(14%), **3**(17%), **4** (17%), **5** (16%), **6** (17%), **7** (16%), **8** (17%).

*Synthesis of Zn^{2+}.**1-8***:

1 (10 mg) was dissolved in 25 mL CH_2Cl_2/CH_3CN (1:2). To this solution anhydrous zinc chloride (51.3 mg, 0.376 mmol) was pre-dissolved in CH_3CN, added 1 drop of 2, 6-lutidine into the solution. After two minutes of stirring, the solvent was removed under reduced pressure. The residue was dissolved in CH_2Cl_2 and excess zinc salt was extracted using distilled water. The organic layer was collected and solvent was removed in *vacuo* and crystallized in n-hexane to afford bluish green product. All zinc complexes reported here were prepared with same procedure. The yields obtained for Zn^{2+}.**1-8** was Zn^{2+}.**1** (98%), Zn^{2+}.**2** (98%), Zn^{2+}.**3** (97%), Zn^{2+}.**4** (98%), Zn^{2+}.**5** (97%), Zn^{2+}.**6** (98%), Zn^{2+}.**7** (98%), and Zn^{2+}.**8** (98%).

Spectroscopic analyses of free base *meta*-benziporphodimethenes and their zinc complex**. 1**: λ_{max} (log ε) 548 (4.31), 517 (4.27), 353 (4.55). ESI-MS (*m/z*): 600.0937 (M + 1) , ^{1}H NMR: 12.32 (br, 1H,NH), 7.93 (s, 1H, 22-ArH), 7.24-7.39 (m,11H, (2,3,4-ArH+ mesoAr-H), 6.81

ACCEPTED MANUSCRIPT

(ab quartet $^{3}J_{H,H}$=4.88Hz, HH, 8,9,18,19-Pyrr H), 6.15 (s,2H, 13,14-Pyrr H), 1.72 (s,12H, CH_3). ^{13}C-NMR (101 MHz, $CDCl_3$, 20°C): 181.79, 153.72, 152.44, 151.77, 147.41, 143.63, 138.84, 138.58, 138.22, 136.53, 133.59, 131.79, 128.68, 127.38, 125.24, 123.15, 121.27, 42.10, 29.06. IR (KBr, 25° C): 3290.6 (N-H Stretch), 2929.5 (C-H Stretch, *sp*^{3} Hybridised), 1691.9 (C=N Stretch), 1582.7, 1502.9 (C=C Stretch Aromatic), 1383.1 (C-H Bending, *sp*^{3} Hybridised out of plane), 799.9, 756.9 (=C-H Bending, Aromatic, out of plane), 717.0 (C-Cl Stretch). Zn^{2+}.**1:** 639 (4.477), 594 (4.216), 351 (4.499). IR (in KBr, 25° C): 2975.5 (C-H Stretch, *sp*^{3} Hybridised), 1672.9 (C=N Stretch), 1545.8, 1491.2 (C=C Stretch Aromatic), 1360.4 (C-H Bending, *sp*^{3} Hybridised, out of plane), 964.1, 804.6 (=C-H Bending, Aromatic, out of plane), 713.5 (C-Cl Stretch). Compound **2**: 542 (4.078), 513 (4.05), 351 (4.344). ESI-Mass (*m/z*): 690.0589 (M + 1). ^{1}H NMR: 12.32 (br, 1H,NH), 7.94 (s, 1H, 22-ArH), 7.31-7.57 (m,11H, (2,3,4-ArH+ mesoAr-H), 6.83 (ab quartet $^{3}J_{H,H}$=5.90Hz, HH, 8,9,18,19-Pyrr H), 6.16 (s,2H, 13,14-Pyrr H), 1.74 (s,12H, CH_3). ^{13}C NMR (101 MHz, $CDCl_3$, 20°C): 182.68, 152.00, 147.06, 138.57, 137.10, 136.45, 133.29, 131.02, 128.52, 127.11, 125.60, 123.56, 123.29, 121.24, 42.25, 28.98. IR (KBr, 25° C): 3281.3 (N-H Stretch), 2924.1 (C-H Stretch, *sp*^{3} Hybridised), 1586.6, 1484.4 (C=C Stretch Aromatic), 1382.8 (C-H Bending, *sp*^{3} Hybridised out of plane), 798.1, 735.7, 703.8 (=C-H Bending, Aromatic, out of plane). Zn^{2+}.**2:** 638 4.45), 594 (4.19), 350 (4.48). IR (in KBr, 25° C): 2969.3 (C-H Stretch, *sp*^{3} Hybridised), 1712.0 (C=N Stretch), 1547.9, 1489.4 (C=C Stretch Aromatic), 1360.6 (C-H Bending, *sp*^{3} Hybridised, out of plane), 967.3, 802.2 (=C-H Bending, Aromatic, out of plane), 465.9 (C-Br Stretch). Compound **3**: 538 (4.22), 508 (4.19), 321 (4.32). ESI-Mass (*m/z*): 670.0478 (M + 1). ^{1}H NMR: 12.16 (br, 1H,NH), 8.06 (s, 1H, 22-ArH), 7.28-7.41 (m,9H, (2,3,4-ArH+ mesoAr-H), 6.82 (doublet $^{2}J_{H,H}$=4.59Hz, HH, 9,18-Pyrr H), 6.56 (doublet $^{2}J_{H,H}$=4.59Hz, HH, 8,19-Pyrr H), 5.86 (s,2H, 13,14-Pyrr H), 1.81 (s,12H, CH_3). ^{13}C-NMR (101 MHz, $CDCl_3$, 20°C):184.33, 162.24, 159.69, 152.99, 146.25, 144.66, 137.77, 135.65,

ACCEPTED MANUSCRIPT

130.61, 127.94, 127.08 , 125.92, 123.59, 123.15, 120.16, 118.37, 111.48, 111.24, 42.50, 29.82, 28.73. IR (in KBr, 25° C): 3300.4 (N-H Stretch), 2967.7 (C-H Stretch, sp^3 Hybridised), 1678.9 (C=N Stretch), 1591.0, 1480.9 (C=C Stretch Aromatic), 1381.7 (C-H Bending, sp^3 Hybridised out of plane), 828.6, 796.8 (=C-H Bending, Aromatic, out of plane), 709.0 (C-Cl Stretch). Zn^{2+}.**3**: 649 (4.517), 602 (4.26), 348 (4.608). IR (in KBr, 25° C): 2880.9(C-H Stretch, sp^3 Hybridised), 1675.2 (C=N Stretch), 1555.1, 1488.8 (C=C Stretch Aromatic), 1321.5 (C-H Bending, sp^3 Hybridised, out of plane), 906.3, 835.5, 797.6 (=C-H Bending, Aromatic, out of plane), 718.7 (C-Cl Stretch). Compound **4**: 533 (4.24), 507 (4.213), 320 (4.372). ESI-Mass (*m/z*): 604.1306 (M + 1). ^{1}H NMR: 12.18 (br, 1H,NH), 7.97 (s, 1H, 22-ArH), 7.35-7.45 (m,3H, (2,3,4-ArH), 6.91-7.05 (m,6H, ArH), 6.83 (doublet $^2J_{H,H}$=4.40Hz, HH, 9,18-Pyrr H), 6.70 (doublet $^2J_{H,H}$=4.22Hz, HH, 8,19-Pyrr H), 6.00 (s,2H, 13,14-Pyrr H), 1.79 (s,12H, CH_3). ^{13}C-NMR (101 MHz, $CDCl_3$, 20°C): 184.35, 162.17, 159.75, 153.00, 146.25, 144.65, 137.78, 135.66, 130.63, 127.95, 127.51, 127.08, 125.94, 123.61, 123.16, 120.18, 118.40, 111.50, 111.26, 42.51, 29.83, 28.74. IR (in KBr, 25° C): 3282.8 (N-H Stretch), 2924.0 (C-H Stretch, sp^3 Hybridised), 1621.6 (C=N Stretch), 1589.3 (C=C Stretch Aromatic), 1381.0 (C-H Bending, sp^3 Hybridised out of plane), 783.6, 753.9, 706.8 (=C-H Bending, Aromatic, out of plane), 1000.3 (C-F Stretch).Zn^{2+}.**4:** 642 (4.36), 598 (4.122), 346 (4.458). ESI-Mass (*m/z*): 666.0491 (M - Cl). IR (in KBr, 25° C): 2881.2(C-H Stretch, sp^3 Hybridised), 1622.1 (C=N Stretch), 1556.9, 1496.0(C=C Stretch Aromatic), 1362.4 (C-H Bending, sp^3 Hybridised, out of plane), 835.3, 787.5, 717.3 (=C-H Bending, Aromatic, out of plane), 1072.7 (C-F Stretch). Compound **5**: 531 (4.287), 508 (4.254), 319 (4.418). ESI-Mass (*m/z*): 712.1006 (M + 1). ^{1}H NMR: 12.08 (br, 1H,NH), 7.89 (s, 1H, 22-ArH), 7.25-7.34 (m,3H, (2,3,4-ArH), 6.90 (doublet $^2J_{H,H}$=4.58Hz, HH, 9,18-Pyrr H), 6.6 5(doublet $^2J_{H,H}$=4.58Hz, HH, 8,19-Pyrr H), 5.98 (s,2H, 13,14-Pyrr H), 1.78 (s,12H, CH_3). ^{13}C-NMR (101 MHz, $CDCl_3$, 20°C): 185.93, 153.54, 145.91, 137.11, 135.14, 128.11,

ACCEPTED MANUSCRIPT

127.31, 126.82, 123.74, 119.90, 119.37, 115.97, 42.64, 28.51. IR (in KBr, 25° C): 3300.0 (N-H Stretch), 2967.2 (C-H Stretch, sp^3 Hybridised), 1651.5 (C=N Stretch), 1594.3, 1494.8 (C=C Stretch Aromatic), 1384.9 (C-H Bending, sp^3Hybridised out of plane), 799.4, 755.0, 706.3 (=C-H Bending, Aromatic, out of plane), 1053.1 (C-F Stretch). Zn^{2+}.**5:** 642 (4.346), 600 (4.108), 346 (4.436). IR (in KBr, 25° C): 2923.8 (C-H Stretch, sp^3 Hybridised), 1652.2 (C=N Stretch), 1561.7, 1495.4(C=C Stretch Aromatic), 1362.7 (C-H Bending, sp^3 Hybridised, out of plane), 931.8, 908.1, 832.8 (=C-H Bending, Aromatic, out of plane), 1074.5 (C-F Stretch). Compound **6**: 539 (4.23), 509 (4.22), 342 (4.414). ESI-Mass (*m/z*): 668.1482 (M + 1). ^{1}H NMR:12.0 (br, 1H,NH), 7.92 (s, 1H, 22-ArH), 7.68 (d,4H-ArH), 7.56 (d,4H-ArH), 7.29 (m,3H-ArH), 6.85 (doublet $^2J_{H,H}$=4.58Hz, HH, 9,18-Pyrr H), 6.75 (doublet $^2J_{H,H}$=4.58Hz, HH, 8,19-Pyrr H), 6.07 (s,2H, 13,14-Pyrr H), 1.75 (s,12H, CH_3). ^{13}C-NMR (101 MHz, $CDCl_3$, 20°C):183.38, 152.24, 146.85, 141.83, 138.51, 136.44, 135.82, 131.86, 128.48, 126.97, 125.94, 124.73, 123.40, 121.28, 42.36, 28.91. IR (in KBr, 25° C): 3278.2 (N-H Stretch), 2968.9 (C-H Stretch, sp^3 Hybridised), 1692.9 (C=N Stretch), 1587.5, 1472.2 (C=C Stretch Aromatic), 1382.5 (C-H Bending, sp^3 Hybridised out of plane), 747.4, 707.1 (=C-H Bending, Aromatic, out of plane), 1322.2 (C-F Stretch)Zn^{2+}.**6:** 641 (4.50), 594 (4.24), 347 (4.57). IR (in KBr, 25° C): 2966.1 (C-H Stretch, sp^3 Hybridised), 1550.3, 1484.9 (C=C Stretch Aromatic), 1362.7 (C-H Bending, sp^3 Hybridised, out of plane), 801.9, 708.1 (=C-H Bending, Aromatic, out of plane), 1322.5(C-F Stretch). Compound **7**: 545 (4.31), 513 (4.27), 378 (4.55). ^{1}HNMR: 12.38 (br, 1H,NH), 7.93 (s, 1H, 22-Ar-H), 7.44 (d, 4 Ar-H $^2J_{H,H}$=8.4 Hz), 7.27-7.32 (m,3H 2,3,4 Ar-H), 6.95 (d, 4 Ar-H $^2J_{H,H}$=8.4 Hz), 6.88 (doublet $^2J_{H,H}$=4.58Hz, HH, 9,18-Pyrr H), 6.77 (doublet $^2J_{H,H}$=4.58Hz, HH, 8,19-Pyrr H), 6.30 (broad s,2H, 13,14-Pyrr H), 3.87 (s,6H, OMe), 1.69 (s,12H, CH_3). IR (in KBr, 25° C): 3337.4 (N-H Stretch), 2926.4 (C-H Stretch, sp^3 Hybridised), 1745.0 (C=N Stretch), 1601.2, 1508.2 (C=C Stretch Aromatic), 1384.5 (C-H Bending, sp^3 Hybridised out of plane), 797.4, 739.7, 711.8

ACCEPTED MANUSCRIPT

(=C-H Bending, Aromatic, out of plane), 1252.7, 1040.1 (C-O Stretch).Zn^{2+}.**7:** 643 (4.48), 592 (4.24), 343 (4.47). IR (in KBr, 25° C): 2882.8 (C-H Stretch, sp^3 Hybridised), 1658.1 (C=N Stretch), 1603.6, 1509.1(C=C Stretch Aromatic), 1360.2 (C-H Bending, sp^3 Hybridised, out of plane), 815.1, 717.3 (=C-H Bending, Aromatic, out of plane), 1254.4, 1033.7(C-O Stretch). Compound **8:** 546 (4.31), 513 (4.27), 376 (4.55**).** ^{1}HNMR: 12.33 (br, 1H,NH), 7.92 (s, 1H, 22-ArH), 7.30 (q, J=5.34 Hz 3H 2,3,4 Ar-H), 6.95 (d,$^2J_{H,H}$=3.81HzHH, 9,18-Pyrr H), 6.80 (d,$^2J_{H,H}$=4.58HzHH, 8,19-Pyrr H), 6.74 (s,4Ar-H (AA'BB')) 6.35 (s,2H, 13,14-Pyrr H), 3.92 (s,6H, para OMe-H's), 3.83 (s,12H, meta OMe-H's), 1.70 (s,12H, CH_3). ^{13}C-NMR (101 MHz, $CDCl_3$, 20°C): 152.45, 147.34, 139.37, 136.53, 133.43, 128.75, 127.29, 125.11, 123.25, 109.62, 61.11, 56.34, 42.07, 29.78, 28.98. IR in (KBr, 25° C): 3300.0 (N-H Stretch), 2923.5 (C-H Stretch, sp^3 Hybridised), 1683.4 (C=N Stretch), 1577.2, 1504.1 (C=C Stretch Aromatic), 1344.3 (C-H Bending, sp^3 Hybridised out of plane), 795.6, 759.6, 717.1 (=C-H Bending, Aromatic, out of plane), 1236.7 (C-O Stretch). Zn^{2+}**.8:** 642 (4.38), 598 (4.12), 346 (4.46). IR (in KBr, 25° C): 2880.3(C-H Stretch, sp^3 Hybridised), 1708.9 (C=N Stretch), 1544.0, 1501.4 (C=C Stretch Aromatic), 1341.0 (C-H Bending, sp^3 Hybridised, out of plane), 934.9, 811.6, 724.8 (=C-H Bending, Aromatic, out of plane), 1232.3 (C-O Stretch).

Single Crystal Structure Determination

Intensity data were collected at 273(2) K on Bruker diffractometer (a single wavelength Enhance X-ray source with MoK_α radiation, λ = 0.71073 Å).[62a] The selected suitable single crystals were mounted using paratone oil on the top of a glass fiber fixed on a goniometer head and immediately transferred to the diffractometer. Pre-experiment, data collection, data reduction and analytical absorption corrections[62b] were performed with the Bruker SAINT

ACCEPTED MANUSCRIPT

program. The crystal structures were solved with SHELXS-97[62c] using direct methods. The structure refinements were performed by full-matrix least-squares on F^2 with SHELXL-97. All programs used during the crystal structure determination process are included in the WINGX software.[62d]

The chemical formula and ring labeling system is shown in Figure 5. Crystal data for compound **8**: $C_{44}H_{45}N_3O_6$, Mw, 711.84; system, monoclinic; space group, P -1; unit cell dimensions, a = 8.7020(4)Å; b = 14.8084(6)Å; c = 15.7963(7)Å; α = 76.9060(10)^0; β =88.9270(10)^0; γ = 76.9610(10)^0; V =1951.82(15)Å^3; Z = 2; T = 298 K; R_{int}, 0.0746; R(all), 0.1046; *Gof* = 0.958; $\Delta_{\rho max}$ = 1.418 e Å^3; $\Delta_{\rho min}$= -1.905 e Å^3.The resolution obtained for the structure of the compounds was limited by the poor quality of the available crystals. The solvent molecule was badly disordered and could not be modeled. All hydrogen atoms were calculated after each cycle of refinement using a riding model, with C-H = 0.93 Å + U_{iso}(H) = 1.2U_{eq}(C) for aromatic H atoms, with C-H = 0.97 Å + U_{iso}(H) = 1.2U_{eq}(C) for methylene H atoms.

Results and Discussion

Synthesis and Spectroscopy

The synthesis of porphyrin analogue, 11, 16-Bis (R-phenyl)-6, 6, 21, 21-tetramethyl-*meta*benzi-6, 21-porphodimethenes with various *meso*-substitutents as shown in Scheme 1 were synthesized using Lewis acid, $BF_3.OEt_2$, catalyzed condensation reaction followed by DDQ oxidation between α, α-dihydroxy-1, 3-diisopropylbenzene, pyrrole and substituted benzaldehydes at room temperature. The desired red color product was obtained after silica gel column chromatography in 15-17% yield alongwith two other products γ-lactam containing *meta*-benziporphodimethenes had *m/z* 18 unit greater than their red powder products, **1**-**8**. All the *meta*-benziporphodimethenes

ACCEPTED MANUSCRIPT

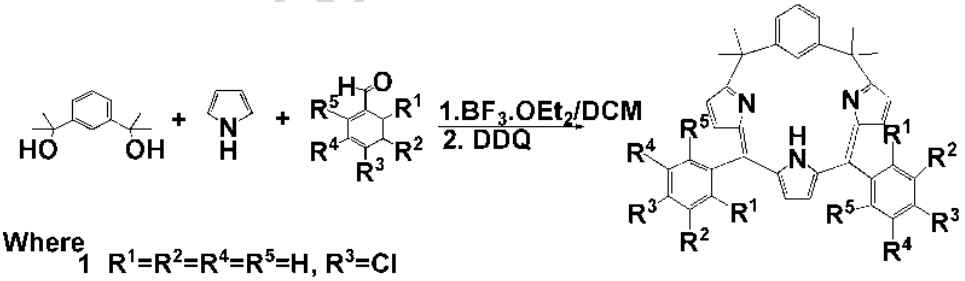
reported in this paper were characterized fully using NMR, UV-Vis and Mass spectroscopy. Their metal complexes were synthesized using metal salt $ZnCl_2$ and reaction was initiated using 2, 6-lutidine. The metallation was confirmed with the instant change in color from red to greenish blue. The formation of complex, Zn^{2+}.**1-8** were confirmed by UV-Vis spectroscopy and change in color from red to greenish blue upon addition of $ZnCl_2$ into acetonitrile solution of free base *meta*-benziporphodimethenes, **1-8**. The UV-Vis spectra of free base *meta*-benziporphodimethenes and their metallated *meta*-benziporphodimethenes complexes are shown in Figure 1A and Figure 1B, respectively. Their UV-Vis spectrum is broad in nature due to presence of sp^3-sp^2 mixed *meso*-carbon atoms non-conjugated system. The ground state absorption spectra characteristics of free base *meta*-benziporphodimethenes and their zinc complexes are tabulated in Table 1. The Soret like high energy band was observed around 342-378 nm for *para* and *ortho*-substituted *meso*-phenyl groups in free base *meta*-benziporphodimethenes, **1**-**8**. The *para*-substituted electron releasing group reduce the Soret like band energy and obtained at 378 and 376 nm, for **7** and **8**, respectively. *Ortho*-halogenations significantly enhance the Soret like band energy and appeared at 321, 320, and 319 nm for **3**, **4**, **5**, respectively. The zinc complexes of *meta*-benziporphodimethenes Soret like high energy band are in the range of 343-353 nm. The Q bands are shifted towards low energy after metallation with zinc. The stokes shift of 80 nm and 100 nm were observed in Q (1-0) and Q (0-0), respectively. The significantly red shifted of Q bands is due to strong interaction of d-orbital of zinc (II) with the macrocycle observed in ground state absorption spectra of zinc complexes of *meta*-benziporphodimethenes with respect to free base *meta*-benziporphodimethenes.[63] Though, the Gouterman four-orbital model is given for porphyrin and other porphyrinoids having complete conjugated systems.[64] But if we assign the bands based on four-orbital model, the highest energy band, Soret like, is S_0-S_2 transition while the low energy bands, Q-bands, are S_0-S_1 transition. The introduction of halogen atoms at *para*

ACCEPTED MANUSCRIPT

positions of the *meso*-phenyl substituents shows bathochromic shift of 1-3 nm with respect to **R** and Zn^{2+}.**R**.[60] *Ortho*-halogenation does not follow the trend and large blue shift was observed when halogenations shift from *para* to *ortho* positions. A large value of blue shift, 28-30 nm, was measured after the replacement of halogen from *para* to *ortho* position in free base *meta*-benziporphodimethenes compared to unsubstituted form, **R**. Addition to support this we also expect there is change in geometry from perturbed to lesser perturbed geometry once metallated with zinc.[60] The compound, **1-8,** forms 1:1 complex with Zn^{2+}. The ESI-Mass spectrum gave a peak of *m/z* at $[M+1]^+$ for free base and $[M - Cl]^+$ for its corresponding metal complexes and shown in supporting information (Figure S1). The mass spectrum also confirms the formation of various *meso*-substituted *m*-benziporphodimethenes and their corresponding metal complexes. The infra-red spectra shows υ (cm^{-1}) for –NH in free base in the range of 3200-3300 cm^{-1} and were absent in case of their corresponding metal complexes (Table S1 & S2 and Figure S2). The sp^3 hybridized –CH stretching frequencies were also observed in all the complexes in the range of 2800-3000 cm^{-1} as expected. The other infra-red stretching frequencies were also observed and comparable to porphyrins macrocycle. These synthesized *meta*-benziporphodimethenes obey the same absorption spectra and NMR spectra pattern as for other reported derivatives (Figure S3).[60-61] ^{1}H NMR spectra of free base, **1-8**, in $CDCl_3$ showed a symmetrical pattern with a singlet in between 1.70-1.81 ppm integrated into twelve hydrogens which corresponds to four methyl groups on two sp^3 hybridized *meso* carbons. In compound **7** a singlet appeared at 3.87 ppm while in the case of **8** having two types of –OCH3 groups, a singlet at 3.92 ppm and 3.83 ppm integrated into six and twelve hydrogens, corresponding to *ortho* and *meta* groups, respectively. The NMR signals for hydrogen on C (22) appeared in the range of 7.92-8.06 ppm for compounds **1-8** and inner core NH proton resonated at 12.0-12.38 ppm as broad signal in compounds, **1-8**. ^{13}C NMR spectra pattern were also observed as expected and shown in supporting information (Figure

ACCEPTED MANUSCRIPT

S4). As a representative data, the spectrophotometric titration of compound **1** was carried out with Zn^{2+} and shown in Figure 2. The change in absorption spectra of **1** with the addition of Zn^{2+} may be correlated to the perturbation of the electronic structure of the compound **1** which in generally attributes to symmetry of molecule. Two isobestic points at 438 and 564 nm, suggesting a neat complex formation. The fluorescence titration was also carried out and shown in Figure 3. The saturation point in fluorescence intensity enhancement was achieved at 2.0 equiv. of Zn^{2+} and 25μM of **1** were used for titration. The stability constants in Hill plot were calculated using increment in absorption spectrum. This analysis gave a value of Hill plot coefficient of 1 and stability constant in the range of 10^5. The large value of stability constant of compound Zn^{2+}.**1** suggests that **1** can be used to detect Zn^{2+} at very low concentration in biological systems. The observed isobestic points and binding constant were in the range of earlier observation reported by Hungs and co-workers.[60]



Where
1 $R^1=R^2=R^4=R^5=H$, $R^3=Cl$
2 $R^1=R^2=R^4=R^5=H$, $R^3=Br$
3 $R^1=R^5=Cl$, $R^2=R^3=R^4=H$
4 $R^1=R^5=F$, $R^2=R^3=R^4=H$
5 $R^1=R^2=R^3=R^4=R^5=F$,
6 $R^1=R^2=R^4=R^5=H$, $R^3=CF_3$
7 $R^1=R^2=R^4=R^5=H$, $R^3=OCH_3$
8 $R^1=R^5=H$,$R^4=R^2=R^3=OCH_3$

Scheme 1. Synthetic route for the synthesis of *meta*-benziporphodimethenes.

ACCEPTED MANUSCRIPT

Compound	λ_{max} in nm		
	Soret like or B (0-0)	Q(1-0)	Q(0-0)
R	349	514	542
Zn^{2+}.**R**	350	593	639
1	353	517	548
Zn^{2+}.**1**	351	594	639
2	351	513	542
Zn^{2+}.**2**	350	594	638
3	321	508	538
Zn^{2+}.**3**	348	602	649
4	320	507	533
Zn^{2+}.**4**	346	598	642
5	319	508	531
Zn^{2+}.**5**	346	600	642
6	342	509	539
Zn^{2+}.**6**	347	594	641
7	378	513	545
Zn^{2+}.**7**	343	592	643
8	376	513	546
Zn^{2+}.**8**	346	598	642

Table 1. Absorption spectra of of *meta*-benziporphodimethenes and thier zinc complexes obtained in degassed acetonitrile. (the values of **R** and Zn^{2+}.**R** were obtained from ref. 60 to discuss the effect of substituent on *meso*-phenyl group; **R** is with unsubstituted *meso*-phenyl)

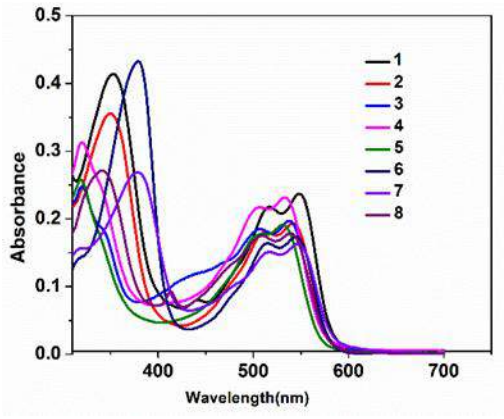


Figure 1A. UV-Vis spectra of compounds **1-8** of 10^{-5} M conc. in acetonitrile solution.

ACCEPTED MANUSCRIPT

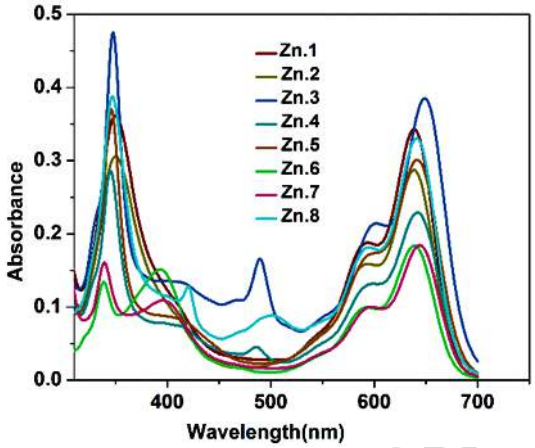


Figure 1B. UV-Vis spectra of compounds Zn^{2+}.**1-8** of 10^{-5} M conc. in acetonitrile solution

]

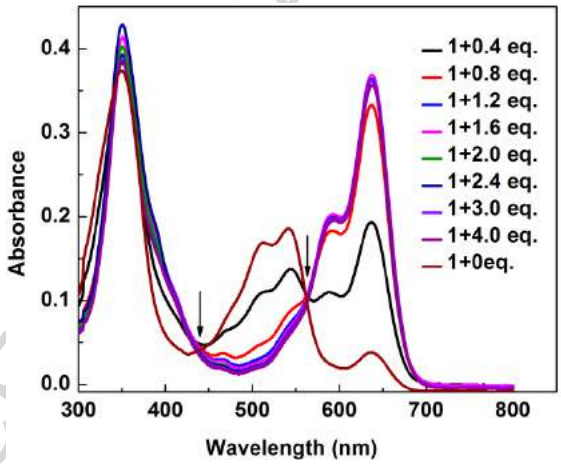


Figure 2. Spectrophotometric titration of **1** with incremental addition of Zn^{2+} in acetonitrile solution. Isobestic points observed at 438 and 564 nm shown by arrow.

ACCEPTED MANUSCRIPT

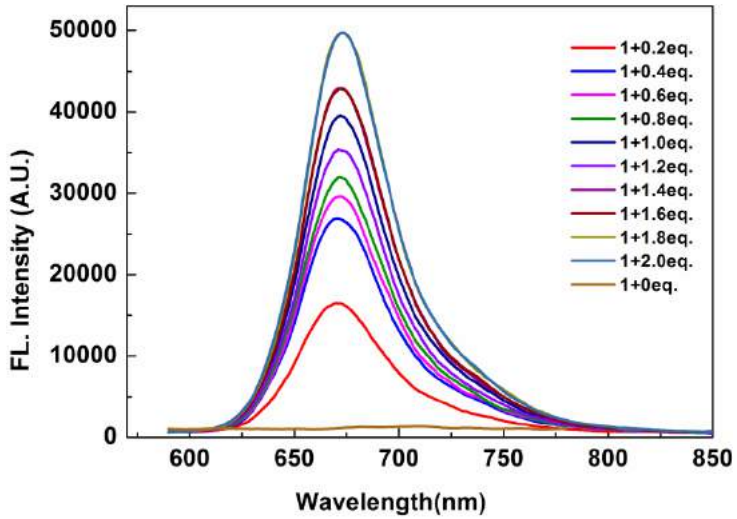


Figure 3. Change in fluorescence intensity of **1** with incremental addition of Zn^{2+} in acetonitrile solution.

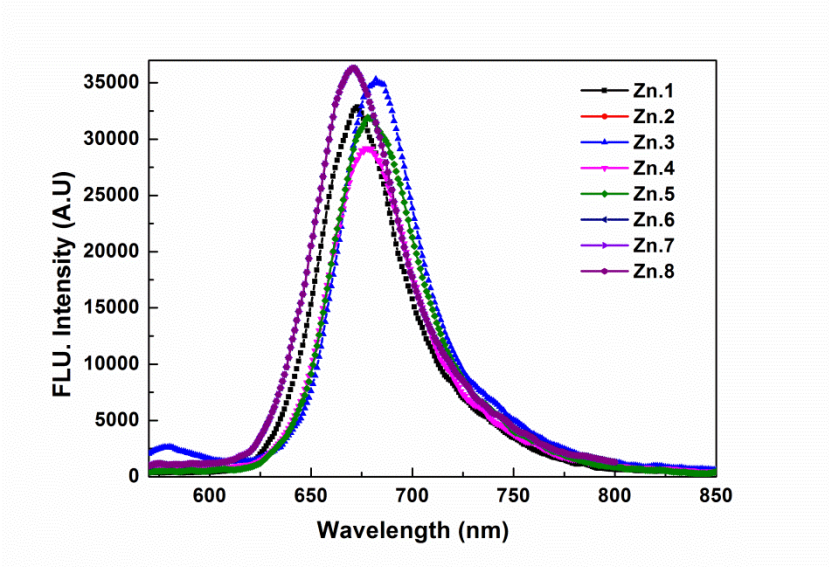


Figure 4. Fluorescence behavior and change in intensity of 10^{-5} M conc. of Zn^{2+}.**1-8** in acetonitrile solution upon excitation at 564 nm.

ACCEPTED MANUSCRIPT

Single Crystal X-ray Structure

Crystal structure of free base *meta*-benziporprphodimethene, **8**, was determined by single crystal X-ray diffraction analyses. The geometry of 8 was found lesser distorted than earlier reported structures of *meta*-benziporphodimethenes.[61] The average deviation of atoms which constitute the macrocycle was measured to be 0.646 Å which is sufficiently lesser as compared to 1.044 Å for free base *meta*-benziporphodimethenes earlier reported by Hung and co-workers.[61] The angle between the phenylene ring plane and three pyrrolicnitrogens of macrocycle is 46.63° which is remarkably lesser. Important and interesting observation in the crystal structure is that the angle between the plane formed by 17 tripyrrin atoms and the vector along the two sp^3*meso* carbons is only 15.45°. These observation confirms that obtained structure of compound 8 is lesser puckered than the earlier reported structures of *meta*-benziporphodimethenes.[60-61] These finding may be attributed to substituents on the *sp*^{3}*meso* carbons of free base *meta*-benziporphodimethenes.

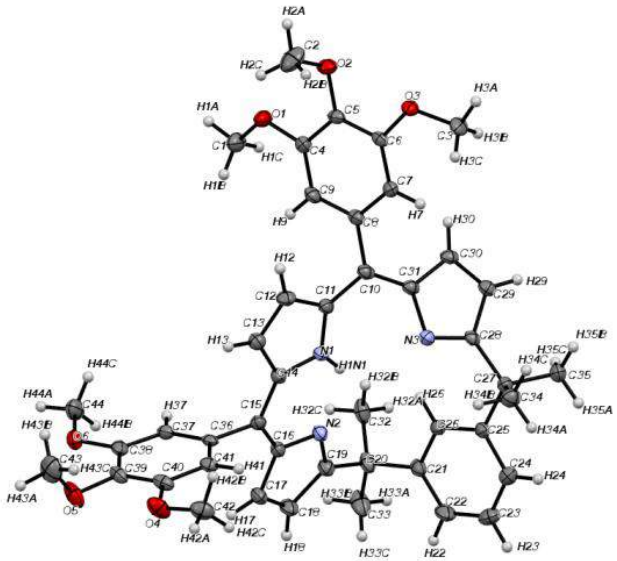


Figure 5. X-ray structure of free base *meta*-benziporphodimethene, **8**.

ACCEPTED MANUSCRIPT

Fluorescence Studies

The important property of fluorescent sensor is its ability to be detected within the complex environment of a cell or organism. The sensitivity of a sensor depends on the stability of a sensors fluorophore and instrument response. Usually the brighter fluorophore need less excitation light thus causing lesser photodamage to the living specimen. The brightness of a fluorophore is examined by the extinction coefficient and quantum yield.[46] These compounds show an excellent chemosensory response after the addition of Zn^{2+}. The free base form in solution is nearly non-fluorescent and become highly fluorescent, emitting between 672-680 nm. The average Stoke's shift is about 33 nm, which is not exciting but nearly similar to other reported sensors for metallated *meta*-benziporphodimethenes.[60] Figure 4 represents the fluorescence behavior of Zn^{2+}.**1-8**. To, the best of our knowledge *meta*-benziporphodimethenes shows higher chelation turn-on fluorescence intensity than any other previously reported zinc specific chemosensors, available in the literature.[51a,f,52,58b] In this study, an attempt was made to focus on the chelation turn-on fluorescence of *meta*-benziporphodimethenes by incorporating the different *meso*-substitutents on tripyrrin moiety. The fluorescence spectra were recorded upon excitation at 564 nm in degassed acetonitrile solution of same concentration. It can be seen from Figure 4 that almost all complexes emitting in the same wavelength range, with a difference of nearly 1-7 nm only. Also, the Figure 4 clearly depicts that *meso*- substituents does not play an important role in tuning the fluorescent spectra to a large extent. This behavior concludes the fact that *meso*-substitutent does not impart any effect on electronic structure of Zn^{2+} metallated *meta*-benziporphodimethenes but related to coplanar tripyrrin moiety in the case Zn^{2+} metallated *meta*-benziporphodimethenes in contrast to the distorted free base form of *meta*-benziporphodimethenes.

ACCEPTED MANUSCRIPT

Compound	τ_s	τ_r	$\varphi=\tau_s/\tau_r$
Zn^{2+}**.1**	3.69	11.88	0.31
Zn^{2+}**.2**	3.53	12.83	0.28
Zn^{2+}**.3**	4.31	11.63	0.37
Zn^{2+}**.4**	4.41	15.59	0.28
Zn^{2+}**.5**	3.98	16.09	0.25
Zn^{2+}**.6**	3.26	24.91	0.13
Zn^{2+}**.7**	3.44	20.52	0.17
Zn^{2+}**.8**	2.77	20.20	0.14

Table 2. Fluorescence quantum yields of zinc complex of *meta*-benziporphodimethenes obtained in degassed toluene calculated using Strickler-Berg relation.

The fluorescence quantum yield (QY) for Zn^{2+}**.1**-Zn^{2+}**.8** were calculated in degassed toluene at room temperature from the ratio of τ_s/τ_r, where τ_s is fluorescence lifetime obtained from fluorescence decay curves recorded with time-correlated single photon counting system combined with Delta diode laser and the radiative life time, τ_r is calculated using Strickler-Berg relation. The calculated fluorescence QY were comparable to the value obtained for 5, 10, 15, 20-tetraphenylporphyrin free base and its zinc complex, 0.11 and 0.033, respectively. The emission spectra of all the zinc complexes are nearly same and are in good agreement with previously reported analogue zinc porphyrin derivatives.[65] The fluorescence quantum yields, φ, calculated for compounds **Zn^{2+}.1-Zn^{2+}.8** are shown in Table 2. The lowest values

ACCEPTED MANUSCRIPT

were obtained for compound Zn^{2+}.**6**, Zn^{2+}.**7** and Zn^{2+}.**8.** It was observed that fluorescence quantum yield are comparatively on higher side when substituent's on *meso*-phenyl are electron withdrawing than electron releasing groups. The observation is opposite to previously reported zinc porphyrin derivatives.[63,65] We believe this may be due to the presence of sp^3-sp^2*meso*-carbons which distinguish these macrocycles from tetraphenylporphyrin and other related porhyrinoids.[65] The fluorescence quantum yield of Zn^{2+}.**7** and Zn^{2+}.**8** are 0.17 and 0.14, respectively which clearly depicts the effect of electron releasing substituents on *meso*-phenyl. The Zn^{2+}.**8** contains three -OMe groups while only one -OMe group on Zn^{2+}.**7**. The presence of halogen on the *meso*-phenyl groups dramatically affect the magnitude of derived fluorescence emission quantum yields. *Para*-halogenation quenches the fluorescence emission in both free base (non-fluorescent) and their zinc derivatives progressively as the atomic number of the attached halogen increases.[63-65] The interaction of halo-substituent to the π-system of the macrocycle has significant effect on the quantum yields. It was also observed that the lowest value for Zn^{2+}.**6** (0.13) indicate that electronegative *para*-substituent effect the fluorescence quantum yield when halo-substituent are on *meso*-phenyl group**.** Contrastingly, *ortho*-chlorination has significant effect and having the highest value of quantum yield (Zn^{2+}.**3**, 0.37). A similar increase in the quantum yield of zinc porphyrin derivatives has been previously reported, but not justified, in the literature.[65-66] *Ortho*-chlorination facilitate smooth interaction between the halo-substituent and the π-system of the macrocycle by locking the position of *meta*-benziporphodimethenes and the *meso*-phenyl group in a perpendicular arrangement and inhibit the indirect conjugation between the induced electron withdrawing halogens and the macrocycle.[67] The strong electronic communication between the π-system of macrocycle and the *ortho*-chlorine overcomes the obvious steric effect of halogens and has been well documented in the literature.[66,68-69] The observed fluorescence quantum yield is consistent with the principles of

ACCEPTED MANUSCRIPT

heavy atom effect of halo-substituent in the case of Zn^{2+}.**1** and Zn^{2+}.**2** as the halo-substituent on *para*-position. The fluorescence quantum yields are not consistent with the principles of heavy atom effect as the position of halo-substituent changes from *ortho* to *para* position (Zn^{2+}.**4** (0.28), Zn^{2+}.**5** (0.25) and Zn^{2+}.**6** (0.13)**).** The observed quantum yields attribute that endocyclic and exocyclic heavy atom effect in the case zinc derivatives oppose each other.[70] *Para*-halogenations seems to withdraw electron density from the macrocycle weakening the electrostatic interaction between the macrocycle and the central metal atom, zinc, and subsequently weakening the endocyclic heavy atom effect. The high quantum yield of *ortho*-chlorinated zinc derivatives (Zn^{2+}.**3**, 0.37) supports additionally the above effect. The observed findings are in good agreement with the reported experimental findings. The placement of the chloro-substituent at *ortho*-position facilitates the 2p-Cl orbital with the π-orbital of the *meso*-carbon. The high electronegative atom strongly interact with the macrocycle and significantly reduce theelectronegativity of the macrocycleand interaction with the central metal atom, zinc, which results in the reduction of endocyclic heavy atom effect.[70-71]

Conclusion

In conclusion, we have extended the series of biologically important fluorescence *switch-on/off* sensor for Zn^{2+} even in very low concentration. In this paper, it is clearly demonstrated that *meso*-substituents does not play any role in tuning the fluorescence intensity. Nevertheless, the. Crystal structure of **8** represents lesser perturbed geometry of free base than values of fluorescence quantum yields obtained are different in each case but higher than tetraphenylporphyrinearlier reported free base *m*-benziporphodimethenes. These chemosensors can be further utilized in physiological imaging and photophysical applications because of their longer excitation and emission wavelengths, which other sensors have deficiency. The use of these complexes in cell imaging is undergoing in our lab.

ACCEPTED MANUSCRIPT

Acknowledgements

RKS thanks to Delhi Technological University for fellowship and AK and LKG thanks to DST, Govt. of India for funding the project under the grant FT/CS-040/2011. MSM thanks DST for providing TCSPC system under FIST project (SR/FST/PSI-164/2011(C)).

Crystallographic data for the structure **8** have been deposited with the Cambridge Crystallographic Data Center (CCDC) under the number CCDC-1411473. Copies of the data can be obtained, free of charge, on application to CCDC 12 Union Road, Cambridge CB2 1EZ, UK [Fax: +44-1223-336033; e-mail: deposit@ccdc.cam.ac.uk or atwww.ccdc.cam.ac.uk.

References

1 T. Mizuno, W. H. Wei, L. R. Eller and J. L. Sessler, *J. Am. Chem. Soc.*, 2002, 124, 1134–1135.

2 P. Anzenbacher, A. C. Try, H. Miyaji, K. Jursikova, V. M. Lynch, M. Marquez and J. L. Sessler, *J. Am. Chem. Soc.*, 2000, 122, 10268–10272.

3 T. L. Kao, C. C. Wang, Y. T. Pan, Y. J. Shiao, J. Y. Yen, C. M. Shu, G. H. Lee, S. M. Peng and W. S. Chung, *J. Org. Chem.*, 2005, 70, 2912–2920.

4 O. Brümmer, J. J. La Clair and K. D. Janda, *Org. Lett.*, 1999, 1, 415–418.

5 A. P. De Silva, H. Q. N. Gunaratne, T. Gunnlaugsson, A. J. M. Huxley, C. P. McCoy, J. T. Rademacher and T. E. Rice, *Chem. Rev.*, 1997, 97, 1515–1566.

6 V. Ramamurthy, K.S. Schanze, ;In Molecular and Supramolecular Photochemistry, Optical Sensors and Switches, vol. 6

7 E. L. Que, D. W. Domaille and C. J. Chang, *Chem. Rev.*, 2008, 108, 1517–1549.

ACCEPTED MANUSCRIPT

8 T. Gunnlaugsson, A. P. Davis and M. Glynn, *Chem. Commun.*, 2001, 2556–2557.

9 T. Gunnlaugsson, P. E. Kruger, P. Jensen, F. M. Pfeffer and G. M. Hussey, *Tetrahedron Lett.*,2003, 44, 8909–8913.

10 R. Meallet-Renault, R. Pansu, S. Amigoni-Gerbier and C. Larpent, *Chem. Commun. (Camb).*,2004, 2344–2345.

11 L. Fabbrizzi, M. Licchelli, P. Pallavicini, A. Perotti, A. Taglietti and D. Sacchi, *Chem. - A Eur. J.*, 1996, 2, 75–82.

12 C. J. Chang, J. Jaworski, E. M. Nolan, M. Sheng and S. J. Lippard, *Proc. Natl. Acad. Sci. U. S. A.*, 2004, 101, 1129–34.

13 F. Pina, M. A. Bernardo and E. García-España, *Eur. J. Inorg. Chem.*, 2000, 2000, 2143–2157.

14 P. Jiang and Z. Guo, *Coord. Chem. Rev.*, 2004, 248, 205–229.

15 R. Krämer, *Angew. Chemie Int. Ed.*, 1998, 37, 772–773.

16 L. Fabbrizzi, M. Licchelli, P. Pallavicini, L. Parodi, A. Taglietti, Perspect. Supramol. Chem., 1999, 5, 93–134.

17 C. C. Woodroofe, R. Masalha, K. R. Barnes, C. J. Frederickson and S. J. Lippard, *Chem. Biol.*, 2004, 11, 1659–1666.

18 M. Taki, J. L. Wolford and T. V. O'Halloran, *J. Am. Chem. Soc.*, 2004, 126, 712–713.

19 Y. Yang, Q. Zhao, W. Feng and F. Li, *Chem. Rev.*, 2013, 113, 192–270.

20 J.-C. G. Bünzli and S. V. Eliseeva, *Chem. Sci.*, 2013, 4, 1939.

21 D. J. Stephens and V. J. Allan, *Science*, 2003, 300, 82–6.

22 W. R. Zipfel, R. M. Williams and W. W. Webb, *Nat. Biotechnol.*, 2003, 21, 1369–1377.

23 H. Kobayashi, M. Ogawa, R. Alford, P. L. Choyke and Y. Urano, *Chem. Rev.*, 2010, 110, 2620–2640.

24 M. Yu, F. Li, Z. Chen, H. Hu, C. Zhan, H. Yang and C. Huang, *Anal. Chem.*, 2009, 81, 930–5.

25 L. Xiong, Z. Chen, Q. Tian, T. Cao, C. Xu and F. Li, *Anal. Chem.*, 2009, 81, 8687–94.

26 H. Su, X. Chen and W. Fang, *Anal. Chem.*, 2014, 86, 891–9.

ACCEPTED MANUSCRIPT

27 M. Chalfie, Y. Tu, G. Euskirchen, W. Ward and D. Prasher, *Science (80-.).*, 1994, 263, 802–805.

28 R. Y. Tsien, *Annu Rev Biochem*, 1998, 67, 509–544.

29 T. Terai and T. Nagano, *Curr. Opin. Chem. Biol.*, 2008, 12, 515–21.(b) H. M. Kim and B. R. Cho, *Acc. Chem. Res.*, 2009, 42, 863–72. (c) Y. Zou, T. Yi, S. Xiao, F. Li, C. Li, X. Gao, J. Wu, M. Yu and C. Huang, *J. Am. Chem. Soc.*, 2008, 130, 15750–1.

30 (a) J.-C. G. Bünzli, *Chem. Rev.*, 2010, 110, 2729–55. (b) Q. Zhao, F. Li and C. Huang, *Chem. Soc. Rev.*, 2010, 39, 3007–30. (c) Q. Zhao, C. Huang and F. Li, *Chem. Soc. Rev.*, 2011, 40, 2508–24.

31 (a) X. Michalet, F. F. Pinaud, L. A. Bentolila, J. M. Tsay, S. Doose, J. J. Li, G. Sundaresan, A. M. Wu, S. S. Gambhir and S. Weiss, *Science*, 2005, 307, 538–44. (b) H. Agadjaniana, J. Maa, A. Rentsendorja, V.Valluripallia, J. Y. Hwang, A. Mahammed, D. L. Farkas, H. B. Gray, Z. Gross and L. K. Medina-Kauwe, *PNAS*, 2009, 106, 6105-6110.

32 (a) P. Chavez-Crooker, N. Garrido and G. A. Ahearn, *J. Exp. Biol.*, 2001, 204, 1433–1444. (b) M. Ghosh, S. K. Sonkar, M. Saxena and S. Sarkar, *Small*, 7 (22), 3170-3177.

33 W. Breuer, S. Epsztejn, P. Millgram and I. Z. Cabantchik, *Am. J. Physiol.*, 1995, 268, C1354–C1361.

34 R. Corradini, A. Dossena, G. Galaverna, R. Marchelli, A. Panagia and G. Sartor, *J. Org. Chem.*, 1997, 62, 6283–6289.

35 Y. Zheng, K. M. Gattás-Asfura, V. Konka and R. M. Leblanc, *Chem. Commun. (Camb).*,2002, 2350–2351.

36 A. Torrado, G. K. Walkup and B. Imperiali, *J. Am. Chem. Soc.*, 1998, 120, 609–610.

37 W.-Y. Lin and H. E. Van Wart, *J. Inorg. Biochem.*,1988, 32, 21–38.

38 J. Rosenthal and S. J. Lippard, *J. Am. Chem. Soc.*, 2010, 132, 5536–7. (b) M. H. Lim, B. A. Wong, W. H. Pitcock, D. Mokshagundam, M. H. Baik and S. J. Lippard, *J. Am. Chem. Soc.*, 2006, 128, 14364–14373.

39 V. Dujols, F. Ford and A. W. Czarnik, *J. Am. Chem. Soc.*, 1997, 119, 7386–7387.

40 T. Gunnlaugsson, J. P. Leonard, K. Sénéchal and A. J. Harte, *Chem. Commun. (Camb).*,2004, 782–3.

41 G. Klein, D. Kaufmann, S. Schürch and J.-L. Reymond, *Chem. Commun.*, 2001, 561–562.

ACCEPTED MANUSCRIPT

42 A. Takeda and H. Tamano, *Brain Res. Rev.*, 2009, 62, 33–44.

43 J. J. R. Frausto da Silva and R. J. P. Williams, The Biological Chemistry of the Elements, Oxford University Press, New York, 2nd edn, 2001

44 S. Y. Assaf and S.-H. Chung, *Nature*, 1984, 308, 734–736.

45 J. M. Berg and Y. Shi, *Science*, 1996, 271, 1081–1085.

46 K. P. Carter, A. M. Young and A. E. Palmer, *Chem. Rev.*, 2014, 114, 4564–4601.

47 N. C. Lim, L. Yao, H. C. Freake and C. Brückner, *Bioorg. Med. Chem. Lett.*, 2003, 13, 2251–2254.

48 E. M. Nolan, J. W. Ryu, J. Jaworski, R. P. Feazell, M. Sheng and S. J. Lippard, *J. Am. Chem. Soc.*, 2006, 128, 15517–15528.

49 R. A. Bozym, R. B. Thompson, A. K. Stoddard and C. A. Fierke, *ACS Chem. Biol.*, 2006, 1, 103–111.

50 R. Yang, K. Li, K. Wang, F. Zhao, N. Li and F. Liu, *Anal. Chem.*, 2003, 75, 612–621.

51 (a) S. C. Burdette, C. J. Frederickson, W. Bu and S. J. Lippard, *J. Am. Chem. Soc.*, 2003, 125, 1778–87. (b) X. A. Zhang, D. Hayes, S. J. Smith, S. Friedle and S. J. Lippard, *J. Am. Chem. Soc.*, 2008, 130, 15788–15789. (c) G. K. Walkup, S. C. Burdette, S. J. Lippard and R. Y. Tsien, *J. Am. Chem. Soc.*, 2000, 122, 5644–5645. (d) E. M. Nolan, S. C. Burdette, J. H. Harvey, S. A. Hilderbrand and S. J. Lippard, *Inorg. Chem.*, 2004, 43, 2624–35. (e) C. J. Chang, E. M. Nolan, J. Jaworski, K. Okamoto, Y. Hayashi, M. Sheng and S. J. Lippard, *Inorg. Chem.*, 2004, 43, 6774–9. (f) S. C. Burdette and S. J. Lippard, *Inorg. Chem.*, 2002, 41, 6816–6823.

52 (a) T. Hirano, K. Kikuchi, Y. Urano and T. Nagano, *J. Am. Chem. Soc.*, 2002, 124, 6555–6562. (b) T. Hirano, K. Kikuchi, Y. Urano, T. Higuchi and T. Nagano, *Angew. Chemie*, 2000, 112, 1094–1096. (c) K. Komatsu, K. Kikuchi, H. Kojima, Y. Urano and T. Nagano, *J. Am. Chem. Soc.*, 2005, 127, 10197–204.

53 N. C. Lim and C. Brückner, *Chem. Commun. (Camb).*,2004, 1094–5.

54 (a) H. Sasaki, K. Hanaoka, Y. Urano, T. Terai and T. Nagano, *Bioorganic Med. Chem.*, 2011, 19, 1072–1078. (b) K. R. Gee, Z.-L. Zhou, W.-J. Qian and R. Kennedy, *J. Am. Chem. Soc.*, 2002, 124, 776–778.

55 B. Tang, H. Huang, K. Xu, L. Tong, G. Yang, X. Liu and L. An, *Chem. Commun. (Camb).*,2006, 3609–11.

56 J. Wang, Y. Xiao, Z. Zhang, X. Qian, Y. Yang and Q. Xu, *J. Mater. Chem.*, 2005, 15, 2836.

ACCEPTED MANUSCRIPT

57 (a) D. Li, S. Chen, E. A. Bellomo, A. I. Tarasov, C. Kaut, G. A. Rutter and W. Li, *Proc. Natl. Acad. Sci. U. S. A.*, 2011, 108, 21063–8. (b) W. Lin, D. Buccella and S. J. Lippard, *J. Am. Chem. Soc.*, 2013, 135, 13512–20.

58 (a) H. C. Roh, S. Collier, J. Guthrie, J. D. Robertson and K. Kornfeld, *Cell Metab.*, 2012, 15, 88–99. (b) A. M. Kim, M. L. Bernhardt, B. Y. Kong, R. W. Ahn, S. Vogt, T. K. Woodruff and T. V O'Halloran, *ACS Chem. Biol.*, 2011, 6, 716–23.

59 (a) S. K. Ghosh, P. Kim, X. Zhang, S.-H. Yun, A. Moore, S. J. Lippard and Z. Medarova, *Cancer Res.*, 2010, 70, 6119–6127. (b) W. Chyan, D. Y. Zhang, S. J. Lippard and R. J. Radford, *Proc. Natl. Acad. Sci. U. S. A.*, 2014, 111, 143–8.

60 C.-H. Hung, G.-F. Chang, A. Kumar, G.-F. Lin, L.-Y. Luo, W.-M. Ching and E. Wei-GuangDiau, *Chem. Commun. (Camb).*,2008, 978–980.

61 (a) G. F. Chang, A. Kumar, W. M. Ching, H. W. Chu and C. H. Hung, *Chem. - An Asian J.*, 2009, 4, 164–173. (b) M. Stępień, L. Latos-Grazyński, L. Szterenberg, J. Panek and Z. Latajka, *J. Am. Chem. Soc.*, 2004, 126, 4566–4580.

62 Bruker CCD System 2003. (b) R. C. Clark, J.S. Reid, 1995, *A51*, 887-897 (c) G. M. Sheldrick, *ActaCryst.* 2008, *A64*, 112-122 (d) L. J. Farrugia, *J. Appl. Cryst.* 2012, *45*, 849-854.

63 F. Nifiatis, J. C. Athas, D. K. Gunaratne, Y. Gurung, K. Monette, and P. Shivokevich, *The Open Spectroscopy Journal*, 2011, 5, 1-12.

64 M. Gouterman, *Journal of Molecular Spectroscopy*, 1961, 6, 138-163.

65 (a) D. J. Quimby and F. R. Longo, *Journal of the American Chemical Society*, 1975, 97, 5111-5116. (b) T. Ding, E. Alemán, D. Modarelli, and C. Ziegler, *J Phys Chem A*, 2005, 109, 7411–7. (c) N. Kobayashi, H. Ogata, N. Nonaka, *Chem. Eur. Journal*, 2003, 9, 5123- 5134**.**

66 S. I. Yang, J. Seth, J.-P. Strachan, S. Gentemann, D. Kim, D. Holten, J. S. Lindsey, D. F. Bocian, *Journal of Porphyrins and Phthalocyanines*, 1999, 3, 117-147.

67 J. P. Strachan, S. Gentemann, J. Seth, *Journal of the American Chemical Society*, 1997, 119, 11191-11201. (b) A Osuka, N Tanabe, and S Kawabata, *Journal of Organic Chemistry*, 1995, 60, 7177-7185.

68 (a) A. Ghosh, *Journal of the American Chemical Society*, 1995, 117, 4691-9 (b)T. Vangberg and A. Ghosh, *Journal of the American Chemical Society*, 1998, 120, 6227-6230.

ACCEPTED MANUSCRIPT

69 W. A. Kalsbeck, J. Seth, and D. F. Bocian, *Inorganic Chemistry*, 1996, 35, 7935-7937.

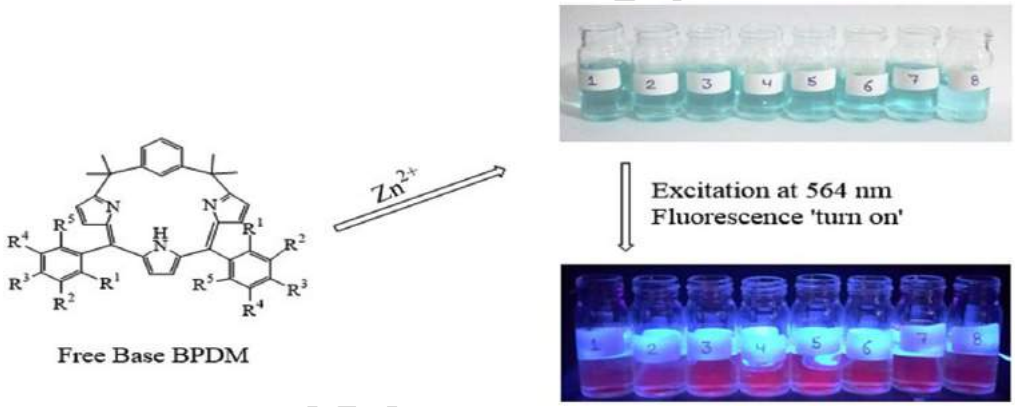
70 D. S .McClure, *Journal of Chemical Physics*, 1949, 17, 905-13.

71 (a) K. N. Solov'ev and E. A. Borisevich, Phys Usp 2005, 48, 231-53. (b) K. N. Solov'ev, M. P. Tsvirko, A. T. Gradyushko and D. T. Kozhich, Opt. Spectrosc. (USSR), 1972, 33, 480.

ACCEPTED MANUSCRIPT

ACCEPTED MANUSCRIPT

Graphical Abstract

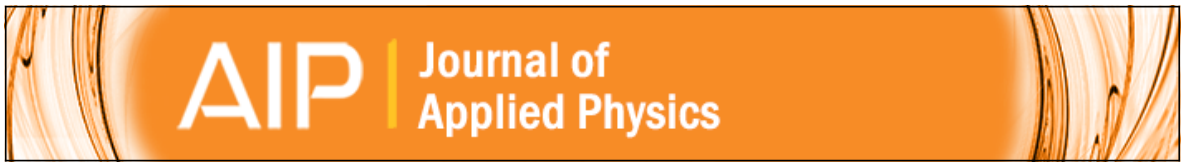


ACCEPTED MANUSCRIPT

Highlights

- Switch-on/off fluorescent molecules
- Sensitive to zinc ions
- High quantum yields in porphyrinoid systems
- Potential to use in cell imaging

ACCEPTED MANUSCRIPT



Tunable unidirectional scattering of ellipsoidal single nanoparticle

Reena, Yogita Kalra, Ajeet Kumar, and R. K. Sinha

Citation: Journal of Applied Physics **119**, 243102 (2016); doi: 10.1063/1.4954675
View online: http://dx.doi.org/10.1063/1.4954675
View Table of Contents: http://scitation.aip.org/content/aip/journal/jap/119/24?ver=pdfcov
Published by the AIP Publishing

Articles you may be interested in

Influence of Au nanoparticles on the photoluminescent and electrical properties of Bi3.6Eu0.4Ti3O12 ferroelectric thin films
J. Appl. Phys. **116**, 034101 (2014); 10.1063/1.4887810

Influence of Cr2O3 nanoparticles on the physical properties of polyvinyl alcohol
J. Appl. Phys. **112**, 093525 (2012); 10.1063/1.4764864

Spectrally tunable magnetic nanoparticles designed for distribution/recollection applications
J. Appl. Phys. **107**, 09B327 (2010); 10.1063/1.3355900

Ag nanoparticle dispersed Pb Ti O 3 percolative composite thin film with high permittivity
Appl. Phys. Lett. **93**, 222901 (2008); 10.1063/1.3037207

Single metal nanoparticle absorption spectroscopy and optical characterization
Appl. Phys. Lett. **88**, 063109 (2006); 10.1063/1.2172143



Reuse of AIP Publishing content is subject to the terms at: https://publishing.aip.org/authors/rights-and-permissions. Download to IP: 14.139.251.107 On: Sun, 03 Jul 2016 10:54:01

JOURNAL OF APPLIED PHYSICS **119**, 243102 (2016)

Tunable unidirectional scattering of ellipsoidal single nanoparticle

Reena,[1] Yogita Kalra,[1] Ajeet Kumar,[1] and R. K. Sinha[1,2,a)]
[1]*TIFAC-center of Relevance and Excellence in Fiber Optics and Optical Communication, Department of Applied Physics, Delhi Technological University (Formerly Delhi College of Engineering, University of Delhi), Bawana Road, Delhi 110042, India*
[2]*CSIR-Central Scientific Instruments Organisation, Sector 30 C, Chandigarh 160 030, India*

(Received 24 February 2016; accepted 5 June 2016; published online 24 June 2016)

We report unidirectional scattering by tri-axial single ellipsoidal dielectric nanoparticle, which is applicable in the design and development of tunable, low-loss and ultra-compact nanoantennas. Based on the orientation and rotation of the ellipsoidal nanoparticle, three types of modes, one longitudinal mode and two transverse modes, have been excited. Electric and magnetic dipoles have been optically induced in the nanoparticle. Generalized Kerker's conditions have been applied at the interference of optically induced electric and magnetic dipoles. Azimuthally symmetric forward scattering with complete suppression of backward scattering using first Generalized Kerker's condition has been achieved at three different wavelengths for the allowed longitudinal mode and transverse modes in the optical region using single ellipsoidal nanoparticle. Due to 3-fold symmetry, forward scattering can be tuned at different wavelengths, using single ellipsoidal nanoparticle just by changing the direction of the incident electric field. *Published by AIP Publishing.*
[http://dx.doi.org/10.1063/1.4954675]

I. INTRODUCTION

Scattering properties of light by various types of nanoparticles have been studied to manipulate and confine electromagnetic waves on the nanometer scale due to their numerous applications such as sensing, nanoantennas, photovoltaics, and medicine.[1–6] Metallic nanoparticles have been used due to their unique property of generation of surface plasmon polaritons at the metal surfaces that has attracted many applications in nanophotonics and metamaterials.[7–9] But metal's losses and absorption affect the quality of the metallic nanostructure.[6,10] Moreover, it is not possible to achieve magnetic resonance in the visible spectrum region using metallic split ring resonators. Therefore, large permittivity dielectrics are being used as the counterpart of metals due to negligible absorption.[11–14] However, absorption is requisite in applications such as photovoltaics[15] and sensing[16] but in case of nanoantennas, absorption should be as low as possible. So, dielectrics with high permittivity are the prevalent choice in application of nanoantennas. First of all, Kuznetsov *et al*. demonstrated experimentally magnetic resonance in the visible spectrum region using high-dielectric nanoparticles.[14] Due to the light-matter interaction, electric and magnetic dipoles are produced in the dielectric nanoparticles of large permittivity at resonant frequencies.[17] Wavelengths at which magnitude of electric and magnetic moments is equal, and generalized Kerker's (GKs) conditions have been applied. When the first generalized Kerker's condition is satisfied, forward scattering takes place by suppressing the backward scattering to zero and when the second generalized Kerker's condition is satisfied, most of the light is scattered in the backward direction.[18] Unidirectional forward scattering (Huygen's source) and backward scattering (Huygen's reflector) are used to design all-dielectric optical nanoantennas.[11,12]

Complete forward scattering and high directivity has been achieved in many symmetrical structures like sphere[5] and cube.[18] Fu *et al*. have calculated forward to backward scattering ratio for spheroidal Si nanoparticles.[19] In spheroidal nanoparticle, two axes are equal and only one axis has different dimensions. But ellipsoidal nanoparticle has all the axes unequal. Ellipsoidal nanoparticle has the advantage that it has three-fold symmetry which leads to three types of modes, two transverse modes (TM) and one longitudinal mode (LM). Our work is based on the ellipsoidal germanium (Ge) nanoparticle. Polarizability of the nanoparticle changes by changing the direction of incident electric field along three unequal axes of the ellipsoid. Hence, the forward scattering can be tuned at different wavelengths by changing the direction of incident electric field, which is not possible in the case of symmetric structures like sphere and cube. Kalkbrenner *et al*. experimentally demonstrated the rotation of the single gold ellipsoidal nanoparticle attached to the tip of glass fiber.[20] Eventually, it is also feasible to rotate dielectric nanoparticle using this technique, so that it is useful in various nanophotonic applications such as optical imaging, energy harvesting, and sensing.

II. DESIGN

Triaxial ellipsoidal dielectric nonmagnetic nanoparticle has been considered with lengths of semi-principal axes as "*a*," "*b*," and "*c*," where length along "*a*" has been taken as semi-major axis. Ellipsoidal particles are classified into three categories based on the relative length of the three principal axes, namely, oblate spheroids ($a = b > c$), prolate spheroids ($a = b < c$), and scalene ellipsoids ($a > b > c$). In this paper, scalene ellipsoid has been considered which leads to three

a)E-mail: dr_rk_sinha@yahoo.com

Reuse of AIP Publishing content is subject to the terms at: https://publishing.aip.org/authors/rights-and-permissions. Download to IP: 14.139.251.107 On: Sun, 03 Jul 2016 10:54:01

distinct modes, one longitudinal mode and two transverse modes. The effective radius of the equivolume sphere for the ellipsoidal nanoparticle is given by $r_{\text{eff}} = (a * b * c)^{1/3}$. Material of the nanoparticle has been taken to be Ge.[21] Ge is a dielectric with high permittivity, $\varepsilon_r = 20$, required for the design of low loss high dielectric nanoantennas. Dimensions of ellipsoid have been taken as $a = 125$ nm, $b = 100$ nm, and $c = 50$ nm. The dimensions of the nanoparticle are chosen in such a way that wavelength of forward scattering falls in the optical region. Incident radiation has been taken to be linearly polarized in the y-direction and propagates in the x-direction. Orientation of the nanoparticle has been shown in Figure 1(a) and rotation of the nanoparticle when major axis is parallel to the x-axis has been shown in Figure 1(b).

III. DIPOLE ANALYSIS

Due to the light-matter interaction, electric and magnetic dipoles are generated at the particular wavelengths λ_{ED} and λ_{MD}. The electric dipole moment "p" and magnetic dipole moment "m" can be expressed as[22]

$$p = \varepsilon_0(1-\varepsilon_r)\oint_V E(r')dV', \tag{1a}$$

$$m = \frac{i\omega(1-\varepsilon_r)}{2c}\oint_V [r \times E(r')]dV', \tag{1b}$$

where i denotes the imaginary part of the complex variable, ω is the angular frequency, ε_0 is the vacuum permittivity, r is the observation point, r' is the source point, c is the speed of light in vacuum, ε_r is the relative permittivity of the nanoparticle, $\times$ denotes the vector product of position vector "r," and electric field vector "$E(r')$". Calculations have been done in the vectorial field with the finite element method (FEM) based "Comsol Multiphysics" software package.

Further, scattering cross section of the nanoparticle for both electric and magnetic dipoles has been calculated as

$$\sigma^p_{sca} = \frac{\langle P_{sca,ED}\rangle}{I_0}, \tag{2a}$$

$$\sigma^m_{sca} = \frac{\langle P_{sca,MD}\rangle}{I_0}, \tag{2b}$$

where I_0 is the incident power density, $\langle P_{sca,ED}\rangle$ and $\langle P_{sca,MD}\rangle$ are the power scattered by electric and magnetic dipole, respectively, which can be expressed as

$$\langle P_{sca,ED}\rangle = \frac{c^2 k_0^4 z_0}{12\pi}|p|^2, \tag{3a}$$

$$\langle P_{sca,MD}\rangle = \frac{c^2 k_0^4 z_0}{12\pi}|m|^2, \tag{3b}$$

where c is the speed of light in vacuum, k_0 and z_0 are the free space wavenumber and free space impedance, respectively. Electric dipole moment "p" and magnetic dipole moment "m" have been calculated using Equations (1a) and (1b), respectively.

Further, the effect of orientation and rotation of the ellipsoidal nanoparticle on electric and magnetic dipole moments has been analyzed. Three distinct modes, one longitudinal mode (LM) and two transverse modes (TM), are excited at distinct combinations of incident angle and rotation angle. LM mode is excited when major axis is parallel to the incident electric field (E) or at $\theta = 90°$. Two TM modes are excited when major axis is perpendicular to the incident electric field or at $\theta = 0°$. One TM mode is excited when $\phi = 0°$ or b-axis is parallel to the incident electric field and another transverse mode is excited when $\phi = 90°$ or c-axis is parallel to the incident electric field.

Scattering cross section has been calculated with Matlab using Equations (2a) and (2b). The variation of scattering cross-section of the ellipsoidal nanoparticle with wavelength for the incident electric field parallel to a-axis has been obtained as shown in Figure 2(a). Peaks in the scattering cross section, one at the wavelength 500 nm corresponds to electric dipole resonance and another at 650 nm, correspond to the magnetic dipole resonance as shown in Figure 2(a). Electric field distribution in the nanoparticle at the wavelengths $\lambda_{\text{ED}} = 500$ nm and $\lambda_{\text{MD}} = 650$ nm has been shown in Figures 2(b) and 2(c), respectively. So, at $\theta = 90°$, LM has been excited at the wavelengths λ_{ED} and λ_{MD}. Figure 2(a) indicates that electric dipole and magnetic dipole interfere at the wavelengths 607 nm and 680 nm. At these wavelengths, electric and magnetic responses are equal.

Further, angle of orientation has been changed from $\theta = 90°$ to $\theta = 0°$, major axis is now parallel to the direction of propagation and two minor axes have been taken to be parallel to the incident electric field one by one. Then two transverse modes are excited, one is called b-TM when $\phi = 0°$ and another is called c-TM when $\phi = 90°$.

First, b-axis has been taken to be parallel to the incident electric field, so b-TM mode has been excited. Scattering cross section has been calculated and has been plotted versus wavelength as shown in Figure 3(a). Peaks in the scattering spectra denote the electric and magnetic dipole resonances.

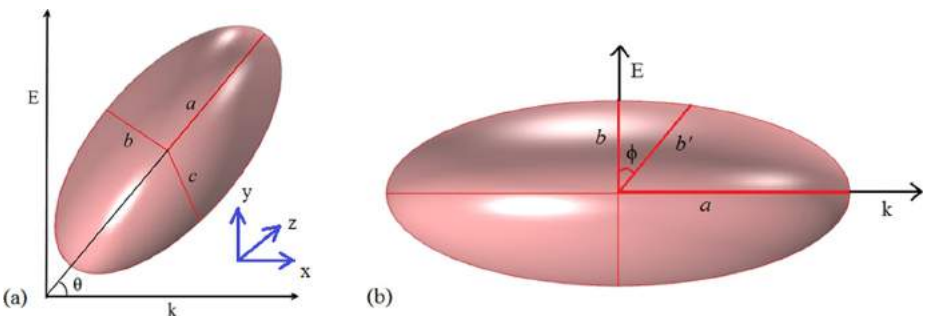


FIG. 1. (a) Orientation of the major-axis of the ellipsoidal nanoparticle in the laboratory frame around the x-axis or the direction of propagation k with angle θ. (b) Rotation of the nanoparticle around the major-axis with angle ϕ.

Reuse of AIP Publishing content is subject to the terms at: https://publishing.aip.org/authors/rights-and-permissions. Download to IP: 14.139.251.107 On: Sun, 03 Jul 2016 10:54:01

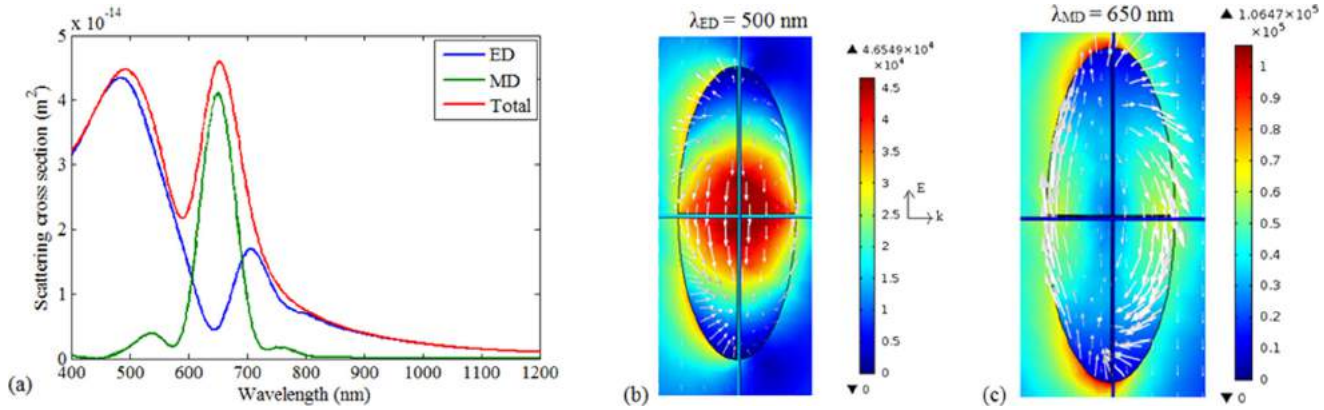


FIG. 2. (a) Scattering cross-section of the ellipsoidal nanoparticle when E || to *a*-axis of the ellipsoid. (b) and (c) Electric field inside the nanoparticle forming electric dipole and magnetic dipole. White arrows indicate electric lines of force.

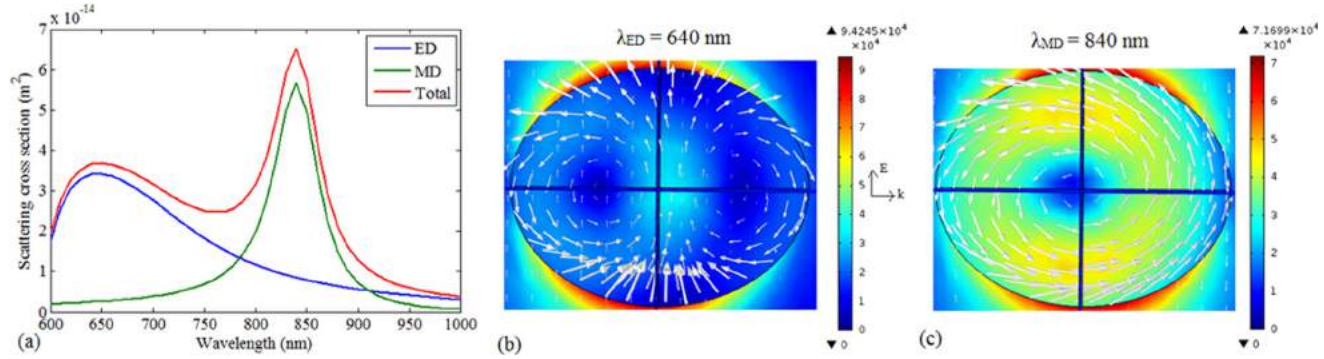


FIG. 3. (a) Variation of scattering cross-section with wavelength when E || *b*-axis of the ellipsoid. (b) and (c) Electric field distribution patterns at the wavelengths where electric dipoles are created.

Electric dipole and magnetic dipole are created at the wavelengths $\lambda_{ED} = 640$ nm and $\lambda_{MD} = 840$ nm, respectively, as shown in Figure 3(a). The electric field distribution at $\lambda_{ED} = 640$ nm and $\lambda_{MD} = 840$ nm has been shown in Figures 3(b) and 3(c), respectively.

Now, *c*-axis has been taken to be parallel to the incident electric field, leading to the excitation of *c*-TM mode. The position of the electric dipole and magnetic dipole has been shifted to the wavelengths $\lambda_{ED} = 560$ nm and $\lambda_{MD} = 660$ nm as shown in Figure 4(a). An electric field distribution at the wavelengths λ_{ED} and λ_{MD} has been shown in Figures 4(b) and 4(c), respectively.

Hence, electric and magnetic dipoles can be tuned at different wavelengths by changing the direction of the incident electric field.

IV. UNIDIRECTIONAL SCATTERING USING GENERALIZED KERKER'S (GK) CONDITIONS

Far field scattering pattern of pure electric and magnetic dipoles is symmetrically distributed in forward and backward directions, when there is no interference between the dipoles.[22] In the case of interference of electric dipole and magnetic dipole, unidirectional scattering takes place. Positions of

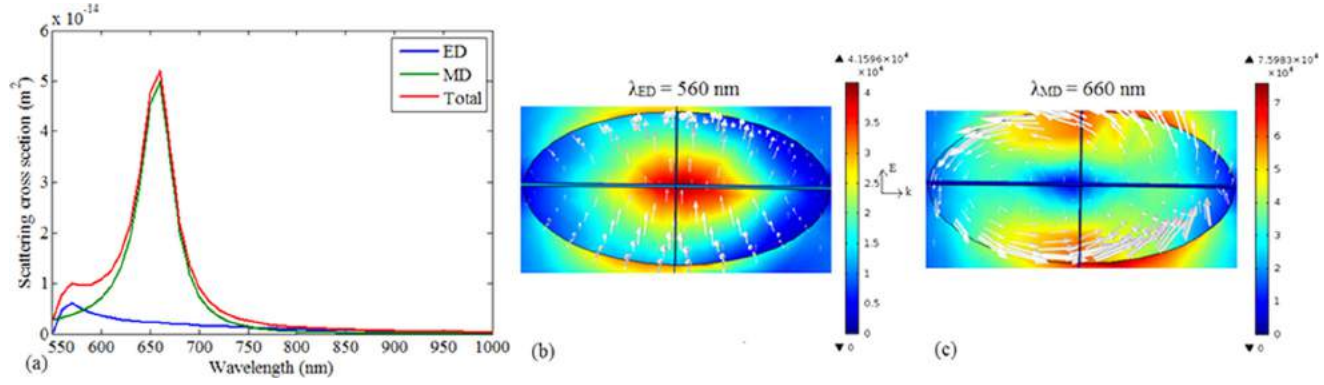


FIG. 4. (a) Plot of scattering cross section with wavelength when E || *c*-axis of the ellipsoidal nanoparticle. (b) and (c) Electric field distribution and direction of electric field shown by white lines.

Reuse of AIP Publishing content is subject to the terms at: https://publishing.aip.org/authors/rights-and-permissions. Download to IP: 14.139.251.107 On: Sun, 03 Jul 2016 10:54:01

electric dipoles, magnetic dipoles, and their interference have been shown in Figures 2–4 for longitudinal as well as transverse modes.

Further, to discriminate whether there is forward scattering or backward scattering, electric polarizability and magnetic polarizability have been calculated and generalized Kerker's conditions have been applied. Electric polarizability α_e and magnetic polarizability α_m can be expressed as

$$\alpha_e = \frac{p_y}{\varepsilon_0 |E_0|}, \tag{4a}$$

$$\alpha_m = \frac{m_x}{|H_0|}, \tag{4b}$$

where E_0 and H_0 are the electric and magnetic fields of the incident plane wave fallen on the nanoparticle, p_y and m_x are the electric dipole moment along y-axis and magnetic dipole moment along x-axis, respectively.[23]

According to the first GK condition, unidirectional forward scattering takes place, when

$$\frac{\alpha_e}{\varepsilon_s} = \mu_s \alpha_m, \tag{5}$$

which results in backward scattering zero or

$$\frac{d\sigma_{sca}}{d\Omega}(180^\circ) = 0, \tag{6}$$

where ε_s and μ_s are the relative permittivity and permeability of the surrounding medium. In our case, surrounding medium is air, so $\varepsilon_s = \mu_s = 1$.

Further, according to the second GK condition, backward scattering takes place when

$$\mathrm{Re}\left(\frac{\alpha_e}{\varepsilon_s}\right) = -\mathrm{Re}(\mu_s \alpha_m), \tag{7a}$$

$$\mathrm{Im}\left(\frac{\alpha_e}{\varepsilon_s}\right) = \mathrm{Im}(\mu_s \alpha_m). \tag{7b}$$

Forward scattering is not zero in this case and has a value equal to

$$\frac{d\sigma_{sca}}{d\Omega}(0^\circ) = \frac{16 k_0^{10}}{9} |\alpha_e/\varepsilon_s|^4. \tag{8}$$

In this case, as medium is taken to be air, so $\varepsilon_s = \mu_s = 1$, so that real part of the electric polarizability is equal to negative of the real part of the magnetic polarizability as shown in Equation (7a). Also, imaginary parts of the electric and magnetic polarizabilities are equal as shown in Equation (7b). In case of backward scattering there is a very small lobe in the forward direction. Thus, forward scattering is not completely suppressed in this case, value of scattered intensity in the forward direction is given by Equation (8).

Now, real and imaginary parts of the electric and magnetic polarizabilities of the nanoparticle have been calculated using Equations (4a) and (4b) and variations have been plotted with respect to the wavelength for all the three distinct modes to analyze the GK conditions of forward scattering and backward scattering as shown in Figures 5(a)–7(a).

Real and imaginary parts of electric and magnetic polarizabilities have been plotted in Figure 5(a) for the longitudinal mode when incident electric field is parallel to the a-axis or semi-major axis. First generalized Kerker's condition is satisfied at the wavelength 680 nm leading to forward scattering at 680 nm. Far field scattering pattern is shown in Figure 5(b). At this wavelength, no backward scattering has been obtained, further verified this fact. At the wavelength of 607 nm, second GK condition is satisfied, thus backward scattering takes place with a small lobe in the forward direction. Far field scattering pattern at this wavelength is shown in Figure 5(c).

Further, electric and magnetic polarizabilities have been calculated for the transverse mode when incident electric field is along the b-axis of the nanoparticle. Here, real and imaginary parts of electric and magnetic polarizabilities are equal at 912 nm as shown in Figure 6(a). Hence, first GK condition is satisfied at this wavelength. Far-field scattering pattern at this wavelength indicates forward scattering shown in Figure 6(b). Second GK condition is satisfied at the wavelength 784 nm. So, there is backward scattering at this wavelength which is also shown by far field scattering pattern in Figure 6(c).

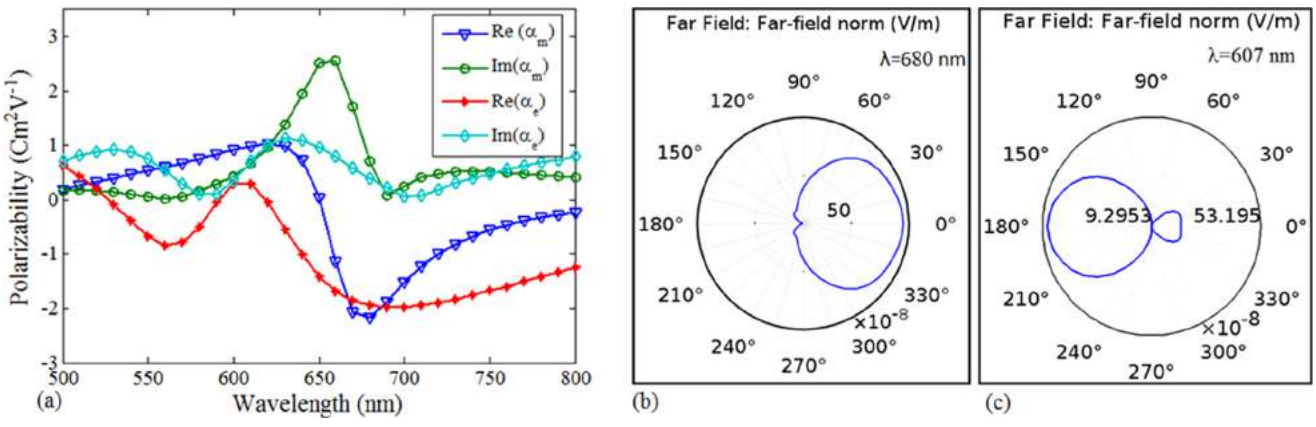


FIG. 5. (a) Plot of real and imaginary parts of electric and magnetic polarizabilities of the nanoparticle with wavelength when E || a-axis. (b)-(c) Far field scattering patterns show forward scattering at wavelength 680 nm and backward scattering at 607 nm.

Reuse of AIP Publishing content is subject to the terms at: https://publishing.aip.org/authors/rights-and-permissions. Download to IP: 14.139.251.107 On: Sun, 03 Jul 2016 10:54:01

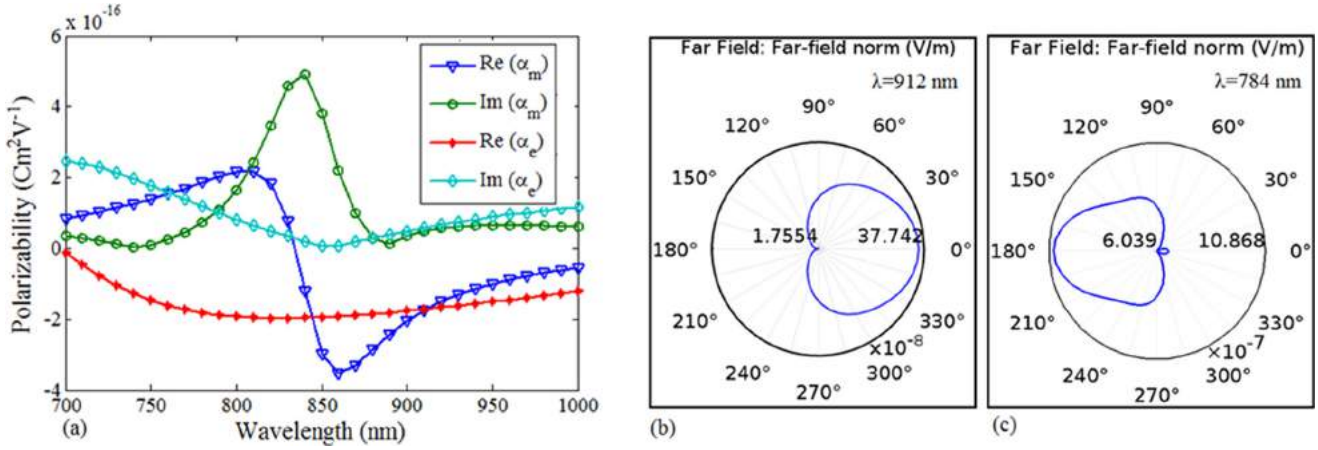


FIG. 6. (a) Variation of electric and magnetic polarizabilities of the nanoparticle with wavelength when E || *b*-axis. (b) and (c) Far field scattering patterns show forward scattering at wavelength 912 nm and backward scattering at 784 nm.

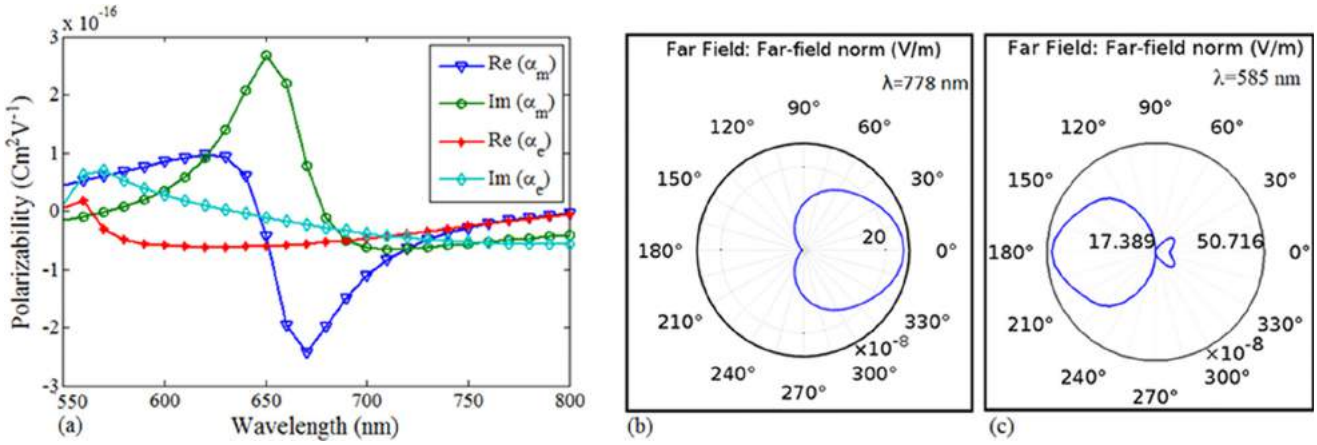


FIG. 7. (a) Wavelength dependence of real and imaginary parts of electric and magnetic polarizabilities of the nanoparticle when E || *c*-axis. (b) and (c) Far field scattering patterns show forward scattering at wavelength 778 nm and backward scattering at 585 nm.

Finally, polarizabilities have been calculated and plotted versus wavelength for the second transverse mode in which incident electric field has been taken along *c*-axis, i.e., smallest axis of the nanoparticle. In this case, first generalized condition is satisfied at the wavelength $\lambda = 778$ nm. Hence, at this wavelength scattering takes place in forward direction which is also verified by far field scattering pattern in Figure 7(b) and backward scattering takes place at the wavelength 585 nm, where far field scattering patterns have been calculated using finite element method. Thereby, ellipsoidal nanoparticles are the suitable candidates for tunable unidirectional applications.

V. CONCLUSION

In this paper, tunable and azimuthally symmetric unidirectional scattering of ellipsoidal dielectric nanoparticle has been analyzed. Electric and magnetic dipoles have been optically induced in the ellipsoidal nanoparticle at the resonance wavelengths, where peaks of the scattering spectra denote the positions of resonance. Due to three fold symmetry, ellipsoidal nanoparticle exhibits three types of resonant modes, one longitudinal mode and two transverse modes. Due to the three types of longitudinal and transverse modes, complete forward unidirectional scattering takes place in the visible and near infrared region at three wavelengths 680 nm, 912 nm, and 778 nm just by changing the direction of incident electric field, satisfying the generalized Kerker's condition. Thus, ellipsoidal nanoparticles can be used to achieve tunable unidirectional scattering. The electric and magnetic resonances have been experimentally demonstrated in the ordered array of nanodisks by Staude *et al.*[24] Tunable unidirectional properties exhibited by these nanoparticles can lead to a large number of applications for the development of low loss and ultra-compact optical nanoantennas, nanolasers, spectroscopy, high resolution near field microscopy, optical imaging and sensing.

ACKNOWLEDGMENTS

The authors gratefully (i) acknowledge the initiatives and the support from TIFAC-Center of Relevance and Excellence in Fiber Optics and Optical Communication at Delhi College of Engineering, now DTU, and Delhi under

Reuse of AIP Publishing content is subject to the terms at: https://publishing.aip.org/authors/rights-and-permissions. Download to IP: 14.139.251.107 On: Sun, 03 Jul 2016 10:54:01

Mission REACH Program of Technology vision-2020, Government of India and (ii) the support through DST-RMES (Indo-Russian) joint research project on "All Dielectric, Plasmonic and Hybrid Photonic Nanostructures."

[1]L. Novotony and B. Hecht, *Principles of Nano-Optics* (Cambridge University Press, 2012).
[2]C. M. Soukoulis and M. Wegener, "Past achievement and future challenges in the development of three-dimensional photonic metamaterials," Nat. Photonics **5**, 523–530 (2011).
[3]W. Xiong, D. Sikdar, M. Walsh, K. J. Si, Y. Tang, Y. Chen, R. Mazid, M. Weyland, I. D. Rukhlenko, J. Etheridge, M. Premaratne, X. Li, and W. Cheng, "Single-crystal caged gold nanorods with tunable broadband plasmon resonances," Chem. Commun. **49**, 9630–9632 (2013).
[4]D. Sikdar, I. D. Rukhlenko, W. Cheng, and M. Premaratne, "Optimized gold nanoshell ensembles for biomedical applications," Nanoscale Res. Lett. **8**, 142–146 (2013).
[5]L. Novotony and N. Van Hulst, "Antennas for light," Nat. Photonics **5**, 83–90 (2011).
[6]S. Lal, S. Link, and N. J. Halas, "Nano-optics from sensing to waveguiding," Nat. Photonics **1**, 641–648 (2007).
[7]M. Alsawafta, M. Wahbeh, and V.-V. Truong, "Plasmonic modes and optical properties of gold and silver ellipsoidal nanoparticles by the discrete dipole approximation," J. Nanomater. **2012**, 457968 (2012).
[8]K. Kishor, M. N. Baitha, R. K. Sinha, and B. Lahiri, "Tunable negative refractive index metamaterial from V-shaped SRR structure: Fabrication and characterization," J. Opt. Soc. Am. B **31**, 1410–1414 (2014).
[9]V. Dillu and R. K. Sinha, "Enhanced Fano resonance in silver ellipsoidal plasmonic crystal cavity," J. Appl. Phys. **114**, 234305 (2013).
[10]U. Kreibig and M. Vollmer, *Optical Properties of Metal Clusters* (Springer-Verlag, Berlin, 1995).
[11]A. E. Krasnok, A. E. Miroshnichenko, P. A. Belov, and Y. S. Kivshar, "Huygens optical elements and Yagi-Uda nanoantennas based on dielectric nanoantennas," JETP Lett. **94**, 593–598 (2011).
[12]A. E. Krasnok, I. S. Maksymov, A. I. Denisyuk, P. A. Belov, A. E. Miroshnichenko, C. R. Simovski, and Y. S. Kivshar, "Optical nanoantennas," Phy. Usp. **56**(6), 539–564 (2013).
[13]A. E. Krasnok, A. E. Miroshnichenko, P. A. Belov, and Y. S. Kivshar, "All-dielectric optical nanoantennas," Opt. Express **20**, 20599 (2012).
[14]A. I. Kuznetsov, A. E. Miroshnichenko, Y. H. Fu, J. Zhang, and B. Luk'yanchuk, "Magnetic light," Sci. Rep. **2**, 492 (2012).
[15]P. Mathew, S. H. Lim, D. Derkacs, C. McPheeters, and E. T. Yu, "Metal and dielectric nanoparticle scattering for improved optical absorption in photovoltaic devices," Appl. Phys. Lett. **93**, 113108 (2008).
[16]D. M. Schaadt, B. Feng, and E. T. Yu, "Enhanced semiconductor optical absorption via surface plasmon excitation in metal nanoparticles," Appl. Phys. Lett. **86**, 063106 (2005).
[17]C. F. Bohren and D. R. Huffman, *Absorption and Scattering of Light by Small Particles* (Wiley, New York, 1983).
[18]D. Sikdar, W. Cheng, and M. Premaratne, "Optically resonant magneto-electric cubic nanoantennas for ultra-directional light scattering," J. Appl. Phys. **117**, 083101 (2015).
[19]Y. H. Fu, A. I. Kuznetsov, A. E. Miroshnichenko, Y. F. Yu, and B. Luk'yanchuk, "Directional visible light scattering by silicon nanoparticles," Nat. Commun. **4**, 1527 (2013).
[20]T. Kalkbrenner, U. Håkanson, and V. Sandoghdar, "Tomographic plasmon spectroscopy of a single gold nanoparticle," Nano Lett. **4**(12), 2309–2314 (2004).
[21]H. H. Li, "Refractive index of silicon and germanium and its wavelength and temperature derivatives," J. Phys. Chem. Ref. Data **9**, 561 (1980).
[22]C. H. Papas, *Theory of Electromagnetic Wave Propagation* (Courier Dover Publications, 2013).
[23]R. Gomez-Medina, B. Garcia-Camara, I. Suarez-Lacalle, F. Gonzalez, F. Moreno, M. Nieto-Vesperinas, and J. J. Saenz, "Electric and magnetic dipolar response of germanium nanospheres: Interference effects, scattering anisotropy and optical forces," J. Nanophotonics **5**, 053512 (2011).
[24]I. Staude, A. E. Miroshnichenko, M. Decker, N. T. Fofang, S. Liu, E. Gonzales, J. Dominguez, T. S. Luk, D. N. Neshev, I. Brener, and Y. Kivshar, "Tailoring directional scattering through magnetic and electric resonances in subwavelength silicon nanodisks," ACS Nano **7**(9), 7824–7832 (2013).

Reuse of AIP Publishing content is subject to the terms at: https://publishing.aip.org/authors/rights-and-permissions. Download to IP: 14.139.251.107 On: Sun, 03 Jul 2016 10:54:01